Principles
of
Applied Geophysics

'This is called practice, but remember to first set forth the theory.'

Leonardo da Vinci
Codex Madrid I (1493–1497)

Principles of Applied Geophysics

D.S. PARASNIS

Professor of Applied Geophysics
University of Luleå, Luleå, Sweden
Fellow of the Royal Swedish Academy of Engineering Sciences

Fourth edition

London New York
CHAPMAN AND HALL

First published in 1962 by
Methuen & Co. Ltd
Reprinted once
Reprint 1971
published by
Chapman and Hall Ltd,
11 New Fetter Lane, London EC4P 4EE
Second edition 1972
Reprinted once
Third edition 1979
Reprinted 1982
Fourth edition 1986

Published in the USA by
Chapman and Hall,
29 West 35th Street, New York, NY 10001

British Library Cataloguing in Publication Data

Parasnis, D.S.
Principles of applied geophysics.—4th ed.
1. Prospecting—Geophysical methods
I. Title
622'.15 TN269

Library of Congress Cataloging in Publication Data

Parasnis, D.S.
Principles of applied geophysics.

Bibliography: p.
Includes index.
1. Prospecting—Geophysical methods. I. Title.
TN269.P32 1986 622'.15 85–32570
ISBN-13: 978-0-412-28330-7 e-ISBN-13: 978-94-009-4113-7
DOI: 10.1007/978-94-009-4113-7

Contents

Preface to the fourth edition

Anyone who compares the present thoroughly revised and enlarged edition of this book with the three previous ones, the first of which was published in 1962, may well ask whether the principles of applied geophysics have become more numerous during the last 25 years or so. Such is not the case and the much larger size of the present edition is due to the principles' having been explained in greater detail than heretofore. There are major and minor alterations, additions and emendations, too numerous to be listed here, throughout the book but I would like to draw attention specifically to some of them.

The chapter on seismic methods is now far more extensive than before and so are also the chapters on electric and electromagnetic methods. There is also a separate chapter on well logging in oil fields giving the essential ideas. Considering the virtual plethora of available books on seismic methods and on well logging I have not thought it necessary to extend these chapters further. This has enabled me to keep the book to a reasonable length and at the same time retain its fairly comprehensive character. Other features of the present edition are solved examples in the text and the problems at the end of all principal chapters. Answers and hints to the latter are given at the end of the book. References (denoted in the text by numbers in square brackets) have been brought up to date but most of the older ones have been purposely retained in the belief that a true understanding of a subject is aided by a glance at its history.

The emphasis is throughout on physical explanations and practical geological applications. Algebraic details have been kept to a minimum in the main text and even these may be skipped for the most part without loss of continuity by readers interested mainly in the qualitative aspects of the various methods. Those who may like to delve deeper into the underlying mathematics will naturally turn to the appendices at the end of the book. However,

whatever the level of mathematical sophistication resorted to in geophysical interpretation, the caution dealt in the preface to the first edition, that 'the success of a geophysical survey depends almost entirely upon an intelligent combination of physics and geology', applies as much today as it did 25 years ago, notwithstanding (or rather because of) the progress in automatic computer processing of geophysical data.

Like all the previous editions the present one contains many topics not to be found in current texts in English devoted to the subject as a whole. Among these may be mentioned a rigorous but simple, logical scheme (hitherto unpublished as far as I know) for the complete determination of the parameters of a thick sheet from its magnetic anomaly, rapid practical procedures for calculating VES curves, Orellana's method of estimating the longitudinal conductance of a stratified earth underlain by a *finitely* resistive substratum, Lee's method for dipping discontinuities, design principles of electromagnetic sensors, radioactive density determinations, statistical considerations in optimum line spacing and a number of others.

SI units are strictly adhered to except in nine figures reproduced from older literature and left intact.

The chapter on seismic methods owes much to the notes of lectures delivered at my department a few years ago by Dr Roy E. White of British Petroleum, London. I am most grateful to him for allowing me to make liberal use of these. Finally, my thanks are due to Irene Lundmark, Department of Applied Geophysics, University of Luleå, for her very efficient help in the intricate task of preparing the manuscript of this edition.

D.S. Parasnis
Luleå, Sweden

1

Introduction

Geophysics is the application of the principles of physics to the study of the earth. The subject includes, strictly speaking, meteorology, atmospheric electricity, or ionosphere physics, but it is in the more restricted sense, namely the physics of the body of the earth, that the word geophysics will be used in this monograph. The aim of pure geophysics is to deduce the physical properties of the earth and its internal constitution from the physical phenomena associated with it, for instance the geomagnetic field, the heat flow, the propagation of seismic waves, the force of gravity, etc. On the other hand, the object of applied geophysics with which this monograph is concerned is to investigate specific, relatively small-scale and shallow features which are presumed to exist within the earth's crust. Among such features may be mentioned synclines and anticlines, geological faults, salt domes, undulations of the crystalline bedrock under a cover of moraine, ore bodies, clay deposits and so on. It is now common knowledge that the investigation of such features very often has a bearing on practical problems of oil prospecting, the location of water-bearing strata, mineral exploration, highways construction and civil engineering. Often, the application of physics, in combination with geological information, is the only satisfactory way towards a solution of these problems.

The geophysical methods used in investigating the shallow features of the earth's crust vary in accordance with the physical properties of the rocks – the last word is used in the widest sense – of which these features are composed, but broadly speaking they fall into four classes. On the one hand are the *static methods* in which the distortions of a static physical field are detected and measured accurately in order to delineate the features producing them. The static field may be a natural field like the geomagnetic, the gravitational or the thermal gradient field, or it may be an artificially applied field like an electric potential gradient. On the other hand, we have the *dynamic methods* in which signals are sent in the ground, the returning signals are detected and their

strengths and times of arrival are measured at suitable points. In the dynamic methods the dimension of time always appears, in the appropriate field equations, directly as the time of wave arrival as in the seismic method, or indirectly as the frequency or phase difference as in the electromagnetic method. There is a further, now considerably important, class of methods which lie in between the two just mentioned. These will be called *relaxation methods*. Their feature is that the dimension of time appears in them as the time needed for a disturbed medium to return to its normal state. This class includes the overvoltage or induced polarization methods. Finally there are what we may call *integrated effect methods*, in which the detected signals are statistical averages over a given area or within a given volume. The methods using radioactivity fall in this class.

The classification of geophysical methods into ground, airborne or borehole methods refers only to the operational procedure. It has no physical significance. Many ground methods can be used in the air, under water or in boreholes as well.

The magnetic, electromagnetic and radioactive methods have been adapted to geophysical measurements from the air. Airborne work has certain advantages. First, on account of the high speed of operations an aerial survey is many times cheaper than an equivalent ground survey provided the area surveyed is sufficiently large and secondly, measurements can be made over mountains, jungles, swamps, lakes, glaciers and other terrains which may be inaccessible or difficult for ground surveying parties.

Compared with ground work, airborne measurements imply a decrease in resolution which means that adjacent geophysical indications tend to merge into one another giving the impression of only one indication. Besides, there is often considerable uncertainty about the position of airborne indications so that they must be confirmed on the ground before undertaking further work like drilling.

In a sense, applied geophysics, excepting the seismic methods, is predominantly a science suited to flat or gently undulating terrain where the overburden is relatively thin. The reason is that whenever the relief is violent, the data of geophysical methods need corrections which are frequently such as to render their interpretation uncertain. On the other hand, when the overburden is too thick the effects produced by the features concealed under it generally lie within the errors of measurement and are difficult ascertain. There is, however, no general rule as to the suitability of any terrain to geophysical methods and every case must be considered carefully on its own merits.

The various methods of applied geophysics will be dealt with in turn in the following chapters.

2

Magnetic methods

2.1 SHORT HISTORY

It was in the year 1600 when William Gilbert, Physician to Queen Elizabeth I, published his book *De Magnete* (abbreviated title), that the concept arose of a general geomagnetic field with a definite orientation at each point on the surface of the earth. In its wake, observations of the local anomalies in the orientation of the geomagnetic field were used in Sweden for iron-ore prospecting, for the first time probably as early as 1640 and regularly by the end of that century. They constitute the first systematic utilization of a physical property for locating specific, small-scale features within the earth's crust. Two centuries later, in 1870, Thalén constructed his magnetometer for comparatively rapid and accurate determinations of the horizontal force, the vertical force and the declination, by the familiar sine and tangent methods used in elementary physics courses. This and its somewhat simplified modification due to Tiberg were in widespread use, especially in Sweden, as a tool for prospecting surveys for more than the following half century.

The large-scale use of magnetic measurements for investigations of geological structures, other than those associated with magnetic ore, did not however begin seriously until 1915, when Adolf Schmidt constructed his precision vertical field balance using a magnetic needle swinging on an agate knife edge. Since then magnetic observations have been successfully employed, not only in the search for magnetite ore, but also in locating buried hills, geological faults, intrusions of igneous rocks, salt domes associated with oil fields, concealed meteorites and buried magnetic objects such as pipe-lines.

2.2 BASIC CONCEPTS AND UNITS

2.2.1 Magnetic field strength, flux density and permeability

A magnetic field strength gives rise to a magnetic flux, just as an electric field strength can give rise to an electric charge flux (current). The magnetic flux

density, that is the flux per unit area, also called magnetic induction, is denoted by B. If H is the field strength then

$$B = \mu H \tag{2.1}$$

where μ is known as the absolute permeability of the medium. In the International System of Units (SI) H is measured in ampere per metre ($A\,m^{-1}$). A convenient way to familiarize oneself with this unit is to note that one $A\,m^{-1}$ is the magnetic field strength that exists at the centre of a one-turn circular coil of diameter 1 metre, placed in air and carrying a current of 1 ampere.

The unit of magnetic flux in SI is volt-second (V s), also named weber (Wb), so that the unit of flux density B is $V\,s\,m^{-2}$ (or $Wb\,m^{-2}$) which is also called tesla (T). The magnetic fields that we measure in practice are flux densities. For most geophysical purposes the tesla is too large as a unit and flux densities are more conveniently expressed in nanotesla ($nT = 10^{-9}$ T). One nT happens to be numerically exactly equal to the older unit of B, namely gamma (γ).

The distinction between H and B should be carefully noted, particularly because B is often called magnetic field in common parlance. Associated with a B-field in a medium is its (postulated) cause, the H-field strength, equal to B/μ.

The absolute permeability μ, being equal to B/H, is easily seen to have the dimensions ohm-second per metre ($\Omega\,s\,m^{-1}$). The absolute permeability of vacuum is a very important quantity and is denoted by μ_0. Thus, a field strength H will create in vacuum a flux density $B_0 = \mu_0 H$. For most practical purposes in geophysics the absolute permeability of air, and even most rocks, may be taken to be μ_0. In the system that we shall adopt in this book, μ_0 has the value $4\pi \times 10^{-7}\,\Omega\,s\,m^{-1}$. Thus if at any point in vacuum (or for practical purposes air) we have a flux density B_0, the corresponding field strength is B_0/μ_0.

2.2.2 Relative permeability, susceptibility and magnetization

If for a medium other than vacuum we write $\mu = \mu_r \mu_0$ we get from (2.1)

$$\begin{aligned} B &= \mu H \\ &= \mu_r \mu_0 H \\ &= \mu_0 H + \mu_0(\mu_r - 1)H \\ &= \mu_0 H + \mu_0 \kappa H \end{aligned} \tag{2.2}$$

where we have put $\kappa = \mu_r - 1$, that is, $\mu_r = 1 + \kappa$. μ_r is a ratio of two permeabilities and therefore a pure number. It is called the relative permeability of the medium. Similarly κ, called the susceptibility, is a pure number. Obviously, for vacuum $\mu_r = 1$ and $\kappa = 0$.

From the last line of (2.2) we see that to obtain in vacuum a flux density equal to the density μH in the medium under consideration, we would need an

additional magnetic field strength κH. This additional field strength that may be said to be present at points of space occupied by a medium subject to a field strength H, is called the *intensity of magnetization* M induced by H. Obviously,

$$M = \kappa H \tag{2.2a}$$

Since κ is a pure number M is also measured in $\mathrm{A\,m^{-1}}$. Since B and H are vectors we write Eq. (2.2) more generally as

$$\mathbf{B} = \mu_0(\mathbf{H} + \mathbf{M}) \tag{2.3}$$

Then, for the x, y, z components of **B** in an orthogonal coordinate system, we have

$$B_x = \mu_0(H_x + M_x), \text{ etc} \tag{2.4}$$

2.2.3 Magnetic moment, magnetic dipole and remanence

If a body of volume V is uniformly magnetized with intensity **M** then $V\mathbf{M} = \mathbf{m}$ ($\mathrm{A\,m^2}$) is called its *magnetic moment*. This is also a vector. If we imagine a particle of infinitesimally small volume but with a very high intensity of magnetization, so that the product VM is nevertheless a finite quantity, we have a magnetic point dipole. The direction of the magnetic moment of a dipole is the dipole axis. The importance of the concept of a point dipole is that a body with non-uniform magnetization can be considered, for the purpose of calculating the field strength as well as the flux density due to it, to be an aggregate of an infinite number of point dipoles, each of moment proportional to the local magnetization intensity at the point in question. Since $\mathbf{M} = \kappa\mathbf{H}$ we have, for a uniformly magnetized body,

$$\mathbf{m} = V\mathbf{M} = V\kappa\mathbf{H} \tag{2.5}$$

An intensity of magnetization can exist in certain bodies (e.g. ordinary magnets) even in the absence of an external field strength. Such magnetization, called permanent or remanent magnetization or simply remanence, is sustained by an internal field strength present at each point within the body. If subjected to an external H-field the body will, in addition, acquire an induced intensity of magnetization.

2.2.4 Hysteresis

If μ in Eq. (2.1) is independent of H the medium is said to be a linear medium. The graph of B against H for such a medium is a straight line as shown in Fig. 2.1 In many substances (e.g. magnetite or pyrrhotite) this is not the case. For example, in an originally non-magnetized sample of, say magnetite, the induction (flux density) B increases with the external field strength H according to the curve (a), which is not a straight line. B does not increase indefinitely but

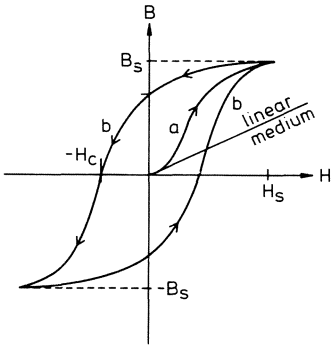

Fig. 2.1 Hysteresis loop.

reaches a saturation value B_s for a certain field strength H_s. On decreasing H from H_s, the flux density follows the left-hand curve (b) and even when $H = 0$ the sample retains a flux density and is seen to possess a remanence. It takes an external field strength H_c in the opposite direction to completely demagnetize the sample. On increasing H further in this direction the sample acquires a saturation flux density $-B_s$, and on reducing $|H|$ again, B follows the right-hand curve (b). So long as H_s is not altered the sample will then continue to follow the loop formed by the curves (b) on repeated increases or decreases of H and will never retrace the curve (a). This loop is called the hysteresis loop of the sample.

A sample that follows a non-linear B–H relation as in Fig. 2.1 cannot be assigned a unique susceptibility value. The κ values quoted for such substances are usually based on the nearly linear initial part of the curve (a), where the sample is in a virgin state and the external field strength H is weak.

2.3 MAGNETIC PROPERTIES OF ROCKS

The magnetic method of applied geophysics depends upon measuring accurately the anomalies of the local geomagnetic field produced by the variations in the intensity of magnetization in rock formations. The magnetization of rocks is partly due to induction by the magnetizing force associated with the earth's field and partly to their remanent magnetization. The induced intensity depends primarily upon the magnetic susceptibility as well as the magnetizing force, and the remanent intensity upon the geological history of the rock. Research in the remanent intensity of rocks, especially since 1950, has given rise to the subject of palaeomagnetism.

2.3.1 Induced magnetism

In accordance with the general classification used in modern physics, rocks (like all substances) fall into three categories, namely diamagnetic, paramagne-

tic and ferromagnetic. The last named category is further subdivided into the truly ferromagnetic, the antiferromagnetic and the ferrimagnetic substances. These terms are briefly explained below.

2.3.1.1 Diamagnetism

In a diamagnetic substance κ in Eq. (2.2) is negative so that the induced intensity in the substance is in a direction opposite to the magnetic field strength and the flux density in such a substance is less than would exist if the corresponding space were vacuum. The origin of diamagnetism lies in the motion of an electron round a nucleus. This motion constitutes a miniature plane current circuit and is characterized by a magnetic moment vector as well as an angular momentum vector, both perpendicular to the plane of the electron's motion. In addition, an electron has an intrinsic magnetic moment, the so-called spin magnetic moment, whose significance will appear later.

An impressed field strength will tend to turn the magnetic moment in its own direction and a mechanical torque will act on the orbital plane. The orbit reacts in a way known, sufficiently well for our purpose, from the behaviour of a top subject to a torque tending to turn its spinning axis. The result, as in the case of the top, is that the angular momentum vector and hence also the magnetic moment vector begin to precess round the magnetizing force. This is known as *Larmor precession.* The additional periodic motion of the electron due to Larmor precession is such as to produce a magnetic moment opposite in direction to the applied field.

It will be realized that there is a diamagnetic effect in all substances including the 'typical' ferromagnetics like iron, cobalt and nickel. But net diamagnetism only appears if the magnetic moments of atoms are zero in the absence of an external magnetizing force, as is the case for atoms or ions having closed electronic shells, because these contain an even number of electrons, half with the spin magnetic moment in one direction and half in the opposite direction. There are many rocks and minerals which show net diamagnetism. Chief among them are quartz, marble, graphite, rock salt, and anhydrite (gypsum).

2.3.1.2 Paramagnetism and the Curie–Weiss law

The susceptibility of paramagnetic substances is positive and decreases inversely as the absolute temperature (Curie–Weiss law). Paramagnetism makes its appearance when the atoms or molecules of a substance have a magnetic moment in the absence of a field and the magnetic interaction between the atoms is weak. Normally the moments are distributed randomly, but on the application of the field they tend to align themselves in the direction of the field, the tendency being resisted by thermal agitation. The paramagnetism of elements is mainly due to the unbalanced spin magnetic moments of the electrons in unfilled shells, like the 3d shells of the elements from Sc to Mn. Many rocks are reported to be paramagnetic, for instance gneisses,

pegmatites, dolomites, syenites, etc. However, it seems certain that their paramagnetism is not intrinsic but is a manifestation of weak ferrimagnetism due to varying amounts of magnetite or ilmenite, or an antiferromagnetism due to minerals like haematite, manganese dioxide, etc.

2.3.1.3 Ferromagnetism

In ferromagnetic materials the atoms have a magnetic moment and the interaction between neighbouring atoms is so strong that the moments of all atoms within a region, called a domain, align themselves in the same direction even in the absence of an external field. In Fe, Co and Ni this interaction takes place between the uncompensated spins in the unfilled 3d shells of the atoms. A state of spontaneous magnetization can therefore exist consisting of an orderly arrangement of the magnetic moments of all atoms. Typical of the ferromagnetics are their hysteresis loops and their large susceptibilities which depend upon the magnetizing force. Ferromagnetism disappears above a temperature known as the Curie temperature. There are no truly ferromagnetic rocks or rock materials.

2.3.1.4 Antiferromagnetism

There exist substances in which the susceptibility has an order of magnitude characteristic of a paramagnetic (10^{-5}) but is not inversely proportional to the temperature. Instead it first increases with temperature, reaches a maximum at a certain temperature, also called the Curie point or the λ point, and decreases thereafter according to the Curie–Weiss law. In these substances the low magnetic susceptibility below the λ point can be explained by assuming an *ordered* state of atoms such that the magnetic moments of neighbouring atoms are equal but directed antiparallel to each other. Thus the two ordered sub-lattices, each reminiscent of the state in a ferromagnetic, cancel each other and their net magnetic moment is zero. This state is called antiferromagnetism and can be confirmed by neutron diffraction studies. Of the rock-forming minerals, haematite (Fe_2O_3) is the most important antiferromagnetic (λ point 675° C).

2.3.1.5 Ferrimagnetism

Among the antiferromagnetic substances there is a class in which, to put it simply, two sub-lattices with metallic ions having magnetic moments are ordered antiparallel as above, but in which the moments of the lattices are unequal, giving rise to a net magnetic moment in the absence of a field. Such substances are called ferrimagnetic. Practically all the constituents giving a high magnetization to rocks are ferrimagnetic, chief among them being magnetite (Fe_3O_4), titanomagnetite ($FeO(Fe, Ti)_2O_3$) and ilmenite ($FeTiO_3$). Spontaneous magnetization and a relatively high susceptibility can also exist in an antiferromagnetic if statistically systematic defects are present, as is

believed to be the case for pyrrhotite (FeS). The temperature dependence of ferrimagnetics is complex, there being theoretically several possibilities.

2.3.2 Susceptibility of rocks

The susceptibility of rocks is almost entirely controlled by the amount of ferrimagnetic minerals in them, their grain size, mode of distribution, etc. and is extremely variable. The values listed in Table 2.1 should nevertheless serve to give a rough idea. Various attempts have been made to represent the dependence of susceptibility on the content of ferrimagnetics, but no simple universally valid relation exists. For particular groups of rocks or for particular ranges of susceptibility a statistically significant correlation can generally be found between the amount of Fe_3O_4, and the susceptibility (Fig. 2.2). However, the scatter is usually such that a prediction based on such correlations must be used with caution.

It will be seen that generally speaking only small susceptibility differences ($\Delta\kappa$) will be encountered between rock formations. The maximum $\Delta\kappa$ (when a deposit of high grade magnetite ore is present) is of the order of ten. As we shall see later, if two very extensive and thick homogeneous formations are separated along a plane vertical contact the peak-to-peak change in the vertical magnetic field in traversing the contact is given by*

$$\Delta B_z = \tfrac{1}{2}\Delta\kappa B_z \tag{2.6}$$

if B_z tesla (T) is the vertical magnetic field (flux density) of the earth. The

Table 2.1 Susceptibilities $\times 10^6$ (Rationalized SI)

Graphite	-100	Gabbro	3800–90 000
Quartz	-15.1	Dolomite	
Anhydrite	-14.1	(impure)	20 000
Rock salt	-10.3	Pyrite	
Marble	-9.4	(pure)	35–60
Dolomite		Pyrite	
(pure)	$-12.5 - +44$	(ore)	100–5000
Granite		Pyrrhotite	10^3–10^5
(without magnetite)	$10 - 65$	Haematite (ore)	420–10 000
Granite		Ilmenite (ore)	$3 \times 10^5 - 4 \times 10^6$
(with magnetite)	25–50 000	Magnetite (ore)	$7 \times 10^4 - 14 \times 10^6$
Basalt	1500–25 000	Magnetite (pure)	1.5×10^7
Pegmatite	3000–75 000		

To convert the above values to the unrationalized system divide by 4π

*This situation is exceptional. In general ΔB depends on $\Delta\kappa$ as well as the individual κ values of the media concerned.

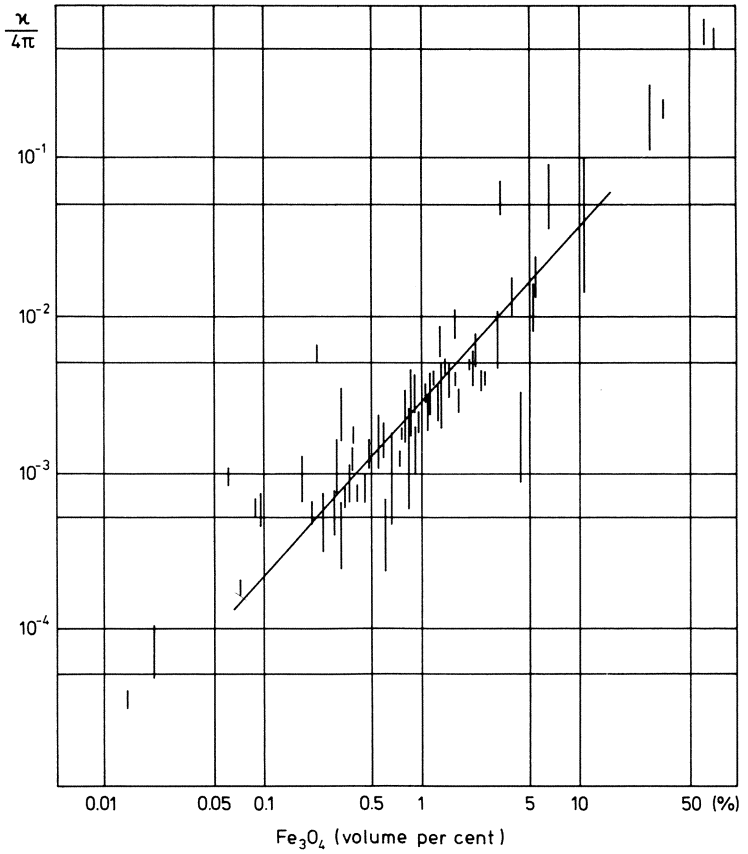

Fig. 2.2 Variation of susceptibility κ (rationalized SI) with magnetite content. After Balsley and Buddington (*Economic Geology*, 1958).

practical limit of determining ΔB_z in most field surveys is about 1 nanotesla (nT) and if $B_z = 50\,000$ nT, substitution in the above equation shows that the practical limit of detecting a susceptibility difference between rock formations will be $\Delta\kappa \approx 4 \times 10^{-5}$. However, the lack of homogeneity in rocks and their impregnation by ferrimagnetic minerals produce random magnetic anomalies, the 'geologic noise' owing to which the limit in reality is some 10–100 times larger.

2.3.3 Remanent magnetism

2.3.3.1 Types of remanence

Researches all over the world have confirmed that both igneous and sedimentary rocks possess remanent magnetization in varying degrees and the

phenomenon is a widespread one. Well-documented examples of rocks, igneous as well as sedimentary, occur in all parts of the world and of all geological ages, in which the remanent intensity is not only strong but has a direction completely different from, at times opposite to, the present direction of the geomagnetic field. Various types of permanent magnetization of rocks are now recognized. One principal type, especially for igneous rocks, is thermoremanent magnetization (TRM) acquired in cooling from high temperatures. Its orientation reflects the orientation of the geomagnetic field prevalent at the time and place of formation. The predominant mechanism in the acquisition of TRM is the alignment of the domains in the ferrimagnetic constituents of the rocks. It is in this respect significant that the TRM of rocks disappears when they are heated above 600° C, which is approximately the Curie point of magnetite [1]. Other principal types of natural remanent magnetization (NRM) of rocks are: isothermal remanent magnetization (IRM) acquired at constant temperature on exposure to a magnetizing force for a short time; viscous (VRM) acquired as a cumulative effect after a long exposure in an ambient field, not necessarily at one and the same temperature; depositional or detrital (DRM) acquired by sediments as the constituent magnetic grains settle in water under the influence of the earth's field; chemical (CRM) acquired during growth or recrystallization of magnetite grains at temperatures far below Curie temperatures.

2.3.3.2 Importance in interpretation

If T is the field strength associated with the earth's flux density the induced magnetization in a rock will be κT. In Table 2.2 are given the values of the Koenigsberger ratio $Q_n = M_n/\kappa T$ where M_n is the natural remanent intensity

Table 2.2 Q_n for some rock specimens

Specimen	Locality	Q_n
Basalt	Mihare volcano, Japan	99–118
Gabbro	Cuillin Hills, Scotland	29
Gabbro	Småland, Sweden	9.5
Andesite	Taga, Japan	4.9
Granite	Madagascar	0.3–10
Quartz dolerite	Whin sill, England	2–2.9
Diabase	Astano Ticino, Switzerland	1.5
Tholeiite dikes	England	0.6–1.6
Dolerite	Sutherland, Scotland	0.48–0.51
Magnetite ore	Sweden	1–10
Manganese ore	India	1–5

Sediments generally low.

for some rock specimens. From this we see that in most igneous rocks like gabbro and basalts, M_n completely dominates the intensity induced by the earth's field strength.

From a study of the magnetic anomalies it is possible to obtain an estimate of the effective magnetic moment **m** of a rock mass of postulated geometry. This is the vector sum of the moments due to induced and remanent magnetism. Thus, if V is the volume of the mass

$$\mathbf{m} = V\kappa\mathbf{T} + V\mathbf{M}_n \tag{2.7}$$

which is a more general form of Eq. (2.5). In the simplest case when T and M_n are parallel we can put

$$m = V\kappa T + VQ\kappa T \tag{2.8}$$

from which we obtain

$$V = \frac{m}{\kappa(1+Q)T} \tag{2.9}$$

If remanence is neglected ($Q = 0$) we shall get the volume estimate $m/\kappa T$ which is larger than the true volume given by (2.9). Similarly, if T and M_n are antiparallel the volume estimate obtained by neglecting remanence will be smaller than the true volume $m/\kappa(1-Q)T$. In the general case, also, the dips of formations may be incorrectly estimated if the vector $\mathbf{M}_n$ in (2.7) is disregarded. A discrepancy between observed dips and those obtained by magnetic interpretation, especially in areas where igneous rocks occur, can be very frequently traced to the existence of a remanent intensity [2].

Methods for determining susceptibility and remanence of rocks are discussed briefly in Appendix 4.

2.4 THE GEOMAGNETIC FIELD

2.4.1 Main or regular field

In order to identify the anomalies in the earth's field it is clearly essential to know its undisturbed character. To a very close approximation the regular geomagnetic field can be represented formally as the field of a point dipole situated almost at the centre of the earth with its magnetic moment pointing towards the earth's geographical south. Physically, the origin of the field seems to be a system of electric currents within the earth. The total geomagnetic flux density B_t at points on the surface varies between about 0.2×10^{-4} T and about 0.6×10^{-4} T. A flux density of, say, 0.6×10^{-4} T is the result of a magnetic field strength of magnitude $0.6 \times 10^{-4}/(4\pi \times 10^{-7}) = 47.8$ A m^{-1} (cf. Section 2.2.1).

At any point on the earth's surface the magnetic flux density vector (or the

Table 2.3 Values of B_h, B_z, D (1975)

Place	Lat.	Long. East	B_h nT	B_z nT	D East
Chelyskin	+77.7°	104.3°	3510	59130	16.9°
Sodankylä	+67.4	26.6	11950	50530	6.2
Hartland	+51.0	355.5	19210	43730	−8.5
San Miguel	+37.8	334.4	25540	38030	−13.3
Hyderabad	+17.4	78.6	39870	14920	−1.6
Tangerang	−6.2	106.6	37190	−23810	0.8
Apia	−13.8	188.2	34450	−20120	12.3
Mauritius (*)	−20.4	57.7	21720	−29030	−16.9
Gnangara	−31.8	116.0	23610	−53500	−3.2
Macquarie Is.	−54.5	159.0	12850	−63930	27.7
Scott Base	−77.8	166.8	10510	−67840	156.4

*Values of B_h, B_z, D for 1976.

magnetic field, as we shall often call the flux density) is completely specified by its horizontal (B_h) and vertical (B_z) components and the declination D, west or east of true north, of B_h. The direction of B_h is the local magnetic meridian. B_z is reckoned positive if it points downwards as in the northern hemisphere generally, and negative if it points upwards as in the southern hemisphere.

The earth's field is not constant at any point on its surface but undergoes variations of different periods. From the standpoint of applied geophysics the most important are the diurnal variations and magnetic storms. Their disturbing effect must be suitably eliminated from magnetic survey observations. Values of B_h, B_z and D for the epoch 1975 at some selected places are given in Table 2.3. The total flux density is given by $B_t = (B_z^2 + B_h^2)^{1/2}$.

2.4.2 Poles and equators

The inclination (I) of B_z from the horizontal, which is of importance in the interpretation of magnetic anomalies, can be found from the equation (cf. Fig. 2.4)

$$\tan I = B_z/B_h \tag{2.10}$$

The points on the earth at which B_h vanishes and hence $I = \pm 90°$ are called the magnetic north and south *dip poles* respectively. There may be any number of such points due to local disturbances, but apart from them there are two main north and south dip poles situated approximately at 72° N, 102° W and 68° S, 146° E. On account of the irregular part of the earth's field they do not

correspond to the intersections of the axis of the imaginary dipole at the earth's centre with the surface which are at 79° N, 70° W and 79° S, 110° E. The latter are called the geomagnetic poles or *axis poles.* The imaginary line on the earth's surface passing through the point $I = 0$ is called the *magnetic equator.* North of it B_z is positive; south of it B_z is negative. The great circle on the earth's surface passing through the imaginary dipole and at right angles to the dipole axis is the *geomagnetic equator.*

2.5 INSTRUMENTS OF MAGNETIC SURVEYING

A variety of instruments suitable for magnetic surveying have been constructed and used in the past. The principal types are described below. It should be noted, however, that two of these, the fluxgate and the proton free-precession magnetometer, have more or less completely replaced the other types in modern work.

2.5.1 Older instruments

2.5.1.1 Pivoted needle instruments

The sensitive element in these is a magnetic needle arranged to swing on pivots. Probably the oldest known instrument of this type is the *Swedish mine compass* in which a compass needle can rotate in the horizontal as well as the vertical plane and take a position along the total intensity vector. In the *Hotchkiss superdip* the total intensity is determined from the deflection of a system consisting of a magnetic needle to which is fastened a counterarm carrying a small weight and making an adjustable angle with the needle. The system is suspended on a horizontal axle in the magnetic meridian. In the *Thalén–Tiberg magnetometer*, a magnetic needle with an adjustable counterweight is suspended on hardened steel bearings in a small glass-covered case which can be swung on a horizontal axle and held in the vertical or the horizontal plane. The case is first clamped in the horizontal position so that the needle swings on a vertical axis. The direction of the local B_h having been noted from the equilibrium position of the free needle, its magnitude is determined by means of an auxiliary magnet of known moment with the Lamont sine method. The procedure in this method consists essentially in swinging the arm on which the magnet is placed (in a horizontal plane) until the needle and the magnet are at right angles to each other. If the needle has then deflected through an angle θ from its free position, $B_h = B_m/\sin\theta$ where B_m is the known field of the magnet at the centre of the needle. The glass case is then held in a plane perpendicular to the magnetic meridian and the inclination of the needle, which is not vertical owing to the counterweight, is used in combination with the calibration constant to calculate B_z.

2.5.1.2 Variometers

These generally measure variations in B_z. In the *Schmidt variometer* a magnetic system is free to swing on an agate knife edge in a vertical plane like the beam of a weighing machine. Its equilibrium position at the reference station is adjusted (by altering the centre of gravity) to be horizontal and the deflections from this position at other stations are read by means of an auto-collimating telescope. The instrument can be calibrated by placing it in the field of a pair of Helmholtz coils. In order to eliminate the effect of B_h, the magnetic system is always oriented at right angles to the magnetic meridian when taking observations.

2.5.1.3 Compensation variometers

These instruments are similar to the Schmidt variometers, but instead of measuring the tilt of the magnetic system from the horizontal they measure the force needed to restore it to that position. The magnetic needle generally hangs on thin wires instead of being balanced on knife edges, and the restoring force is obtained by turning or moving compensating magnets or by means of varying the torsion in the suspension wire. Since the deflection moment due to B_h is zero when the needle is horizontal, the azimuthal orientation of compensation-type variometers is not critical. In variometers designed to measure B_h the magnetic system is initially vertical and restored to this position. The plane of rotation in this case is in the magnetic meridian.

2.5.2 Modern magnetometers

2.5.2.1 Fluxgate instruments

In these instruments use is made of the fact that the magnetic flux density B induced in certain materials depends non-linearly on the magnetizing force H as shown by the curve (a) in Fig. 2.1. Strictly speaking the B–H relation is represented by the hysteresis curve (b) in Fig. 2.1 but it will be sufficient for us to consider the curve (a) in Fig. 2.1. Within the range $|H| \leqslant H_s$ the B–H curve can be quite accurately described by an equation of the type

$$B = \mu_0 H(a - bH^2) \tag{2.11}$$

where a and b are constants which depend on how quickly the material is magnetically saturated. Now, consider a pick-up coil of effective area A wound tightly around, say, a long thin rod of the material. If the magnetic flux in the rod varies as a result of variations in H, the magnitude of the voltage induced in the coil will be given by the law of electromagnetic induction as

$$V = A\frac{dB}{dt} \tag{2.12}$$

If $H = H_0 + p \sin \omega t$ where H_0 is a steady ambient magnetic field and $p \sin \omega t$ is an alternating field produced by an alternating current flowing through an exciting coil wound round the rod, we have from (2.13) and (2.14)

$$V = \mu_0 A[(a - 3bH_0^2 - \tfrac{3}{4}bp^2)p\omega \cos \omega t - 3bH_0 p^2 \omega \sin 2\omega t + \tfrac{3}{4}bp^3 \omega \cos 3\omega t] \tag{2.13}$$

It will be seen that the output voltage contains the second and third harmonics in addition to the first but that while the first and third harmonics are always present, the second harmonic appears only if $H_0 \neq 0$. Moreover the amplitude of the second harmonic is directly proportional to H_0. By filtering out the second harmonic in the output voltage and measuring its amplitude, the ambient steady flux density $B_0 = \mu_0 H_0$ in the direction of the rod ('the fluxgate element') can be determined. In contrast to most of the instruments in the previous sections, fluxgate instruments can be made to read absolute flux densities in the element and not just relative ones.

The fluxgate instruments used in practice differ considerably from each other in construction details but the principle of a very common construction is as follows. The element consists of two juxtaposed, identical cores of a highly permeable magnetic material like mumetal or permalloy, with the windings of the exciting coil in opposite senses around the two cores. A pick-up coil is wound round the entire assembly. Since the signs of the amplitudes p of the two exciting fields are then opposite to each other, the first and third harmonics will be absent in the output voltage from the pick-up coil, as can be seen from Eq. (2.13), and a pre-filtered signal is thus obtained. The amplitude of the exciting field is greater than H_s and the frequency is normally a few kHz. Much higher frequencies have, however, been used in some fluxgate instruments. Construction details of some types of fluxgate instruments are available in several papers [3–6].

2.5.2.2 Proton free-precession magnetometer

Often called 'proton magnetometer' for short, the correct name of this type of instrument is as above and the principle on which it works is as follows. A proton has a magnetic moment **m** as well as an angular momentum **J** (joule second), the relation between the two vectors being

$$\mathbf{m} = \gamma \mathbf{J} \tag{2.14}$$

where $\gamma = 2.67520 \times 10^8 \, \mathrm{T^{-1} \, s^{-1}}$ is an accurately known constant of atomic physics called the gyromagnetic ratio of a proton. The magnetic moment vectors of the protons in, say, a bottle of water in the earth's magnetic field (B) align themselves parallel and antiparallel to the field. An excess number, in the proportion $\exp(2mB/kT)$ where k is Boltzmann's constant and T is the absolute temperature, will point parallel to the field (the state of lower energy). If a strong magnetic field differing in direction from the earth's field is applied

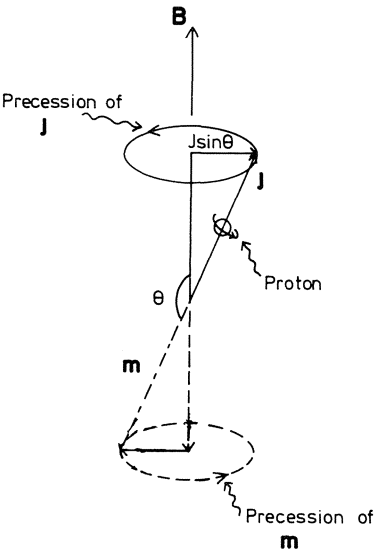

Fig. 2.3 Precession of protons.

to the water bottle the magnetic vectors gradually align in the direction of the resultant of the two fields. In water it takes approximately five seconds for all the moments to align themselves.

If the additional field is removed rapidly (within about 30 μs), the magnetic moments cannot follow the instantaneous resultant during the removal, and are left in the direction of the original resultant. They are now under the influence of the prevalent earth's field which exerts a torque $mB \sin \theta$ on each proton where θ is the angle between **m** and **B** (Fig. 2.3). On account of its angular momentum the proton, however, reacts to this torque as would a spinning top, that is, by precessing round the vector **B**. The component of **J** perpendicular to **B** is $J \sin \theta$ and the angular velocity of precession is obtained from the theory of gyroscopes as

$$\omega = \frac{mB \sin \theta}{J \sin \theta} = \gamma B \tag{2.15}$$

An alternating voltage will be induced in a coil wound round the water bottle, the frequency ν of which can be measured, and it follows from (2.15) that

$$B = \frac{\nu}{(\gamma/2\pi)} = 23.4868\nu \text{ nT} \tag{2.16}$$

The signal voltage decays exponentially as the precession is damped out and the protons spiral back to their original distribution.

It should be observed that the precession frequency does not depend on the angle between **m** and **B** and hence the direction of the exciting field is immaterial except that it must not coincide with the direction of **B**. If it does no precession will take place and the signal voltage will be zero, but this unlikely situation is easily remedied in practice by simply holding the water bottle in another orientation and taking a new reading. It should also be noted that the quantity measured is *essentially* the frequency of the signal voltage and not its amplitude, so that the orientation of the pick-up coil is also immaterial.

One great advantage of the proton magnetometer is that it requires no levelling. Consequently it is admirably suited to airborne and shipborne measurements. Its disadvantage is that it measures the magnitude of the total ambient field and not its direction. We shall see later that the interpretation of such measurements is inherently more approximate than that of, say, vertical field measurements. For the details of the construction of a proton free-precession magnetometer reference may be made to papers by Waters and Philips [7] and Gupta Sarma and Biswas [8].

2.5.2.3 High-sensitively alkali vapour magnetometers

Like the proton magnetometer these instruments, which are also known as optical-pump or absorption-cell magnetometers, exploit the phenomenon of magnetic resonance. Although, for example, helium gas has also been employed in such magnetometers, it is the alkali metal vapours that yield the highest sensitivities and among these rubidium and caesium are the most widely used elements. The atoms of alkali metals possess a magnetic moment mainly due to the spin of the single peripheral electron but also due to the spin of the nucleus. Each atom is normally in a ground state of energy and there are also (discrete) energy states to which the atom may be excited. When the atom is placed in a magnetic field each energy state is split into several discrete sub-levels (the so-called Zeeman effect) corresponding to the possible discrete orientations that the magnetic moment may take with respect to the magnetic field. The projections of some of the magnetic moments on the magnetic field are parallel to the field while others are antiparallel.

If a cell with alkali atoms in a magnetic field is illuminated appropriately with circularly polarized light it is possible to 'pump' all the ground state atoms with parallel moment-projections into energy states where the projections are antiparallel to the field. As long as this 'optical pumping' is going on the intensity of the light transmitted through the cell is low but once the ground states are empty there is no further absorption of energy and the intensity is maximum.

Suppose now that an electromagnetic field of adjustable frequency is applied to the cell in a direction different from that of the static field **B**. If the frequency is such that $h\nu = \Delta E$ where h is Planck's constant and ΔE is the energy difference between the ground state levels with parallel and antiparallel

moment-projections, some atoms absorb energy from the field and go back to ground states with parallel moment-projections, the 'pump' restarts and the intensity of the light transmitted through the cell drops sharply. It can be shown that

$$2\pi\nu = \frac{m_a B}{J_a}$$

or

$$B = \frac{\nu}{2\pi(m_a/J_a)} \tag{2.17}$$

where m_a is the atomic moment and J_a the atomic spin (angular momentum).

The factor $2\pi(m_a/J_a)$ is known accurately for many atoms. For the naturally occurring isotopes ${}^{87}_{85}\mathrm{Rb}$ and ${}^{133}_{55}\mathrm{Cs}$ the values are 4.67 and 3.498 Hz nT^{-1}. Like proton magnetometers the vapour magnetometers measure only the magnitude of the ambient field. Also they do not need any levelling. Since ν can be determined very accurately on account of the sharpness of the resonance, sensitivities of the order of 0.01 nT can be obtained with alkali vapour magnetometers. The construction of a caesium magnetometer has been described in some detail by Giret and Malnar [9]. They used an absorption cell of 100 ml volume containing free atoms of Cs in equilibrium with the metal, at a presssure of about 267 μPa (2 nmHg).

2.5.3 Comparison of magnetometer features

The accuracy of pivoted needle instruments is scarcely better than $\pm$ 100 nT and they are now seldom used. The Schmidt- and compensation-type variometers are precision instruments having accuracies better than $\pm$ 5 nT, although the accuracy of some instruments of this type, intended for rough reconnaissance surveys, is not better than $\pm$ 20–50 nT. These instruments have also largely fallen out of use now but it is worth noting that in some situations, e.g. areas with high power-line or other electric noise, the fluxgate or proton instruments may fail to operate and recourse must be had to mechanical magnetometers.

The fluxgate, proton free-precession and alkali vapour magnetometers have the advantage that their sensitive elements and the measuring or the recording system can be widely separated by cables. They can, therefore, be conveniently used under certain circumstances (e.g. in boreholes, under water, in airborne work, etc.) where the design of older instruments would be highly complicated. Their other characteristic is the speed of measurement, some 10 s, in contrast to the older instruments which may need a minute or so for one measurement.

The accuracy of fluxgate and proton magnetometers is of the order of 1 nT although the requirement of levelling for fluxgate instruments leads in practice to accuracies more like $\pm$ 5–10 nT and much less in borehole and airborne

work. Proton magnetometers of special construction give accuracies of the order of 0.1 nT, while alkali vapour instruments are superior in accuracy by a factor of ten as has already been seen. Fluxgate instruments have the advantage over both these that they can measure *components* of the flux density. It is also worth noting that if the external magnetic field is strongly inhomogeneous the decay of proton precession is so fast that no signal is obtained. The limit of admissible gradient in the best designs appears to be about 500 nT m^{-1}. The high sensitivity of alkali vapour magnetometers can be useful for surveys in areas (e.g. sedimentary basins) where magnetic field variations are small from point to point, provided uncertainties in measurements due to other causes can be avoided.

2.6 SURVEY LAYOUT AND FIELD PROCEDURE

2.6.1 Absolute and relative measurements

Magnetic measurements in applied geophysics have often been carried out as relative determinations in which the values of one or more elements of the magnetic field at any point are measured as differences from the values at a suitably chosen base point. As seen above, however, many modern instruments read directly the values of, for example, the total field or the vertical field. When such absolute measurements are made, which is practically always the case nowadays, the normal field value in the area is usually subtracted from the observations and only the resulting anomalies are used for interpretation. If the area of investigation is relatively small, say a few square kilometres, the normal geomagnetic field may be considered to be substantially constant within it and its value determined by an inspection of the observations. In very large areas, say more than a hundred square kilometres, the variation of the normal field may be significant and should be allowed for. This may be advisable in a large-scale aerial survey or in connecting surveys in several small areas.

2.6.2 Ground surveys

2.6.2.1 Area staking and precautions

When the area for magnetic investigations has been selected a base line is staked parallel to the geological strike (the trace of the rock strata on the plane represented by the surface of the earth) and measurements are made at regular intervals (say 20 m or 40 m) along lines perpendicular to the base. In detailed surveys the station separation may even be as close as 1–2 m. If no geological strike is discernible the base line may be initially laid in some convenient direction. In reconnaissance surveys measurements are often made along lines not belonging to any grid system but detailed and systematic surveys need a

well-staked grid of measurement stations. If relative measurements are resorted to, a reference point far from artificial disturbances such as those due to power lines, railways etc. is chosen and the magnetic field values at all other points are measured as positive or negative differences from the field at this point.

Certain precautions must be taken in magnetic measurements. Magnetic materials in the wearing apparel of the observer, like keys, penknives, wrist watches (also, or rather especially, 'non-magnetic' ones!) etc. can totally vitiate the observations and ought to be entirely removed, although this may not be so critical in measurements with the proton magnetometer if the measuring element is relatively far from the observer.

2.6.2.2 Corrections to observations

The principal correction that must be applied to a set of magnetometer observations is for the diurnal variation of the earth's field. An auxiliary instrument may be kept at some convenient station within the area and read at intervals or the readings may be continuously recorded. The algebraic difference between the readings of this instrument at any time, t, and the reference time, $t = 0$ (corrected, if necessary for the temperature coefficient) is subtracted from the reading at the field station, which was also measured at time t. If great accuracy is not desired, it is sufficient to repeat at 1–2 hours' interval the reading at a previously occupied station and distribute the difference over the stations measured during this interval. The correction thus obtained includes both the diurnal variation and the drift of the instrument.

Modern instruments are either temperature compensated or are inherently indifferent to temperature variations (e.g. proton magnetometer) so that temperature corrections are not usually needed in modern work.

The influence of topographic relief on magnetic observations is usually negligible, but if the terrain is rough and appreciable height differences are present it may be necessary to allow for the variation of the earth's normal field with height (cf. Table 2.4) to reduce the observations to some standard level.

An interesting approach to reducing the measured magnetic anomalies to a single horizontal plane, above or through the highest point of the topography, to overcome topographic effects has been indicated by Roy [10]. But it

Table 2.4 Variation of B_h, B_z, B_t at geomagnetic latitude of 50°

	B_h	B_z	B_t
With height	− 0.96 nT/100 m	− 2.27 nT/100 m	− 2.47 nT/100 m
With latitude towards N	− 3.79 nT/km	6.35 nT/km	4.40 nT/km

requires a Fourier transformation of the field and is probably not practical to use for routine processing.

2.6.3 Airborne surveys

Modern aeromagnetic surveys are nearly always measurements of the total-intensity amplitude by means of proton magnetometers. The data are very often digitally recorded for automatic production of contoured maps. The principles of interpretation are exactly the same as those described later for ground surveys. One point worth noting in this connection is that aeromagnetic profiles often tend to give an impression of a single anomaly where actually there are more than one anomalies. This lack of resolution increases with increasing altitude at which the survey is carried out. Most aeromagnetic surveys are flown at a height between about 70 m and 200 m but much lower altitudes (30–35 m) are standard in Finland and Sweden. The anomaly resolution in the latter is vastly superior to that of higher–altitude surveys.

A consequence of the decreased resolution in high-altitude aeromagnetic surveys is that if the causative feature is actually composed of several geologic bodies at shallow depth, the interpretation gives consistently too large depths to the bodies. The difference can be quite considerable and this danger should be constantly borne in mind in interpreting high-altitude aeromagnetic data.

2.7 RELATIVE MERITS OF HORIZONTAL, VERTICAL AND TOTAL-FIELD MEASUREMENTS

Among the magnetic elements the direction of the field is the element least sensitive to changes in the dimensions and magnetic properties of a sub-surface body. It is therefore never used by itself in accurate work. Of the remaining, namely B_h, B_z and B_t, any one or more can be chosen for measuring the respective anomalies ΔB_h, ΔB_z and ΔB_t. Since ΔB_h and ΔB_t are associated with a change in direction as well, the interpretation of these anomalies becomes somewhat complicated. The anomalous vector in the total field is $\Delta \mathbf{B}_t = \mathbf{B}_t - \mathbf{B}_{0t}$ where $\mathbf{B}_{0t}$ is the normal flux density in the area and the magnitude of this vector is

$$\Delta B_t' = |\mathbf{B}_t - \mathbf{B}_{0t}| = (\Delta B_z^2 + \Delta B_h^2)^{1/2} \tag{2.18}$$

However, since proton or alkali vapour magnetometers measure only the magnitudes B_t and B_{0t}, the anomaly magnitude obtained from measurements with them is not (2.18) but

$$\Delta B_t = |\mathbf{B}_t| - |\mathbf{B}_{0t}| = B_t - B_{0t} = (B_z^2 + B_h^2)^{1/2} - (B_{0z}^2 + B_{0h}^2)^{1/2} \tag{2.19}$$

The distinction between the two magnitudes $\Delta B_t'$ and ΔB_t will be evident from Fig. 2.4(a).

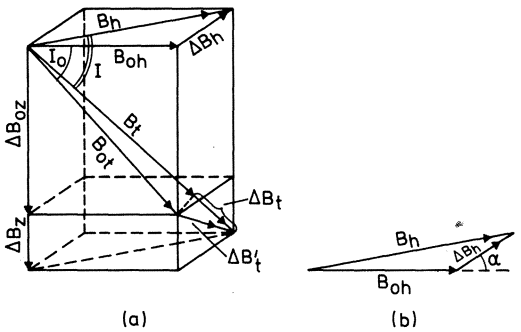

Fig. 2.4(a) Anomalous vectors of the geomagnetic field. (b) Azimuth of ΔB_h.

If α is the angle that ΔB_h makes with B_{0h} (Fig. 2.4(b)) the cosine theorem of elementary geometry gives

$$B_h^2 = B_{0h}^2 + 2B_{0h}\Delta B_h \cos\alpha + \Delta B_h^2$$

Also,

$$B_z^2 = (B_{0z} + \Delta B_z)^2 = B_{0z}^2 + 2B_{0z}\Delta B_z + \Delta B_z^2$$

Hence, from (2.19)

$$\Delta B_t = (B_{0t}^2 + 2B_{0h}\Delta B_h \cos\alpha + 2B_{0z}\Delta B_z + \Delta B_z^2 + \Delta B_h^2)^{1/2} - B_{0t} \quad (2.20)$$

Provided $\Delta B_z \ll B_{0t}$ and $\Delta B_h \ll B_{0t}$ this can be simplified to

$$\Delta B_t = \frac{B_{0h}}{B_{0t}}\Delta B_h \cos\alpha + \frac{B_{0z}}{B_{0t}}\Delta B_z$$

$$= \Delta B_h \cos\alpha \cos I + \Delta B_z \sin I \quad (2.21)$$

where I is the normal geomagnetic inclination in the area.

From the theoretical standpoint measurements of ΔB_z are to be preferred to those of ΔB_h or ΔB_t since the sub-surface picture can be visualized much more readily from ΔB_z but the present practice in geophysical surveys, even on ground, is strongly towards using proton magnetometers for determining ΔB_t, owing no doubt to the great convenience that levelling or orientation is not necessary and the speed of surveys is higher than for ΔB_z measurements of comparable accuracy. Sometimes both ΔB_z and ΔB_h are measured (for example, by suitable fluxgate instruments). In a survey over an area which may be considered to be virtually an infinite plane, such a procedure offers no additional information if observations of only ΔB_z are made sufficiently densely, and is therefore superfluous because both ΔB_h and ΔB_t can then be calculated. This rather surprising result, the converse of which is not true (except for the case when $\Delta \mathbf{B}_h$ is determined), follows from Green's theorem in potential theory and will be proved in the chapter on gravitational methods.

However, in certain special cases (e.g. in underground work) where the measurements cannot be carried out over a plane (or a closed surface) or where a sufficiently dense network of points is not available, the knowledge of both $\Delta\mathbf{B}_h$ and $\Delta\mathbf{B}_z$ can be of some additional help.

Another surprising result of practical importance is that the total change in ΔB_z across geological features such as thin dikes or spherically shaped masses is always (that is, even in low magnetic latitudes) greater than or equal to that in ΔB_h (cf. Figs 2.6 and 2.15). Thus, from this point of view too, measurements of ΔB_z are to be preferred to those of ΔB_h *all over the world.*

2.8 QUALITATIVE INTERPRETATION OF MAGNETIC ANOMALIES

2.8.1 Initial preparation

A first step towards interpretation is the preparation of a 'magnetic map' on which the intensity values at different stations are plotted and on which the contours of equal $\Delta B_h, \Delta B_z$ or ΔB_t (isoanomalies) are drawn at suitable intervals. The interpolation necessary in contour drawing is particularly easy if the observation points form a square network. In such cases, the most accurate contours are obtained if the interpolation is carried out mainly along the approximate direction of the isoanomalies, since this is the direction in which the gradients are low. A trial isoanomalous line is first sketched to obtain the trend and is subsequently corrected by more exact interpolation. Contouring of geophysical maps, especially of large-scale surveys like airborne surveys, is nowadays often done on automatic plotters using computer programs for interpolation.

Most geophysical anomaly maps are coloured using suitable colour schemes and colour gradations for the areas enclosed between successive contours. Colouring is a very valuable aid in the qualitative interpretation of a geophysical map in general and should not be underestimated. Many a feature of geological interest is first discernible when a map is suitably coloured.

An important point in considering the anomalies in an area is the zero level, that is the readings of the instrument at points where the field is the normal undisturbed geomagnetic field. If the readings remain constant, or vary randomly so as to suggest a geologic noise only, over a sufficient length of a measuring profile, say 100–500 m, the reading at any point on this stretch may be taken to be the zero reading and the anomalies at all other points in the area referred to it. If distinct magnetically anomalous masses are evident in the area, the zero level can be determined from the flanks of an anomaly curve, since they approach it asymptotically at great distances from the mass. Regional anomaly gradients, terrain characteristics, or contacts between rock formations of differing magnetizations sometimes make it impossible to use the same zero level throughout the area.

2.8.2 Some basic magnetic anomaly patterns

Certain qualitative conclusions are readily drawn from a magnetic map. Anomalous conditions in the sub-surface are indicated, for instance, by successive closed contours with the anomaly values increasing or decreasing towards a 'centre', while the direction of elongation of the closed curves may be identified with the strike of the anomalous body. Another indication is given by high horizontal anomaly gradients. They are often associated with contacts between rocks of different susceptibilities or unequal total intensities of magnetization, the contact lying shallower the steeper the gradient.

A considerable amount of qualitative interpretation of magnetic maps consists in recognizing and delineating anomaly patterns. These can be classified, especially on the so-called regional maps covering comparatively large areas, into some basic shapes and their modifications. The following list is not exhaustive but will be found to be adequate in the first analysis of most regional magnetic maps.

(1) Circular features or features of roughly the same extent in all horizontal directions.
(2) Long, narrow anomaly features.
(3) Dislocations when one part of an anomaly pattern is displaced with respect to the other part.
(4) Extensive high-intensity areas ('sheets') with no regular pattern of contours but considerable relief in the field values.
(5) 'Quiet' areas with little relief in the field values showing no distinctive pattern of contours.

Naturally, the various patterns do not necessarily occur isolated from each other but may be found superimposed. Experience shows that each pattern has its distinctive geological counterpart although the exact nature of this may differ from area to area. For instance, circular patterns are often associated with granitic as well as basic intrusions or with ore bodies, while long, narrow patterns are very frequently due to dikes, tectonic shear zones, isoclinally folded strata with magnetic impregnation or long ore bodies. Dislocations are indicative of geological faults while basaltic flows, large gabbro intrusives, greenstone belts etc. will typically given rise to 'sheets' of anomalies. In many instances quartzitic rock formations, monzonite, limestones etc. can be delineated by typical 'quiet' areas with low field values but this is not invariably the case since, for example, many limestones with skarn minerals or quartzites with magnetite impregations as well as monozonites can be associated with fairly high magnetic anomalies. The interpretation of the various anomaly patterns on a magnetic map in terms of rocks must be made in conjunction with available field geological observations. Conversely, the availability of a magnetic map is of the greatest use in constructing the geology in areas with sparse rock outcrops.

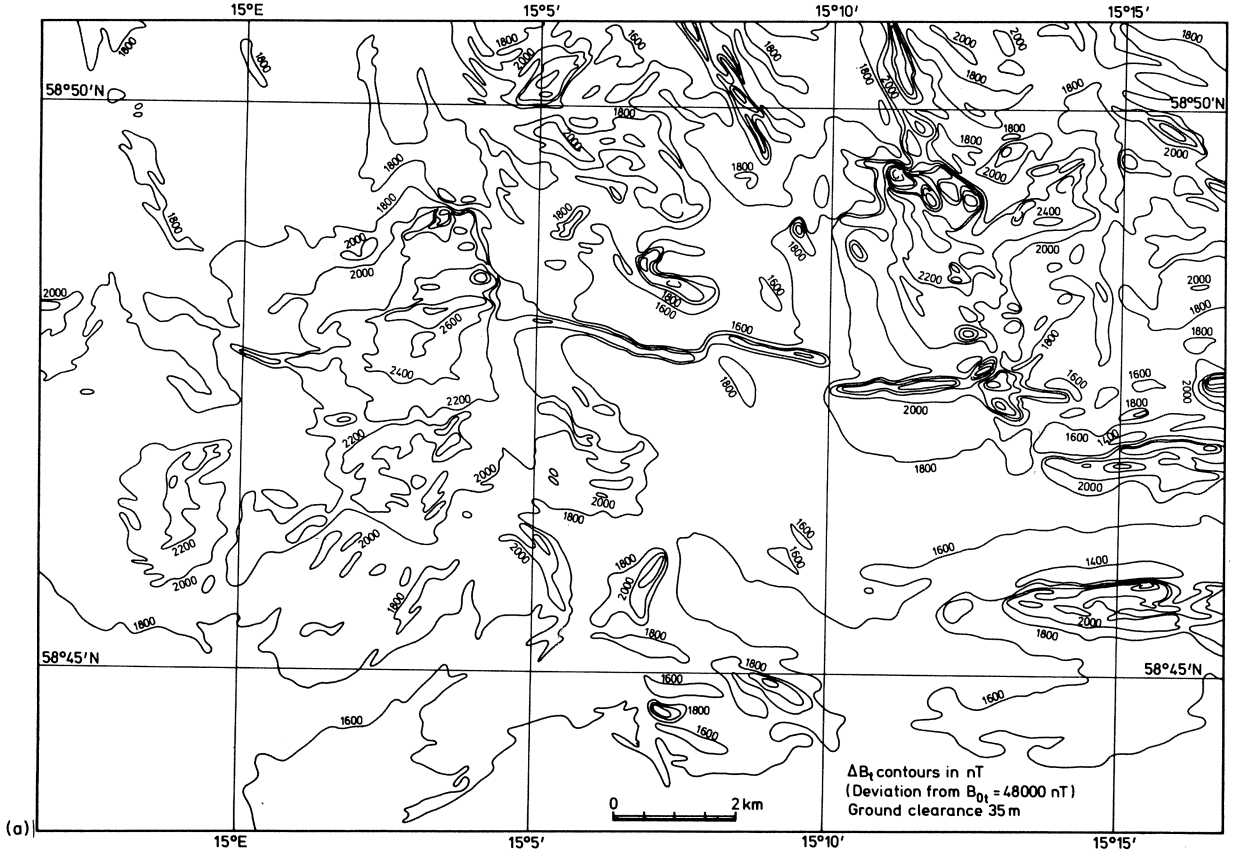
15°E
15°5′
15°10′
15°15′
58°50′N
58°45′N
ΔBt contours in nT
(Deviation from B0t = 48000 nT)
Ground clearance 35 m
0
2 km

(a)

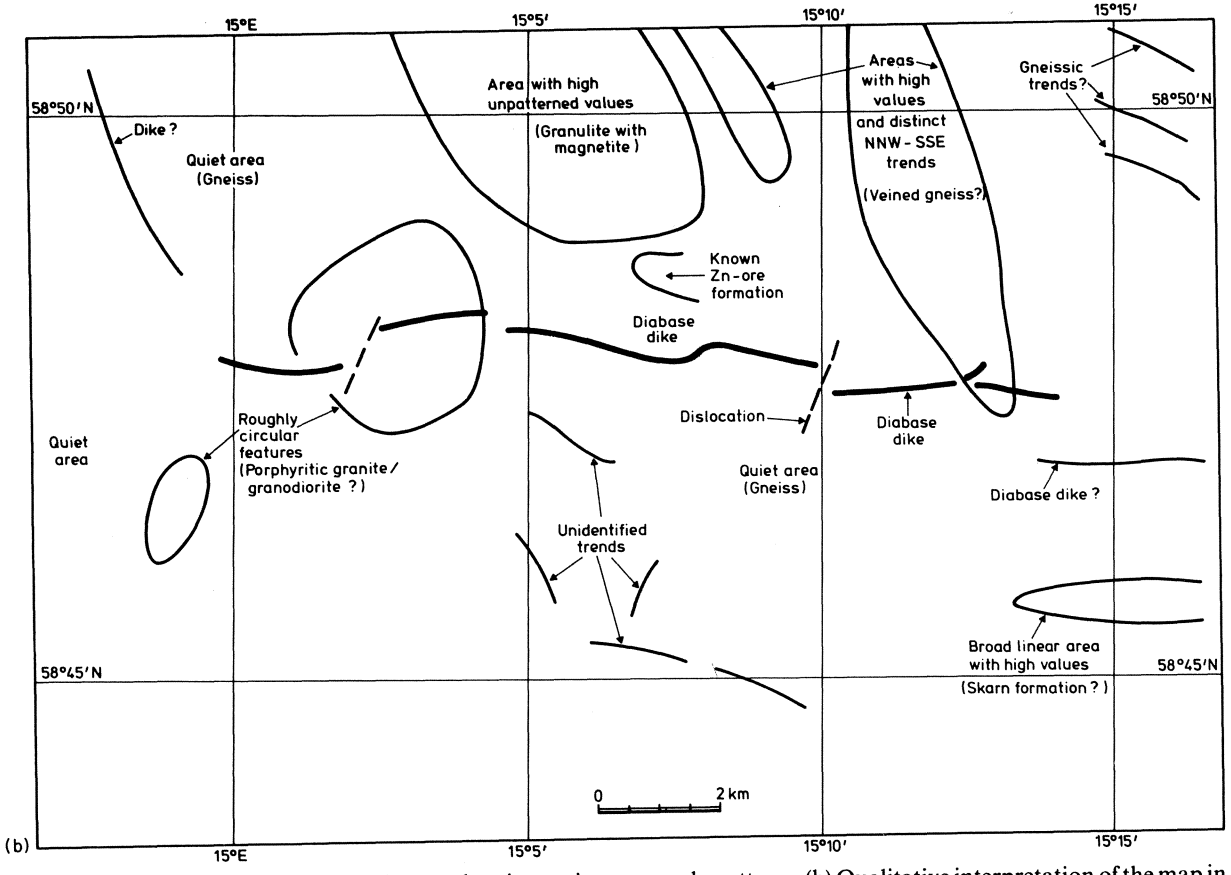

Fig. 2.5(a) Example of an aeromagnetic map showing various anomaly patterns. (b) Qualitative interpretation of the map in Fig. 2.5(a).

Figure 2.5(a) shows an example of an aeromagnetic map on which most of the above mentioned patterns can be observed. Figure 2.5(b) shows the corresponding geological picture constructed from a combination of field geological observations and aeromagnetics.

2.8.3 Caution concerning strike direction

It was mentioned above that the directions of the elongation of closed isoanomaly contours suggests the strike direction of the corresponding geological feature. However, a caution is in place in this respect because in low magnetic latitudes bodies of finite length, striking north–south, produce anomaly patterns which indicate an apparent east–west strike. The effect is easily understood by considering the field created by the longitudinal magnetization of the body by the horizontal component of the earth's magnetizing force. In fact, the anomaly pattern in this case closely resembles that in Fig. 2.6 discussed later. For strike directions of the body deviating from the north too, the anomaly patterns in low magnetic latitudes indicate apparent strikes significantly different from true ones [11]. In high magnetic latitudes the effect of a strong, almost horizontal remanent magnetization may similarly cause the anomaly patterns to deviate from the true strike.

2.9 QUANTITATIVE INTERPRETATION

2.9.1 Basic limitations of theory

The usual procedure in interpreting magnetic anomalies quantitatively is to guess a body of suitable form, calculate its field at the points of observation and compare it with the measured values. It is then possible to adjust the depth and dimensional parameters of the body by trial and error or by automatic optimizing methods until a satisfactory agreement is achieved between the calculated and observed values. In nearly all quantitative interpretation this agreement is only secured in practice along one or more selected profiles and not over the entire area. It is important to bear this in mind because the structure must be altered (or even discarded in favour of another) if a satisfactory agreement is not found to exist along other profiles than the initially selected ones. Any such model is moreover one of an infinity of possible models. Despite this non-uniqueness the interpretation of magnetic anomalies is not so seriously hampered in practice as might be imagined. The reason is that on the basis of geological information, which is usually available, or on grounds of plausibility, it is normally possible to reduce the number of alternatives to a moderate one from which only a few need to be selected initially as working hypotheses.

The calculation of the magnetic effect of a body of arbitrary shape and susceptibility, magnetized by an external field, is a very complicated problem,

as will be evident from its outline in Appendix 1. To bring the calculation within reasonable analytical or numerical effort, it is very often assumed that the body is homogeneously magnetized and is situated in a non-magnetic medium. Homogeneous magnetization is, however, only possible in a homogeneous, isolated body bounded by a second-degree surface, namely a sphere, an ellipsoid, an infinitely long cylinder of elliptic cross-section, a non-truncated paraboloid, a non-truncated hyperboloid and a non-truncated cone. Geologic structures do not conform to these shapes (or to the prerequisite of homogeneity) except in very rare instances and even then only approximately. At points inside a geologic body far from its bounding surface, the assumption of homogeneous magnetization may be more or less true, but at the edges and corners it definitely fails. Consequently, all calculations of the magnetic field of a geological structure based on the postulate of homogeneous magnetization are approximations of varying degree and conform better to the true field the greater the distance from the structure.

2.9.2 Anomalies of a sphere

Although a sphere as a geologic body is rare, it is useful to study its magnetic anomalies as they incorporate many important features of the anomalies of bodies of complex but roughly isometric shape. A detailed mathematical analysis will be found in Appendix 3 and, based on this, Fig. 2.6 shows the ΔB_z and ΔB_t maps that will be obtained in three different magnetic latitudes above an inductively magnetized sphere of susceptibility 0.01, just touching the ground surface. The centre of the sphere is vertically below the origin of coordinates.

It will be seen that in high magnetic latitudes the ΔB_z and ΔB_t strongly resemble each other and in all cases the line through the most positive and the most negative anomaly coincides with the south–north direction which is also the direction of the horizontal component of the sphere's (induced) magnetic moment. If the sphere has a remanent magnetization besides that induced by the earth's field, this line on an anomaly map will deviate from north–south and indicate the direction of the horizontal component of the net magnetic moment of the sphere instead.

A study of Fig. 2.6 also reveals that in high magnetic latitudes the centre of the sphere is more or less exactly below the point of most positive anomaly if I is positive (or below the most negative anomaly if I is negative). Note also that the dominating feature in the low-latitude ΔB_t maps has an east–west strike although the causative body is perfectly isometric!

2.9.3 Anomalies of thin, sheet-like bodies

Thin and thick sheets are very useful shapes for approximating many geological features. A thin sheet can often satisfactorily model ore veins or

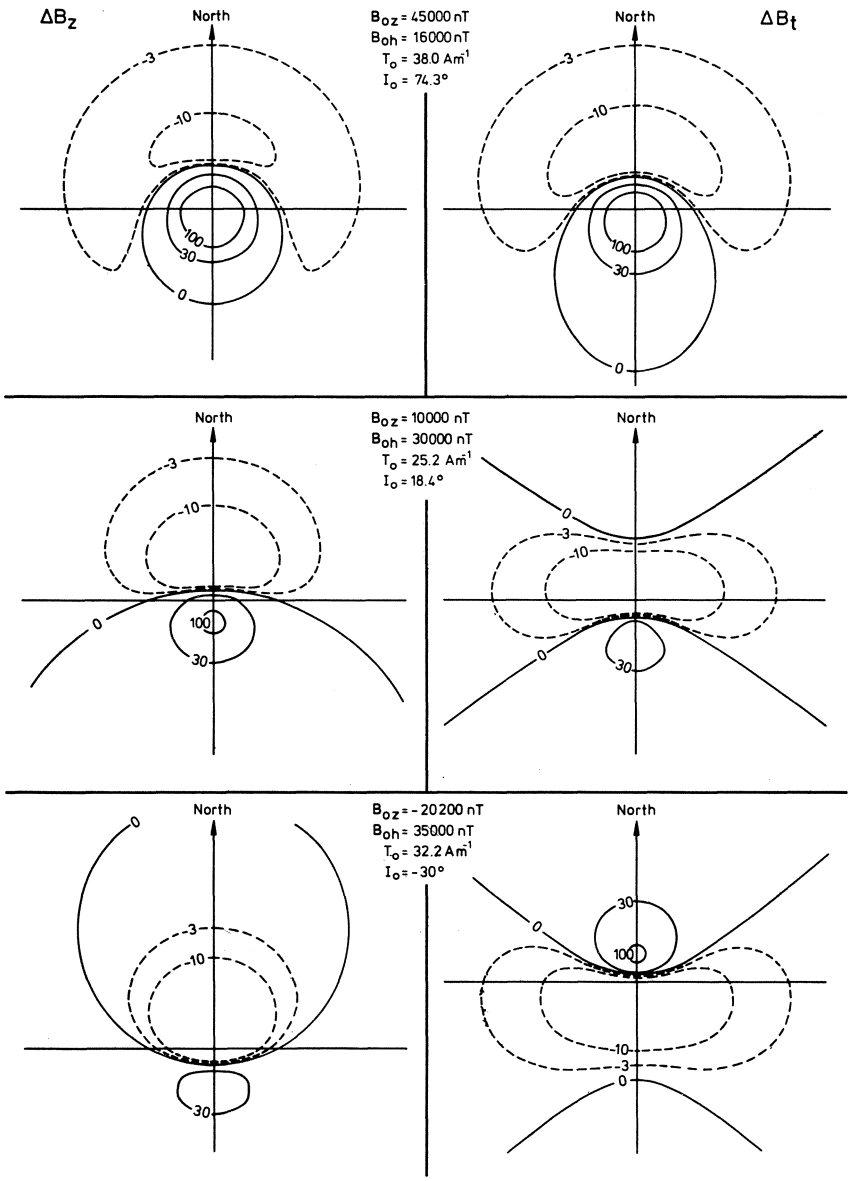

Fig. 2.6 Magnetic anomaly maps over a buried sphere just touching the ground surface in three different magnetic latitudes.

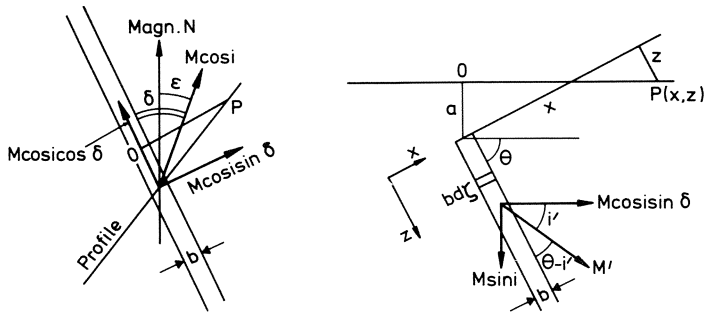

Fig. 2.7 Thin, magnetized sheet in plan (a) and section (b). (Note that in the final formulae x is used to denote the distance OP and not a coordinate with respect to the x, z axes shown.)

dikes while a thick sheet may approximate to a broad magnetically impregnated zone or a thick dike. We shall consider first a thin sheet of infinite length as well as depth extent, and assume that it is uniformly magnetized although such magnetization is, in fact, not possible for a body of this shape. We must now consider its various geometrical relations rather carefully.

If the magnetization vector **M** makes with the horizontal an angle i (not necessarily equal to the inclination I of the earth's field at the place) the horizontal component of **M** is $M\cos i$ and the vertical component is $M\sin i$. Fig. 2.7(a) shows the trace of the upper edge of a dipping thin sheet of thickness b, with the horizontal component of magnetization making an angle δ with the strike direction of the sheet and an angle ε with the north direction.

The component $M\cos i$ can be resolved in its turn into a component $M\cos i\cos\delta$ in the strike direction and $M\cos i\sin\delta$ perpendicular thereto. The component $M\cos i\cos\delta$ is of no interest if the strike length is infinite since it does not give rise to any anomaly. If now we take a vertical section at right angles to the strike, the situation will look as in Fig. 2.7(b) where M' denotes the resultant of the component $M\cos i\sin\delta$ and the vertical component $M\sin i$, and i' denotes the inclination of M' with the horizontal. Obviously

$$\tan i' = \frac{M\sin i}{M\cos i\sin\delta} = \frac{\tan i}{\sin\delta} \tag{2.22}$$

or

$$i' = \tan^{-1}(\tan i/\sin\delta) \tag{2.23}$$

Further,

$$M'^2 = M^2(\cos^2 i\sin^2\delta + \sin^2 i)$$

or, putting $\sin^2\delta = 1 - \cos^2\delta$ and simplifying,

$$M' = M(1 - \cos^2 i\cos^2\delta)^{1/2} \tag{2.24}$$

It is convenient to introduce the magnetization intensities $M'_{\parallel}$ and $M'_{\perp}$ along the dip of the sheet and perpendicular to the sheet respectively. From Fig. 2.7(b) we see that

$$M'_{\parallel} = M' \cos(\theta - i') \tag{2.25a}$$

$$M'_{\perp} = M' \sin(\theta - i') \tag{2.25b}$$

The anomalies of a thin sheet can now be calculated by integrating the effect of elementary strips of cross-sectional area $b\,\mathrm{d}\zeta$. The details of the calculation are given in Appendix 5 and the final result for the horizontal-field and vertical-field anomalies is

$$\Delta B_h = -\frac{\mu_0}{4\pi} 2b \frac{xM'_{\parallel} + aM'_{\perp}}{a^2 + x^2} \tag{2.26}$$

$$\Delta B_z = \frac{\mu_0}{4\pi} 2b \frac{aM'_{\parallel} - xM'_{\perp}}{a^2 + x^2} \tag{2.27}$$

where x is the distance of a point P on a profile perpendicular to the strike from the point O vertically above the edge of the sheet and is positive in the direction from which i' and the dip θ are measured. It should be noted that while i' may have any value between $-90°$ and $+90°$, θ is to be measured from $0°$ to $180°$. ΔB_h is directed parallel to OP since, by symmetry, there cannot be a horizontal flux density in the strike direction. The azimuth α of ΔB_h with respect to the magnetic north is evidently $90° - \delta + \varepsilon$.

If the magnetization of the sheet is due purely to induction in the earth's field M will be in the magnetic meridian ($\varepsilon = 0$) and we shall have $i = I$, $i' = \tan^{-1}(\tan I / \sin \delta) = I'$ (say) and $\alpha = 90° - \delta$. Then, for the total-field anomaly we get from Eq. (2.21)

$$\Delta B_t = \Delta B_h \sin \delta \cos I + \Delta B_z \sin I \tag{2.28}$$

Since in this case $M' = \kappa T'_0$, where T'_0 is the component of the earth's total magnetic field strength in the plane of Fig. 2.7(b), we have

$$M'_{\parallel} = \kappa T'_0 \cos(\theta - I') \tag{2.29a}$$

$$M'_{\perp} = \kappa T'_0 \sin(\theta - I') \tag{2.29b}$$

Equations (2.26) and (2.27) can then be written, after replacing $\mu_0 T'_0$ by B'_0 and taking out $\cos(\theta - I')$, as

$$\Delta B_h = -\frac{b\kappa B'_0 \sin(\theta - I')}{2\pi} \frac{a + x \cot(\theta - I')}{a^2 + x^2} \tag{2.30}$$

$$\Delta B_z = \frac{b\kappa B'_0 \cos(\theta - I')}{2\pi} \frac{a - x \tan(\theta - I')}{a^2 + x^2} \tag{2.31}$$

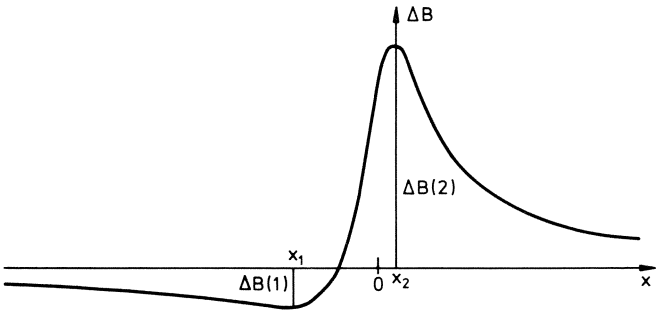

Fig. 2.8 General magnetic anomaly profile across a thin sheet.

where $B'_0 = B_0(1 - \cos^2 I \cos^2 \delta)^{1/2}$ is the component of the earth's normal flux density B_0 in the plane of Fig. 2.7(b), just as M' (and T'_0) are the components in this plane of M (and T_0).

The total-field anomaly can be expressed in the present case using (2.26), (2.27) and (2.28) by

$$\Delta B_t = \frac{b\kappa B'_0 \sin(2I' - \theta)}{2\pi} \frac{\sin I}{\sin I'} \frac{a - x\cot(2I' - \theta)}{a^2 + x^2} \tag{2.32}$$

It will be seen that all the three equations (2.30–2.32) are special cases of the equation

$$\Delta B = F \frac{a - kx}{a^2 + x^2} \tag{2.33}$$

Thus, irrespective of whether ΔB_h, ΔB_z or ΔB_t is measured, an anomaly profile across a thin sheet looks, in general, like that in Fig. 2.8.

2.9.3.1 Parameter determination with solved example

Next, we shall see how the parameters of a thin sheet of infinite depth extent and length can be determined from a measured magnetic anomaly profile. It should be realized, however, that in practice the values obtained are only estimates and must be further adjusted somewhat to secure a best possible agreement with the calculated and observed anomalies at all the measurement points. The estimates are obtained from a profile at right angles to the strike by means of the following exact scheme.

Let $\Delta B(1)$ and $\Delta B(2)$ denote the extreme values of ΔB (cf. Fig. 2.8) where $\Delta B(2)$ is *numerically* the greater of the two.

(1) *Lateral position of top edge.* Seek the point on the profile (between the extreme values) at which $\Delta B = \Delta B(1) + \Delta B(2)$. The top edge will be exactly below the corresponding observation point which will be the origin of

coordinates (cf. Fig. 2.7). The positive direction of x is already defined, this being the direction from which I' (minus or plus) is measured.

(2) *Depth a of the edge.* Let x_1, x_2 denote the x coordinates of $\Delta B(1)$ and $\Delta B(2)$ respectively. Of these x_1 will always be *numerically* the greater if $|\Delta B(2)| > |\Delta B(1)|$. Then $a = (-x_1 x_2)^{1/2}$. (Either x_1 or x_2 is negative so that $-x_1 x_2$ will always be positive.)

For a nearly symmetric profile x_1 will be numerically very large while $x_2 \approx 0$ so that this formula fails. In this case we proceed by finding the two points on the profile at which ΔB is half the central maximum (or minimum) anomaly. The distance between these points is exactly $2a$.

(3) *k and dip θ.* For k we simply have $k = 2a/(x_1 + x_2)$. Then, depending on whether $\Delta B_h, \Delta B_z$ or ΔB_t is the measured anomaly, we obtain θ from $\theta - I' = \cot^{-1}(-k), \theta - I' = \tan^{-1}(k)$ or $2I' - \theta = \cot^{-1}(k)$ respectively. On account of the properties of trigonometric functions, a value of θ outside the range $0 \leqslant \theta \leqslant 180°$ may be obtained. In such a case the simple expedient of adding (or subtracting) an appropriate multiple of 180 to the angle found will immediately give the correct θ in the range 0–180°. It is this θ that is to be used in subsequent calculations.

(4) F can now be calculated from either of the two expression below provided the profile is not near-symmetric ($|x_1|$ very large, $k \approx 0$):

$$\Delta B(1) = -\frac{F}{2a}\frac{k^2}{\sqrt{(k^2+1)+1}} \tag{2.34}$$

$$\Delta B(2) = \frac{F}{2a}\frac{k^2}{\sqrt{(k^2+1)-1}} \tag{2.35}$$

For a *symmetric profile*

$$\Delta B(1) \approx 0; \qquad \Delta B(2) = F/a \tag{2.36}$$

$\Delta B(2)$ is, this case, the central anomaly.

For an almost *antisymmetric profile** ($x_1 \approx -x_2; \Delta B(1) \approx -\Delta B(2); k \approx \infty$) the two expressions reduce, on the other hand, to

$$\Delta B(1) = -F/2a; \qquad \Delta B(2) = F/2a \tag{2.37}$$

(5) *Estimate of bκ.* Except when a profile is almost perfectly antisymmetric ($k \approx \infty$) the product $b\kappa$ can be calculated from the relevant expression for F in Eqs (2.30)–(2.32) since its value is now known.

For a nearly antisymmetric profile, however, the factor $\sin(\theta - I')$, $\cos(\theta - I')$ or $\sin(2I' - \theta)$ in Eqs (2.30)–(2.32), as the case may be, approaches

*This is a profile whose one half can be obtained by reflection of the other half, first in the x axis and then once more in the y axis.

zero and $b\kappa$ becomes indeterminate if we attempt to use the expression for F in question. It can be rigorously shown that in this case all that we have to do to determine $b\kappa$ is simply to omit the factor $\sin(\theta - I')$, $\cos(\theta - I')$ or $\sin(2I' - \theta)$, and equate the remaining factor to the value of F calculated from (2.37).

The validity of the entire scheme above is easily verified if we note that on putting the derivative of ΔB in Eq. (2.33) with respect to x equal to zero we obtain the equation

$$kx^2 - 2ax - k^2 = 0 \tag{2.38}$$

The two roots of this equation (x_1, x_2) are

$$x_1, x_2 = \frac{1 \pm \sqrt{(1 + k^2)}}{k} a \tag{2.39}$$

from which it follows that

$$x_1 + x_2 = 2a/k \qquad \text{and} \qquad x_1 x_2 = -a^2 \tag{2.40}$$

It is also easy to prove that $\Delta B(1) + \Delta B(2) = \Delta B(0)$, the anomaly at $x = 0$.

We shall illustrate the above procedure by reference to Fig. 2.9 which shows the total-field anomaly profile across a dike striking at 52° W from the north ($\delta = +52°$), at a place where $I = -33°$ and $B_0 = 44\,160$ nT. Here we have

$$\tan I' = \frac{\tan(-33°)}{\sin 52°} = -0.7930, \quad I' = \tan^{-1}(-0.7930) = -52.5°$$

$$\cos I = 0.8387, \quad \cos\delta = 0.6157; \qquad B'_0 = 37\,817 \text{ nT}$$
$$\sin I = -0.5446, \quad \sin I' = -0.7934$$

From Fig. 2.9 we obtain the following measured values:

$$\Delta B(1) = +238 \text{ nT}, \qquad \Delta B(2) = -543 \text{ nT}, \qquad \Delta B(1) + \Delta B(2) = -305 \text{ nT}$$

(The *numerically* greater value is -543 nT and is denoted by $\Delta B(2)$.)

There are two measuring points on the profile at which $\Delta B = -305$ nT but only one of them, marked 0, lies between the extreme values. The axis of x is positive to the right in this figure as I' has been measured from this direction. With 0 determined as the origin we then get

$$x_1 = +28 \text{ m}, \qquad x_2 = -12 \text{ m}, \qquad a = \sqrt{(28 \times 12)} = 18.3 \text{ m}$$
$$k = 36.6/(28 - 12) = 2.29, \qquad F = -5680 \text{ nT}$$

Since the profile is for ΔB_t we have, from (2.32) and (2.33),

$$k = \cot(2I' - \theta)$$
$$2I' - \theta = \cot^{-1}(k) \tag{2.41}$$

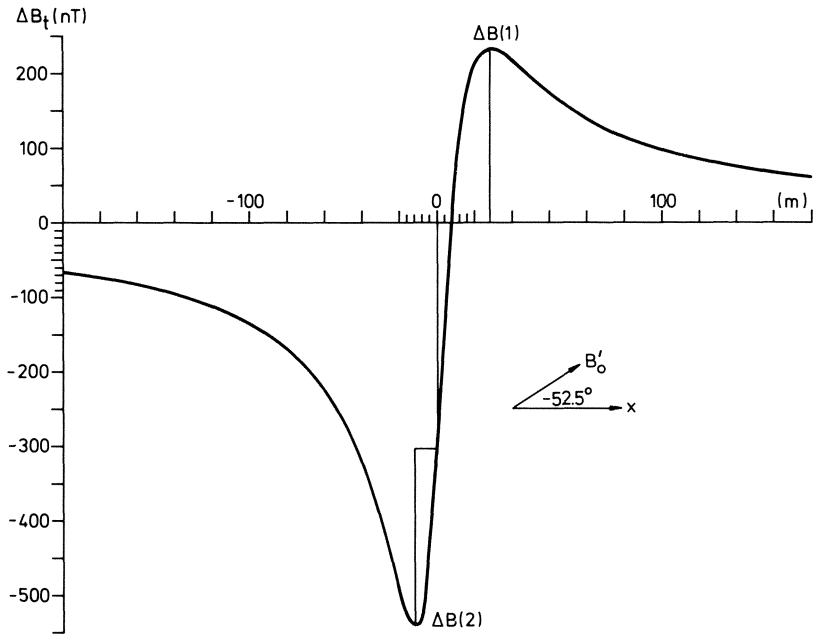

Fig. 2.9 Magnetic profile across a thin sheet ($\delta = +52°$, $I' = -33°$, $B_0 = 44\,160$ nT).

and

$$F = \frac{b\kappa B_0' \sin(2I' - \theta)}{2\pi} \frac{\sin I}{\sin I'} \tag{2.42}$$

From Eq. (2.41),

$$\begin{aligned} 2I' - \theta &= \cot^{-1}(2.29) = 23.6° \\ \theta &= -105° - 23.6 \\ &= -128.6° \end{aligned} \tag{2.43}$$

As this value lies outside the range $0 \leqslant \theta \leqslant 180°$ we add 180° to the right-hand side and obtain 51.4° as the dip θ. It is this value of θ that is to be introduced in Eq. (2.42), or the corresponding expression when ΔB_h or ΔB_z is the field in question. In other words, the value of $2I' - \theta$ as obtained from Eq. (2.41) is not to be used in (2.42) except, of course, when θ obtained at the stage represented by Eq. (2.43) is already in the range $0 \leqslant \theta \leqslant 180°$. In the present case we therefore put $\sin(2I' - \theta) = \sin(-105° - 51.4°) = \sin(-156.4°) = -0.400$ in Eq. (2.42) and get

$$b\kappa = 3.55 \text{ m}$$

2.9.3.2 Vertical field of thin sheet with no transverse magnetization

It is of considerable interest to study this case which implies a dip parallel to the effective magnetic field ($\theta = I'$). It arises typically in high magnetic latitudes over steeply dipping magnetite ores and is one instance in which the strike length of the sheet can also be estimated in case the thin sheet is not infinitely long.

For a thin sheet with $\theta = I'$ and in which, moreover, there is no remanent magnetization, (2.31) can be written as

$$\Delta B_z = \frac{b\kappa B_0'}{2\pi a} \frac{1}{1 + x_a^2} \tag{2.44}$$

where $x_a = x/a$. It is obvious that in this case ΔB_z is maximum at $x = 0$ and

$$\Delta B_z(\max) = \frac{b\kappa B_0'}{2\pi a} \tag{2.45a}$$

and

$$x_{1/2} = a \tag{2.45b}$$

where $x_{1/2}$ is the distance at which $\Delta B_z = \Delta B_z(\max)/2$. Eqs (2.45a) and (2.45b) give the depth and the product $b\kappa$.

If the sheet is not infinitely long but has a strike length L its anomaly $\Delta B_z(L)$ can be shown to be (exactly)

$$\Delta B_z(L) = \tfrac{1}{2}\Delta B_z(\infty)[f(d_{1a}) + f(d_{2a})] \tag{2.46}$$

where $d_{1a} = d_1/a$ and $d_{2a} = d_2/a$ are the horizontal distances of the profile from the two ends of the sheet in terms of the depth a and

$$f(d_a) = \frac{d_a}{(x_a^2 + d_a^2 + 1)^{1/2}} \tag{2.47}$$

$\Delta B_z(\infty)$ is, of course, the anomaly given by Eq. (2.44). The distance $x_{1/2}$ referred to below is defined as above but for the central profile.

If, on the other hand, $y_{1/2}$ is the distance at which the anomaly falls to half the maximum value along a line parallel to and directly above the sheet, the ratio $x_{1/2}:y_{1/2}$ depends on L/a and has the limiting values 1.000 ($L = 0$, the sheet dwindling down to a thin vertical 'wire') and 0 ($L = \infty$). Similarly $a/x_{1/2}$ will be a function of L/a and has the limiting values 1.305 and 1.000 respectively.

In Fig. 2.10 are plotted $x_{1/2}:y_{1/2}$, $a/x_{1/2}$ and the parameter

$$\frac{b\kappa B_0'}{4\pi x_{1/2}\Delta B_z(\max)}$$

against L/a. The last mentioned parameter is equal to $\frac{1}{2}$ for an infinitely long sheet as can be seen from Eqs (2.45a) and (2.45b). If $x_{1/2}:y_{1/2}$ can be determined

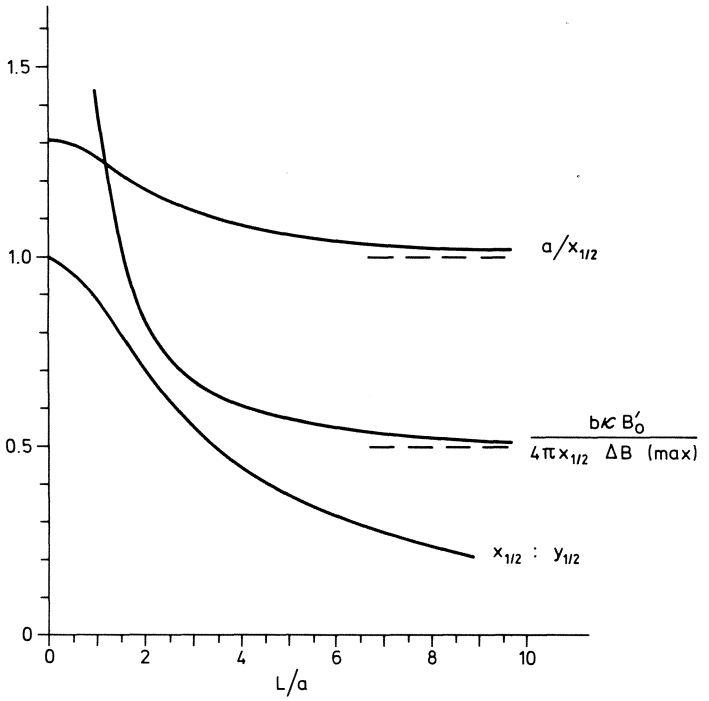

Fig. 2.10 Parameters of a thin sheet having no transverse magnetization, as a function of sheet length.

from a map of ΔB_z, the depth a to the upper edge, the length L and the product $b\kappa$ for a body that can be approximated by a thin sheet of very large depth extent and no transverse magnetization may be estimated from Fig. 2.10. How this diagram is to be used in pertinent cases will be shown later.

If it is desired to take into account the effect of a finite depth extent, ΔB_z may be calculated from Eqs (2.44) and (2.46) by subtracting from their right-hand sides expressions of identical forms but with a', the depth of the lower edge of the sheet, replacing a. In this case the lower edge must, of course, be shifted sideways to an appropriate extent to take account of the dip (Fig. 2.11). It is easy to see that the shift required is $(a' - a)/\tan\theta$. Some examples of anomaly curves of such magnetic 'double lines' are shown in Fig. 2.12 for the case of vertical dip. The ratio $a/x_{1/2}$ depends in this case upon L as well as a' (Table 2.5) so that the depth of the upper edge cannot be estimated without a reasonable assumption about the depth of the lower one.

As seen from Fig. 2.12 an effect of the lower edge is that there is a negative side-extremum in ΔB_z (if the principal anomaly is positive, and vice versa). The ratio $\Delta B_z(\text{min})/\Delta B_z(\text{max})$ depends on the ratio a'/a and can be used to estimate

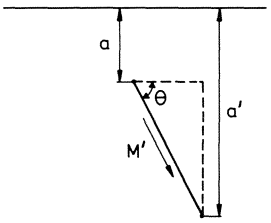

Fig. 2.11 Dipping thin sheet of finite depth extent.

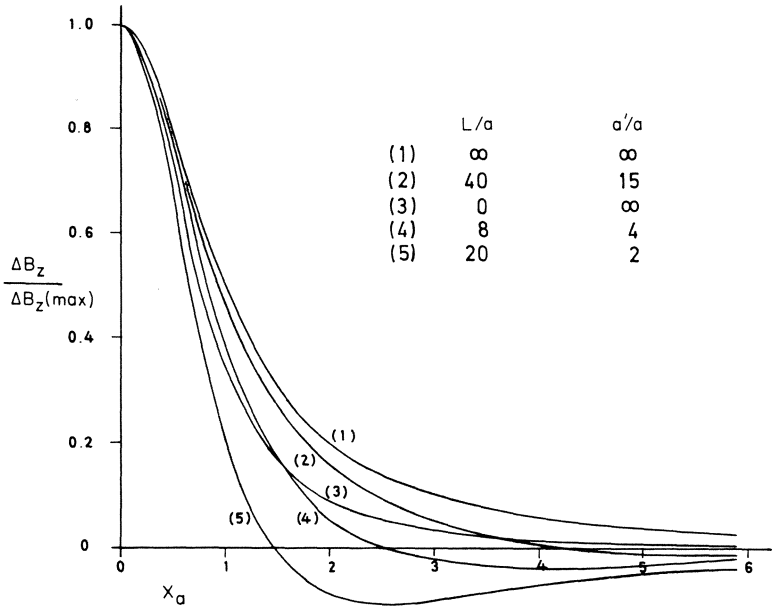

Fig. 2.12 ΔB_z across some thin vertical sheets of various depth extents and lengths.

Table 2.5 $a/x_{1/2}$ for magnetic thin plates with no transverse magnetization

	a'/a			
L/a	1	2	4	∞
0	1.99†	1.54	1.37	1.305
2	1.91‡	1.45	1.26	1.18
4	188‡	1.43	1.21	1.08
8	2.02‡	1.48	1.20	1.03
∞	2.06‡	1.53	1.26	1.00

†Point dipole ‡Linear dipoles

it. A diagram for the purpose pertaining to a vertically dipping sheet is given in Fig. 2.13.

2.9.4 Anomalies of sheets of arbitrary thickness

A long sheet of arbitrary thickness and infinite depth extent may be considered to be built up of an infinite number of thin sheets and the anomaly found by integration. Fig. 2.14 shows the geometry of the case, the notation being

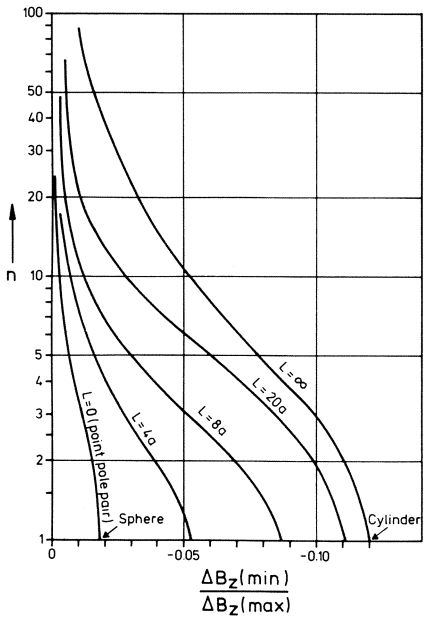

Fig. 2.13 Relation between side-extremum and depth extent for a thin, dipping sheet with no transverse magnetization.

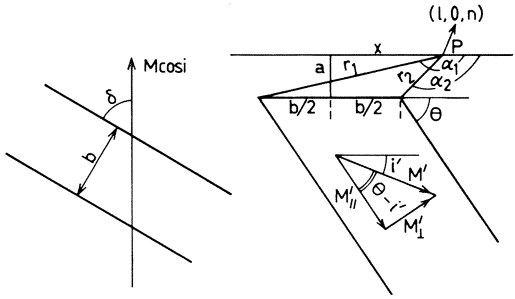

Fig. 2.14 Sheet of arbitrary thickness in plan and section.

similar to that in Fig. 2.7, but to begin with we shall consider the slightly more general situation in which the magnetization of the sheet is at an angle i different from the inclination of the earth's at the place so that $i \neq I$ and $i' \neq I'$. This means that the sheet has a remanent magnetization as well. As with a thin sheet all the three anomalies can be expressed by a *single* equation with appropriate values for the parameters involved, namely,

$$\Delta B = \left(\frac{\mu_0}{2\pi}\right) M' C \sin\theta [(\alpha_1 - \alpha_2) - k \ln(r_1/r_2)] \tag{2.48a}$$

The derivation of this equation will be found in Appendix 5.3.

For computational purposes Eq. (2.48a) can be written as

$$\Delta B = \left(\frac{\mu_0}{2\pi}\right) M' C \sin\theta \left[\cos^{-1}\left(\frac{r_1^2 + r_2^2 - b^2}{2r_1 r_2}\right) - k \ln(r_1/r_2)\right] \tag{2.48b}$$

where

$$r_1 = [(x + b/2)^2 + a^2]^{1/2}$$
$$r_2 = [(x - b/2)^2 + a^2]^{1/2}$$

The angle yielded by the $\cos^{-1}$ term will lie between 0 and π.

The values of C and k for $\Delta B_h, \Delta B_z$ and ΔB_t are given in Table 2.6. The $\cos^{-1}$ term in the above equation corresponds to the term $a/(a^2 + x^2)$ in Eq. (2.33). Both terms are symmetrical in x, that is, they retain their sign and magnitude if we change the sign of x. The logarithm in Eq. (2.48) corresponds to the term $x/(a^2 + x^2)$ in Eq. (2.33). These two terms are antisymmetric in x, that is, they change in sign but not in magnitude when x changes sign.

If the sheet is purely inductively magnetized, so that $i' = I'$, the k values in Table 2.6 are obviously exactly the same as those in Eqs (2.30)–(2.32). Conversely, if the thin sheet has a remanent magnetization, so that i' differs from I', the relevant k factors in Eqs (2.30)–(2.32) will be simply replaced by the corresponding general ones in Table 2.6.

Figs 2.15(a) and 2.15(b) show ΔB_h and ΔB_z curves across a sheet ($b = 2a$) dipping at various angles. These are quite general as far as strike angle

Table 2.6

Anomaly	C	k
ΔB_h	$-\sin(\theta - i')$	$-\cot(\theta - i')$
ΔB_z	$\cos(\theta - i')$	$\tan(\theta - i')$
ΔB_t	$\dfrac{\sin I}{\sin I'} \sin(I' + i' - \theta)$	$\cot(I' + i' - \theta)$

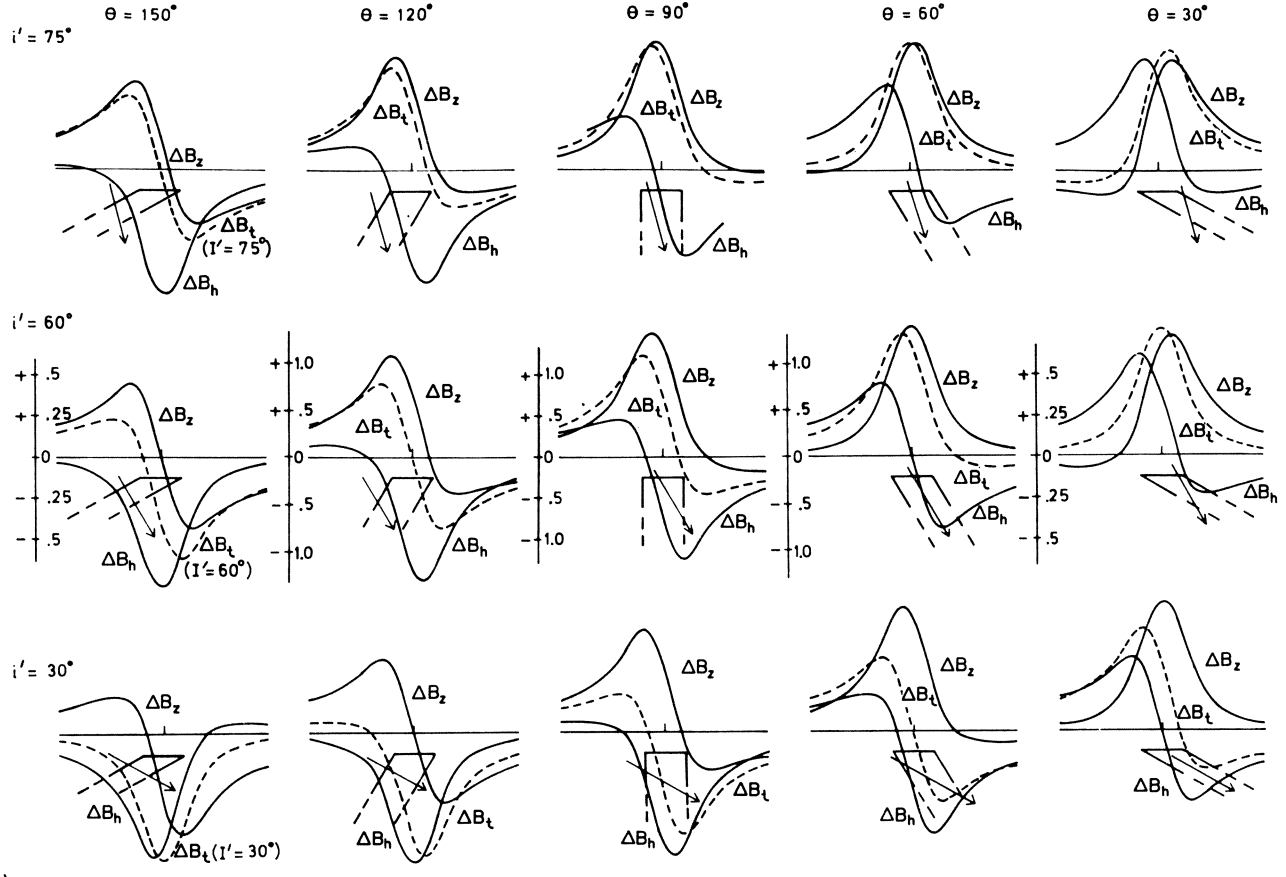
θ = 150°
θ = 120°
θ = 90°
θ = 60°
θ = 30°
i′ = 75°
i′ = 60°
i′ = 30°
ΔBz
ΔBt
ΔBh
(I′= 75°)
(I′= 60°)
(I′= 30°)
+ .5
+ .25
0
- .25
- .5
+ 1.0
+ .5
0
- .5
- 1.0

(a)

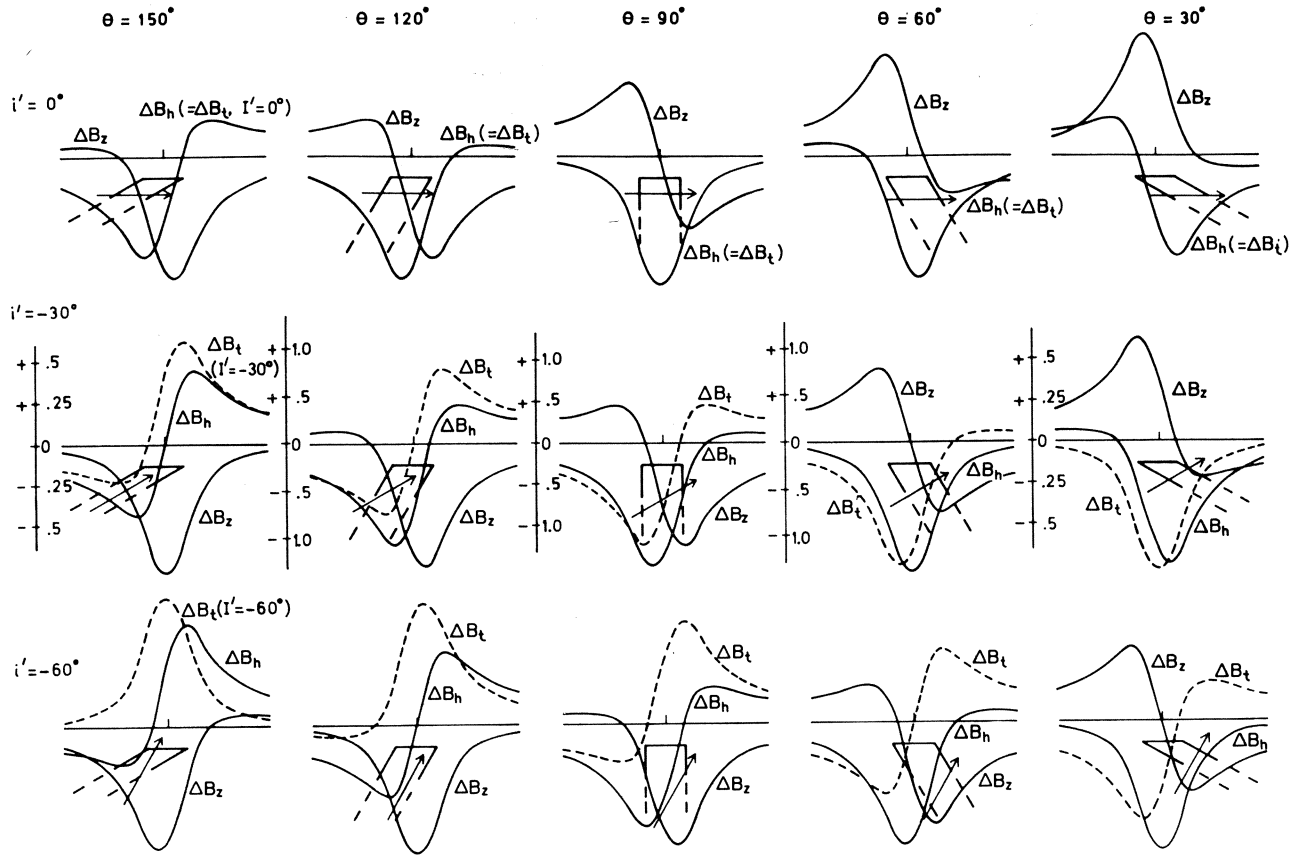

(b)

Fig. 2.15(a) and (b) Magnetic anomalies ΔB_z, ΔB_h, and ΔB_t across a thick sheet ($b = 2a$). In the absence of remanence or with remanence coinciding with the direction of the earth's field, $I' = \tan^{-1}(\tan I/\sin\delta)$ where δ is the strike angle. All ΔB_t curves shown are, however, for east-west strike of sheet only ($\delta = 90°, I' = I$) and no remanence.

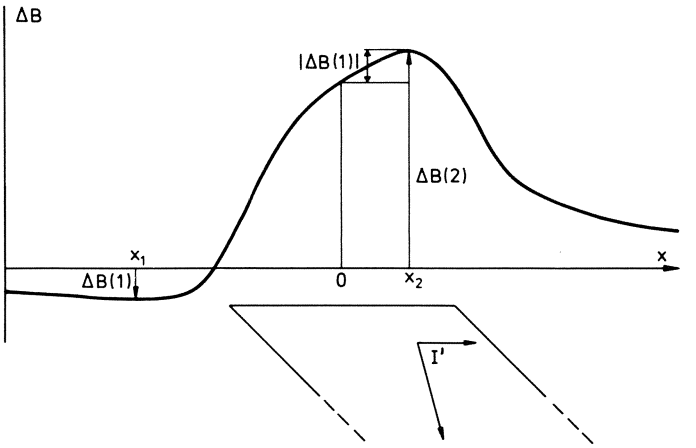

Fig. 2.16 Principal features of a magnetic profile across a thick sheet.

δ and magnetization direction in the sheet are concerned so long as the equation $i' = \tan^{-1}(\tan i/\sin\delta)$ is satisfied. Thus, for example, if the direction of remanence coincides with the earth's field (or if there is no remanence), $i = I$ and $i' = I'$, and each of the curves is then valid for any strike angle $\delta = \sin^{-1}(\tan I/\tan I')$ measured from the magnetic meridian (positive anticlockwise in plan). The curves labelled ΔB_t show the total-field anomaly for east–west strike of the sheet and no remanence.

The curves in Figs 2.15(a) and 2.15(b) resemble the anomaly curve for a thin sheet (Fig. 2.8) because the thickness is only twice the depth to the upper surface. For a substantially thicker sheet, however, the curves can be significantly different as the illustration in Fig. 2.16 shows.

2.9.4.1 Parameter determination for thick sheet

As in the case of a thin sheet a single exact and logical scheme can be devised to obtain estimates of the thick-sheet parameters from an anomaly profile, be it ΔB_h, ΔB_z or ΔB_t, at right angles to the strike of the sheet. This scheme will be described below. The proof of its validity is somewhat involved and is given in Appendix A5.4. The notations below are the same as for the thin-sheet scheme and it is assumed that $i = I$ and $i' = I'$.

(1) *Position of centre of sheet.* Seek a point on the profile, lying between the two extreme anomalies, at which $\Delta B = \Delta B(1) + \Delta B(2)$. The *numerically* greater extreme value is denoted by $\Delta B(2)$. The centre of the sheet is exactly below the observation point corresponding to ΔB. This point is our origin O. The positive direction of x is already known as this is the direction from which I' is

measured. The coordinates x_1, x_2 for $\Delta B(1)$ and $\Delta B(2)$ respectively are thus now known. The *numerically* greater one is x_1.

(2) *Width b and depth a of the sheet.* To find these, form first the ratios

$$d' = \frac{x_1 + x_2}{x_1 - x_2} \quad \text{and} \quad Q = \frac{\Delta B(2) + \Delta B(1)}{\Delta B(2) - \Delta B(1)}$$

and then enter the diagram in Fig. 2.17 to determine

$$b' = \frac{b}{|x_1 - x_2|} \tag{2.49}$$

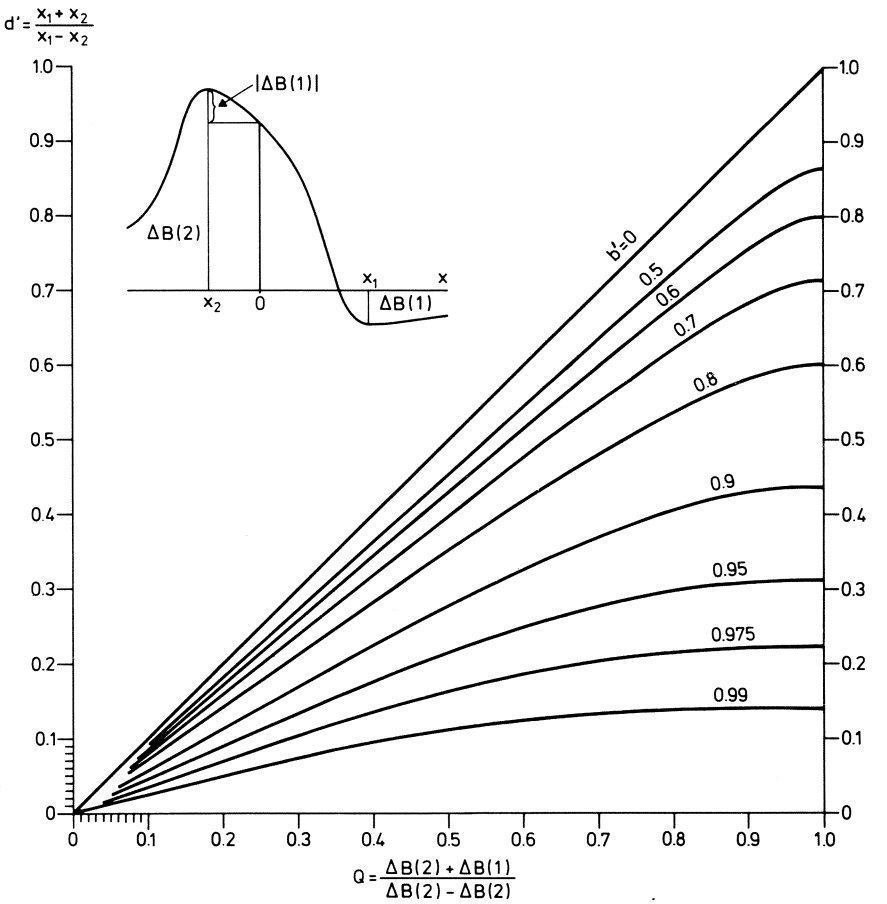

Fig. 2.17 Exact diagram for determining the thickness of a sheet from anomaly features in Fig. 2.16.

Fig. 2.17 is based on an exact transcendental equation derived in Appendix 5.4. Eq. (2.49) immediately gives b. Note that b here is the width in the horizontal plane.

With the knowledge of b, the depth a is calculated from

$$a = (-x_1 x_2 - b^2/4)^{1/2} \tag{2.50}$$

Either x_1 or x_2 is necessarily negative and x_1 numerically sufficiently large so that the bracketed quantity in Eq. (2.50) is always positive.

The above procedure fails when the profile is nearly symmetric since in this case, although the origin may be placed at the central maximum (or minimum) without much error, it may not be possible to locate the other extreme value on the profile and its coordinate. Therefore, we must proceed in some other way to determine b. One method is as follows.

Let $|x_{1/2}|$ and $|x_{1/4}|$ denote the absolute values of the coordinates of the points at which ΔB falls to one half and one fourth of the central value. (There will be one point of each category on either side of the origin. Since a profile is rarely perfectly symmetrical in practice, we should take the mean $|x_{1/2}|$ and the mean $|x_{1/4}|$.) Let

$$\xi = \frac{x_{1/4}}{x_{1/2}} \tag{2.51}$$

Then it can be shown that

$$a = \frac{(\xi^2 - 1)x_{1/2}}{2} \qquad \text{Symmetric profile} \tag{2.52}$$

and

$$b = 2(x_{1/2}^2 - a^2)^{1/2} \qquad \text{Symmetric profile} \tag{2.53}$$

Fig. 2.17 is also of no avail for a nearly antisymmetric profile ($x_1 \approx -x_2$, $\Delta B(1) \approx -\Delta B(2)$) because in this case d' and Q tend to be nearly zero so that b' is indeterminate, as can be seen from the figure. For a nearly *antisymmetric profile* we locate the coordinate $x_{1/2}$ of a point at which the anomaly is one half of one of the two extreme values. There will be four such points, two for each of the two extreme values (Fig. 2.18). Let us, for the sake of concreteness, consider that half of the antisymmetric profile in which ΔB is positive in Fig. 2.18. Denote by η the ratio $x_1/x_{1/2}$. (Theoretically it does not matter which one of the two $x_{1/2}$'s is used!!) Then the following exact equation (Problem 2.6) gives the width b:

$$b^2 = (1 + \eta^2)(4\eta - 1 - \eta^2)x_{1/2}^2 \qquad \text{Antisymmetric profile} \tag{2.54}$$

The depth a is then obtained from Eq. (2.50).

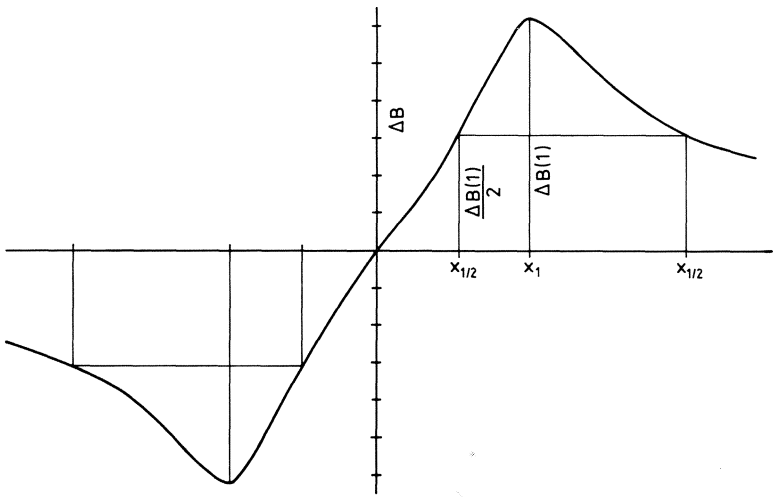

Fig. 2.18 Features to be used for a nearly antisymmetric profile.

(3) *k and θ*: As in the case of a thin sheet we get k from the formula

$$k = \frac{2a}{x_1 + x_2} \tag{2.55}$$

after which $\theta - I'$ or $2I' - \theta$ can be obtained by using the appropriate expression for k in Table 2.6. (We are assuming that $i' = I'$, as already stated.) If the value of θ thus found lies outside the range $0 \leqslant \theta \leqslant 180°$ a suitable multiple of 180° is simply added to or subtracted from the value and this will then give the correct θ, as in the case of a thin sheet. *It is this θ that is to be used in subsequent calculations.* (θ may be modified by a correction for the so-called demagnetization effects, but these will be considered in a later section.)
For a near-symmetric profile, $k \approx 0$.

(4) *Magnetization intensity M′ of the sheet*: Except when a profile is almost perfectly antisymmetric ($k \approx \infty$), M' can now be calculated from the formula:

$$\left(\frac{\mu_0}{2\pi}\right) M' C \sin\theta = \frac{\Delta B(1) + \Delta B(2)}{2} \frac{1}{\tan^{-1}(b/2a)} \tag{2.56}$$

where the left-hand side is the common factor in Eq. (2.48) and C is the appropriate expression in Table 2.6 depending upon the anomaly field in question. As we have already seen $\Delta B(1) + \Delta B(2)$ is the anomaly $\Delta B(0)$ at

$x = 0$. This may be difficult to ascertain with sufficient accuracy for nearly antisymmetric profiles.

For a *nearly antisymmetric profile*, C in (2.48) becomes zero too, and the attempt to find M' by means of an equation like (2.56) fails. It can be rigorously shown that for this case M' can be determined from the equation

$$\left(\frac{\mu_0}{2\pi}\right) M' \sin\theta = \frac{-\Delta B(1)}{\ln[(2x_1 + b)/(2x_1 - b)]} \tag{2.57}$$

Alternatively $-\Delta B(1)$ may be replaced by $\Delta B(2)$ in which case we replace x_1 by x_2 on the right-hand side.

Note that it is not necessary to know the normal geomagnetic field B_0 to obtain M'. However, if it is known we can go one step further and find the effective susceptibility from the definition of M', namely

$$M' = \kappa T'_0 = \kappa(B'_0/\mu_0) \tag{2.58}$$

We have called κ in (2.58) the effective susceptibility to allow for the possibility that M' may contain a remanent component parallel to T'_0 besides that induced by T'_0 and that the body itself may not have uniform susceptibility.

It was mentioned in Section 2.9.3.1 that b and κ cannot be separately determined for a thin sheet. On the other hand, they can be determined separately for a thick sheet! Although this might appear paradoxical, since there is no sharp boundary between a 'thick' sheet and a 'thin' one, the scheme in section 2.9.3.1 and the scheme for a thick sheet are not contradictory in this respect (Problem 2.4).

It should be noted that, in practice, the values of the various parameters obtained will only give us estimates and it may be necessary to adjust these further to secure the best possible agreement between the measured and the calculated anomalies along the entire profile.

Throughout this and the previous section we have assumed that the upper surface of the sheet is horizontal in the strike direction and not plunging. Likewise the measurement profile is assumed to be horizontal. If these conditions are not postulated the algebra becomes very complicated. This general case has been treated very thoroughly by Werner [12], although in parts with a somewhat different notation from that adopted here.

Finally, one fact of notation that should be kept in mind is that whereas b in Fig. 2.7 for a thin sheet is the width perpendicular to the plane of the sheet, b in Fig. 2.14 is the horizontal width. The width as measured perpendicular to the sides of the thick sheet is $b\sin\theta$. This is why the factor $\sin\theta$ appears in Eq. (2.48) on the right-hand side but not in Eqs (2.30)–(2.32).

2.9.4.2 Solved example of thick sheet anomaly

ΔB_z *profile at Vallenar, Chile.* Fig. 2.19 shows an aeromagnetic profile originally cited by Gay [13]. At Vallenar we have $I = -25°$ and the strike angle of the linear anomaly in question is $\delta = +23°$. Assuming that there is no remanence, Eq. (2.23) yields $I' = -50°$.

Denoting by $\Delta B(2)$ the numerically greater extremum in ΔB_z we deduce the following parameters from the figure:

$$\Delta B(2) = -1566\,\text{nT}, \quad \Delta B(1) = +133\,\text{nT}, \quad \Delta B(2) + \Delta B(1) = -1433\,\text{nT}$$
$$x_2 = 47.8\,\text{m}, \quad x_1 = -373.0\,\text{m}, \quad x_1 + x_2 = -325.2\,\text{m},$$
$$x_1 - x_2 = -420.8\,\text{m}$$
$$d' = 0.773, \quad Q = \frac{-1433}{-1699} = 0.843$$

Hence

$b' = 0.46$ (Fig. 2.17), $b = |-420.8| \times 0.46 = 193.6\,\text{m}$ (Eq. 2.29)
$a = 92\,\text{m}$ (Eq. 2.50), $k = -0.566$ (Eq. 2.56), $b/2a = 1.052$

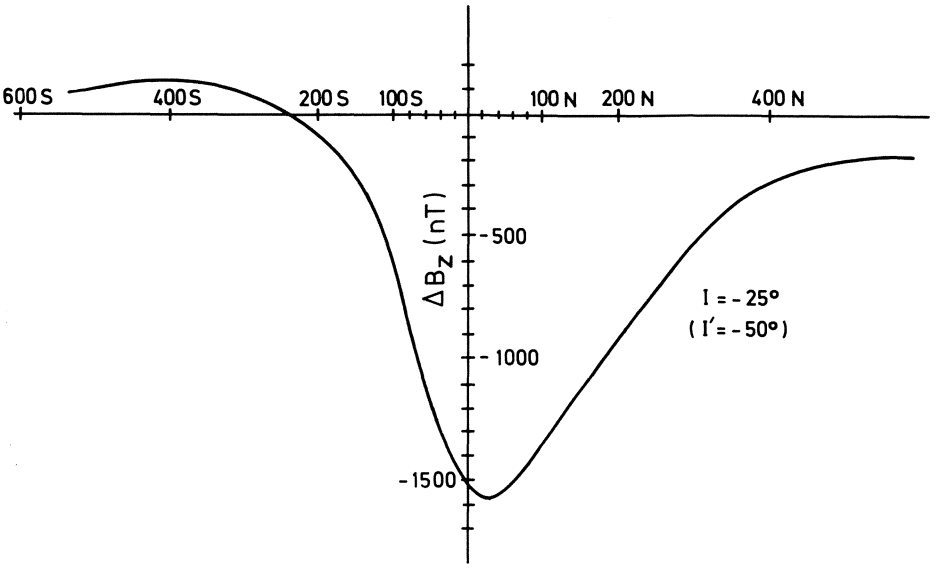

Fig. 2.19 ΔB_z profile at Vallenar, Chile ($\delta = 23°$, $I = -25°$). (For interpretation, see text.) After [13].

(The actual depth found by drilling, as cited by Gay, is 97 m.)

Since the profile is a ΔB_z profile, Table 2.6 shows that

$$\theta - I' = \tan^{-1}(-0.566) = -29.5°$$

Hence,

$$\theta = I' - 29.5° = -50° - 29.5° = -79.5°$$

This value of θ is outside the range $0 \leqslant \theta \leqslant 180°$. Therefore we add a suitable multiple of 180°, in this case only one multiple, and get the dip as

$$\theta = -79.5° + 180° = 100.5° \tag{2.59}$$

In subsequent calculations we must use this θ so that

$$\theta - I' = 100.5° - (-50°) = 150.5° \tag{2.60}$$

Table 2.6 shows that $C = \cos(\theta - I')$ in the present case so that using Eq. (2.56) we obtain (with $\mu_0 = 4\pi \times 10^{-7}\,\Omega\,s\,m^{-1}$, as usual):

$$2M' \times 10^{-7} = \frac{-1433 \times 10^{-9}}{2} \frac{1}{\cos(150.5°)\sin(100.5°)} \frac{1}{\tan^{-1}(1.052)}$$

The angle $\tan^{-1}(1.052) = 46.45°$ must, of course, be expressed in radians, namely 0.813 rad. Further

$$\cos(150.5°) = -0.8704, \qquad \sin(100.5°) = +0.9833$$

Thus,

$$M' = 5.145\ A\,m^{-1} \tag{2.61}$$

At Vallenar $B_0 \approx 28\,000$ nT, i.e. $B'_0 = 15\,400$ nT and $T'_0 = B'_0/\mu_0 = 15\,000 \times 10^{-9}/(4\pi \times 10^{-7}) = 12.25\ A\,m^{-1}$. Eq. (2.61) then yields the effective susceptibility

$$\kappa = 0.42 \tag{2.62}$$

2.9.5 Finite depth extent and strike length

Equation (2.48) is valid for sheets extending to infinity in either direction perpendicular to the plane of Fig. 2.14 and with the lower face at infinite depth. If the depth extent is finite we obtain an infinitely long two-dimensional prism. Its magnetic anomaly can be calculated by subtracting from the right-hand side of (2.48) the corresponding expression for a second sheet of infinite depth extent and identical thickness and dip but with the upper surface at a depth equal to the depth of the lower face of the prism.

Fig. 2.20 shows an example of such an interpretation. The surface magnetic map of ΔB_z in this case showed a long magnetic feature with a strike angle $\delta = 20°$. Various combinations of k and the depth of the lower face were tried, with $k = -1.564$ and the depth extent shown in the figure giving the most satisfactory fit between the observed and calculated ΔB_z anomalies.

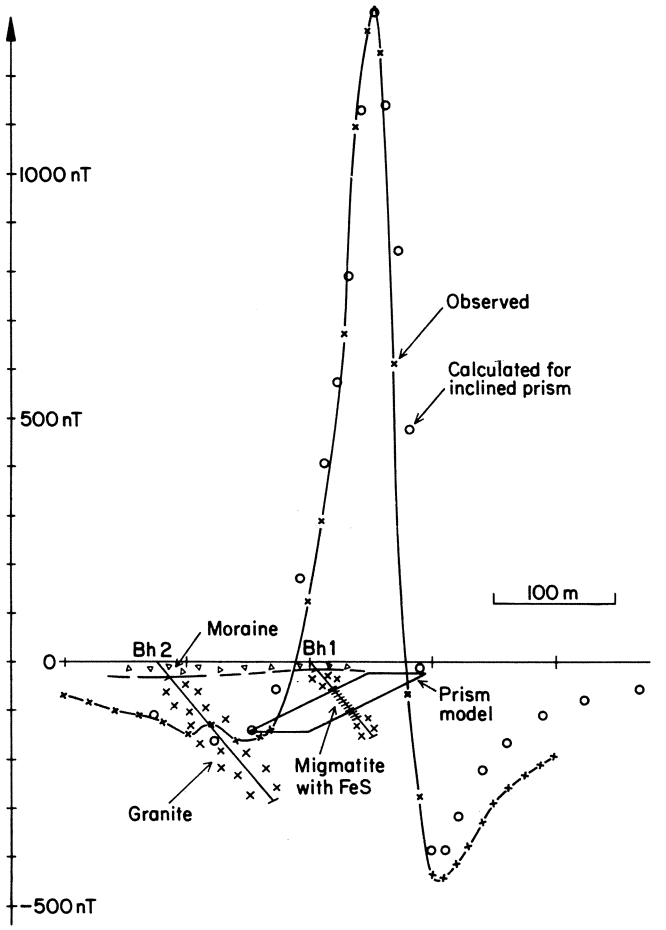

Fig. 2.20 Observed and calculated ΔB_z across an inclined prism-like body ($k = -1.564$).

Assuming only induced magnetization ($I = 75°$ in the area) we find $I' = \tan^{-1}(\tan 75°/\sin 21°) \approx 85°$. From Table 2.6, $\theta - I' = \tan^{-1}(-1.564) = -57°$. This gives $\theta = 28°$, as shown in the figure. Two holes were drilled on the basis of this interpretation, the deeper one specifically to verify the inference about the depth extent. The shallower hole encountered migmatite with pyrrhotite at the expected depth while the deeper hole was barren and confirmed the interpreted depth extent.

By combining a number of different sheets we can simulate more complicated cross-sections and calculate the anomalies of very long geologic bodies of uniform cross-section. However, it must be mentioned in passing

that the procedure is not theoretically correct and is acceptable only if the susceptibilities of the individual prisms are low ($\lesssim 1$).

The magnetic anomalies of prisms of uniform cross-section whose length and depth extent are finite have been studied in some detail by Hjelt [14]. It is evident from this study that the effect of finite strike length is very complex and no simple description of it can be given.

2.9.6 Sloping step simulating fault, flexure, lava flow etc.

It is interesting to note that the anomalies over this feature are again given by Eq. (2.48a), but not by Eq. (2.48b), with the symbols as in Fig. 2.21. However, the scheme of Section 2.9.4.1 is not applicable here. This figure also shows two of the many possible shapes of ΔB_z curves across a step. The shapes of ΔB_h and ΔB_t curves can likewise take a very wide variety of forms and general rules for determining the parameters of the sloping step are very difficult to formulate. Although θ can be estimated from the value of k that gives the best fit with the observed data, it is not possible to estimate b by any simple rule, contrary to the case for the thick sheet, so that adjustments in interpretation are much more difficult to make for the sloping step.

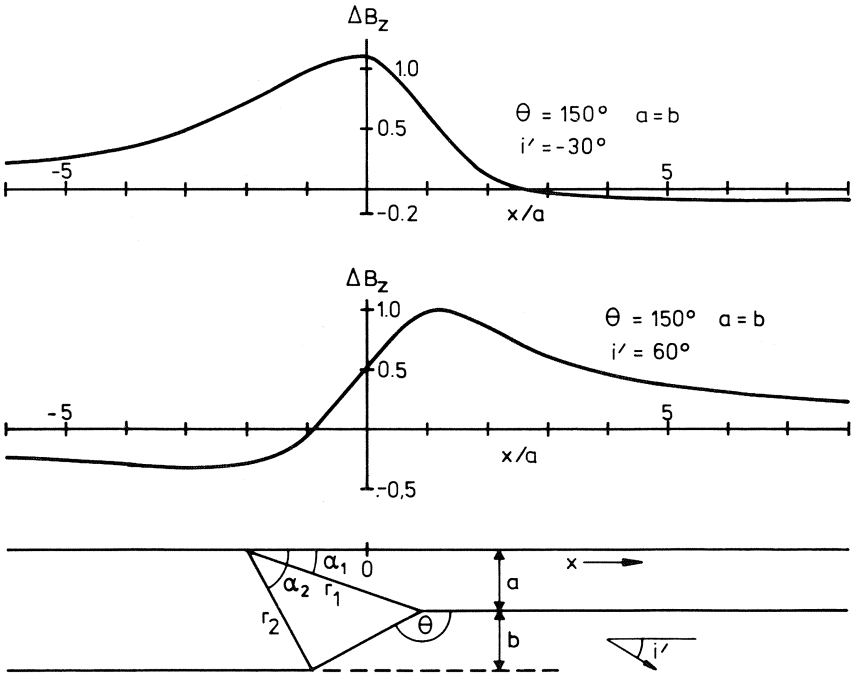

Fig. 2.21 Sloping step.

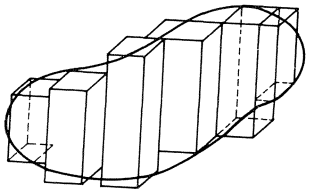

Fig. 2.22 Arbitrarily shaped body approximated by prisms.

2.9.7 Bodies of arbitrary shape

The calculation of magnetic field due to bodies of arbitrary shape leads to formulae which are generally unmanageable, even for numerical computation on high-speed computers, unless simplifying assumptions are made. One such approach is to subdivide the body into a number of rectangular prisms (Fig. 2.22) and sum the effect of each prism at a point of observation. Again, the procedure of simply summing up the effects of individual prisms is not theoretically correct, but is acceptable in practice if the susceptibilities of the prisms are low. The expressions for the magnetic anomalies of a single rectangular prism can be derived exactly if we assume homogeneous magnetization [15].

Another approach is to approximate the body by a polyhedron whose faces are plane polygons. This method has been treated by Coggon [34] who extends it to gravity calculations as well.

2.10 EFFECT OF DEMAGNETIZATION

It is implicit in the defining equation (2.2a) that H is the actual magnetic field strength at the point under consideration. Within a finite body the local field strength is not equal to the strength of the inducing field at that point. For instance, within a sphere of susceptibility κ on which is acting a homogeneous external magnetic strength H_0, the internal H is everywhere $H_i = H_0/(1 + \kappa/3)$, $< H_0$ if $\kappa > 0$ (Appendix 2). The reduction in the internal H field is tantamount to a 'demagnetizing force' within the sphere equal to

$$H_0 - \frac{H_0}{1 + \kappa/3} = \frac{\kappa H_0}{3 + \kappa}$$

acting opposite to H_0.

By analogy with the sphere, the internal field strength in a direction α within a body of arbitrary shape may be written as

$$H_{i\alpha} = \frac{H_{0\alpha}}{1 + N_\alpha \kappa_\alpha} \tag{2.63}$$

where N_α is a demagnetizing 'factor' in the direction α. It should be noted that only for bodies bounded by a second-degree surface are H and N constant

within the body, e.g. for a sphere $N = \frac{1}{3}$ in all directions. For all other shapes $\mathbf{H}_i$, N and the intensity of magnetization ($\kappa\mathbf{H}_i$) vary from point to point. If, therefore, we understand by $H_{i\alpha}$ in Eq. (2.63) the *average* internal magnetizing force in the direction α we get an 'average demagnetization factor'

$$N_\alpha = \frac{1}{\kappa_\alpha}\left(\frac{H_{0\alpha}}{H_{i\alpha}} - 1\right) \tag{2.64}$$

N depends on κ, but the dependence is not so simple as would appear from Eq. (2.63) because H_i is also a function κ. $H_{i\alpha}$ needed for estimating N_α has to be calculated by solving the appropriate integral equations numerically. This is a very difficult problem and apart from bodies bounded by second-degree surfaces (for which the integral equations can be solved exactly), H_i and N have only been evaluated for very simple shapes like prisms and sheets.

If, in solving the integral equations, it is assumed (contrary to fact) that H_i is uniform within a body, the corresponding N turns out to be independent of κ (although not of position) and for rectangular prisms it is then expressible exactly in terms of elementary functions. Eskola [224] has shown that this assumption is acceptable only if $\kappa \gtrsim 1$. Nevertheless it is commonly resorted to in geophysical work for all κ because the detailed calculation of H_i, which incidentally requires a knowledge of κ (!), is a formidable numerical problem even for simple shapes like prisms.

Demagnetization effects influence the magnetic interpretation in the following way. The value of k obtained in the adjustment described in Sections 2.9.3 and 2.9.5 yields $\theta - i'$, the angle between the dip and the inclination of M'. If M' has a remanent as well as an induced component, i' is unknown and hence also θ. However, even if there is no remanence ($i' = I'$), when M' will be expected to be in the direction of I', it will deviate from this direction. This can be understood by reference to Fig. 2.23. The magnetization $M'_\parallel$ of the prism of infinite strike length in the cross-sectional plane will not be $\kappa T'_0 \cos(\theta - I')$ according to Eq. (2.29a) but instead

$$M'_\parallel = \frac{\kappa}{1 + N_\parallel \kappa} T'_0 \cos(\theta - I') \tag{2.65}$$

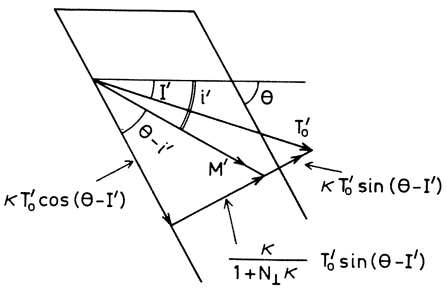

Fig. 2.23 Effect of demagnetization.

in view of Eq. (2.63), where $N_\parallel$ is the demagnetization factor in the direction of the depth extent. Similarly the transverse magnetization will not be as in Eq. (2.29b) but

$$M'_\perp = \frac{\kappa}{1 + N_\perp \kappa} T'_0 \sin(\theta - I') \tag{2.66}$$

Strictly speaking even the κ's in these equations should be replaced by $\kappa_\parallel$ and $\kappa_\perp$ but we shall not make this refinement.

It should be observed that the demagnetization effect tends to deflect M' so as to make it less inclined to the sloping sides of the sheet.

For infinite depth extent, as in Fig. 2.14, it can be shown that $N_\parallel = 0$ and $N_\perp = 1$ (Appendix 6) so that (2.65) and (2.66) give

$$\frac{M'_\perp}{M'_\parallel} = \frac{\tan(\theta - I')}{1 + \kappa} \tag{2.67}$$

Now, for a ΔB_z profile, for example, $M'_\perp / M'_\parallel = k$ (p. 32) and hence, from (2.67), for a ΔB_z profile

$$\tan(\theta - I') = (1 + \kappa)k$$

or

$$\theta = I' + \tan^{-1}[(1 + \kappa)k] \tag{2.68}$$

For a prism of finite depth extent we get from (2.65) and (2.66)

$$\theta = I' + \tan^{-1}\left(\frac{k(1 + N_\perp \kappa)}{1 + N_\parallel \kappa}\right) \tag{2.69}$$

(Eqs (2.68) and (2.69) are also valid for a thin sheet.)

We now revert to the ΔB_z profile in Section 2.9.4.2 and estimate θ by taking account of demagnetization. We assume that the susceptibility of the sheet in question is 0.42 as given by Eq. (2.62). Then from (2.68) we have

$$\begin{aligned} \theta &= -50° + \tan^{-1}(1.42 \times -0.566) \\ &= -50° - 38.8° \\ &= -88.8° \end{aligned}$$

that is $-88.8° + 180° = 91.2°$ as the true dip, instead of 100.5° (Eq. 2.59). In this case the difference is about 10° and may be inconsequential but if κ is appreciable we may be led to grossly erroneous conclusions about the dip if demagnetization effects are disregarded.

2.11 SOME EXAMPLES OF MAGNETIC INVESTIGATIONS

The examples below are chosen to illustrate some geologic points in magnetic interpretation. A general method of attack on any problem is hard to find especially when igneous rocks or chromite and manganese ore bodies, all of which are notorious for the capricious character of their remanent magnetiz-

ation, are the objects of investigation. Every case of magnetic investigation needs a careful study of the geology and the topography of the area.

2.11.1 Magnetite ore in Central Sweden

The map in Fig. 2.24 shows the results of a survey in Central Sweden. The choice of the area was dictated by general geological considerations; the exact location of the magnetic disturbance is the outcome of the geophysical work. The magnetic anomaly shows an approximately east–west strike. From profiles going over points in the immediate vicinity of the anomaly centre the mean $x_{1/2}:y_{1/2}$ (Section 2.9.3.2) was found to be about 0·55 which gave $L/a \approx 3$ and $a/x_{1/2} \approx 1.1$ (Fig. 2.10). The mean value of $x_{1/2}$ over the central profiles was 58 m, hence $a = 65$ m. The observed and calculated anomalies using this depth and a magnetic width $(b\kappa) = 86$ also estimated from Fig. 2.10 are shown in Fig. 2.24(b). A slight effect of the transverse magnetization was also taken into consideration in these calculations. A drill-hole placed as shown encountered rich magnetite ore of total horizontal width of 10 m. This would indicate an average apparent susceptibility of about 8.6 for the ore (cf. Table 2.1). A hole parallel to the one shown was drilled initially along a line through the anomaly centre but encountered pegmatite at the expected ore depth and, owing to the peculiar disposition of the pegmatite dike, continued to be in it without giving any ore. This illustrates well the uncertainties that lurk in geophysical work even when the anomaly is a 'textbook example' and the agreement between observations and calculations is almost as good as might be desired.

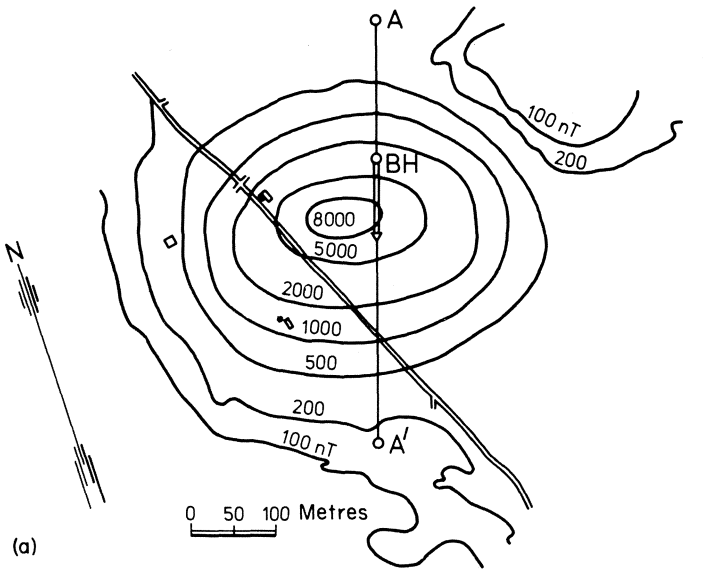

Fig. 2.24(a) A magnetic survey (ΔB_z) in Central Sweden.

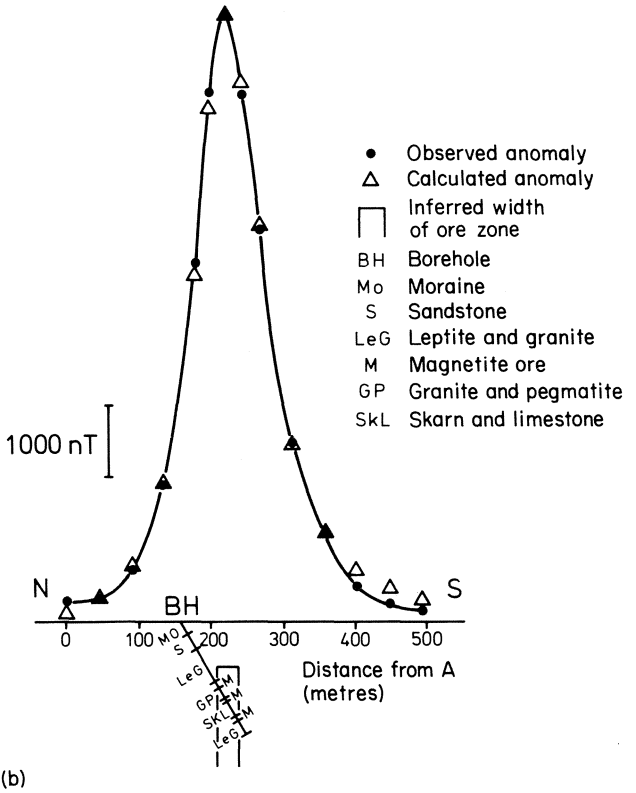

(b) Profile AA′ in Fig. 2.24(a).

2.11.2 Chromite deposits

Magnetic anomalies over two chromite masses (one known before the work) in the Guleman concession area in Turkey (approximately 39°50′ E and 30°30′ N) are shown in Fig. 2.25 [16]. According to Yüngül, the susceptibility of the ore masses is, on the average, 2–18 times smaller than the surrounding ultrabasic or basic rocks (serpentines, peridotites, norites) so that negative anomalies should be expected over the ores. This is at variance with the observations the positive values of which must, therefore, be attributed to permanent magnetization pointing downwards. Now both Cr_2O_3 and $FeCr_2O_4$ occurring in chromite ores are antiferromagnetic, the former with a weak susceptibility. It is, however, conceivable that the latter compound has ferrimagnetic properties so that spontaneous magnetization of the mass may therefore be possible.

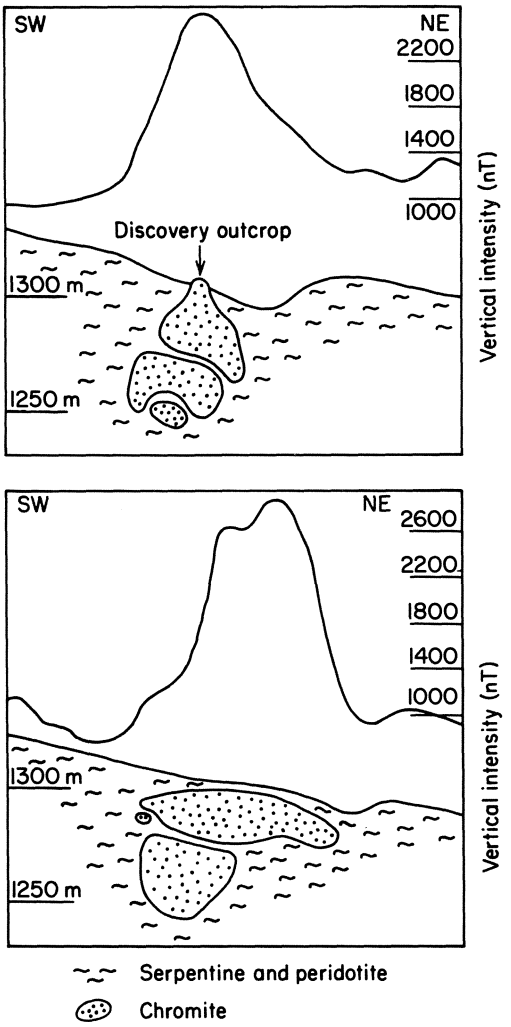

Fig. 2.25 ΔB_z profiles across chromite masses. After [16].

2.11.3 Sulphide body near Lam (Bavarian Forest)

The country rock in this area consists mainly of quartzitic shales and evinces a typical layered structure. The dip of the layers is about 70–80° towards the north. The ore occurs in an impregnation zone as veins concordant with the shales. It contains pyrite, chalcopyrite, pyrrhotite and galena carrying values in silver. Some magnetite is also present.

Two magnetic profiles over the ore are shown in Fig. 2.26 after Zachos [17].

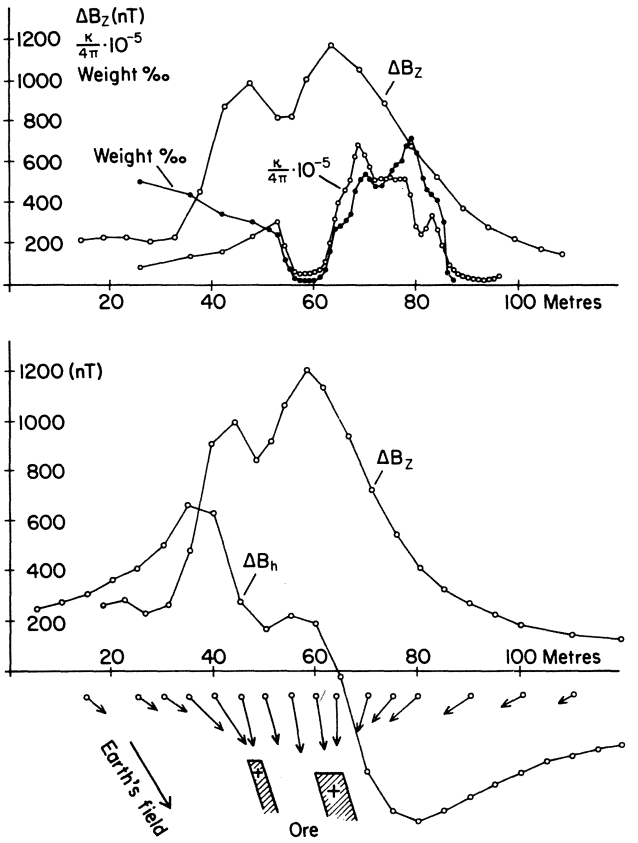

Fig. 2.26 Magnetic profiles across sulphide veins. After [17]. Arrows emanating from open rings in the lower part denote anomalous total field in magnitude and direction.

Maxima in ΔB_z and inflection points in ΔB_h corresponding to each of the two parallel veins are readily evident. The arrows in the lower profile represent anomalous total intensity vectors.

In the upper profile are also plotted (1) the susceptibility (κ) of the rock samples at different places along an underground gallery leading to the ore and (2) the estimated proportion of the total magnetic constituent in the samples. The susceptibility and B_z curves run roughly parallel to each other but the maxima in the former are displaced about 10 m to the north. Zachos attributes this difference to the northerly dip of the veins.

The weight per thousand curve departs from the susceptibility curve at several points. This apparent discrepancy has been attributed to variations in the *magnetite:pyrrhotite* proportion in the samples.

PROBLEMS

2.1 A deep-seated long, thin magnetic ore vein strikes 23° west of north in an area where $I = 27.4°$. From a shaft to the north–east of this body two adits at 200 m and 250 m depth are driven towards the ore perpendicular to the strike. The total-field anomaly was found to be zero at a distance of 567 m from the shaft in the upper adit and 617 m in the lower adit. The vertical-field anomaly was zero at a distance of 28 m from the shaft in the upper adit.

Calculate the dip and depth of the ore vein.

2.2 (a) Determine the parameters of the thick sheet that gives the following near-symmetric vertical-field anomaly along a profile perpendicular to the strike, given that $I = 54°$, $\delta = 30°$. The coordinates are in metres, the 'E' coordinate being in the direction of the horizontal component of the geomagnetic field along the profile.

x	40W	20	0	20E	40	60	80	100	120E
ΔB_z(nT)	180	255	365	525	775	1195	1960	3490	6515

x	140E	160	180	200	220	240	260	280E
ΔB_z(nT)	10295	12745	13970	14485	14465	13755	11805	8265

x	300E	320	340	360	380	400	420	440E
ΔB_z(nT)	5105	3340	2380	1805	1435	1180	995	885

(b) What dip would be indicated if the above anomalies were in the total field?

2.3 A long magnetic dike striking north–south has a rectangular cross-section and a width of 40 m. The depth to the upper surface is 20 m. The component of B_{0z} in a plane at right angles to the strike is 45 000 nT. Exactly above the centre of the dike $\Delta B_z = 260$ nT. The dike has a susceptibility of 0.0112 and a remanent intensity 0.6 A m^{-1} in the same direction as the induced one.

Calculate the depth to the lower face of the dike, neglecting demagnetization effects.

2.4 Verify from Eq. (2.56) that as $b \to 0$ it is only possible to determine the product bM' but not b and M' separately.

2.5 Verify that if, with the convention in Section 2.9.4, $|x_1| > |x_2|$ for the extreme points in ΔB, then $|B$, then $|\Delta B(2)| > |\Delta B(1)|$.

2.6 Prove the result stated in Eq. (2.54).

3

Gravitational methods

3.1 INTRODUCTION

3.1.1 Newton's law and gravitational potential

Newton's law of gravitation states that the force (in newtons) between two *point* masses m_1, m_2 is equal to Gm_1m_2/r^2 where r is the distance between the masses and $G = 6.67 \times 10^{-11}$ [$\approx (20/3) \times 10^{-11}$] $\mathrm{m^3\,kg^{-1}\,s^{-2}}$. The force is one of attraction and acts along the line joining the two point masses. We say that the point mass m_2 is in a field of force (the gravitational field) due to m_1 and vice versa. Since 'Force = Mass × Acceleration', the acceleration of m_2 will be Gm_1/r^2. Indeed, it is evident that the acceleration of *any point* mass due to m_1 will be Gm_1/r^2 towards m_1.

A point mass placed in the vicinity of any body will be in the gravitational field of the body and experience an acceleration if free to move. The total force on the mass due to the body (and hence the acceleration) in any desired direction can be calculated by applying Newton's law to infinitesimal, point mass elements of the body and integrating over the entire volume.

We shall define the gravitational potential due to a *point* mass m at a distance r from itself as

$$V = \frac{Gm}{r} \tag{3.1}$$

With this definition* the acceleration ($\mathrm{m\,s^{-2}}$) of any point mass towards m,

*This is the same definition as that adopted by Kellogg in his classic book on potential theory [18] and (implicitly) by Jeffreys [19], among others. As defined in this manner, V has the dimensions of [$\mathrm{m^2 s^{-2}}$] and represents the work done *by the field* per kilogram of a *point* mass m_0 when m_0 moves from infinity to a distance r from m.

namely Gm/r^2, is given by $-\mathrm{d}V/\mathrm{d}r$, while

$$\frac{\mathrm{d}V}{\mathrm{d}r} = -\frac{Gm}{r^2} \tag{3.2}$$

represents the acceleration in the direction of r. To be more general, with this definition the derivative of V in any direction gives the acceleration of a point mass in that direction. If we are using, say, rectangular coordinates the total acceleration will be the vector sum of the accelerations in the x, y and z directions. This resultant is the gradient of V and is denoted by grad V.

The gravitational potential of an arbitrarily shaped body at a point P, whether inside or outside the body, is

$$V = \int \frac{G\rho \,\mathrm{d}v}{r} \tag{3.3}$$

where $\rho \,\mathrm{d}v$ is the mass of an infinitesimal volume element $\mathrm{d}v$ situated at the point Q of the body, ρ is the density at Q, r is the distance PQ and the integral is taken over the entire volume of the body. The acceleration of a point mass in the vicinity of the body will be grad V as said above.

3.1.2 Potential of a homogeneous spherical shell

To illustrate the application of Eq. (3.3) let us consider a very thin spherical shell of density ρ, radius R and thickness t, and a point P at a distance r from its centre (Fig. 3.1). Since each infinitesimal mass element of the ring AB is at the same distance x from P, the potential $\mathrm{d}V$ at P due to the ring is obtained from Eq. (3.1) simply by replacing r by x and m by the mass of the ring, which is $2\pi R^2 \sin\theta \,\mathrm{d}\theta \times \rho t$. Thus

$$\mathrm{d}V = G\frac{2\pi R^2 \sin\theta \,\mathrm{d}\theta \times \rho t}{x} \tag{3.4}$$

However, with the notation as in Fig. 3.1

$$x^2 = R^2 + r^2 - 2Rr\cos\theta$$

$$x\,\mathrm{d}x = Rr\sin\theta\,\mathrm{d}\theta$$

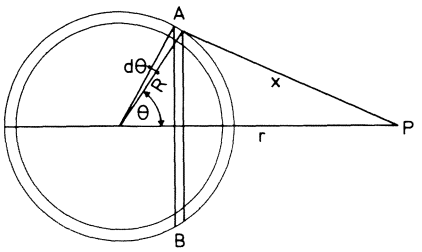

Fig. 3.1 Spherical shell.

Inserting this in Eq. (3.4) and integrating with respect to x, we get the potential V due to the whole shell:

$$V = \frac{2\pi GR\rho t}{r} \int_{r-R}^{r+R} dx$$

$$= \frac{GM_s}{r} \tag{3.5}$$

if P is outside the shell and $M_s = 4\pi R^2 \rho t$ is the mass of the shell. Thus the potential outside the shell is as if the entire mass of the shell were concentrated into a point mass at the centre.

If P is inside the shell the lower limit of the integral above becomes $R - r$ so that

$$V = 4\pi G\rho tR$$

$$= \frac{GM_s}{R} \tag{3.6}$$

The potential at a point inside the shell does not depend on the point's distance from the centre but is constant and equal, in view of (3.5), to the value on the surface of the shell.

3.1.3 Gravitational acceleration due to a homogeneous sphere

A sphere can be considered to be built up of an infinite number of thin shells. For a point outside the sphere we sum the potentials of all these shells as given by (3.5) but since r is the same for all shells the summation simply involves adding the masses of all the shells and this gives the potential of the sphere as

$$V = \frac{GM}{r} \tag{3.7}$$

where M is the mass of the sphere. The gravitational acceleration at the external point is

$$\frac{dV}{dr} = -\frac{GM}{r^2} \tag{3.8}$$

in the direction of r or $+GM/r^2$ towards the centre of the sphere. The acceleration at a point outside the sphere is as if the whole mass of the sphere were concentrated into a point mass at the centre. If the radius of the sphere is R, the acceleration on the surface towards the centre is $GM/R^2 = (4\pi/3)G\rho R$ if ρ is the density of the sphere.

The situation at a point P *inside* the sphere is different. If r is P's distance from the centre, P is on the surface of a sphere of radius r and the acceleration

due to this inner sphere will be $(4\pi/3)G\rho r$ towards the centre. The remaining solid shell between the radius r and the surface of the big sphere can be considered to be built up of an infinite number of thin shells. As the potential of every such shell at P is independent of r, its derivative with respect to r is zero so that the outer solid shell as a whole will not produce any acceleration at P. Thus the gravitational acceleration at a point inside the sphere is $(4\pi/3)G\rho r$ towards the centre, that is, $-(4\pi/3)G\rho r$ in the direction of r, and is proportional to r in contrast to the acceleration outside the sphere which varies as the inverse square of r.

3.2 GRAVITATIONAL FIELD OF THE EARTH

3.2.1 Geopotential and geoid

Besides the acceleration produced by the earth's gravitational potential V, any body attached to the earth experiences a centrifugal acceleration due to the rotation of the earth equal to $\omega^2 d$ if ω is the angular velocity of the earth's rotation and d is the perpendicular distance of the body from the rotation axis.

Let, now, ξ, η, ζ be the coordinates of the body with respect to non-rotating, rectangular axes at the earth's centre, the ζ axis being along the rotation axis. Then the components of the centrifugal acceleration in the three directions are $\omega^2\xi, \omega^2\eta, 0$ since $\xi, \eta, 0$ are the respective perpendicular distances of the body from the rotation axis. These three components can be seen to be the ξ, η, ζ derivatives of a 'centrifugal potential' $\frac{1}{2}\omega^2(\xi^2 + \eta^2)$, and the total potential at the body can therefore be written as

$$W(\xi, \eta, \zeta) = V(\xi, \eta, \zeta) + \tfrac{1}{2}\omega^2(\xi^2 + \eta^2) \tag{3.9}$$

W is called the *geopotential.* A surface on which W has the same value everywhere is called an equipotential surface. The acceleration of a freely falling body on the earth, commonly called the gravity g at the place, is the gradient of W and, as such, is perpendicular to the surface of constant W. A spirit level at a place indicates the horizontal plane and is tangent to an equipotential surface through the place. Hence g is, by definition, in the vertical direction. If we now take an arbitrary point (not lying in the plane of the spirit level) as origin, and define a local x, y, z coordinate system with the x, y plane parallel to the plane of the spirit level, then the gravity at the place of the spirit level is

$$g = \frac{\mathrm{d}W}{\mathrm{d}z} \tag{3.10}$$

where the derivative is to be evaluated at the spirit level. If the earth were a non-rotating homogeneous sphere the z axis (the vertical) would coincide with the radius of the earth but this is not so for the real earth.

The undisturbed surface of the ocean is part of an equipotential surface, the value of W on which is denoted by W_0. This surface and its imagined continuation under the continents, which of course is not accessible, together constitute the *geoid.* On account of its complicated shape the geoid is not a convenient surface of reference to describe the figure of the earth. Instead, in modern descriptions, the earth is approximated by an ellipsoid of revolution containing a mass equal to the earth's actual mass and having an ellipticity (equatorial minus polar radius divided by equatorial radius) = 1/298.25. The surface of this reference ellipsoid is an equipotential surface $W = U_0$ and it follows very closely the mean surface of the ocean for which $W = W_0$.

3.2.2 International gravity formula

On account of the centrifugal acceleration, which varies with latitude, being greatest at the equator and zero at the poles, and to a lesser extent because the earth is not a perfect sphere but flattened at the poles, the value of gravity varies systematically with the latitude ϕ. The variation of g on the reference ellipsoid is defined by the following formula adopted by the International Union of Geodesy and Geophysics in 1967 after a critical evaluation of the available absolute g values on the earth [20]:

$$g = 9.780\,318(1 + 0.005\,3024 \sin^2 \phi - 0.000\,0059 \sin^2 2\phi)\ \mathrm{m\,s^{-2}} \quad (3.11)$$

This formula reproduces the actual values on the earth at sea level within 1 μm s^{-2}. The formula previously adopted by the IUGG in 1930 is still in use for calculating 'normal gravity' at sea level. The difference between the g values calculated from these two formulae is given to the accuracy quoted above by

$$g_{1967} - g_{1930} = (-172 + 136 \sin^2 \phi)\ \mu\mathrm{m\,s^{-2}}$$

3.3 MEASUREMENT OF GRAVITY: ABSOLUTE AND RELATIVE MEASUREMENTS

Some of the most accurate absolute determinations of gravity were made in the 19th century by Kater with his reversible pendulums. The method consists in principle of adjusting the moments of inertia of a bar pendulum such that its periods of oscillation (t) about two knife edges located on either side of the centre of gravity are equal. The distance between the knife edges l is then the length of an ideal simple pendulum of the same period so that $g = 4\pi^2 l/t^2$. Other methods of absolute determination have also been devised, e.g. the free-fall of a mass or the determination of the paraboloid of revolution obtained by revolving a vessel containing mercury around a vertical axis. The free-fall method has now superseded the accuracy of any other method [21].

In applied geophysics, a knowledge of the absolute gravity is not of

immediate interest. We are concerned, as in the magnetic methods, with relative measurements. These give the gravity difference Δg between an observation point and a base point. Appropriate corrections (Section 3.6) must be applied to the differences measured within any region to take account of any known causes of the difference. The corrected Δg values, called the anomalies, yield information about the changes of density within the earth as well as about the surfaces that bound regions of differing density. The information is, however, always subject to certain fundamental ambiguities inherent in the theory of the Newtonian potential (Section 3.9).

Gravity anomalies, being differences in acceleration, can be expressed fundamentally in the SI unit $m\,s^{-2}$ but more conveniently in the sub-unit $\mu m\,s^{-2}$. One $\mu m\,s^{-2}$ is also called a gravity unit (g.u.). In most current geophysical literature before the adoption of SI the unit gal ($cm\,s^{-2}$), named after Galileo, and its sub-multiple, the milligal, are used (1 mgal = 10 g.u.). Since the value of g given by Eq. (3.11) varies between the relatively narrow limits of 9.780 318 and 9.832 177 $m\,s^{-2}$ from the equator to the poles, one g.u. is roughly one ten-millionth (10^{-7}) of the normal gravity at any place on the earth. The maximum gravity anomalies (on the surface) due to concealed features such as salt domes, oil bearing structures, ore bodies, undulations of rock strata etc. are of the order of a few tens to a few hundreds of g.u. and, in fact, for small-scale or deeply buried structures, they may be only a few g.u. Away from such maxima, the distortions in the normal gravity field of the earth may be even smaller, say, $1-10$ parts in 10^8. Apart from the geologic structures just mentioned, large cavities and fracture zones in rocks can also produce significant gravity anomalies that can be used to locate these features.

3.4 GRAVIMETERS

It is clear from the above that relative gravity measurements, if they are to have any wide application, must be made with an accuracy better than a few parts in 10^7 and, preferably, with an accuracy approaching 1–5 parts in 10^8. This aim is achieved in instruments known as *gravimeters*. A number of ingenious gravimeter designs have been proposed during the last fifty years but fundamentally they fall into only two categories, the stable and the unstable types. To this may be added a third type, namely the dynamic, but this has seldom been used for geophysical purposes.

The stable gravimeter can be described briefly as a highly sensitive balance. It contains a responsive element, usually a spring carrying a weight, which is displaced from the equilibrium position when the force of gravity changes. The displacements are always extremely small (of the order of a few tenths of a nanometre) and must be magnified optically, mechanically or electrically. The unstable gravimeter is designed so that when its sensitive element is displaced due to a change in the gravity, other forces tending to increase the

displacement come into play. The gravity change can be measured by the force necessary to return the element to its equilibrium position. Brief descriptions of some gravimeter designs are given below to illustrate the principles.

3.4.1 Stable types

3.4.1.1 Askania

In this instrument (Fig. 3.2(a)) a beam carrying a mass at one end is held horizontally by means of a main spring (*S*). A mirror placed on the mass reflects a light beam into a double photoelectric cell. The movement of the mass due to a change in the gravity is indicated by the deflection of a galvanometer through which the differential current from the photoelectric cell is led. The mass is restored to the equilibrium position by varying the tension in the auxiliary spring (*S'*). Calibration can be effected by means of small known weights brought on the beam by tilting the instrument.

3.4.1.2 Gulf (Hoyt)

This gravimeter utilizes a helical spring formed from a ribbon (Fig. 3.2(b)). One end of the spring is rigidly clamped while the free end carries a mass with a mirror. An elongation of a helical ribbon spring is always accompanied by a rotation of the free end. In the Gulf gravimeter the rotation is much greater (and therefore can be read more accurately) than the elongation (or the contraction) of the spring caused by a change in the gravity. The range of the instrument is only about 300 g.u. so that a readjustment of the tension in the

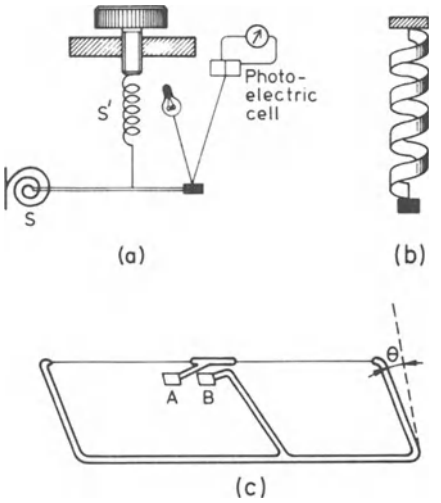

Fig. 3.2 Stable gravimeters.

helix is necessary if gravity differences larger than this amount are to be measured. The accuracy is of the order of 0.2–0.5 g.u.

3.4.1.3 Nörgaard

This is one of the gravimeters (Fig. 3.2(c)) combining a wide range (about 20 000 g.u.) with a relatively high accuracy (about 1 g.u.). A small quartz beam carrying a mirror A is supported horizontally from a quartz thread, the torsion in the latter counteracting the force of gravity. The mirror A is initially parallel to the fixed mirror B as is indicated by the coincidence of two index lines in the field of a telescope. When the beam deflects due to a change in the gravity, coincidence can be achieved again by tilting the entire frame through an angle θ. There are two such positions of the frame, one on each side of the initial position. At coincidence the torsion moment of the thread must always be the same (mg_0l) so that if g and g_0 are the gravity values at two stations then $g \cos \theta = g_0$.

The instrument can be calibrated by tilting it at small known angles.

3.4.2 Unstable types

3.4.2.1 LaCoste–Romberg

This gravimeter is essentially an adaptation of the long-period LaCoste seismograph [22, 23] which uses a 'zero-length' spring. Such a spring is wound so that its extension is equal to the distance between the points at which its ends are fastened. Thus, the length defined as the actual physical length minus the extension is zero. The zero length spring S (Fig. 3.3(a)) is attached rigidly to the frame at C and balances the mass M at the end of a beam. With the geometry as in the figure, it is easy to show that the net torque on the mass is $(Mg \times \overline{AM} - k \times \overline{AB}^2) \sin \theta$ where k is the spring constant. If $Mg \times \overline{AM} = k \times \overline{AB}^2$ the torque becomes zero, the period infinite and the equilibrium unstable. The instrument is then very sensitive to variations in g.

Readings are taken by restoring M to the original position by raising or lowering C by means of a screw with a calibrated dial. The accuracy is of the order of 0.2 g.u.

3.4.2.2 Worden

The principle of this instrument is very similar to that of the LaCoste–Romberg gravimeter. The mass, M (Fig. 3.3(b)), is kept in unstable equilibrium by the zero length quartz spring, BC, whose one end is attached to an arm AB inclined at a fixed angle α to AM. Both AM and AB are hinged at A to a torsion thread. If θ is the deflection of AM from the horizontal the net torque on the beam system is easily seen (on applying the elementary sine theorem to the

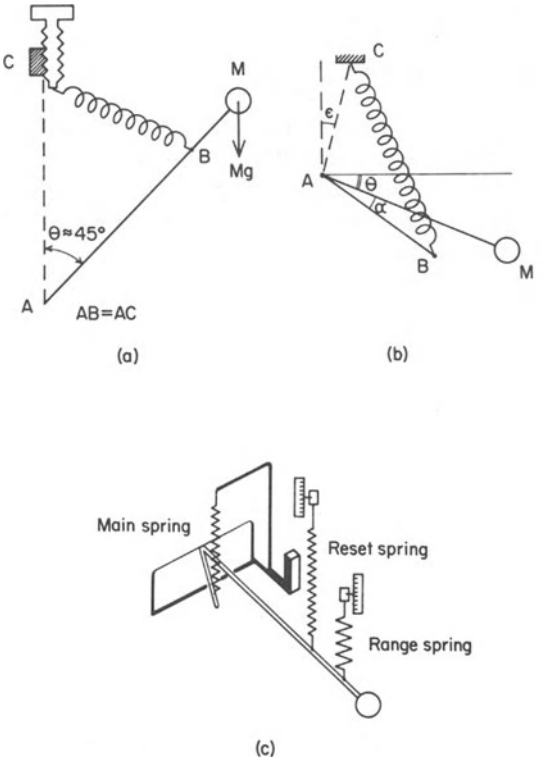

Fig. 3.3 Unstable gravimeters.

triangle ABC) to be $mg\overline{AM}\cos\theta - \tau(\theta+\theta_0) - k\overline{AC}\times\overline{AB}\cos(\alpha+\theta-\varepsilon)$ where θ_0 is the permanent torsion in the quartz thread and τ is the torsion constant.

By suitable choice of the different constants and the position of C ($\varepsilon \approx 0$), the equilibrium can be made unstable and the system becomes very sensitive to variations in g. The equilibrium is restored by means of auxiliary springs arranged as shown in Fig. 3.3(c), one of which determines the range of g measurable by the instrument and the other compensates for the variations in g for a particular setting of the range spring. The instrument is temperature compensated by auxiliary quartz springs and, moreover, the entire system, except for the reading dials, levels, etc. is kept in a small sealed thermos flask. The total weight of the instrument including the case is about 5 kg but the mass M (made out of fused quartz) weighs only a few milligrams. The accuracy is 0.1–0.2 g.u. and the range of the instrument is wide, namely about 20 000 g.u.

3.5 FIELD PROCEDURE

3.5.1 Primary and secondary base nets

In most, now probably in all, countries of the world values of g have been established at a number of topographically and geographically well defined reference stations. These form the *primary base nets* of gravity stations. In all but a few handfuls of cases these values have been established indirectly by measurements of the difference of g between a base station and a place where g is already known, ultimately derived, of course, from one of the direct absolute determinations of g in the world. Once a primary net has been established any two stations in it with adequate gravity difference can, in turn, be used to calibrate a gravimeter. As the primary stations are generally sparsely distributed it is often found convenient in large-scale exploration surveys to establish a *secondary net* within the area of interest, connected to one or more stations of the primary net. In many exploration surveys, however, when only changes in g are deemed to be of interest no connection with the primary net is made and the differences are simply referred to a local base at which the value of g is arbitrarily designated as zero.

3.5.2 Local and regional surveys

Gravimeter observations are usually made at the corners of a square grid. The length of the side of the square will depend upon the anticipated dimensions of the features to be located. In oil prospecting the grid side may be of the order of 0.5–1 km or more, while in mineral exploration the stations must often be spaced on a grid with sides no larger than 10–50 m. For other purposes, such as the location of dikes or geological faults, the spacing may be anywhere between these extremes. In large-scale or regional surveys it is also the general practice to establish gravimeter stations along roads.

The geographical positions and the elevations of gravimeter stations must be accurately known in order to reduce the readings to standard reference conditions, as described below. The elevations may be determined by spirit-levelling or barometrically [24].

3.5.3 Drift of gravimeters

The readings of all gravimeters drift more or less with time, due to elastic creep in the springs. This apparent change in the gravity at a station may be from a few tenths of a g.u. to about 10 g.u. per hour. In order to correct for it, the measurements at a set of stations are repeated after 1–2 h and the differences obtained are plotted against the time between two readings at a station. A 'drift curve' can then be drawn and the corrections read off it. In accurate work it is

advisable to determine the drift curve by a least squares adjustment. This is usually straightforward since most gravimeters drift linearly with time. Parabolic or other drift functions are, however, not uncommon.

3.6 CORRECTIONS TO GRAVITY OBSERVATIONS

The gravity difference between two stations is in part due to factors other than the attraction of unknown anomalous masses. These factors and the corrections due to them are as follows.

3.6.1 Latitude

The value of gravity increases with the geographical latitude. By differentiating Eq. (3.11) we get

$$\frac{dg}{d\phi} = 51\,859 \sin 2\phi \text{ g.u./rad}$$

If the latitude difference between two stations is small the correction becomes

$$\delta g = 0.081 \sin 2\phi \text{ g.u. per } 10\,\text{m (north–south)} \tag{3.12}$$

since the mean radius of the earth is $R = 6368$ km.

It must be substracted from or added to the measured gravity difference accordingly as the station is on a higher or lower latitude than the base station. The correction is linear to distances in the N–S direction of the order 1–2 km (about 0.5–1 minute of latitude) on either side of the base. If the measurements extend beyond this distance a new base station must be selected and the difference between the normal gravity at it and the first base must be determined by reference to Eq. (3.11).

If the north–south distance of a station from the base is known to within 10 m, an accuracy which it is normally not in the least difficult to achieve, the latitude correction will be known to better than one tenth of a g.u.

3.6.2 Elevation

The force of gravity outside the earth varies in inverse proportion to the square of the distance from the earth's centre. If g_1 be its value at the datum level (not necessarily the sea level), then at a height h above it,

$$g = g_1 \frac{R^2}{(R+h)^2} \approx g_1(1 - 2h/R) \tag{3.13}$$

if powers of h/R higher than the first are neglected. In most practical cases the distance of the datum level from the earth's centre may be taken to be equal to the mean radius of the earth. The correction for the elevation (the 'free-air

correction') is then

$$\delta g = \frac{2g_1}{R}h = \begin{cases} 3.072\,h \text{ g.u. } (h \text{ in metres}) & \text{at the equator} \\ 3.088\,h \text{ g.u.} & \text{at the poles} \end{cases} \tag{3.14}$$

The mean amount 3.080 g.u. per metre of elevation, which is sufficiently accurate for most purposes, must be added to a measured gravity difference if the station lies above the datum level and substracted if it lies below it.

If an accuracy of 0.1 g.u. is aimed at in relative gravity measurements, elevation differences from the datum level must be known to be better than 4 cm.

3.6.3 Material between station levels

It will be realized by reference to Fig. 3.4 that while the gravity at B will be less than that at A by an amount $2g_1h/R$ (free-air correction), it will be greater by an amount $\delta g = 2\pi G\rho h$. This is the additional attraction exerted on a unit mass by the slab of rock material of density ρ (kg m^{-3}) between the levels of A and B. The correction

$$\delta g = 0.4191 \times 10^{-3}\rho \text{ g.u. per metre (of elevation)} \tag{3.15}$$

is called the Bouguer correction. It must be substracted from the measured gravity difference if a station lies above the level of the base station and added if it lies below.

In the above we have assumed that the slab between A and B is of infinite extent in all horizontal directions, but actually this is not the case. For a point like B whose distance from any edge of the slab is large compared with h the slab may be considered to be of infinite extent. But for a point E near an edge the correction according to (3.15) is overestimated, because the attraction of material that actually does not exist (to the left of E in this simple illustration) has also been removed. To get the proper correction this attraction must be

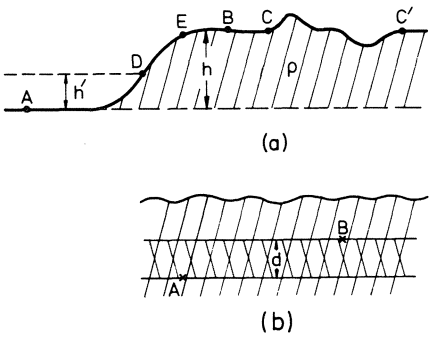

Fig. 3.4 Topographic correction.

estimated and re-added! For a point D on the slope the situation after applying (3.15) is that, not only has the attraction of non-existent material of thickness h' been subtracted from the measured Δg, but the upward attraction of *existing* material to the right of D and above its level has not been accounted for.

In fact, for points like E or D it is advisable to dispense with the Bouguer correction of Eq. (3.15) altogether and calculate instead the attraction of the topography as a whole by dividing it into a number of suitable masses (e.g. semi-infinite slabs, prisms etc.). The attraction of an individual mass, calculated by formulae like those in Section 3.9, is then subtracted from the measured Δg if the mass lies below the level of the point of observation and added it it lies above. This is, strictly speaking, the only proper manner of estimating the *topographic correction* at any observation point, but for points like B or C considerable labour is saved by dividing the topographic correction into a *Bouguer correction* according to Eq. (3.15) and a *terrain correction* for local relief described in the next section.

When measurements are made below the earth's surface the slab of material between A and B (Fig. 3.4(b)) exerts an attraction on a unit mass placed at A as well as B. The attractions being in opposite directions, the difference of gravity between A and B due to the slab is $4\pi G\rho d$ and the Bouguer correction is doubled ($0.8382 \times 10^{-3}\,\rho$ g.u. per metre).

3.6.4 Local relief

At a point like C the major contribution to Δg that comes from topography is removed by the Bouguer correction. However, a nearby local terrain irregularity (hill, knoll etc.) will also exert an attraction directly proportional to its density. The vertical component ($T\rho$) of this attraction will be directed upwards and reduce the gravity at C. A term of this magnitude must therefore be added to the measured value of gravity at C. A valley such as that near C' is a negative mass and the vertical component of its attraction will also be directed upwards leading again to an additive terrain correction.

The terrain correction is often calculated by dividing the area around a station in compartments bounded by concentric rings and their radii drawn at suitable angular intervals (ϕ). The mean elevation (z) in each compartment is determined from a topographic map, without regard to sign, that is by treating a hill as well as a valley as a positive height difference from the station level. The correction due to the attraction of the material in such a compartment is

$$\delta g = T\rho = G\rho\phi[r_2 - r_1 + \sqrt{(r_1^2 + z^2)} - \sqrt{(r_2^2 + z^2)}] \qquad (3.16)$$

where r_1, r_2 are the radii of the inner and outer rings bounding the compartment.

Tables of the bracketed expression in (3.16) have been published, but with the general availability of small programmable calculators it has become easy,

and is in fact preferable, to prepare one's own tables by choosing r_1, r_2 values that best suit the survey and the terrain in question. The calculation of terrain corrections is very tedious and it is therefore fortunate that they are not needed as a rule except for stations in the immediate vicinity of a 'violent' topographic irregularity. There is no compelling reason for a circular division of the terrain except some convenience in *manual* calculations. For computer-adapted procedures a rectangular grid division is preferable. In a method suggested by Ketelaar [25] the terrain surface is approximated by square prisms with sloping upper surfaces. The correction due to a prism characterized by the matrix indices i, j, and surface slope α, is shown to be

$$\delta g(i, j) = G\rho D(1 - \cos\alpha)K(i, j)$$

where D is the grid side. The matrix $K(i, j)$ can be calculated once for all.

There is no real difference in the procedure for calculating the topographic correction at points like D and the terrain correction at C.

3.6.5 Tides

The attractions of the sun and the moon may change the gravity at a station cyclically with an amplitude of as much as 3 g.u. during the course of a day. The correction cannot be calculated in any simple way and recourse must therefore be had to tables regularly published in advance for each year [26]. The drift correction to gravimeter readings includes, in part, the tidal correction.

3.7 THE BOUGUER ANOMALY

It will be seen now that the corrected gravity difference between a station at a point like C in Fig. 3.4 and a base is

$$\Delta g_{\text{corr}} = \Delta g_{\text{obs}} + 3.080h - 0.4191 \times 10^{-3}h\rho + T\rho \text{ g.u.} \qquad (3.17a)$$

where h is positive if the station is above the base and negative if it is below. The latitude and tidal corrections are included in the term Δg_{obs}. The last two terms on the right-hand side will be replaced by a single topographic correction term for points like D or E in Fig. 3.4(a). The density of the topographic irregularity in Fig. 3.4 has been assumed to be the same as that of the infinite slab, namely ρ. This assumption may not always be justified.

The numerical coefficient of the third term on the right-hand side must be doubled if measurements are made underground. In such measurements T may be negative if, for instance, tunnels are situated *above* the level of a station.

The difference Δg_{corr} is called the *relative* Bouguer anomaly. In many regional surveys when absolute values of g are determined it is usual to calculate the *absolute* Bouguer anomaly. This is given by

$$\Delta g_{\text{B}} = g - (g_0 - 3.086H + 0.4191 \times 10^{-3}\rho H - T\rho) \qquad (3.17b)$$

where g_0 is the sea-level value given by (3.11) at the latitude in question and H is the height of the station above sea level. The bracketed quantity in (3.17b) is the expected value of gravity under the assumptions underlying Eq. (3.11) and the assumptions involved in the estimates of the three correction terms in the bracket.

The variations of Δg_{corr} or Δg_{B} within an area can be properly attributed to the variations of density below the respective datum level (level of base station or that of the sea) *only provided* the total topographic correction accounts exactly for the whole geometry of the topography and for all inhomogeneities in the material between the station level and the datum level. Since this situation is not realized in practice even remotely, the Bouguer anomaly actually represents the attraction, at points on the physical surface of the earth, of all inhomogeneities in the earth, above as well as below the datum level. The reader should also be on guard against the loose expression that Δg_{corr} or the bracketed quantity on the right-hand side in (3.17b) is the 'gravity reduced to the datum level'. It should be realized that the gravity measured on the datum level, at a point B', vertically below B in Fig. 3.4(a), for example, will *not* differ from that at B by Δg_{corr}, even if it were possible to calculate the topographic correction absolutely perfectly, because the effect of any inhomogeneities below the datum level is not the same at B as at B'.

3.8 DENSITY DETERMINATIONS

Strictly speaking, any value may be chosen for ρ for the reductions in Eq. (3.17). However, it is clearly desirable to eliminate the effect of surface features as far as possible by using the true (average) value for their density.

The density may be estimated by laboratory measurements on samples of the rocks exposed within the area of interest. But such estimates suffer from the fact that the samples may be weathered or in other ways unrepresentative. Furthermore, the density of the rocks at depth may be different from that of the surface samples, owing to a variable water content and, in the case of 'loose' rocks like clays, marls, moraine, etc., owing to significant compaction even at moderate depths. Therefore various 'field' methods have been suggested for the determination of ρ. In Nettleton's method [27], the Bouguer anomalies at the stations on a line of measurement are calculated assuming different values of ρ. The anomalies that show the least correlation with the topography are adopted as the true anomalies, the corresponding ρ being adopted as the true average density of the surface rocks. Nettleton's original method is graphical, but Jung [28] pointed out that it can be translated into exact mathematical language by putting the correlation coefficient between Δg_{corr} and h equal to zero. We then get

$$\rho = \rho_0 + \frac{\sum(\Delta g_{\text{corr}} - \overline{\Delta g}_{\text{corr}})(h - \bar{h})}{0.000\,4191 \sum(h - \bar{h})(h - \bar{h} + T - \bar{T})} \tag{3.18}$$

where ρ_0 is an appropriate assumed value of ρ to which a 'correction' term must be added to obtain the true ρ.

In a method proposed by Parasnis [29], $\Delta g_{obs} + 3.086h$ in Eq. (3.17) is plotted against $(-0.0004191\ h + T)$ and the slope of the straight line (determined by least squares) is adopted as the true ρ. This is equivalent to assuming Δg_{corr} (the Bouguer anomaly) to be a random error. In this case

$$\rho = \rho_0 + \frac{\sum(\Delta g_{corr} - \overline{\Delta g}_{corr})(h - \bar{h} + T - \bar{T})}{0.0004191 \sum(h - \bar{h} + T - \bar{T})^2} \tag{3.19}$$

The essential prerequisite for Nettleton's method, on the other hand, is that the topographic relief must be due purely to erosion. While the two equations (3.18) and (3.19) reduce to identical forms if $T = 0$, the two values differ but little (a few parts in a thousand) in a normal actual case even if $T \neq 0$.

The above methods deal with stations along a 'line'. Strictly speaking, the density obtained from (3.18) and (3.19) is valid only for these stations and the intermediate points. Legge [30] and Jung [31] have shown that the least squares method leading to (3.19) can be generalized to apply to a set of measurements over an area also.

3.9 INTERPRETATION

Generally speaking we may say that a Bouguer anomaly that is negative with respect to the surrounding anomalies indicates masses of density lower than the density of the surrounding rocks. Similarly positive Bouguer anomalies indicate masses of higher density than the surroundings. The anomalies in gravity arise from relatively small density differences (δ) between rock

Table 3.1 Densities ($kg\,m^{-3}$)

Oil	900	Granite	2500–2700
Water	1000	Anhydrite	2960
Sand, wet	1950–2050	Diabase	2500–3200
Sand, dry	1400–1650	Basalt	2700–3300
Coal	1200–1500	Gabbro	2700–3500
English chalk	1940	Zinc blende	4000
Sandstone	1800–2700	Chalcopyrite	4200
Rock salt	2100–2400	Chromite	4500–4800
Keuper marl	2230–2600	Pyrrhotite	4600
Limestone		Pyrite	5000
(compact)	2600–2700	Haematite	5100
Quartzite	2600–2700	Magnetite	5200
Gneiss	2700	Galena	7500

formations and the interpretation is naturally sensitive to the adopted density values. It is, therefore, important to obtain reliable density estimates of the rocks in an area, preferably by a combination of the laboratory and field methods of the previous section. The densities of some commonly encountered rocks and minerals will be found in Table 3.1.

We must now discuss a problem which very frequently appears in gravity interpretation and which must be resolved before proceeding to a quantitative interpretation of gravity data in terms of the sizes and shapes of concealed masses.

3.9.1 Regionals and residuals

Fig. 3.5 shows a map of absolute Bouguer anomalies and a profile in the area. We note here, especially from the profile, that a slow change of Δg with distance from one end of the map to the other is found to be superimposed on a faster variation apparent in the central part. These two types of variation are termed regional and local respectively. Either may be the object of detailed interpretation and is then separated from the other, in which case it is called the *residual* variation. More commonly it is the local variations that are of immediate interest in a small-scale survey and the term residual is commonly understood to imply these while a regional variation is termed a trend. What is often called *trend analysis* is essentially a process of separating regionals and residuals.

It is important to realize from the outset that there is no unique way of separating regionals and residuals on the basis of gravity data alone, analytically or otherwise. The reason is simply the obvious fact that a given number cannot be uniquely decomposed into two or more numbers whose sum it is unless extraneous constraints are placed. Nevertheless, for the sake of speed and uniformity in treating the data, it is often desirable to use some standardized procedure to separate different types of gravity variations.

One method is to take the average of a set of symmetrically placed values around a point, subtract it from the value at the point, and prepare a map of the residuals thus obtained. A more sophisticated procedure is to express the gravity field in the area by a low-order polynomial, e.g.,

$$\Delta g(x, y) = Ax + By + 2Cxy + Dx^2 + Ey^2 + F$$

and determine the coefficients $A, B \ldots$ etc. by a least squares adjustment. The residuals are obtained by subtracting the polynomial values from the measured ones. The polynomial, being of low order, represents slow or large-scale variations which are usually attributed to deeper causes, although this need not be their origin, a point that is easily overlooked.

Still more sophisticated procedures using Fourier transformation of the data have also been suggested [32]. In the other extreme, graphical methods in

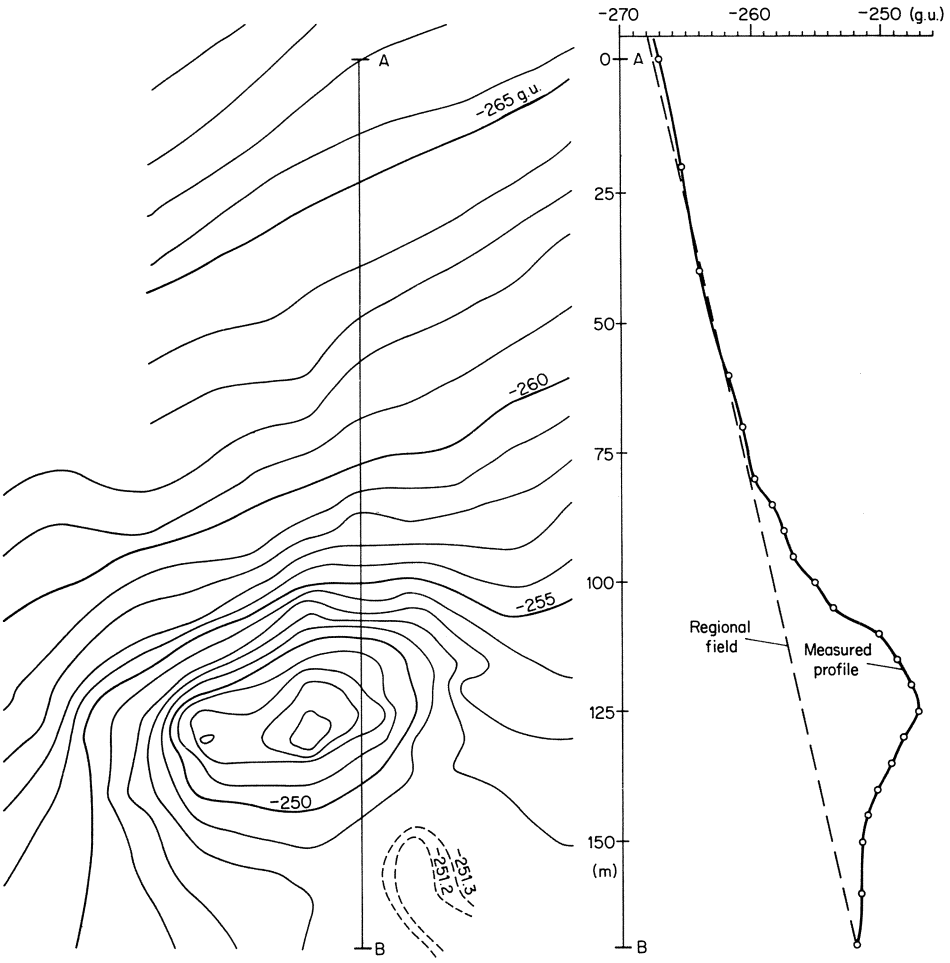

Fig. 3.5 Map of absolute Bouguer anomalies and profile showing regional gravity gradient.

which contours or profiles are smoothed freehand to separate a smooth trend and local variations may be found to be adequate in many cases.

Finally it should be remembered that there are trends that cannot be satisfactorily approximated by a polynomial, no matter of what degree. An example is a trend like the Δg curve in Fig. 3.6(c). More complicated functions, for example $\Delta g = C \tanh mx$, may be necessary in treating such trends analytically.

3.9.2 Anomalies of different bodies

The quantitative interpretation of gravity anomalies in terms of sub-surface mass distributions follows a pattern similar to the interpretation of magnetic

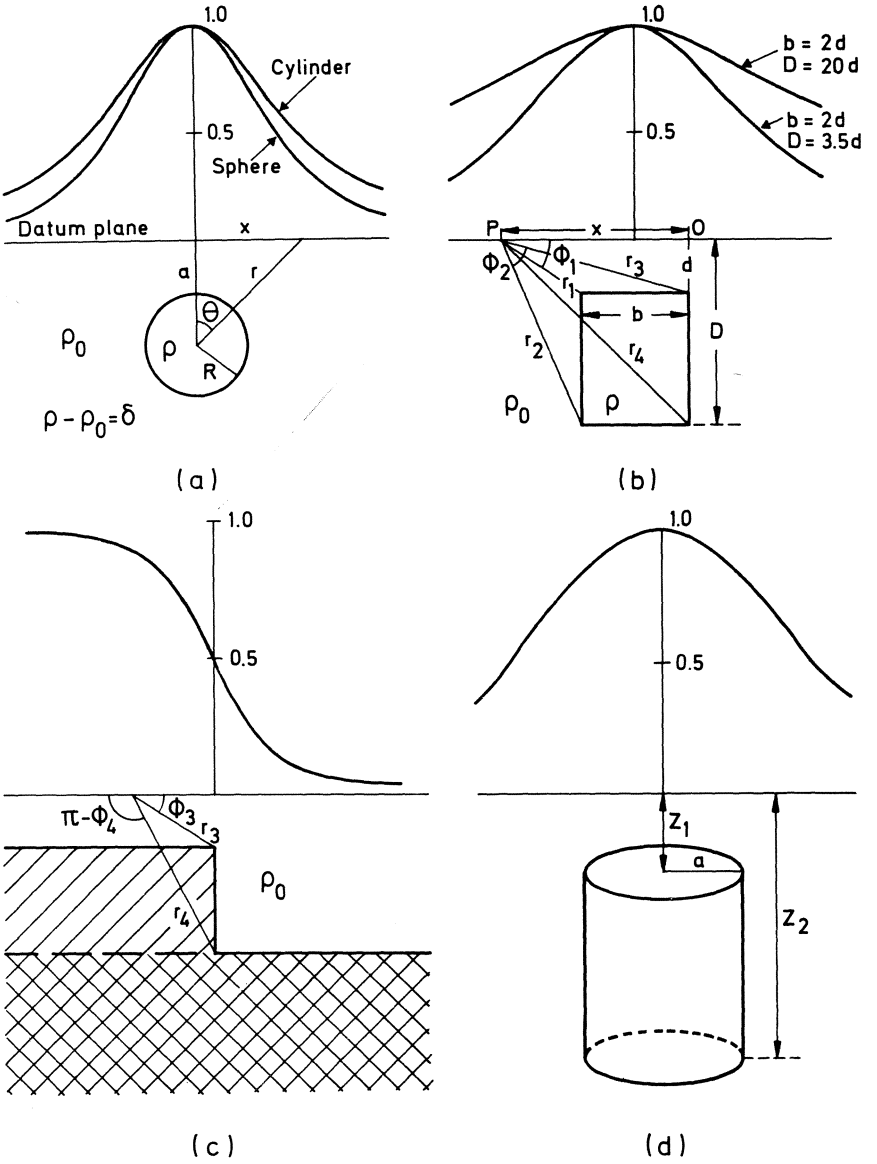

Fig. 3.6 Gravity anomalies across some bodies of simple geometrical shape.

anomalies (Chapter 2). The mass distribution is assumed to correspond to some plausible simple structure and the parameters of the structure are adjusted until its calculated anomaly at all points agrees satisfactorily with the observed anomaly. (The adjustment can be done by computer optimization programs.) For this purpose we need to know the gravity anomalies produced

by a variety of type-structures (Fig. 3.6). Some formulae for such anomalies will be discussed below. Their derivation is generally elementary.

3.9.2.1 Sphere

We have already found the gravitational attraction of a sphere in Eq. (3.8). The gravity anomaly due to a spherical body is the vertical component of this attraction. Then denoting by δ the density excess of the sphere over its surroundings we get, in the notation of Fig. 3.6(a),

$$\Delta g = \frac{4}{3}\pi R^3 G\delta \frac{\cos\theta}{r^2}$$

$$= \Delta g_{\max}/(1 + x_a^2)^{3/2} \tag{3.20}$$

where $\Delta g_{\max} = \Delta g$ at $x = 0$ and $x_a = x/a$. It should be noted that even if the cause of an anomaly is *known* to be a spherical body, its radius and density difference from the surrounding rock cannot be separately determined with the knowledge of the gravity field alone. This is because all spheres with the same value for the product $R^3\delta (R < a)$ and having the same centre produce identical gravity fields at the surface.

As an example of an approximately spherical body we may take a boulder. A boulder of 1 m radius is buried in an otherwise homogeneous moraine with which it has a density contrast $\delta = 1000\,\mathrm{kg\,m^{-3}}$. If it just touches the surface of the ground, the gravity anomaly directly above its centre will be 0.28 g.u.

3.9.2.2 Long, horizontal cylinder

We take Fig. 3.6(a) to represent an infinitely long cylinder striking at right angles to the plane of the paper. Its gravitational attraction at an external point is $2G\mu/r$ towards the axis, μ being the mass per unit length. The gravity anomaly along a line of the ground, perpendicular to the cylinder, is therefore

$$\Delta g = \frac{2\pi G R^2 \delta}{r}\cos\theta$$

$$= \frac{2\pi G R^2 \delta a}{r^2}$$

$$= \frac{\Delta g_{\max}}{(1 + x_a^2)} \tag{3.21}$$

where $\Delta g_{\max} = 2\pi G R^2 \delta/a$. Note that $\Delta g_{\max}$ decreases as the first power of the depth to the cylinder axis.

As an example we may note the following. A long, horizontal underground tunnel of circular cross-section (radius 1 m), driven in a rock with density $2700\,\mathrm{kg\,m^{-3}}$ will produce a maximum decrease of 0.113 g.u. in the gravity at the surface if the axis of the tunnel is at a depth of 10 m.

3.9.2.3 Long prism of rectangular cross-section

The cross-section of an infinitely long prism striking perpendicular to the plane of the paper is shown in Fig. 3.6(b). The angles made by the lines $r_1, r_2, \ldots$, etc. with the horizontal are denoted by $\phi_1, \phi_2, \ldots$, etc. We have then

$$\Delta g = 2G\delta\left[x \ln\frac{r_1 r_4}{r_2 r_3} + b \ln\frac{r_2}{r_1} + D(\phi_2 - \phi_4) - d(\phi_1 - \phi_3)\right] \qquad (3.22)$$

This formula can be obtained as a special case of Eq. (3.26) for the anomaly of a rectangular parallelepiped by letting the parallelepiped extend to infinity in one of the horizontal directions.

The rectangular prism is one of the versatile models which can be used to approximate a wide variety of geological features, as we shall see below.

Ridge or undulation. If we imagine the lower boundary face to be extended indefinitely in the horizontal plane, the figure would represent a buried ridge (horst) or sharp undulation of the bedrock. The formula (3.22) is not altered in any way provided the density of the material beneath the extended lower surface is the same as that of the prism material.

Graben, buried channel etc. If we imagine the upper boundary surface to be extended indefinitely in the horizontal plane and assume that the surface slab thus obtained has the same density ρ as the prism, the structure will approximate a graben or buried valley, channel etc. with steep sides. The formula (3.22) remains the same. In this case, the effect of the surface slab will appear as a constant, superposed anomaly that will be removed in the interpretation as a regional trend.

Infinite slab. If the vertical faces be moved in opposite directions to infinity, $r_1 \to r_2, r_3 \to r_4, \phi$ and $\phi_2 \to \pi, \phi_3$ and $\phi_4 \to 0$ so that Eq. (3.22) reduces to

$$\Delta g = 2\pi G\delta(D - d) \qquad (3.23)$$

The anomaly of an infinite slab depends only on the thickness ($D - d$ in Eq. (3.23)) and not on the depth to the top surface of the slab. Equation (3.23) is the basis of the Bouguer correction in Section 3.6.3.

Infinitely long vein or dike. If the lower surface of the prism were moved downwards to a very large depth, Fig. 3.6(b) would correspond to a vein or dike. In this case $r_2 \to r_4 \approx D$ and $D(\phi_2 - \phi_4) \to b$ in Eq. (3.22). The anomaly of an infinitely long dike increases indefinitely with its depth extent since $r_2 \to \infty$ in the second term but the increase is very slow.

Step structure or fault. The structure shown in Fig. 3.6(c) is a special case in which one of the vertical faces of the prism is moved to infinity. The prism then becomes the singly-hatched portion of the diagram. The anomaly of this configuration is obtained from (3.22) by putting $r_1 = r_2$ and $\phi_1 = \phi_2 = \pi$ but δ in this case will be the density difference between the materials of the singly-hatched and the empty portions of the figure, assuming that the substratum

(doubly hatched portion) has some uniform density:

$$\Delta g = 2G\delta\left[x \ln\frac{r_4}{r_3} + \pi(D-d) - D\phi_4 + d\phi_3 \right]$$

If the two hatched portions have the same density we have either a buried erosional *escarpment* or a *geologic fault* in which the rock block on one side of a vertical plane has been thrust downwards or upwards with respect to the block on the other side. The 'throw' of the fault is $(D-d)$. It is easily verified that total variation of Δg across a fault is $2\pi G\delta(D-d)$.

If the density of the doubly hatched portion is different from the densities of both overlying materials, the singly-hatched portion will represent a laccolith, a thick flat-lying lava bed etc.

3.9.2.4 Vertical cylinder

The anomaly of a vertical cylinder (Fig. 3.6(d)) at a point on its axis is given by

$$\Delta g = 2\pi G\delta[z_2 - z_1 + (z_1^2 + a^2)^{1/2} - (z_2^2 + a^2)^{1/2}] \tag{3.24a}$$

If $z_2 \to \infty$,

$$\Delta g = 2\pi G\delta[(z_1^2 + a^2)^{1/2} - z_1] \tag{3.24b}$$

and, if, in addition, $z_1 \to 0$,

$$\Delta g = 2\pi G\delta a \tag{3.24c}$$

These equations show that the attraction of a vertical cylinder remains finite as its depth extent increases, in contrast to the attraction of an infinitely deep-going dike.

The anomaly at a point off the axis is difficult to calculate and cannot be expressed in a simple form like Eq. (3.24a) above [33].

The vertical cylinder is a useful model for features like certain diapirs, salt domes and mine shafts.

3.9.2.5 Rectangular parallelepiped

A surprisingly large number of geological structures can be adequately represented by the above regular shapes and their combinations, especially the prism of polygonal cross-section. However, a prism of infinite length is not a good approximation to geological structures whose length in the strike direction is comparable to the largest linear dimension in the cross-section, or when it may be necessary (as in estimating topographic corrections) to divide a structure into finite blocks. In such cases a rectangular parallelepiped is often a very useful 'building block'.

The anomaly due to a homogeneous rectangular parallelepiped with density contrast $\delta = \rho - \rho_0$ (Fig. 3.7) can be calculated easily. With the origin of coordinates at the observation point P and the axes as shown, the

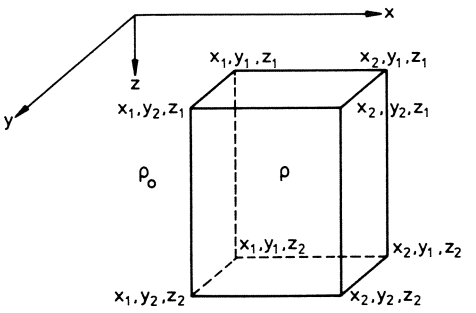

Fig. 3.7 Rectangular parallelepiped.

gravitational attraction due to a mass element $\delta \times dx\,dy\,dz$ towards the element is obtained from Eq. (3.2) simply by replacing m by $\delta \times dx\,dy\,dz$. The gravity anomaly $d(\Delta g)$ due to the element is the vertical component of the attraction, so that

$$d(\Delta g) = \frac{G\delta \times dx\,dy\,dz}{r^2} \cos\theta$$

$$= \frac{G\delta \times dx\,dy\,dz}{r^2} \frac{z}{r}$$

$$= \frac{G\delta \times z\,dx\,dy\,dz}{(x^2 + y^2 + z^2)^{3/2}}$$

The anomaly due to the entire parallelepiped is then

$$\Delta g = G\delta \int_{x_1}^{x_2} \int_{y_1}^{y_2} \int_{z_1}^{z_2} \frac{z\,dx\,dy\,dz}{(x^2 + y^2 + z^2)^{3/2}} \tag{3.25}$$

The successive definite integrals can be found from a table of elementary integrals. The algebra is somewhat tedious but quite straightforward, and the final result can be expressed in a form convenient for computer (or calculator) programming as

$$\Delta g = \sum_{\substack{i,j,k \\ =1,2}} (-1)^{i+j+k-1} f(x_i, y_j, z_k) \tag{3.26}$$

where the eight terms in the summation are functions of the coordinates $x_i, y_j, z_k (i, j, k = 1, 2)$ of the eight corners of the parallelepiped with

$$f(x, y, z) = G\delta \left[x \ln \frac{y + r}{(x^2 + z^2)^{1/2}} + y \ln \frac{x + r}{(y^2 + z^2)^{1/2}} + z \tan^{-1}\left(\frac{zr}{xy}\right) \right] \tag{3.27}$$

and

$$r = (x^2 + y^2 + z^2)^{1/2}$$

Gravity anomalies of general polyhedra, that is, of bodies bounded by faces that are arbitrary polygons, have been dealt with by Coggon [34]. Graphical methods for estimating the gravity effects of finite bodies have also been devised [35, 36, 37] but these are now of largely historical interest, since the necessary computations, such as those in Eq. (3.26), can be made quite easily even on simple programmable electronic calculators.

3.10 DEPTH DETERMINATIONS

3.10.1 Bodies of postulated shapes

If we postulate some regular shape for an anomalous mass, it is generally possible to devise rules which unambiguously determine the depth to its top surface or centre of gravity. As in magnetic interpretation (p. 37), the rules are often based on the distance at which the gravity anomaly or its horizontal gradient falls to a given fraction of the maximum value [38]. It is perhaps worth emphasizing that the converse is not true; that is, the geometry of a mass cannot be uniquely determined by assuming a depth to its top surface or centre of gravity. This can be seen as follows.

Suppose that we have such a mass capable of explaining a given gravity field. Let us now add to this mass another one distributed on a horizontal plane at a depth z below the ground surface, in the form of a thin layer whose surface density ($\mathrm{kg\,m^{-2}}$) varies in the horizontal direction (x) as $A\cos(2\pi x/\lambda)$. The attraction of this distribution on the ground surface can be shown (see Problem 3.4) to be $2GA\pi\exp(-2\pi z/\lambda)\cos(2\pi/\lambda)x$. Obviously this can be kept less than any quantity, however small, if the wavelength λ of the distribution is kept sufficiently short. The additional mass considered here is geologically unrealistic but it is possible to show that realistic mass distributions can be added without affecting the anomaly of the originally determined mass by more than any given arbitrarily small quantity.

3.10.2 Limiting depths

When no assumptions are made about the anomalous body the shallowest possible mass distribution may lie on the surface of the earth itself, or, if we refer to a volume distribution, it may lie with its top surface just touching the earth's surface at one or more points, unless geological or other data preclude such distributions. On the other hand it can be shown that the top surface of a distribution cannot lie at an arbitrarily *large* depth, but that there must be a limiting depth to it. For the rapid estimate of this maximum possible depth (h) from the observed gravity field, Bott and Smith [39] and Smith [40] have obtained a variety of important, rigorous results. Some of them are briefly discussed below. They apply to gravitating bodies whose density contrast

with the surrounding rock is either entirely positive or entirely negative. No other restrictions need be placed on the magnitude or variation of the density contrast or on the shape and location of the body. The assumption is thus very light and can be satisfied in a very large number of geological situations.

(1) If Δg_{max} and $\Delta g'_{max}$ are respectively the maximum values of the gravity anomaly and its horizontal gradient, then

$$h \leqslant 0.86 \Delta g_{max} / |\Delta g'_{max}| \tag{3.28}$$

The inequality is particularly suitable when Δg_{max} and $\Delta g'_{max}$ occur close to each other.

(2) For all x we have

$$h \leqslant 1.50 \Delta g(x) / |\Delta g'(x)| \tag{3.29}$$

This inequality can be used when only part of the whole anomaly is known.

For 'two-dimensional' density distributions such as those in Figs 3.6(b) and (c) the numerical factor may be replaced by 0.65 in the inequality (3.28) and by 1.00 in (3.29).

(3) If $|\delta|_{max}$ is the absolute value of the maximum density contrast and $\Delta g''$ the second horizontal gradient of Δg,

$$h \leqslant 5.40 G |\delta|_{max} / |\Delta g''|_{max} \tag{3.30}$$

This inequality may be inverted to find the lower limit of $|\delta|_{max}$ if a plausible value for h can be assigned on other data. If it is assumed that $\delta \geqslant 0$ throughout the body, the inequality can be improved by replacing the symbol $|\delta|_{max}$ by $|\frac{1}{2}\delta|_{max}$.

The above formulae have been generalized by Smith [41] in an interesting manner. For instance, suppose that the body lies wholly between the planes $z = h, z = l$. Let $\overline{\Delta g}(d)$ be the average value of $\Delta g(x, y)$ around a circle of radius d lying in the plane $z = 0$ and having its centre at $(x, y, 0)$.

$$D = \overline{\Delta g}(d) - \Delta g(x, y, 0) \tag{3.31}$$

Then Smith has shown that

$$|D| \leqslant G |\delta|_{max} d[J(\alpha) - J(\beta)] \tag{3.32}$$

where $\alpha = h/d, \beta = l/d, J(t)$ is the function plotted in Fig. 3.8 and $|\delta|_{max}$ is, as before, the maximum density contrast. For large values of $t, J(t) = 1.752/t$ while $J(0) = 6.591$.

The inequality (3.32) can be used in a number of ways depending upon the information already available about the body (see, for example, Section 3.14.2). If it is assumed that $\delta \geqslant 0$ throughout the body $|\delta|_{max}$ may be replaced by $\frac{1}{2}|\delta|_{max}$.

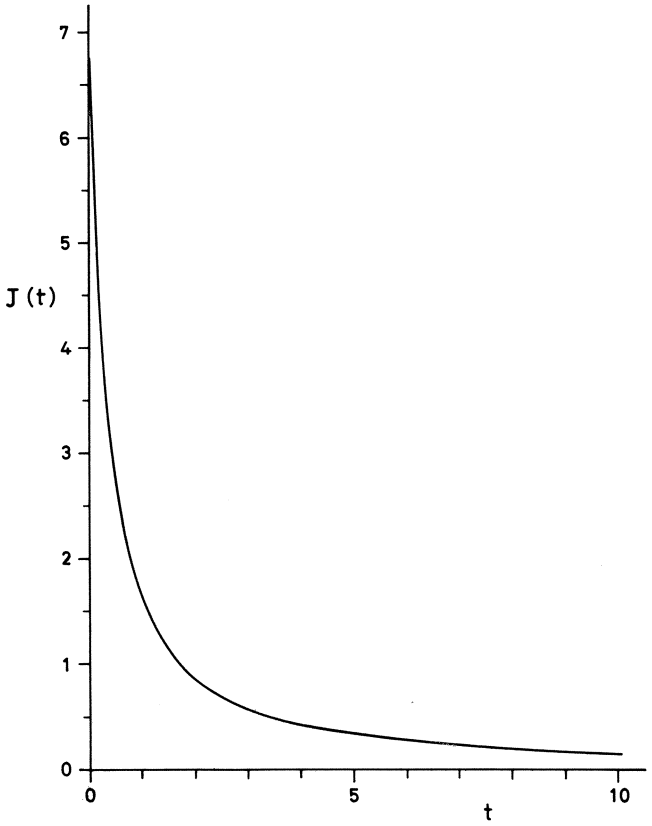

Fig. 3.8 Smith's function $J(t)$.

3.11 SOME THEORETICAL ASPECTS OF GRAVITY INTERPRETATION

3.11.1 Green's equivalent stratum and ambiguity

The discussion hitherto may be called the 'forward' approach to gravity interpretation. That is, given a mass distribution we determine its gravity field on the earth's surface for comparison with measured values. The real problem in applied geophysics is, however, the inverse one: given a gravity field Δg over what is virtually an infinite horizontal plane, to determine the mass distribution producing the field. The problem of magnetic interpretation (p. 28) is essentially the same because here too we are concerned with a field of force derivable from a Newtonian potential as the potential in Eq. (3.3).

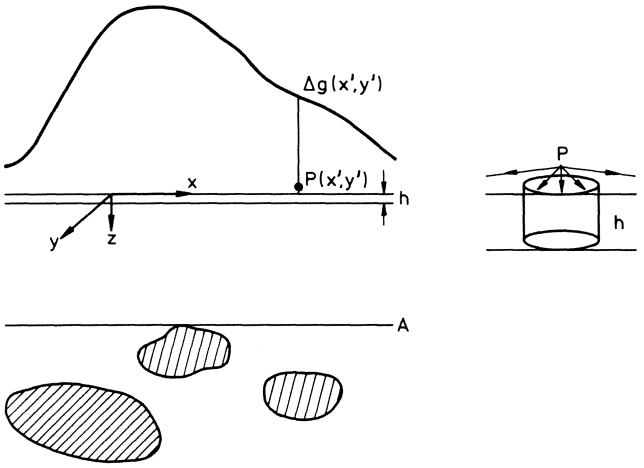

Fig. 3.9 Green's equivalent stratum.

Suppose now that we have measured an anomalous gravity field on the ground surface and that the masses producing it lie entirely below some plane A (Fig. 3.9). Let $\Delta g(x', y')$ be the anomaly at a point $P(x', y')$. Let us now suppose that instead of the original masses there is a very thin layer of matter on the ground surface whose thickness h is constant while its density varies from point to point, the ground being otherwise homogeneous. We shall denote the density contrast between the layer and the remaining ground by $\delta(x', y')$. The gravity due to this layer at any point P can be easily found as follows.

Since P is infinitesimally close to the ground surface, only the attraction of the matter in the immediate neighbourhood of P has a vertical component. The attraction of the more distant matter is nearly horizontal and its vertical component is negligible (see enlarged inset in Fig. 3.9). Consider therefore a very small circular area with P as centre. The attraction of the matter in the thin layer within this area is immediately obtained as $2\pi G\delta(z_2 - z_1)$, by putting $z_1 \approx z_2$ in Eq. (3.24a) since the last two terms in the equation will cancel each other. But $z_2 - z_1$ is h in the present case so that the attraction at P due to the entire layer will be simply $2\pi G\delta(x', y')h = 2\pi G\sigma(x', y')$ where $\sigma(x', y')$ denotes the surface density ($\mathrm{kg\,m^{-2}}$) of the thin layer at the point x', y'.

Now if we choose for the surface density of the fictitious layer a value $\Delta g(x', y')/2\pi G$ the attraction of the layer at P will obviously be exactly the measured anomaly $\Delta g(x', y')$. This fictitious layer is known as *Green's equivalent stratum* since as far as the gravity anomaly is concerned it is entirely equivalent to the masses actually producing the anomaly.

We shall now see that infinitely many exactly equivalent layers of this type

can be constructed. To illustrate the principle only we shall simplify the algebra by assuming that the measured gravity anomaly is two-dimensional, and symmetric as in Fig. 3.10. It can be shown (Appendix 13) that Δg, which is now a function of x' only, can be expressed as the integral

$$\Delta g(x') = \int_0^\infty A(\lambda) \cos(2\pi x'/\lambda)\, d\lambda \tag{3.33}$$

where the function $A(\lambda)$ can be uniquely determined from the values of Δg along the entire profile in Fig. 3.10.

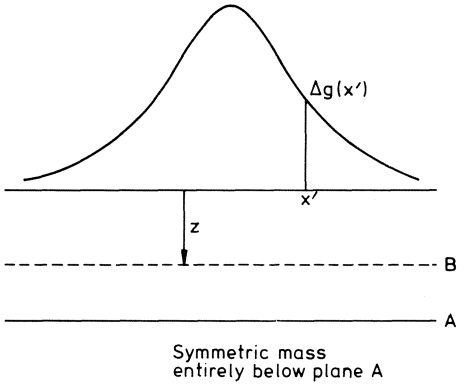

Fig. 3.10 Ambiguity in gravity interpretation.

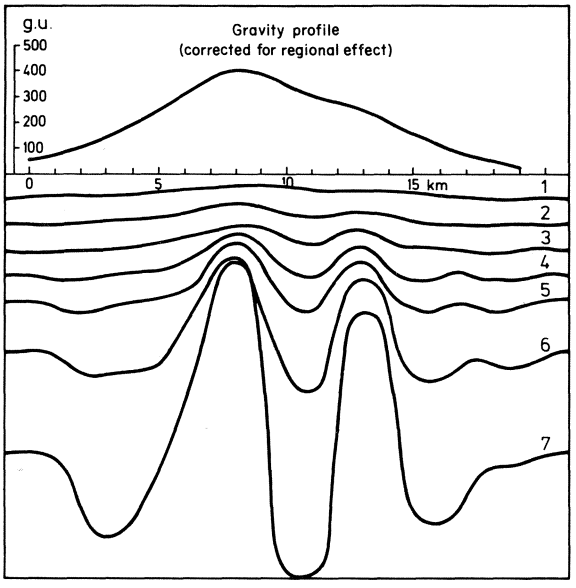

Fig. 3.11 (a)

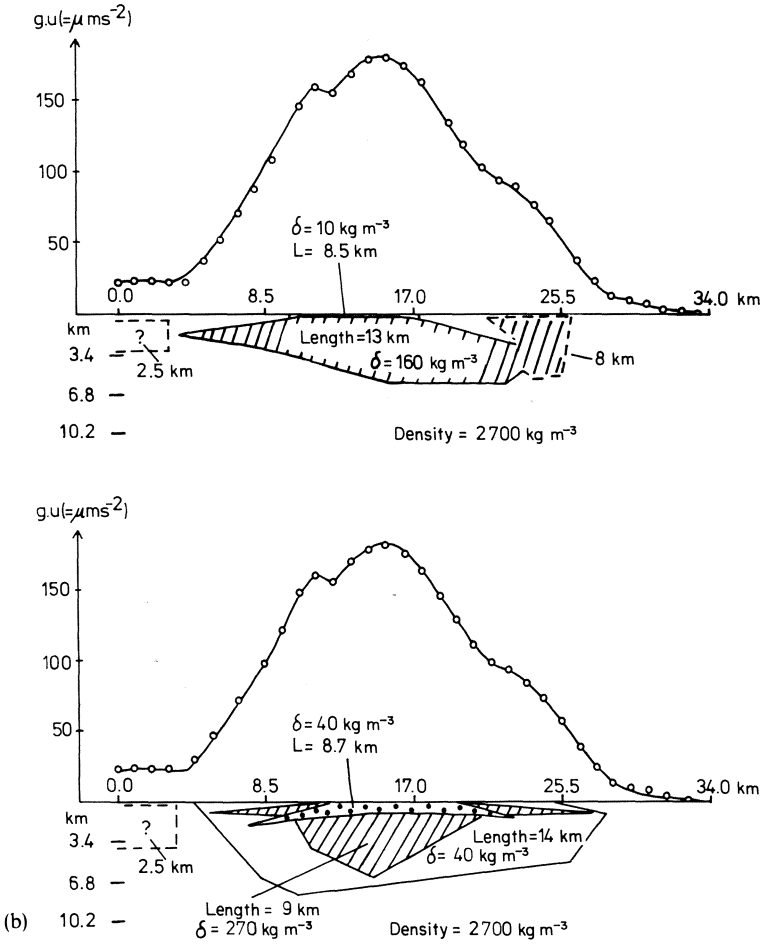

Fig. 3.11(a) Alternative basement reliefs (1–7) each of which explains a given gravity anomaly exactly ($\delta = 200\ \text{kg m}^{-3}$). After [42]. (b) Alternative structures producing the same gravity anomaly within the accuracy of measurements.

Consider the expression $A(\lambda)\cos(2\pi x'/\lambda)$ for some definite value of λ and a plane such as B in Fig. 3.10 at a depth z. From the result quoted towards the end of Section 3.10.1 it will be apparent that a surface density distribution

$$\frac{A(\lambda)}{2\pi G} e^{+\lambda z} \cos(2\pi x'/\lambda) \tag{3.34}$$

on B will exactly produce an anomaly $A(\lambda)\cos(2\pi x'/\lambda)$ on the ground surface. By letting λ have all values between 0 and ∞ in (3.34) we obtain a fairly complicated but a definite total surface density distribution on B. It is obvious

that this total distribution must then produce the measured anomaly $\Delta g(x')$.

The above reasoning can be applied to any plane between A and the ground surface. (The maximum depth of B is limited by the rules in Section 3.10.2 and is the depth of A.) Thus, an infinite number of Green's equivalent strata can be constructed to explain a given gravity field. The concept of Green's equivalent stratum is geologically implausible in most (though not all) practical situations but it serves to illustrate the inherent ambiguity in the interpretation of gravity (and magnetic) measurements made on the earth's surface. We shall now take two concrete examples of ambiguity.

Fig. 3.11(a) is an example where a given gravity anomaly has been explained exactly by each of the alternative basement reliefs. Automatic optimization techniques in no way reduce the fundamental ambiguity as the example in Fig. 3.11(b) shows. Either of the two complex structures explains the measured gravity within the limits of accuracy. The structures have the finite lengths shown perpendicular to the plane of the figure, but do not extend symmetrically on either side of the plane. The dotted structures lie entirely on one side of the plane of the figure.

It will now be obvious that the interpretation of gravity measurements in terms of sub-surface mass distributions can never be unique unless some external control (e.g. geological information, drill-hole data, etc.) is available. The mere fact that the calculated anomaly of some mass distribution, whose geometrical parameters are appropriately adjusted, agrees everywhere with the measured values, is no guarantee that the distribution occurs in reality, however good the agreement may be.

3.11.2 Analytic continuation

3.11.2.1 Basic equations

An important consequence of the fact that the anomalous masses below the plane A in Fig. 3.9 can be replaced by an anomalous layer of surface density $\Delta g(x', y')/2\pi G$ is as follows. The anomalous mass of a volume element of the layer is $\delta(x', y')\,\mathrm{d}v$. But if $\mathrm{d}S$ is a surface element,

$$\begin{aligned}\delta(x', y')\,\mathrm{d}v &= \delta(x', y')\,h\,\mathrm{d}S \\ &= \sigma(x', y')\,\mathrm{d}S \\ &= \frac{\Delta g(x', y')}{2\pi G}\,\mathrm{d}x'\,\mathrm{d}y'\end{aligned}$$

Then from Eq. (3.3) we get the gravitational potential V at any point $D(x, y, z)$ above the earth (Fig. 3.12) as

$$V = \int_{y'=-\infty}^{\infty}\int_{x'=-\infty}^{\infty} \frac{\Delta g(x', y')}{2\pi G r}\,\mathrm{d}x'\,\mathrm{d}y' \tag{3.35}$$

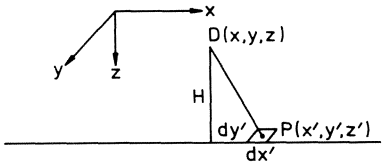

Fig. 3.12

where $r = [(x-x')^2 + (y-y')^2 + (z-z')^2]^{1/2}$ is the distance of D from the surface element $dx'\,dy'$.

Thus the potential at D can be found solely from a knowledge of $\Delta g(x', y')$ on the ground surface. It is not necessary to know what the actual masses producing $\Delta g(x', y')$ are!

If the positive z axis is in the downward direction then, according to our convention (cf. Eq. (3.10)), the gravity at the point D will be given by dV/dz. Then from Eq. (3.35),

$$\Delta g(x, y, z) = -\frac{z-z'}{2\pi}\iint \frac{\Delta g(x', y', z')\,dx'\,dy'}{[(x-x')^2 + (y-y')^2 + (z-z')^2]^{3/2}} \tag{3.36}$$

If we chose the origin of coordinates to lie on the ground surface we can put $z' = 0$. The z coordinate of D will then be $-H$ if H is the height of D above the surface. Hence

$$\Delta g(x, y, -H) = \frac{H}{2\pi}\iint \frac{\Delta g(x', y', 0)\,dx'\,dy'}{[(x-x')^2 + (y-y')^2 + H^2]^{3/2}} \tag{3.37}$$

This same equation applies to the magnetic case if we replace Δg by ΔB_z. For the magnetic case, however, one more possibility should be noted, namely that by differentiating both sides of (3.35) with respect to x and y in turns, the horizontal components of the magnetic field can also be found from a knowledge of the vertical field ΔB_z alone. Clearly, therefore, measurements of the horizontal magnetic field on the surface of the earth will not yield any additional information if sufficiently dense and precise vertical field measurements are available (cf. p. 23).

3.11.2.2 Upward and downward continuation

The procedure implied by Eq. (3.37) of calculating the field at a higher level when it is given on the ground surface is known as *upward analytic continuation*. If we transfer the origin to the plane $z = -H$, Eq. (3.37) becomes

$$\Delta g(x, y, 0) = \frac{H}{2\pi G}\iint \frac{1}{r^3}\Delta g(x', y', H)\,dx'\,dy' \tag{3.38}$$

which we may regard as an integral equation for determining $\Delta g(x', y', H)$, that

is the field on a deeper level, when the field on the ground surface $\Delta g(x, y, 0)$ is given. This process is called *downward analytic continuation.*

The idea behind undertaking analytic continuation of gravity and magnetic fields is as follows. Consider two equal spherical masses at depths a_1 and a_2 ($> a_1$). The ratio of their maximum gravitational attractions (deeper mass: shallower mass) will be a_1^2/a_2^2. At a height z above the surface the ratio will be

$$\frac{(a_1+z)^2}{(a_2+z)^2} = \frac{a_1^2(1+z/a_1)^2}{a_2^2(1+z/a_2)^2}$$

$$> \frac{a_1^2}{a_2^2}$$

Thus the effect of the deeper mass is relatively enhanced by upward continuation of the field whereas downward continuation will achieve the opposite effect.

Upward continuation is a straightforward numerical problem. The faithfulness with which the field can be reproduced at the higher level is only limited by the extent of the area on the ground surface within which the field is given, the denseness of the data and the fineness of the mesh (size of $dS = dx'\,dy'$) into which the datum plane can be divided for numerical integration.

Downward continuation is a more difficult numerical problem than upward continuation although a formal procedure for it is readily devised (Appendix 13.2.1). It has also an inherent limitation in that the continued field is physically meaningful only when the sub-surface point at which it is calculated is outside the body (or bodies) causing the given field.

The gravity anomalies on a deeper level, calculated analytically starting from the surface field, begin to fluctuate between positive and negative values at some stage even if the original field is of one sign only. If there are rapid variations of gravity in the data (anomalies varying over short distances) the fluctuations are discernible at shallow depths of continuation. For slow variations they may not be noticeable until a greater depth. There is never a sharp depth at which the fluctuations can be said to start. When the depth of continuation exceeds a certain depth the fluctuations become particularly violent. This 'critical' depth may sometimes coincide roughly with the top surface of the body but strictly it represents the maximum depth at which an anomalous mass of one sign only may occur in its most concentrated form, namely as a mass of infinite density and zero volume [43]. However, this depth can be directly obtained by the rules in Section 3.10.2 and downward continuation towards this purposes does not repay the labour involved (even using digital computers).

The situation in practice where analytical continuation is most likely to be useful is the case where it is desired to tie together aeromagnetic measurements in two adjacent areas that have been surveyed at two different heights, and it is

not feasible to re-fly. The field of the survey at the lower height should be continued upwards in this case.

3.12 DETERMINATION OF TOTAL ANOMALOUS MASS

It is interesting to note that although gravity measurements alone cannot uniquely determine the distribution of anomalous masses, they do provide a unique estimate of the *total* anomalous mass. This is a corollary of Gauss' flux theorem in potential theory and for our purpose it is very easily established as follows.

Suppose we have some mass distribution as in Fig. 3.13. The gravity anomaly on the surface due to an element dm at depth a is given by (cf. Eq. (3.20) for a sphere)

$$\frac{Ga\,dm}{(R^2+a^2)^{3/2}} \tag{3.39}$$

where R is the distance of the observation point from the epicentre of the element. If we integrate (3.39) over the entire ground surface we have

$$Ga\,dm\int\int\frac{dS}{(R^2+a^2)^{3/2}} = Ga\,dm\int_{R=0}^{\infty}\int_{\theta=0}^{2\pi}\frac{R\,dR\,d\theta}{(R^2+a^2)^{3/2}} \tag{3.40}$$

since the element dS can be expressed as $R\,dR\,d\theta$ as shown in the figure. Since the integrand is obviously independent of θ the integral over θ gives 2π and (3.40) becomes

$$\begin{aligned} &2\pi Ga\,dm\int_0^{\infty}\frac{R\,dR}{(R^2+a^2)^{3/2}} \\ &= 2\pi Ga\,dm\left[-\frac{1}{(R^2+a^2)^{1/2}}\right]_0^{\infty} \\ &= 2\pi G\,dm \end{aligned}$$

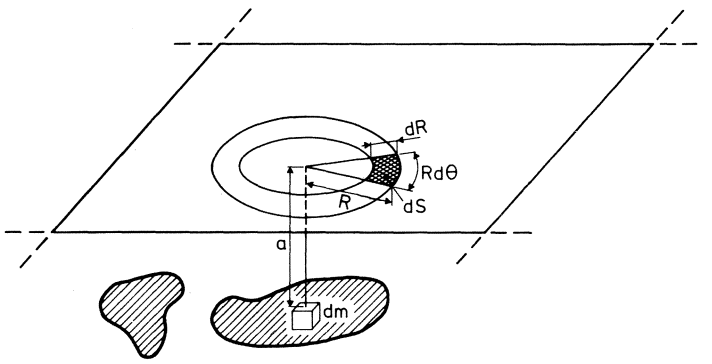

Fig. 3.13 Theorem of Gauss.

Thus the surface integral of the gravity anomaly of the element dm is simply $2\pi G\,\mathrm{d}m$. It is easy to see that the surface integral of the gravity anomaly of the entire mass M will be $2\pi G\int \mathrm{d}m = 2\pi GM$. Thus

$$M = \frac{1}{2\pi G}\int\int \Delta g\,\mathrm{d}S \tag{3.41}$$

In practice the integration, which is strictly speaking over the whole ground surface, will be replaced by a summation over the area of measurement. If Δg is expressed in g.u. and an element ΔS in square metres, we get from (3.41)

$$M = 2.39\sum(\Delta g \Delta S)\ \text{metric tons} \tag{3.42}$$

The sum in (3.42) gives the total anomalous mass, that is, the difference between the mass of a body and the mass of the country rock occupying an identical volume. If a body has a density ρ_1 and is embedded in a rock of density ρ_0, its *actual* mass will be

$$2.39\frac{\rho_1}{\rho_1 - \rho_0}\sum(\Delta g \Delta S)\ \text{tons} \tag{3.43}$$

If the mass distribution is such that some parts of it have a higher density than the surroundings and others lower, the formula (3.42) will naturally give the net difference between the anomalous masses of these various parts.

In the application of (3.42) in practice, Δg is generally the local anomaly obtained after the removal of any regional trends. Consequently the estimate of M will depend to some extent on the regional trends assumed. Furthermore, since the summation in (3.42) is over a finite area while the integration in (3.41) is over an infinite plane, the estimate of M is in a sense an underestimate of the actual tonnage.

3.13 VERTICAL DERIVATIVES OF GRAVITY

Let us again suppose as in Section 3.11 that we have two spherical masses at depths a_1 and $a_2 (> a_1)$. While the ratio of their maximum gravity anomalies (shallower mass: deeper mass) is a_2^2/a_1^2, the maximum values of the vertical derivatives $\partial(\Delta g)/\partial z$ will be in the proportion $a_2^3/a_1^3 (> a_2^2/a_1^2)$, those of the second derivatives $\partial^2(\Delta g)/\partial z^2$ in the proportion $a_2^4/a_1^4 (> a_2^3/a_1^3)$ and so on. Thus, the successive vertical derivatives of gravity accentuate the relative effect of the shallower mass. This is the opposite of what happens in analytic continuation. Now, the vertical derivative of gravity of any order, at any point on the ground or above it, can be calculated merely from the knowledge of gravity on the ground surface. This follows from Eq. (3.36) for we may perform repeated differentiations with respect to z on both sides and evaluate the resulting double integral numerically. For example, by differentiating both

sides of (3.36) with respect to z and transferring the origin to the ground surface we get for the first vertical derivative of Δg at D.

$$\frac{\partial \Delta g}{\partial z} = -\frac{1}{2\pi}\iint \Delta g(x', y', 0)\left(\frac{1}{r^3} - \frac{3z^2}{r^5}\right) dx'\, dy' \tag{3.44}$$

The integral can be evaluated numerically in practice.

Many different methods of varying precision have been proposed for computing vertical derivatives (or fields at higher level) from surface data [44]. We must remember, however, that a knowledge of vertical derivatives (or field at higher level) does not in any way reduce the fundamental ambiguity in gravity interpretation. The reason is that the derivatives (and fields) being directly deducible from sufficiently dense and precise surface data do not contain any additional information not inherent in the original data. This does not preclude, of course, that the maps thus constructed may show some 'optical' advantages in that some features of the field might be easier to spot on these maps than on the map of the original data. For example, adjacent maxima or minima in the gravity field are often better resolved in a map of the second vertical derivative than in that of the field itself. On the other hand, the effect of surface irregularities is far more serious in the derivatives so that if, say, the second derivative is measured directly, the topographic corrections to it will be considerably more uncertain than the corresponding corrections to the gravity.

3.14 ILLUSTRATIONS OF GRAVITY SURVEYS AND INTERPRETATION

3.14.1 West Midlands (England)

This example is taken from a paper by Cook *et al.* [45]. The contours of the Bouguer anomalies in the area of measurements are shown in Fig. 3.14. The general geologic section is as follows. Rocks of Triassic age (Keuper Marl and Sandstones) are underlain by Coal Measures which contain coal seams and rest upon strata of Old Red Sandstone. Beneath the O.R.S. follow the rocks of Silurian and Cambrian age. All the strata are generally flat or have gentle dips but there is considerable faulting. Igneous intrusions occur at some places. The trias is exposed in the Forest of Arden and in the area between the Forest of Wyre and South Staffordshire coalfields. In these coalfields and in the Warwickshire coalfield to the east the surface rocks are composed of Coal Measures.

The first step in the interpretation is to estimate the attraction of the surface rocks. Their thickness is fortunately well known over most of the area. However, this estimate cannot be made directly because although the density of the surface rocks may be known, the attraction is proportional to the

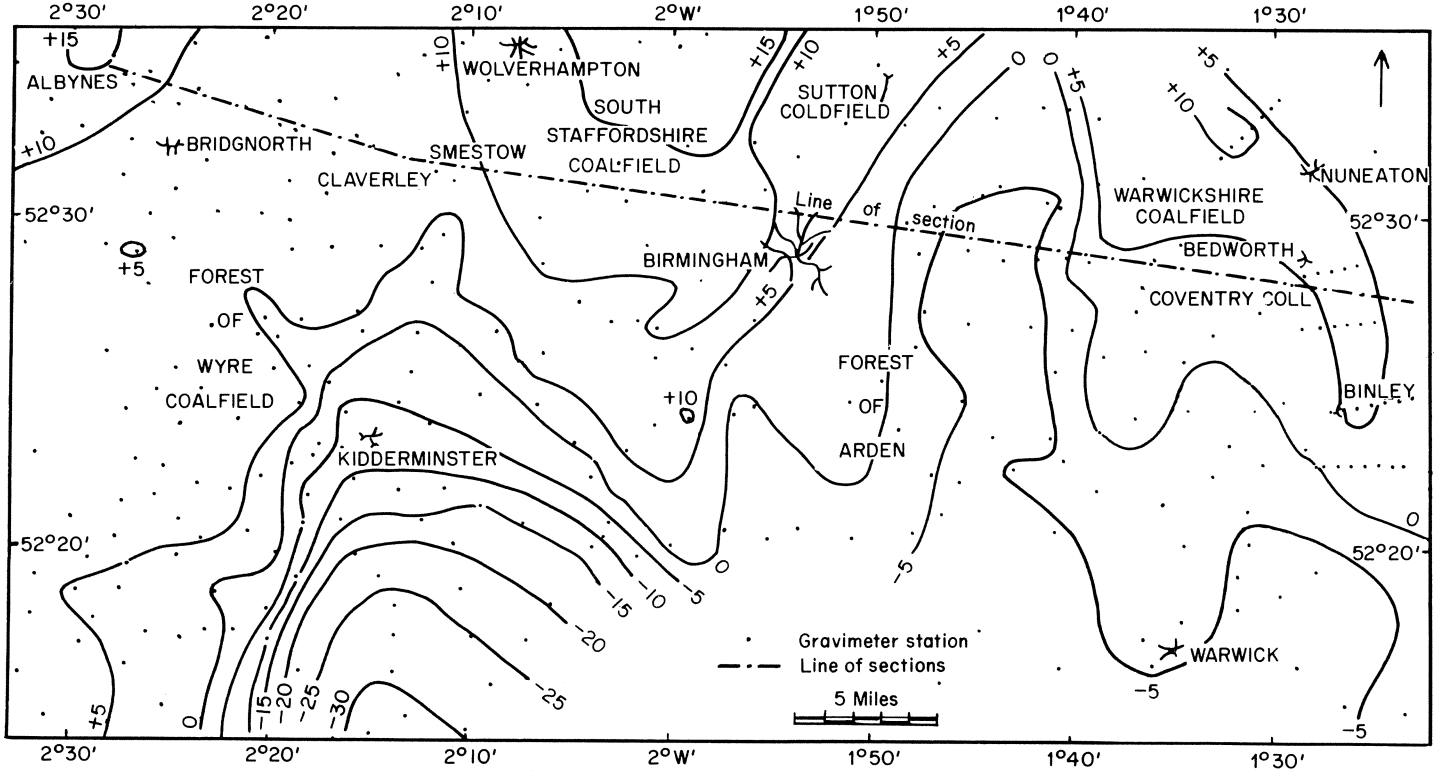

Fig. 3.14 Absolute Bouguer anomalies in West Midlands, England. After [45]. Contours in milligal, 1 mgal = 10 μm s^{-2} = 10 g.u.

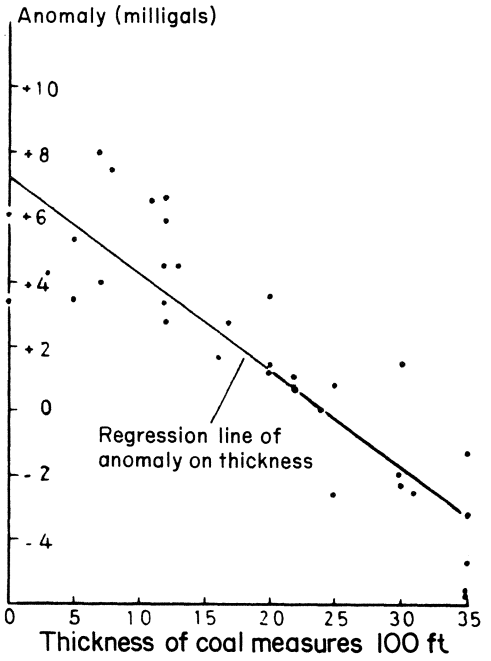

Fig. 3.15 Regression of anomaly on thickness. After [45]. (1 mgal = 10 g.u.)

difference of this density from that of the underlying rocks, which is not known. Cook therefore proceeds by plotting the anomalies against the thicknesses of the surface rocks concerned, say Coal Measures, at the observation stations. It will be appreciated from Section 3.7 that the points thus obtained will lie approximately on a straight line with a slope $0.419 \times 10^{-3}\delta$ g.u./m ($0.128 \times 10^{-4}\delta$ mgal/ft) where δ is the difference of the density of the Coal Measures from that of the rocks below them. The plot for the Warwickshire coalfield (Fig. 3.15) yields $\delta = 230 \pm 20\,\text{kg m}^{-3}$. Similarly the density difference between the Trials and the underlying rocks (Coal Measures) is found to be $250 \pm 140\,\text{kg/m}^{-3}$. The Bouguer anomalies then must be corrected for the attraction of the known Trias and Coal Measures, adopting the above density differences.

Fig. 3.16 shows the residual anomalies along a line from the Albynes to Bedworth. They indicate a large structure under the Trias cover between the Birmingham Fault and the Western Boundary Fault of the Warwickshire coalfield. It seems plausible from the geology that the low anomaly values in this part are caused by a slab of Coal Measures resting on the heavier Palaeozoic rocks. The western boundary of the slab is the known Birmingham Fault. Assuming the eastern one to be a vertical step the thickness of the slab

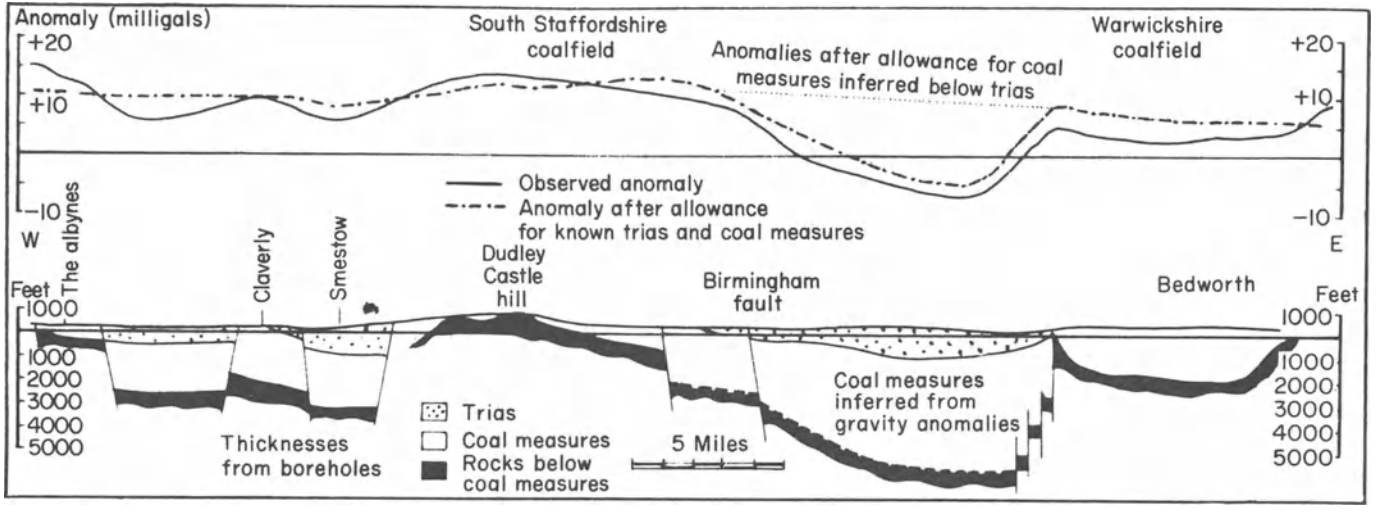

Fig. 3.16 Section along line in Fig. 3.14.

can be estimated from Equation (3.23) to be about 4000 ft. The maximum horizontal gradient over a vertical step is $2\pi G\delta \ln(D/d) = 48$ g.u./1000 ft. The observed value is only 10 g.u./1000 ft which indicates that the eastern margin is not vertical but slopes down (to the west) perhaps as a result of a number of step faults as shown.

3.14.2 Camaguey Province, Cuba

The measurements discussed here were included in a prospecting campaign for chromite ore (Davis *et al.* [46]). The area is relatively flat except for a few scattered hills, mine dumps and excavations. The chromite deposits occur in serpentinized peridotite and dunite near their contact with felspathic and volcanic rocks. The Bouguer anomalies are shown in Fig. 3.17. The isoanomalous lines clearly indicate that apart from the local, roughly circular disturbance in the centre, there is a general ('regional') gravity trend consisting of an increase in the values from the southwest to the northeast (dotted contours). The residual anomalies obtained on subtracting this trend are shown in Fig. 3.18.

The maximum residual anomaly is 2.1 g.u. and its maximum horizontal gradient 1.6 g.u./20 m. Substituting in the inequality (3.28) we get $h \leqslant 23$ m for the depth to the top surface of the chromite deposit. In fact, the ore was found

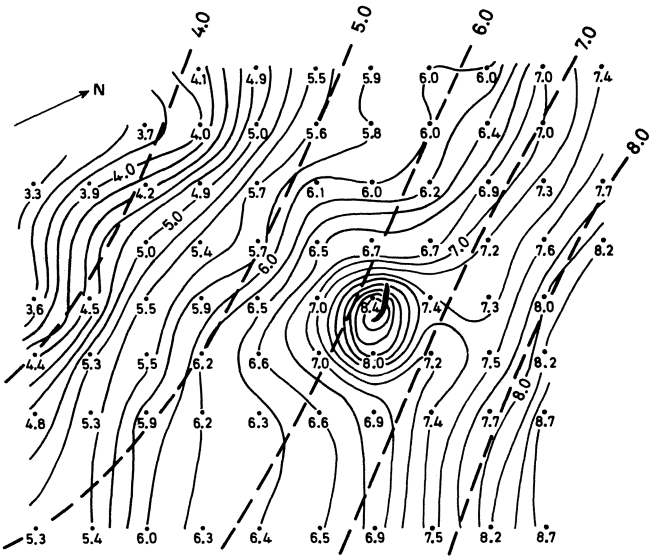

Fig. 3.17 Relative Bouguer anomalies on a chromite deposit, values and contours in g.u. After [46].

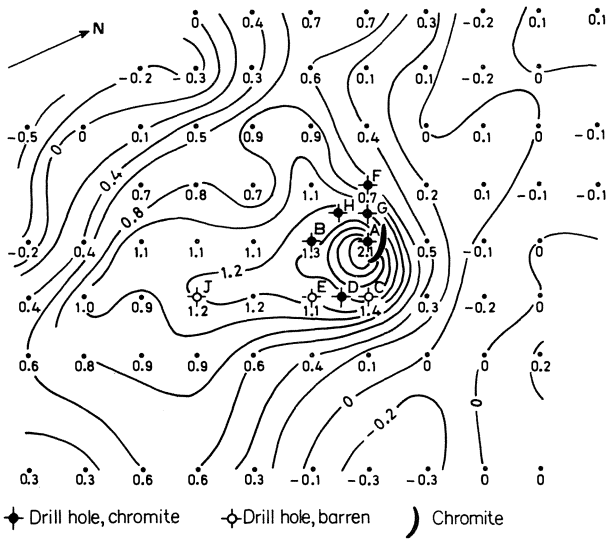

Fig. 3.18 Map in Fig. 3.17 after regional correction. Residual anomalies in g.u.

to be exposed inconspicuously in a pit and later uncovered more fully by a shallow trench as shown.

The average value of the anomaly around a circle of radius $d = 20$ m centred at the maximum is 0.98 g.u. Thus, in the equation (3.31) $|D| = 2.10 - 0.98 = 1.12$ g.u. If we suppose that the ore body lies entirely between 0 and 60 m (the latter limit is suggested by the drilling results), $\alpha = 0$ and $\beta = 60/20 = 3.0$. From Fig. 3.8 we read off $J(0) = 6.591$ and $J(3.0) = 0.579$. Then assuming $\delta \geqslant 0$ throughout the body the inequality (3.32) becomes

$$\tfrac{1}{2}G\delta d \times (6.591 - 0{\cdot}579) \geqslant 1.12 \times 10^{-6}\,\mathrm{m\,s^{-2}}$$

leading to a minimum density difference $\delta = 280\,\mathrm{kg\,m^{-3}}$ between the chromite ore and the surrounding serpentinized peridotite. The latter is reported to have a density of $2500\,\mathrm{kg\,m^{-3}}$ so that the density of the chromite deposit must everywhere be equal to, or greater than, $2780\,\mathrm{kg\,m^{-3}}$. This, in turn, means that the grade of the deposit must be better than 13.9% chromite (by volume) in all parts of it. Note that in these estimates we have not made any assumption as to the shape of the ore body, its depth, or its location sidewise.

Since the grid in Fig. 3.18 is a close and regular 20 m square array we may associate $\Delta S = 400\,\mathrm{m^2}$ with every observation point for estimating the anomalous mass according to (3.42). After inserting interpolated points between the last two rows in Fig. 3.18 we obtain $\sum \Delta g = 30.5$ g.u. for the 86 points in the figure. The total anomalous mass is therefore $2.39 \times 400 \times 30.5 = 29\,158$ metric tons. If the body causing the anomaly has a density of, say,

4000 kg m^{-3} and lies in serpentinized peridotite its actual mass will be some 77 000 tons (cf. Eq. (3.43)). The ore ascertained from the drill holes amounts to only 24 000 tons. That the gravity anomaly is not entirely accounted for by the known chromite is evident also from the high anomaly values to the south of the maximum. The remaining mass, of course, need not be chromite.

3.15 NOTE ON MARINE GRAVITY MEASUREMENTS

3.15.1 General

Nearly 70% of the earth's surface is covered by oceans and our knowledge of the earth's interior would be much less than what it is without geophysical measurements of various kinds at sea. There is no particular difficulty in making magnetic measurements at sea by proton magnetometers as these do not require a stable platform. Gravimeter measurements at sea are necessarily more complicated because no stable platform is available. Nevertheless instruments for the purpose have been devised, the earliest one being a three-pendulum apparatus of Vening Meinesz from the 1920s. This is no longer used. Present measurements are made by gravimeters mounted on gyro-controlled stabilized platforms. There are a variety of such instruments, some of which have been described by Dehlinger and Chiburis [47]. Most of these designs are adaptations of gravimeters used for land work although there are exceptions.

3.15.2 Eötvös correction

Gravity measurements on board ship are affected by the earth's attraction as well as by ship motion. The effects of horizontal and vertical accelerations due to the ship's motion and the cross-coupling effects between these two vary from one instrument design to another and are computer corrected in modern instruments. But apart from these, and apart from the corrections described for land work, there is a new, fundamental correction in gravity work at sea explained below.

The centrifugal acceleration experienced by a mass, at rest relative to the earth's surface at latitude ϕ, due to the earth's rotation from west to east, is $V_\phi^2/(R\cos\phi)$ where V_ϕ is the linear velocity of the mass due to the earth's rotation. Its component in the radial, that is, vertical direction (V_ϕ^2/R) tends to reduce the earth's gravitational pull. In land work this is included in the net measured value of g. For an instrument on board a ship moving with easterly velocity V_E the centrifugal acceleration is $(V_\phi + V_E)^2/(R\cos\phi)$ and its vertical component is $(V_\phi + V_E)^2/R$. The vertical acceleration due to a northerly speed V_N is, however, V_N^2/R. The additional acceleration due to the ship's motion is then easily seen to be $(2V_\phi V_E + V^2)/R$ where $V = (V_E^2 + V_N^2)^{1/2}$ is the ship's speed. Since $V_\phi = R\omega\cos\phi$ where ω is the earth's angular velocity the

acceleration can be written as

$$\delta g_E = (75\, V_E \cos\phi + 0.04 V^2)\, \mu m\, s^{-2}$$

where V and V_E are in knots.

The correction δg_E is called the *Eötvös correction* and is to be added to the measured value of gravity. (V_E is negative for a westerly speed.) Some gravity work under water is done by lowering a gravimeter enclosed in a pressure-tight spherical shell on to the sea bottom. Levelling of the instrument is executed by remote control devices. The Eötvös correction does not, of course, arise in such measurements. The overall accuracy of sea gravity measurements is between about 10 and 100 $\mu m\, s^{-2}$ depending upon errors in ship speed, ship heading, positioning etc. For the LaCoste–Romberg ocean bottom gravimeters, however, an accuracy of 1 $\mu m\, s^{-2}$ and better has been claimed.

Since the principal application of marine gravity measurements at present is in global rather than prospecting geophysics we shall not consider them further except to note that marine gravity interpretation proceeds as a rule from free-air anomalies and not from Bouguer anomalies.

PROBLEMS

3.1 A protuberance of height h on an otherwise flat homogeneous ground may be considered to be a spherical cap whose base is a circle of diameter d. What is the difference in gravity between a point exactly on top of the protuberance and one far away from the protuberance after the free-air and latitude corrections have been made? There is no density difference between the material in the protuberance and the rest of the ground.

3.2 A pit in a bedrock of density ρ is filled with material of density ρ_0 and can be approximated by a truncated paraboloid of revolution $x^2 = \lambda(a - z)$ whose flat surface is the horizontal ground surface. The origin is at the centre of the face and the z axis is vertically downwards. What is the gravity anomaly at the centre of the pit on the ground surface?

3.3 An E–W striking structure in a bedrock ($\rho = 2700\, kg\, m^{-3}$) is suspected to be a fault. Total Δg in traversing the structure in a N–S direction is 6 $\mu m\, s^{-2}$ while the maximum ΔB_z is 62 nT. The area is at the magnetic equator ($B_{0f} = 35\,000$ nT) and the ground surface is flat. The loose material covering the bedrock is non-magnetic with a density of 2000 $kg\, m^{-3}$. The bedrock susceptibility is known to lie somewhere between 0.01 and 0.03. There is no remanence.

Estimate the probable maximum and minimum depth to the top of the structure assuming that the fault has a vertical throw.

3.4 Jordan's lemma in integral calculus states that

$$\int_0^\infty \frac{\cos mx}{x^2 + a^2}\, dx = \frac{\pi}{2a} e^{-ma}$$

Use this result, and the result that an infinitely long line of mass μ per unit length exerts at a distance r an attraction $2\mu G/r$ towards itself, to verify the anomaly of the surface distribution $A\cos(2\pi x/\lambda)$, stated in Section 3.10.1.

3.5 A very long horizontal underground tunnel of radius 2.5 m is driven very deep down in a homogeneous bedrock of density 2500 kg m^{-3}. Assuming that the free-air correction has been made, find the residual gravity anomaly on the axis of the tunnel and at a roof point vertically above the axis.

3.6 Estimate the maximum possible depth to the topmost point of the bedrock in Fig. 3.11(a).

3.7 Estimate the total anomalous mass of the local structure causing the anomaly in Fig. 3.5.

3.8 The upper surface of an intrusion (diameter 20 km) causing a nearly circular gravity anomaly with a maximum value of 404 μm s^{-2} is at a depth of 100 m. The average density of the intrusion is 2900 kg m^{-3}, that of the surrounding rock is 2750 kg m^{-3}. Assuming the intrusion to be a vertical cylinder, estimate its depth extent.

4

Electrical methods

4.1 INTRODUCTION

The electrical properties of the sub-surface can be explored either electrically or electromagnetically. The two electrical methods to be discussed in this chapter are: (a) self-potential (SP) and (b) earth resistivity (ER). The induced polarization (IP) method, although it can be classified as an electrical method from the field-operational point of view, is discussed separately in the next chapter. The SP method was used by Fox as early as 1830 on the sulphide veins in a Cornish mine but the systematic use of the SP and ER methods dates from about 1920.

4.2 SELF-POTENTIAL METHOD

4.2.1 Occurrence of self-potentials

The SP method, as its name implies, is based upon measuring the natural potential differences which generally exist between any two points on the ground. The potential differences, partly constant and partly fluctuating, are associated with electric currents in the ground. We shall revert to the fluctuating part in a later chapter. The constant and unidirectional potential differences between any two points can arise due to various electrochemical mechanisms as we shall see below.

Ranging normally from a fraction of a millivolt to a few tens of millivolts self-potentials sometimes attain values of the order of a few hundred millivolts and much more. Such large anomalous potentials are often (but not always) observed over sulphide and graphite ore bodies, magnetite and several other electronically conducting minerals. Large SP values are also found on coal and manganese deposits. Unless superimposed by other self-potentials these

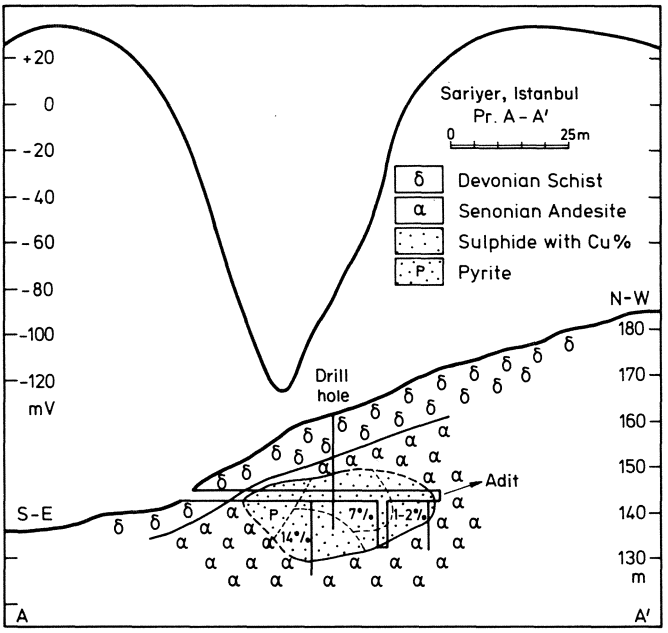

Fig. 4.1 SP profile across a pyrite mass. After Yüngül (*Geophysics*, 1954, **19**, 458).

'mineral potentials' are invariably negative with respect to a point far away from the mineral occurrence when the dips are steep but they may be flanked by positive maxima as in Fig. 4.1. Positive principal SP maxima on the ground surface over the above mentioned minerals are found in the case of flat dips. Distinct, although considerably smaller in magnitude, are the anomalies often observed on other features like quartz veins, pegmatite etc. These are positive.

4.2.2 Field procedure

The measurement of self-potentials is quite easy. Any millivoltmeter with a surface over the above mentioned minerals are found in the case of flat dips. some 10–15 cm into the ground and read off. Alternatively a usual potentiometer circuit of the null type can also be employed with advantage. The electrodes must be non-polarizable (e.g. Cu in $CuSO_4$ solution or Pt-calomel in KCl solution); ordinary metal stakes will not generally do since electrochemical action at their contact with ground tends to obscure the natural potentials.

Two alternative procedures are in use for SP surveys. The electrodes, say 20 m apart, are advanced together along staked lines or else one electrode connected to one end of a long cable on a reel is kept at a base point while the

other electrode, the reel, and the voltmeter, are carried to different points as the cable is laid off. The stationary electrode is connected to the negative terminal of the voltmeter. A new base point is chosen when the cable length is exhausted and its potential with respect to the old base point is measured so that data can be finally referred to one single reference point. When the observed potential difference is divided by the electrode separation the first procedure gives approximately the gradient of the potential ($mV\,m^{-1}$). In the second procedure we are measuring the 'absolute' SP. The *zero level* necessary for obtaining a map of absolute SP is determined as in the magnetic method, that is, by an inspection of the data.

4.2.3 Origin of self-potentials

There has been considerable speculation concerning the electrochemical mechanisms producing self-potentials and even now it cannot be said that the question has been satisfactorily settled. However, the main mechanisms appear to be as follows.

4.2.3.1 Electrofiltration

Electrofiltration or streaming potentials (also called zeta potentials) are a manifestation of a phenomenon first studied in detail by Helmholtz in the 19th century, that an electric potential difference is developed between the ends of a capillary tube through which an electrolyte is flowing. The effect is believed to be due to the attachment of ions to the walls of the capillary, combined with the unequal flow velocities of positive and negative ions. It is found that the electric field ($V\,m^{-1}$) along the capillary can be expressed as

$$E = \frac{\varepsilon \rho \zeta}{4\pi\mu} p \tag{4.1}$$

where ε = dielectric constant of the electrolyte ($F\,m^{-1}$), ρ = the resistivity of the electrolyte ($\Omega\,m$), ζ = a parameter (streaming potential, V) that depends upon the material of the capillary wall and the electrolyte, p = pressure gradient ($Pa\,m^{-1}$) and μ = dynamic viscosity of the electrolyte (Pa s). E is thus in the same direction as the pressure gradient, that is opposite to the direction of electrolyte flow.

In geophysical work electrofiltration potentials can be found associated with the flow of water through sand, porous rocks, moraine etc. High ground is generally found to be more negative than low ground, indicating that the electric current due to these potentials tends to flow uphill, which is in accordance with Eq. (4.1). Thus a potential of $-1842\,mV$ associated with alunite (a basic sulphate of Al and K) has been reported on a mountain top near Hualgayoc, Peru [48] and $-1940\,mV$ over unmineralized quartzites on a hill in Shillong, India [49].

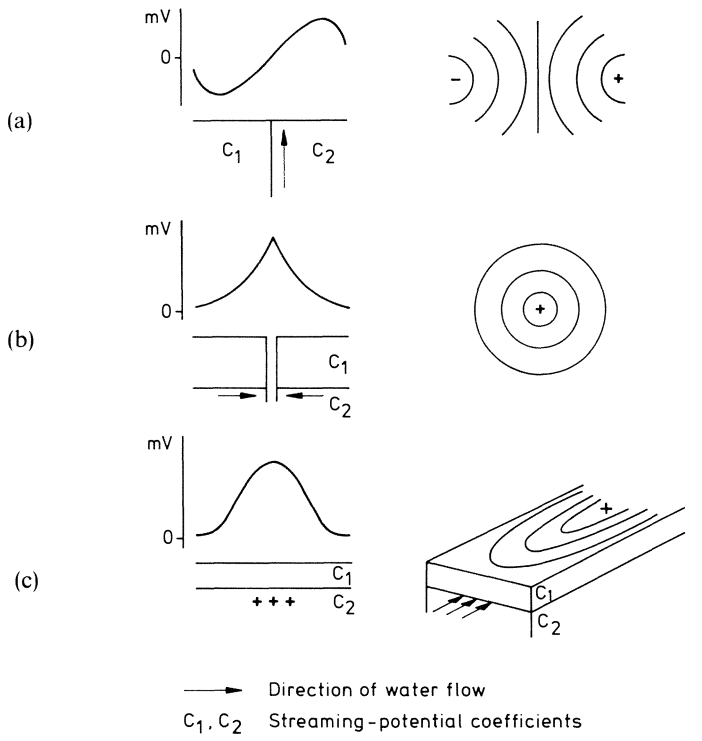

Fig. 4.2 Idealized electrofiltration SP (profiles and maps) on some flow models. After [50]. (a) Vertical boundary; (b) pumping from a well; (c) horizontal boundary flow.

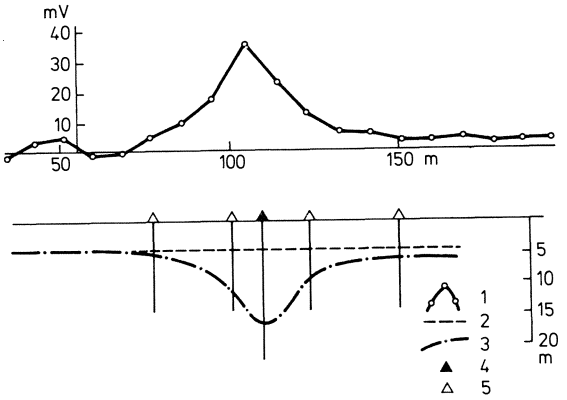

Fig. 4.3 SP caused by pumping of ground-water. After [52]. (1) Measured SP; (2) water table before pumping; (3) water table during pumping; (4) exploitation borehole; (5) piezometric borehole.

The flow of water due to a pressure gradient is not a sufficient condition for electrofiltration anomalies to arise. It is necessary that the flow takes place parallel to the boundary between two rock media for which the effective ζ of Eq. (4.1) is different. Some flow models of hydrogeological interest and their expected electrofiltration anomalies are shown schematically in Fig. 4.2.

Electrofiltration potentials have been used to detect leakage spots on submerged slopes of earth-dam water reservoirs [51], to detect concealed karstic, springs etc. and to study the effect of pumping on the ground-water table (Fig. 4.3).

4.2.3.2 Concentration differences (diffusion)

It has been suggested that differences in the concentration of electrolytes in the ground from place to place may be the cause of the ubiquitous 'blackground' SP anomalies of the order of fractions of a millivolt to some tens of millivolts. Let us imagine an electrolytic cell such as the one in Fig. 4.4 with two metal electrodes in two electrolytic solutions of concentrations C_1, C_2 in contact with each other. We shall assume the system to be such that when the cell is in action the net transfer of charge from one electrode to the other within the cell takes place through positive ions. For instance, Cu electrodes in $CuSO_4$ solutions form exactly this type of cell. It can be shown that the overall electromotive force (the difference 'potential of electrode 2 minus potential of electrode 1') of such a cell is

$$U = \frac{2v}{u+v}\frac{RT}{nF}\ln\frac{C_1}{C_2} \tag{4.2}$$

where u, v are respectively the velocities ($m\,s^{-1}$) of the positive and negative ions in the electrolyte when the cell is in action, R = the universal gas constant ($8.314\,J\,K^{-1}\,mol^{-1}$), T = absolute temperature (K), F = Faraday's constant ($96\,487\,C\,mol^{-1}$) and n = valence of the ions. If the charge transfer takes place through negative ions u and v in (4.2) will be interchanged.

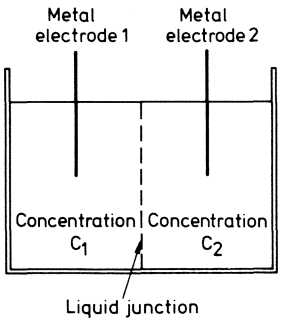

Fig. 4.4 Electrolytic concentration cell.

Now, suppose an electrolyte is so chosen that $u = v$. The e.m.f. of this cell will be

$$U_0 = \frac{RT}{nF} \ln \frac{C_1}{C_2} \tag{4.3}$$

However U_0 is simply $U_{M2}(C_2) - U_{M1}(C_1)$ if $U_M(C)$ be the potential of the metal electrode involved in contact with an electrolyte of concentration C. The e.m.f. U_0 obviously exists in the cell of Eq. (4.2) as well, so that the difference $(U - U_0) = U_j$ must be attributed to the fact that $u \neq v$. It is easily seen that

$$U_j = -\frac{u - v}{u + v} \frac{RT}{nF} \ln \frac{C_1}{C_2} \tag{4.4}$$

U_j is called the 'liquid-junction potential' although its cause is not the junction as such but rather the unequal velocities of the positive and negative ions when the cell is in action. Equation (4.4) is written with the convention that U_j represents the difference 'potential of solution on the right minus potential of solution on the left'.

If the concentration of electrolytes in the ground varies locally, potential differences will be set up in accordance with Eq. (4.2). This is plausible but the difficulty with this theory is that over the passage of time any concentration differences in the ground will disappear owing to the diffusion of the more concentrated solute to the less concentrated one. Hence it becomes necessary to postulate a source that will continuously regenerate concentration differences. No such source has been positively identified in actual natural systems but exchange with atmospheric oxygen is a strong candidate.

One of the most common solutes in natural electrolytes is NaCl. Differences in NaCl concentrations produce SP anomalies that are of great significance in well logging. This topic is considered in more detail later (Chapter 9).

4.2.3.3 Adsorption

SP anomalies of the order of + 20 to + 40 mV are characteristically obtained over pegmatite and quartz even when the rocks are completely concealed under an overburden. In the example of Fig. 4.5 the boundaries of gneiss intruded by pegmatite veins are clearly shown by the sharp gradients. Such self-potentials have been attributed to the adsorption of positive ions on the surface of the veins (although what is actually measured is, of course, the ordinary ohmic drop due to a flow of current) but the details of the electrochemical mechanism are by no means clear. Self-potentials observed over clays probably also belong to this category.

4.2.3.4 Mineral potentials

These are often called by the less general name of 'sulphide' potentials since they are as a rule strongest on ores like pyrite and chalcopyrite but their

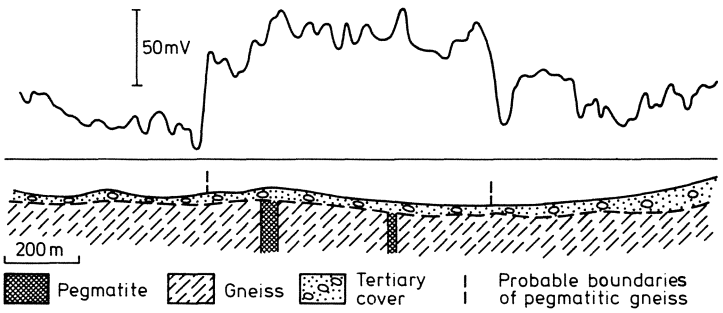

Fig. 4.5 SP on pegmatite dikes. After [52].

common feature is really that they are observed on electronically conducting minerals. Most theories have attributed mineral self-potentials to the oxidation of parts of a mineral deposit above the water table, but such an explanation cannot fit graphite, which shows high SP anomalies but does not normally undergo significant oxidation. Moreover, oxidation implies loss of electrons so that the upper end of a mineral deposit should become positively charged whereas almost invariably a negative SP anomaly is observed on the ground surface above ore bodies (cf. Fig. 4.1). However, it was pointed out by Sato and Mooney [53] that the ore body need not directly take part in the electrochemical reactions. Their theory amounts briefly to the following.

Since we are concerned with an electronic conductor (the ore) in contact with an ionic conductor (electrolytes in the country rock), there must be an electrochemical action at their boundary. It is plausible to assume that, just as a metal electrode (Me) dipped in an electrolyte liberates ions in the electrolyte according to the reaction $Me \rightarrow Me^{+} + e^{-}$, an electronically conducting ore sulphide MeS will liberate ions according to the reaction $MeS \rightarrow Me^{2+} + S + 2e^{-}$ where e^{-} is the electronic charge. There may also be more complex reactions in some cases liberating negative ions such as OH^{-} or SO_4^{2-}. If the concentration of ions in the electrolyte is different near the top and the bottom parts of the ore body, as may well happen if the electrolytic solution pressures are different, an ionic current will flow in the surrounding electrolyte. The mechanism may be compared to the concentration cell referred to in Section 4.2.3.2 when it is in action. The directions of current and ion flow implied by a negative SP centre over an ore are shown in Fig. 4.6. Evidently, the ore body, being a good electronic conductor, serves to transport the electrons from the lower part to the upper part.

The theory of Sato and Mooney explains the prevalence of negative centres over pyrite, graphite etc. as well as some converse phenomena, e.g. the absence of SP anomalies on sphalerite (ZnS) or haematite (Fe_2O_3) which are very poor conductors. Sato and Mooney also calculate the maximum potential dif-

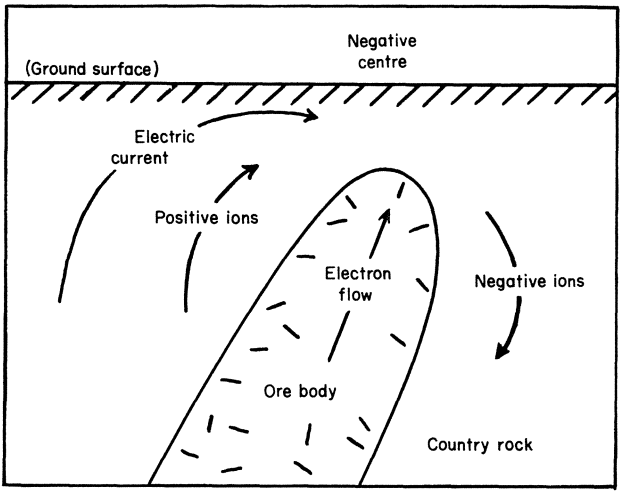

Fig. 4.6 Current and ion flow in the vicinity of an ore body.

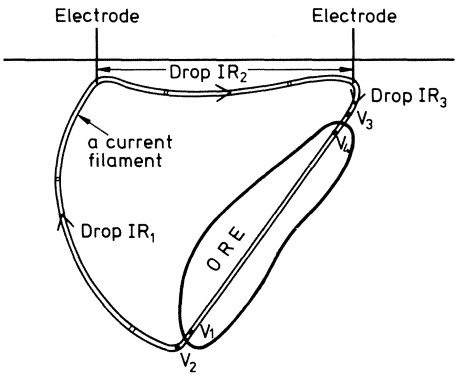

Fig. 4.7 Potential drops in SP observations.

ferences that could be observed on various types of electronically conducting ores. However, Kilty [54] has pointed out that these calculations postulate equilibrium electrochemical conditions in that they disregard the effect of the ohmic potential drop in the electrolyte due to current flow. We shall therefore look somewhat more closely at the phenomenon.

The field measurement of SP is essentially a measurement of the ohmic drop IR between two potential electrodes where I is the current and R the electric resistance along the current filament between the electrodes. Fig. 4.7 shows such a current filament. We shall assume that the electrolytes near the top and bottom of the ore are chemically identical except for the ionic concentrations. The interface reactions that liberate ions cause a potential difference between

the ore and the solution in contact with it. Thus the potentials V_1 and V_4 at the two ends are different from V_2 and V_3 just outside the ore. Of course V_1 and V_4 are not directly accessible to observation. The interface potential drops at the top and bottom are therefore

$$\Delta\phi_b = V_1 - V_2, \qquad \Delta\phi_t = V_4 - V_3 \tag{4.5}$$

In addition, along the current filament there are the ohmic potential drops IR_1, IR_2 and IR_3 where R_1, R_2, R_3 denote the electric resistances along the different sections of the current path. What we measure as the SP anomaly at a point is the drop IR_2.

According to Kirchhoff's law in electric theory the sum of all potential drops along a closed current path is zero. Hence

$$(V_1 - V_2) + IR_1 + IR_2 + IR_3 + (V_3 - V_4) + V_4 - V_1 = 0$$

that is, the observed SP is

$$IR_2 = -V_{ore} + \Delta\phi_t - \Delta\phi_b - I(R_1 + R_3) \tag{4.6}$$

where V_{ore} is the potential drop $V_4 - V_1$ within the ore. (Kilty has denoted $\Delta\phi_t, \Delta\phi_b$ by $\Delta\phi_e, \Delta\phi_d$ respectively.) For V_{ore}, Eq. (4.6) gives

$$V_{ore} = \Delta\phi_t - \Delta\phi_b - IR \tag{4.7}$$

where IR is the total ohmic drop in the electrolyte along the filament. The theory of Sato and Mooney assumes $I = 0$ (which is not the case in nature). If $I = 0, \Delta\phi_t$ and $\Delta\phi_b$ can be found from appropriate electrochemical tables. But since $I \neq 0$, Eq. (4.7) shows that V_{ore} is less than the equilibrium value $\varepsilon(0) = \Delta\phi_t - \Delta\phi_b$ and that as the current in the circuit increases the potential drop across the ore decreases. However, $\Delta\phi_t - \Delta\phi_b$ is not constant but is a function $\varepsilon(I)$ of the current in the system, and since $V_{ore} = IR_{ore}$, Eq. (4.7) gives

$$\begin{aligned} IR + IR_{ore} &= \varepsilon(I) \\ &= \varepsilon(0) + \frac{d\varepsilon}{dI} I \end{aligned} \tag{4.8}$$

provided the current I is very small. This is the equation that then determines the current involved in an SP anomaly.

From a study of the self-potentials on the ground and in boreholes on the Joma ore body in Norway, Logn and Bølviken [55] estimated current densities in the area to vary between about $0.001\,\mu A\,m^{-2}$ and about $0.7\,\mu A\,m^{-2}$, while Kilty obtained a value of 0.067 from another anomaly.

4.2.4 Interpretation of SP anomalies

It should be realized that the magnitude or pattern of SP anomalies is no unfailing guide to their ultimate cause. Two almost equally strong, adjacent

anomalies may be due to two entirely different causes, as Fig. 4.8 illustrates. The interpretation may also be complicated because anomalies of two or more different types, or of the same type but due to different sources, are superimposed. In certain cases, however, a combination of geological and topographical data and SP measurements allows one to frame working hypotheses for distinguishing the origin of different SP anomalies in the area of investigation. This is often experienced in well logging for oil or coal as will be seen later (Chapter 9).

For the quantitative interpretation of SP anomalies it is necessary to assume a suitable model of a polarized body and calculate its electric potential under the appropriate boundary conditions. The problem is in fact complicated and formulae for only some simple models can be derived analytically. In general, numerical methods are required [56].

The simplest model is a perfectly conducting sphere polarized in the vertical direction (Fig. 4.9(a)), for which it can be shown that the self-potential U at a point P of the ground (outside the sphere) is given by

$$U = C\left(\frac{a-z}{r^3} + \frac{a+z}{r'^3}\right) \tag{4.9}$$

where $r^2 = x^2 + (a-z)^2, r'^2 = x^2 + (a+z)^2$, a = depth of centre of the sphere, x = horizontal distance of P from the sphere's centre, z = depth of P below the

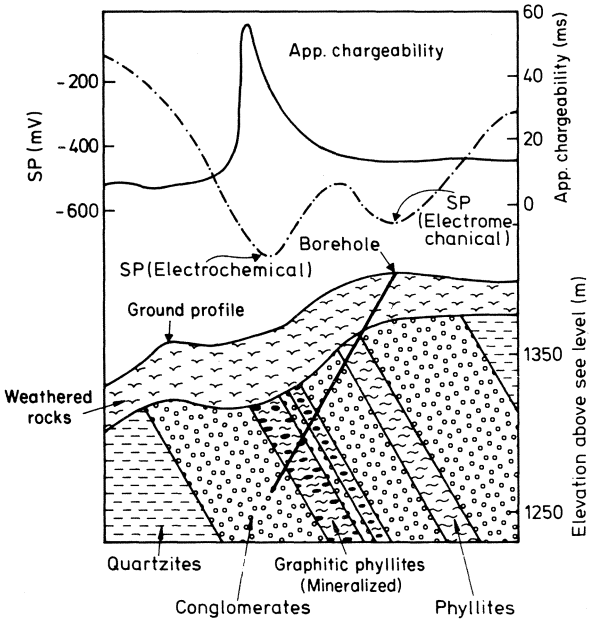

Fig. 4.8 Adjacent SP anomalies due to two different causes. After [49].

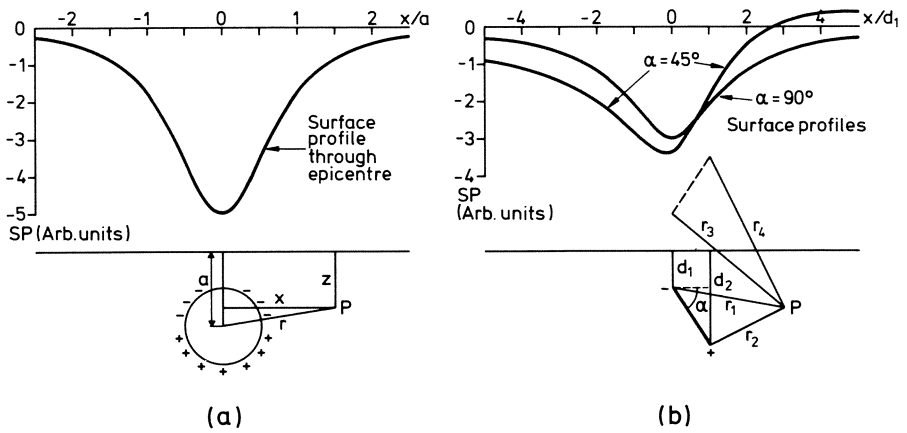

Fig. 4.9 SP anomalies over (a) a polarized sphere and (b) a thin dipping plate.

ground surface and C = the maximum anomaly on the ground surface ($z = 0$). It can easily be shown that for a profile through the epicentre on a horizontal ground surface, the distance between the points at which the SP anomaly falls to $C/2$ is

$$w_{1/2} = 2a(4^{1/3} - 1)^{1/2}$$

from which we obtain the depth rule

$$a \approx 0.65\, w_{1/2} \tag{4.10}$$

Another simple model is a perfectly conducting, infinitely long, inclined thin plate with horizontal edges (Fig. 4.9(b)) polarized in the direction of its dip. In this case

$$U = C \ln\left(\frac{r_1 r_3}{r_2 r_4}\right) \tag{4.11}$$

where r_1, r_2 are the shortest distances of P from the top and bottom edges of the plate respectively, and r_3, r_4 are the corresponding distances from the images of the edges in the horizontal ground surface. For points on a profile on the ground and at right angles to the plate edges, U can be expressed as

$$U = C \ln \frac{x^2 + d_1^2}{(x - l\cos\alpha)^2 + d_2^2} \tag{4.12}$$

where d_1, d_2 are the depths of the top and bottom edges of the plate, x is the distance of P from the profile point O vertically above the top edge, α is the dip and l is the plate's extent in the dip direction. Actually $l\cos\alpha = (d_2 - d_1)\cot\alpha$ but it is preferable to use $l\cos\alpha$ since Eq. (4.12) then remains valid without

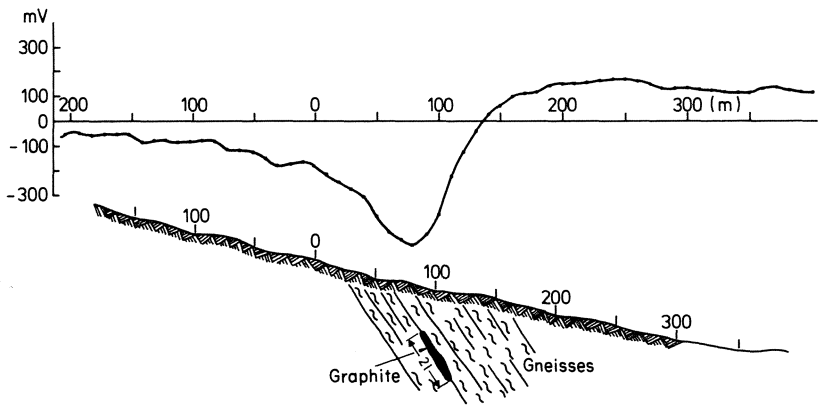

Fig. 4.10 SP on a graphite occurrence resembling a dipping plate. After P. Meiser (*Geophysical Prospecting*, 1962, p. 212).

modification even when the dip is zero. The equation can also be written as

$$U = C \ln \frac{x^2 + d_1^2}{x^2 - 2l(x \cos \alpha - d_1 \sin \alpha) + d_1^2 + l^2} \tag{4.13}$$

No *exact* scheme like the one in Section 2.9.3.1 for magnetic anomalies seems so far to have been devised for determining the parameters l, d_1 and α of Eq. (4.13) from SP anomalies, so that adjustment by trial and error must be resorted to at some stage. In the case where the SP anomaly is accompained by a magnetic one from the same structure, the initial parameter estimates can be obtained from the magnetic curve.

Fig. 4.10 shows a field example on a graphite occurrence that resembles a dipping plate.

4.3 EARTH RESISTIVITY

4.3.1 Basic idea and scope

In the ER method a direct commutated or low-frequency alternating current is introduced into the ground by means of two electrodes (metal stakes or suitably laid out bare wire) connected to the terminals of a portable source of e.m.f. The resulting potential distribution on the ground, mapped by means of two probes (metal stakes or, preferably, non-polarizable electrodes), is capable of yielding information about the distribution of electric resistivity below the surface. The method has been used mainly in the search for water-bearing formations, in stratigraphic correlations in oil fields and in prospecting for conductive ore bodies. An application to an archaeological problem has been reported by Ginzburg [57].

4.3.2 Electric conduction in continuous media

The electric current I (A) in a short, thin, linear conductor of uniform cross-section is given by Ohm's law as

$$I = -\frac{\mathrm{d}V}{R} \tag{4.14}$$

where $\mathrm{d}V$ is the potential difference (V) between the ends of the conductor and R (Ω) is the resistance of the conductor. The minus sign expresses the fact that the current flow is from high to low potential, that is, in a direction opposite to that of the increase of potential (the gradient). R is directly proportional to the length $\mathrm{d}l$ (m) of the conductor and inversely to the cross-section s (m^2) so that

$$R = \rho\frac{\mathrm{d}l}{s} \tag{4.15}$$

where the constant of proportionality ρ is the *resistivity* (Ω m) of the material of the conductor. We should note carefully the distinction between resistance and resistivity. The resistance is a characteristic of a particular path of an electric current whereas resistivity is a physical property of a material.

From Eqs (4.14) and (4.15) we get

$$\frac{I}{s} = -\frac{1}{\rho}\frac{\mathrm{d}V}{\mathrm{d}l} \tag{4.16}$$

The left-hand side of this equation is the current density j (current per unit area of cross-section, $\mathrm{A\,m^{-2}}$), while $-\mathrm{d}V/\mathrm{d}l$ on the right-hand side is the electric field E ($\mathrm{V\,m^{-1}}$) in the direction of the current density vector. Hence

$$j = E/\rho \qquad \text{or} \qquad E = \rho j \tag{4.17}$$

Alternatively

$$j = \sigma E \tag{4.18}$$

where $\sigma\,(=1/\rho)$ is the conductivity of the material, siemen per metre ($\mathrm{S\,m^{-1}}$), also called mho per metre ($\Omega^{-1}\,\mathrm{m}$), the word 'mho' being 'ohm' spelt backwards.

If we let the length $\mathrm{d}l$ in (4.16) tend to zero and consider the linear conductor as an element of a homogeneous and isotropic continuous medium, e.g. a homogeneous rock mass, then either of the equations (4.17) or (4.18) expresses Ohm's law for such a medium. In an isotropic medium σ and ρ are independent of the direction of current flow.

4.3.3 Point current electrode on homogeneous earth

Consider a point electrode on the surface of a homogeneous isotropic earth extending to infinity in the downward direction and having a resistivity ρ.

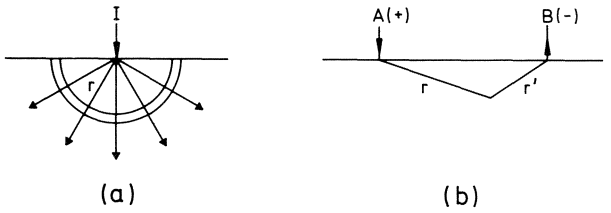

Fig. 4.11 Point electrodes on the surface of a homogeneous earth.

Describe a hemispherical shell of radius r and thickness dr around the electrode (Fig. 4.11(a)). By symmetry, the current at any point of the shell will be along the radius. If the total current passing through the electrode into the ground is I the potential drop dV across the shell can be written, using Eq. (4.16), as

$$\mathrm{d}V = -\frac{I\rho\,\mathrm{d}r}{2\pi r^2}$$

Integrating, we get for the potential at a distance r from a point current source

$$V(r) = \frac{I\rho}{2\pi}\frac{1}{r} + C$$

where C is an arbitrary constant. If V is chosen to be zero at $r = \infty$, then $C = 0$ and we get

$$V(r) = \frac{I\rho}{2\pi}\frac{1}{r} \tag{4.19}$$

In practice we have, of course, two electrodes, one positive (A), sending current into the ground, and the other negative (B), collecting the returning current (Fig. 4.11(b)). The total potential at any point P in the ground will then be

$$V = \frac{I\rho}{2\pi}\left(\frac{1}{r} - \frac{1}{r'}\right) \tag{4.20}$$

where r, r' are the distances of P from the two electrodes.

4.3.4 Buried current electrode in homogeneous, isotropic earth

This is a slightly more general situation than the one considered above. In finding the potential in this case we must take into account the boundary condition that there is no current density at the ground surface perpendicular to the surface, that is, in the vertical or z direction. This condition happens to be automatically inherent in the solutions of the previous case. There as well as now, all the current at the surface flows in the horizontal direction (Fig. 4.12).

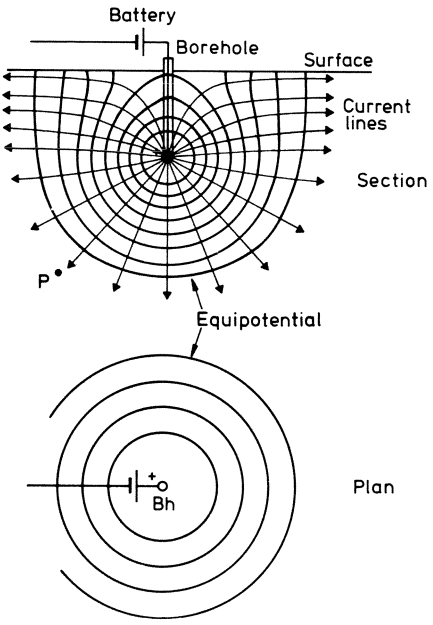

Fig. 4.12 Buried point electrode.

From Eq. (4.16) it is evident that V must therefore satisfy the condition $(1/\rho)(\partial V/\partial z) = 0$ at the ground surface. The expression that satisfies this condition and Laplace's equation (Appendix A7.1) is

$$V = \frac{I\rho}{4\pi}\left(\frac{1}{r_1} + \frac{1}{r'_1}\right) \tag{4.21}$$

where r_1, r'_1 are the distances of the point P from the current electrode and its image in the ground surface respectively. Fig. 4.12 also shows the current and equipotential lines on a vertical plane through the electrode. The complete equipotential surfaces can be visualized by imagining the figure revolved round an axis through the electrode and perpendicular to the ground surface. On the ground surface the equipotential lines will be circles centred around the electrode epicentre.

With two buried electrodes, a positive and a negative one as usual, the potential becomes

$$V = \frac{I\rho}{2\pi}\left(\frac{1}{r_1} + \frac{1}{r'_1} - \frac{1}{r_2} - \frac{1}{r'_2}\right) \tag{4.22}$$

where r_2, r'_2 are the distances of P from the negative electrode and its image respectively.

4.4 SOME PRACTICAL ASPECTS OF RESISTIVITY WORK

4.4.1 Resistivity of rocks and minerals

On a non-homogeneous earth the measured potentials when current is introduced into the ground will differ from those calculated under the assumption that the ground is homogeneous. The magnitude of the electric anomalies on a non-homogeneous earth depends upon the resistivity differences between different rocks.

The resistivity of rocks is an extremely variable property ranging from about $10^{-6}\,\Omega$m for minerals such as graphite to more than $10^{12}\,\Omega$m for dry quartzitic rocks. Most rocks and minerals are insulators in the dry state. In nature they almost always hold some interestitial water with dissolved salts and therefore acquire an ionic conductivity which then depends upon the moisture content, the nature of the electrolytes and the degree to which the open spaces in a rock (pores, microfissures, cracks, fractures etc.) are saturated with water. The form of the pores in a rock plays a subordinate role in determining the conductivity but the degree of pore interconnection is very important. In rocks like basalt or granite, for example, the conductivity can vary enormously depending upon the degree of pore interconnection or lack of it, from thousands of Ωm in compact, non-porous masses down to 10–50 Ωm in rocks like porous, water-bearing basalts in most tropical areas. Water-bearing fracture zones in rocks usually have fairly low resistivities while the resistivity of clays depends on the proportion of clay minerals and other material.

Some minerals, notably graphite, pyrrhotite, pyrite, chalcopyrite, galena and magnetite, are relatively good electronic conductors (Table 4.1). A dissemination of such minerals within a rock can also make it a better

Table 4.1 Electric resistivities (Ωm)

Rocks and sediments		Ores	
Limestone (marble)	$> 10^{12}$	Pyrrhotite	10^{-5}–10^{-3}
Quartz	$> 10^{10}$	Chalcopyrite	10^{-4}–10^{-1}
Rock salt	10^{6}–10^{7}	Graphite shales	10^{-3}–10^{1}
Granite	5000–10^{6}	Pyrite	10^{-4}–10^{1}
Sandstones	35–4000	Magnetite	10^{-2}–10^{1}
Moraine	8–4000	Haematite†	10^{-1}–10^{2}
Limestones	120–400	Galena	10^{-2}–300
Clays	1–120	Zinc blende	$> 10^{4}$

†Stoichiometric Fe_2O_3 Insulator

conductor but very much depends upon the nature of the dissemination. Pyrite, chalcopyrite, pyrrhotite etc. can occur as 'rolled' crystals or flakes with intimate contact between crystal surfaces. Ores containing these minerals are very often good conductors. Galena and magnetite have a tendency to form individual, euhedral crystals, more or less isolated from each other, so that galena and magnetite ores are as a rule poorer conductors than, for example, pyrite ores.

Practically all rocks and minerals are semiconductors, their conductivity increasing with increasing temperature according to the equation

$$\sigma = \sigma_0 e^{-E/kT} \tag{4.23}$$

where T is the absolute temperature (K), k is Boltzmann's constant and E is the so-called energy gap or activation energy for the substance in question. The activation energies are, however, poorly known for most of the naturally occurring minerals. Stoichiometric haematite and zinc blende are insulators but certain impurities in haematite, for example, can reduce the resistivity considerably. These so-called donor or acceptor impurities also play a great part in determining the magnitude of the conductivity of naturally occurring sulphides and oxides. Modern solid state theory provides an explanation of these phenomena based on quantum mechanics [58].

The resistivity of porous, water-bearing rocks (free of clay minerals) follows Archie's law, $\rho = \rho_0 f^{-m} s^{-n}$ where ρ_0 is the resistivity of the water filling the pores, f is the porosity (volume fraction pores), s is the fraction of pore space filled by the water and n, m are certain parameters. The value of n is usually close to 2.0 if more than about 30% pore space is water-filled but can be much greater for lesser water contents.

The value of m depends upon the degree of cementation or, as this is often well correlated with geologic age, upon the geologic age of the rock. It varies from about 1.3 for loose, Tertiary sediments to about 1.95 for well-cemented Palaeozoic ones, but can be outside this range for individual formations.

Archie's law is of considerable importance in electric well logging (Chapter 9). It is an empirical law but a theoretical basis for it has been indicated recently by Korvin [59] in a very interesting paper.

The determination of the resistivity of rock samples is, in principle, simple and need only involve measuring the current density in, and the potential difference across, a rectangular or cylindrical sample with plane end faces. The application of Eq. (4.16) then gives the resistivity. In practice several problems arise due to the inhomogeneous nature of most natural samples and due to electrode polarization caused by electrochemical action when a current is passed through a sample. To overcome the latter problem it is necessary to make the measurements with an alternating current of a suitably high frequency (e.g. 100–1000 Hz).

4.4.2 Apparent resistivity

Let A, B be the current electrodes, positive and negative respectively, placed on the ground surface and M, N the potential probes. If ΔV is the voltage difference between M and N it follows from (4.20) that

$$\rho = 2\pi \frac{\Delta V}{IG} \tag{4.24a}$$

where

$$G = \frac{1}{AM} - \frac{1}{BM} - \frac{1}{AN} + \frac{1}{BN} \tag{4.24b}$$

Equation (4.24) yields the resistivity of a homogeneous earth. In an actual case, ρ will vary on altering the geometrical arrangement of the four electrodes or on moving them on the ground without altering their geometry. That is, $\Delta V/I$ will not be directly proportional to G as on a homogeneous earth. The value of ρ, obtained on substituting the measured $\Delta V/I$ and the appropriate G in Eq. (4.24), is called the *apparent resistivity* (ρ_a). It can be calculated for given electrode arrangements for a number of sub-surface resistivity distributions by solving the boundary value problem involved.

4.4.3 Point-electrode configurations

A variety of electrode arrangements are possible but we shall restrict ourselves to some of the common arrays in use. Throughout the following A, B will denote the current electrodes and M, N the potential probes. For the time being, we shall only consider arrays placed on the ground surface, assumed to be flat.

4.4.3.1 Wenner

In this array (Fig. 4.13(a)) the four electrodes are collinear and the separations between adjacent electrodes are equal (a), with M, N in between A, B as shown.

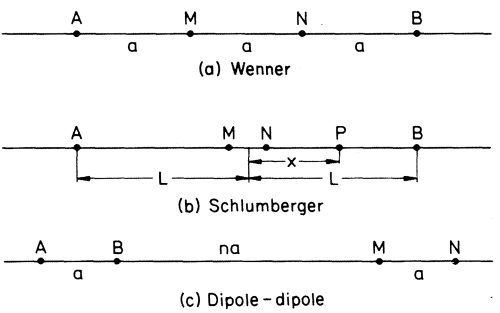

Fig. 4.13 Some electrode configurations.

Equation (4.24) reduces then to

$$\rho_a = 2\pi a \frac{\Delta V}{I} \tag{4.25}$$

4.4.3.2 Schlumberger

The M, N electrodes in this array (Fig. 4.13(b)) are also between A, B and placed symmetrically at the centre, but $MN(=2l) \ll AB(=2L)$. At an arbitrary point P on the line $AMNB$ we get, using Eq. (4.24) and measuring x from the centre of the line,

$$V = \frac{I\rho}{2\pi}\left(\frac{1}{L+x} - \frac{1}{L-x}\right)$$

from which

$$\frac{dV}{dx} = -\frac{I\rho}{2\pi}\left(\frac{1}{(L+x)^2} + \frac{1}{(L-x)^2}\right) \tag{4.26}$$

At the centre ($x = 0$), therefore,

$$\frac{dV}{dx} = -\frac{I\rho}{\pi L^2}$$

which gives for the apparent resistivity

$$\rho_a = \frac{\pi L^2}{I}\left(-\frac{dV}{dx}\right) \tag{4.27a}$$

If MN is sufficiently small, we may put $(-dV/dx) = \Delta V/2l$ where ΔV is the measured voltage difference between M and N (potential of M minus the potential of N). Then

$$\rho_a = \frac{\pi L^2}{2l}\frac{\Delta V}{I} \tag{4.27b}$$

where $\pi L^2/2l$ is the array constant.

4.4.3.3 Axial bipole–bipole ('dipole–dipole')

The arrangement shown in Fig. 4.13(c) is usually referred to as dipole–dipole but we shall see below that it would be preferable to call it an axial bipole–bipole system. In this array M, N are outside A, B and on the same line, each pair having a constant mutual separation a. If na is the distance between the two innermost electrodes (B, M) then Eq. (4.24) yields

$$\rho_a = \pi n(n+1)(n+2)a\frac{\Delta V}{I} \tag{4.28}$$

4.4.3.4 Various dipole–dipole arrays

The product of I and the length AB is called the dipole moment of the current source. If AB is made vanishingly small and I is increased at the same time, keeping $I \times (AB)$ constant, we obtain an ideal point current dipole of moment $I \times (AB)$ ampere metre. In practice, the electric field produced at a point P by a pair of current electrodes may be considered to be produced by a point dipole if the distance of P from A and B is large compared with the dipole length AB. If the separation MN of the potential probes, between which P is situated, is likewise small compared to P's distance from A and B we speak of a *potential dipole* MN. If the lengths AB and MN, instead of being small, are comparable to the distance between their centre points, we speak of a *bipole–bipole* system. We may also have a hybrid system like bipole–dipole.

The potential at P of the current dipole in Fig. 4.14 on homogeneous ground is

$$V = \frac{I\rho}{2\pi}\left(\frac{1}{AP} - \frac{1}{BP}\right)$$

$$= \frac{I\rho}{2\pi}\frac{BP - AP}{(AP)(BP)} \tag{4.29}$$

However, when the distance of P is large, $AP \approx BP = r$ and $BP - AP \approx BP - MP = BM = AB\cos\alpha$ if AM is the perpendicular from A to BP. When r is large the angle α may be put equal to θ, which is the angle between BA and the line joining P to the dipole centre O. With all the substitutions made in Eq. (4.29) we get

$$V = \frac{\rho I}{2\pi}\frac{(AB)\cos\theta}{r^2} \tag{4.30}$$

as the dipole potential. From this we can obtain the gradient of V in the desired direction, namely the direction of the potential dipole. The measured gradient when substituted in this expression will yield the apparent resistivity corresponding to the particular dipole–dipole orientation.

Several different dipole–dipole configurations have been suggested and given

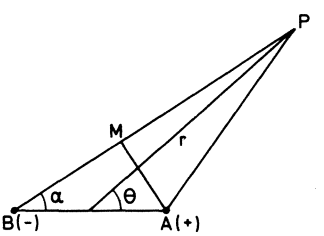

Fig. 4.14 An electric dipole.

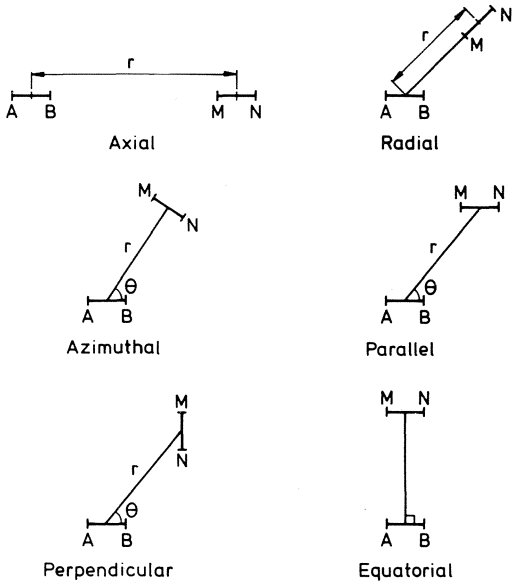

Fig. 4.15 Various dipole–dipole configurations.

characteristic names as shown in Fig. 4.15. The derivation of the ρ_a formulae is indicated in Appendix 8. As can be seen from Fig. 4.15 the main geometrical features of the various arrangements are as follows.

In the *axial* configuration A, B, M, N are collinear. In the *radial* one the MN dipole is oriented along the line joining the dipoles. The axial array is a special case of the radial. In the *azimuthal* configuration the MN dipole is perpendicular to the line joining the dipoles. In the *parallel* configuration the dipoles are parallel but not collinear. A special case of it ($\theta = 90°$) is the *equatorial* configuration in which the MN dipole centre is always on the line joining the dipoles. When the dipoles are perpendicular to each other we have the *perpendicular* array.

The advantage of dipole–dipole arrays is that the distance between the current source and the potential dipole can be increased almost indefinitely, being subject only to instrument sensitivity and noise, whereas the increase of electrode separations in the Wenner and Schlumberger arrays is limited by cable lengths.

4.4.3.5 Pole–dipole and pole–pole

When one of the current electrodes, say B, is very far removed from the measurement area the electrode A is referred to as a current pole. The MN array may be a dipole (length $MN \ll$ distance AM) or a bipole. We have then a

pole–dipole (or a pole–bipole) array. Conversely, when one of M, N is far removed, the remaining electrode is referred to as a potential pole. If the current dipole AB is then short compared with its distance from the potential pole we have a *dipole–pole* array. Finally, a *pole–pole* arrangement will be obtained when one of A, B and one of M, N are removed to 'infinity'. Figs 4.11 and 4.12 really imply an ideal pole–pole arrangement.

The pole–dipole or dipole–pole arrangements are not uniquely defined by these names alone since the orientation of the dipole (or bipole, as the case may be) with respect to the dipole–pole line remains to be specified. In their particular forms in which the electrodes are collinear these arrangements are, for obvious reasons, often referred to as *three-electrode arrays* while the pole–pole is often referred to as a *two-electrode array*. A particular case of pole–dipole is the *half-Schlumberger* in which A (or B) of Fig. 4.14(b) is effectively at infinity.

The expressions for the apparent resistivity for the pole–dipole, dipole–pole and pole–pole are left to the reader as exercises.

4.4.3.6 Reciprocity theorem

It can be seen from Eq. (4.24b) that if the electrodes A, B are interchanged for M, N respectively and vice versa, the expression for G is unaltered. Then Eq. (4.24a), which is true for a homogeneous earth, of resistivity ρ, shows that the voltage ΔV between the new potential electrodes will also be unaltered if the current passing through the new current electrodes in kept the same as before. Actually, this is a special case of the reciprocity theorem which is also valid for an inhomogeneous earth consisting of any number of separate regions, each of which is a homogeneous medium whose conductivity is independent of the current density. It follows that if this condition is met, the apparent resistivity obtained with any configuration of Section 4.4.3.5 remains the same if the A, B and M, N pairs are interchanged and the current is kept the same, no matter how complicated the resistivity distribution in the sub-surface.

The reciprocity of A, B and M, N pairs is easily verified in practice. It must be remarked, however, that if the experiment is made with a small distance between the two pairs, a different value of ρ_a may be obtained after an interchange because at the high current densities near the potential electrodes in such a case, the conductivity of the ground may not be independent of the current density.

4.5 VERTICAL ELECTRICAL SOUNDING (VES)

4.5.1 Sounding and mapping

The properties of the sub-surface may be explored by two main procedures often called, by analogy, electric sounding (or drilling) and electric mapping (or

trenching). In this section we shall deal with sounding, leaving mapping for a subsequent one. The object of sounding is to determine the variation of electric conductivity with the depth. Strictly speaking, the idea is meaningful only for an earth in which the conductivity varies merely with depth without any lateral variations. Good to excellent approximations to this situation are commonly found in sedimentary areas with gently dipping or flat-lying beds and VES has been the most important geophysical method of water prospecting in many such areas. Less favourable for VES, because of lateral inhomogeneities in them, are areas like moraine-covered Precambrian terrain or areas of deep *in situ* weathering with fresh bedrock underneath, where the method is often used to estimate the thickness of the overburden.

The essential idea behind VES, assuming conductivity variation with depth only, is the fact that as the distance between the current and potential electrodes is increased the current filament passing across the potential electrodes carries a current fraction that has returned to the surface after reaching increasingly deeper levels. This will be appreciated from Fig. 4.16(a). Here, the current filament 2 flowing across the electrode pair M_2, N_2 carries current that has returned to the surface from a deeper level than the filament 1 flowing across the pair M_1, N_1 nearer to the current source A, B. Thus the potential difference ΔV_2, and hence the apparent resistivity ρ_{a2} in the position M_2N_2, are relatively more influenced by the conductivity at deeper levels than are the quantities ΔV_1 and ρ_{a1}. An analogous argument applies when M, N are kept at the same place but A, B are moved instead (Fig. 4.16(b)). Thus a sounding can be performed by moving either the pair A, B or the pair M, N or, in fact, both. Note that as long as the distance AB is not altered, which is the case shown in 4.16, the current distribution as such in the earth is not altered, that is, the fraction of the total injected current penetrating below any given level before returning to the surface is exactly the same irrespective of the

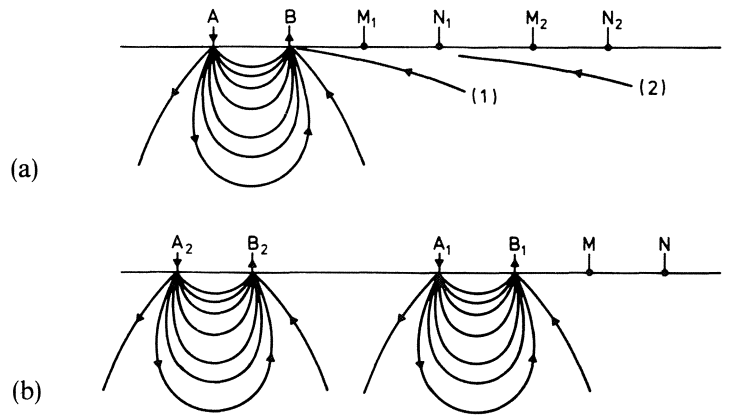

Fig. 4.16 Essential idea behind VES.

relative positions of the A, B and M, N pairs. This fraction will, however, alter if the distance AB is changed.

4.5.2 Field procedure in VES

4.5.2.1 Wenner sounding

In this case the distance a (Fig. 4.13(a)) is increased by steps, keeping the midpoint of the configuration fixed. The apparent resistivity is obtained from Eq. (4.25) but it must be remembered that here, as in all earth resistivity measurements, ΔV represents the measured voltage between M and N *minus* any self-potential voltage between M and N observed before the current is passed.

4.5.2.2 Schlumberger sounding

The M, N electrodes (Fig. 4.13(b)) are kept fixed and A, B are moved outward symmetrically in steps. At some stage the MN voltage will, in general, fall below the reading accuracy of the voltmeter in which case the distance MN is increased (e.g. five- or ten-fold), maintaining, of course, the condition $MN \ll AB$. It is advisable then to have an overlap of two or three readings with the same AB and the new as well as the old MN distance. The ρ_a values with the two MN distances but the same AB may sometimes differ significantly from each other and if, in this case, the results are plotted as ρ_a against AB (or $AB/2$), each set of ρ_a values obtained in the overlapping region with one and the same MN will be found to lie on separate curve segments, displaced from each other (Fig. 4.17).

The different segments must be suitably merged to obtain a single smooth sounding curve. Often, it is sufficient to shift a segment obtained with a larger MN towards the adjoining previous one obtained with the smaller MN, as shown in Fig. 4.17, the reasoning being that $\Delta V/(MN)$ measured for a smaller MN value is nearer to the true gradient in Eq. (4.27) than the value with the larger MN. The predominant contribution to the shifts comes, however, in practice from the differing effect of local inhomogeneities at the old and new

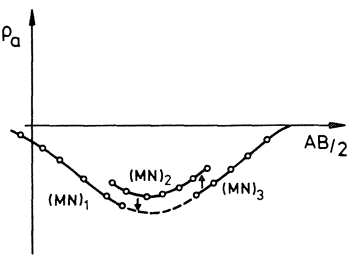

Fig. 4.17 Displacement of segments in Schlumberger sounding.

positions of M and N electrodes. The effect exists in Wenner sounding as well and is, in fact, more serious since all the four electrodes are moved, but it is concealed and not readily identifiable.

4.5.2.3 Dipole–dipole sounding

The basic procedure in this case is already evident from Fig. 4.16 which shows an axial 'dipole–dipole' system. The apparent resistivity is given by Eq. (4.28). Soundings can be made, in principle, with any of the dipole configurations in Fig. 4.15 but in most other cases the field routine will be inconvenient.

Similarly, the pole–pole, pole–dipole and dipole–pole arrangements (Section 4.4.3.5) could also be used, but the effect of the far electrode (B or N) is hardly ever negligible in practice and the measurement becomes, to all intents and purposes, a four-electrode one, so that it is then just as well to use one of the three principal sounding procedures described above.

4.5.3 Layered earth

4.5.3.1 Slichter–Langer theorem

It was shown by Slichter [60] and Langer [61] that if the conductivity σ in the earth varies with depth only, it can be determined uniquely from a knowledge of the surface potential produced by a single point electrode. No further physical or geological data are needed for the purpose. It is instructive to contrast this problem with its theoretical possibility of a unique solution with the inverse magnetic and gravity problems which are fundamentally indeterminate. It must be noted, however, that the determination of σ solves the *electric* problem but not necessarily the *geological* one.

One type of conductivity distribution to which the Slichter–Langer theorem undoubtedly applies is an earth composed of several horizontal strata with no variation of conductivity in the horizontal direction in any stratum. This model adequately describes many geological situations and is of particular importance in prospecting for ground water by the earth resistivity method. However, because of the practical numerical difficulties involved in applying the Slichter–Langer theorem, in practice one must, as a rule, resort to a trial-and-error technique in which the surface potential or apparent resistivity due to a current source is calculated for an assumed stratified conductivity distribution and compared with the observations.

4.5.3.2 Apparent resistivity on a horizontally-layered earth

We have seen in Section 4.3.3 that the surface potential of a point electrode placed on the surface of a homogeneous earth is $I\rho/2\pi x$ at a distance x from the electrode. In Appendix 9 it is shown that on a horizontally-layered earth the

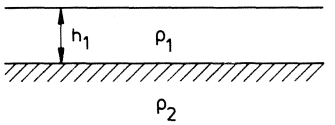

Fig. 4.18 Two-layer earth.

potential is given by

$$V(x) = \frac{I\rho_1}{2\pi}\frac{1}{x}\left(1 + 2x\int_0^\infty K(\lambda)J_0(\lambda x)\,\mathrm{d}\lambda\right) \tag{4.31}$$

where ρ_1 is the resistivity of the top layer, J_0 is the Bessel function of order zero and $K(\lambda)$ is a function of the integration variable λ as well as of the resistivities and thicknesses of all the layers and of the resistivity of the infinite substratum. The integral evidently represents a 'disturbance potential' due to the layered structure. In general it must be numerically evaluated. To take an example of $K(\lambda)$ we have for a two-layer earth (Fig. 4.18):

$$K(\lambda) = \frac{-k_1\exp(-2\lambda h_1)}{1 + k_1\exp(-2\lambda h_1)} \tag{4.32}$$

where h_1 is the thickness of the top layer; ρ_1, ρ_2 are the resistivities of the layer and the substratum respectively; and $k_1 = (\rho_1 - \rho_2)/(\rho_1 + \rho_2)$.

With the knowledge of V it is possible to calculate ρ_a from Eq. (4.24) for any electrode configuration. For example, denoting the second term in the large brackets in Eq. (4.31) by $F(x)$, ρ_a for the Wenner configuration is easily shown to be

$$\rho_{aw} = \rho_1[1 + 4F(a) - 4F(2a)] \tag{4.33}$$

To obtain ρ_a for the Schlumberger configuration we proceed as follows. From Eq. (4.31) the electric field at the distance x is

$$-\frac{\mathrm{d}V}{\mathrm{d}x} = \frac{I\rho_1}{2\pi}\frac{1}{x^2}\left(1 + 2x^2\int_0^\infty K(\lambda)J_1(\lambda x)\lambda\,\mathrm{d}\lambda\right) \tag{4.34}$$

since

$$\frac{\mathrm{d}J_0(x)}{\mathrm{d}x} = -J_1(x)$$

where $J_1(x)$ is the Bessel function of order one. Now, in the Schlumberger configuration (Fig. 4.13(b)) we have one positive and one negative electrode at the same distance L on each side of the central point so that the electric field at the centre is twice that given by (4.34) or, replacing x by $L(= AB/2)$, it is

$$\frac{I\rho_1}{\pi}\frac{1}{L^2}\left(1 + 2L^2\int_0^\infty K(\lambda)J_1(\lambda L)\lambda\,\mathrm{d}\lambda\right)$$

Substituting this for $(-\mathrm{d}V/\mathrm{d}x)$ in Eq. (4.27) we get

$$\rho_{aS} = \rho_1 \left(1 + 2L^2 \int_0^\infty K(\lambda) J_1(\lambda L) \lambda \, \mathrm{d}\lambda \right) \tag{4.35}$$

4.5.3.3 General features and types of VES curves

We shall now confine ourselves to the Schlumberger array in the following discussion but *mutatis mutandis* the same remarks will apply to any other configuration. The ratio ρ_a/ρ_1 for a two-layer case, calculated from (4.35), is shown in Fig. 4.19 on a double logarithmic plot as a function of L/h_1, for values of ρ_2/ρ_1 from 0 (perfectly conducting substratum) to ∞ (perfectly insulating substratum).

It will be seen that ρ_a approaches ρ_1 when the current electrode separation is small compared with the thickness of the top layer and ρ_2 when it is large. The

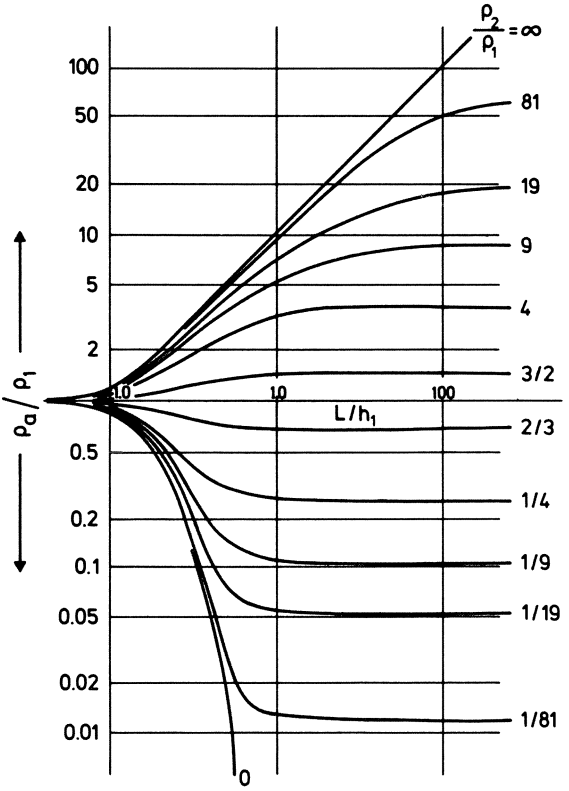

Fig. 4.19 Master curves of Schlumberger apparent resistivity on a two-layer earth.

transition from ρ_1 to ρ_2 is, however, smooth and no simple general rule based on specific properties of the curve (e.g. the gradient) can be devised to find the thickness h_1.

With the addition of a third layer (h_2, ρ_2) sandwiched between the top layer (h_1, ρ_1) and the substratum (ρ_3), the problem becomes much more complicated. The apparent resistivity curve can then take four basic shapes known as Q (or DH, descending Hummel), A (ascending), K (or DA, displaced anisotropic) and H (Hummel type with minimum), depending upon the relative magnitudes of ρ_1, ρ_2, ρ_3 (Fig. 4.20). In every case, however, ρ_a approaches ρ_1 for small values of L and ρ_3 for large ones. At intermediate values of L it is influenced by the resistivity of the middle layer.

For more than three layers the variety of possible VES curves is virtually beyond simple classification. In none of the cases, however, is there any simple relation between the coordinates of the turning points or the inflection points and the layer parameters $h_1, h_2, \ldots$ and $\rho_1, \rho_2, \ldots$ etc.

4.5.3.4 Characteristic function and resistivity transform

The function $K(\lambda)$ in Eq. (4.31) is often called the kernel function of resistivity. This is somewhat of a misnomer since in integral equation theory it is $J_0(\lambda r)$ that is known as the kernel function. We shall call $K(\lambda)$ the 'characteristic

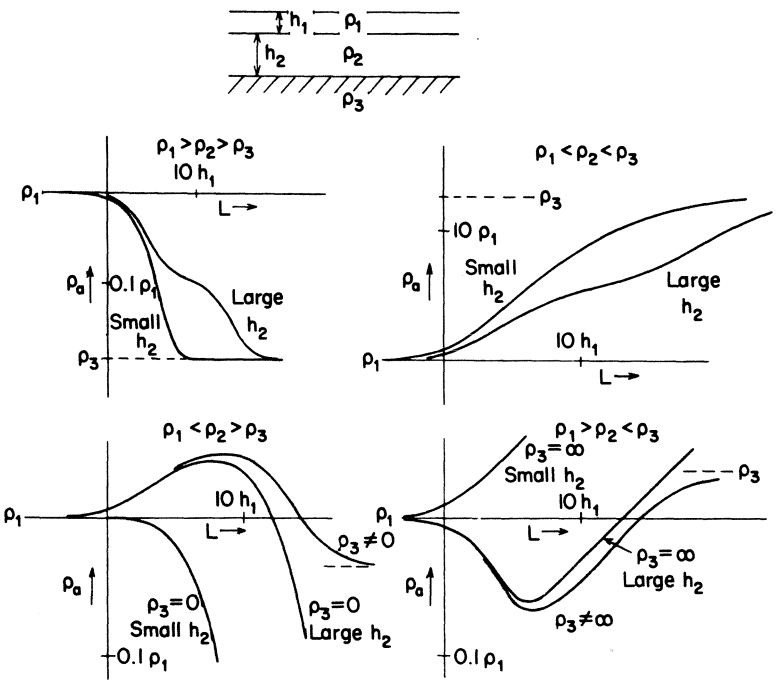

Fig. 4.20 Q (or DH), A, K (or DA) and H-type curves in vertical electrical sounding.

function'. Eq. (4.31) can be rewritten as

$$V = \frac{I\rho_1}{2\pi}\left(\frac{1}{x} + 2\int_0^\infty K(\lambda)J_0(\lambda x)\,d\lambda\right)$$
$$= \frac{I\rho_1}{2\pi}\left(\int_0^\infty J_0(\lambda x)\,d\lambda + 2\int_0^\infty K(\lambda)J_0(\lambda x)\,d\lambda\right)$$
$$= \frac{I}{2\pi}\int_0^\infty T(\lambda)J_0(\lambda x)\,d\lambda \qquad (4.36)$$

where we have used the result $\int_0^\infty J_0(\lambda x)\,d\lambda = 1/x$ in Bessel function theory and put $T(\lambda) = \rho_1[1 + 2K(\lambda)]$. $T(\lambda)$ is known as the resistivity transform. It plays an important role in the modern theory of the interpretation of resistivity sounding as we shall see later. Note that whereas the characteristic function $K(\lambda)$ is dimensionless, $T(\lambda)$ has the dimensions of ohm metre.

Using the result $\int_0^\infty J_1(\lambda x)\lambda\,d\lambda = 1/x^2$ it can be shown similarly that Eq. (4.35) can be written as

$$\rho_a(L) = L^2\int_0^\infty T(\lambda)J_1(\lambda L)\lambda\,d\lambda \qquad (4.37)$$

giving the apparent resistivity for $(AB/2) = L$ in terms of $T(\lambda)$. Corresponding expressions can be derived for all configurations.

4.5.4 VES interpretation

4.5.4.1 Plotting

The first step in the interpretation of VES measurements is to plot these in a graph, either manually or on a CRO terminal screen. For two of the interpretation methods described below it is necessary to use paper.

If we have a Wenner sounding the measured ρ_a is plotted on the y axis and the electrode separation $a(= AB/3)$ on the x axis. The data of a Schlumberger sounding are plotted with $L(= AB/2)$ along the x axis. For dipole–dipole soundings the distance between the centres of the dipoles is the most convenient one to plot along the x axis. Although the plotting may be done on a linear scale, there are so many practical and theoretical advantages in using a logarithmic scale along both axes that VES data are virtually never plotted except on a double logarithmic graph.

In what follows we shall be dealing, unless stated specifically otherwise, with Schlumberger soundings.

4.5.4.2 Curve matching by master diagrams

This method involves a comparison of the measured curve with a set of theoretically calculated master curves. It can be used provided that (1) the data can be plausibly referred to the number of layers for which the master curves

are calculated and (2) the curves have been calculated for the electrode configuration in question. Except for the two-layer case (Fig. 4.19) master curves cannot be presented in a single diagram covering all possible combinations of the thickness and resistivity parameters. Extensive catalogues are needed and have been published elsewhere [e.g. 62, 63]. Master curves are calculated assuming $\rho_1 = 1\,\Omega\text{m}$ and $h_1 = 1\,\text{m}$ and plotted double-logarithmically. The manner of using them is very simple and as follows.

The observed ρ_a is plotted against L on transparent double logarithmic paper with the same modulus (decade length in mm) as the master curves paper. Keeping the respective axes parallel, the transparent paper is slid on various master curves in succession until a satisfactory match is obtained with some curve (if necessary an interpolated one). The value of L coinciding with the point 1.0 on the x axis of the matching curve gives h_1 and the measured value of ρ_a coinciding with the point 1.0 on the y axis gives ρ_1. The values of $h_2, \rho_2, h_3, \rho_3, \ldots$ etc. are obtained from the appropriate parameter belonging to the matching master curve. A self-explanatory example of a measured three-layer curve is shown in Fig. 4.21.

To grasp the validity of the above procedure it will be sufficient for us to study the two-layer case. From Eqs (4.32) and (4.35) we have

$$\rho_a = \rho_1 \left(1 + 2L^2 \int_0^\infty \frac{-k_1 \exp(-2\lambda h_1)}{1 + k_1 \exp(-2\lambda h_1)} J_1(\lambda L) \lambda \, d\lambda \right) \tag{4.38}$$

Putting $\lambda = p/L$, $d\lambda = dp/L$ we get

$$\frac{\rho_a}{\rho_1} = 1 + 2 \int_0^\infty \frac{-k_1 \exp[-2p(h_1/L)]}{1 + k_1 \exp[-2p(h_1/L)]} J_1(p) p \, dp \tag{4.39}$$

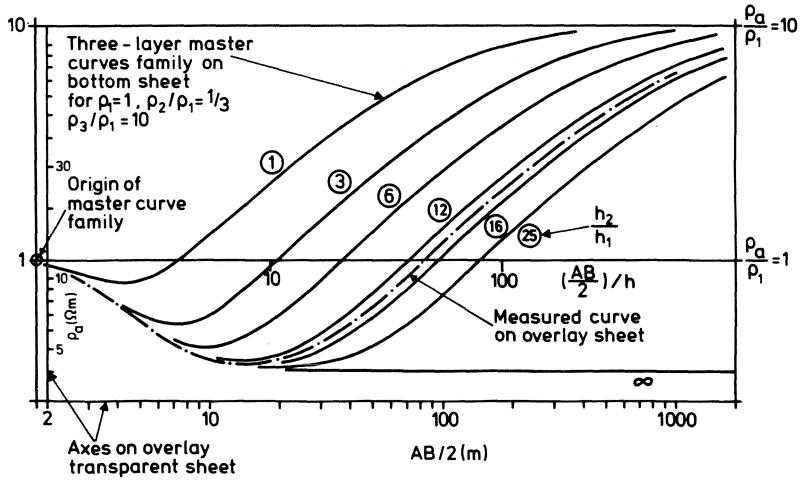

Fig. 4.21 Example of curve matching.

This equation shows that the ratio ρ_a/ρ_1 does not depend on h_1 and L separately but only on the ratio h_1/L. Suppose now that we have two different two-layer earths with parameters ρ_1, ρ_2, h_1 and ρ'_1, ρ'_2, h'_1. On these we have the apparent resistivities ρ_a, ρ'_a respectively, for $AB/2 = L, L'$ respectively. Then, provided k is the same in both cases, Eq. (4.39) shows that

$$\frac{\rho'_a}{\rho'_1} = \frac{\rho_a}{\rho_1} \qquad \text{if} \qquad \frac{L'}{h'_1} = \frac{L}{h_1} \tag{4.40}$$

We now choose an arbitrary value for ρ_1 and one for h_1, and calculate ρ_a/ρ_1 as a function of L/h_1 from Eq. (4.39) for different k values. If we choose $\rho_1 = 1\,\Omega\,\text{m}$ and $h_1 = 1\,\text{m}$ it only remains to choose a suitable scale for drawing graphs of $\rho_a(\Omega\,\text{m})$ against $L\,(\text{m})$ along the x axis. Such a set of standard graphs is the one already shown in Fig. 4.19. When the measured curve $\rho'_1(L')$ on a two-layer earth matches one of the curves in the standard set, and we read the value of ρ'_a on the *measured* curve corresponding to $\rho_a = 1\,\Omega\,\text{m}$ of the *standard* set, the first of Eqs (4.40) shows that this value is just ρ'_1, since $\rho_1 = 1\,\Omega\,\text{m}$. Similarly the second equation shows that the value of L' for the measured curve corresponding to the point $L = 1\,(\text{m})$ in the standard set is equal to h'_1, the first-layer thickness of the unknown earth. Since, according to Eq. (4.39), the two matching curves must have the same k, we have

$$\frac{\rho'_1 - \rho'_2}{\rho'_1 + \rho'_2} = \frac{\rho_1 - \rho_2}{\rho_1 + \rho_2}$$

that is,

$$\frac{\rho'_2}{\rho'_1} = \frac{\rho_2}{\rho_1}$$

But ρ_2/ρ_1 is known from the parameter printed beside the matching standard graph and since ρ'_1 is already known we immediately get ρ'_2. Thus, all the parameters ρ'_1, ρ'_2, h'_1 of the actual two-layer earth are now known.

Exactly the same principle of dimensionless ratios applies to more than two layers, except that a standard curve then will not have just one parameter like ρ_2/ρ_1 attached to it but others like $\rho_3/\rho_1, h_2/h_1, \ldots$ etc. as well. But once ρ_1 and h_1 are known all the other unknowns are easily obtained.

The curve matching technique by means of standard curves is practicable only when the number of layers is small, say up to four. Even for four layers the number of reasonable parameter combinations is so large and the collection of curves so bulky that interpretation by matching becomes generally impracticable and for a larger number of layers it is virtually impossible. Fortunately modern developments described later have rendered the above type of curve matching technique largely obsolete.

4.5.4.3 The auxiliary point method

This method can be traced back to Hummel [64] although it has been subsequently refined and improved by several workers [65]. Let us take a

three-layer case (ρ_1, ρ_2, ρ_3) of Fig. 4.20 with $h_2 \gg h_1$. Clearly, as long as the current electrode separation does not exceed a certain value the apparent resistivity curve will not differ appreciably from a two-layer case with the same ρ_2/ρ_1 as that in the three-layer case under consideration. At large electrode separations the third layer, that is, the infinite substratum (ρ_3), will influence the measurements.

Hummel showed that for sufficiently large separations the apparent resistivity curve obtained is virtually the same as for a two-layer case with the same substratum but with an overlying layer of thickness $H = h_1 + h_2$ and a resistivity ρ_m given by $H/\rho_m = h_1/\rho_1 + h_2/\rho_2$. It will be noticed that ρ_m is derived by applying Kirchhoff's law for resistances in parallel. The equation is easily rearranged as

$$\frac{\rho_m}{\rho_1} = \frac{\rho_2/\rho_1}{\rho_2/\rho_1 - 1 + H/h_1} \frac{H}{h_1} \tag{4.41}$$

By matching the initial branch of a measured resistivity curve with an appropriate curve in Fig. 4.19 we obtain ρ_2 and h_1 (ρ_1 is known from the asymptote of ρ_a for very small electrode separations). Similarly, by matching the branch obtained with large electrode separations we get ρ_3/ρ_m and H again with the help of Fig. 4.19. Since ρ_2/ρ_1 and H/h_1 are now known, ρ_m can be obtained from (4.41) and hence ρ_3, since ρ_3/ρ_m has been determined. The calculation for ρ_m is avoided if the right-hand side of (4.41) is plotted on an auxiliary master diagram as a function of the dimensionless parameter H/h_1. A family of curves for various ρ_2/ρ_1 values is obtained and ρ_m can be read off as the ordinate of the appropriate curve.

The method can be extended in principle to a sounding curve on any number of layers by the alternate use of the two-layer master curves in Fig. 4.19 and the family of auxiliary curves based on Eq. (4.41). The 'drill' with the auxiliary point method can be illustrated by the hypothetical example in Fig. 4.22.

An inspection of the curve in the figure suggests that there must be at least four layers of which the second must be more resistive than the surface layer, the third must be less resistive than the second (as the descending branch shows) and the fourth (substratum) must be more resistive than the third.

A transparent paper on which the sounding curve has been traced is slid on Fig. 4.19 (the logarithmic modulus must be equal on both drawings!) keeping the respective axes parallel to each other until a reasonably long portion of the first branch of the measured curve coincides with one of the master curves. In the example, the coinciding master curve is one for which $\rho_2/\rho_1 = 3$ (dashed in Fig. 4.22). The origin (1, 1) of the master collection is marked on the tracing (circle A with cross in Fig. 4.22). The coordinates of A give ρ_1, h_1.

The tracing is now placed on the auxiliary diagram (Fig. 4.23) on which the family (4.41) has been drawn (again on a logarithmic scale of the same

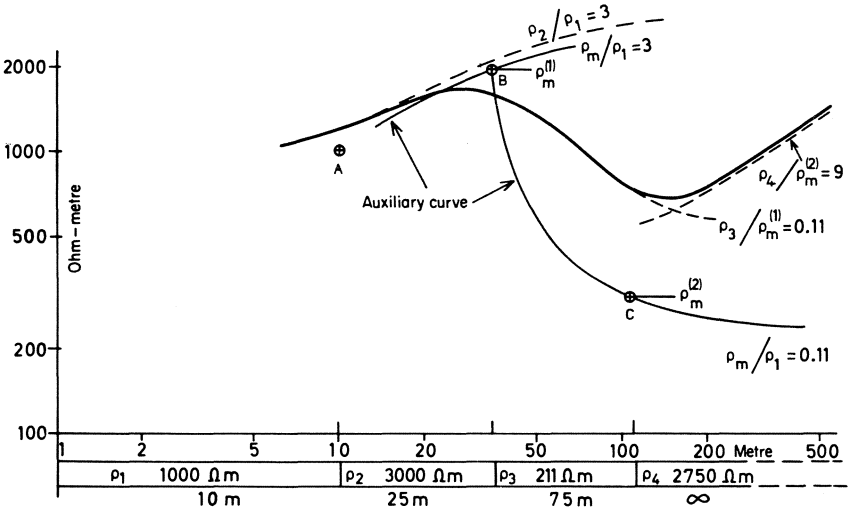

Fig. 4.22 Hypothetical example of auxiliary point method of VES interpretation.

modulus) with A coinciding with the origin of the auxiliary diagram (the auxiliary point!), the respective axes being parallel. The auxiliary curve for which $\rho_2/\rho_1 = 3$ is copied on the tracing for a sufficient length. This is the curve marked $\rho_m/\rho_1 = 3$ in Fig. 4.22.

The tracing is now again transferred to Fig. 4.19 and slid over it, keeping the axes parallel, *and with the origin always on the copied curve* $\rho_m/\rho_1 = 3$, until a further reasonably long portion of the measured sounding curve (in this example the descending branch) coincides with one of the curves in Fig. 4.19. In Fig. 4.22 this is the dashed curve $\rho_3/\rho_m^{(1)} = 0.11$. The origin of Fig. 4.19 is again marked on the tracing (point B). The coordinates of B give $h_1 + h_2$ and $\rho_m^{(1)}$ which is ρ_m of Eq. (4.41).

The tracing is now once more placed on the auxiliary diagram and the curve for 0.11 copied. On re-transferring the tracing to Fig. 4.19 and repeating the procedure above to obtain a coinciding master curve ($\rho_4/\rho_m^{(2)} = 9$) we locate the point C, the coordinates of which give $\rho_m^{(2)}$ and $h_1 + h_2 + h_3$ where

$$\frac{h_1 + h_2 + h_3}{\rho_m^{(2)}} = \frac{h_1}{\rho_1} + \frac{h_2}{\rho_2} + \frac{h_3}{\rho_3}$$

The resistivities of the various layers are easily obtained by multiplying the ratios found by $\rho_1, \rho_m^{(1)}$ and $\rho_m^{(2)}$. The complete interpretation is shown at the bottom in Fig. 4.22.

The most serious limitation of the auxiliary point method is that it requires the thickness of each successive layer to be much greater than the *combined thicknesses* of all the overlying layers. The method has nevertheless been

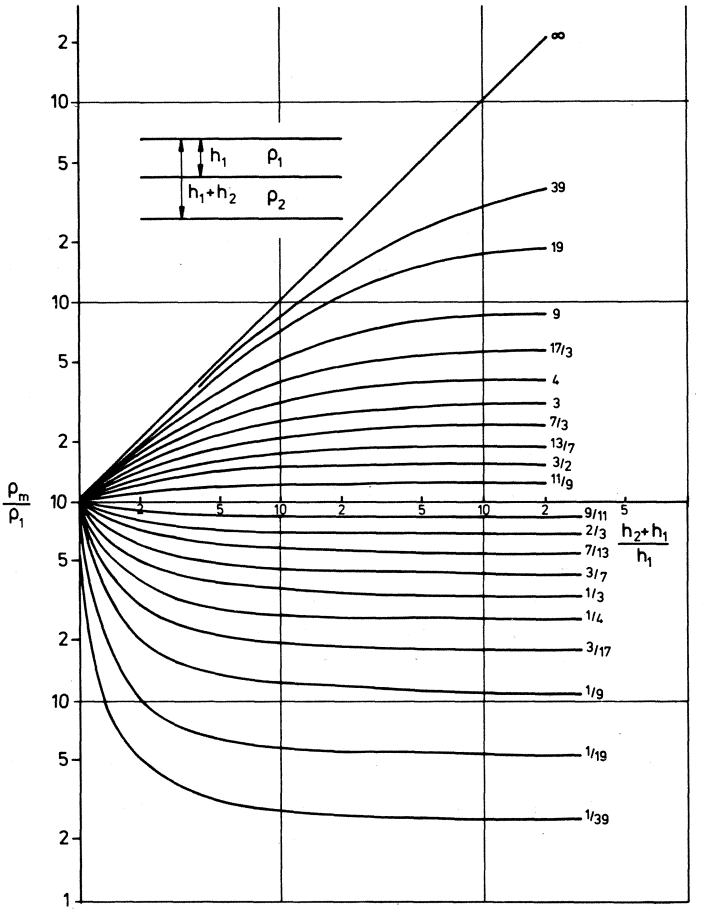

Fig. 4.23 Auxiliary diagram based on Eq. (4.41) for VES interpretation.

extensively used and can give satisfactory results in experienced hands, especially if certain modifications of Eq. (4.41) are used [65]. The risk of misleading results is, however, very great since the basic condition is a severe geological restriction. Now that fast computer methods are available the main use of the auxiliary point method is in locating a trial solution for subsequent optimization.

4.5.4.4 VES curves by linear filters

This trial-and-error method is basically a curve-matching procedure in which the entire VES curve for a specified layered model is calculated at the time of the interpretation itself for comparison with the measured one and the layer parameters are adjusted until a model is arrived at that yields a curve closely

fitting the observed curve and is also satisfactory in the light of any other information that may be available. The procedure requires rapid evaluation of the right-hand side of Eq. (4.37) or the equivalent equation for other electrode configurations. This feat is now possible, thanks to the pioneering work of Ghosh [66] who showed that the evaluation can be made with sufficient accuracy for any value of the distance $L(= AB/2)$ in Eq. (4.37) by means of a small number of fixed coefficients, calculated once and for all. Such a set of coefficients is called a digital linear filter. The computation of a sounding curve involving virtually any number of layers is now a matter of minutes, if pocket-size programmable calculators are used, and of seconds if desk-top or larger computers are available.

(*a*) *Basic procedure and a numerical example.* The mathematical background of Ghosh's idea will be found in for example Kofoed [71] but the practical procedure, divided into two stages, is simple and is illustrated below using the filter originally proposed by Ghosh. Many other filters have been designed subsequently.

(1) In the first stage, sampled values $T_m(m = 0, 1, 2, \ldots)$ of $T(\lambda)$, the transform function corresponding to the layering in question, are calculated from the recurrence relations in Appendix 9 for successive discrete values of λ in the ratio $10^{1/3}$, that is 2.154. The distance along the x axis is $1/\lambda$ and the sampling rate corresponds on a logarithmic plot to three equidistant $T(\lambda)$ values per decade. Any starting value of λ may be used but it is convenient to start with $\lambda = 1$ and calculate for $\lambda < 1$ as well as > 1.

(2) In the second stage, the value of apparent resistivity for the λ corresponding to any m is obtained as

$$(\rho_a)_m = \sum_{j=-3}^{5} b_j T_{m-j} \quad (m = 0, 1, 2, \ldots) \tag{4.42}$$

where b_j are the nine coefficients in Table 4.2. Due to the particular manner in which the b_j's have been calculated by Ghosh, each $(\rho_a)_m$ value obtained from Eq. (4.42) refers, not to the abscissa $1/\lambda$ of the corresponding T_m, but to an abscissa that is about 5% to the left*. Thus, for example, $(\rho_a)_m$ corresponding to T_m at $1/\lambda = 21.54$ is to be plotted at $1/\lambda = 20.46$† etc. On a logarithmic plot of modulus 62.5 mm, for example, this simply means shifting the whole calculated curve by $62.5 \times \log(0.95) = -1.4$ mm, that is, 1.4 mm to the left.

If desired, a second set of transform values may be defined in between those of the first set and the calculation in (4.42) repeated to obtain $(\rho_a)_m$ at a closer spacing.

*To be exact, $(100 \ln 1.05)\% = 4.879\%$.
†More exactly 20.49.

Table 4.2 Ghosh coefficients for calculating ρ_a (Schlumberger array)

b_{-3}	b_{-2}	b_{-1}	b_0	b_1	b_2	b_3	b_4	b_5
0.0225	−0.0499	0.1064	0.1854	1.9720	−1.5716	0.4018	−0.0814	0.0148

If we write out Eq. (4.42) for a particular m we have

$$(\rho_a)_m = b_5 T_{m-5} + b_4 T_{m-4} + b_3 T_{m-3} + b_2 T_{m-2} + b_1 T_{m-1} + b_0 T_m + B_{-1} T_{m+1} + b_{-2} T_{m+2} + b_{-3} T_{m+3} \tag{4.43}$$

If m represents the largest value of $1/\lambda$ at which ρ_a is to be calculated, Eq. (4.43) shows that it is necessary to have five extra T_m values, namely $T_{m-5}, \ldots, T_{m-1}$, to the left of this distance. Similarly if m represents the smallest value of $1/\lambda$ at which $(\rho_a)_m$ is to be calculated we need three extra T_m values, T_{m+1}, T_{m+2} and T_{m+3}, to the right of this distance.

We shall now calculate as an example the ρ_a curve for a Schlumberger sounding on the five-layer earth shown in Fig. 4.24. Referring to Eq. (A9.9), p. 373 we find that $T_1(\lambda)$, which is the same as $T(\lambda)$ of Eq. (4.37), is given by

$$T_1 = \frac{W_1(\lambda) + T_2(\lambda)}{1 + W_1(\lambda) T_2(\lambda)/\rho_1^2} \tag{4.44}$$

where

$$W_1(\lambda) = \rho_1 \frac{1 - u_1}{1 + u_1} \qquad \text{and} \qquad u_1 = \exp(-2h_1\lambda) \tag{4.45}$$

T_1 involves T_2, T_2 involves T_3 and T_3 involves T_4. The expressions for T_2 and T_3 are obtained by simply replacing the subscript 1 in (4.44) and (4.45) by the subscript 2 or 3. Since the substratum in our case is given by $n = 5$ we need only go as far as T_4 according to Eq. A9.8, p. 373. Evidently

$$T_4(\lambda) = \rho_4 \frac{1 - k_4 u_4}{1 + k_4 u_4} \tag{4.46}$$

$$k_4 = \frac{20 - 400}{20 + 400} = -\frac{19}{21}, \qquad u_4 = \exp(-2h_4\lambda) = e^{-50\lambda} \tag{4.47}$$

As a concrete case we shall calculate the transform $T(\lambda)$ for $\lambda = 0.01$.

ρ_1 = 10 Ωm	h_1 = 2 m
ρ_2 = 50 Ωm	h_2 = 15 m
ρ_3 = 100 Ωm	h_3 = 20 m
ρ_4 = 20 Ωm	h_4 = 25 m
ρ_5 = 400 Ωm	substratum

Fig. 4.24 A five-layer earth.

Inserting $\lambda = 0.01$ in (4.46) and (4.47) we get

$$T_4(0.01) = 68.633\,\Omega\,\text{m}$$

The following sequence of values can then be easily checked by the reader, even using a slide rule (preferably one with the exponential function) if a pocket calculator is not available.

$u_3 = 0.6703, \quad W_3 = 19.739, \quad T_3(0.01) = 77.826\,\Omega\,\text{m}$

$u_2 = 0.7408, \quad W_2 = 7.445, \quad T_2(0.01) = 69.225\,\Omega\,\text{m}$

$u_1 = 0.9608, \quad W_1 = 0.1999, \quad T_1(0.01) = T(0.01) = 60.990\,\Omega\,\text{m}$

Table 10 shows the values of $T(\lambda)$ calculated as above for different λ's in the ratio $10^{1/3}$. To calculate ρ_a corresponding to, say, $\lambda = 0.01$, the coefficient series of Table 4.2 is placed as shown in the fourth column of Table 4.3 with b_0 against $\lambda = 0.01$ and with $b_5, b_4, \ldots$ etc. in the order shown, each one against a $T(\lambda)$ value. Notice that the order of the b's is such that the subscript of b decreases as λ decreases, an easy rule to remember.

We now multiply each $T(\lambda)$ by the coefficient against it and add all the results. The sum gives the value of ρ_a, to be referred to the distance $1/\lambda$ against which b_0 occurs. In the example in the table,

$$12.326 \times 0.0148 + 17.864 \times (-0.0814) + \cdots + 227.12 \times 0.0225 = 62.09\,\Omega\,\text{m}$$

occurs at $1/\lambda = 100$ m. As mentioned earlier, however, this is, in reality, the value of ρ_a at $1/\lambda = 95$ m and not at $1/\lambda = 100$ m.

Table 4.3 Calculation of ρ_a from $T(\lambda)$

λ	$\lambda(=L)$	$T(\lambda)$	Ghosh series	ρ_a
21.54	0.046	10.00		
4.64	0.216	10.00		
2.154	0.464	10.0024		10.09
1	1	10.247		10.28
0.464	2.15	12.326	0.0148	11.55
0.215	4.64	17.864	−0.0814	16.87
0.1	10	26.549	0.4018	27.26
0.046 4	21.5	37.706	−1.5716	39.65
0.021 5	46.4	47.210	1.9720	52.92
0.01	100	60.990	0.1854	62.09
0.004 64	215.5	94.976	0.1064	88.58
0.002 154	464	153.71	−0.0499	153.37
0.001	1000	227.12	0.0225	
0.000 464	2155	294.97		
0.000 215 4	4642	343.10		

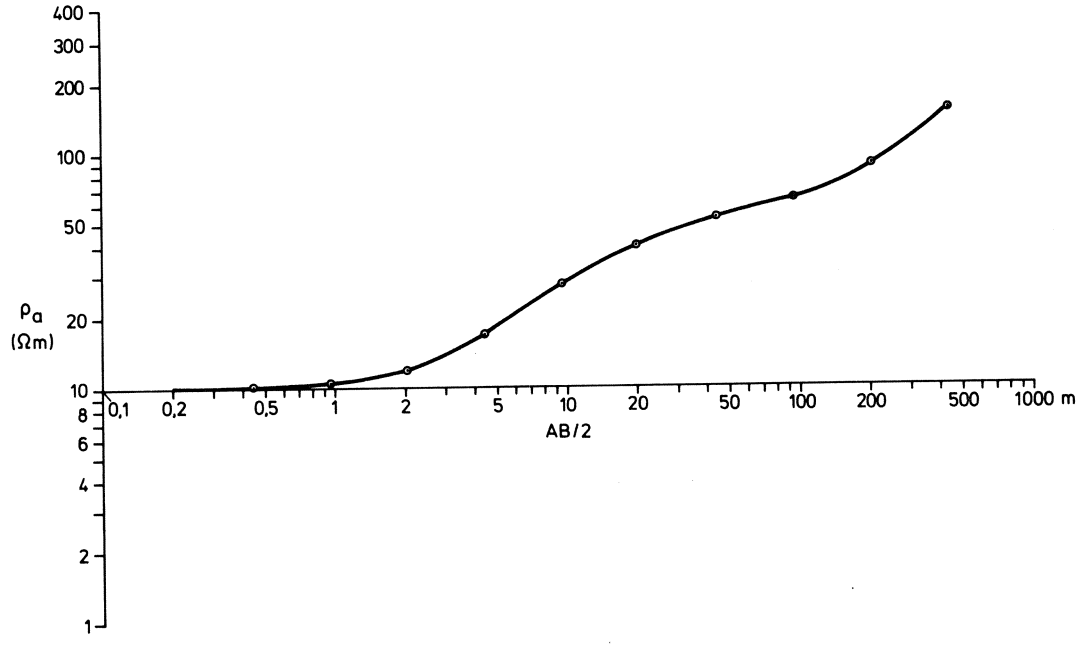

Fig. 4.25 ρ_a curve for the earth in Fig. 4.24 calculated by means of digital linear filter.

The coefficient series is now slid one step up or down and the procedure above is repeated. Fig. 4.25 shows the calculated curve for the five-layer case in question. The 5% leftward shift has been made in the plotting.

Sometimes it may be desired, and is in fact necessary in the optimization method described in Section 4.5.4.5, to calculate ρ_a at a given value of L, rather than of λ as above. If Table 4.2 is used, $T(\lambda)$ must then be calculated at nine values of λ, in the ratio $10^{1/3}$, 'centred' at $\lambda = (1 - \ln 1.05)/L = 0.951\,21/L$. Thus, if we wish to calculate ρ_a for, say, $L = 85$ m, then the nine values of λ will be 0.519, 0.241, 0.0519, 0.0241, 0.0112, 0.005 19, 0.002 41, 0.001 12 where the underlined value is the 'central' λ value.

(*b*) *Guptasarma's filters.* The accuracy of Ghosh's filter (Table 4.2) is of the order of 3% for resistivity curves that do not have steep branches. However, if there are steep branches as, for example, in the Q and K type curves in Fig. 4.20, the filter can give completely erroneous results. This is due, among other things, to the small number of coefficients and the sparseness of sampling (three points per decade). If a large computer is available it is not necessary to restrict the number of coefficients to nine or the number of sampled $T(\lambda)$ values to three per decade. Thus, Johansen [67] used 140 fixed coefficients, calculated to eight decimals, and sampled $T(\lambda)$ at ten points per decade, achieving a relative accuracy of the order of 1 part in 10^{-6} in the computation of ρ_a, the time being less than one second on a CDC 6400 computer, even for a model containing as many as ten layers.

Much research has gone into designing efficient filters with a small number of coefficients so that computations can be made without recourse to large computers. The most significant advance in this direction is the work of Guptasarma whose excellent paper [68] on the optimum design of resistivity filters should be consulted by the interested reader in the original. For our present purpose of practical calculations it is sufficient to refer to Table 4.4 which is one of the filters designed by him. The manner of using this seven-point filter is as follows.

We wish to calculate the Schlumberger apparent resistivity for $AB/2 = L$. First determine $T(\lambda_r)$ for seven values of λ_r where

$$\lambda_r = 10^{(a_r - \log_{10} L)} \tag{4.48}$$

where a_r are the abscissa values (column 1) in Table 11. Then

$$\rho_a(L) = \sum_{r=1}^{7} \phi_r T(\lambda_r) \tag{4.49}$$

where ϕ_r are the seven filter coefficients corresponding to the abscissa values a_r.

The accuracy of the ρ_a values calculated from Guptasarma's filter, like that from all filters, depends upon the layering as well as L. However, under

Table 4.4 Guptasarma's seven-point filter for calculating ρ_a (Schlumberger array)

a_r	ϕ_r Filter coefficient rounded to four decimal places
−0.174 45	0.1732
0.096 72	0.2945
0.367 89	2.147
0.639 06	−2.1733
0.910 23	0.6646
1.181 4	−0.1215
1.452 57	0.0155

(It is necessary to retain all decimals in a_r and ϕ_r during calculation.)

identical conditions, Guptasarma's filter gives ρ_a values whose error is much less than, for example, the Ghosh filter of Table 4.2. We used the latter filter in Section 4.5.4.4 for the purpose of demonstrating the calculation procedure only. For all practical VES interpretation, the reader is urged to use Table 4.4 rather than Table 4.2.

4.5.4.5 Optimization methods

Once a layered structure that approximately reproduces the observed ρ_a curve is found, modifications to it can be readily made and further ρ_a curves calculated quickly by the filter technique, to obtain better and better agreement with observations. However, it might not always be easy to make a suitable initial guess. The auxiliary point method can, of course, be used with advantage to find a trial solution. Another method is to let the computer seek an optimum model by an iterative procedure and use this as the starting point for 'manual' fine adjustments to the structure. Optimization methods are generally based on minimizing the sum of squares of the differences between the observed and calculated ρ_a values.

Let $P_j (j = 1, 2, \ldots, m)$ be a starting model with n resistivities and $(n-1)$ layer thicknesses, the nth layer being the substratum so that $m = 2n - 1$.

Let y_i be the N measured values of ρ_a for the N separations $x_i (i = 1, 2, \ldots, N)$ between the current electrodes. The problem is to find a set of values P_j that minimizes the sum

$$S = \sum_{i=1}^{N} [y_i - \rho_a(x_i, P_j)]^2 \tag{4.50}$$

where $\rho_a(x_i, P_j)$ is the apparent resistivity for x_i on the model represented by the set P_j and is, of course, nothing but the ρ_a given by Eq. (4.37). It should be

realized that the optimized model is not unique and different optimized models will be arrived at from different starting models.

Equation (4.50) is a non-linear equation. The theory of optimization need not detain us here. Some details of it will be found in papers by Johansen [69], Inman *et al.* [70] and in a monograph by Kofoed [71]. It will be sufficient to note here that the optimization procedure can be programmed to produce certain extremal parameter sets showing the limits within which some or all parameters can stay and yet give a satisfactory agreement with measurements. This is a very valuable feature of optimization methods but such programs need large computers. Experience shows, however, that it is often more convenient to obtain information of this sort 'manually' by direct interactive calculations of ρ_a curves on a graphic computer terminal by successively changing a selected parameter of a fitting model in one and the other direction, until the calculated curve just begins to depart from the best fitting curve.

*4.5.4.6 Pekeris–Kofoed method of direct determination**

The electric conductivity of a layered earth is a function of depth only. According to the Slichter–Langer theorem, therefore, the knowledge of the surface potential due to a point electrode – or of quantities, like apparent resistivity, derived from the potential – should suffice in theory to determine the thicknesses and resistivities of the various layers. An interpretation method based on this approach was suggested initially by Pekeris [72] for measurements of the potential and modified by Kofoed [71] to suit the modern practice of expressing the data as apparent resistivity. A practical procedure is outlined below.

To start with we note without proof that according to a result in Bessel function theory, Eq. (4.37) can be 'inverted' and written as

$$T_1(\lambda) = \int_0^\infty \frac{\rho_a(L)}{L} J_1(\lambda L)\, dL \tag{4.51}$$

Equation (4.51) shows that $T_1(\lambda)$ can be computed from measurements of ρ_a as a function of L. $T_1(\lambda)$ is used on the left here, instead of $T(\lambda)$, to emphasize that we are dealing with a transform function when measurements are made on the surface of the first layer on top of a number of layers below. If the first layer is removed and measurements are imagined to be made on the surface of what was until now the second layer, the transform obtainable from them will be denoted by $T_2(\lambda)$. Removal of layer 2 will lead to $T_3(\lambda)$ and so on. We shall revert to the details of computing $T_1(\lambda)$ later but suppose for the present that $T_1(\lambda)$ has been computed for a set of small to large λ values from the observed ρ_a curve.

Now, the resistivity of the first layer ρ_1 may be taken to be known as this is

*This entire section may be omitted on a first reading of the book.

the asymptote of the measured ρ_a curve for small values of L. Then it can be shown that the function

$$G_1(\lambda) = \frac{T_1(\lambda) - \rho_1}{T_1(\lambda) + \rho_1} \tag{4.52}$$

has the asymptotic form

$$G_1(\lambda) \sim -k_1 \exp(-2\lambda h_1) \tag{4.53}$$

for large values of λ where h_1 is the first-layer thickness and

$$k_1 = \frac{\rho_1 - \rho_2}{\rho_1 + \rho_2} \tag{4.54}$$

(In the definition of k_1 many authors, including Kofoed (*loc. cit.*), use $\rho_2 - \rho_1$ in the numerator of (4.54).)

Equation (4.53) means that if $\ln|G_1(\lambda)|$ is plotted on the y axis against λ on the x axis of a graph the points for large values of λ will lie on a straight line of slope $-2h_1$ which gives h_1 while the intercept of the line on the y axis will be $\ln|k_1|$, which yields $|k_1|$. The sign to be assigned to k_1 is the *opposite of the sign* of $G_1(\lambda)$ in Eq. (4.52). Hence, taking proper cognizance of the sign of k_1, Eq. (4.54) gives ρ_2.

The next step is to compute $T_2(\lambda)$ mentioned above for different λ. This is actually easy since from Eq. (4.44) we find that

$$T_2(\lambda) = \frac{T_1(\lambda) - W_1(\lambda, h_1)}{1 - W_1 T_1/\rho_1^2} \tag{4.55}$$

and $T_1(\lambda)$ is already known for a set of λ while W_1, defined by Eq. (4.45), can be computed for these λ values as h_1 is now known.

A function $G_2(\lambda)$, exactly analogous to $G_1(\lambda)$, is then calculated for different values of λ by replacing T_1 by T_2 and ρ_1 by ρ_2 in (4.52), whereupon $\ln|G_2(\lambda)|$ is plotted against λ.

The points corresponding to large λ values will now lie on a straight line of slope $-2h_2$, giving h_2 while the intercept $\ln|k_2|$ yields $|k_2|$ and hence ρ_3 (taking proper cognizance of the sign of k_2). Functions $T_3(\lambda)$ and $G_3(\lambda)$ are then constructed analogously and the process repeated until at some stage in the calculations the $\ln|G(\lambda)|$ values for all λ (large or small) are found to lie on a single straight line. This indicates that we have now reached the stage of the lowermost layer resting on the infinite substratum. This final log-plot yields the thickness of the bottom layer and the resistivity of the substratum. (It is generally more convenient to use an ordinary semi-logarithmic paper to the base 10 and plot $|G(\lambda)|$ on its log scale and λ along its linear scale. The slope of the large-λ straight lines on this paper is $-0.8686h$ and the intercept is equal to $\log_{10}|k_1|$.)

The main computational task in the Pekeris–Kofoed method is the

Table 4.5 Ghosh coefficients a_j for calculating T_m (Schlumberger sounding)

a_{-2}	a_{-1}	a_0	a_1	a_2	a_3	a_4	a_5	a_6
−0.0723	0.3999	0.3492	0.1675	0.0858	0.0358	0.0198	0.0067	0.0076

determination of $T_1(\lambda)$. The other successive transforms follow easily, as Eq. (4.55) shows, since at each stage the previous T, W ρ are known. The starting function $T_1(\lambda)$ can be calculated by means of a digital filter. The procedure is analogous to that for calculating ρ_a from $T(\lambda)$, described in Section 4.5.4.4, as will be seen from the following, but the filter is different. There are two main steps.

(a) The first step is to sample the (smoothed) ρ_a curve, plotted on a double logarithmic paper, at equidistant points along the x axis. In using the filter in Table 4.5 (valid for Schlumberger sounding) the sampling rate must be three points per decade. The sampling may be started anywhere but it is convenient to start with a 'round' value like 1 or 10 m and read off the equidistant ρ_a values for greater as well as smaller L. A list $R_0, R_1, R_2 \ldots$ is made where R_0 denotes the value read at the shortest L at which the ρ_a curve is sampled, R_1 the value at the next L etc.

(b) The second step is to calculate the sum defined by

$$T_m = \sum_{j=-2}^{6} a_j R_{m-j} \tag{4.56}$$

corresponding to the mth distance L_m, where a_j are the nine coefficients in Table 4.5. Then T_m is the value of $T_1(\lambda)$ for $\lambda = 1/L_m$. In this way $T_1(\lambda)$ is calculated for the set of λ values $1/L_0, 1/L_1, \ldots$ etc. Equation (4.56) is similar to Eq. (4.42) and the manner of handling it, with due alteration of details, will be apparent from a study of Section 4.5.4.4.

Values of $T_1(\lambda)$ at values of λ intermediate between $1/L_0, 1/L_1$ etc. can be calculated by a second sampling of the ρ_a curve starting from another L than the one used first.

As an example, let us suppose that the ρ_a curve in Fig. 4.25 is a measured VES curve. If the reader refers again to Section 4.5.4.4 it will be obvious that sampling this curve at the rate of three points per decade, starting from $L = 0.4642$ m, will give us the series of ρ_a values in the last column of Table 4.3. To calculate T_1 for, say, $L = 46.42$ m ($\lambda = 1/46.42 = 0.021\,54$) we position the a_j series in Table 4.5 with a_0 against the value $\rho_a = 52.92$ and calculate the sum

$$\begin{aligned} T_1(0.02154) = {} & 10.09 \times 0.0076 + 10.28 \times 0.0067 \\ & + 11.55 \times 0.0198 + 16.87 \times 0.0358 \end{aligned}$$

$$+ 27.26 \times 0.0858 + 39.65 \times 0.1675$$
$$+ 52.92 \times 0.3492 + 62.09 \times 0.3999$$
$$+ 88.58 \times (-0.0723)$$
$$= 46.86$$

(The exact value is 47.210 as can be seen from the table. The discrepancy is due to rounding-off errors and the shortness of the filters.)

Patella [73] has given another method to calculate $T_1(\lambda)$ but it is not as quick as the above one based on Ghosh-type coefficients.

Although the Pekeris–Kofoed method is theoretically elegant it has certain disadvantages in practice. First, in its above form, it involves rather a large number of calculations and many subtle decisions although Kofoed (*loc. cit.*) has devised an automatized version of it which avoids some of these disadvantages. However, the most serious disadvantage is that the method is extremely sensitive to irregularities in the data and the results are generally unreliable except on theoretical inputs given to a very high degree of precision. Also, the conversion of ρ_a values into $T(\lambda)$ values means that primary data are tampered with. In contrast, the matching method of Section 4.5.4.4 leaves the primary data intact.

A solution obtained by any direct method should be regarded as a trial solution in practice and should be checked against the measured ρ_a curve by a forward calculation. Slight adjustments will still be needed in general to obtain the best fitting curve.

4.5.4.7 Principles of equivalence and suppression

In the actual application of the various interpretation methods to a particular field problem limitations are set by the maximum distance from the current source to which the electric field is given, and by the irregularities in the field due to surface inhomogeneities. Furthermore all measurements have a finite accuracy. On account of all these causes, widely different resistivity distributions may lead to ρ_a curves which, although they are not identical, cannot be distinguished in practice. This introduces ambiguity in the interpretation.

The mathematical formulation of two simple types of equivalence is easily obtained. Consider, for example, a relatively thin layer sandwiched between two layers whose resistivities are much higher than that of the sandwiched layer. The current flow in the earth will then tend to concentrate into the middle layer and will be almost parallel to the layer (Fig. 4.26(a)). The resistance of an elementary block of length Δl and cross-section $h\Delta m$ to such a current flow is $R = \rho\Delta l/(h\Delta m)$ and this will be unaltered if we increase ρ but at the same time increase h in the same proportion. Thus all such middle layers for which the ratio h/ρ is the same (within certain limits on h and ρ) are electrically equivalent.

On the other hand, if the resistivity of the middle layer is much larger than

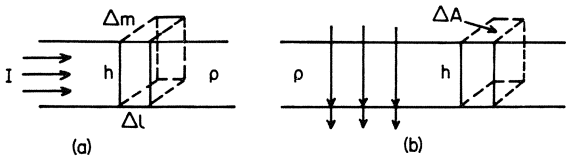

Fig. 4.26 Principle of equivalence.

that of the layers on either side, the electric current will tend to avoid it and take the shortest route to the lower layer. The lines of current flow will be almost perpendicular to the layer (Fig. 4.26(b)). The resistance of an elementary block to this flow will be $R = \rho h/\Delta A$ where ΔA is the cross-section. In this case all layers for which the product $h\rho$ is the same are electrically equivalent so that, again, h and ρ cannot be determined separately.

Another very important type of equivalence arises when the resistivity of a layer is anisotropic. This we shall consider in Section 4.7.

If the thickness of a layer is very small compared with its depth (and its resistivity is neither infinite nor zero) its effect on the ρ_a curve is so small that the presence of the layer will be suppressed.

In a general sequence of several layers most of the h and ρ parameters are subject to the principles of equivalence and some to suppression but the parameters can, in general, only vary within certain limits. These limits can be found by the optimization procedure discussed in Section 4.5.4.5. Consider, for example, the measurements shown in Fig. 4.27 and the best fitting curve due to a five-layer sequence. The lack of fit in the central part is probably due to local inhomogeneities. In Table 4.6 are shown *some* of the equivalences for this case.

Apart from the equivalences arising from keeping h/ρ (or $h\rho$, as the case may be) constant, two or more layers can often be suitably combined into a single layer without significant change in the VES curve. For instance, suppose once more that the originally five-layer curve in Fig. 4.25 is a measured curve. If layers 2 and 3 in Fig. 4.24 are coalesced into one of thickness $H = 20 + 15 = 35$ m and resistivity $\rho_m = 70\,\Omega$m using Eq. (4.41), an identical VES curve is obtained. Whether a five-layer or a four-layer curve is to be matched with the measurements will then depend very much upon available geological information and/or VES curves at neighbouring survey points.

As another illustration of equivalence and its limit, we take the measurements in Fig. 4.28 which indicate a four-layer case. The calculated curve corresponding to an acceptable four-layer sequence is also shown. The substratum here is salt water which acts as an excellent conductor. One problem in this area was to estimate the maximum thickness that layer 3 could have assuming that the parameters determined for the other layers are more or less the actual ones. The case corresponds to that in Fig. 4.26(b) so that h_3, ρ_3

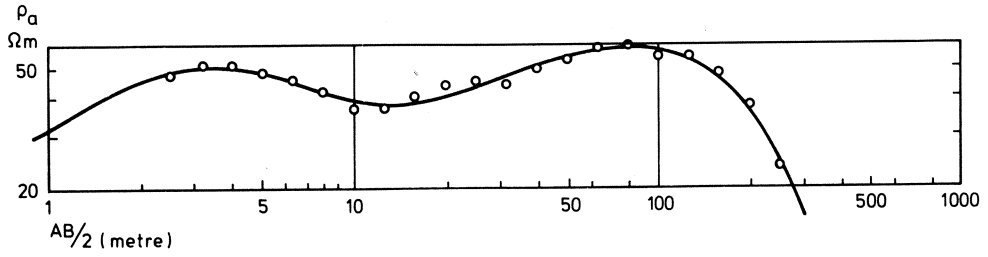

17.76	208.50	28.76 Ωm	68.70	1.83

Fig. 4.27 A VES curve and its interpretation (Area: Wilhelmsborg, Denmark).

Table 4.6 Some equivalences for the example Fig. 4.27 (h in m, ρ in Ω m)

Solution of Fig. 4.27

ρ_1	h_1	ρ_2	h_2	ρ_3	h_3	ρ_4	h_4	ρ_5
17.76	0.48	208.52	0.52	28.76	8.26	68.70	99.50	1.83

Each of the following solutions fits the measured curve as well as the solution above. They form a subset of many possible equivalences obtained by extremizing various parameters of the problem.

1. *Models extremizing* ρ_1

h_1, ρ_1 may vary arbitrarily provided ρ_1 lies between extremes cited and h_1/ρ_1 lies between the corresponding limits (almost constant).

ρ_1 max.	35.24	0.98	194.33	0.52	28.76	8.24	68.70	99.46	1.85
ρ_1 min.	6.06	0.17	442.04	0.26	28.98	8.45	68.74	99.27	1.90

2. *Models extremizing* h_2

h_2, ρ_2 may vary arbitrarily provided h_2 lies between extremes cited and $h_2\rho_2$ lies between the corresponding limits (almost constant).

h_2 max.	17.66	0.46	105.61	1.07	28.35	8.00	68.58	99.80	1.84
h_2 min.	9.29	0.27	658.45	0.16	29.24	8.60	68.81	9.07	1.91

3. *Models extremizing* h_4

h_4, ρ_4 may vary arbitrarily provided h_4 lies between extremes cited and $h_4\rho_4$ lies between the corresponding limits.

h_4 max.	17.28	0.48	218.08	0.52	27.56	7.29	66.09	109.78	0.62
h_4 min.	16.73	0.45	220.58	0.48	29.79	9.27	71.40	91.63	3.14

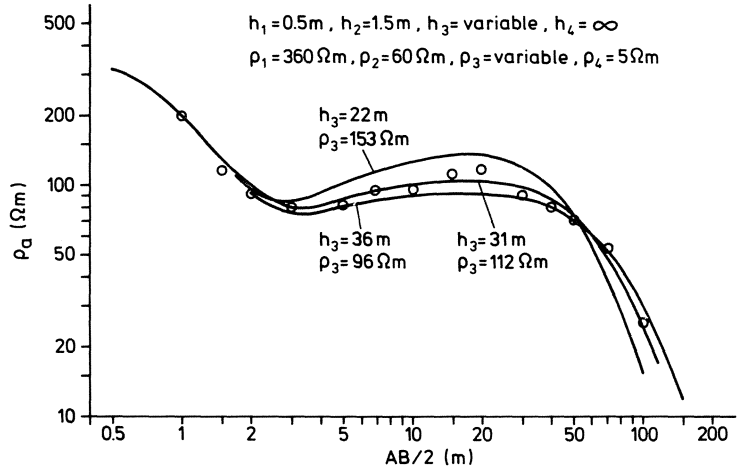

Fig. 4.28 Example of limits of equivalence.

are to be varied while keeping $h_3\rho_3 = 3472\,\Omega\,m^2$. It is found that the calculated curve begins to depart significantly from the measurements when $h_3 \approx 36\,m$, the corresponding ρ_3 being $96\,\Omega\,m$. It is also found as the figure shows that h_3 cannot be less than about 25 m under the same assumptions.

Finally, it should be noted that the Pekeris–Kofoed (or any other) direct method is not exempt from the principle of equivalence since a unique straight line cannot be passed through the '$\ln|G(\lambda)|, \lambda$' curve for large λ values because there is no unique definition of 'large' λ and, more rigorously, even in the ideal case the points do not lie on a straight line but on a *curve* whose asymptote is a straight line.

4.5.4.8 Geologic section from VES

By means of systematic soundings on a grid system or along a profile, it is possible to build a geologic section. Fig. 4.29 shows an example near the town of Weener in Germany. The object of this investigation was to locate permeable sand beds bearing fresh water as a catchment area for water works. Certain qualitative correlations will be readily recognized between the nature of the sounding graph at each point and the stratification inferred at that point on its basis. It is interesting to see, for example, that curve 78 seems to possess a weak maximum after the initial dip due to the highly conductive clay. The reality of this maximum is confirmed on comparing the curve with sounding 59 (not shown) and 60. The maximum is due to the less conductive sands thinning out below this point but the presence of this layer could hardly have been reliably inferred here without the comparison. As Flathe [74] has pointed out in this regard, 'On its own, graph no. 78 would admit of a wide variation in the interpretation.'

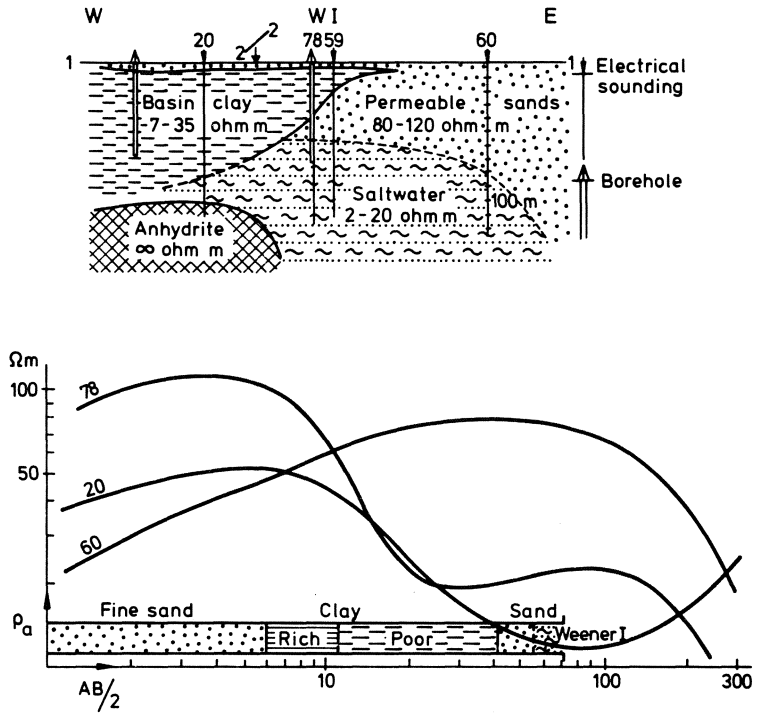

Fig. 4.29 Geologic section constructed from VES interpretation. After [74].

4.5.4.9 Determination of longitudinal conductance

The quantity

$$S = \frac{h_1}{\rho_1} + \frac{h_2}{\rho_2} + \cdots + \frac{h_{n-1}}{\rho_{n-1}} \qquad \text{(siemen} \equiv \text{mho)} \tag{4.57}$$

which is the sum of all the thickness/resistivity ratios of $n-1$ layers overlying an infinite substratum of resistivity ρ_n is called the longitudinal conductance of the layering in question. This quantity is of some interest in the interpretation of VES curves *with an ascending final part* whose asymptote indicates a substratum resistivity $\rho_n > \rho_{n-1}$, because it can be uniquely estimated from this part. No layer-solution for such curves, inconsistent with this estimate of S, can be accepted.

We shall first consider the mathematically simpler case of an infinitely resistive substratum and return to finite ρ_n values later. It can be shown that when $\rho_n = \infty$, the apparent resistivity for large L is given in Schlumberger sounding by the asymptotic equation

$$\rho_a \sim L/S \tag{4.58}$$

Obviously, for large L, then

$$\log \rho_a = -\log S + \log L \tag{4.59}$$

and we see that on the usual double-logarithmic plot of ρ_a against L, the VES curve for sufficiently large L will be a straight line of slope 1, that is, of inclination 45° with the axes, *if the substratum is insulating.* An example is the final branch of the curve marked 20 in Fig. 4.29.

If we put $\rho_a = 1\,\Omega\text{m}$ in Eq. (4.59) (or, for that matter, in (4.58)) we find that the corresponding value of L is numerically equal to S. Hence, to obtain S from the VES plot we simply produce the 45° straight line so as to meet the horizontal line through the point $\rho_a = 1\,\Omega\text{m}$ on the plot and simply read off the value of L at the point of intersection (Fig. 4.30(a)).

It should be realized that no rising portion of a VES curve, final or otherwise, on a horizontally layered earth can have an inclination of more than 45° with the L axis (on a double-logarithmic plot) and that once the curve starts to show this inclination there cannot be any further branch of it with smaller inclination since an inclination of 45° indicates an infinitely resistive substratum. No information can be obtained on horizontally layered structures below this substratum as no current can penetrate below it. Inclinations greater than 45° (or branches beyond such a segment) indicate more or less severe departures from the condition of horizontal layering, errors of measurement, presence of lateral inhomogeneities etc. Inclinations greater than 45° are also obtained when alternating current is used instead of direct current and at the same time the upper layers are highly conductive. The use of a.c. (even of very low frequency) should be avoided in electrical sounding.

We now consider the case when $\rho_n \neq \infty$ (but of course $> \rho_{n-1}$). The equation of the ρ_a curve for large values of L corresponding to (4.59) is difficult to derive in this case but it has been shown by Orellana [75] to be

$$\rho_a \sim -\frac{\pi}{2}\frac{L^2}{S^2\rho_n}\left[H_{-1}\left(\frac{L}{S\rho_n}\right) + Y_1\left(\frac{L}{S\rho_n}\right)\right] \tag{4.60}$$

where H_{-1} is the so-called Struve function of order -1 and Y_1 is the Bessel function of the second kind (also called Neumann function) of order 1. Both these are rather complicated functions but we shall presently see that Eq. (4.60) can be used to estimate S without going into a study of the two functions as such. The equation can be written as

$$\frac{\rho_a}{\rho_n} \sim -\frac{\pi}{2}x^2[H_{-1}(x) + Y_1(x)] \tag{4.61}$$

where we have put $L/S\rho_n = x$.

The right-hand side of Eq. (4.61) has been plotted as a function of x in Fig. 4.30(b).

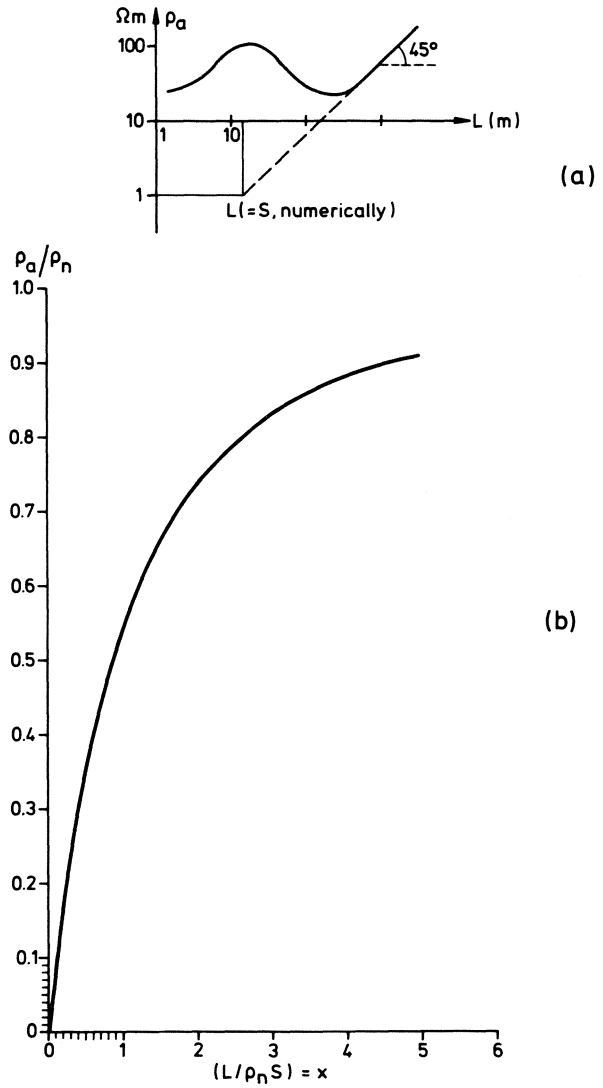

Fig. 4.30 Determination of longitudinal conductance for a layered earth with (a) infinitely resistive substratum and (b) substratum of finite resistivity.

If measurements have been made up to sufficiently large L, a good estimate of the substratum resistivity ρ_n can often be made by extrapolation of the VES curve to infinitely large values of L. Then, taking the measured ρ_a value at some definite large L on the observed VES curve we calculate the ratio ρ_a/ρ_n and entering the diagram in Fig. 4.30 read the corresponding x. Then S is immediately obtained as $L/x\rho_n$.

As an example let us suppose the curve in Fig. 4.25 to be a measured VES curve. Extrapolation of the final ascending branch indicates, say, $\rho_n = 300\,\Omega\,\text{m}$ (although we know in this case that $\rho_n = 400\,\Omega\,\text{m}$). For $L > 200\,\text{m}$ the curve seems to follow its asymptotic form fairly closely. For $L = 190\,\text{m}$, say, the 'measured' ρ_a is $82\,\Omega\,\text{m}$ giving $\rho_a/\rho_n = 0.273$. From Fig. 4.30 we then get $x = 0.375$ and hence $S = 1.8$, which should be compared with the true longitudinal conductance of 1.95 siemen for this case.

4.5.4.10 Dipping discontinuities

We have so far considered a perfectly horizontally layered earth. This idealized situation is very rarely encountered in practice. In most cases the contacts between various layers are dipping and sometimes even undulating. Dipping discontinuities were discussed by Maeda [76] and by de Gery and Kunetz [77] as far back as 1955. There is no simple way of estimating the effect of dip or of the departure from the postulate of plane discontinuities. However, a reasonably practical attempt for the quantitative interpretation of sounding data on such discontinuities seems to be due to Lee [78].

Lee's method for determining the configuration of such a surface S (e.g. an undulating bedrock surface below a homogeneous top-layer) is briefly as follows. Measure ρ_a (in the sense of Schlumberger) on a profile in the strike direction z, say. Then it can be shown that for large values of λ

$$T(\lambda) = \int_0^\infty \frac{\rho_a}{z} J_1(\lambda z)\,\mathrm{d}z \simeq \rho_1[1 + 2kN\exp(-2\lambda d)]$$

$$= H(\lambda), \text{ say} \qquad (4.62)$$

where N is the number of times a horizontal cylinder of the smallest radius d, and axis along the profile of measurement, is tangential to S.

The parameters $2kN$ and $2d$ are easily found from a plot of $\ln|H/\rho_1 - 1|$ against λ for several large values of λ. Circles of radii d centred on the respective profiles are drawn in a plane representing the vertical plane perpendicular to the strike direction.

For a plane discontinuity $N = 1$. For undulating surfaces N for each profile must be determined by inspection of the various kN values in such a way that $k = (\rho_1 - \rho_2)/(\rho_2 + \rho_1)$ is the same for all profiles. Appropriately many lines tangential to each of the circles are finally drawn and the picture smoothed to obtain the simplest structure.

A degenerate case arises when S is a plane discontinuity perpendicular to the ground surface as in Fig. 4.35. For this $2k$ in (4.62) must be replaced by k.

4.6 ELECTRICAL MAPPING

The object of mapping is to determine the lateral variations in the conductivity of the ground. Mapping is primarily useful for detecting local, relatively

shallow inhomogeneities and is employed typically in ore prospecting and in delineating geologic boundaries, fractures, cavities etc. Very often the problem is to find such features below a relatively uniform overburden like soil, deeply weathered rock, glacial drift etc., in which case it is necessary to know, and control in field work, the fraction of injected electric current penetrating below the overburden. We shall study this problem somewhat closer.

4.6.1 Current penetration

4.6.1.1 Current penetration in homogeneous, isotropic ground

Although this case is not of great practical interest we shall treat it as it illustrates the idea involved rather easily. Current is injected into the ground by a positive electrode A and collected by a negative one B (Fig. 4.31). If a rectangular coordinate system is chosen with the origin midway between A and B, the potential at any point x, y, z is found from Eq. (4.20) to be

$$V(x,y,z)=\frac{I\rho}{2\pi}\left(\frac{1}{[(L+x)^2+y^2+z^2]^{1/2}}-\frac{1}{[(L-x)^2+y^2+z^2]^{1/2}}\right)$$

where $2L=$ the distance AB. The y direction is perpendicular to the plane of the figure.

At each element $\mathrm{d}x\,\mathrm{d}y$ of a horizontal plane at depth z there is a vertical current density j_z. Fig. 4.31 shows that a current $j_z\,\mathrm{d}x\,\mathrm{d}y$ passes downwards through an element left of the origin and a corresponding quantity returns on the right-hand side after having penetrated below the depth z. The total current that penetrates below z is obtained by integrating $j_z\,\mathrm{d}x\,\mathrm{d}y$ from $x=-\infty$ to $x=0$ and from $y=-\infty$ to $y=+\infty$. Now, j_z can be obtained from the expression for V since

$$j_z=-\frac{1}{\rho}\frac{\partial V}{\partial z}$$

Hence the current in question is

$$\int_0^{\infty}\int_{-\infty}^{0}\frac{Iz}{2\pi}\left(\frac{\mathrm{d}x\,\mathrm{d}y}{[(L+x)^2+y^2+z^2]^{3/2}}-\frac{\mathrm{d}x\,\mathrm{d}y}{[(L-x)^2+y^2+z^2]^{3/2}}\right)$$

Both the double integrals are easily evaluated using standard tables of

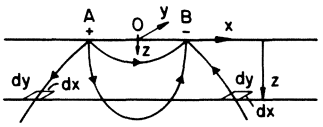

Fig. 4.31 Current penetration in homogeneous ground.

integrals. The first double integral yields

$$\frac{I}{\pi}[\pi - \tan^{-1}(z/L)] \tag{4.63}$$

and the second (including in it the minus sign) gives

$$-\frac{I}{\pi}\tan^{-1}(z/L) \tag{4.64}$$

Hence the *fraction* of the total current penetrating below the depth z, the sum of (4.63) and (4.64) divided by I, is

$$g = 1 - \frac{2}{\pi}\tan^{-1}(z/L) \tag{4.65}$$

The fraction $f = 1 - g$ is confined on the other hand between the ground surface and the horizontal plane at z. We see from this that as much as 50% of the total current injected and collected on a homogeneous ground by means of a pair of point electrodes has never penetrated below the depth $z = L(\tan^{-1} 1 = \pi/4)$ and as much as 70.5% never below $z = 2L$.

4.6.1.2 Current penetration in two-layered earth

The current penetration in an earth composed of several strata can be calculated from the expression for the potential in Eq. (4.31) using the modern transform theory discussed in Section 4.5.3. It was worked out by other methods as far back as 1941 by Muskat and Evinger [79]. Fig. 4.32

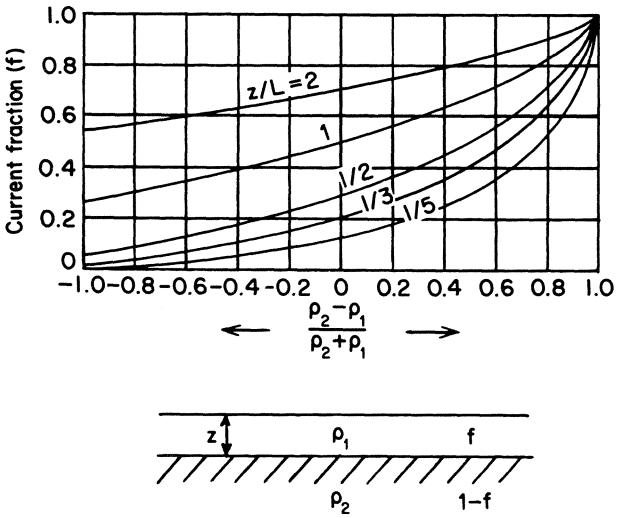

Fig. 4.32 Penetration of electric current in a two-layer earth. After [79].

reproduced from their paper showing the penetration in a two-layer earth can be used in relevant practical situations to estimate the electrode separation necessary to ensure that a desired fraction of the injected current penetrates below the overburden.

4.6.2 Mapping procedures

4.6.2.1 Wenner mapping

The usual routine in this procedure is to move the Wenner array of Fig. 4.13(a), with a fixed separation, as a whole in suitable steps along the line of the array itself. When one traverse is finished the array is moved to the next parallel line and so on until the area of investigation is covered. Usually the array is moved so that each of the four electrodes advances through a distance equal to the array separation a. The apparent resistivity values (Eq. (4.25)) are plotted on a map at positions corresponding to the centre of the array and the map is contoured.

4.6.2.2 Schlumberger mapping

The procedure is similar to the above in that all four electrodes are moved through the same distance but the Schlumberger array of Fig. 4.13(b) is used instead. The apparent resistivity (Eq. (4.27b)) is referred, as in the Wenner case, to the centre of the array in plotting the values on a map.

4.6.2.3 Gradient array mapping

In this procedure the A, B electrodes are fixed and the M, N electrodes with a constant mutual separation are moved along the A–B line (Fig. 4.33). If the MN separation $2l$ is small compared to the distances of M and N from the nearest current electrode the quantity $\Delta V/2l$, where ΔV is the voltage difference between M and N (voltage at M minus that at N), may be considered to be the potential gradient $-\mathrm{d}V/\mathrm{d}x$ at the point P midway between M and N. The apparent resistivity is easily shown using Eq. (4.26) to be given by

$$\rho_a = \frac{\pi (L^2 - x^2)^2}{I} \frac{\Delta V}{(L^2 + x^2)} \frac{}{2l} \tag{4.66}$$

where $2L = AB$ and x is the distance of P from the point O midway between A and B.

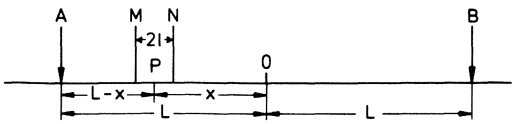

Fig. 4.33 Gradient-array mapping.

In gradient mapping AB is generally large (1 km or more) while MN is kept at 10 or 20 m and observations at distances from A or B less than, say, ten times MN are avoided. When the traverse is complete A, B are moved to the next parallel line.

4.6.2.4 Dipole–dipole mapping

A collinear dipole–dipole configuration such as the one in Fig. 4.13(c) can be moved as a whole along lines parallel to the array keeping the values of a and n fixed. The apparent resistivity (Eq. (4.28)) may be referred to the centre of array or to the centre of one of the dipoles and plotted on a map. The configuration is, however, commonly used in mapping in a somewhat different way as follows.

Measurements are made along a profile with a selected a (e.g. 60 m) and with $n = 1$, at suitable intervals (usually equal to a). In plotting the measurements on paper, lines making an angle of 45° with the line representing the profile are drawn from the centres of the current and potential dipoles in opposite directions, and the value of ρ_a obtained for that position of the array is plotted at the intersection of these two lines (Fig. 4.34). The measurements along the profile are repeated for $n = 2, 3, \ldots$, and plotted in a similar way. It is easy to see that the measurements for $n = 2$ in such a plot will appear along a line below the line on which those for $n = 1$ appear, those for $n = 3$ will be plotted along a line still 'deeper' and so on. Contours of equal ρ_a are then drawn on this plot. The picture thus obtained is called a vertical pseudo-section of the ground because while measurements along a profile are indicative of lateral conductivity variations, measurements for a larger value of n may be supposed to contain more information about deeper inhomogeneities than those for a small n (cf. Fig. 4.16). An example of a pseudo-section will be found in Fig. 5.5.

The idea of pseudo-section plotting is not exclusive to dipole–dipole measurements but it has seldom been exploited for other arrays. For example, pseudo-sections can be easily constructed for Schlumberger or Wenner mapping measurements, if made with different-sized arrays, by plotting each ρ_a value vertically below the array centre at a distance proportional to $AB/2$ or a.

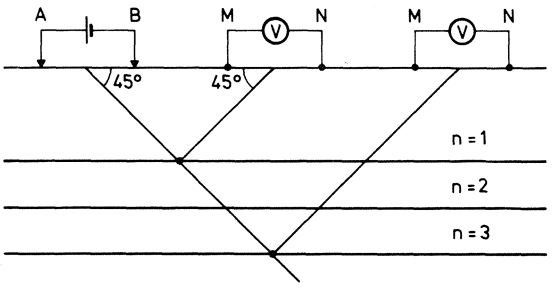

Fig. 4.34 Plotting of dipole–dipole ρ_a data.

4.6.2.5 Line electrode mapping

In areas with a well-defined strike, more or less constant in direction, it is often of operational advantage to use line instead of point sources for electrical mapping. Two bare, parallel copper wires are laid evenly on, or preferably pegged, at short (e.g. 5 m) intervals, to the ground, the four extremities of the wires forming a rectangle. Measurements of the potential gradient are made between the two wires along profiles at right angles to the wires. The potential of an infinitely long line electrode on a homogeneous earth can be easily found by an argument similar to that in Section 4.3.3 for a point source. It is given by $(J\rho/\pi)\ln r + C_\infty$ where J is the current per metre of electrode length, C_∞ is an infinite constant and r is the perpendicular distance from a point in the ground to the wire. With two parallel, infinitely long electrodes, one positive and the other negative, the potential will be $(J\rho/\pi)\ln(r_1/r_2)$ where r_1, r_2 are the perpendicular distances of the point from the two wires. In practice, the line electrodes are necessarily finite in length and the logarithmic term is somewhat more complicated (Problem 4.11).

4.6.3 Outcropping lateral discontinuities

4.6.3.1 Vertical contact

The case of two homogeneous, isotropic rock formations separated by a plane vertical boundary (Fig. 4.35) can be treated easily by the method of images (Appendix A7.2) or by more general methods of solving Laplace's equation. Suppose that we have a single point electrode C situated in medium 1 at a distance a from the contact, B being at infinity, and that we make a gradient mapping along a line through the electrode perpendicular to the strike of the contact. (Actually we are now using a pole–dipole configuration mentioned in Section 4.4.3.5.) On a homogeneous medium the potential gradient is given according to Eq. (4.19) by

$$\frac{dV}{dr} = -\frac{I\rho}{2\pi}\frac{1}{r^2}$$

Hence the apparent resistivity in our pole–dipole mapping will be given by

$$\rho_a = \frac{2\pi r^2}{I}\left(-\frac{dV}{dr}\right) \tag{4.67}$$

Using the appropriate expression for V depending on whether the measurement point is in medium 1 or 2 (Appendix A7.2) we get

$$\begin{aligned} \rho_a &= \rho_1\left(1 - \beta_1\frac{r^2}{(2a-r)^2}\right) \quad r < a \text{ (medium 1)} \\ \rho_a &= \rho_1(1+\beta_1) \qquad\qquad\quad r > a \text{ (medium 2)} \end{aligned} \tag{4.68}$$

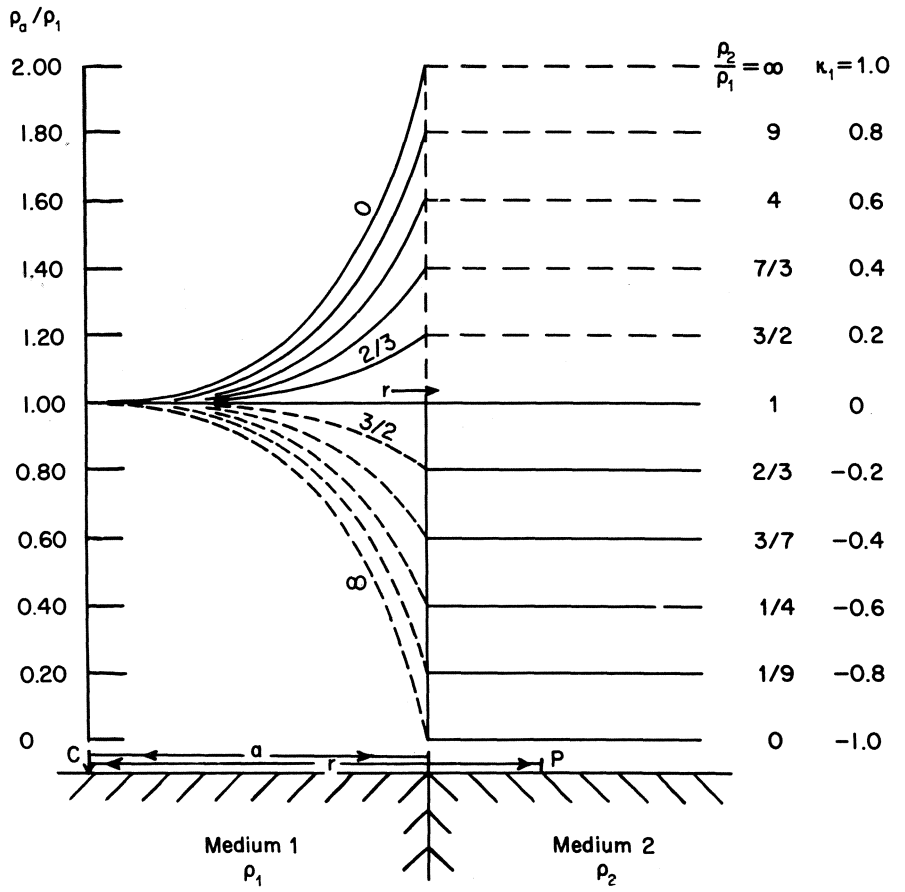

Fig. 4.35 Gradient mapping across a vertical contact.

where $\beta_1 = (\rho_2 - \rho_1)/(\rho_2 + \rho_1)$. Typical curves are given in Fig. 4.35.

It will be seen that the apparent resistivity is discontinuous at the boundary. The discontinuity will be evident in practice as a more or less steep gradient of the resistivity curve if there is an overburden and the contact is not outcropping.

4.6.3.2 Vertical dike or broad zone

In this commonly encountered case the apparent resistivity profile can be visualized qualitatively, provided the dike or zone is very broad, by a combination of a profile across two contacts (Fig. 4.36). The exact theoretical solution is, on the other hand, complicated and is anyhow of limited use in practice since it can only be obtained when there is no overburden. A special

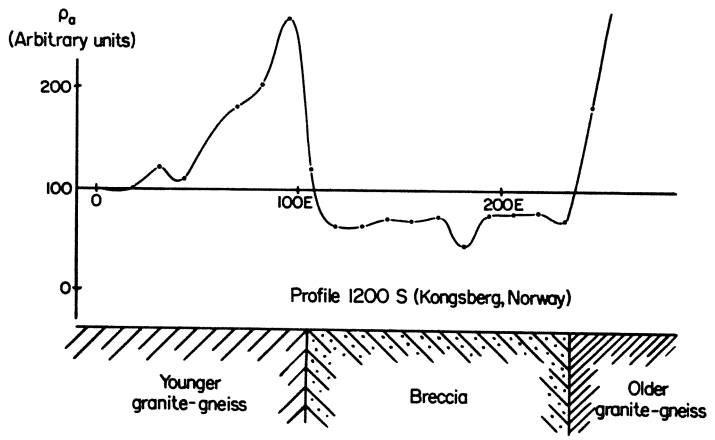

Fig. 4.36 Example of ρ_a measurements across steep geological contacts. After [80].

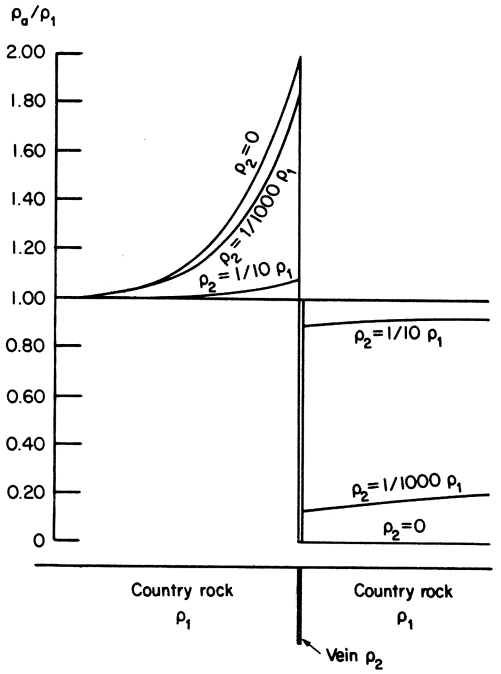

Fig. 4.37 ρ_a across a thin vein. After [80].

case is that of an outcropping thin dike or vein cutting through the surrounding rock. Some apparent resistivity curves for a pole–dipole mapping profiles across such a dike are shown in Fig. 4.37.

Figs 4.35 and 4.37 incorporate two features which are worth a special mention since they apply to all work with the resistivity methods. First, small resistivity contrasts cause comparatively large departures of the ratio ρ_a/ρ_1 from 1.0. Secondly, the ratio is practically unchanged whether the resistivity contrast is moderately large, say $\rho_2/\rho_1 = 10$, or very large, say $\rho_2/\rho_1 = 10\,000$. This is often known as the 'saturation effect'. Consequently, while the resistivity method is efficient in detecting small variations in the conductivity of the ground, it is ill adapted for distinguishing, say, a good conductor from a very good conductor, although both will be readily detected.

Finally, in this connection, Fig. 4.38 shows the results of an electrical mapping survey in an ore-bearing area using parallel electrodes, 200 m long and 1200 m apart. The potential probes (40 m apart) were moved along lines perpendicular to the current electrodes and between them. The country rock in

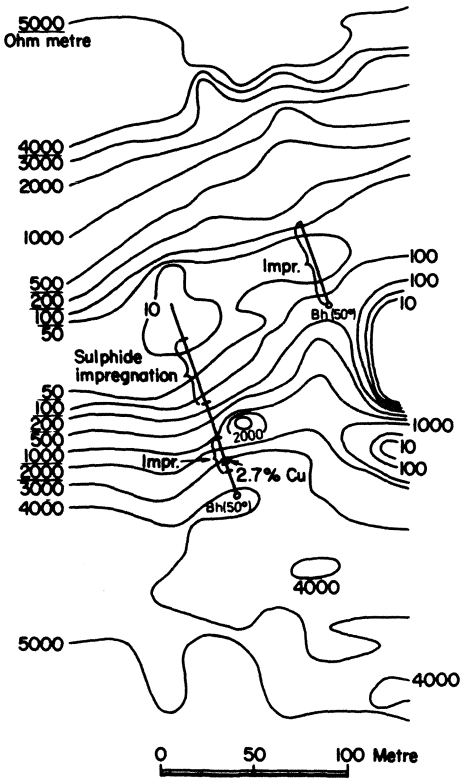

Fig. 4.38 Resistivity map of an area in North Sweden.

the region, with apparent resistivities less than 1000 Ω m, is more or less uniformly impregnated with pyrite and pyrrhotite with mineable concentrations of chalcopyrite in places. The boundaries between the barren and the impregnated rock are clearly indicated by the steep gradient in the resistivity contours.

4.6.3.3 Hemispherical sink

This model (Fig. 4.39) is of some significance in mapping depressions in bedrock, small ore bodies, cavities, etc. In this case it is possible to obtain an analytical solution for the potential in the presence of a point electrode on the surface [81] but as the solution is rather complicated we shall consider instead the special case when the normal electric field is homogeneous far away from the sink. Such a field can be simulated in practice by means of two current electrodes very far from each other. Even this restricted case, however, yields some insight into how the electric field and ρ_a can vary under more complicated conditions.

We choose the centre of the sink as the origin, the x axis in the direction of the normal field E_0, the z axis vertically downwards and the y axis perpendicular to the plane of Fig. 4.39. Then the electric field ($-\mathrm{d}V/\mathrm{d}x$) on the surface ($z = 0$) is found to be

$$E_1 = E_0 - E_0 \frac{2\beta}{3+\beta} b^3 \left(\frac{2x^2 - y^2}{(x^2+y^2)^{5/2}} \right) \quad \text{outside the sink} \qquad (4.69a)$$

$$E_2 = 3E_0 \frac{1+\beta}{3+\beta} \quad \text{on the sink} \qquad (4.69b)$$

where $\beta = (\rho_2 - \rho_1)/(\rho_2 + \rho_1)$ and b = radius of the sink.

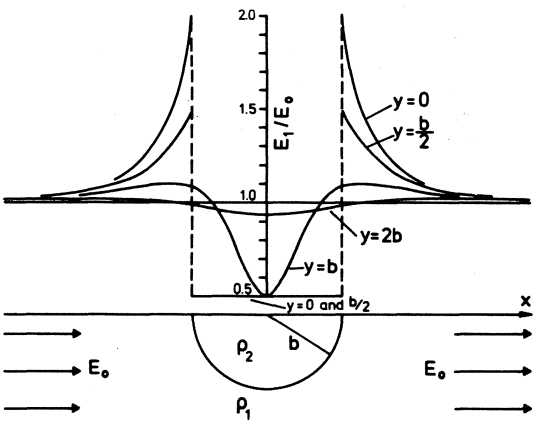

Fig. 4.39 ρ_a profiles over an outcropping hemispherical sink.

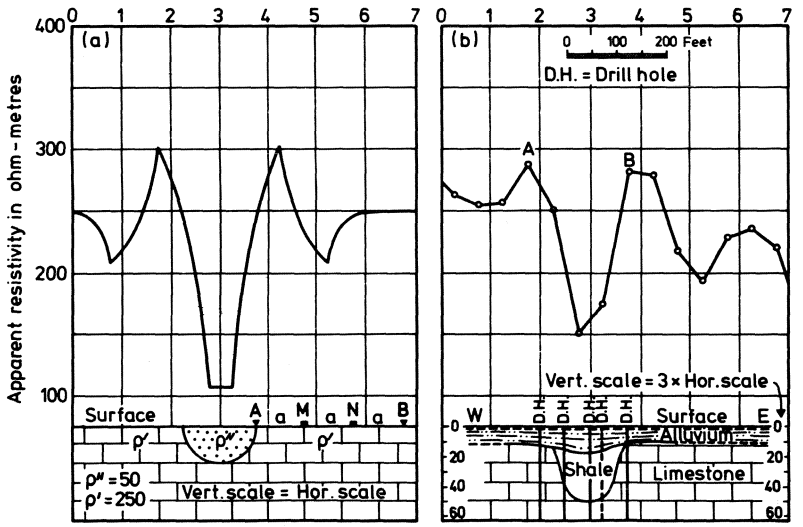

Fig. 4.40 Wenner ρ_a across hemispherical sinks. After [81].

We see from Eq. (4.69b) that the field on the sink is homogeneous and in the direction of E_0. (This, incidentally, is so at all points within the sink and not only on the surface.)

Fig. 4.39 also shows the normalized fields E_1/E_0 and E_2/E_0 along four x profiles at distances of 0, $b/2$, b and $2b$ from the centre, for a sink filled with material one fourth as resistive as the surrounding medium. Since only the two potential electrodes are moving in a gradient mapping, the profiles are generally easier to interpret than in other procedures. If all the four electrodes move, as in Wenner mapping, for example, the ρ_a curve takes a form which is not always easy to visualize intuitively. An interesting sample is shown in Fig. 4.40(a). Here the theoretical curve has been calculated for the Wenner arrangement taken across a hemispherical sink embedded in an otherwise homogeneous ground. The curve shows several cusps as each of the four electrodes crosses the sink boundary in succession. Fig. 4.40(b) is a field curve over a deposit which approximates to this form.

4.6.4 Inhomogeneity of arbitrary shape

Apparent resistivity curves over lateral inhomogeneities of arbitrary shape cannot be calculated analytically and some sort of numerical method must be resorted to. The theoretically most exact method uses integral equations [82, 83] but an approach using the finite element method has also been made [84]. All such calculations need fairly large computers. A detailed discussion of

the subject is beyond the scope of this book and the reader is referred for further details to the papers cited above.

4.7 ANISOTROPIC EARTH

4.7.1 Generalized Ohm's law

Although we have considered homogeneous as well as non-homogeneous earth it has been tacitly assumed that all the media concerned are electrically isotropic. However, many rocks such as shales, slates, laminated ores and also many other rock formations are markedly anisotropic and serious errors can arise in the interpretation if this fact is neglected.

To start with we shall see the form that Ohm's law takes for an anisotropic medium.

In Eq. (4.17) or (4.18) the current density j and the electric field E are assumed to be in the same direction, which is the case for a homogeneous isotropic medium. Thus for a current density in the x direction, for example, $j_x = \sigma E_x$. In general, however, not only the field E_x but also the fields E_y, E_z may give rise to a current density in the x direction. If the additional current densities are proportional to the fields we may write them as $\sigma_{xy}E_y$ and $\sigma_{xz}E_z$ respectively where σ_{xy}, σ_{xz} are constants of proportionality. For the sake of consistency we then write the contribution σE_x to j_x as $\sigma_{xx}E_x$. The total current density in the x direction is the sum of these three terms. The same reasoning holds for the current densities j_y, j_z in the y and z directions. In general, therefore,

$$\begin{aligned} j_x &= \sigma_{xx}E_x + \sigma_{xy}E_y + \sigma_{xz}E_z \\ j_y &= \sigma_{yx}E_x + \sigma_{yy}E_y + \sigma_{yz}E_z \\ j_z &= \sigma_{zx}E_x + \sigma_{zy}E_y + \sigma_{zz}E_z \end{aligned} \tag{4.70}$$

If the nine constants $\sigma_{xx}, \sigma_{xy}, \ldots$, characterizing the medium are independent of the electric fields E_x, E_y and E_z the medium is said to be *linear*. The system (4.70) is the generalized form of Ohm's law (Eq. 4.18) for a homogeneous, anisotropic medium. An alternative form of the law, corresponding to Eq. (4.17), is:

$$\begin{aligned} E_x &= \rho_{xx}j_x + \rho_{xy}j_y + \rho_{xz}j_z \\ E_y &= \rho_{yx}j_x + \rho_{yy}j_y + \rho_{yz}j_z \\ E_z &= \rho_{zx}j_x + \rho_{zy}j_y + \rho_{zz}j_z \end{aligned} \tag{4.71}$$

This system is, in fact, simply the solution of the system of linear simultaneous equations (4.70) and vice versa. It should be realized that, in general, $\sigma_{xx} \neq 1/\rho_{xx}, \sigma_{xy} \neq 1/\rho_{xy}, \ldots$, and so on for the other constants.

4.7.2 Point electrode on anisotropic earth

We shall now consider a somewhat simpler situation, namely one in which the current density in any of the three directions x, y, z depends on the electric field and conductivity in that direction only. Then the 'off-diagonal' components like $\sigma_{xy}, \sigma_{xz}, \ldots$, etc. or $\rho_{xy}, \rho_{xz}, \ldots$, etc. in (4.70) and (4.71) are zero and only $\sigma_{xx}, \sigma_{yy}, \sigma_{zz}$, the conductivities in the three directions, exist. These we now denote simply by $\sigma_x, \sigma_y, \sigma_z$. Correspondingly we have the three resistivities ρ_x, ρ_y, ρ_z. For this particular situation we have, in addition, $\sigma_x = 1/\rho_x, \ldots$, etc.

We have seen that the potential of a point electrode on the surface of a homogeneous isotropic earth (Eq. 4.19) is

$$V = \frac{I\rho}{2\pi} \frac{1}{(x^2 + y^2 + z^2)^{1/2}} \tag{4.72}$$

It can be shown that the potential on our homogeneous, anisotropic earth is (Appendix 10)

$$V = \frac{I(\rho_x \rho_y \rho_z)^{1/2}}{2\pi} \frac{1}{(\rho_x x^2 + \rho_y y^2 + \rho_z z^2)^{1/2}} \tag{4.73}$$

Equation (4.72) shows that the equipotential lines $V =$ constant on the surface ($z = 0$) of the isotropic earth are given by

$$x^2 + y^2 = \text{constant} \tag{4.74}$$

They are thus circles of different radii with the current electrode as the centre. On the surface of the anisotropic earth the equipotential lines are seen, from Eq. (4.73), to satisfy the equation

$$\rho_x x^2 + \rho_y y^2 = \text{constant} \tag{4.75}$$

This is an equation for an ellipse with its centre at the origin. Writing it in the form

$$\frac{x^2}{\sigma_x} + \frac{y^2}{\sigma_y} = \text{constant}$$

we see that the major axis of any elliptical equipotential contour on the surface is in the direction of the greater of the two *conductivities* σ_x, σ_y. The ratio of the two axes of the ellipse is the square root of the ratio of the two conductivities in their directions.

4.7.3 Anisotropy paradox

In most practical situations where anisotropy is significant, e.g. in sandstones, shales, slates, clays and many other sedimentary rocks as well as crystalline rocks like gneisses, there are two predominant resistivities, namely ρ_1

(longitudinal resistivity) parallel to the layering and ρ_t (transverse resistivity) perpendicular thereto. The number $\lambda = (\rho_t/\rho_l)^{1/2}$ is called the coefficient of anisotropy and is always greater than one (see Problem 4.8). For most sedimentary rocks it is of the order of 1.1–2.5 but much higher values can be found, particularly in metamorphosed sediments, gneisses, banded ores etc. There is no upper limit to λ.

Let us now consider a *vertically* stratified earth and take the x axis perpendicular to the stratification, the y axis parallel to the strike and the z axis vertically downwards. Then we have

$$\rho_x = \rho_t \qquad \text{and} \qquad \rho_y = \rho_z = \rho_l \tag{4.76}$$

and Eq. (4.73) can be written after taking ρ_x out of the bracket in the denominator as

$$V = \frac{I\rho_m}{2\pi} \frac{1}{(\lambda^2 x^2 + y^2 + z^2)^{1/2}} \tag{4.77}$$

where we have put $\rho_m = (\rho_t \rho_l)^{1/2}$, the geometrical mean of ρ_t and ρ_l.

It is easy to see that

$$\rho_m = \lambda\rho_l = \rho_t/\lambda \tag{4.78}$$

Take a profile on the surface in the x direction, that is, in the direction of the transverse resistivity and passing through the electrode. For this profile $z = 0$ and $y = 0$ in Eq. (4.77) so that

$$V = \frac{I\rho_m}{2\pi\lambda} \frac{1}{x}$$

$$= \frac{I\rho_l}{2\pi} \frac{1}{x} \tag{4.79}$$

Comparing this equation with Eq. (4.72) we see that for measurements on the surface in the x direction, that is in the direction of the transverse resistivity ρ_t, the anisotropic earth behaves as if it has the longitudinal resistivity ρ_l! This result is known as the *anisotropy paradox*. For surface measurements along a profile in the y direction through the electrode ($x = 0, z = 0$) Eq. (4.77) gives

$$V = \frac{I\rho_m}{2\pi} \frac{1}{y} \tag{4.80}$$

Thus for measurements in the direction of the longitudinal resistivity, the effective resistivity of the anisotropic earth is neither ρ_l nor ρ_t but the geometric mean ρ_m.

We have considered above strata dipping vertically and a profile either parallel or perpendicular to the strike. However, for a general dip α and a profile at an angle ϕ with the strike, the apparent resistivity of the anisotropic

earth is

$$\rho_a = \frac{\rho_m}{[1 + (\lambda^2 - 1)\sin^2\phi \sin^2\alpha]^{1/2}} \tag{4.81}$$

The special cases above can be immediately verified by putting $\alpha = 90°$ and $\phi = 90°$ or $0°$.

4.7.4 Maillet's equivalence

Another important practical consequence of anisotropy is as follows. Suppose we have an anisotropic layer of thickness h between two highly resistive layers. We have then the situation as in Fig. 4.26(a). The current will be flowing in the direction of ρ_l and the equivalence rule takes the form $h/\rho_l = \text{constant}$. Now, we have the identity

$$\frac{h}{\rho_l} \equiv \frac{h}{(\rho_l\rho_t)^{1/2}}\left(\frac{\rho_t}{\rho_l}\right)^{1/2} = \frac{\lambda h}{\rho_m}$$

From this we see that the h/ρ_l ratio will not be changed if we replace the anisotropic layer of thickness h and resistivities ρ_l, ρ_t by an isotropic layer of thickness λh and a resistivity ρ_m. The same holds true if an anisotropic layer has much higher resistivities than the two layers on either side and the current flow is as in Fig. 4.26(b).

Conversely, any layer of thickness h and isotropic resistivity ρ in a sequence of interpreted VES layers may be replaced by an anisotropic layer of thickness h/λ (!) and resistivities $\rho_t = \lambda\rho, \rho_l = \rho/\lambda$ by choosing any value of $\lambda(> 1)$. The ambiguity in VES interpretation introduced by this fact is obvious. It can only be resolved by some knowledge of the geology and the properties of the strata in question.

It should be realized that the equivalence of layers discussed in Section 4.5.4.7 is due to the inaccuracy of all practical measurements but the equivalence between an isotropic layer and an anisotropic layer having appropriate parameters is *exact*. The two alternatives cannot be distinguished even if we have infinitely accurate measurements. This impossibility was first pointed out by Maillet [85] and proved by him for any current distribution in an anisotropic layer and not only for the two special cases of Fig. 4.26 as here.

The possibility of corrections to the interpreted layer-thicknesses in electrical sounding arising due to anisotropy should always be borne in mind.

PROBLEMS

4.1 A current of 1 A is supplied to homogeneous ground of resistivity 500 Ω m with $AB = 200$ m. Calculate the current density (a) at a point 50 m vertically below the midpoint of AB and (b) at a point at the same depth but vertically below one of the electrodes.

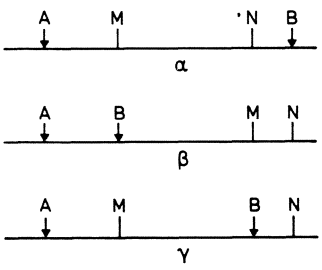

Fig. 4.41

4.2 What is the maximum MN distance if $\Delta V/MN$ in the Schlumberger array of Fig. 4.13(b) is to be within 1% of the true gradient on a homogeneous earth if $AB = 200$ m?

4.3 Fig. 4.41 shows three electrode arrarys (α, β, γ) in which the distances between adjacent electrodes are the same in the three cases. If α, β, γ also denote the potential differences measured between M and N when the same current is passed through the earth in all arrays show, assuming the reciprocity theorem, that

$$\alpha + \beta = \gamma$$

(Note 1: An answer involving changes of symbols in Eq. (4.24) is not valid since that equation is true for homogeneous earth only. The problem assumes a general, inhomogeneous (but linear) earth. No integrations are required.

Note 2: The equation above has often been inconsistently written in the literature with a minus sign.)

4.4 A sounding interpretation gave the following parameters: $h_1 = 2.7$ m, $\rho_1 = 8020\,\Omega$m; $h_2 = 15$ m, $\rho_2 = 370\,\Omega$m; $h_3 = 15$ m, $\rho_3 = 1520\,\Omega$m; $\rho_4 = 250\,\Omega$m. A drill-hole showed a dry surface layer of thickness 3.1 m, an argillaceous sandy layer (13.8 m) and a gravelly layer of thickness 4.1 m before the hole reached the substratum. What is the probable reason that h_3 differs so much from the true thickness?

4.5 Interpret the 'measured' ρ_a curve of Table 4.3 by the auxiliary point method and compare the result with the remark in 'Answers'.

4.6 The following ρ_a values were obtained in a Schlumberger sounding. Draw the VES curve on a double logarithmic paper and sample it to calculate T_m at $AB/2 = 22.6$ m using Table 4.5. Extrapolate if necessary. Compare T_m with the exact T_1 (22.6) for the model $h_1 = 0.7$ m, $\rho_1 = 500\,\Omega$m; $h_2 = 5.0$, $\rho_2 = 80$; $h_3 = 35$, $\rho_3 = 260$; $h_4 = \infty$, $\rho_4 = 2.5$.

$AB/2$(m)	0.7	1	1.5	2	3	5	7	10	15	20	30	40	50	70	100
ρ_a(Ω m)	480	434	285	182	115	76	92	111	145	167	201	197	188	132	65

4.7 A three-layer earth has the following parameters: $h_1 = 5\,\text{m}$, $\rho_1 = 110\,\Omega\text{m}$; $h_2 = 20\,\text{m}$, $\rho_2 = 450\,\Omega\text{m}$; $\rho_3 = 2\,\Omega\text{m}$. Calculate using Table 4.4 ρ_a in a Schlumberger sounding for $AB/2 = 100\,\text{m}$.

4.8 Consider a rectangular prism consisting of two layers of thickness h_1, h_2 and resistivities ρ_1, ρ_2 respectively. Derive an expression for the anisotropy coefficient λ of this prism and show that $\lambda > 1$.

4.9 In a gneissic area with an extremely thin overburden, values of $\rho_a = 3480\,\Omega\text{m}$ and $4890\,\Omega\text{m}$ were obtained along two mutually perpendicular profiles, one of which was parallel to the strike. The dip of the gneissic schists is known to be 45°.

(a) Which of the two profiles is the one parallel to the strike?

(b) Calculate the true resistivities of the rock and anisotropy coefficient.

(c) What value of ρ_a would have been obtained parallel to the strike if the dip had been 60°?

4.10 The overburden in an area is fairly uniform in thickness (15 m) and has a resistivity of $180\,\Omega\text{m}$. The underlying rock has a resistivity of $420\,\Omega\text{m}$. Estimate the minimum AB distance in mapping if at least 60% of the current is to penetrate below the overburden.

The following examples require a closer study of the theory in this chapter and in Appendix 7.

4.11 Two parallel linear current electrodes, each of length $2b$, are laid on the ground surface so that the four ends are at the corners of a rectangle. The electric field is measured along profiles perpendicular to the line electrodes. Derive the expression for the apparent resistivity, if $2L$ is the current electrode separation.

4.12 A second current electrode B (negative, if C is positive) is placed on the ground surface in Fig. 4.35 in medium 2 at a distance b from the contact. Show that the apparent resistivity in gradient mapping will be given in medium 1 by

$$\rho_a/\rho_1 = 1 + \beta_1 \frac{1 - (d+b)^2/(d+a)^2}{1 - (d+b)^2/(d-a)^2} \qquad d > a$$

$$\rho_a/\rho_1 = 1 + \beta_1 \frac{1 - (b+d)^2/(a+d)^2}{1 + (b+d)^2/(a-d)^2} \qquad d < a$$

where d is the distance of the measurement point from the contact.

(Note: To avoid ambiguity concerning positive and negative distances, choose the origin of coordinates at C in solving the problem.)

4.13 A Wenner electrode configuration $AMNB$ with $AM = MN = NB = l$ is moved across the contact in Fig. 4.35 along a line perpendicular to the strike of the contact. Derive the expressions for the potential difference between M and N for the following three principal cases: (a) All electrodes in medium 1, (b) A, M, N in medium 1 and B in medium 2, (c) A, M in medium 1 and N, B in medium 2.

5

Induced polarization

5.1 INTRODUCTION

If an electric current in the ground is interrupted the voltage across M, N (Fig. 4.13) does not drop to zero instantaneously. It is found instead to relax for several seconds (or minutes) starting from an 'initial' value which is a small fraction of the voltage (V) that existed when the current was flowing (Fig. 5.1). This phenomenon has been termed *induced polarization* and is easily observed when electronically conducting minerals or clay minerals are present in the ground. It was noted in geophysical work by C. Schlumberger some time before 1920 but modern application of the phenomenon to geophysical exploration dates from about 1948 although several, largely inconclusive, experiments were reported between 1920 and 1948.

The phenomenon has been known to electrochemists studying the passage of electric currents in electrode–electrolyte systems and has in this connection been called *overvoltage*. That a very similar effect exists in pure dielectrics has also been known for a considerable time [86].

It takes a finite, although short, time before the voltage V is reached when a current is switched on. This implies that for an uninterrupted current flow induced polarization should manifest itself as a dependence of the ground impedance on the frequency of the current. This is, in fact, borne out by observations.

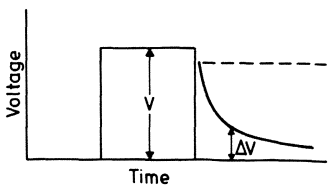

Fig. 5.1 IP phenomenon.

Thus, the IP phenomenon can be observed in the time as well as the frequency domain. It is an exceedingly complex phenomenon although it superficially resembles the discharge of a capacitor (time domain) or the variation of the impedance of an RC circuit (frequency domain). An adequate explanation of all aspects of the IP phenomenon has yet to be given but we shall consider some of the theories advanced later on.

5.2 MEASURES OF IP

5.2.1 Time domain

When measurements are made by passing d.c. pulses of duration T in the ground the magnitude of the observed IP is often expressed as $\Delta V/V$ (millivolt per volt or per cent) where ΔV is the voltage remaining at a definite time t after current cut-off. This measure of IP, which we shall denote by P_t^T, is called the *polarizability*. Commonly used values of T are in the range of 1–20 s while t is a fraction of T.

It is usual to send the d.c. pulse first in one direction and then in the reverse direction, after a current-off time following the measurement of P_t^T. The cut-off time is generally of the same order of magnitude as T.

It is essential to choose t properly. It must be long enough for the electromagnetic induction effects in the ground to have substantially disappeared but short enough for ΔV not to fall below the sensitivity of the detecting device.

The ratio $\Delta V/V$ is independent of V, at least for the current densities in the ground in normal field operations.

Sometimes the normalized time integral $(1/V)\int_{t_1}^{t_2}\Delta V_{\mathrm{IP}}\,\mathrm{d}t$ representing the area under the decay curve is used to express IP as millivoltsecond per volt or as millisecond. This measure is known as *chargeability* (denoted M_{t_1,t_2}^T).

A quantity that implicitly contains some information about the shape of the decay curve is the ratio L/M where M is as defined above and L is the corresponding quantity representing the area 'above' the curve, that is, between the dashed line in Fig. 5.1 and the decay curve between t_1 and t_2.

5.2.2 Frequency domain

In the frequency domain, the apparent resistivity of the ground is measured by any one of the innumerable electrode configurations possible (Section 4.4.3) at two frequencies F and $f(<F)$. IP is expressed as the apparent frequency effect $\mathrm{FE}_{F,f}=(\rho_{af}-\rho_{aF})/\rho_{af}$. The term per cent frequency effect is also used if this ratio is expressed as a percentage change in ρ_a.

f is usually in the range 0.05–0.5 Hz and F in the range 1–10 Hz.

Another frequency domain measure of IP is the *metal factor* $MF_{F,f}=$

$A(\rho_{af} - \rho_{aF})/(\rho_{af}\rho_{aF}) = A(\sigma_{aF} - \sigma_{af})$ where A is a suitable numerical coefficient (10^5 or $2\pi \times 10^5$ are values that are often used) and the σ_a's are the apparent conductivities. In SI units, MF has the dimensions siemen per metre.

The time-domain measure corresponding to $MF_{F,f}$ will be IP/ρ_a where $IP = P_t^T$ or M_{t_1,t_2}^T, but this does not appear to have been used.

A third measure of the IP effect in the frequency domain is the phase difference ϕ between the voltage between M, N and the current injected into the ground. Maximum values of ϕ in practice are usually a few hundredths to a tenth of a radian at a frequency of, say, 1 Hz.

5.3 ORIGIN OF IP

5.3.1 Electrode and membrane polarizations

The electric conduction paths in the ground are normally ionic but they may sometimes be hindered to a greater or lesser extent by mineral particles (e.g. pyrite grains) in which the carriers of current are electrons.

It is well known that when a current passes across a metal electrode (electronic conductor) dipped in an electrolyte, charge can pile up continuously at the interface when all the processes in the electrolytic reaction are not equally rapid. This produces the familiar back e.m.f. or electrode polarization. The extra piled-up charge diffuses back into the electrolyte when the current is stopped, re-establishing the original equilibrium in which a thin layer of negative ions is fixed to the metal electrode. The IP observed over sulphide ores or other electronically conducting minerals like graphite or magnetite is basically a manifestation of such 'electrode polarization'. The effect will be enhanced if the mineral grains are dispersed rather than in a compact mass since it is essentially a surface phenomenon and the polarization charge will be large owing to the large total surface of the particles. Values of more than 10% for $\Delta V/V$, for example, are not uncommon on such ores (Fig. 10.2).

Induced polarization is also observed in the absence of electronically conducting minerals. The presence of clay particles appears to be a necessary condition for this effect for it is not observed on clean quartz sand or similar media devoid of clay minerals. 'Membrane polarization', as this effect has been termed, is most probably due to ionic exchanges and the setting up of diffusion potentials somewhat as follows.

The surface of clay particles, the edges of layered and fibrous materials or cleavage faces normally have unbalanced negative charges that attract a cloud of positive ions from the surrounding electrolyte. When an electric current is forced through a clay–electrolyte system, positive ions can readily pass through this cloud but negative ions are blocked forming zones of ion concentration.

The return of the ions to the former equilibrium distribution after the

current is stopped constitutes a residual current and appears as the IP effect. Superficially, as far as observations are concerned, membrane and electrode IP effects resemble each other. No diagnostic feature that can distinguish these two effects unambiguously has yet been found for field observations.

5.3.2 Macroscopic theories

It is beyond the scope of this monograph to discuss in detail the various attempts that have been made to explain the IP phenomenon quantitatively. For an excellent résumé of these the reader is referred to the monograph of Bertin and Loeb [87] and for a qualitative account to Sumner's monograph [88]. Here we shall indicate some of the main lines in these theories.

The two principal features of the phenomenon that must be explained by any IP theory are the shape of the decay curve and its counterpart in the frequency domain, namely the variation of the (complex) resistivity with frequency. It should be realized that the decay curve is not a simple exponential but more like a sum of several exponentials. In some cases the variation is also found to be of the type $\Delta V = At^{-n}$ where t is the time after current cut-off.

Many of the experimental results including the above two can be conveniently approximated by the assumption that the current density j in the ground is given by

$$j = (\sigma + \mathrm{i}\varepsilon_{\mathrm{IP}}\omega)E \qquad (\mathrm{i} = \sqrt{(-1)}) \tag{5.1}$$

where σ and E are the conductivity and the electric field, ω is the angular frequency and $\varepsilon_{\mathrm{IP}}$ is a parameter of the nature of a dielectric constant.

The dielectric constant of rocks is of the order of $5\text{–}100\varepsilon_0$ where ε_0 is the dielectric constant of vacuum (8.854×10^{-12} farad per metre). Various estimates of $\varepsilon_{\mathrm{IP}}$ have been made from IP observations [87]. Even the lowest of these indicate $\varepsilon_{\mathrm{IP}} \approx 10^4\text{–}10^5\varepsilon_0$ and some of the highest ones $\varepsilon_{\mathrm{IP}} \approx 10^{11}\varepsilon_0$! It is clear that ordinary dielectric properties cannot explain IP and the observed decay constants of IP voltage imply 'abnormally' high interface capacitances at mineral gains.

The macroscopic or phenomenological theories attempt to explain the observations by means of certain *ad hoc* parameters and relations, of which the above discussion gives one example.

Another such attempt is Seigel's assumption that the source of IP signal is a secondary current density vector $\mathbf{m} = m\mathbf{j}_0$ where m is a dimensionless parameter ('chargeability') and $\mathbf{j}_0$ is the current density at the end of a charging process. The electric potential in the medium is then given by the analogue of Eq. (A1.10) and Seigel showed [89] that the assumption amounts to an effective decrease of σ to $\sigma(1 - m)$ during the charging or the discharging processes. With these assumptions it is possible to calculate the IP response of

polarizable bodies. This approch does not, of course, intend to explain the time dependence of IP.

In considering time dependence we recall that the voltage across a charged capacitor in parallel with a resistor decays exponentially with time. As mentioned above the IP decay curve is of a more complicated type. Various attempts have therefore been made to explain the observed time dependence of IP and the frequency dependence of the complex resistivity by simulating suitable, more elaborate resistor–capacitor combinations [87]. While such networks explain the results of specific experiments they cannot be said to explain the *physical* origin of IP.

5.3.3 Microscopic theories

The object of microscopic or physical theories is to explain the IP phenomenon by consideration of the forces acting on the electric charge carriers involved and their motion under these forces. Suppose, for example, that the ions in the ground electrolytes move only under diffusion forces obeying the diffusion equation

$$\frac{\partial C}{\partial t} = D\frac{\partial^2 C}{\partial x^2} \tag{5.2}$$

where C is the ion concentration (mol m^{-3}) and D the diffusion coefficient (m^2 s^{-1}), a suggestion made by Warburg already in 1899 for explaining the response of non-polarizable electrodes to alternating current.

If C undergoes a sinusoidal variation of frequency f at $x = 0$ the general solution of Eq. (5.2) is known to be of the form $C = C_0 \exp[-x(\pi f D)^{1/2}] \sin[2\pi ft - x(\pi f/D)^{1/2}]$ which suggests that the amplitude of the IP voltage should depend on $f^{1/2}$. Accurate experiments show that it in fact depends on f^{α} where $\alpha \neq \frac{1}{2}$. In the time domain it can be shown [87] that the time constants derived from this theory are several orders of magnitude smaller than those observed in practice for the IP phenomenon.

Simple diffusion is thus not sufficient to explain the IP phenomenon. Of the attempts made to improve upon the diffusion hypothesis two will be mentioned here.

Bertin and Loeb in the monograph cited above assume that the anions and cations in the electrolyte under consideration are subject to electrical forces in addition to diffusion forces. They then arrive at the following modification of (5.2):

$$\frac{\partial C}{\partial t} = \frac{\partial}{\partial x}\left(uCE - D\frac{\partial C}{\partial x}\right) \tag{5.3}$$

(E = electric field V m^{-1}, u = ionic mobility m^2 V^{-1} s^{-1}.)

Equation (5.3) is assumed to be satisfied separately by the anions and cations. The signs of u will be opposite to each other for the two species.

Considering the situation at the end of the charging process when no flow of matter takes place any longer, Bertin and Loeb are able to explain the order of magnitude of ε_{IP} on the basis of (5.3).

Nilsson [90] starts with slightly different assumptions and taking into account the thermal agitation forces derives a non-linear differential equation for the electric field at a distance x from a plane electrode,

$$\frac{\partial E}{\partial t} = D\left(\frac{\partial^2 E}{\partial x^2} - \frac{ze}{kT}E\frac{\partial E}{\partial x}\right) \tag{5.4}$$

where z denotes the number of electrons lost per atom in the formation of the cations, e is the electronic charge, k is Boltzmann's constant and T is the absolute temperature.

A numerical integration of this equation under appropriate boundary conditions seems to reproduce the time dependence of IP. Nilsson also makes the interesting suggestion that IP and SP have the same origin, the latter being the static field obtained as a function of x for $\partial E/\partial t = 0$. (In consulting Nilsson's paper the reader should note that it contains an inordinate number of misprints.)

It is interesting to note that if the concentration of ions is postulated to be proportional to the electric field and u to be independent of E, Eq. (5.3) is essentially the same as (5.4).

The full implication of these equations and of other similar attempts is still to be worked out and the physical theory of IP is not yet in a final shape.

5.4 ELECTROMAGNETIC COUPLING

Electromagnetic induction in the ground creates potential differences that are superimposed on those due to the true IP effect. These coupling effects can be troublesome in IP measurements when the current-supply lines are long and the ground is highly conductive. They must be assessed before the true IP effect can be estimated.

A universally applicable method of correcting for electromagnetic coupling does not exist. In practice one must assume an electrical structure for an area (e.g. a layered sequence) and calculate, for the electrode configuration in question, the spurious IP parameter magnitude that can arise due to electromagnetic induction. This is then subtracted from the measured value of the parameter. An approach of this type is a matter of expediency and, although used widely, its theoretical basis is qualitative at best.

Hohmann [91] among others has treated in some detail the problem of electromagnetic coupling in frequency-domain methods. Figs 5.2 and 5.3, after him, give an idea of the spurious per cent frequency effect that will arise for a

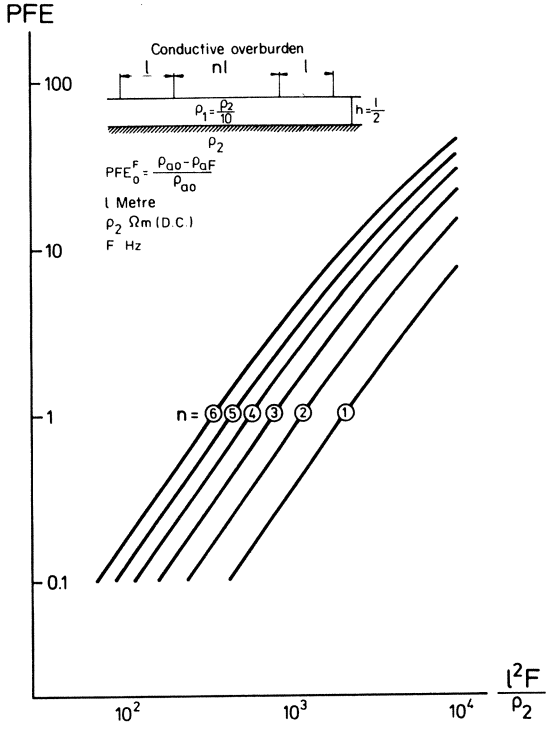

Fig. 5.2 Per cent frequency effect (PFE) due to electromagnetic coupling in frequency-domain IP for a dipole–dipole configuration on the two-layer earth shown. After [91].

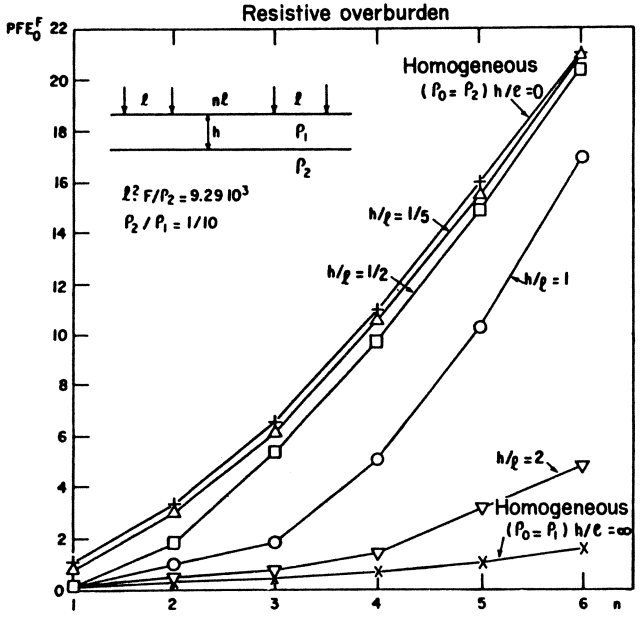

Fig. 5.3 Per cent frequency effect (PFE) due to e.m. coupling as a function of overburden thickness and n in a dipole–dipole array. After [91].

dipole–dipole configuration (Section 4.3.3) on the two-layer earth shown. Similar calculations for the time-domain method have been published by Rathor [92] and for the phase difference IP method by Wynn [93].

As a rule it is advisable to select a measurement technique that minimizes electromagnetic coupling effects rather than try to estimate them. For example, for a Schlumberger array (Fig. 4.13) L for time-domain work should be such that $\mu L^2/\rho \ll \sim 1\,\mathrm{s}$ where μ is the magnetic permeability ($= 4\pi \times 10^{-7}\,\Omega\,\mathrm{s\,m^{-1}}$ for most practical purposes) and $\rho(\Omega\,\mathrm{m})$ the resistivity of the ground. For frequency-domain work Sumner [88] suggests that the ratio a/d (a = electrode spread and $d = (\rho/\pi f\mu)^{1/2}$) should be less than 0.1.

Similarly, configurations in which the current electrodes line is at right angles to the potential electrodes line minimize the effect of electromagnetic coupling.

5.5 EXAMPLE OF AN IP SURVEY

Although IP measurements have sometimes been undertaken as vertical soundings [94] like the resistivity work described in the previous chapter, most of the present IP work is of the mapping type. The advantage of IP soundings (as a complement to VES) is that they are able to distinguish between clay layers (high IP) and some other low-resistivity strata like salt-water beds (no IP).

Fig. 5.4 is an example of a ρ_a and IP (frequency domain) survey [95]. It should be evident from Section 5.2 that an IP measurement necessarily involves a concomitant resistivity measurement. The measurements in Fig. 5.4 were made by using a number of dipole–dipole arrays (Fig. 4.34) with different n values. The manner of plotting the readings should be clear from the inset. As already mentioned in Section 4.6.2.4 a diagram obtained in this manner is qualitatively regarded as representing 'an electrical vertical section' or rather 'pseudo-section' through the profile, since increasing n values give information from increasingly larger depths, but the plot must not be taken too literally. Vertical tabular bodies of constant thickness, for example, can be shown to give wedge-shaped anomalies on this plot. Thus the patterns in Fig. 5.4 do not by any means necessarily indicate a broadening of the mineralization towards the deeper levels.

An example of a time-domain in IP profile will be found in Fig. 10.2.

PROBLEMS

5.1. The overburden in an area is 20 m thick and has a resistivity of $2\,\Omega\,\mathrm{m}$. The underlying bedrock has a resistivity of $20\,\Omega\,\mathrm{m}$. A frequency-domain measurement with a dipole–dipole configuration having $AB = 40\,\mathrm{m}$ and $BM = 160\,\mathrm{m}$ is planned. Estimate with the help of Fig. 5.3 (or 5.4) the

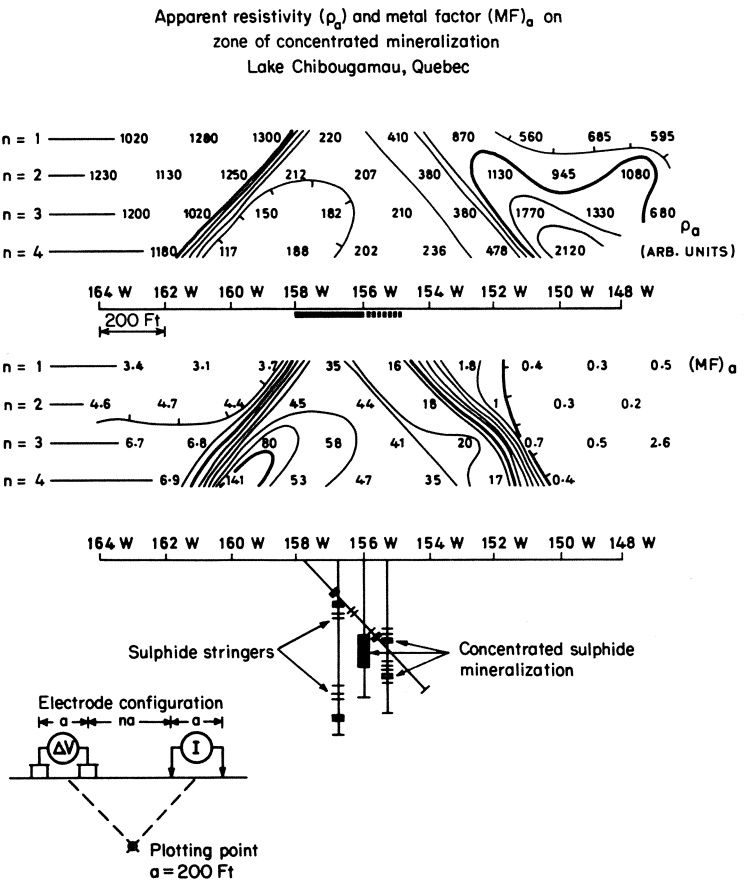

Fig. 5.4 A frequency domain IP survey with the dipole–dipole configuration. After [95].

highest frequency that may be used in order to keep the PFE due to e.m. coupling less than 1%.

5.2. The following voltages were measured at the times given, after the interruption of a direct current that was sent into the ground for 120 s. The potential during the current-on time was 214 mV. Calculate two values for the polarizability and one for the chargeability.

Time (s)	60	150	300	600	900	1200	1800
ΔV(mV)	9.5	6.5	5.0	3.2	3.0	2.1	1.5

6

Electromagnetic continuous wave, transient-field and telluric methods

6.1 INTRODUCTION

If a time-varying electromagnetic field is produced on the surface of the ground currents will flow in sub-surface conductors in accordance with the laws of electromagnetic induction. These currents give rise to secondary electromagnetic fields which modify the total field observed at any point on the surface. In general, the resultant field, which may be picked up by a suitable search coil, will differ from the primary field in intensity, phase and direction and reveal the presence of the conductors.

If the primary field is transient the secondary currents and their field will decay gradually when the primary field has ceased to exist. The decay is faster the higher the resistivity of the medium in which the currents flow. In this case we cannot talk of any unique phase relations since the signal contains an infinite number of frequencies.

A great advantage of the electromagnetic methods is that they can be successfully applied even when conductive ground connections, indispensable for the methods of the last two chapters, cannot be made owing to highly resistive (or insulating) surface formations. This is frequently the case in arid tracts in the polar and sub-polar regions where the ground may be frozen to a considerable depth.

On the other hand one of the troublesome effects in the electromagnetic methods is that the secondary currents in superficial layers of good conductivity, e.g. clays, graphitic shales, etc. may screen the deeper conductors partially or wholly from the primary field. The latter, which are the real objects of exploration, will then produce weak or no distortions (anomalies) in the total field and may therefore be indetectable.

6.2 ELECTROMAGNETIC INDUCTION

6.2.1 Neumann's law

The basis of electromagnetic methods is the law of induction, the precise formulation of which is due to F. Neumann, although the phenomenon of electromagnetic induction as such was discovered by Michael Faraday in 1832. In the form that we shall find most useful, the law states that if the magnetic flux normal to a plane circuit changes with time, an electromotive force equal in magnitude to the time rate of change of flux is induced in the circuit and that if the circuit is closed, an electric current will flow in it in such a direction that its magnetic field will tend to oppose the change of flux. At this point it will be convenient to recall the rule that the direction of the magnetic field at a point, due to a linear current element, is the direction in which the tip of the handle of a right-handed corkscrew tends to move when the screw tends to advance in the direction of the current. Thus, if the magnetic flux normal to the circuit in Fig. 6.1 is increasing with time upwards the induced current must flow in the direction shown in the figure in order that its magnetic field inside the loop be downwards to oppose the increase.

The bearing on electromagnetic prospecting of the fact, that the time-varying magnetic flux must have a component normal to the plane of the circuit, is that the transmitter in a survey must be suitably oriented so that its primary magnetic field can be expected to cut a presumed geological conductor.

Neumann's law does not describe all the phenomena of the electromagnetic field and needs to be supplemented by other laws. We shall deal with these later.

6.2.2 Phase relations

Consider now a sinusoidally varying field of frequency $\nu (1/\nu = \text{period } T$, angular frequency $\omega = 2\pi\nu)$. Such a field can be represented in a plane diagram as a rotating vector. One whole period of the field corresponds to a rotation of the vector through 360° (2π radian). If a vector representing a field **A** makes an anticlockwise angle ψ in this diagram with the vector representing a field **B**, then **A** is ahead of **B** in phase and goes through its maximum, minimum or any other corresponding phase $T\psi/2\pi = \psi/2\pi\nu$ seconds before **B**.

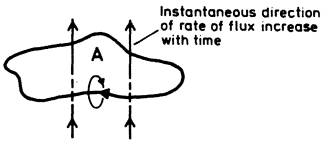

Fig. 6.1 Plane circuit.

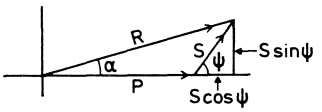

Fig. 6.2 General phase diagram.

The secondary field S at an observation point due to currents induced in the sub-surface conductors will, in general, differ in phase from the primary field P. In Fig. 6.2, the x axis represents the phase of P, and S is shown to be ahead of P in phase by the angle ψ. In general, of course, ψ can take any value and S may lie in any of the four quadrants. The vector sum of P and S is the resultant vector R.

The component $S\cos\psi$ of S, in phase with P, is called the *real* component, and the component $S\sin\psi$, 90° (one quarter period) ahead of P, is the *imaginary* component. These components are often called the in-phase component and the out-of-phase (or quadrature) component respectively. There are sound reasons, historical and logical, to retain the names real and imaginary, as we shall do in this book. A diagram like Fig. 6.2 representing the phase relations between various periodic fields is called a vector (or a phasor) diagram. The following relations are easily obtained from the diagram by elementary geometry and trigonometry.

$$\text{Resultant-field amplitude } R = (P^2 + S^2 + 2PS\cos\psi)^{1/2} \tag{6.1}$$

$$\text{Resultant-field phase } \alpha = \tan^{-1}\frac{S\sin\psi}{P + S\cos\psi} \tag{6.2}$$

$$\text{Secondary-field amplitude } S = (P^2 + R^2 - 2PR\cos\alpha)^{1/2} \tag{6.3}$$

$$\text{Secondary-field phase } \psi = \tan^{-1}\frac{R\sin\alpha}{R\cos\alpha - P} \tag{6.4}$$

$$R\sin\alpha = S\sin\psi \tag{6.5}$$

The last equation expresses that the imaginary component of the resultant field is the same as the imaginary component of the secondary field. What we can actually measure in practice is the magnitude of R and its phase α in relation to P but the magnitude of P at an observation point can be calculated from a knowledge of the source geometry and Eqs (6.3) and (6.4) then give S and ψ.

6.2.3 Single-turn circular coil (Fig. 6.3)

The current systems induced in geological conductors like ores, water-bearing strata etc. by a time-varying primary field that acts upon them are, in general, very complicated but the phenomena arising can be qualitatively well understood from a study of the response of a single-turn circular coil. This is

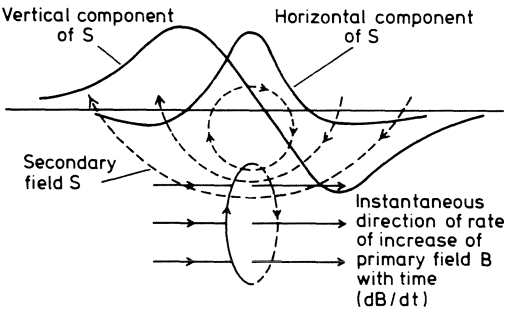

Fig. 6.3 Single-turn coil in alternating magnetic field.

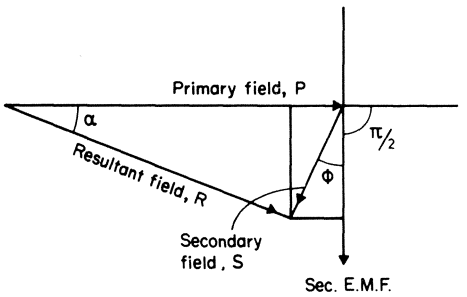

Fig. 6.4 Phase relations for a single-turn loop.

because in very many cases the complicated current systems are predominantly currents flowing along the edges or outer surfaces of the bodies, forming closed loops. We shall consider the case of a single-turn circular coil in a homogeneous sinusoidally varying magnetic field of frequency $\nu = \omega/2\pi$. The mathematical analysis of this circuit is relatively simple (Appendix A11.1) and shows that the induced e.m.f lags 90° in phase behind the primary field while the current in the coil, and consequently the secondary field in the vicinity of the coil, lags behind the e.m.f. by a further angle $\phi = \tan^{-1}(\omega L/R)$ where L is the inductance of the coil and R its resistance. Consequently $\psi = -(\pi/2 + \phi)$.

The phase relations between the primary, the secondary and the resultant fields in this case are shown in Fig. 6.4 from which we see that the real component of S is $-S\sin\phi$ and the imaginary component is $-S\cos\phi$.

It will be seen from the expression for ϕ that a very good conductor produces a secondary field almost opposite in phase to the primary field ($R \to 0, \phi \to \pi/2$) while a bad conductor produces a field that lags 90° behind the primary one ($R \to \infty, \phi \to 0$). The same phase effects are obtained on increasing or decreasing the frequency of the primary field (or the inductance of the coil).

As with ϕ, the magnitudes of the real and imaginary components of the

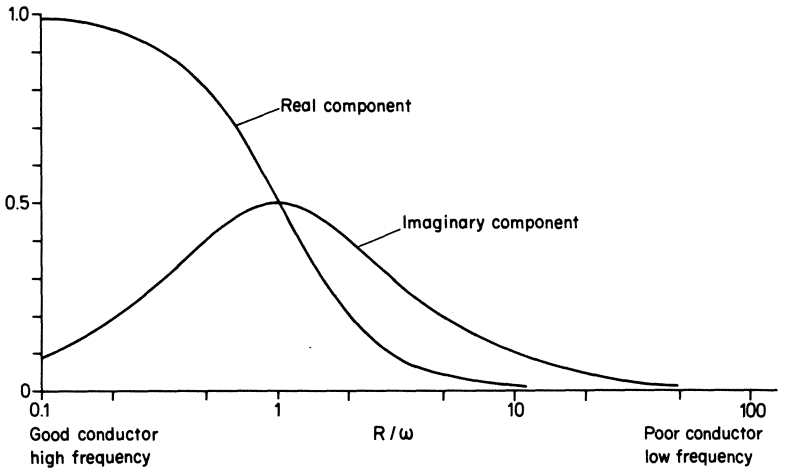

Fig. 6.5 Secondary-field response of a single-turn loop to a sinusoidal field.

secondary field of a single-turn loop depend on the ratio of ω and R (assuming L to be constant), rather than on ω and R separately. They are plotted in Fig. 6.5 against R/ω. This figure is interesting because it reproduces qualitatively every essential detail of the induction response of many complicated geological conductors to sinusoidal fields, homogeneous or otherwise. Thus, the real component of S decreases in magnitude as the frequency is decreased while it increases if the frequency is increased but reaches a saturation value as $\omega \to \infty$ ($R/\omega \to 0$ in Fig. 6.5). On the other hand the imaginary component increases as the frequency is increased from very low values, reaches a maximum, and thereafter decreases with further increase in frequency.

Fig. 6.5 also shows that for a poor conductor the imaginary component will increase if the frequency is increased while on an excellent conductor it will decrease if the frequency of the primary field is increased. This furnishes a simple rule to judge the quality of a conductor from dual frequency measurements. Other simple rules may be formulated from Fig. 6.5. Thus, a good conductor produces a large real but a small imaginary component while a bad conductor produces a relatively large imaginary but a small real component. If the conductor has a 'medium' resistivity both the components are moderately large. Quantitatively, the ratio of magnitudes 'real/imaginary' is often used, this being greater than one for good and less than one for bad conductors. Such rules of thumb are generally valid only on isolated conductors. If the fields of two or more conductors in the ground interact strongly with each other these rules may fail.

In Fig. 6.3 is shown a qualitative sketch of the horizontal and vertical secondary fields along a line above the single-turn loop, perpendicular to the

plane of the loop, on which is acting a homogeneous, horizontal oscillating field. The real and imaginary components of each of the two fields vary in these fashions along the line. The horizontal component directly above the loop is in the same direction as the instantaneous direction in which the primary field is increasing and is therefore reckoned positive. The vertical component, on the other hand, is (in this case) arbitrarily reckoned positive upwards. The secondary-field components show a variation along the profile which is similar to that of the respective components of the magnetic field on a plate magnetized perpendicular to its plane, as a comparison with the case for $i' = 0°$ and $\theta = 90°$ in Fig. 2.15(b) will show. A loop carrying a current I has, in fact, a magnetic moment equal to IA (A m^2) if A is its area, and the direction of the moment is that of the advance of a right-handed corkscrew placed at the loop's centre when the tips of the handle are turned in the direction of the current in the loop. At the epoch conceived in Fig. 6.3 the moment is instantaneously directed towards the left but it is, of course, oscillating with the same frequency as the primary field but is $\pi/2 + \phi$ in phase behind it, since this is the phase lag of the current in the loop, as we have already seen.

6.3 ELLIPTIC POLARIZATION

Let us now consider the total fields X and Y in the horizontal and vertical directions at any point in the vicinity of the loop in Fig. 6.3. These are easily seen to be

$$\begin{aligned} X &= B_0 \cos \omega t + s \cos(\omega t - \pi/2 - \phi) = C \cos \omega t + D \sin \omega t \\ Y &= s' \cos(\omega t - \pi/2 - \phi) = C' \cos \omega t + D' \sin \omega t \end{aligned} \tag{6.6}$$

where s, s' are the amplitudes of the horizontal and vertical components of the secondary field at that point.

Eliminating ωt from (6.6) we can obtain

$$(C'^2 + D'^2)X^2 + (C^2 + D^2)Y^2 - 2(CC' + DD')XY - (CD' - C'D)^2 = 0 \tag{6.7}$$

which is the general equation of an ellipse in an x, y coordinate system. This means that the resultant field at any point is elliptically polarized, the vector $R = \sqrt{(X^2 + Y^2)}$ describing an ellipse $\omega/2\pi$ times per second. In fact, the resultant field is, in general, always elliptically polarized irrespective of the nature of the primary field or the number or nature of the secondary circuits.

The plane of the ellipse of polarization is manifest in practice from the circumstance that no signal is induced in a receiver coil held with its plane parallel, that is with its axis perpendicular, to the plane of the ellipse at the observation point. The receivers in many modern electromagnetic prospecting systems are solenoids rather than plane coils. A solenoid has to be held perpendicular to the ellipse of polarization to have no signal induced in it.

The angle that the plane of the ellipse of polarization makes with the

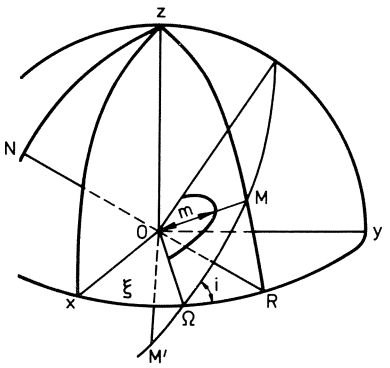

Fig. 6.6 Dip, tilt and azimuth of the polarization ellipse.

horizontal is the *dip* of the field while the angle that the major axis makes with the horizontal is the *tilt* of the field. That these two angles are distinct is easily appreciated if we take the case of a vertical primary field. Then, whatever the angle made by the secondary field with the horizontal the plane of the ellipse will be vertical, that is the dip will be 90°. However, the angle between the major axis of the ellipse and the horizontal need not (in fact, will not) be 90°. Finally, the *azimuth* of the resultant field is the angle between a specified direction (for example, the north) and the line of intersection of the plane of the ellipse with the horizontal.

The concepts of the dip, tilt and azimuth of a rotating field when the plane of polarization is arbitrarily oriented are illustrated in Fig. 6.6. The great circle $M\Omega M'$ of the sphere with centre O represents the plane of the ellipse. The ellipse, or rather a part of it, is drawn in this plane by a thick line and its semi-major axis is marked by *m*. $xOyR$ is the horizontal plane so that the dip is the angle marked *i*. ON is a line perpendicular to the ellipse plane so that the angle NOz between it and the vertical is also *i*. If Ox is a reference direction, the angle $xO\Omega$ is the azimuth. zMR represents the vertical plane through the major axis cutting the horizontal plane along the line RO so that angle MOR is the tilt of the major axis. The angle $ZOM (= 90° - \text{tilt})$ may be called the co-tilt. (Sometimes the two terms tilt and co-tilt are interchanged.) The angle xOR is the azimuth of the major axis. Note that the azimuth of the plane of the ellipse and the azimuth of the major axis of the ellipse are two different angles, in general.

All the above angles and the sizes of the major and minor axes of the ellipse of polarization can be determined if the primary-field components $(P_x, P_y, P_z)\cos\omega t$ and the secondary-field ones $(S_x, S_y, S_z)\cos(\omega t + \psi)$ are known. Alternatively they can be measured directly. However, such complete determinations are rarely undertaken in practice. In most methods using polarization, only the tilt is measured.

6.4 FREE-SPACE MAGNETIC FIELDS OF LOW-FREQUENCY SOURCES

6.4.1 Biot–Savart law

The primary field of an electromagnetic source is the field in free space (vacuum) or, for practical purposes, in air provided any influence of the ground can be neglected. The free-space field must be removed from the resultant electromagnetic field to obtain the secondary field of subsurface conductors. It can be calculated by applying the Biot–Savart law to the source circuit. This law states that a current element of length dl carrying a current I creates at any point P in free space a magnetic flux density given by

$$dB = \frac{\mu_0 I\, dl}{4\pi r^2} \sin\theta \quad (\mathrm{Wb\,m^{-2}}) \tag{6.8}$$

where r is the distance between P and the element, while θ is the angle between the element and the line joining it to P and $\mu_0 = 4\pi \times 10^{-7}\ \Omega\,\mathrm{s\,m^{-1}}$. The field is perpendicular to the plane contained by dl and the joining line, and its direction is given by the corkscrew rule of Section 6.2.1. The Biot–Savart law is, strictly speaking, only true for steady currents but it may be applied to time-dependent currents provided they are varying slowly. In the following we shall assume sinusoidally varying fields of low frequency and consider three of the commonly employed sources in electromagnetic prospecting.

6.4.2 Horizontal cable on the ground (Fig. 6.7(a))

If the cable is carrying a current $I_0 \cos\omega t$, the field at a point on the same level as the cable is vertical and equal to

$$P_0 \cos\omega t = \frac{\mu_0 I_0 \cos\omega t}{4\pi r}(\cos\beta_1 + \cos\beta_2) \quad \mathrm{Wb\,m^{-2}}$$

$$= \frac{100 I_0 \cos\omega t}{r}(\cos\beta_1 + \cos\beta_2)\ \mathrm{nT} \tag{6.9}$$

where β_1, β_2 are the angles shown in the figure. The formula is easily obtained from (6.8) by appropriate integration.

If the cable is infinitely long $\beta_1 = 0, \beta_2 = 0$ so that

$$P_0 \cos\omega t = \frac{200 I_0 \cos\omega t}{r} \quad \mathrm{nT} \tag{6.10}$$

at a distance r from the cable. In a vertical plane perpendicular to the cable the field lines are circles with the 'cable' as the centre (Fig. 6.7(b)).

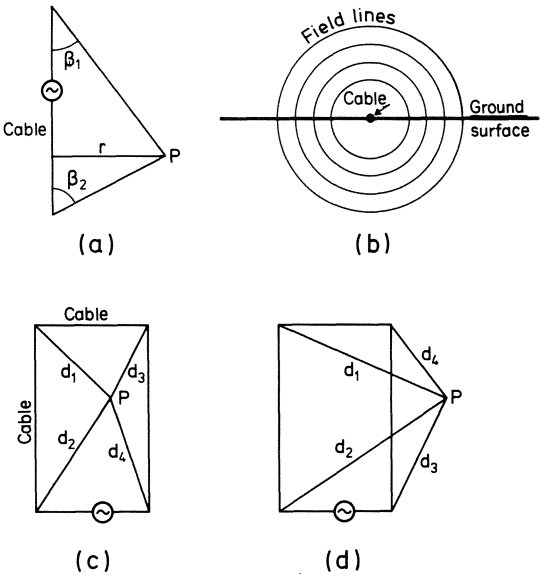

Fig. 6.7(a) Long cable as source; (b) Free-space magnetic field of a long cable; (c) Point inside rectangular loop-source; (d) Point outside rectangular loop-source.

6.4.3 Horizontal rectangular loop (Fig. 6.7(c))

The field at a point on the same level as the loop is vertical and given by

$$P_0 \cos \omega t = 100 I_0 \cos \omega t \left(\frac{d_1}{A_1} + \frac{d_2}{A_2} + \frac{d_3}{A_3} + \frac{d_4}{A_4} \right) \quad \text{nT} \qquad (6.11)$$

where the A's are the areas of the rectangles having the respective d's as diagonals. If P is outside the loop (Fig. 6.7(d)) the last two terms in the bracket have a minus sign before them. Equation (6.11) is obtained very easily by applying (6.9) to each side of the rectangle and using the elementary formula for the area of a rectangle.

6.4.4 Field of a current dipole

This is the field of small circular coil or short solenoid at distances greater than a few times its dimensions. At any point P (Fig. 6.8) the field is entirely in the plane contained by the direction of the dipole, that is, the axis of the coil or the solenoid, and the line joining the dipole centre to P. It can be resolved into a component $B_{\parallel}$, parallel to the instantaneous dipole direction, and a component $B_{\perp}$, perpendicular to the dipole and directed away from it. These

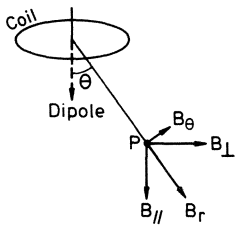

Fig. 6.8 Current-carrying coil as dipole.

components are given by

$$B_{\parallel} = \frac{\mu_0 m_0 \cos \omega t}{4\pi r^3}(3\cos^2\theta - 1) \qquad \text{Wb m}^{-2} \tag{6.12a}$$

$$B_{\perp} = \frac{\mu_0 m_0 \cos \omega t}{4\pi r^3} 3\sin\theta\cos\theta \qquad \text{Wb m}^{-2} \tag{6.12b}$$

where $m_0 \cos \omega t$ is the instantaneous magnetic moment (A m^2) of the dipole (= area of coil × instantaneous current $I_0 \cos \omega t$). These equations are algebraically the same as those for the field of a magnetic dipole particle (Appendix A2.3) but, strictly speaking, they need to be proved from the law of Biot and Savart. As this proof is somewhat lengthy it will be omitted here.

Since the dipole field is of considerable importance in practice we shall look a little more closely at it. Its lines of force are shown in Fig. 6.9 for a vertically oriented dipole. The entire diagram can be rotated through 90° to obtain the picture for a horizontally oriented dipole or through any other angle to obtain the picture with the dipole oriented in a desired direction.

It is easily seen from Eq. (6.12b) that along the dipole axis, that is for $\theta = 0$ or 180°, there is no field perpendicular to the dipole. There is also no such field along a line at right angles to the dipole and through its centre ($\theta = \pm \pi/2$). Along this line the field is antiparallel to the dipole and is half as strong as the field at the same distance along the dipole axis. Finally, at points for which $\cos^2\theta = \frac{1}{3}$, that is $\tan^2\theta = 2$, we have $B_{\parallel} = 0$ and the field is exactly perpendicular to the dipole. This is the case in Fig. 6.9 for points lying on the dotted lines making angles $\tan^{-1}\sqrt{2} = 54.7°$ with the dipole.

Instead of the fields parallel and perpendicular to a dipole it is often necessary to know the field B_r at any point in the direction of the radius vector from the dipole to the point and the field B_θ perpendicular to the radius vector (in the direction of increasing θ). These fields are:

$$B_r = \frac{\mu_0 m_0 \cos \omega t}{2\pi r^3}\cos\theta \qquad \text{Wb m}^{-2} \tag{6.13a}$$

$$B_\theta = \frac{\mu_0 m_0 \cos \omega t}{4\pi r^3}\sin\theta \qquad \text{Wb m}^{-2} \tag{6.13b}$$

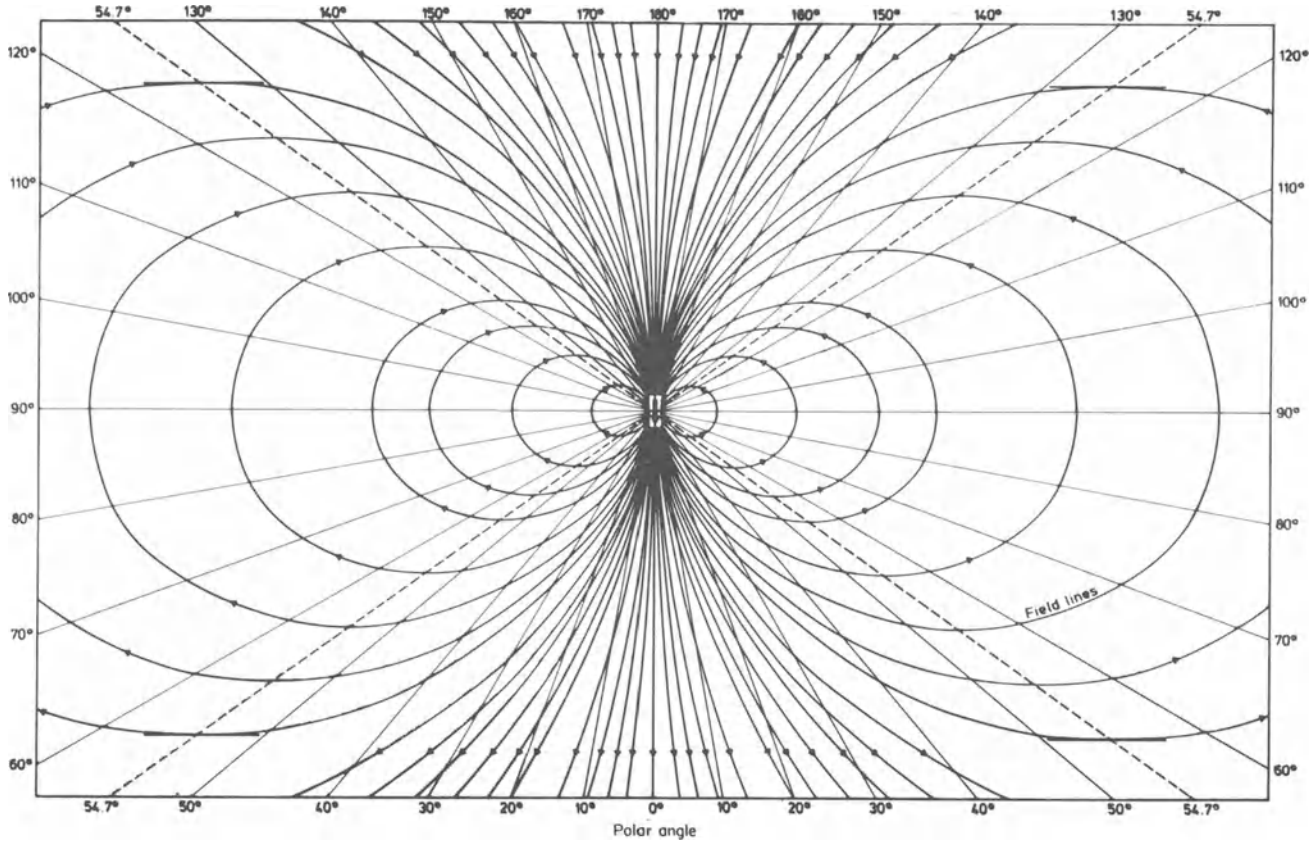

Fig. 6.9 Dipole field.

6.5 NEAR AND FAR FIELDS

Neumann's law and the law of Biot and Savart do not describe electromagnetic phenomena completely. For a complete description we must resort to Maxwell's equations (Appendix A11.2). It can be shown from these that if we have a time-dependent electric current instead of a steady one there is at every point in a medium not only a magnetic field but also an electric one, both varying with time.

Consider, for example, an oscillating magnetic dipole. We shall now find it convenient to express its magnetic moment as $m_0 \exp(-i\omega t) = m_0(\cos \omega t - i \sin \omega t)$ where $i = \sqrt{(-1)}$ rather than as $m_0 \cos \omega t$. If the dipole is situated in a homogeneous isotropic medium of resistivity ρ, dielectric constant ε and magnetic permeability μ, the fields B_r, B_θ are found from Maxwell's equations to be

$$B_r = \frac{\mu m_0}{2\pi r^3}(1 - ikr)e^{-i(\omega t - kr)} \cos \theta \tag{6.14a}$$

$$B_\theta = \frac{\mu m_0}{4\pi r^3}(1 - ikr - k^2r^2)e^{-i(\omega t - kr)} \sin \theta \tag{6.14b}$$

where

$$k = (\omega^2 \varepsilon \mu + i\omega\mu/\rho)^{1/2} = a + ib \quad \text{(say)} \tag{6.15}$$

The real and imaginary components, a and b, of k are calculated in Appendix A11.3 from which we find that

$$|k| = (a^2 + b^2)^{1/2} = \left(\frac{\mu\omega}{\rho}\right)^{1/2} (\rho^2 \varepsilon^2 \omega^2 + 1)^{1/4} \tag{6.16}$$

It can be seen from Eqs. (6.14) that at sufficiently small distances r from the dipole such that $|k|r \to 0$,

$$B_r \approx \frac{\mu m_0}{2\pi r^3} e^{-i\omega t} \cos \theta \tag{6.17a}$$

$$B_\theta \approx \frac{\mu m_0}{4\pi r^3} e^{-i\omega t} \sin \theta \tag{6.17b}$$

These expressions can be derived by means of the Biot–Savart law for the field of a magnetic dipole in a medium of permeability μ. The real components of (6.17a) and (6.17b) are identical to (6.13a) and (6.13b) respectively if $\mu = \mu_0$. Thus, for a given medium and a given frequency there is a region ($|k|r \approx 0$) in the vicinity of the dipole where we can, with reasonable accuracy, express the magnetic field by Eqs (6.17). This is the so-called *near field or induction region* in which the field amplitude varies as $1/r^3$ and the field is in phase with the dipole.

For very large distances ($|k|r \to \infty$) we find from Eqs (6.14) that B_r decreases

as $1/r^2$ and B_θ as $1/r$ so that when r is sufficiently large the total field is simply B_θ. Thus, in this so-called *far-field or radiation region* the field of the dipole varies as the inverse distance from it, that is, much more slowly than in the near-field region. The field structure is more complicated in the *intermediate* region. In particular, the field is elliptically polarized in this region, whereas in the near and far regions it is linearly polarized, that is, at any point the field vector oscillates along a straight line. There are, of course, no sharp boundaries between the various regions but a practical limit for the extent of the near-field region may be defined by $|k|r \leqslant 0.1$.

For practically all rocks, with a few notable exceptions such as waterlogged soils, wet clays etc., ε is of the order of 90 picofarad per metre. If, now, $v\rho \lesssim 10^8\,\Omega\,\mathrm{m\,s^{-1}}$ then $\rho\varepsilon\omega = 2\pi\rho\varepsilon v \ll 1$ can be neglected in Eq. (6.16), while for μ we may put $\mu_0 = 4\pi \times 10^{-7}\,\Omega\,\mathrm{s\,m^{-1}}$ (cf. Table 1). Under these conditions the near-field region is seen, for practical purposes, to be defined by $r \leqslant 35.6(\rho/v)^{1/2}$ m. For frequencies commonly employed in geophysical work (maximum about 20 kHz) the condition $v\rho < 10^8\,\Omega\,\mathrm{m\,s^{-1}}$ is satisfied with a good margin in many, if not most, areas. If, however, ρ, is very large so that $\rho\varepsilon\omega \gg 1$, or is actually infinite as for free space, the near-field region, defined as $|k|r \leqslant 0.1$, is easily shown, using the free-space value $8.854\,\mathrm{pF\,m^{-1}}$ for ε, to be given by $r \leqslant (5000/v)$ km.

It should be realized that the definition $|k|r \leqslant 0.1$ used above for the near-field region is arbitrary. Many authors consider the intermediate zone to begin at $|k|r \approx 1$ and with this convention the near-field zone will extend to 10 times the distances obtained above.

The importance of distinguishing the near- and far-field zones is that in the interpretation of electromagnetic measurements in the near-field zone it is mostly sufficient to use Neumann's law while for the interpretation of measurements in the far zone it is often necessary to take account of phenomena like the refraction and reflection of electromagnetic waves.

6.6 CLASSIFICATION OF ARTIFICIAL SOURCE, CONTINUOUS WAVE METHODS

The continuous wave (CW) electromagnetic methods using artificial – also called controlled – sources may be divided fundamentally into near-field and far-field methods. The former operate typically at relatively low frequencies (*c.* 100 Hz–*c.* 400 Hz) and with source–receiver separations of the order of a few tens to a few hundreds of metres, while the latter use frequencies higher than *c.* 10 kHz and source–receiver separations of several kilometres to thousands of kilometres. It must be remembered, however, that what is a near-field operation in one area may, on the same frequency, be a far-field operation in another, more conductive, area and conversely. Since the CW methods use sinusoidally varying fields they are also called harmonic-field methods.

The principal CW methods will be discussed briefly below. Nearly all of them can be used on the surface, in boreholes, under water or in the air, although the technical details of instrumentation and the logistics of operation will naturally differ in each situation.

6.7 NEAR-FIELD CW METHODS

6.7.1 Tilt-angle methods

These techniques are also known as dip-angle techniques but as we have made a distinction between dip and tilt (Section 6.3) they will be called tilt-angle methods here. Generally the tilt of the magnetic field vector is measured in the vertical plane through the line of measurement and not in the plane of the polarization ellipse. Thus the tilt measured is that of the projection of the major axis of the ellipse on the measurement plane. Unless the azimuth and the dip of the polarization plane deviate considerably from that of the vertical plane through the line of measurement the measured tilt differs little from the true tilt, but this potential source of deviation should be kept in mind.

Tilt angles can be measured with an accuracy of about 0.5°–1° and somewhat better if the transmitter and receiver are supported on tripods.

6.7.1.1 Broadside technique

In this case the transmitter dipole (T) and receiver dipole (R), which may be plane coils or solenoids, are moved simultaneously along separate, parallel lines perpendicular to the geological strike. T is held with its axis horizontal in the line direction and therefore at right angles to the T–R line. In the absence of conductors the field at the receiver, being the primary field only, will be horizontal and along the line on which R is moved. Normally, there will be no signal in R if it is held with its axis vertical.

If conductors are present their secondary field will cause the resultant field

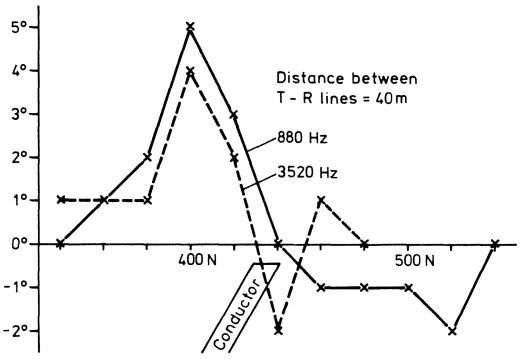

Fig. 6.10 Tilt-angle profile with a broadside system.

vector to tilt out of the horizontal in general, and then R must be turned around the T–R line as axis to make the signal in it minimum. The tilt of the field for certain geometries of conductors will be in opposite directions on the two sides of a sheet conductor when the coil system traverses it, so that the tilt profile shows an inflection (commonly called 'cross-over') directly above the conductor as Fig. 6.10 illustrates.

6.7.1.2 Shoot-back technique

Another tilt-angle technique ('in-line') in which T and R, instead of being on separate lines as above, are on the same line, one behind the other, suffers from the fact that it gives 'false' tilt angles if there is a height difference between T and R, in contrast to the above broadside technique in which the normal field at the receiver position is always horizontal. A version of the in-line method, devised by J.D. Crone, eliminates the effect of topography and is useful in reconnaissance surveys. The procedure is as follows.

The coils are constructed so that either can be used as a transmitter or a receiver. The axis of coil 1 is directed towards 2, but downwards at an angle of 15° to the horizontal. Coil 1 transmits on the selected frequency and coil 2, acting as a receiver, is turned (for minimum signal) around a horizontal axis perpendicular to the line 1–2. The tilt α_1 of the field is noted. Thereafter coil 2 transmits but with the axis pointing 15° upwards. The tilt α_2 of the field is measured at coil 1, now acting as a receiver. In the absence of conductors α_1 and α_2 are very nearly equal regardless of the elevation difference between the coils so that any difference $\alpha_1 - \alpha_2$ is taken as a measure of the anomaly due to a sub-surface conductor.

6.7.1.3 Other variations

Variations of the tilt-angle technique using artificial sources include the use of fixed large loops or grounded cables, instead of dipole transmitters, as sources. In one version a large transmitter loop is set up in the vertical plane and the receiver is moved along a line of measurement that is relatively distant from the transmitter. The axis of the transmitter is directed towards successive receiver positions while the tilt is measured. When a large loop or a long cable is laid on the ground the normal orientation of the receiver dipole axis for no signal will be horizontal as the normal field at it is vertical. The tilt (or the co-tilt, if we prefer to call it so) of the field from the vertical shows a maximum above a steep conductor, since the secondary horizontal field is strongest here, and not a cross-over as when the normal field is a horizontal one.

6.7.2 Fixed source systems

6.7.2.1 The compensator or Sundberg method

(*a*) *Layout and field procedure.* The primary layout in this method that was introduced by Sundberg [97] consists of a straight cable, some 400 to 4000 (or

more) metres long, grounded at both ends, through which an alternating current of low frequency (< 1000 Hz) is passed. A large horizontal loop, usually rectangular, may also be laid on the ground instead of the cable. The cable (or the long side of the primary loop) is generally placed approximately parallel to the geological strike in the area and the electromagnetic field is investigated at regular intervals along lines perpendicular to the strike. In the case of the loop, observations can be made inside as well as outside the loop.

For many, if not most, purposes it would be sufficient to measure the amplitude and phase of either the vertical or the horizontal component of the resultant field, but measurements of both may be called for in detailed work. A search coil consisting of several turns of copper wire on a suitable frame is held horizontally (to measure the vertical component) or vertically (to measure the horizontal component) and the voltage induced in it is compared with a reference voltage. The latter is obtained from an auxiliary ('feeding') coil stationed near the primary layout. A method has also been tried in which the reference voltage is instead transmitted by a UHF carrier-wave modulated at the frequency of the primary current.

The comparison of voltages is made on a compensator, essentially an a.c. potentiometer, in which the inclusion of a reactive element enables one to determine phase differences. A simple circuit of this type is shown in Fig. 6.11. The real component is balanced by the voltage across the resistor R and the imaginary one by that across the variometer I, the balance being indicated by a zero signal in the detector. For a discussion of other types of compensators see [96]. The real and imaginary signals in the receiver can be expressed after calibration as nanotesla per ampere primary current. In earlier papers, the field has been expressed as microgauss per ampere. It should be noted that $1\ \mu G = 0.1$ nT. The phase of the received field with respect to the primary field is given by $\tan^{-1}$ (imag./real). However, circuits can be devised that give a phase reading directly.

The normal primary field of the layout must be subtracted from the observed real component. The imaginary component needs no correction. These considerations are valid provided the field is linearly polarized. However, it is evident from Section 6.5 that at appreciable distances from the

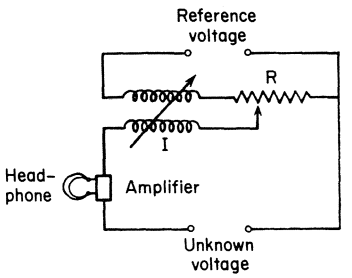

Fig. 6.11 Compensator circuit in principle.

layout the field may be elliptically polarized and a simple correction for the normal field may not be sufficient.

Assuming, however, that we are in the near-field zone the measured vertical field (amplitude V_0) in the receiver can be written as

$$V_0 \cos(\omega t + \alpha) = KI_0 \cos \omega t + S_{v0} \cos(\omega t + \psi) \tag{6.18}$$

where K is the relevant geometrical factor (cf. Eqs (6.10) and (6.11)) depending on the source and S_{v0} is the amplitude of the vertical secondary field. The real and imaginary components of the secondary field are then seen to be

$$S_{v0} \cos \psi = V_0 \cos \alpha - KI_0 \tag{6.19a}$$

$$S_{v0} \sin \psi = V_0 \sin \alpha \tag{6.19b}$$

Dividing by I_0 we get the components per ampere of primary current amplitude.

Real component
$$\frac{S_{v0}}{I_0} \cos \psi = \frac{V_0}{I_0} \cos \alpha - K \quad \text{nT A}^{-1} \tag{6.20a}$$

Imaginary component
$$\frac{S_{v0}}{I_0} \sin \psi = \frac{V_0}{I_0} \sin \alpha \quad \text{nT A}^{-1} \tag{6.20b}$$

The division V_0/I_0 can be made automatically in the instrument. This way of expressing the field components obviates the need to hold the primary current amplitude constant and simplifies the instrument design and field operation.

(*b*) *Topographic corrections.* The real component of the secondary field obtained from (6.19a) or (6.20a) will be erroneous if K does not correspond to its nominal value in Eqs (6.10) and (6.11) as may happen when the cable (or loop) and the receiver are not on the same horizontal level. The imaginary component is obviously not affected as it does not involve K. The correction to the vertical-field real component for any difference in height is easily calculated. Referring to Fig. 6.12 we see that the primary vertical field in the receiver is

$$\begin{aligned} &\frac{200I_0}{r} \cos \theta \quad \text{nT} \\ &= \frac{200I_0}{r} \left(1 - \frac{h^2}{r^2}\right)^{1/2} \\ &\approx \frac{200I_0}{r} \left(1 - \frac{h^2}{2r^2}\right) \qquad \text{if } h \ll r \end{aligned} \tag{6.21}$$

$(1 - h^2/2r^2)$ is thus the correction factor to K due to the difference in level between the cable and the receiver.

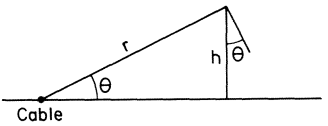

Fig. 6.12 Topographic effect in the Sundberg method.

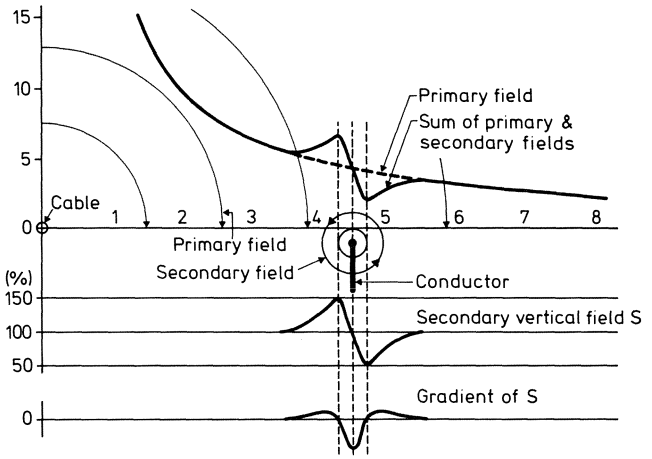

Fig. 6.13 Origin of anomaly in the Sundberg method.

There is no horizontal component if the cable and the receiver are on the same level. Any non-zero horizontal component indicates an anomaly but a 'false' anomaly of 200 $I_0(h/r^2)$ will be obtained in the horizontal real component in case of a height difference but the horizontal imaginary component will still be zero.

The relative insensitivity of the imaginary component to changes in the primary field will be easily appreciated from the above. It is common to all electromagnetic methods.

(*c*) *Interpretation.* Coming now to the interpretation of the data of the Sundberg method the general shape of the secondary vertical field profile across a steeply dipping sheet conductor in a non-conducting or a poorly conducting environment should be evident from a study of Fig. 6.13. If the conductor is very long and relatively thin the secondary field conforms fairly well to that of a long current concentration along the top edge of the sheet both in the vertical and the horizontal component. The latter will show a maximum above the edge instead of the cross-over shown by the vertical field. In general, however, the main features of the secondary field are more correctly visualized

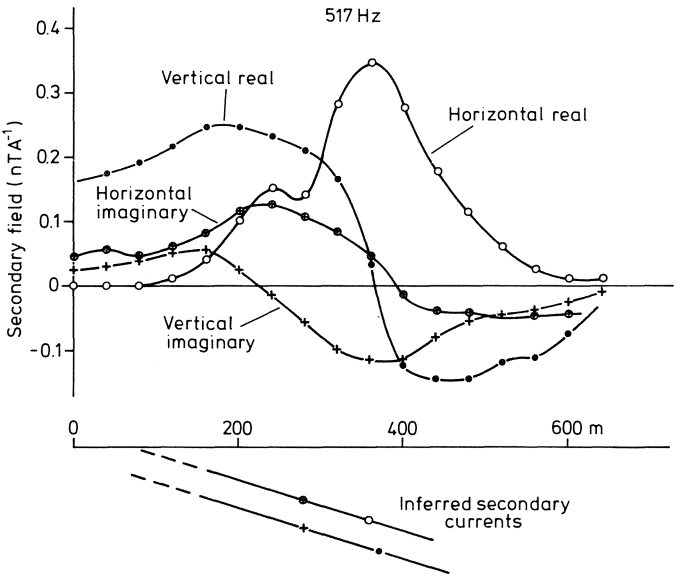

Fig. 6.14 Example of Sundberg-method measurements.

by replacing the secondary current distribution by a magnetized sheet with a magnetization at an appropriate angle to the plane of the sheet. Conversely, if the measured vertical or horizontal secondary field curve is compared with one of the corresponding magnetic field curves in Figs 2.15(a) and 2.15(b), the closest resembling curve and the sketch of the sheet below it will give a reasonably good idea of the position and dip of the conducting sheet.

Fig. 6.14 is an example of a profile with the Sundberg method showing the real and imaginary components in the vertical as well as the horizontal secondary field across a very good conductor.

6.7.2.2 The Turam method

The compensator method requires a direct connection between the primary layout and the observation point and therefore becomes cumbersome when large areas are to be covered. This operational disadvantage is overcome in the Turam method devised by Hedström [98].

The primary field is produced as before by a long cable or a large loop, and two search coils, 10–50 m apart, are carried along the line of measurements. For each position of the coils the ratio of the amplitudes of and the phase difference between the voltages induced in them are measured on a bridge-type compensator, the former with an accuracy of about 0.005, the latter about 0.02°.

The coils are usually held horizontally (so as to compare the vertical components of the resultant field) but one may sometimes be kept vertical and the other horizontal, to measure the horizontal field in the former. We shall restrict the discussion to the case of two horizontal coils.

The quantities measured in Turam work are $V_1/V_2, V_2/V_3, \ldots$, etc. and $\alpha_2 - \alpha_1, \alpha_3 - \alpha_2, \ldots$, etc. where the V's are the amplitudes, and α's the phases of the vertical electromagnetic field at the stations $1, 2, 3, \ldots$. To correct for the variation of the primary field (p) with the distance from the source the measured ratios are divided by the normal amplitude ratios $p_1/p_2, p_2/p_3, \ldots$, etc. This is particularly easy in the case of the long cable since the normal ratio of the vertical fields at any two points is simply the inverse ratio of the distances of the points from the cable, unless one or both of the coils are on a level different from the cable, when an easily calculable correction must be applied.

The normalized or reduced ratios $V_1p_2/V_2p_1, V_2p_3/V_3p_2, \ldots$, etc. will all be equal to unity in the absence of sub-surface conductors.

The normal phase differences are, of course, zero provided the ground is non-conducting. This statement is not strictly true because the phase of an electromagnetic field varies by 2π over a distance of one wavelength. However, the air-wavelength of the low frequency primary field used in geoelectric work is of the order of several hundred kilometres. This is very long compared with the distance from the cable of a kilometre or so, up to which the measurements can usually be made so that the normal phase changes, although not strictly zero, are quite negligible.

On conductive ground, however, the phase may change appreciably within relatively short distances. Moreover, the field will be elliptically polarized, the inclination of the ellipse becoming more and more horizontal away from the cable. In accurate and detailed work these effects must be taken into account in order to correct as far as possible for the conductivity of the country rock and the overburden [99, 100, 101]. It is evident that deviations of the reduced ratio from unity and the phase difference from zero indicate anomalous sub-surface conditions.

Now, whereas it is obvious that if c is the constant separation between the receivers, $(\alpha_2 - \alpha_1)/c$ is a measure of the horizontal gradient of the phase of the resultant field, the significance of the reduced ratio (RR) needs to be considered further.

If V, p are the amplitudes of the resultant vertical and primary vertical fields at a point, those at a neighbouring point a small distance c further away from the source can be written as $V + \mathrm{d}V, p + \mathrm{d}p$. Then

$$\mathrm{RR} = \frac{V(p + \mathrm{d}p)}{(V + \mathrm{d}V)p}$$

$$= \frac{1 + \mathrm{d}p/p}{1 + \mathrm{d}V/V} \qquad (6.22)$$

Neglecting second-order small quantities Eq. (6.22) can be written as

$$\begin{aligned} \mathrm{RR} &= \left(1+\frac{\mathrm{d}p}{p}\right)\left(1-\frac{\mathrm{d}V}{V}\right) \\ &= 1+\frac{\mathrm{d}p}{p}-\frac{\mathrm{d}V}{V} \\ &= 1-\mathrm{d}\left[\ln\left(V/p\right)\right] \\ &= 1-c\frac{\mathrm{d}}{\mathrm{d}x}\left(\ln\frac{V}{p}\right) \end{aligned} \tag{6.23}$$

Thus the departures of the reduced ratio from unity are a measure of the negative horizontal gradient of the vertical field amplitude expressed in terms of the local primary field.

Typical vertical field indications obtained along three parallel Turam profiles across a sheet-like conductor are shown in Fig. 6.15. The conductor in question is a large pyrite ore body in an environment of porphyry rocks. It dips about 68° NE and the depth to its top surface is 14 m [102]. The frequency of the primary field was 540 Hz in this work and the source was at 400NE. The marked asymmetry in the curves is probably due to the dip of the conductor.

It is worth remembering that in the case where a sheet-like conductor has an attitude parallel to the primary field-lines at it, there will be no ratio and phase-difference anomalies above the conductor. Moreover, the signs of either

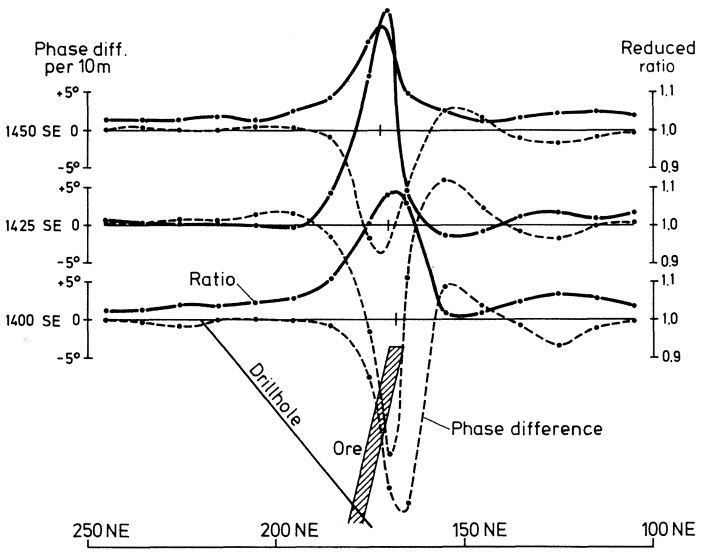

Fig. 6.15 Turam ratio and phase difference anomalies.

indication will be reversed if the dip towards the source is shallower than this value, presuming throughout that the surrounding rocks are non-conducting.

It will be noticed that the ratio and phase difference curves show extremum values directly above the conductor and that they resemble the negative x derivative of the curve for the vertical field in Fig. 6.13.

6.7.3 Moving source and receiver systems (tandem outfits)

(*a*) *Basic configurations and field procedure.* The layout of this method is shown in Fig. 6.16. A battery-operated portable oscillator (1–2 W) delivers an alternating voltage to a transmitter coil or solenoid. The receiver is spaced at a fixed distance from the transmitter, usually between 25 and 100 m, and is connected to a compensator which is also fed by the reference voltage from the transmitter. The layout is, in principle, the same as that in the Sundberg method except that the transmitter is now movable. Commercial outfits go under various names like Slingram, MaxMin, EM-Gun, Demigun, HEM etc. but they are basically all alike.

The field acting on the receiver is measured in per cent of the primary field present at it when the system is in free space. Exactly corresponding to Eq. (6.18) for the Sundberg system we can write (using R_0 for the amplitude of the field picked up by the receiver)

$$R_0 \cos(\omega t + \alpha) = P_0 \cos \omega t + S_0 \cos(\omega t + \psi) \tag{6.24}$$

where $P_0 \cos \omega t$ is the appropriate free-space field (Eq. (6.12) and Fig. 6.17) at the selected nominal distance from the transmitter. The real and imaginary components of the resultant field are then $P_0 + S_0 \cos \psi$ and $S_0 \sin \psi$ respectively. The instrument is calibrated to read $100[1 + (S_0/P_0) \cos \psi]$ in per cent units on the real component display and $100 (S_0/P_0) \sin \psi$ in per cent units on the imaginary component display. In some outfits the normal primary field at the receiver is 'bucked out' and the real component display reads the *anomaly* $100(S_0/P_0) \cos \psi$.

In principle, any mutual orientation of the transmitter and receiver may be

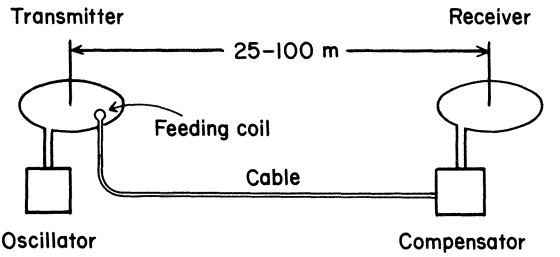

Fig. 6.16 Moving source–receiver system.

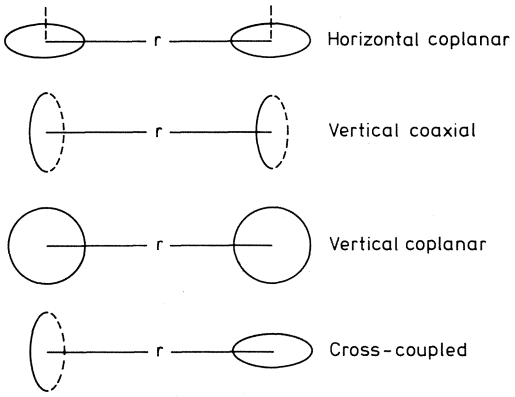

Fig. 6.17 Various moving source–receiver systems.

used but most surveys are carried out with both dipoles either horizontal or vertical. Four of the common arrangements are shown in Fig. 6.17. The transmitter–receiver layout is moved as a whole along their joining line and readings taken at suitable intervals. For horizontal coplanar coils and vertical coaxial coils the direction of movement is perpendicular to the geological strike to ensure that the primary field cuts any conductors since these generally follow the geology. Vertical coplanar coils should be moved along lines parallel to the strike in ground work as otherwise the reference cable will have to cut across trees, bushes, etc.

(*b*) *Corrections due to changes in primary field.* In Eq. (6.24) $P_0 \cos \omega t$ is the actual primary field at the receiver and if this changes because of, for example, a change in the coil separation, a false anomaly in the real component will be read even if S_0 is zero. Since the dipole primary field varies as $1/r^3$ a change of 1% in the nominal separation causes of 'false' anomaly of 3% to be read in the real component. This shows the necessity of maintaining the selected coil separation as constant as possible during a survey. No anomaly appears in the imaginary component due to an error in coil separation or in the nominal orientation if $S_0 = 0$ and even if $S_0 \neq 0$ the error in the imaginary component reading due to a 1% change in P_0 will be 1% of the reading itself in per cent units. As the imaginary component is thus relatively insensitive to changes in P_0 much more reliance can be placed on it in rough terrain. Although corrections to the real component readings due to a change in mutual separation, or orientation of the coils etc. can be calculated easily (Problem 6.2) it is preferable in rough terrain to sight the coils towards each other in such a way that their nominal orientation (e.g. coplanarity) is maintained, automatically eliminating the correction to a large extent.

(*c*) *Typical conductor responses.* The response of a conductor in free space or in a poorly conducting environment is easily visualized in a qualitative manner by elementary arguments.

Consider, for instance, a long, *thin* vertical plate below the plane of the transmitter and the receiver, both of which are horizontal, the plate being perpendicular to the transmitter–receiver line (Fig. 6.18). Suppose that at a particular instant the oscillating transmitting dipole is directed downwards so that the primary field cuts the plate as shown. The secondary currents in the plate will be into the plane of the figure at the top edge of the plate and out of it at the bottom. At any point R_1 on the same side of the plate as the transmitter the secondary field will be directed upwards, that is, in the same sense as the primary field at it. At a point such as R_2, however, the two fields will be in opposite directions and the resultant field will be less than the primary. Furthermore it is easy to see that if either the transmitter or the receiver is directly above the plate the field indicated by the compensator will be equal to the primary field.

Thus as the horizontal transmitter–receiver system with a fixed spacing is carried across the plate, the field picked up by the receiver will have the appearance as in Fig. 6.18(a). The maximum damping in the field (negative anomaly) is obtained when the midpoint of the system is directly above the plate.

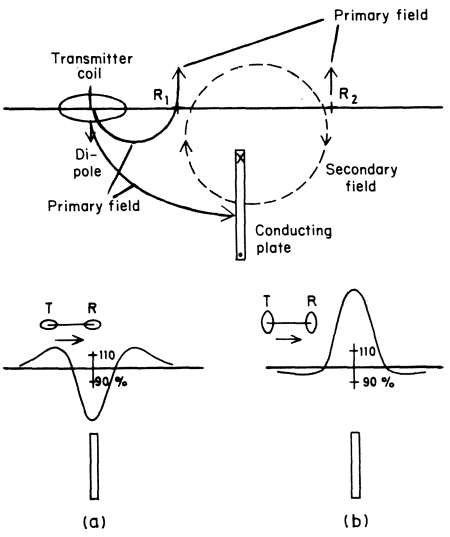

Fig. 6.18 Origin of the electromagnetic anomalies in the moving source–receiver system.

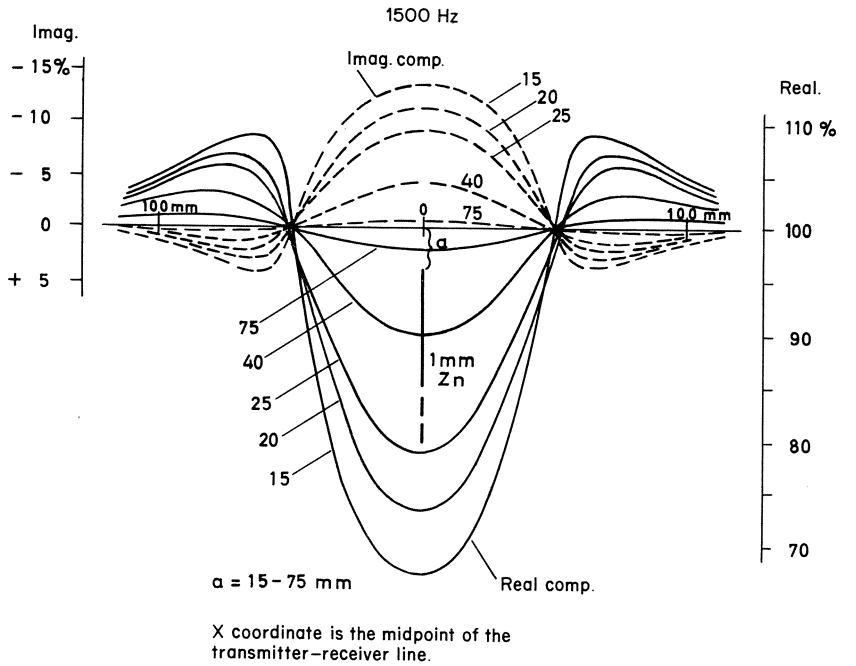

Fig. 6.19 Model electromagnetic experiments on a Zn conductor.

Similarly, it can be seen that if both coils are held vertically and are coaxial, the field will, under certain conditions, have the appearance as in Fig. 6.18(b), there being a maximum *augmentation* of the primary field (a positive anomaly) when the plate is midway between the transmitter and the receiver. However, the response to this coil configuration varies in a rather complicated manner with the depth to the top edge of the plate and is generally difficult to predict correctly from simple arguments alone.

In Fig. 6.19 are shown the results of some small-scale laboratory experiments on a 1 mm thick zinc plate at different depths below the plane of the coils, these being horizontal and 100 mm apart. Fig. 6.20 is a simplified vector diagram on which are plotted the maximum real and imaginary component anomalies measured above several vertical conducting plates at two different depths (20 and 40 mm) and with different values for the factor ρ/vd where ρ is the resistivity of the plate, d its thickness and v the frequency. It will be noticed that a single field observation suffices to determine the depth and ρ/vd for a *thin* plate and also that, for the same depth, the field of all plates with the same ρ/vd is practically identical. (The resistivities of the plates used are Cu 16.5, Al 29, Zn 60 and Pb 210 nΩm.)

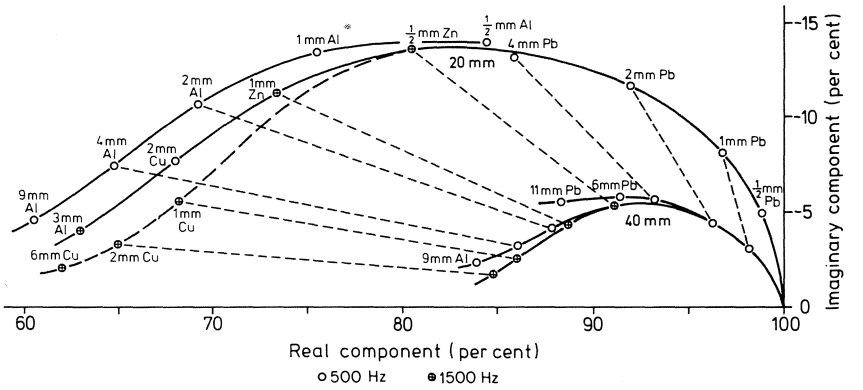

Fig. 6.20 Vector diagram for vertical conducting plates at two depths for the system in Fig. 6.18(a). The anomalies plotted are for the position when the system midpoint is directly above a plate. Coil distance = 100 mm. Note that the axis of the imaginary component is negative upwards.

Experiments show that if the factor ρ/vd is kept constant the thickness d must not exceed a certain value d_{max} if the field is to remain unchanged. This value depends upon ρ and v. For a given v, d_{max} is smaller the better the conductor and for a given ρ it is smaller the higher the v. The result of this limitation on d is that the vector curve for each depth splits up as shown. This makes it possible, within certain limits, to estimate ρ and d separately by appropriately varying the frequency [103].

Vector diagrams as in Fig. 6.20 are of great value in the quantitative interpretation of field surveys. Sets of them for different depths, conductor dips, lengths etc. have been published by Nair *et al.* [104]. The use of vector diagrams will be described in more detail in Section 6.9.3.

The response of *inclined* plates to the horizontal transmitter–receiver system is shown in Fig. 6.21. In all these cases there is a minimum in the imaginary component (the imaginary scale is negative upwards!) almost exactly above the top edge of the conductor. The minimum in the real component occurs at a point slightly towards the 'inside' of the plate. However, on a conductor poorer than that shown both minima are shifted towards the inside.

The real and imaginary responses *along the line of measurements* are plotted in Fig. 6.21(b) as vector diagrams. The figure furnishes an interesting comparsion of how of the secondary vector 'swings' in the various cases as the coils are brought towards the conductor from infinity. This is the vector drawn from the point 100, 0 in the figure to a point on the locus curve (cf. Fig. 6.3 noting that the imaginary scale in Fig. 6.21 is negative upwards). The origin of the vector diagram in 6.21, as that of the diagram in Fig. 6.20, is to the left, outside the figure.

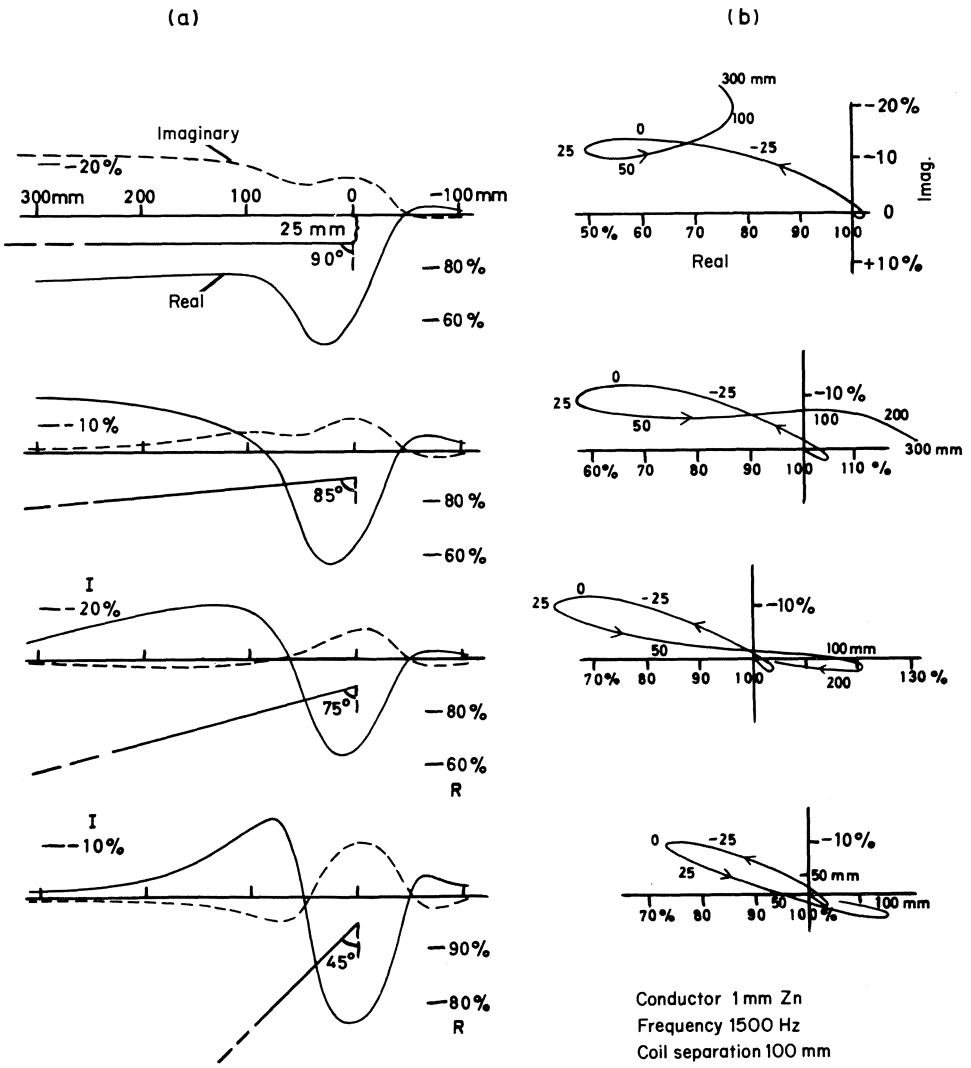

Fig. 6.21 Real and imaginary component anomalies with the system in Fig. 6.18(a) across thin dipping sheets of great lateral extents.

In Fig. 6.22 are reproduced the results of some field measurements on two thin sulphide conductors containing about 1% copper as chalcopyrite, $CuFeS_2$. The conductor has a gentle dip of 10° with the horizontal. The measurements were made at two different frequencies and two transmitter–receiver separations. The smaller coil separation maps more detail in the

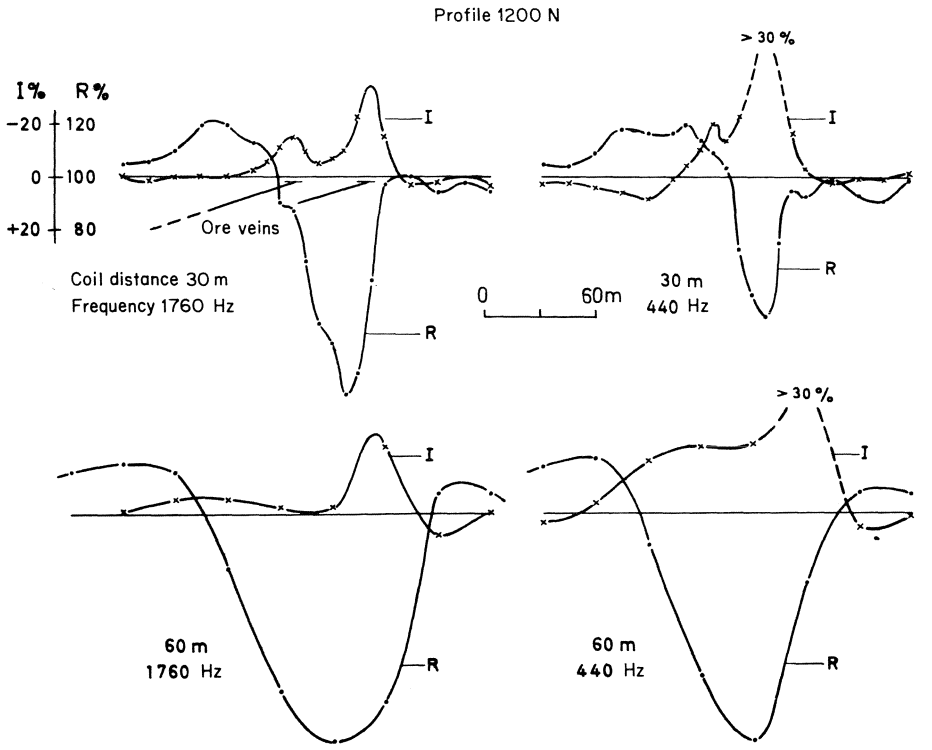

Fig. 6.22 Survey profiles with the moving source–receiver configuration in Fig. 6.18(a).

anomalies but the effect of near-surface conductivity variations is liable to be accentuated. At the same time, however, the use of a lower frequency emphasizes the relatively deeper conductivity variations. By a judicious application of such measurement techniques it is possible to derive considerable detailed information about the conductors evinced by the electromagnetic anomalies obtained with the moving source–receiver system [103]. It will be observed that the imaginary component anomaly increases when the frequency is reduced while the real component response is affected but little. From the discussion in Section 6.2.3 and from Fig. 6.4 (as well as Fig. 6.20) it will be evident that this indicates that the ore veins must be very good conductors. It should be noted that the anomaly profiles for 60 m separation resemble in shape the curves obtained in the model experiments in Fig. 6.21(a) on a plate dipping approximately 5° from the horizontal, indicating that the dip of the ore veins is fairly flat.

6.8 FAR-FIELD METHODS

6.8.1 VLF transmitters and the distant field in air

The electromagnetic methods thus far described operate essentially in the near-field region. The effects of the intermediate region may at times manifest themselves, as has already been hinted at in connection with fixed source systems, but the far-field region (Section 6.5) is almost never involved in these methods.

When an oscillating source radiates electromagnetic waves the far field dominates beyond a few wavelengths from the source. In the methods dealt with hitherto the source is generally not powerful enough for measurements at large distances. However, such measurements are possible in the field of strong sources and we now turn to these.

Powerful radio transmitters situated in different countries transmit unmodulated carrier waves, either continuously or with Morse code, for purposes of military communication, on frequencies in the band 15–25 KHz. Some examples are: NAA, Cutler, USA, 17.7 k Hz, 1 MW; GBR, Rugby, England, 16.0 kHz, 500 kW; ROR, Gorki, USSR, 17.0 kHz, 315 kW; NWC, North West Cape, Australia, 15.5 kHz, 1 MW. In radio technology these frequencies are known as very low frequencies (VLF), although it should be borne in mind that they are not low in the sense of the electromagnetic methods of applied geophysics, and the name is therefore improper in this connection.

The antenna of a VLF transmitter constitutes an oscillating *electric* dipole that sends out electric and magnetic fields. In the previous pages we have several times considered a vertical *magnetic* dipole and its magnetic, but not electric, field although it emits the latter type of field also. In the present case of the electric dipole we shall deal with both the fields. Also, we shall now refer to the magnetic field strength $H(\mathrm{A\,m^{-1}})$ instead of the flux density $B(=\mu H\,\mathrm{Wb\,m^{-2}})$ that we employed when dealing with the near-field methods.

The propagation of VLF waves from an electric dipole on the actual surface of the earth is a very complex phenomenon involving a ground wave, a space wave and a wave guided by the ionosphere and the earth's surface but it will be sufficient for our purpose to note that at large distances from the transmitter the field of a dipole may, for practical purposes, be considered to be uniform within a small area. The structure of the field at such a point is shown in Fig. 6.23 where the transmitter bearing (the propagation direction of the ground wave) is designated as the x direction. It will be seen that the incident magnetic field strength has only the horizontal component H_{iy} perpendicular to the transmitter bearing and that there is no vertical magnetic field. The incident electric field has a horizontal component E_{ix} in the direction of the

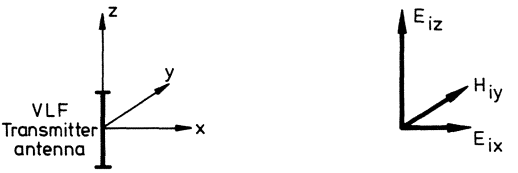

Fig. 6.23 VLF field at a distant point.

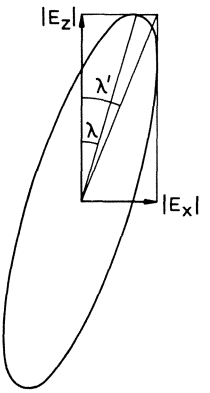

Fig. 6.24 Distinction between λ and λ'.

transmitter bearing and a vertical component E_{iz} but no component in the y direction.

It was shown by Norton [105] as far back as 1937 that on homogeneous, conductive ground E_{ix} leads E_{iz} in phase by 45° so that the vector **E** is elliptically polarized and further that, along the ground, at distances beyond about one wavelength from the antenna, the angle λ that the major axis of the ellipse makes with the vertical, and the ratio of the ellipse axes on such an earth, remain virtually constant at all points. Furthermore $E_z \gg E_x$. The exact expression for λ is complicated. Fortunately, since $\rho\varepsilon\nu \ll 1$ (p. 194) in geophysical applications, it can be simplified and then gives for the field in air at the surface:

$$\begin{aligned} \tan\lambda &= (\pi\rho\nu\varepsilon_0)^{1/2} \\ &= 0.527 \times 10^{-5}(\rho\nu)^{1/2} \end{aligned} \tag{6.25}$$

where

$$\varepsilon_0 = 8.854\,\text{pF m}^{-1}.$$

It will be seen that even if $\rho = 10\,\text{k}\Omega\,\text{m}$ and $\nu = 20\,\text{kHz}$, λ is barely 4.5°, so that the major axis is practically vertical. (The angle λ must not, of course, be confused with the angle λ' made by the resultant of the amplitudes of E_x and E_z with the vertical. The latter angle is given by (Fig. 6.24) $\tan\lambda' = (2\pi\rho\nu\varepsilon_0)^{1/2}$.)

6.8.2 VLF wave in the ground

Owing to the almost infinite conductivity of the ground compared with air, the VLF wave arriving at any point is refracted vertically downwards into the ground irrespective of its angle of incidence. In the wave transmitted into the ground the horizontal field E_{tx} *lags* 45° in phase behind the vertical field E_{tz} and, moreover, $E_{tx} \gg E_{tz}$. The electric vector $\mathbf{E}_t$ of the transmitted field is therefore also elliptically polarized but the major axis of the ellipse is now nearly horizontal. If its inclination with the *horizontal* is denoted by λ, the equation for it is again (6.25). The transmitted magnetic field has only the component H_{ty} in the y direction.

The electric and magnetic field strengths in the transmitted wave can be written as

$$E_{tx} = (\mu\rho\omega)^{1/2} H_{ty}(0) \exp(-bz) \cos(\omega t + \pi/4) \tag{6.26}$$

$$H_{ty} = H_{ty}(0) \exp(-bz) \cos \omega t \tag{6.27}$$

where z is the depth, $b = (\mu\omega/2\rho)^{1/2}$ and $H_{ty}(0)$ is the amplitude of the magnetic field strength at the surface. These equations show that the amplitudes of E_{tx} and H_{ty} decrease exponentially and that E_{tx} is ahead of H_{ty} in phase by $\pi/4$. Also, the ratio of the amplitudes of E_{tx} and H_{ty} is seen from (6.26) and (6.27) to be

$$\left|\frac{E_{tx}}{H_{ty}}\right| = (\mu\rho\omega)^{1/2} \tag{6.28}$$

6.8.3 Measurements with VLF station in strike direction

6.8.3.1 H-field anomaly

This case, in which a station is situated so that the VLF ground wave arrives in the geological strike direction in the area of measurement, is illustrated in Fig. 6.25. It is often referred to as 'E polarization' since the **E** vector lies in the vertical plane through the strike direction. The transmitted field H_{ty} induces currents in the sheet conductor shown in the figure but their secondary magnetic field H^s is not, in general, horizontal. Moreover as the fields H_{iy} and H^s are not in phase their resultant is polarized and describes an ellipse, changing in magnitude cyclically as it rotates.

At distant points on a profile like the one drawn in the figure, a solenoid held vertically will show no signal. In the vicinity of the conductor a signal is induced in it due to the secondary magnetic field. In most VLF measurements in practice the solenoid is now tilted in the vertical plane through the profile (the y–z plane) to make the signal a minimum. In this position the solenoid is perpendicular to the major axis of the ellipse and the residual signal in it is due to the field along the minor axis. The tilt of the solenoid axis from the vertical is

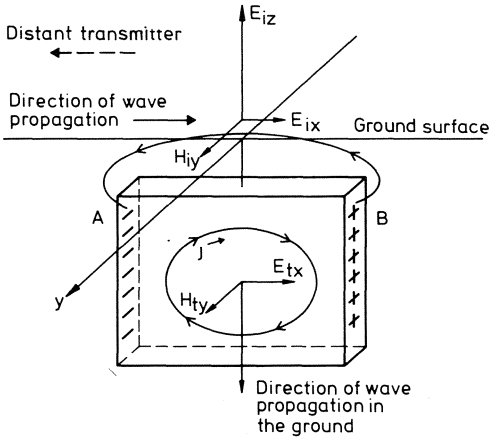

Fig. 6.25 Conductor striking parallel to the propagation direction of the VLF ground wave ('*E* polarization').

equal to the tilt of the major axis of the ellipse of polarization from the horizontal. The procedure assumes the ellipse to be in the vertical plane through the profile which, though not always justified, is very nearly the case for long conductors. The tilt is above the horizontal on one side of the conductor and below it on the other with a cross-over directly above the conductor where the tilt is zero.

A second solenoid at right angles to the first and with its axis in the same vertical plane will pick up the field corresponding to the major axis. A comparison of the signals in the two solenoids gives the ratio b/a of the minor axis field (b) to the major axis field (a). (In much geophysical VLF literature this has been improperly called the eccentricity which, by mathematical convention, is $(a^2 - b^2)^{1/2}/a$.)

The upper part of Fig. 6.26 shows a profile across two parallel sulphide conductors, each several kilometres long, in N. Sweden. Also shown for comparison are the anomalies with the moving source–receiver method (1600 Hz). A moment's reflection with reference to the lower part of the figure will convince that the tilt is such that at any measurement point, the solenoid axis in the minimum signal position, if produced downwards, will point towards the conductor! Further examples of H-field anomalies will be found elsewhere [106, 107].

If ΔV is the amplitude of the vertical component of H^s, θ is the tilt and ψ is the phase difference between H_{iy} and H^s, it can be shown (Appendix A11.4) that $\tan 2\theta \approx 2\Delta V \cos\psi / H_{iy}(0)$. Since usually $\Delta V \ll H_{iy}$ we may put $\tan 2\theta \approx 2\theta$ and hence $\theta \approx \Delta V \cos\psi / H_{iy}(0)$. Now $\Delta V \cos\psi$ is the real (or in-phase) component of ΔV. Hence $100 \times \theta$ (in radian), which is the quantity read

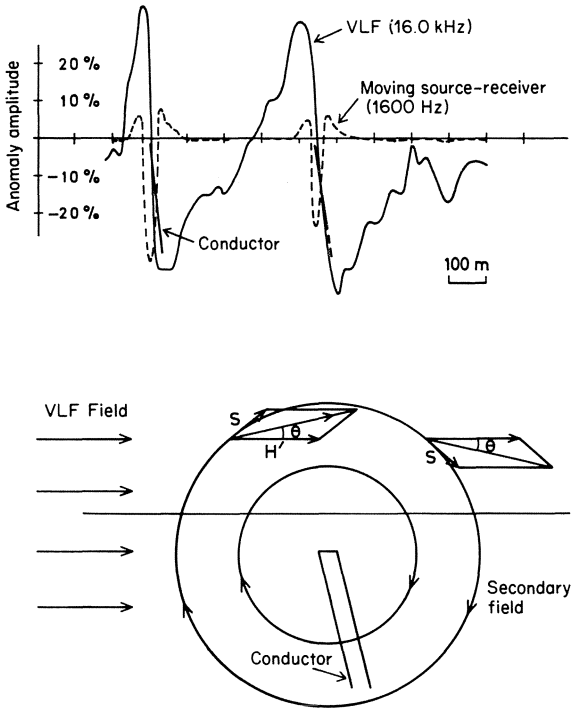

Fig. 6.26 Example of VLF tilt-angle anomaly.

on the instrument, measures the real component of the vertical secondary field in per cent of the primary VLF magnetic field strength.

The axes ratio b/a can be shown to be approximately $\Delta V \sin \psi / H_{iy}(0)$, that is, the imaginary (or quadrature) component of the secondary vertical field as a fraction of the primary field strength.

It has been assumed above that the incident field H_{iy} is exactly at right angles to the strike. Generally this is not the case in practice. If α is the angle between the strike and H_{iy}, the effective inducing field is $H'_{ty} = H_{ty} \sin \alpha < H_{ty}$. However, the strength of the induced currents and their secondary field is reduced in the same ratio, namely $\sin \alpha$, and to a very good first approximation neither the magnitude of θ nor the ratio b/a along a profile perpendicular to the strike is affected in practice.

6.8.3.2 E-field anomaly and apparent resistivity

The electric field in the ground is effectively only the horizontal field E_{tx}. On account of this field an (oscillating) electrical charge density is developed on the faces of the conductor marked A and B in Fig. 6.25 in contact with the host

rock. Its secondary electric field E^s is opposite to the incident field E_{ix} at all points along the profile and is, of course, especially strong directly above the conductor. If the electric field is measured at different points along the profile by means of an electric antenna (a wire) laid *perpendicular to the profile* it will be minimum above the conductor.

If should be realized in this connection that the horizontal fields E_x and H_y (but not the vertical field E_z) are continuous at the ground surface, that is, $E_{ix} = E_{tx}$ and $H_{iy} = H_{ty}$ at the surface. Hence, hereafter we shall suppress the subscripts i and t for fields measured by a wire antenna laid on the ground and by a solenoid held near the ground surface with its axis horizontal, and denote the fields by E_x and H_y.

In practice modern VLF instruments for prospecting do not measure the E_x field as such but the ratio E_x/H_y and the phase difference between E_x and H_y. The ratio has the dimension of 'ohm' and is called the wave impedance. From Eq. (6.28) we find (putting $\mu = \mu_0$) that

$$\rho = \frac{1}{2\pi\mu_0 \nu}\left|\frac{E_x}{H_y}\right|^2 (\Omega\,\mathrm{m}) \tag{6.29}$$

Thus the measurement of the amplitude ratio E_x/H_y will yield the resistivity of a homogeneous ground.

On non-homogeneous ground we may define an *apparent resistivity* ρ_a by Eq. (6.29). The dials of VLF instruments are calibrated to read ρ_a and the phase difference directly. The latter is, as Eqs (6.26) and (6.27) show, 45° on homogeneous ground and differs from this value on non-homogeneous ground.

If ρ_a according to Eq. (6.29) is measured along a profile across the conductor in Fig. 6.25 it will show a minimum above the conductor because the net E_x is reduced, as explained above.

Thus, when a VLF wave arrives in the strike direction, a geological sheet conductor gives an electric as well as a magnetic field anomaly.

6.8.4 Measurements with station-bearing perpendicular to strike

This case, illustrated in Fig. 6.27, is sometimes referred to as H polarization since the incident magnetic field vector lies in the vertical plane through the strike direction. It is evident that the transmitted magnetic field will not induce any currents in the plane of the conductor and there will be no secondary magnetic field along the measurement profile. The transmitted electric field E_{tx} (at the instant assumed) induces a positive charge density on the conductor's face abcd and a negative one on the face efgh. The secondary electric field due to these charges is opposite to E_{ix} above the conductor so that the conductor will be indicated by a minimum in the apparent resistivity calculated from Eq. (6.29). In contrast to the earlier case of E polarization the electrical

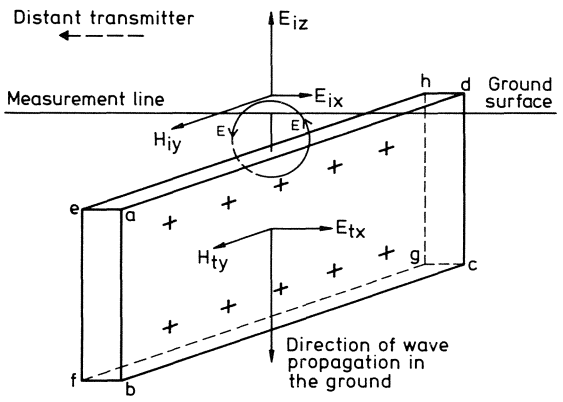

Fig. 6.27 Conductor striking perpendicular to the propagation direction of the VLF ground wave ('*H* polarization').

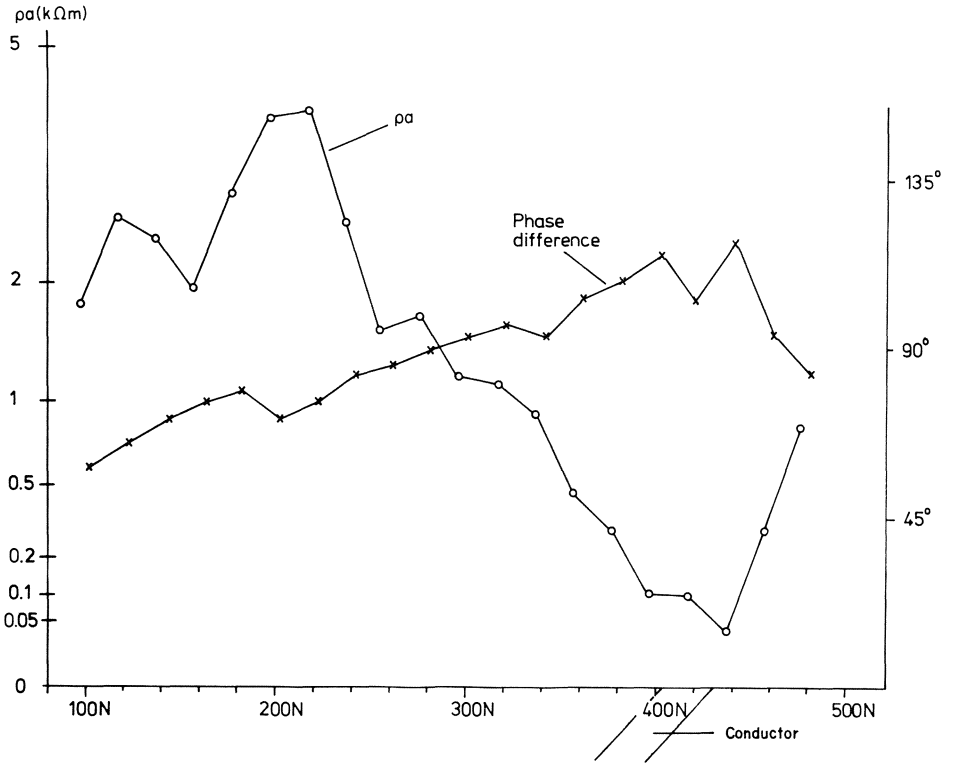

Fig. 6.28 ρ_a obtained from wave impedance measurements across a conductor (the scale for ρ_a is quadratic).

antenna in the present case is trailed *along* the profile of measurement while the solenoid for picking up the magnetic field is perpendicular to the profile and, of course, horizontal.

We see that when a VLF wave arrives at right angles to the geological strike there is only an electrical but no magnetic anomaly over a sheet conductor.

Fig. 6.28 shows a ρ_a profile obtained from VLF measurements across an ore conductor. The variation of the phase difference between E_x and H_y is also shown.

6.8.5 Effect of topography on VLF observations

At the ground surface the electric current necessarily follows the topography. A wire antenna laid on the surface will measure the true tangential electric field in its own direction since the other electric component at the surface is exactly perpendicular to the surface and does not affect the measured field. It follows that the influence of topography on the E_x anomalies in the VLF method is negligible.

The situation concerning the magnetic field is not so simple because when the VLF wave arrives at an inclined ground surface it is reflected but the reflected magnetic field has both a horizontal and vertical component and these are not in phase with the primary field. The magnetic field therefore becomes polarized and a tilt anomaly is obtained even if the earth be homogeneous. Fig. 6.29, reproduced from a paper by Eberle [108], who has made a mathematical analysis of the problem, can be used to estimate the readings of the VLF instrument in per cent ($100 \times \theta$ (radian) and $100(b/a)$) due to topography. Towards this end it is necessary to calculate first, τ, the angle of wave incidence with the ground surface.

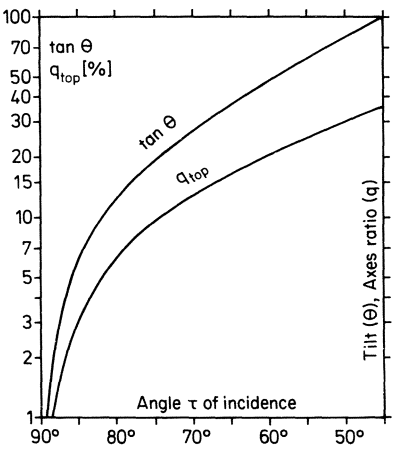

Fig. 6.29 Topographic effect in H-field VLF measurements. After [108].

This is obtained from the following simple equation:

$$\tan \tau = \cot \beta' \frac{\sin \xi_2}{\sin \xi_1} \tag{6.30}$$

where β' = inclination of ground surface along the survey line, ξ_1 = angle between the direction of the incoming magnetic field and strike of the ground morphology and ξ_2 = angle between the survey line and strike of the morphology.

In broad terms the effect of topographic relief is that the VLF instrument readings are positive going up a slope and negative going down, with a cross-over at the crest of a ridge or the bottom of valley. The shape of the tilt profile is thus very similar to that in Fig. 6.26. The possible effect of topography must be assessed before a VLF tilt-angle anomaly can be ascribed to a deeper geological conductor.

6.9 INTERPRETATIONAL AIDS IN EM PROSPECTING

6.9.1 Theoretical approaches

The problem of calculating theoretically the response of a conductor to an electromagnetic field is that of solving Maxwell's equations under appropriate boundary conditions. In the absence of any conductors the voltage induced in a receiver as a result of a current I in a primary source is $Z_0 I$ where Z_0 is the mutual impedance between the source and the receiver in vacuum. However, this voltage is also equal to KB_0 where B_0 is the flux density at the receiver. In the presence of a conductor the voltage will be $ZI = KB$, K being the same as before since it is a purely instrumental constant. Obviously, $B/B_0 = Z/Z_0$.

Thus, put in another way, the problem of finding the electromagnetic response is essentially that of calculating the mutual impedance of the source and the receiver in the presence of the conductor system of interest. In general the problem is extremely complicated and treatments were confined initially to simple conductor models such as a sphere [109–111], a semi-infinite earth, a cylinder [112], vertical and horizontal sheets [113, 114] and an earth whose conductivity is a function of the depth only [115, 116]. Very great progress has been made, however, in treating more complicated models such as a sphere enclosed by spherical shells [117] or a conductivity inhomogeneity in a layered half-space [118, 119], etc. The reader will also find two special issues of *Geophysics* [120, 121], a paper by Weidelt [122] and a monograph by Wait [123] illuminating from the theoretical point of view.

6.9.2 Model experiments

Although the formal solution of many of the theoretical problems may be available, the numerical computations are generally formidable and require recourse to a computing machine. Fortunately, however, the response of a

'natural' conductor can be exactly duplicated in the laboratory on a small, convenient scale. This is most easily seen from dimensional considerations.

Let the response of a conductor be measured in the dimensionless form S/P where S and P are the secondary and primary fields at a point. Since displacement currents are neglected the only relevant parameters producing this response are: $\rho(\Omega\,\mathrm{m})$, $\nu(\mathrm{s}^{-1})$, the absolute permeability $\mu(\Omega\,\mathrm{s\,m}^{-1})$ and the linear scale of the experiment characterized by some length $d(\mathrm{m})$. It is immediately verified that the quantity $\gamma = \rho/\mu\nu d^2$ formed from these four parameters is dimensionless. Therefore every system which has the same γ must produce the same dimensionless response S/P irrespective of the actual values of ρ, μ, ν and d.

Suppose now that $d_{\text{full scale}}/d_{\text{laboratory}} = n$ and that the frequency of the laboratory experiment is the same as the 'full-scale' experiment which it is supposed to represent. Then equating the γ's,

$$\left(\frac{\rho}{\mu}\right)_{\text{f.s.}} = n^2\left(\frac{\rho}{\mu}\right)_{\text{lab.}} \tag{6.31a}$$

Since, however, in both cases we are generally concerned with 'non-magnetic' conductors $\mu = \mu_0$, the permeability of free space, so that

$$\rho_{\text{f.s.}} = n^2\rho_{\text{lab.}} \tag{6.31b}$$

This means that if the linear dimensions in the laboratory experiment are n times smaller than those in the full-scale work, a laboratory conductor with resistivity ρ will correspond to a geometrically similar full-scale conductor of resistivity $n^2\rho$.

Thus suppose that $10^{-3}\,\mathrm{m}$ (1 mm) in the laboratory is chosen to represent 1 m in full scale ($n = 10^3$). A transmitter–receiver separation of 100 m will then be represented by 100 mm, a conductor depth of 50 m by 50 mm and so on for all the other lengths involved. The response of a 1 mm thick zinc plate ($\rho = 6.0 \times 10^{-8}\,\Omega\,\mathrm{m}$) will then be the same as that of 1 m thick full-scale conductor, e.g. an ore vein, of resistivity $6.0 \times 10^{-8} \times 10^6 = 0.060\,\Omega\,\mathrm{m}$.

The choice of model conductors is limited more or less to metal sheets and these do not show a very wide range of conductivities. However, since we have the scale factor, the frequency, and to some extent the magnetic permeability as additional variables at our disposal, a wide range of conductors in full scale can be electromagnetically simulated in the laboratory.

Model experiments have already been referred to in Section 6.7.3. It should be easy now on the basis of the above discussion to 'translate' these to full scale.

It should be noted that the parameter $\rho/\mu\nu d$ has the dimensions of length. Consequently its full scale value is n times the laboratory value if the relative response S/P is the same for both systems. Since we put $\mu = \mu_0$ in full scale and in the laboratory this means

$$\left(\frac{\rho}{\nu d}\right)_{\text{f.s.}} = n\left(\frac{\rho}{\nu d}\right)_{\text{lab.}} \tag{6.31c}$$

6.9.3 Vector diagrams and example of use

The results of electromagnetic theoretical calculations or model experiments are usually plotted as vector diagrams, also called phasor diagrams, an an aid to interpretation. We have already come across vector diagrams. A curve in such a diagram is the locus of the common tip of the resultant and secondary field vectors in Fig. 6.2 when the phase angles α and ψ change with frequency or the properties of the secondary circuit. A vector diagram like that in Fig. 6.20 is valid only for the measuring system, the conductor geometry and the field at a definite receiver position, for which it is constructed. The diagram in Fig. 6.20 is constructed, for example, for a horizontal loop system, a single vertical sheet conductor and the field read when the midpoint of the loop system is exactly above the sheet. In this particular case an alternative vector diagram could be constructed, if desired, by plotting the positive side maxima in the real and imaginary components (or, in fact, any other value on the anomaly curve except, of course, a zero value).

The use of vector diagrams in interpretation is fairly straightforward provided the geological situation approximates the conductor geometry behind the vector diagram. Suppose that field measurements across a long geological conductor with a horizontal loop system (coil separation 60 m, frequency 880 Hz) have given a symmetric curve resembling Fig. 6.19 and that the central fields are 96.1% and -6.5% in the real and imaginary components respectively.

A symmetrical curve indicates a vertical or steeply dipping conductor so that Fig. 6.20 is applicable. Entering this diagram we find (by interpolation) that the observed anomaly corresponds to the anomaly of a 1.5 mm thick Pb plate ($\rho = 210\,\text{n}\Omega\,\text{m}$) on 500 Hz and at a depth of 30 mm, which is $0.3 \times$ coil separation in the laboratory. Hence the depth of the geological conductor is $0.3 \times 60 = 18$ m. Since the full scale coil separation is 600 times the laboratory one we have $n = 600$ in Eq. (6.31) which gives

$$\left(\frac{\rho}{\nu d}\right)_{\text{f.s.}} = 600\left(\frac{210 \times 10^{-9}}{500 \times 1.5 \times 10^{-3}}\right)$$

With $\nu_{\text{f.s.}} = 880$ Hz we get

$$\left(\frac{\rho}{d}\right)_{\text{f.s.}} = 0.148\,\Omega$$

for the resistivity/thickness ratio of the geological conductor. Frequently the result is expressed as the 'conductivity $\times$ thickness' product which is the reciprocal (σd) of ρ/d or, in the present case, 6.76 siemen.

In order to avoid having to refer to the parameters of the laboratory experiment each time, the depth for each vector locus (the 'semicircles' in Fig. 6.20) and the $\rho/\nu d$ parameter corresponding to each thin dashed line can

be marked on the vector diagram in terms of the coil separation. It is then only necessary to multiply either of these parameters by the coil separation in full scale to obtain the depth and the (ρ/vd) product of the geological conductor.

6.10 DEPTH PENETRATION

The question of how deep electromagnetic waves penetrate into the ground is of great importance in geophysics. If the ground were perfectly insulating the waves could penetrate to any distance. However, owing to the finite conductivity of most surface formations and of the underlying rocks the incident energy is absorbed and the amplitude of the waves decreases exponentially in traversing the conductors, due to absorption alone. In addition there will be a 'geometric decrease' as the wave spreads. This decrease depends upon the character of the source (cf. Eq. (6.14)). It is therefore convenient to discuss the topic of depth penetration with reference to plane waves, for which there is no such geometric decrease.

The amplitude of a plane wave is reduced to 1/e of its surface value within a distance $\delta = 1/b$ where b is defined in Eq. (6.15). We shall call this distance the depth penetration. Two important extreme cases can now be distinguished.

If displacement currents are negligible ($v\rho \lesssim 10^8\,\Omega\,\mathrm{m\,s^{-1}}$) then, for 'non-magnetic' conductors ($\mu = \mu_0$)

$$\delta = 503.3\left(\frac{\rho}{v}\right)^{1/2} \text{ metres} \tag{6.32}$$

which shows that for this case the depth penetration decreases with a decrease in resistivity and an increase in frequency.

If $\rho = 2000\,\Omega\,\mathrm{m}$, a value typical of many glacial moraines, sandy clays, wet sandstones and chalk, the depth penetration will be about 700 m at $v =$ 1000 Hz and 225 m at $v = 10\,000$ Hz. However, owing to the presence of water containing dissolved salts many surface formations have resistivities as low as $100\,\Omega\,\mathrm{m}$ and δ may be reduced to about 150 m even at $v = 1000$ Hz. In sedimentary formations clays and shales with resistivities of the order of $1\,\Omega\,\mathrm{m}$ are quite common and in such cases frequencies as low as 10 Hz will be required to obtain a depth penetration of 150 m.

The relative response of deep-seated conductors increases and that of shallow ones decreases as the frequency is lowered. The use of very low frequencies for deep exploration is, however, limited by the fact that the absolute magnitude of the signals decreases more or less in proportion to the frequency.

In the other extreme when displacement currents are appreciable ($v\rho \gtrsim 10^{10}\,\Omega\,\mathrm{m\,s^{-1}}$) we have (again for non-magnetic media),

$$\delta = 1784\varepsilon^{1/2}\rho \text{ metres} \tag{6.33a}$$

Taking $\varepsilon = 90\,\text{pF m}^{-1}$ as representative of most earth materials,

$$\delta = 16.9 \times 10^{-3} \rho \text{ metres} \tag{6.33b}$$

In this case δ is independent of frequency.

We see from Eq. (6.33b) that if frequencies of, say, 10 MHz and higher are to penetrate more than a few tens of metres, the resistivity must be at least a few thousand ohm metre. Experiments have been reported in which radio and radar frequencies penetrated several hundred metres of rock. From the above it is clear that these rocks must have been highly resistive. In special circumstances (e.g. glacier ice) it may, of course, be possible to obtain a penetration of several kilometres even at radar frequencies [124].

It should be noted that if $v\rho$ lies between $\sim 10^8$ and $\sim 10^{10}$ it is generally preferable to estimate δ from the exact expression obtained from Eq. (6.15), namely

$$\frac{1}{\delta} = b = \left(\frac{\omega\mu}{2\rho}\right)^{1/2} [(\rho^2\varepsilon^2\omega^2 + 1)^{1/2} - \rho\varepsilon\omega]^{1/2} \tag{6.34}$$

Apart from the depth penetration defined above there is another magnitude which is often referred to as the (practical) depth penetration. This is the maximum depth at which a conductor may lie and yet give a recognizable electromagnetic anomaly. This depth depends on the nature and magnitude of the stray anomalies ('noise') caused by near-surface conductivity variations, on the geometry of the deep conductor and on the instrumental noise. Experiments show that in the ideal case where the first noise type can be neglected, the maximum practical depth penetration of the various electromagnetic arrangements is between about 1 and 5 times the separation between the transmitting and receiving systems.

6.11 INFLUENCE OF OVERBURDEN CONDUCTIVITY

Most targets of exploration are found beneath some thickness of overburden. In passing through a thickness of conductive overburden equal to that given by Eq. (6.32), the amplitude of the primary field decreases by the factor e. In addition, after a passage through this distance – also known as 'skin depth' – the phase of the field is changed by 1 radian (57.3°). A smaller overburden thickness will cause proportionally smaller attenuation and phase change. The phase of the field actually exciting the conductor is therefore not that of the primary field emitted at the surface by the source. The secondary field of the conductor in its turn will also suffer attenuation and change of phase in arriving at the receiver on the surface. If we consider, for the sake of concreteness, the horizontal loop system of Fig. 6.18(a) and a thin vertical sheet conductor, the net result can be that the phase is changed so much that

the imaginary component, instead of being negative, becomes positive. It might be thought that the amplitude of the secondary field [(real comp.)^2 + (imag. comp.)^2]$^{1/2}$ will be smaller than if the overburden were non-conducting and that the effect will be aggravated in view of Eq. (6.32) if the frequency were increased. In fact, the opposite can happen as the multi-frequency measurements in Fig. 6.30 illustrate. The overburden here is soil and 17 m thick weathered basalt (vertical thickness) and the conductor below consists of two steeply dipping strata of carbonaceous shale, 17 m and 15 m thickness along the hole, separated by 27 m of unweathered trap. It will be seen that the secondary real component *increases* (up to 1344 Hz) as the frequency is increased, and although the imaginary component shows a decrease from

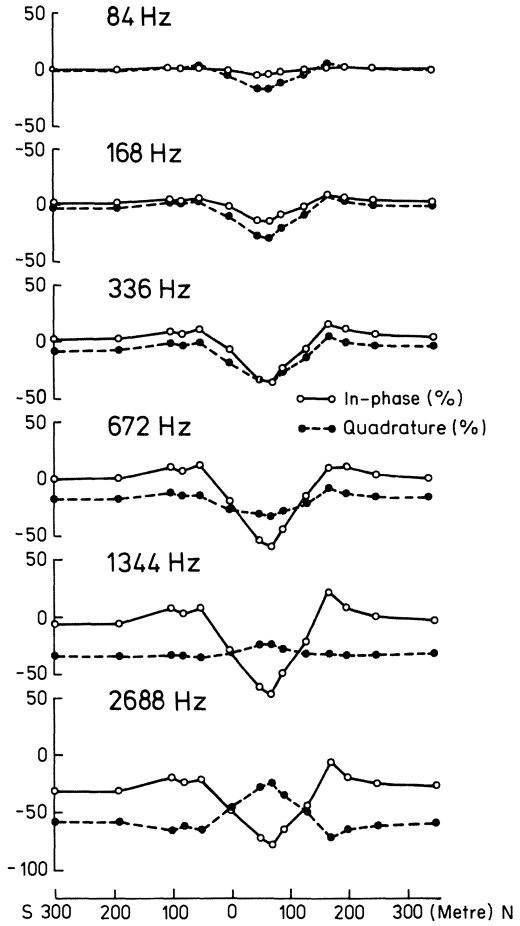

Fig. 6.30 Multifrequency measurements with a horizontal loop system. After [125].

336 Hz to 672 Hz, after an increase from 84 Hz to 336 Hz, it increases again to a large value at 2688 Hz. It changes sign at 1344 Hz. The total amplitude of the secondary field, however, increases continuously as the frequency is increased from 84 Hz to 2688 Hz.

The above type of increase in anomaly when a decrease is expected due to the 'screening effect' of the conductive overburden is often called 'negative screening'. Its explanation is that the currents induced in the overburden by the primary field are channelled into the target conductor because of its high conductivity and the resulting current density in it is higher than it would be by pure induction if the target were in free space. The higher the frequency the stronger are the induced overburden currents that are channelled into the conductor below. This increase continues of course only so long as the skin depth in the overburden material is large compared with the thickness of the overburden. Then the attenuation is still moderate. When the frequency is sufficiently high, of course, the currents in the overburden are confined to the surface and screen the underlying material. The anomaly of the target then decreases and will eventually disappear altogether as the frequency is increased.

It will be seen that in Fig. 6.30 the response of overburden is clearly visible at a frequency as low as 336 Hz when the secondary component is distinctly non-zero on the flanks, away from the anomaly of the shales.

Experiments on models in free space must therefore be used with caution when the conductivity of the overburden, or that of the host rock in which the target is situated, is appreciable. Multifrequency measurements will be called for under these circumstances for obtaining an adequate geological picture [103, 125].

6.12 TRANSIENT-FIELD METHODS (TIME-DOMAIN EM)

6.12.1 Introduction

Electromagnetic energy can be supplied to the ground by transient pulses instead of by continuous waves which we have been discussing so far. When a circuit (e.g. a large circular or rectangular loop) is carrying a steady electric current, the constant magnetic flux due to its passes, of course, through any electric conductor that may be present in the environment but no secondary currents are induced since the flux is not varying with time. If the steady current is suddenly switched off the flux falls from its initial steady value to the value zero but during a short interval it is obviously varying with time and currents will therefore be induced in a conductor in accordance with Neumann's law (Section 6.2.1). Their secondary field decays with time as the currents gradually dissipate on account of the electrical resistance in the conductor. This time-dependent field will, in its turn, induce a transient electromotive force in a receiver circuit on which it may be acting.

In practice, the primary current and flux cannot be switched off perfectly instantaneously, but only more or less suddenly. A commonly used procedure is to bring the flux from its steady value B_0 to the value zero, linearly with time within a short interval τ of the order of microseconds. The rate of change of flux, B_0/τ, and hence any induced electromotive force due to it, will, in this case, be proportional to B_0 and therefore also to the primary current. Consequently, the secondary field acting on a receiving circuit and the e.m.f. induced in it will also be proportional to the initial steady current in the primary circuit. Hence, the receiver signal in the transient-field EM method is expressed as microvolt per ampere primary current.

6.12.2 Transient field of single-turn circular loop

This is a particularly easy case to study. Suppose that the primary field in Fig. 6.3 is a steady field and we suddenly switch it off. Then the induced current I in the loop follows the equation

$$RI + L\frac{dI}{dt} = 0 \tag{6.35}$$

where t is the time, R the resistance and L the self-inductance in the loop. Integrating we get $I = I_0 \exp[-(R/L)t]$ where I_0 is the current at $t = 0$, that is, immediately after the primary field is switched off. As the magnetic field of a current is proportional to the current, the signal induced in a receiver due to I will also decay exponentially with time and may be written as $S = S_0 \exp[-(R/L)t]$. It is then evident that a graph of ln S against t in this case will be a straight line of slope $-R/L$.

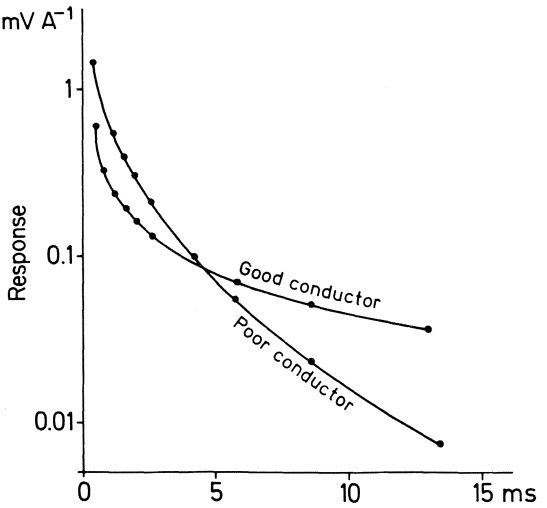

Fig. 6.31 Transient EM signals on typical conductors.

If R is large the slope is steep and the signal vanishes quickly. If R is small the signal persists for a relatively longer time. This is essentially true even when we have a massive conductor, rather than a single-turn loop, and we cannot speak of a resistance in the conductor but must consider the resistivity (or its reciprocal, the conductivity) of the conductor. For such cases, into which category geological conductors also fall, the ln S against t plot is not a straight line, but the rate of fall of the 'signal versus time' curve nevertheless indicates the quality of the conductor (Fig. 6.31).

6.12.3 TEM survey procedures

The transmitter in a TEM survey is generally a square or rectangular loop, the square one being the more common of the two. Typical dimensions are 80 m × 80 m or 200 m × 200 m although smaller and larger loops have also been used. In principle, a long grounded cable could also be used as a source but there are difficulties in injecting pulses of sufficient energy in such a source. It is interesting to note that since transient-field measurements are made after the primary field has been turned off, the transmitter loop itself can be used as a receiver. Fig. 6.32 shows this and other common layouts.

A typical procedure of measurement using a single square loop as transmitter and receiver (Fig. 6.32(a)) is as follows. A known current is sent for, say, 10 s in the loop and switched off. The loop is automatically connected to a detecting device, as soon as the primary field has ceased to exist. The signal voltage in the loop is sampled at suitable predetermined intervals from, say, 4 ms to 200 ms, divided by the primary current, and the values ($\mu V A^{-1}$) for different times are stored in the memory of a microcomputer. A second primary pulse is sent after a no-current period of 10 s and the signals received are added to the corresponding stored values. The current direction in the transmission is usually reversed for each pulse, to avoid effects due to ground polarization. In this case the sign of the received signal is reversed for every second pulse before stacking. The procedure of stacking is repeated a desired number of times and the final series of values is printed out after dividing it automatically by the number of stackings. The loop is then moved, parallel to one of its sides, by a distance equal to the side.

In practice, it is not necessary to move the entire loop bodily, but only the cable lengths forming two of its sides, as indicated in Fig. 6.33, which speeds up the survey. The layouts in Figs 6.32(a)–(c) measure the vertical component of the secondary field while the arrangement of Fig. 6.32(d), using a small orientable receiver coil or solenoid, enables the horizontal component to be measured also.

As we have seen before, the secondary current system in a geological conductor can often be replaced by a single current flowing along the edges of the conductor. It is then easy to see that the profiles of the vertical and

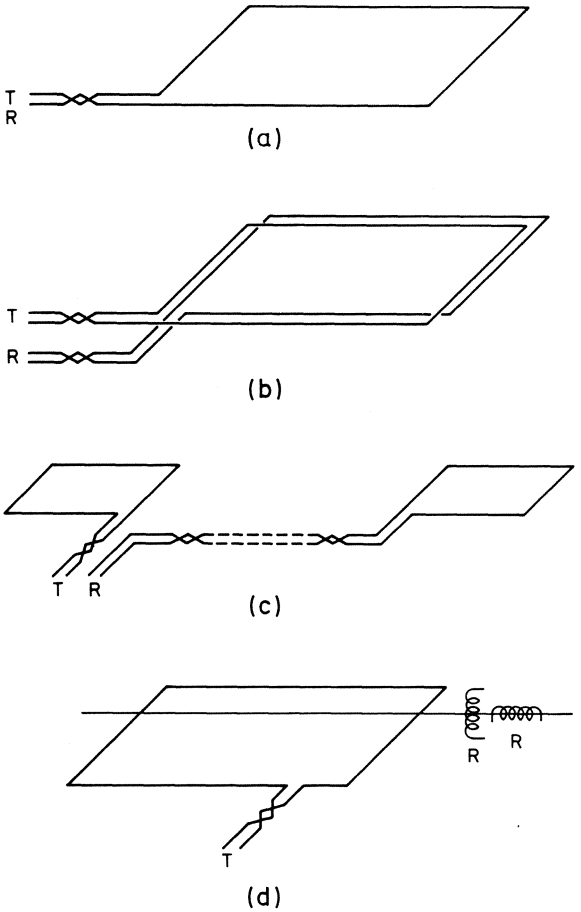

Fig. 6.32 Transient-field measurement layouts. (a) One loop as transmitter (T) and receiver (R). (b) Separate coincident loops. (c) Spaced loops. (d) Fixed loop and orientable receiver.

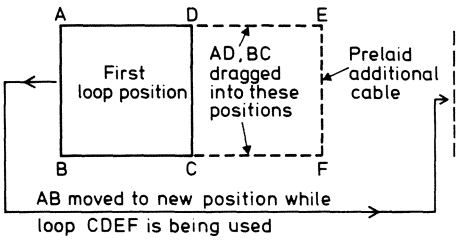

Fig. 6.33 Speeding up TEM field work.

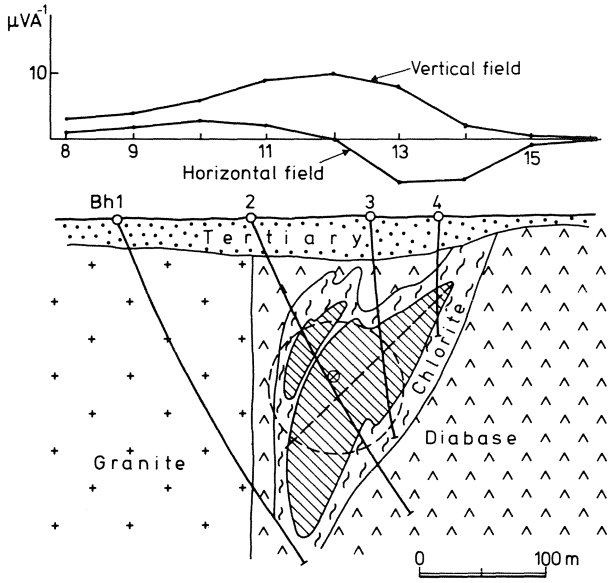

Fig. 6.34 Field example of TEM measurements. After [130].

horizontal fields measured across a steeply dipping conductor, at one and the same instant after current cut-off with the layout of Fig. 6.32(a) or (b), will resemble the profiles in Fig. 6.3. A field example from a survey in Caucasus (USSR) is shown in Fig. 6.34. The circle in the figure and the dashed line represent an equivalent sphere and an equivalent thin plate respectively, giving the same field values as the ore.

Similarly it will be seen that a profile with a system such as that in Fig. 6.32(c), in which both the transmitter and the receiver are moved, will resemble the anomaly profile in Fig. 6.18(a).

6.12.4 Comparison of TEM and CW methods

The transient and the continuous wave methods are related to each other through the Fourier transform (Appendix 13) according to which a transient pulse can be decomposed into an infinite number of sine and cosine waves. The transient signal received is a superposition of the secondary field response of a conductor to each of these frequency components. Hence, a transient-field measurement over a sufficiently long time interval implicitly contains roughly the same information as a multifrequency measurement with the same layout and vice versa.

If we take a transmitter loop laid horizontally on a homogeneous,

conductive ground the transient current system induced in it due to a pulse in the loop may be approximated, immediately after the pulse is over, to a single circular transient current at the surface, coincident with the loop but flowing in a direction opposite to the primary current before it was switched off. This transient current-ring will induce another ring below it and so on. Each of these rings is larger than the previous one and the entire response of the ground may be considered qualitatively to be the field of the first ring diffusing into the ground with the velocity of electromagnetic waves and broadening at the same time, somewhat like a smoke ring puffed into the air from a cigarette [126]. From this we can infer that the signals measured at later times are governed by the part of the ground lying at depths greater than the depths that govern the earlier signals. From Section 6.10 it is evident that a high frequency is damped out at a shallower depth than a low frequency. Thus, qualitatively speaking, the early time response in the transient-field method is analogous to the high frequency response of the continuous wave method while the late time response corresponds to the response at low frequencies. Theoretically it is not possible, however, to attach a definite frequency to a definite time and vice versa. The equivalence should only be looked upon in broad terms.

Transient methods possess certain advantages. It is clear from Section 6.10 that either very great primary field strengths at high frequencies or, if the field strengths are moderate, very low frequencies must be used in the continuous wave methods, if subsurface conductors below highly conductive overburden are to be excited. In either case the instrumentation becomes very difficult, cumbersome and costly. The production of very high transient field strengths, on the other hand, is easier although the difficulties involved should by no means be underrated. Experiments have been reported in which a power of 700 kW was dissipated in 100 ms through a square single-turn loop of side 300 m [127, p. 342].

Several instances have been reported of sulphide ore bodies being detected by transient-field methods below highly conducting overburden [128, 129]. It has been suggested, though not explicitly, that such a detection is impossible by continuous wave methods. The problem deserves a more detailed experimental and theoretical study than has been made hitherto, in view of the theoretical equivalence between continuous wave and transient techniques referred to above.

Another advantage of transient-field methods is that the exact geometry of the source with respect to the receiver is largely immaterial since the measurements, carried out in the absence of a primary field, are purely those of the secondary field and no knowledge of the primary field strength is required to obtain the secondary field. In this respect, transient-field measurements are exactly comparable to those of the imaginary component or the phase shift in continuous-wave methods. It follows that the effect of topographic irregularities is often negligible in transient-field measurements.

The main disadvantages of TEM methods are a relatively slow speed of operation and the proneness of the receiving circuit to electrical noise since the circuit has to respond to a broad band of frequencies and cannot be tuned to a particular frequency in order to enhance the received signal, as can be done in a continuous-wave equipment.

6.12.5 Transient-field theory and model experiments

Although the systematic development of transient-field methods started nearly forty years after that of harmonic-field methods, the methods are now well entrenched in applied geophysical work and are even reported to be more or less the only usable EM methods in certain areas (e.g. Australia and USSR). Much of the pioneering transient-field development is due to Soviet scientists [130] but their papers, being in Russian, are unfortunately not widely known in the west.

Considerable theoretical work now exists on the responses of various types of conductors to transient pulses of different shapes [131–137] and a coherent development is also given in a treatise by Kaufman and Keller [138]. As with harmonic-field methods the theoretical treatments are at present confined to relatively simple conductors. To obtain the response of complicated geological structures it is often necessary to resort to model experiments in the laboratory.

The principle of TEM model experiments is exactly the same as in Section 6.9.2 but there are some differences in detail. In the transient-field mode the common dimensionless parameter for two electromagnetically equivalent systems is $\gamma' = \rho t/\mu d^2$. The dimensionless response, which was S/P in the harmonic-field methods, is formulated from the following considerations. Since the transmitter loop in full scale may have a different number of turns from that in the laboratory scale we must reckon in either case with the effective primary current NI where N is the number of turns. Further, the e.m.f.'s in the two receivers must be compared for some standard condition, e.g. for a receiver loop of unit geometrical area and one turn only. Then if U is the voltage actually developed in the receiver coil we must consider the quantity U/Ma where M is the number of turns in the receiver loop of area a.

From the physical quantities involved, namely the time t, any length d in the system, the effective primary current NI, the standardized receiver voltage U/Ma and the magnetic permeability μ, we can form $Utd/(MaNI\mu)$ as the only fundamental dimensionless ratio. This has to be the same in full scale and the laboratory model. If we restrict attention to 'non-magnetic' conductors ($\mu = \mu_0$) and measure the signal (U/I) at the same absolute time (after current-off) in full scale and in the laboratory model, it is easily shown that the full scale signal $U_{\text{f.s.}}/I_{\text{f.s.}}$ and the laboratory model signal $U_{\text{lab}}/I_{\text{lab}}$ are related by the following simple equation:

$$\frac{U_{\text{f.s.}}}{I_{\text{f.s.}}} = \frac{1}{n}\frac{M_{\text{f.s.}}}{M_{\text{lab.}}}\frac{N_{\text{f.s.}}}{N_{\text{lab.}}}\frac{a_{\text{f.s.}}}{a_{\text{lab.}}}\frac{U_{\text{lab.}}}{I_{\text{lab.}}} \tag{6.36}$$

where $n = d_{\text{f.s.}}/d_{\text{lab.}}$ is the geometrical scale factor.

Equation (6.36) is valid irrespective of whether the transmitter and receiver loops are identical or not. The corresponding loops in the two systems must, of course, be geometrically similar to each other. For example, if the receiver in full scale is a dipole it must also be a dipole in the laboratory scale.

Since $\gamma'_{\text{f.s.}} = \gamma'_{\text{lab.}}$ for two equivalent systems, we get $\rho_{\text{f.s.}} = n^2 \rho_{\text{lab.}}$ which is the same rule as for harmonic-field model experiments.

6.13 INFLUENCE OF MAGNETIC PERMEABILITY

We have assumed so far that the magnetic permeability of conductors is equal to that of vacuum. This however is not justified for some natural conductors, e.g. magnetite ores, for which the relative permeability may be as much as 10.

From Section 6.9.2 it is evident that the effect of increasing the permeability n times is the same as that of increasing the conductivity $(1/\rho)$ n times. However, besides the field due to induced currents there is, in the case of magnetic conductors, a purely *magnetic* secondary field due to the oscillating induced magnetism. This latter field is in phase with the primary field and is, generally speaking, opposed to the real component of the induction part of the secondary field.

For example, for the single-turn loop of Section 6.2.3, the primary field is $P \cos \omega t$ and the real component of the secondary field due to the coil current is $-S \sin \phi \cos \omega t$. If we imagine a very small needle or bar (susceptibility κ) to be situated at the centre of the loop, the field due to its magnetic moment will be equal to a geometrical constant times $\kappa P \cos \omega t$, which is opposite in sign to the real component of the current-created field of the loop. The latter's amplitude increases with frequency while the magnetic moment amplitude is independent of frequency. There is therefore a certain frequency for a magnetic conductor above which its response is typically inductive (e.g. damping in the real component) and below which it is predominantly magnetic (e.g. with an appearance as for the field of a body statically magnetized in the direction of the primary field).

The effect can also be studied by means of the vector diagram in Fig. 6.35 where OP represents the phase and amplitude of the primary field, and $PA = S$ the amplitude of the current-created secondary field at a low frequency. The phase of this field with respect to OP is $-(\pi/2 + \phi)$ and its real and imaginary components are $-S \sin \phi$ and $-S \cos \phi$. The diagram is typical of the anomaly obtained with a moving source–receiver system when it straddles a steeply dipping conductor (e.g. Fig. 6.19). If the conductor is highly magnetic it will produce an additional in-phase component **AM** so that the amplitude and

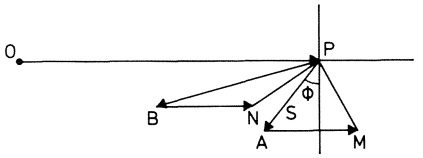

Fig. 6.35 Typical effect of magnetic permeability on EM anomalies.

phase of the resultant field will be as shown by the vector **PM**. We see that while the secondary imaginary component is unchanged the secondary real component is positive, unlike the case when the conductor is non-magnetic.

At a sufficiently high frequency the current-created secondary field will be represented, in phase and amplitude, by the vector **PB** since ϕ as well as the amplitude S increases with frequency (cf. Section 6.2.3). If the conductor is magnetic the additional in-phase component is **BN** but its magnitude is independent of frequency and therefore equal to AM. The real and imaginary components of the resultant secondary field, represented by vector **PN**, are now both seen to be negative as in the case when there is no magnetic permeability influence. As before, the secondary imaginary component is not affected by the magnetic permeability.

The effect of magnetic permeability in electromagnetic work generally manifests itself in that anomalies which are 'normally' positive are rendered negative and vice versa (Fig. 10.3). The influence of permeability must be carefully considered in field work when magnetic conductors are suspected in an area [139, 140].

6.14 CONTROLLED-SOURCE ELECTROMAGNETIC SOUNDING

Electromagnetic methods can be used to determine the parameters of a layered earth like the purely electrical methods (Section 4.5). The basis of EM sounding is the fact that the depth of penetration of an EM field depends upon the frequency (Eq. 6.32) or the fact that, if the field is transient, it gradually diffuses into the ground. A variety of procedures have been suggested, using artificial sources like oscillating magnetic dipoles, loops, cables carrying alternating current, oscillating electric dipoles and transient sources of similar geometries.

6.14.1 Frequency and geometric sounding

Let us consider the system of Fig. 6.16 (coil separation r) on the plane surface of a semi-infinite stratified earth. If B_{0z} is the vertical field at the receiver when the system is in free space and B_z the field on the stratified earth, it can be shown

[e.g. 138, 141] that

$$\frac{B_z}{B_{0z}} = 1 - \int_0^\infty r^3 R(\lambda, h, \rho, v) J_0(\lambda r) \lambda^2 \, d\lambda \tag{6.37}$$

where h, ρ are thickness and resistivity vectors $(h_1, h_2, \ldots, h_{n-1}; \rho_1, \rho_2, \ldots, \rho_n)$ and v is the frequency. $R(\lambda)$ is a *complex* function corresponding to $K(\lambda)$ in Eq. (4.31) and like $K(\lambda)$ it can be found for any stratification by means of recurrence relations. Similar equations exist for other source–receiver configurations.

The real and imaginary parts of B_z/B_{0z} can be measured for different separations r and constant v (*geometric sounding*) or for different frequencies v but constant r (*frequency sounding*). The measurements thus obtained can then be fitted to a model of the earth by calculating the right-hand side of (6.37). Digital filters, like those for calculating VES curves in Chapter 4, have been devised [141] but, in general, the computations in the electromagnetic case are much more complicated.

An example of electromagnetic geometrical sounding at two different frequencies, made for water prospecting, is shown in Fig. 6.36. Unfortunately, the mathematical expressions in electromagnetic sounding, like Eq. (6.37), do not allow a presentation of the measured data in the form of apparent resistivities over the entire range of frequencies or source–receiver distances so that the geological structure cannot be immediately conjectured from EM sounding curves as it can be from VES curves.

However, in the near-field $((\omega\mu/\rho)^{1/2} r \ll 1)$ and in the far-field region $((\omega\mu/\rho)^{1/2} r \gg 1)$ the data can be expressed as apparent resistivities, but we shall not enter into this question further. The expression for the apparent resistivity ρ_a in the near-field region is nevertheless worth quoting here as it is the basis of calibrating the readings of certain moving source–receiver systems used in mapping near-surface resistivity variations. For the horizontal-loop system of Fig. 6.16, for example, we have

$$\rho_a = \frac{2\pi v \mu r^2}{4[Im]}$$

$$= 1.974 \times 10^{-6} \frac{v r^2}{[Im]} \tag{6.38}$$

where $[Im]$ is the imaginary component of the field at the receiver as a fraction of the primary field there. Typical operational values are $v = 1600$ Hz, $r = 20$ m (or appropriate combinations such that $vr^2 =$ constant).

A theoretical limitation on the frequency in EM sounding is that the depth of penetration (Eq. 6.32) at each frequency used must be significantly greater than the thickness of any layer sounded. With the usual resistivities of common geological materials this is generally not a serious limitation.

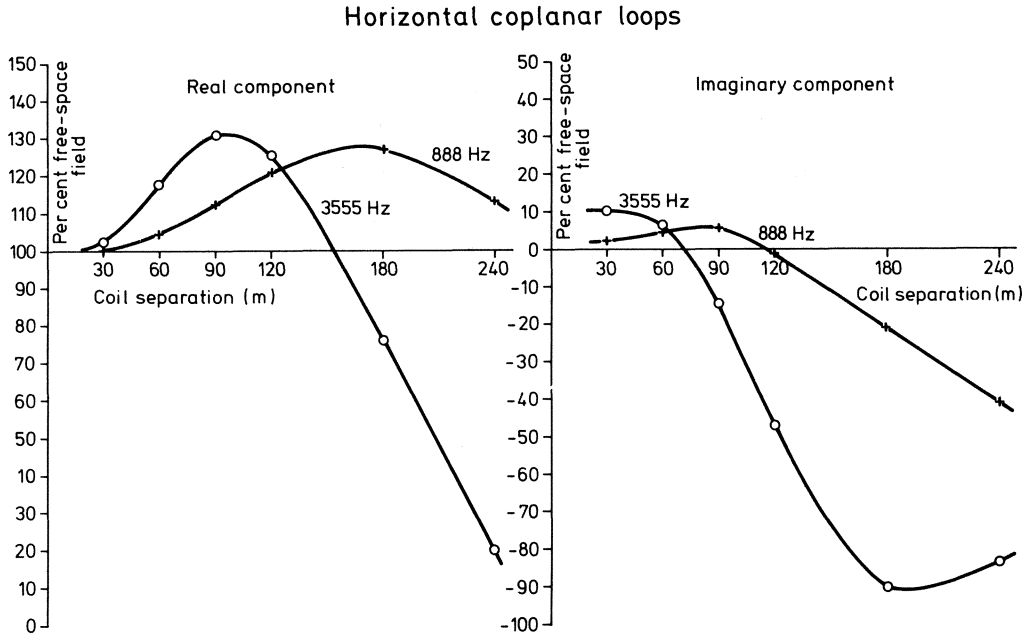

Fig. 6.36 Example of electromagnetic sounding. (The measurements are at the same point as in Fig. 4.27.)

6.14.2 Transient-field soundings

We shall again confine attention to the dipole system of Fig. 6.16 although many other systems have been proposed for these soundings. In transient-field soundings it is possible to express the measured data at early times or late times as apparent resistivities. At intermediate times the theoretical expressions for the response of a layered earth are too complicated to permit such a representation. For the system in question, early and late times are defined by the criteria $(\mu/2\rho t)^{1/2} r \gg 1$ and $\ll 1$ respectively, r being the coil separation. These conditions correspond to the far-field and near-field regions in the frequency domain. It should be noted that late (or early) times in the absolute sense (seconds) will vary with r.

For our system, the apparent resistivity is defined by

$$\rho_a = \frac{\mu}{4\pi t}\left(\frac{2\mu a_T a_R}{5t(U/I)}\right)^{2/3} \tag{6.39}$$

where a_T, a_R are the effective areas of the transmitter and receiver coils and U/I is the signal (volt per ampere primary current) in the receiver.

In Figs 6.37(a) and (b) are plotted some theoretical curves over a two-layer earth for the case $r = h$, the thickness of the top layer. The abscissa is the parameter d/h where

$$d = 2\pi\left(\frac{2\rho t}{\mu}\right)^{1/2} \tag{6.40}$$

It is evident that $\rho_a \to \rho_2$ for large values of d, and consequently of t, when the induced currents may be supposed to have diffused into the lower substratum. However, for small values of t the ρ_a curve does not approach ρ_1 indefinitely, as one would naively expect by analogy with VES curves (Fig. 4.19), but only shows a nearest-approach. The reason is that with the given r the late-time condition is not satisfied at this end and Eq. (6.39) ceases to be applicable. For a smaller value of r, however, the ρ_a curve will approach the value ρ_1 more closely for the same t, but for any given r in practice there will always be some t at which Eq. (6.39) fails. The late-time condition further implies that the behaviour of the ρ_a curve at short times is dependent on ρ_1 as well so that the smaller the value of ρ_1 the earlier does Eq. (6.39) cease to be applicable. Conversely, if the early-time formula for ρ_a corresponding to Eq. (6.39) is used, it will fail at some stage when t is sufficiently large for given values of r and ρ_1 and the approach of the ρ_a curve at the right-hand side will not be asymptotic to the second-layer resistivity. Similar situations arise in frequency soundings when data are expressed as ρ_a at the low-frequency or high-frequency end.

The above brief discussion should indicate some of the complications that arise in electromagnetic soundings. For a fuller account the reader is referred to the excellent treatise of Kaufman and Keller [138].

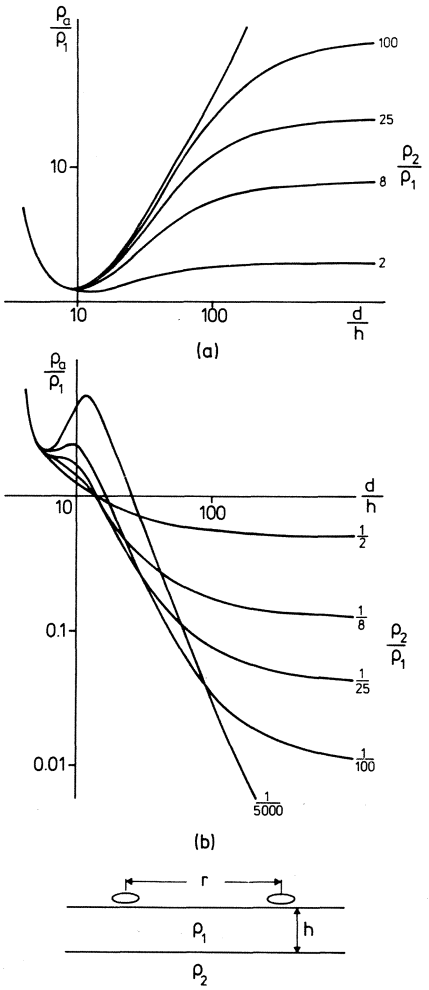

Fig. 6.37 ρ_a curves over a two-layer earth in transient-field sounding.

In transient-field soundings we can define a 'diffusion depth' analogous to the penetration or skin depth of Eq. (6.32) by

$$\delta = \left(\frac{2t\rho}{\mu}\right)^{1/2} = 503.3(t\rho)^{1/2} \tag{6.41}$$

The maximum measuring time must be such that δ is greater than the thickness of any layer sounded. If δ is much smaller than the thickness of a particular layer no information can be obtained of the layers below as the currents will not have diffused below the layer in question during the duration

of the measurement. As in frequency sounding the condition on δ is not a serious limitation in practice.

6.15 NATURAL-FIELD METHODS

6.15.1 The telluric method

It has been known for a long time that electric currents of different kinds are flowing through the ground producing a potential difference between two points. Some of these currents are artificial, caused by electric railways, power lines, etc., while others may be natural, e.g. those due to the self-potentials of sulphide ores. Besides these local phenomena creating potential differences in limited regions there are currents caused by astronomical phenomena, such as the solar electron streams, the rotation of the earth, etc., which cover extremely large areas. These currents flow in vast sheets involving the entire surface of the earth and are therefore called telluric currents, from Tellus, the Earth Goddess in Roman mythology.

The telluric electric fields are of the order, say, of $10\,\mathrm{mV\,km^{-1}}$ and are constantly fluctuating in direction and magnitude at any point.

If X and Y are two orthogonal components of the telluric field at any point on the earth's surface they are related to the components X_0 and Y_0 simultaneously existing at a base point by the simple linear equations:

$$\begin{aligned} X &= aX_0 + bY_0 \\ Y &= cX_0 + dY_0 \end{aligned} \tag{6.42}$$

The matrix $\|ab/cd\|$ is characteristic of the electric properties of the surface down to a depth of a few kilometres at the point under consideration.

On account of the linear form of Eq. (6.42) the relationships between the time derivatives of components are exactly the same as those between the components themselves. In the telluric method the variations $\Delta X, \Delta Y$, $\Delta X_0, \Delta Y_0$ in successive intervals of, say, 10 s are determined from the simultaneous photographic records of the potential difference between two X and two Y electrodes at the field point and two X_0 and two Y_0 electrodes at the base.

It is easy to see that the successive normalized components $\Delta X_0/\Delta R_0$ and $\Delta Y_0/\Delta R_0$ where $\Delta R_0^2 = \Delta X_0^2 + \Delta Y_0^2$ define a circle while the vectors $\Delta X/\Delta R_0$ and $\Delta Y/\Delta R_0$ define an ellipse. The ratio of the area of the ellipse to that of the circle at the base is a convenient measure of the relative telluric disturbance at the field point.

Telluric currents obey the ordinary laws of electricity. Thus, for instance, if E is the electric field at a point, then $E = \rho j$ (Ohm's law) where j is the associated current density. Consider a vertical contact between two media (Fig. 4.35) and

imagine a telluric current density in the plane of the figure. If $\rho_2 < \rho_1$, then j normal to the contact will increase as we approach the contact from medium 1 and by Ohm's law E, that is $\Delta R/\Delta R_0$, will also increase. Conversely, $\Delta R/\Delta R_0$ will fall as we approach the contact from medium 2. E must therefore be discontinuous across the contact. Actually its variation is very similar to that of ρ_a in Fig. 4.35 or 4.36.

In general, all geologic structures which tend to disturb the uniform flow of the telluric current sheets, e.g. salt domes, folded strata, buried ridges, etc. will cause telluric anomalies. Detailed descriptions of the telluric method will be found elsewhere [142–144].

6.15.2 The magneto-telluric method

This is in a sense a further development of the telluric method. Briefly, it involves a comparison of the amplitudes and phases of the electric and magnetic fields associated with the flow of telluric currents.

The measurement of the electric field is relatively easy as indicated above, but that of the magnetic field is considerably more difficult since we are concerned with frequencies around 1 Hz and down to 0.001 Hz or less. It is necessary to have coils with highly permeable cores and some 20–30 000 turns of wire. Such a coil can be about 2 m long and weigh some 30–40 kg. The voltages induced in the coil are detected by very high gain, low-noise amplifiers and the entire equipment for the measurement of the magnetic field can easily weigh some 70 kg or thereabouts.

Consider a telluric current sheet of frequency v flowing in an electrically homogeneous earth of resistivity ρ. The depth penetration of such a sheet, that is, the depth at which the current density in it falls to 1/e of its value at the surface, is given by Eq. (6.32).

It can be shown that the surface electric and magnetic fields are horizontal and orthogonal and that their amplitudes, E_x and H_y, are related by the same equation as Eq. (6.29). Some workers prefer to consider the quantity measured by a magneto-telluric coil in air as the flux density B_y (Wb m^{-2} or T) rather than as the magnetizing force H_y(A m^{-1}). Since $B_y = \mu_0 H_y$ we get

$$\rho = \frac{\mu_0}{2\pi v}\left|\frac{E_x}{B_y}\right|^2 \tag{6.43}$$

Here E_x is in V m^{-1}. Expressing E_x in mV km^{-1} and B_y in nT we can write (6.43) as

$$\rho = \frac{0.2}{v}\left|\frac{E_x}{B_y}\right|^2 \tag{6.44}$$

where ρ is in Ωm. The phases of E_x and H_y(or B_y) differ by $\pi/4$, H_y lagging behind E_x.

If, then, we measure E_x and H_y at a definite frequency the first indication of the non-homogeneity of the earth will be that the phase difference θ will not be

$\pi/4$. Secondly, ρ calculated from measurements at different frequencies will not be the same. However, we can always define an *apparent* resistivity ρ_a by Equation (6.43).

On determining ρ_a and θ as functions of frequency by actual measurements we obtain magneto-telluric soundings in a manner analogous to the electric soundings in Chapter 4 where, however, the current penetrates deeper because the electrode separation is increased.

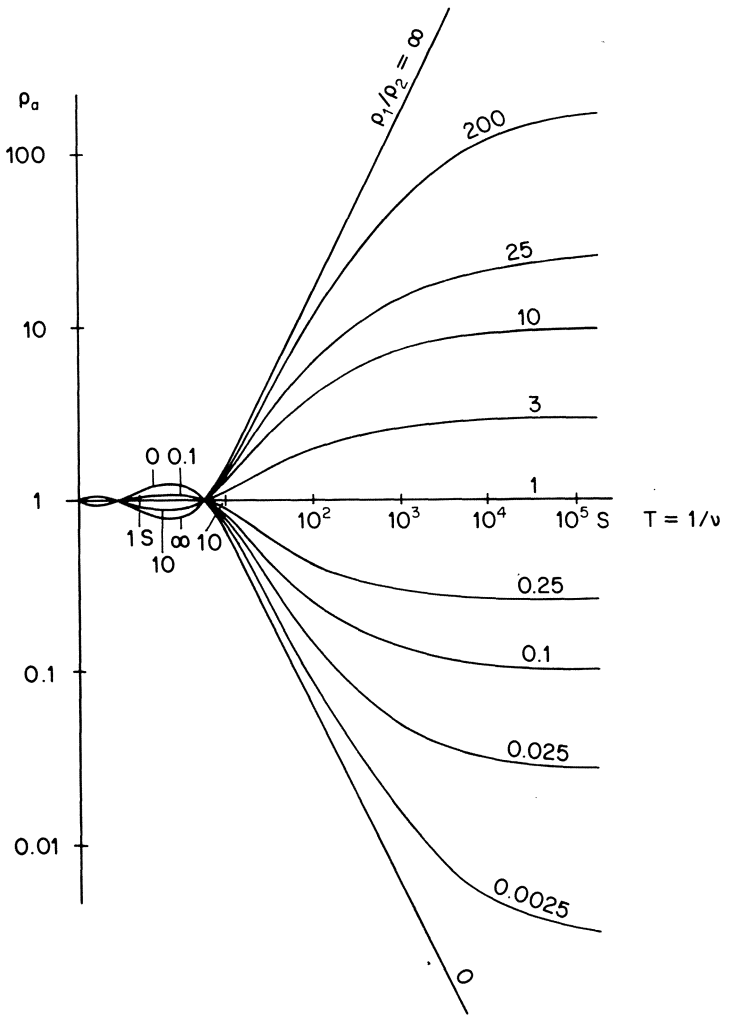

Fig. 6.38(a) Magneto-telluric sounding: ρ_a against $T(=1/\nu)$ on a two-layer earth. This figure and Fig. 6.38 (b) assume a first-layer thickness of 1 km and a resistivity of 1 Ω m.

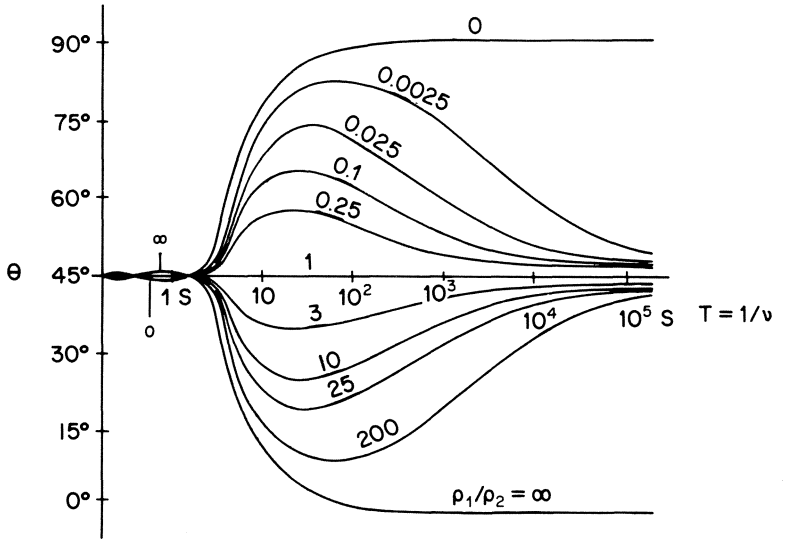

Fig. 6.38 (b) Magneto-telluric sounding: θ against $T(=1/\nu)$ on a two-layer earth.

Theoretical calculations of ρ_a and θ as functions of ν for a horizontally stratified earth have been made by Cagniard who has also given one of the classic accounts of this method [145].

Figs 6.38(a) and (b) show ρ_a and θ for a two-layer earth. The major application of this method in the future is likely to be in elucidating very deep structures. In fact, soundings down to several tens of kilometres, and even a couple of hundred kilometres, have already been claimed. The utility of magneto-tellurics in shallow prospecting is probably limited, but one possible application may be in some areas with highly conductive overburden. It should be noted that, with *a given source–receiver separation*, the d.c. resistivity methods are handicapped by the short-circuiting effect of a high-conductivity near-surface layer whereas the magneto-telluric (and similar but artifical source) methods can 'see' through the layer to the required depth if one chooses an appropriately low frequency.

The reader should not, however, be unduly optimistic about the possibilities of the magneto-telluric method from the above, because usually the scatter of the observed ρ_a values prohibits an unambiguous interpretation of the ρ_a versus ν curves. Furthermore, the principle of equivalence (p. 147) also applies here.

One of the basic assumptions in the application of the telluric methods is

that of uniformity of the fields ('plane wave approach'). There has been considerable discussion as to its validity but the fact that, in areas with uniform sedimentary strata, magneto-telluric data are repeatable and independent of time has been interpreted to mean that the fields are uniform. It has also been pointed out [146] that ρ_a may depend on the direction in which E and H are measured and therefore a correct interpretation of sounding graphs in some cases requires a tensor analysis of the ρ_a–v curves.

A good review of the theoretical and observational work in magneto-tellurics up to 1970 has been given by Keller [147] and the method has also been described in a coherent way in monographs by Porstendorfer [148] and Kaufman and Keller [149].

6.15.3 Afmag

Natural magnetic fields of all frequencies from very low to very high ones are reaching all points on the earth. The frequencies that are exploited in the magneto-telluric methods are below about 1 Hz. The corresponding energy comes from complicated interactions between plasma emitted from the sun and the earth's magnetic field. Above 1 Hz the energy of the natural electromagnetic fields seems largely to come from local and distant thunder-storms and man-made electrical disturbances. Depending upon local and seasonal variations the main part of their energy seems to be in the region of a few hundred Hz to a few kHz.

The space between the ionosphere and the earth's surface acts as a waveguide for these fields with the result that their vertical component is normally very small. Their amplitudes and directions tend to be random or rather quasi-random. Normally a search coil at any point will show a marked horizontal plane of polarization for these waves and a diffuse azimuth in that plane. However, in the vicinity of highly conductive bodies the plane of polarization tilts out of the horizontal while the azimuth becomes more definite, and the presence of the conductor is thereby revealed. Usually the field strength shows an inflection point above the conductor and is flanked on the sides by a maximum and a minimum (cf. Fig. 6.26).

The name AFMAG is derived from the fact that the fields picked up by the search coil are *a*udio *f*requency *mag*netic fields. On account of the relatively high frequency the coil weight need be only a fraction of that required in the magneto-telluric method. The tilt measurements are made for two different frequencies, one high and one low, and the response ratio 'low/high' provides a measure of the conductivity of the conductor. It will be seen from the discussion in Section 6.2.3 that if $S\cos\phi$ or α is used as a measure of the response such a ratio is greater than 1 for good conductors and less than 1 for bad ones.

6.16 AIRBORNE MEASUREMENTS

The airborne electromagnetic methods are adaptations of the ground systems described so far. A large number of modifications exist but the principal types may be summarized as follows.

6.16.1 Continuous wave systems (near-field)

6.16.1.1 Helicopter and wing-tip

In its typical version this system employs vertical, coaxial transmitter and receiver coils with the dipole axis parallel to the line of flight (cf. Fig. 6.17). The coils are often compact ferrite-core coils with a diameter of approximately 10 cm and are mounted about 10–20 m apart at the ends of a very rigid boom installed underneath a helicopter. The boom is carefully designed to minimize the motion of the coils relative to each other so that spurious signals in the in-phase component are eliminated.

The system is flown at a height of about 45–50 m and the in-phase and out-of-phase field components at the receiver are continuously registered (usually in parts per million of the primary field at the receiver) on the automatic recorder. Typical anomalies from subsurface conductors range from a few hundred to a thousand parts per million, and conductivities are estimated semi-quantitatively by the 'in-phase/out-of-phase' response ratio. The shapes of the anomalies can be visualized by the same type of arguments as for ground systems (p. 199 or p. 205).

The coils can also be mounted on the wing-tips of a small aircraft. In that case they are situated in the same vertical plane (instead of being coaxial as in the helicopter system) with their axes in the flight direction (Fig. 6.17).

The practical depth penetration of the two systems is of the order of 20–30 m below ground level (about 75 m below flight level).

6.16.1.2 Dual frequency phase shift method

The fixed-wing aircraft has certain advantages (longer range, higher survey speed, greater payload, etc.) over the helicopter. However, the desired constancy of the coil distance (less than about 1 cm in about 15–20 m) is difficult to achieve with the coils on the wing-tips.

Now, the out-of-phase component of an electromagnetic field is a purely secondary phenomenon and is very nearly independent of the variations in the coil distance. In the phase shift system only the out-of-phase component is recorded at two frequencies, one low (e.g. 400 Hz) and one high (e.g. 2300 Hz). The response ratio 'low/high' instead of the ratio 'in phase/out-of-phase' provides a measure of the conductivity of the anomalous body.

The transmitter is at the aeroplane while the receiving coil is towed behind in a 'bird' at the end of a cable, some 150 m long. The plane must be flown at a

height of at least 120–150 m in order that the bird may not hit the tree tops and get lost. Over undulating terrain and in 'bumpy' weather it might be necessary to fly it still higher. Measurements of the in-phase component are out of the question due to the violent movements of the receiver bird.

On account of the comparatively high altitude at which such a system must be flown the signals of deeper conductors fall to very low levels and are often no greater than the signals due to lateral variations in surface conductivity. In this sense, then, the depth penetration of the method is poor unless the system is flown very low, which however is rarely possible for technical reasons.

The out-of-phase component of very good conductors varies little with frequency and such conductors cannot be detected by phase-shift measurements alone. This disadvantage may, however, be offset in areas with conducting host rock and/or overburden because good conductors may collect the phase-displaced currents induced in the rock or the overburden and give rise to a measurable electromagnetic field. (This is often the reason behind the strong imaginary component anomalies obtained over grounded rails, metal pipes etc., which, in themselves, represent almost infinitely good conductors to electromagnetic prospecting systems. Their intrinsic imaginary component responses are zero.)

The system has been discussed in more detail elsewhere [150, 151].

6.16.1.3 Rotating field

This method was devised in Sweden with a view to overcoming the disadvantages of the systems under Sections 6.16.1.1 and 6.16.1.2, namely the small depth penetration and, in the second, also the inherent impossibility of in-phase measurements.

The transmitter of the system consists of two coils, one horizontal and the other vertical, fed by alternating currents of the same amplitude and frequency but with a phase difference of 90°. The primary electromagnetic field at any point in the surrounding space is therefore a rotating elliptically polarized field.

The receiver consists likewise of two mutually perpendicular coils and is placed at a distance, say a, from the transmitter (Fig. 6.39). Along the line joining the transmitter and receiver in Fig. 6.39 the ellipse of polarization is a circle.

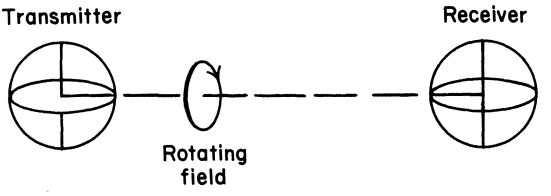

Fig. 6.39 Principle of the airborne rotating field system.

It is evident that if m is the dipole moment of either transmitting coil the primary field acting on the horizontal as well as the vertical receiving coil has an amplitude m/a^3. The voltages induced in the two receiver coils can be balanced against each other after shifting the phase of one of them, say that of the vertical coil voltage, by 90° so that the reading of a meter or a recorder is normally zero.

When a secondary field from a subsurface conductor acts on the receiver there is an imbalance since the field will in general affect the two receiver coils unequally. The net voltage in the vertical coil is added (after shifting its phase by 90°) to the voltage in the horizontal coil. The resultant has two components, one in phase with the primary field in the horizontal receiving coil and the other out of phase with it. These unbalanced components can be measured in terms of volts, amperes, tesla or any other convenient unit by suitably calibrating the deflection of the recorder connected to the receiver. It is, however, preferred to express them as percentages of the primary voltage induced in either receiver coil when a has a standard, specified value a_0.

It will be noticed that in contrast to the other airborne systems the rotating field system does not require a direct cable connection between the transmitter and the receiver. Also, the balance of the primary fields is independent of the variations in a since these affect the fields on both receiver coils in exactly the same way. It is therefore possible to place the transmitter in one aeroplane while the receiver is towed on a short cable (about 15–30 m) from another plane, flying in tandem at a distance of about 150–300 m. Such a system can be flown fairly low (about 60–80 m) and is not so dependent on weather conditions as the dual frequency system with its long towing cable.

Theoretically, the low flight height and the large transmitter–receiver distance should combine to give the system a depth range of more 100 m below ground [152, 153]. However, the response of superficial horizontal conductors (e.g. soil layers) to the rotating field system is often very complicated, masking the anomalies of deeper conductors and making the interpretation difficult. According to tests in areas of high surface conductivity (East Africa) the practical penetration of the rotating field system in these areas appears to be only slightly better (40–50 m) than that of the wing-tip systems [154] although in areas of low surface conductivity (e.g. some pre-Cambrian shield areas) the predicted figure may perhaps be approached.

6.16.1.4 Turair

This system is based on the principle of the Turam ground method. It is a semi-airborne system in that the transmitter (large loop or long cable) is laid on the ground and traverses are made across it with the two Turam receiver coils towed from an aircraft. The corrections for the normal ratios are made by graphically removing the 'regional' gradient that appears on the profile record. They could, of course, be made by computation if the aircraft position with

respect to the transmitter is known, but this would probably add greatly to the cost of the method. The interpretation of the anomalies obtained is exactly as in ground work, a remark that applies to all airborne work.

6.16.2 Afmag

This system (Section 6.15.3) has also been adapted to airborne work [155]. A receiver consisting of two mutually perpendicular search coils, each making an angle of 45° with the horizontal, is towed behind an aircraft with the axes of the coils and the line of flight in the same vertical plane.

The flight direction is chosen perpendicular to the geologic strike in the region. Since the natural magnetic fields tend to be polarized perpendicular to the geologic strike the mean polarization vector then lies in the vertical plane through the flight line and the coil axes. If the vector has a tilt α from the horizontal, the voltages induced in the coils are proportional to $\cos(45° - \alpha)$ and $\cos(45° + \alpha)$. The difference of the two voltages is recorded in such a way that the deflection of a pen is approximately proportional to α. As in the ground AFMAG the tilt is recorded at two frequencies (150 and 510 Hz) so that relative estimates of the conductivities of anomalous conductors can be made.

6.16.3 Radiophase (VLF)

This is a system for combined H- and E-mode measurements from the air on the VLF band (Section 6.8). A block diagram of the system is shown in Fig. 6.40.

There are two electrical antennae, one vertical ('whip') and the other horizontal ('trail antenna'). Similarly there are two mutually orthogonal coils for picking up the magnetic field.

Since the amplitude of the vertical component (E_z) of the electric vector **E** is 100–200 times larger than that of the horizontal component (E_x), small departures from orthogonality between the two antennae cause large variations in the amplitude of the total signal picked up by the trail antenna. Hence a direct measurement of the ratio between the whip and the trail antenna voltages in out of the question. What is measured instead is the amplitude of the component of the trail antenna voltage that is 90° out-of-phase with the whip antenna voltage, in terms of the latter's amplitude. It is easily seen that the measured quantity is $(E_x \cos\gamma/E_z)\sin\phi$ where ϕ is the phase difference ($\approx 45°$) between E_x and E_z, and γ is the instantaneous angle made by the trail antenna with the horizontal. It is not possible to relate this quantity to the tilt of the polarization ellipse without a knowledge of γ, and since this is impossible in airborne work, we cannot calculate an apparent resistivity. The method is therefore only of semi-quantitative use for mapping conductivity variations.

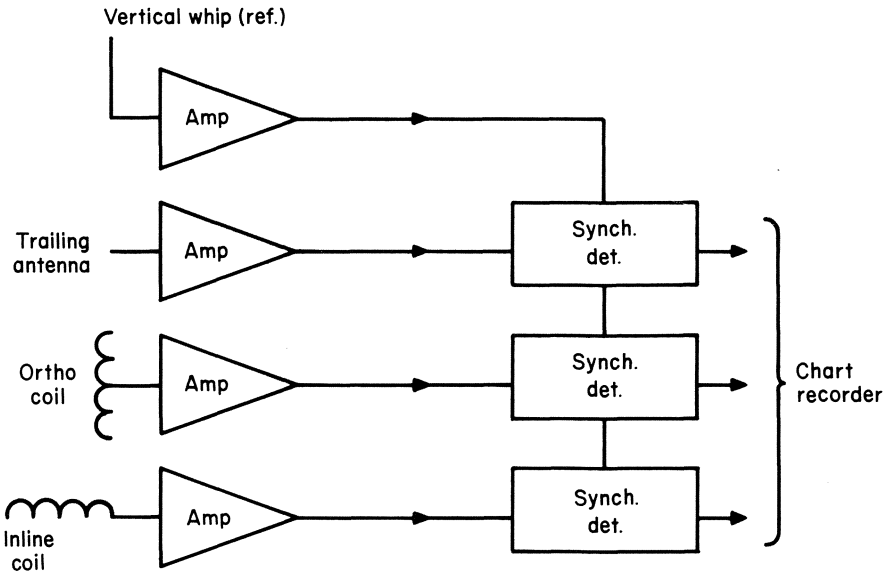

Fig. 6.40 Block diagram for the airborne Radiophase VLF system.

The *H*-mode measurements are carried out in a similar manner. The components of the signals in the two coils that are 90° out of phase with the whip antenna voltage are measured and r.m.s. summed to give a measure of the amplitude of the secondary magnetic field. The measure is not theoretically exact.

As in ground work, the scope of the airborne VLF method is primarily limited, on account of the high frequency involved, to the mapping of superficial conductivity variations, e.g. of soils, moraine cover, permafrost areas etc.

6.16.4 Airborne transient field (INPUT)

Transient pulses have been employed for aerial electromagnetic work. In the *in*duced *pul*se *t*ransient (INPUT) system a wire is strung from the aircraft nose, around each wing-tip and beneath the tail, thus forming a large loop transmitter. Pulses of some 2 kW are sent through this horizontal loop at a repetition rate of several hundred times a second. A small 'bird' towed on a cable about 150 m long houses the coil which receives the secondary decaying signal from the ground. The signal is sampled (between the transmission pulse) at several pre-selected decay times (channels) from about 100 μs after current cut-off to about 2000 μs. The results can be expressed as ratios of the signals on different channels to, say, the signal in channel 1. A rapid decay (low late-

channel signal) indicates a poor conductor in the ground, a slow decay a good conductor.

An advantage of the INPUT system is that since measurements are made during the time the primary field is cut off, the transmitter–receiver orientation geometry is of no consequence. Hence the sensitivity of the (broadband) receiver can be increased very considerably so that extremely weak signals can be detected. However, at the same time, we have no absolute reference for the strength of the recorded signals. In this the INPUT system resembles purely phase-measuring systems above. It is, in principle, a multifrequency phase-measuring system, the later sampling times corresponding to successively lower frequencies. The lowest frequency that is effectively exploited cannot, of course, be less than the repetition rate of the pulse and the highest cannot be greater than the reciprocal of the time (after power cut-off) at which channel 1 is sampled.

The details of an INPUT instrumentation have been described by Gupta Sarma *et al.* [156] and some theoretical aspects have been treated by Verma [157].

6.17 NOTE ON THE DESIGN OF ELECTROMAGNETIC COILS

The design of electromagnetic coils is a matter of some complexity. Here only the barest principles can be touched upon. We shall consider only flat, air-cored, circular coils (diameter D) for the moving source–receiver system of Fig. 6.16 with a separation (r) of 60 m, and derive the requirements for power (P), diameter (d) of winding wire, number of turns (N) in a coil, etc.

Suppose the r.m.s. noise field strength in an area (due to atmospheric disturbance, man-made disturbance etc.) is $1.6 \times 10^{-8}\,\mathrm{A\,m^{-1}}$ within a bandwidth of 0.1 Hz around a measuring frequency $f = 3600$ Hz. If a signal-to-noise ratio of 250:1, say, is desired at the receiver the r.m.s. normal field (H_0) at it should then be $4 \times 10^{-6}\,\mathrm{A\,m^{-1}}$.

Now for the coil configuration in question

$$H_0 = \frac{NIA}{4\pi}\frac{1}{r^3}(\mathrm{A\,m^{-1}}) \tag{6.45}$$

where I is the r.m.s. current in the transmitter (area A). For a coil of reasonable size, say $D = 0.60$ m, we get then

$$NI = 39 \text{ ampere turns} \tag{6.46}$$

Suppose the transmitter is wound of Cu wire (resistivity ρ, density δ). Then if R is the resistance of the coil

$$P = RI^2 = \frac{\rho N \pi D I^2}{(\pi d^2/4)} \quad (\mathrm{W}) \tag{6.47}$$

$$M = \delta N D \pi \frac{\pi d^2}{4} \text{ (kg)} \tag{6.48}$$

Hence

$$P = \rho\delta(NI)^2 D^2 \pi^2 / M \tag{6.49a}$$

Putting $\rho = 1.7 \times 10^{-8}\,\Omega\,\text{m}$ and $\delta = 8930\,\text{kg m}^{-3}$ we get

$$P = \frac{0.82}{M} \text{ (W)} \tag{6.49b}$$

Usually $R \ll 2\pi f L$ where L is inductance of the coil so that if V is the r.m.s. supply voltage

$$I = \frac{\sqrt{2}V}{2\pi f L}$$

which can be written as

$$N = \frac{\sqrt{2}V}{2\pi f N I} \frac{N^2}{L} \tag{6.50}$$

The value of N^2/L can be found from inductance tables (e.g. Jahnke and Emde, *Tables of Functions*, Dover, New York, pp. 86–89). For a flat coil of length, say, 60 mm and $D = 0.60$ m we find from the tables that $N^2/L = 8.33 \times 10^5$.

Suppose $V = 30$ V; then for the example under consideration $N = 40$ turns. If we choose $M = 1$ kg it is then easily shown that $d = 1.4$ mm. For a coil of this weight (and the remaining specifications as above) we then get $P = 0.82$ W from (6.49b). Also, it follows that $L = 1.9$ mH and $Q = 2\pi f L/R = 52$.

It is preferable to construct *the receiver coil* with the same specifications as the transmitter coil. The minimum induced voltage in the receiver for the above example will be $1.3\,\mu\text{V}(-\text{i}\omega\mu_0 N H_0 A)$ before tuning the coil, and $52 \times 1.3 = 66\,\mu$V after tuning.

Here we have only considered the principles. For a discussion of the optimum design of electromagnetic sensing coils the reader may be referred to an article by Becker [158].

PROBLEMS

6.1 Make a qualitative sketch of the variation of R and α in Fig. 6.4 with frequency for a single-turn loop.

6.2 What is the spurious real-component anomaly in the following cases involving moving source–receiver systems?

(a) Horizontal coils 40 m apart; receiver coil elevation 5 m above the transmitter coil.

(b) Transmitter coil axis vertical, receiver coil on the same level but with its axis making a small angle θ with the vertical.

(c) Vertical coaxial coils (= collinear horizontal dipoles) with elevation difference h ($\ll$ coil separation r_0).
(d) Vertical coplanar coils, elevation difference h. Is it necessary to impose the restriction $h \ll r_0$?

6.3 What is the diagram for a single-turn loop corresponding to Fig. 6.21?

6.4 Sketch the E_x field along a profile in the x direction in Fig. 6.25 and the H_y field along the y direction in Fig. 6.27.

6.5 Measurements made on a frequency of 5000 Hz on a 5 m wide, long ore vein ($\rho = 2\,\Omega$m) are to be simulated in a laboratory model on a scale of 1:1000. The ore lies under a 10 m thick overburden ($\rho = 100\,\Omega$m). As ore only zinc plates of 1 mm thickness ($\rho = 60\,n\Omega$m) are available. (a) How many zinc plates should be used to simulate the ore? (b) What frequency should be used in the laboratory experiment? (c) What should be the thickness and resistivity of the material simulating the overburden?

6.6 Two groups with identical systems of the type in Fig. 6.16 (coil separation for each = 40 m) are measuring in the same area along separate parallel lines. What is the closest permissible distance between the lines if one group is not to disturb the readings of the other group by more than 1% of the normal field at the receiver?

6.7 A horizontal-loop system (60 m coil distance) gave an anomaly of + 4% in the real component and 0% in the imaginary component at a very low frequency, when placed with its midpoint above a thin, sheet-like, steeply dipping magnetic conductor. When the frequency was increased to 500 Hz the anomalies obtained were: real, − 4.1% imaginary, − 11.7%.
(a) Estimate the depth to the upper edge of the sheet and its resistivity/thickness ratio using Fig. 6.20.
(b) What anomalies would be obtained on this magnetic conductor if the frequency were 1000 Hz?
(c) That part of the anomaly on 500 Hz which is due to induced currents is to be simulated in laboratory model experiments. The laboratory equipment has a coil separation of 100 mm. Only one frequency (f) and only Zn plates are available for the model experiments. What thickness of Zn plates should be used?

7

Seismic methods

7.1 INTRODUCTION

The seismic methods of geophysical exploration utilize the fact that elastic waves travel with different velocities in different rocks. The principle is to initiate such waves at a point and determine at a number of other points the time of arrival of the energy that is refracted or reflected by the discontinuities between different rock formations. This then enables the position of the discontinuities to be deduced.

The importance of the seismic methods lies above all in the fact that their data, if properly handled, yield an almost unique and unambiguous interpretation.

The incomparably most important application of seismic methods is in oil prospecting but they are also employed for site investigations in building large-scale structures and other civil engineering projects like determination of depth to bedrock, delineation of sand and gravel deposits, detection of water-bearing fracture zones etc.

7.2 ELASTIC CONSTANTS AND WAVES

7.2.1 Hooke's law

The basis of the seismic methods is the theory of elasticity. The elastic properties of substances are characterized by elastic moduli or constants which specify the relation between the *stress* and the *strain*. A stress is measured as force per unit area. It is compressive (or tensile) if it acts perpendicular to the area and shearing if it acts parallel to it. A system of compressive stresses changes the volume but not the shape of a body, one of shearing stresses changes the shape but not the volume.

The strains in a body are deformations which produce restoring forces

Table 7.1 Elastic constants

Substance	Bulk modulus ($Nm^{-2} \times 10^{-10}$)	Shear modulus ($N\,m^{-2} \times 10^{-10}$)
Marbles and limestones	3.7–5.7	2.1–3.0
Granites	2.7–3.3	1.5–2.4
Sudbury diabase	7.3	3.7
Ohio sandstone	1.25	0.61
Iron (wrought)	16.0	7.7
Iron (cast)	9.5	5.0
Glass (crown)	5.0	2.5
Quartz (fibre)	1.5	3.0

opposed to the stresses. Tensile and compressive stresses give rise to longitudinal and volume strains which are measured as the change in length per unit length or change in volume per unit volume. Shearing strains are measured as angles of deformation. It is usually assumed that the strains are small and reversible, that is, a body resumes its original shape and size when the stresses are relieved.

Hooke's law states that the stress is proportional to the strain, the constant of proportionality being known as the elastic modulus or constant. The law is not strictly true and more general stress–strain relationships have also been introduced in applied seismology, notably by Ricker [159, 160]; yet Hooke's law carries us a long way in the theory of elasticity.

The two moduli of immediate interest for the study of the elastic waves in the earth are the bulk modulus (k) and the shear modulus (μ). Their values for some rocks and for a few common substances will be found in Table 7.1. The bulk modulus is also referred to as the *incompressibility* and the shear modulus as *rigidity*. Liquids and gases offer no resistance to deformation so that for them $\mu = 0$.

7.2.2 Elastic waves

If the stress applied to an elastic medium is released suddenly the condition of strain propagates within the medium as an elastic wave. There are several kinds of elastic waves:

(1) In the longitudinal, compressional or P waves the motion of the medium is in the same direction as the direction of wave propagation. These are, in other words, ordinary sound waves. Their velocity is given by

$$V_P = \left(\frac{k = 4\mu/3}{\rho} \right)^{1/2} \tag{7.1}$$

where ρ is the density of the medium.

(2) In the transverse, shear or S waves the particles of the medium move at right angles to the direction of wave propagation and the velocity is given by

$$V_S = \left(\frac{\mu}{\rho}\right)^{1/2} \tag{7.2}$$

It is evident that $V_P < V_S$. Shear waves do not propagate through liquids and gases ($V_S = 0$).

Shear waves can be polarized in such a way that the particles oscillate along a definite line perpendicular to the direction of wave propagation. In geophysical context these polarized waves are known as SH and SV waves depending upon whether the particle motion is horizontal (parallel to the ground surface) or vertical (perpendicular to the surface).

(3) If a medium has a free surface there are also surface waves in addition to the above two which are 'body waves'. In the *Rayleigh* waves the particles describe ellipses in the vertical plane that contains the direction of propagation. At the surface the motion of the particles is retrograde with respect to that of the waves. The velocity of Rayleigh waves is about 0.9 V_S. Rayleigh waves are very commonly referred to as *ground roll.*

Analogous to Rayleigh waves are the *Stoneley* waves which are also surface waves but propagated under rather special conditions along the interface between two media.

(4) Another type of surface waves the *Love* waves. These are observed when the S wave velocity in the top layer of a medium is less than in the substratum. The particles oscillate transversely to the direction of the wave and in a plane parallel to the surface. The Love waves are thus essentially shear waves. Their velocity for short wavelengths is equal to V_S in the upper layer and for long wavelengths V_S in the substratum.

(5) In addition to the above there are *guided* waves. These are confined to a particular layer (e.g. water layer, coal seam etc.) and their velocity depends upon the wavelength and layer thickness, as well as on density and elastic constants.

The frequency spectrum of body waves in the earth extends from about 15 Hz to about 100 Hz; the surface waves have frequencies lower than about 15 Hz.

In applied seismology only the P waves are of importance as exploration tools. In principle, however, S waves could also be used but the difficulty is to get S waves of sufficient energy. Explosions, which are the common means of generating powerful elastic waves, produce predominantly, if not exclusively, P waves. These are converted in part to S waves on oblique reflection and although some work has been reported with such S waves they have not been put to any great use in applied geophysics.

Surface waves are incapable of giving information about structures at depth

Table 7.2 Elastic velocities ($m\,s^{-1}$)

	Compressional	Shear
Air	330	–
Sand	300–800	100–500
Water	1450	–
Glacial moraine	1500–2700	900–1300
Limestones and dolomites	3500–6500	1800–3800
Rock salt	4000–5500	2000–3200
Granites and other deep-seated rocks	4600–7000	2500–4000

and are of no avail in exploration geophysics. The interest attached to them, particularly the Rayleigh waves, is due to the fact that they constitute an unwanted signal on the seismic record which has to be suppressed to enhance the desired signals.

7.2.3 Velocities in rocks

Typical values for the velocity of P and S waves in some rocks are given in Table 7.2. The velocities are generally found to be greater in igneous and crystalline rocks than in sedimentary ones. In the sedimentary rocks they tend to increase with depth of burial and geologic age. Many empirical attempts have been made to represent this increase. For shales and sands Faust [161] finds that

$$V = 46.5(ZT)^{1/6}\,m\,s^{-1} \tag{7.3}$$

where Z is the depth in metres and T the age in years.

Seismic velocities can be measured in the field as well as in the laboratory on samples of rocks. Several methods for laboratory determinations using magnetostrictive pulses, ultrasonic pulses, resonances etc. have been developed [162–164]. Well velocity surveys are also a common method of obtaining information on velocities. A seismometer (Section 7.3.2.2) is lowered into a borehole, a shot is fired close to the surface and the travel time to the seismometer is noted. The seismometer is then lifted a short distance and another travel time is measured. From the difference in these times the average velocity in the material between the two positions of the seismometer can be calculated. We shall revert to this topic in later sections.

Seismic velocities often show anisotropy in stratified media; the velocity parallel to the strata is generally greater than that normal to them by an amount of the order of 10–15%.

7.2.4 Reflection and refraction (Snell's law)

The surfaces in a medium on which the wave motion is the same at all points are called *wavefronts*. If the wavefront surface is plane we talk of a plane wave. The normal to a wavefront at any point is the direction of a *ray* and is the instantaneous direction of wave propagation at that point. In a medium of constant seismic velocity the rays are straight lines. In inhomogeneous media the rays are curved. It is often more convenient to describe wave propagation by means of rays rather than wavefronts.

When seismic rays fall on the interface between two media they may be reflected or refracted. In addition a mode conversion occurs, that is, an incident P wave, for example, is reflected or refracted partly as a P wave and partly as an S wave (Fig. 7.1). If θ is the angle made by any ray with the normal to the interface then Snell's law states that $(\sin\theta)/V = \text{constant}$ where V is the velocity of the wave in question. Thus, with θ_1 as the angle of incidence of the P-wave ray shown we have

$$\frac{\sin\theta_1}{V_{P1}} = \frac{\sin\theta_2}{V_{P1}} = \frac{\sin\theta_3}{V_{S1}} = \frac{\sin\theta_4}{V_{P2}} = \frac{\sin\theta_5}{V_{S2}} \tag{7.4}$$

Corresponding equations exist if the incident wave is an S wave.

At normal incidence ($\theta_1 = 0$) an incident P wave produces no S waves and an incident S wave produces no P waves.

7.2.5 Huygen's principle and diffraction

Rays are primarily useful for describing wave propagation in homogeneous media or when waves hit an interface whose radius of curvature is large in

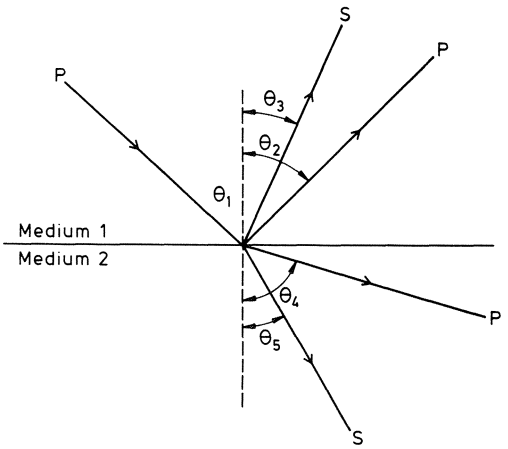

Fig. 7.1 Snell's law.

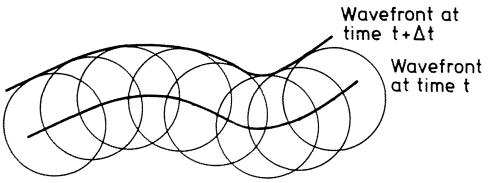

Fig. 7.2 Huygen's principle.

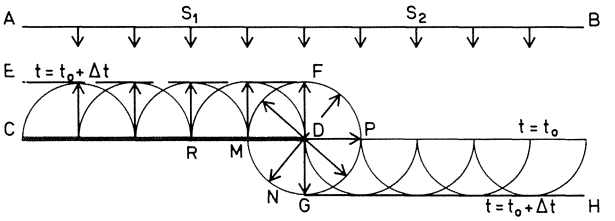

Fig. 7.3 Diffraction at an edge. *CD* is a thin layer in an otherwise homogeneous medium.

comparison with the wavelength λ as in Fig. 7.1 where, the interface being plane, its radius of curvature is infinite. When an obstacle in the path of a wave has a curvature radius that is small compared with λ we must turn to Huygen's principle for a description of wave propagation.

Huygen's principle states that every point on a wavefront may be considered to be a secondary source that emits waves travelling radially outward from the point. The envelope of the wavefronts of all such spherical waves defines the position of the primary wavefront at a later instant (Fig. 7.2). Only that part of the envelope which is in the direction of the wave advance is considered in Huygen's construction. Reflection, refraction and Snell's law can be derived from Huygen's principle but, more importantly, it describes correctly the situation when a wave hits a small obstacle, an edge or any similar discontinuity in a medium.

Consider, for example, a plane wavefront impinging at time $t = t_0$ on the horizontal layer *CD* that terminates abruptly at *D* (Fig. 7.3). The envelope, at time $t_0 + \Delta t$, of all spherical waves emanating from points on *CD* is the reflected plane wavefront *EF* at this time. To the right of *D* the downward travelling wavefront has reached the position *GH* at $t = t_0 + \Delta t$ since there is no obstacle in its path. In addition to *EF* and *GH* there is a wavefont *MFPGN* that emanated from *D* and has now reached this position. This represents the *diffracted wave* travelling outwards from *D* and it should be noted that it is present even in the segment *GNM* which is in the geometrical shadow of the primary wave. A point S_1 on a surface *AB* receives two waves, the reflected one

RS_1, and the diffracted one DS_1. At a point S_2 only the diffracted wave DS_2 is received.

Since for seismic waves λ is of the order of 100 m or more, many geologic features give rise to diffracted waves. We shall consider diffraction again in a later section.

7.2.6 The seismic pulse

7.2.6.1 Group and phase velocities (dispersion)

We have hitherto tacitly assumed that the elastic disturbance consists of a sinusoidal wave of single frequency v with no beginning or end in time. The velocity V of this wave is obtained from the distance travelled by any surface of constant phase (e.g. maximum compression) in unit time. This is the *phase velocity* of the wave.

However, when a charge is detonated on land or in water a seismic pulse of a certain shape and finite duration ('breadth') is generated. According to Fourier's theorem (Appendix 13) the pulse can be considered to consist of an infinite number of sinusoidal waves of infinitesimally close-spaced frequencies from zero to infinity. If the velocity of a wave depends upon frequency each of these component waves travels with its own velocity with the result that the initial form of the pulse is distorted as it propagates in the medium. More specifically, the pulse broadens with increasing time, that is, with the distance travelled (Fig. 7.4).

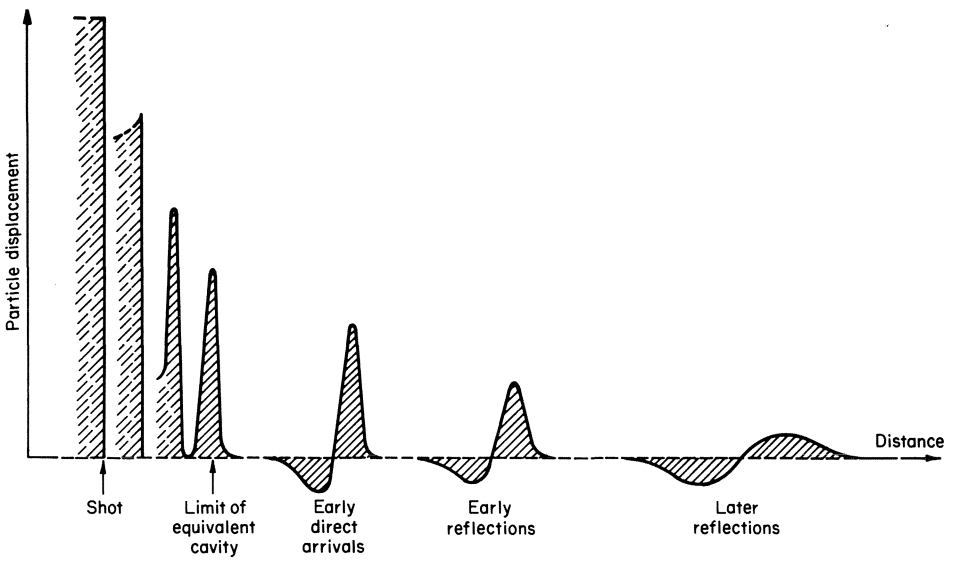

Fig. 7.4 Broadening of a seismic pulse.

Although there is no specifiable point on the pulse (peak, trough or any other) which travels with a constant velocity, the pulse as a whole (or rather its centre of energy) travels with a constant velocity U (provided energy is not absorbed on the way). This is the *group velocity* of the elastic disturbance.

The phenomenon of the distortion of pulse form during propagation due to a dependence of phase velocity on frequency, and through it on the wavelength λ since $V = \nu\lambda$, is called *dispersion.* Between V and U we have the relation

$$U = V - \lambda \frac{dV}{d\lambda} \tag{7.5}$$

The dispersion of seismic body waves (P or S) is too small to be detected in practice. It is, however, appreciable for surface waves.

7.2.6.2 Attenuation

Seismic waves are reduced in amplitude as they are propagated through the earth due to three factors: geometrical divergence, partial transmission and reflection at acoustic boundaries and absorption of energy in the medium of transmission.

The influence of the first factor is well known and can be allowed for, e.g. at large distances from the source spherical waves reduce in amplitude in inverse proportion to the distance travelled.

The transmission and reflection coefficients of a geological interface are functions of the elastic contrast between the layers in contact. In principle, a comparison of the amplitudes of the reflected pulses should provide some information about such contrasts, and the attenuation suffered.

It should be noted that elasticity theory based on Hooke's law involving reversible stresses and strains does not admit of any attenuation due to absorption of energy, in contrast to electromagnetic theory which predicts such attenuation for electromagnetic waves (Chapter 6). The attenuation due to geometric divergence only means that energy is spread over larger and larger areas with distance from the source but none of it is lost. However, it is observed in practice that seismic waves do lose energy through absorption in rocks with the amplitude A very nearly following the (empirical) equation $A = A_0 \exp(-\delta\nu x/V)$ where δ is the logarithmic decrement and x the distance. Typical values of δ for earth materials in bulk would be around 0.02–0.03. We see from this that high-frequency waves are attenuated more quickly than low-frequency ones.

Two absorption mechanisms, viscosity and solid friction, have been suggested. Both mechanisms are observed in rocks but it seems that solid friction generally predominates. The presence of water apparently increases the decrement and at the same time leads to a predominance of viscous damping.

Work on the absorption of seismic waves has been reported by Datta [165], where also references to several other papers on the subject will be found.

7.2.7 Basic appearance of a time–distance graph

It will be convenient now to visualize how a seismic recording might look. Fig. 7.5 shows the graph of the arrival times of the principal waves in the sample case of a uniform overburden on top of a substratum. The arrival times of the direct P wave and the ground roll or Rayleigh wave (GR) increase in direct proportion to the distance and therefore lie on the respective straight lines. The arrivals of the wave reflected at the overburden–substratum interface lie on a curve (hyperbola, as we shall see later). From a certain distance (marked $2h \tan \theta_c$) onwards the disturbances produced by the refracted wave travelling along the interface arrive earlier than the reflections. Again, from a certain distance (marked x_c) they overtake the direct wave. These 'refracted arrivals' also lie on a straight line since the increments in their travel time are in direct proportion to the increments in distance.

In plotting Fig. 7.5 we have disregarded S waves. Similarly, waves reflected repeatedly between overburden base and ground surface are also disregarded. In an actual situation there will, in general, be several layers and these may in

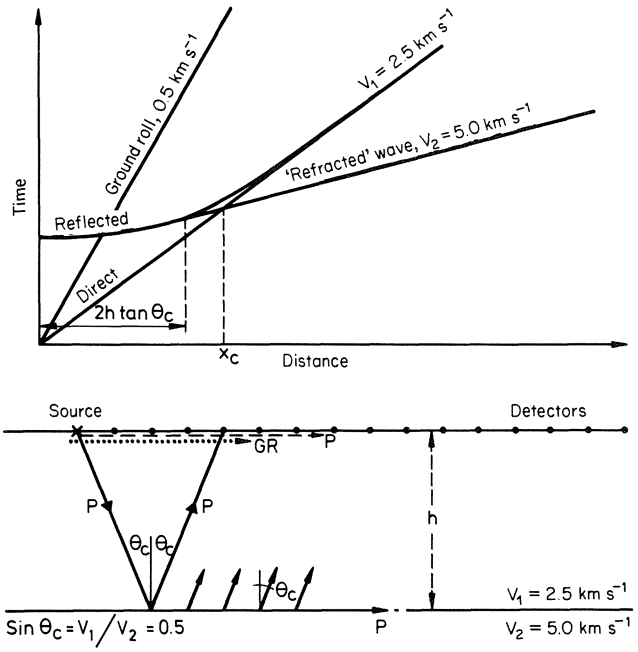

Fig. 7.5 Basic appearance of a time–distance graph.

addition be inhomogeneous. We shall consider these and other complications later but it is worth noting here that the time–distance graphs then obtained, although much more involved, nevertheless show a basic similarity with the graph in Fig. 7.5.

7.3 THE REFLECTION METHOD

7.3.1 Principles

7.3.1.1 Reflection hyperbola

The depth to an interface between two rock formations can be determined by measuring the travel time of a seismic wave generated at the surface and reflected back from the interface. The energy of P as well as S waves is reflected partly as P and partly as S waves. If the reflected and the incident waves are of the same kind (both P or both S) the ordinary law of reflection applies, namely, angle of incidence = angle of reflection, as Eq. (7.4) shows.

It is generally assumed that the observed reflections are only P–P reflections. This assumption is justified as a rule since near the shot point most of the explosion energy is transmitted as P waves.

It is easily deduced from Fig. 7.6 that if V is the uniform velocity above the reflecting horizon the reflected wave arrives at G after a time

$$t = \frac{2}{V}\sqrt{(h^2 + x^2/4)} \tag{7.6}$$

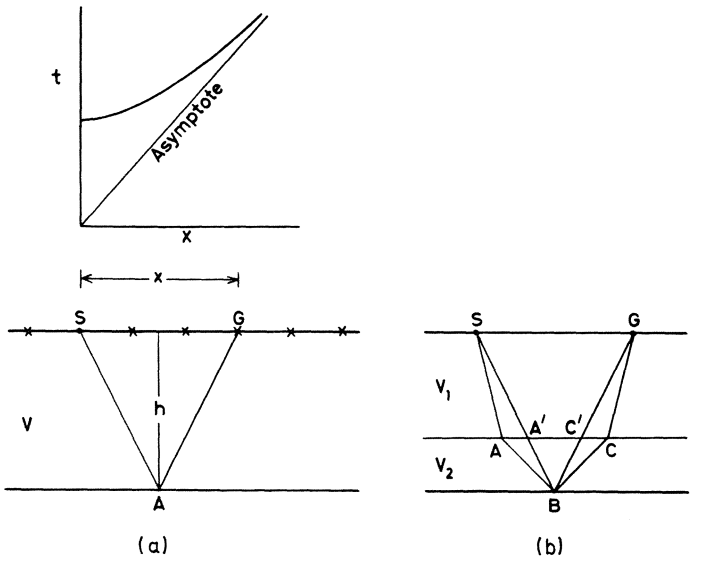

Fig. 7.6(a) Reflection hyperbola. (b) Reflection of refracted rays.

so that

$$h = \tfrac{1}{2}\sqrt{(V^2t^2 - x^2)} \tag{7.7}$$

Either equation shows that the x–t curve is a hyperbola convex towards the x axis and with the t axis as the axis of symmetry. The line through $x = 0$, $t = 0$ with a slope $1/V$ is its asymptote. The time t in Eq. (7.6) is referred to as the two-way time (TWT).

Only one branch of the hyperbola is shown in Figs 7.6(a) and 7.5. The other branch will correspond, of course, to the arrivals at detectors left of S. Almost without exception time–distance graphs in reflection seismics are plotted with

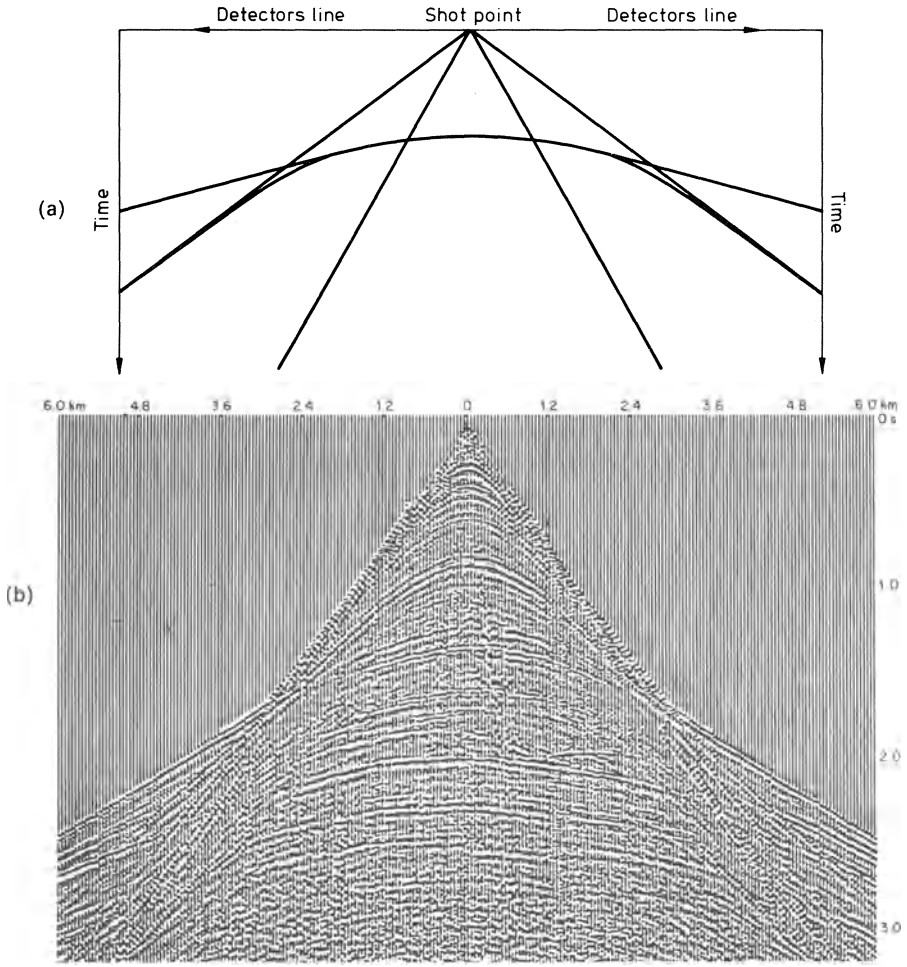

Fig. 7.7(a) Fig. 7.5 as a time section. (b) An actual time section.

the time axis downwards. Using this convention and adding complementary halves to the graphs in Fig. 7.5 we obtain Fig. 7.7. A display of this type is called a *time section.*

If there are two or more reflecting horizons which separate layers with different velocities it is generally the practice to disregard the refraction of rays. A ray such as $SABCG$ (Fig. 7.6(b)) is replaced by the ray $SA'BC'G$. This is justified in as much as the rays may be considered to be almost vertical on account of the small shot–detector separation (in comparison with the shallowest interface of interest) that is used in reflection seismics. The 'reflection spread' in Fig. 7.7 is considered to extend on either side of the source to a maximum distance of $x_m = 2h \tan \theta_c$. It will be seen in Section 7.4.2 that $\sin \theta_c = V_1/V_2$ so that

$$x_m = \frac{2(V_1/V_2)}{[1-(V_1/V_2)^2]^{1/2}} h \tag{7.8}$$

It is instructive to compare Fig. 7.7(a) with an actual field record (Fig. 7.7(b)) without bothering at this stage about the details of seismic data acquisition.

7.3.1.2 Diffraction hyperbola

We have seen in Section 7.2.5 that a point of abrupt change in seismic properties of the ground is a secondary source of waves. If we consider now Fig. 7.8 and imagine a primary source exactly above the edge at D it follows that in addition to the reflected arrivals to the right of S, which give the hyperbola of Eq. (7.6), there will also be diffracted arrivals, whereas to the left of S there will be diffracted arrivals but no reflections. The arrival time t_d of the diffracted wave is easily seen to be

$$t_d = \frac{h}{V} + \frac{(x^2+h^2)^{1/2}}{V} \tag{7.9}$$

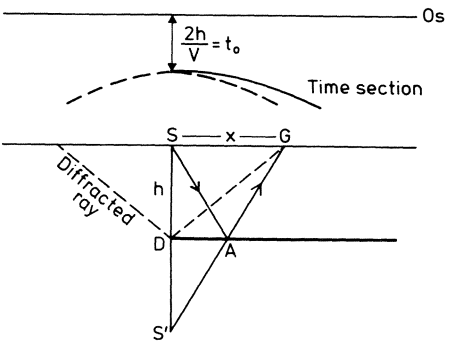

Fig. 7.8 Diffraction hyperbola (dashed).

in which the first term is the time for the primary wave to go from S to D, where it is diffracted, and the second term the time for the diffracted wave to go from D to G. Equation (7.9) is also an equation for a hyperbola, termed the *diffraction hyperbola.*

The length of the path travelled by the diffracted wave is $SD + DG = S'D + DG$, if S' is the image of S in the reflector, while the path length for the reflected wave is $SA + AG = S'A + AG = S'G$ and obviously $S'D + DG > S'G$. Hence t_d is always greater than the reflection time t given by Eq. (7.6), except at the source ($x = 0$) where $t_d = t$.

The time section corresponding to Fig. 7.7(a) for the case in Fig. 7.8 is shown in the upper part of the latter figure.

7.3.1.3 Normal-incidence time section

It was mentioned in Section 7.3.1.1 that the incident and reflected rays SB and BG in Fig. 7.6(b) can be considered to be almost vertical provided the detector is very close to the source. If S and G are coincident the two rays will be exactly normal to the reflector. If we now associate a source with each of the detectors and plot the respective TWTs below each detector, the graph will obviously be a horizontal straight line instead of the curved hyperbola in Fig. 7.7. If the reflector, instead of being horizontal, is dipping or curved only the reflected ray corresponding to an incident ray that hits an interface normally will arrive back at the detector. Whatever the path (straight, broken or curved) that the incident ray takes in reaching the point of reflection, it will bounce back and retrace exactly the same path *if the incidence at the reflector is normal.* (This is an illustration of what is known as a reciprocity theorem.)

The concept of normal incidence enables us to construct time sections when the geological structure is more complicated than in Fig. 7.6 or 7.8. The principle is illustrated in Fig. 7.9 where a curved reflector is shown and the material above it is assumed to have constant seismic velocity. In this case the TWT of a normal-incidence ray such as S_1A_1 will be proportional to the path length $2S_1A_1$. It is plotted at B_1 below S_1, the length S_1B_1 representing the TWT on some suitable scale. For a source–detector combination at S_2 there will be two normally incident rays, namely, S_2A_2 and S_2A_3. Their TWTs are

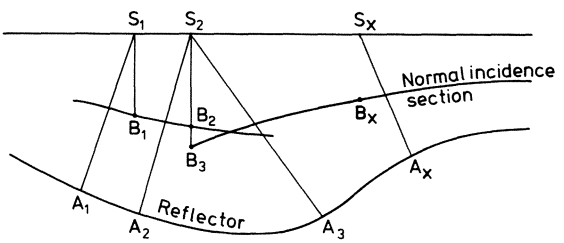

Fig. 7.9 Construction of normal-incidence section over curved reflector.

plotted at B_2 and B_3. Continuing in this way we obtain the normal-incidence time section shown. Since the diagram is only intended to illustrate the principle, reflections other than those at the curved reflector have been disregarded.

For a complicated multilayer situation with varying velocity the refractions at each interface must be taken into account to trace the path of a ray and the TWT for it must be calculated with due regard to the path length and velocity in each layer (Problem 7.1).

7.3.1.4 Acoustic impedance and partition coefficients

While an elastic disturbance is passing over a point in a homogeneous medium the stress at the point is varying with time and the point itself is moving from its equilibrium position with a certain velocity. The magnitude of the ratio 'stress/point velocity' at any instant is a constant characteristic of the medium and is called its *acoustic impedance* for the disturbance concerned (P, S etc.). It can be shown (Appendix 12) that the acoustic impedance, denoted by Z, is the product of the density ρ of the medium and the *phase velocity* V of the disturbance.

Consider now a plane P wave in medium 1 (acoustic impedance Z_1) falling at normal incidence on the interface with medium 2 (acoustic impedance Z_2). The wave is then partly reflected and partly transmitted. At normal incidence there is no change of direction of the transmitted wave, that is, no refraction (cf. Eq. (7.4)). If the *displacement amplitude* of the incident wave is 1.0, the displacement amplitude of the reflected wave is

$$R = \frac{Z_2 - Z_1}{Z_2 + Z_1} = \frac{\rho_2 V_2 - \rho_1 V_1}{\rho_2 V_2 + \rho_1 V_1} \tag{7.10a}$$

in the direction of the *reflected* wave. The amplitude of the transmitted wave is

$$T = 1 - R = \frac{2Z_1}{Z_2 + Z_1} \tag{7.10b}$$

where R and T are known as reflection and transmission coefficients. Together they are known as partition coefficients since they determine the partitioning of the energy of the incident wave, although the coefficients as given by Eqs (7.10a) and (7.10b) are for amplitude and not energy.

It should be noted that for reflection to occur $\rho_2 V_2$ and $\rho_1 V_1$ must differ from each other while for refraction it is sufficient that V_2 and V_1 differ. R is negative if $Z_2 < Z_1$. In such a case an incident compression is reflected as dilatation and vice versa. If R is positive a compression is reflected as a compression and a dilatation as a dilatation.

In general, $R < 1$ but if $Z_1 = 0$, we have $R = 1$, in which case all the incident energy is reflected. This is almost the case, for example, for a wave falling on the surface of the sea from a source in air. If $Z_2 = 0$, then $R = -1$ and, again all

energy is reflected, but a compression as a dilatation and vice versa. An example is a wave arriving at the surface of the sea from a source in the water.

Table 7.3 gives some typical reflection coefficients. Many factors like porosity, water content, degree of lithification etc. affect the acoustic impedance of rocks. In a sedimentary column ρ and V generally increase with depth due to compaction and the acoustic impedances in various layers tend to become more like each other so that R decreases, with the result that the reflections from deeper interfaces are generally weaker than those from shallower ones. In addition there are transmission losses in the pulse energy due to geometrical divergence and absorption.

7.3.1.5 Superposition (convolution)

A seismic record is primarily a record of the amplitude of the wave disturbance arriving at the detector at different times. Consider a sub-surface made of reflecting interfaces spaced so that the travel time between successive reflectors is a constant, τ. Suppose a seismic source produces a very sharp pulse (Fig. 7.10). Such a pulse is often called a spike. The reflection record will then look as in Fig. 7.11, where the relative heights are proportional to the original

Table 7.3 Typical seismic reflection coefficients (R)

Interface	Approximate R
Air over sea	1.0
Sea over limestone	0.65
Sea over boulder clay	0.45
Sea over recent sand/clay	0.3
Clays over gas sand, 500 m	−0.30
Sea-bed multiples	0.25
Sand/shale over limestone, 1500 m	0.20
10% change in acoustic impedance	±0.05

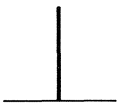

Fig. 7.10 A spike pulse.

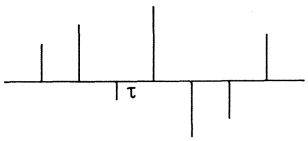

Fig. 7.11 Reflections of a spike from various reflectors.

spike height and to the various reflection coefficients. A medium that exhibits this proportionality is said to be linear. However, the ideal situation of Fig. 7.10 is never obtained in reality, not least because the seismic source pulse is not a 'spike'.

Now consider a more realistic source pulse shown in Fig. 7.12(a). It will be sufficiently accurate for our purpose to characterize this pulse by a series of uniformly spaced ordinates $0, -4, -12, -8, 40, 16, -24, -8, 0$ in arbitrary units. In other words we consider the pulse to be made up of a succession of spikes or impulses following each other at equal intervals of time. If the pulse is reflected from an interface with an ideal reflection coefficient 1 the ground disturbance as a function of time will be exactly a replica of the pulse (assuming the ground is a linear medium and the pulse undergoes no change of shape in propagation). Suppose there is an interface 1 with reflection coefficient 0.5. On

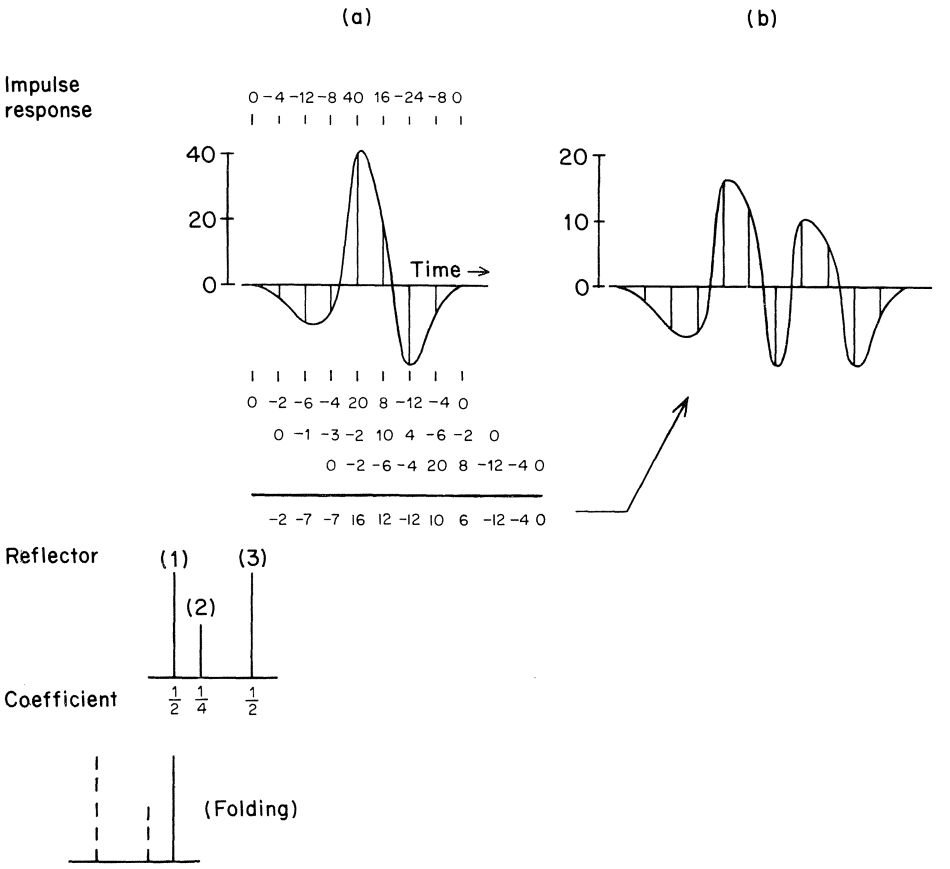

Fig. 7.12 Superposition and convolution.

reflection from this, the arriving pulse will produce half as much disturbance, which is written as the series $0, -2, -6, \ldots$, in Fig. 7.12(a).

The ground disturbance due to a reflection from another interface, 2, one half time unit 'deeper' than interface 1 (that is, $V/2$ depth units apart from 1) will start one time unit later (since the outward going pulse has to travel to and back from interface 2 in being reflected from it). Suppose the reflection coefficient of interface 2 is 0.25. Then a series of ordinates $0, -1, -3, -2, 10, 4, -6, -2, 0$ displaced one time unit in relation to the earlier series $0, -2, -6, \ldots$, will represent the ground motion due to this reflection. Similarly a third reflector one time unit deeper than interface 2 and having, say, a reflection coefficient 0.5, will produce a disturbance displaced two units in time. Adding (i.e. superposing) the disturbances we see that the resultant ground disturbance will be represented by the pulse in Fig. 7.1(b) with sampled ordinates $0, -2, -7, -7, 16, 12, -12, 10, 6, -12, -4, 0$ (or more stringently expressed, by the ordinates series which we may use to reconstruct a first approximation of the pulse form).

Exactly the same result can be obtained if, instead of superposition, we use the following procedure. The string of reflection coefficients (1), (2) and (3) is folded back on itself (convolved, cf. the aptly named genus of plants *convolvulus*) and slid past in discrete steps of one time unit, across the series $0, -4, -12, \ldots$, etc. For each position of the string we multiply each of the three reflection coefficients by the pulse ordinate of this series found directly above that coefficient, and then add the three results together. We obtain again the series $0, -2, -7, \ldots$. This procedure is known as convolution and, as seen, its outcome is exactly the same as that of superposition.

The final appearance of a seismic record is, of course, also influenced by multiple reflections, diffractions, refractions, the change of pulse in transmission etc. but, mainly, the record is the convolution of a basic wavelet with the long string ('log') of all the various reflection coefficients in the ground.

The procedure of convolution using discrete evenly spaced 'samples' can be mathematically written as follows. Let a denote the series of reflection coefficients in the reverse order to which they occur and b the pulse series (in the forward order). Then the pth term in the final series c is given by

$$c_p = \sum_{m=0}^{p} a_m b_{p-m} \tag{7.11}$$

An important condition for the application of Eq. (7.11) is that the sampling interval must be uniform and the same for both a and b. It will be noticed that in the example of Fig. 7.12, the interval is not uniform in the folded (or the original) series of reflection coefficients. Before applying Eq. (7.11) it is therefore necessary in this case to insert a coefficient $a_2 = 0$ between the two dashed spikes of the folded series so that the series a in this case becomes the evenly spaced series $0.5, 0, 0.25, 0.5$. A reflector of coefficient 0 midway between

reflector 2 and 3 is implicit in the calculation of Fig. 7.12(a) for it will merely produce a row of zeroes.

We have already come across convolution in connection with the calculation of VES curves in Section 4.5.4.4. The mathematical formulation of the convolution procedure for continuous functions is indicated in Appendix 13.

7.3.1.6 Deconvolution

It is evident from Fig. 7.12(b) that the effect of convolving the seismic pulse with the reflection coefficient log is to broaden the seismic record. If the seismic record were to consist only of this and were free of unwanted signals (e.g. ground roll, direct waves, multiple reflections etc.) the object of seismic interpretation could be stated to be the recovery of the original log. This process is called deconvolution or inverse filtering and is illustrated below for the idealized example in Fig. 7.12.

Here the position is that the seismic record or its desired appearance, namely the series $c_0, c_1, \ldots, c_9$ ($c_0 = -2, \ldots, c_9 = -4$), is known. Further, it may be assumed that we know (or can find out from experiments) the pulse form $b_0, b_1, \ldots, b_7$ ($b_0 = -4, \ldots, b_7 = -8$) sent out by the source. The problem then is to determine the series $a_0, a_1, \ldots$, etc.

From Eq. (7.11) we note that

$$c_0 = a_0 b_0$$

Therefore $a_0 = c_0/b_0 = (-2)/(-4) = 1/2$.

$$c_1 = a_0 b_1 + a_1 b_0$$

Therefore $a_1 = (c_1 - a_0 b_1)/b_0 = [-7 - \frac{1}{2}(-12)]/(-4) = 1/4$.

$$c_2 = a_0 b_2 + a_1 b_1 + a_2 b_0$$

Therefore $a_2 = (c_2 - a_1 b_1 - a_0 b_2)/b_0 = [-7 - \frac{1}{4}(-12) - \frac{1}{2}(-8)]/(-4) = 0$.

$$c_3 = a_0 b_3 + a_1 b_2 + a_2 b_1 + a_3 b_0$$

Therefore $a_3 = 1/2$.

$$c_4 = a_0 b_4 + \cdots$$

Therefore $a_4 = 0$.

$$\cdots$$

$$c_9 = a_0 b_9 + \cdots$$

Therefore $a_9 = 0$.

Thus, we have recovered the series $a_0 = 1/2, a_1 = 1/4, a_2 = 0, a_3 = 1/2$, $a_4 = 0 \ldots$. The reader can verify the calculation of a_3 to a_9 from the above. It should be noted that $a_2 = 0$ is the 'missing' reflection coefficient already

mentioned. The coefficients from a_4 onwards are zero since there are no further reflectors.

In practice the seismic record contains unwanted signals and the source pulse is only inexactly known. Consequently, the above procedure is only of theoretical interest and more sophisticated ones have to be devised in practice.

Deconvolution is also used for the removal or suppression of unwanted signals from the seismic record. This aspect of inverse filtering is taken up later in connection with the processing of data.

7.3.2 Data acquisition

7.3.2.1 Seismic sources

(*a*) *Land sources.* The standard method of producing seismic waves on land is to explode a dynamite charge in a hole. Another commonly used explosive is ammonium nitrate. Explosive sources like Geoflex and Primacord (trade names) are explosive cords that can be buried in the ground at a depth of about 0.3–1 m in ploughed furrows, instead of in drill holes, but this needs soft ground. Attempts have been made to obtain the seismic energy by mechanical means. The Geograph or Thumper involves dropping a weight of about 3000 kg from a height of about 3 m and the records from some 30–50 shots at the same impact point are stacked together to enhance the signal. Instead of the freely falling weight a source known as the Dinoseis explodes a mixture of propane and oxygen in an expandable chamber driving the movable bottom plate of the chamber against the ground.

The energies produced by mechanical sources are not generally sufficient and the equipment is massive so that these methods have found only a limited application. One exception is the Vibroseis which falls in a class by itself on account of its continuous vibratory signal. It is treated separately later on in Section 7.3.5.

(*b*) *Marine sources.* A very considerable part of seismic reflection work nowadays is carried out on water which in this context implies work in water deeper than about 10 m needing sizeable ships (about 50 m in length).

The most widely used source in marine operations is the *airgun* which discharges highly compressed air into the water. PAR, Seismojet, Terrapak and Unipulse are the trade names of some of the sources of this type. Very similar to the Dinoseis land source are the *gas guns* Aquapulse and Deltapulse while Aquaseis and Maxipulse use small dynamite charges (200 g) or a long detonating cord (up to 100 m) respectively. The Vaporchoc uses superheated steam instead of chemically explosive gases.

Implosive sources (Hydroseis, Flexichoc) may be said to be the converse of airguns in that they initiate a pulse when the hydrostatic pressure of external water makes the walls of an adjustable evacuated chamber collapse on the sudden removal of the restraint keeping the walls apart.

Sources using electrical energy (Boomer, Pinger, Sono Probe, Sparkarray etc.) depend for their action on the sudden movement of a piston or a plate by a transducer device.

As will be seen there is a large variety of sources for marine operations. A technical description of them is beyond the scope of this book and the interested reader should refer to specialized literature for details [166].

7.3.2.2 Detectors

(*a*) *Land work.* In the early days seismic waves were detected by a mechanical seismometer which consisted, in principle, of a heavy mass suspended as a pendulum. The mass remained stationary on account of its inertia while the suspension frame moved with the earth. Such mechanical devices have now been completely replaced in applied geophysical exploration by small, lightweight electric detectors or geophones.

The simplest type is the electromagnetic geophone. A coil attached to a frame is placed between the poles of a magnet which, in turn, is suspended from the frame by leaf springs. The magnet acts as an inertial element while the coil moves with the earth. The relative motion of the coil and the magnet produces an e.m.f. proportional to the *velocity* of the earth's motion. Instead of the magnet being the inertial element the coil can be made the inertial element of the geophone. This latter type (Fig. 7.13) is probably the more common of the two in modern work. There is a large variety of geophones on the market, some of them weighing no more than 50 g.

The natural frequencies of electromagnetic geophones in reflection seismic work are usually between about 5 Hz and 30 Hz but high-resolution work may call for higher frequencies. If pulses arrive at a geophone in succession the oscillations set up by the first pulse will mask later pulses unless the geophone is damped in the meanwhile. The damping of modern geophones is usually electromagnetic. A critically damped geophone just fails to oscillate after responding to the arriving pulse by a peak displacement that decays gradually with time. The damping chosen in practice is usually 70% of the critical but although the geophone response for this case is an oscillating one, even the first 'overshoot' in the direction opposite to the initial peak response is only about 4.5% for this value of damping (cf. Fig. 7.13(b)). If v_0 is the natural frequency of the geophone the first overshoot occurs about $0.75/v_0$ seconds after a pulse has set the geophone oscillating. The geophone is therefore virtually in its rest position at $1/v_0$ seconds, assuming the pulse to be an ideal spike.

The interested reader will find the details of the theory of electromagnetic geophones in a paper by Dennison [167].

(*b*) *Marine work.* The detectors for marine work, called *hydrophones*, utilize the phenomenon of piezoelectricity that certain materials (e.g. quartz among the natural ones and barium zirconate or barium titanate among the synthetic ones) develop electrical charges when subjected to mechanical stress. The

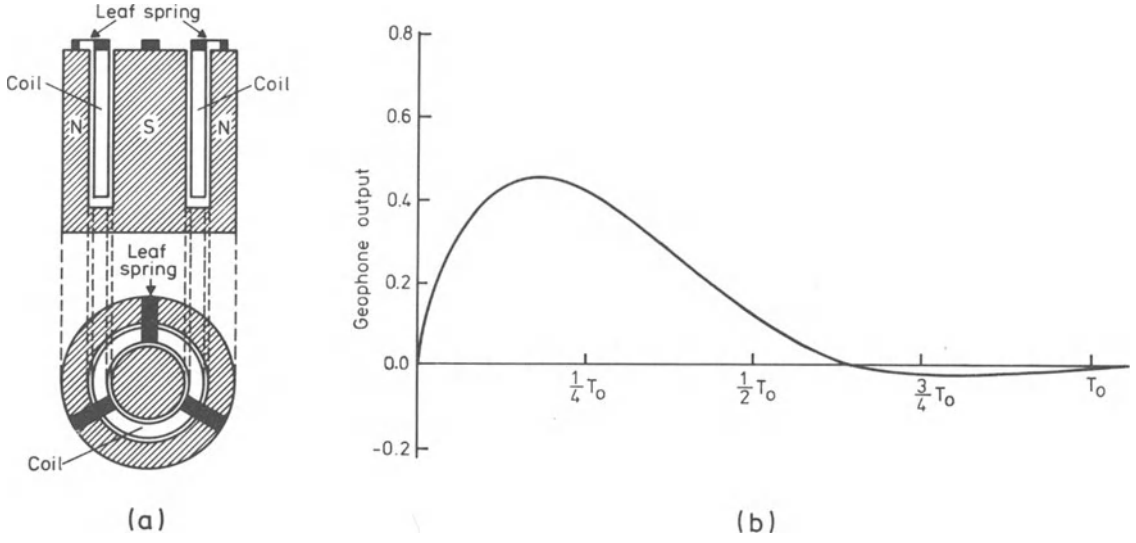

Fig. 7.13 (a) Geophone. (b) Damping of a geophone with overshoot.

material used in hydrophones is one of the synthetic ones, either in the form of a disc or in the form of a hollow cylinder. In the latter case the cylinder is closed at the ends by brass caps. When subjected to bending due to a pressure wave a piezoelectric disc will develop opposite charges on its two faces. Similarly, the outside and inside of a hollow cylinder will become oppositely charged. In either case the voltage between the surfaces is the output of the hydrophone and this is proportional to the pressure in the water in contrast to the output of geophones which is proportional to the velocity of the ground surface.

The output of a single piezoelectric element is extremely small and normally each hydrophone consists of up to fifty series-coupled elements.

7.3.2.3 Field procedure

(*a*) *Land operations.* When the area of investigations has been decided upon the first step in a seismic survey on land is to select locations for shot holes. If only shallow holes are needed they can be prepared by augering, but generally drilling by machine is necessary in deep exploration since the shot holes may be as much as a hundred or more metres deep. The depth of holes and weight of dynamite for the shot (a few grams to several kilograms) are important factors controlling the quality of the seismic record.

The next step is to plant the geophones firmly on the ground, which may sometimes entail burying them below the surface. In most of the work the geophones are placed along a straight line (called a profile) through the point on the surface vertically above the shot (epicentre). This procedure is known as profile shooting, but other shooting and geophone patterns adapted to particular problems are also used. Also, the detector points are not single geophones but groups of geophones, as we shall see in the next section.

The geophones are connected to the recording equipment by long cables, the amplifier gains and filters are appropriately set and when the recording system is started the shot is fired. The recording is stopped after a few seconds when the ground motion has substantially subsided. The moment of the shot is registered on the recording medium, now almost without exception a magnetic tape. We shall consider an outline of the complete data acquisition system in Section 7.3.2.7.

(*b*) *Marine operations.* In marine operations it is not feasible to 'plant' detector groups individually. Instead these are contained in a several kilometres long tube, called a *streamer*, that is reeled off and positioned in the water astern a ship, while the ship is still arriving in the area of work (Fig. 7.14). This is followed by the seismic source units. Shots are fired (about every 25 m) and recordings made while the ship is moving. This is necessary as otherwise the trailing streamer cannot be kept in position. Detailed monitoring of data quality is naturally not possible because of the ship's motion. Work proceeds generally on a 24 hr basis but not all the time can be spent in shooting.

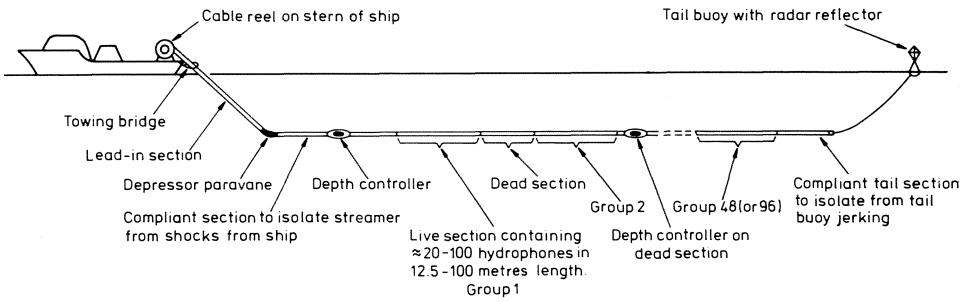

Fig. 7.14 Ship with streamer for marine seismic work. After [168].

A major problem in marine operations is to know the position of the ship at any time. Many navigation systems using radio waves, acoustic waves, satellite observations etc. are available. A knowledge of them is not necessary for our present purpose.

7.3.2.4 Detector arrays and noise suppression

(*a*) *Types of noise.* We have seen (e.g. Fig. 7.7) that the seismic record contains unwanted signals besides the reflections that we are seeking. All unwanted signal is called *noise.* Noise is classified into *coherent* (or correlated) and *incoherent* (uncorrelated or random).

Coherent noise is more or less similar at all detectors and is predictable from one detector to another. The dominant coherent noise in land work is due to surface waves while streamer noise is dominant at sea. Multiple reflections of the most varied kind (some are shown in Fig. 7.15) also constitute coherent noise, often called *signal-generated* noise. The most significant such noise in marine work is reverberation or ringing due to multiple reflections between the water surface and the sea bed.

Incoherent noise is completely unpredictable from one detector to another. Noise due to wind-shaking of geophones, microseisms, traffic (in some measure) etc. falls in this category. Instrumental noise is not a significant component any longer in the seismic record.

(*b*) *Frequency filtering.* Where the frequency content of the noise differs markedly from that of the signal it is possible to use frequency filters. The common practice in filtering is to cut off the low-frequency ground roll by a high-pass filter and the high-frequency wind noise by a low-pass filter.

Filters have a disadvantage, however, in that they necessarily distort the shape of the signal pulse. In particular the pulse is lengthened and, moreover, its phase is shifted, that is, characteristics such as crests and troughs are displaced in time as illustrated in Fig. 7.16 for a pulse that initially has the shape

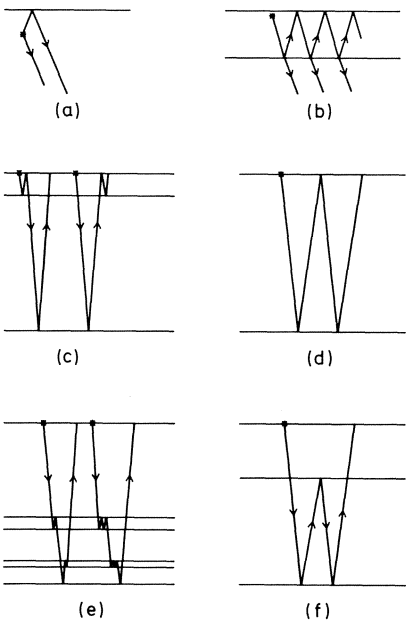

Fig. 7.15 Multiple reflections of a few different types: (a) ghost; (b) reverberation; (c) water-layer peg-leg; (d) simple surface multiple; (e) short-period internal; (f) long period internal.

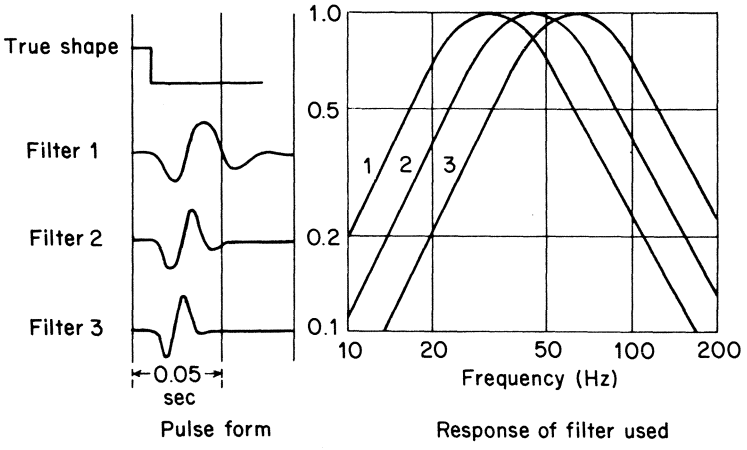

Fig. 7.16 Effect of filtering.

of a step. The result is that filters create interference patterns on the seismogram in addition to those created by the signals.

(*c*) *Multiple-detector arrays.* Besides filtering, another method is also used to eliminate or minimize the noise in seismic records. The detectors are placed along the profile with very close separations (e.g. 10 m) and the outputs of several adjacent detectors are added together and recorded as a single trace.

Consider a surface wave of some definite wavelength. If the geometry of the detector groups is appropriately selected the instantaneous motion of the ground due to the vertical component of this surface wave will be upwards at some detectors and downwards at others, so that the sum of the outputs will eliminate the surface wave from the record.

Actually, the effect of multiple arrays is more complicated than the brief description above would indicate. For one thing, it is unrealistic to consider only one isolated wavelength because seismic signals and noise in practice contain a continuous spectrum of waves. For this reason an array should be such that its length exceeds the longest wavelength in the surface waves and the detector spacing does not exceed half the shortest wavelength. Detector groups in land work can, however, be in other patterns than a straight line (e.g. a cross, star, etc.). The centroid of the group is treated as the observation point.

Broadly speaking it can be shown that if n inputs containing the same signal but random noise are added together the root-mean-square signal in the output is increased by a factor n (provided the n signals are coherent) whereas the r.m.s. noise is increased by a factor $\sqrt{n}$. Hence the signal-to-noise ratio in the output is improved by the factor $\sqrt{n}$. The coherent noise is supposed to be eliminated by the design of the array.

7.3.2.5 Vertical stacking and CDP stacking

The summation of signals from a number of similar input channels for the purpose of increasing the signal-to-noise ratio is known as *stacking*. There is a large variety of stacking layouts but we shall consider only two of these.

(*a*) *Vertical stacking.* In *vertical stacking* we have one shot point and one detector group, both of which are kept at fixed locations. The outputs of the group for a number of shots are added, either in the field or later, in the processing of data. The procedure is mainly used when the energy source is weak (e.g. weight dropping). It is time consuming in land work and the improvement after the first few stackings is small. For instance, a total of nine stackings will improve the signal-to-noise ratio (assuming noise to be random) by a factor of three but a further nine stackings will improve the ratio only by an additional factor of $\sqrt{2}$.

Vertical stacking in marine work rarely involves more than four records because at normal ship speed (about 10 km h^{-1}) the ship moves so far between

shots that the locations of detectors and shots cannot any longer be considered to be fixed as required by the concept of stacking.

(*b*) *CDP stacking. Common depth point* (CDP) or, as it is also called common reflection point (CRP), stacking was originally suggested by Mayne [169] to enhance weak reflections in relation to background noise, but it has also proved to be useful for reducing the signals from multiple reflections. The principle of CDP stacking can be seen from Fig. 7.17 where the dots represent the traces numbered 1 to 24 on a record and the crosses 1 to 6 are six successive shots. For each shot we record outputs from all 24 detectors along a line. As already mentioned each output usually represents the signal from a group of detectors at a location and not just a single detector. As a matter of convenience, the detector set-ups for the different shots are shown in Fig. 7.17 as displaced from each other. In reality, the line is one and the same.

Assuming a horizontal reflector we see that trace 24 on the record for shot 1 has the same reflection point as trace 20 for shot 2, trace 16 for shot 3, etc. The traces 24, 20, 16, 12, 8 and 4 for shots 1, 2, 3, 4, 5 and 6 respectively are collectively known as a *CDP gather*. Another CDP gather is, for example: shot 1–trace 21, shot 2–trace 17, shot 3–trace 13, shot 4–trace 9, shot 5–trace 5 and shot 6–trace 1. The number of traces in a gather is the *fold* of the stack. In the example shown we have a 6-fold stack. Other arrangements with more numerous channels and shots will, of course, give a higher stacking multiplicity. In general,

$$\text{fold} = \frac{\frac{1}{2}(\text{channel spacing} \times \text{number of channels})}{\text{shot spacing}} \tag{7.12}$$

A correction called 'normal moveout correction', to be discussed in Section 7.3.3.6, is applied to each CDP gather so that the reflection hyperbolas are straightened out, after which the six traces are summed to give one trace in the final stacked section (Fig. 7.18) corresponding to the depth point in question.

It should not be imagined from Fig. 7.17 that the whole line of detector groups is pulled two detector spacings to the left after each shot. In practice a sufficient number of extra detector groups (in this case eight) will have been laid out and appropriate connections to the amplifiers can be made simply by a switch, called a roll-along switch, without moving the detectors. It should be noted that one and the same detector has a different trace number for different shots in this description of CDP.

Although the CDP procedure implies a considerable degree of redundancy nearly all reflection seismic surveys now use it routinely.

7.3.2.6 Analogue recording and displays

(*a*) *Recording.* Although analogue recording for data acquisition – as distinct from data monitoring – may be said to be obsolete now, it is

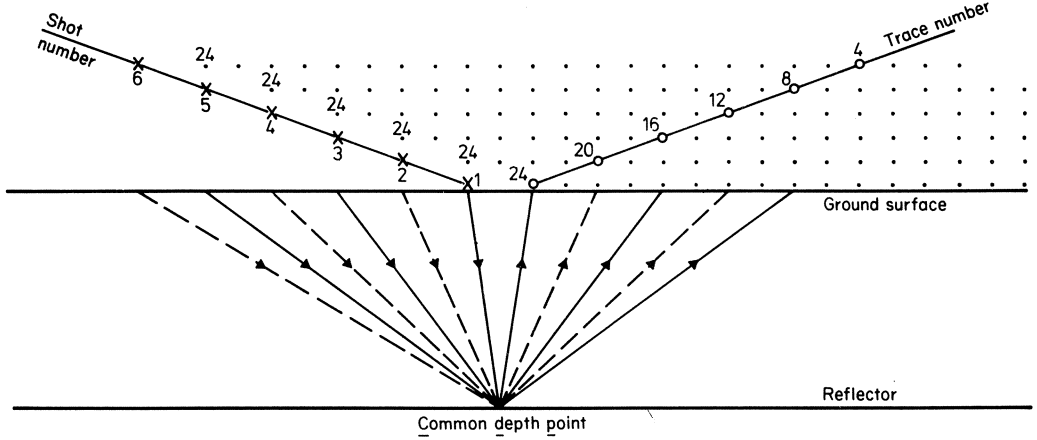

Fig. 7.17 Common depth point stacking.

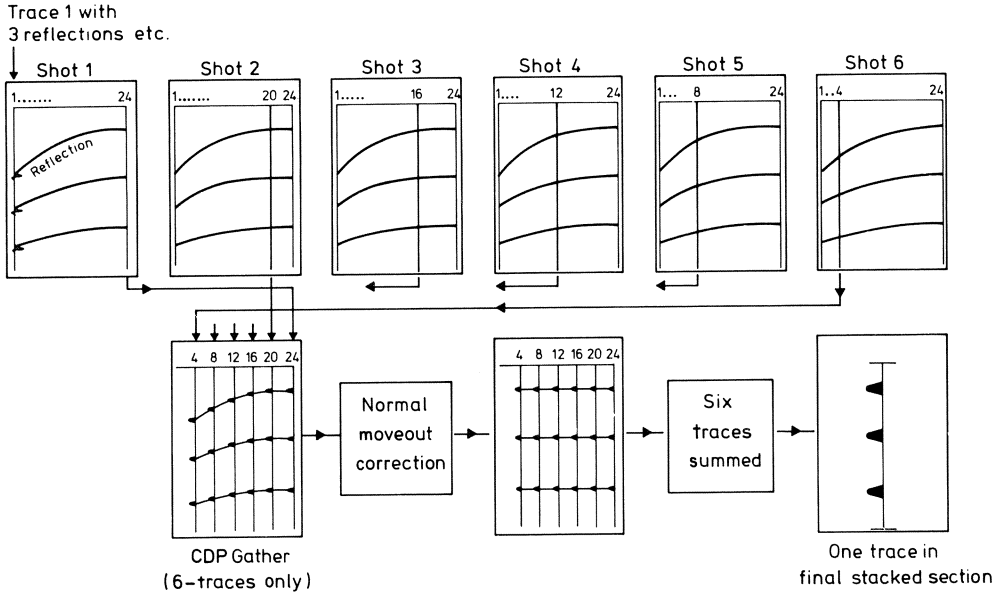

Fig. 7.18 Processing of CDP gather.

instructive to take a brief look at it, not least because even with modern digital recording the final display of a time section is always in analogue visual form.

In optical analogue recording the voltage from the geophone is fed into an amplifier, usually over a transformer for reasons of impedance matching, and is then passed on to a galvanometer. Most amplifiers are provided with automatic gain control and a number of high-pass and low-pass filters which allow a selection of the frequencies to be recorded.

The galvanometer deflections are registered by means of a mirror and light-source system on a continuously running photographic film. A single film may carry signal traces from as many as 48 geophones. The record is called a *seismogram.*

Vertical time lines, generally running across the entire width of the film, are superposed on the record. These are generated by a light beam which passes intermittently through a slot in a rotating disc whose speed is accurately controlled by a suitable device such as a tuning-fork-driven oscillator. Events on a seismogram can be read to a millisecond.

Magnetic analogue recording uses a magnetic tape instead of the photographic film as the recording medium, the galvanometers being replaced by recording heads, one for each trace. The variations of the geophone output are recorded as corresponding variations of the magnetization intensity of the tape.

(*b*) *Display.* The seismic record (whether on photographic paper or on a magnetic tape) consists of wiggles. Part of a typical reflection seismogram recorded on photographic paper is shown in Fig. 7.19. A wiggle on a single trace may represent a reflected pulse or ground movement due to other pulses

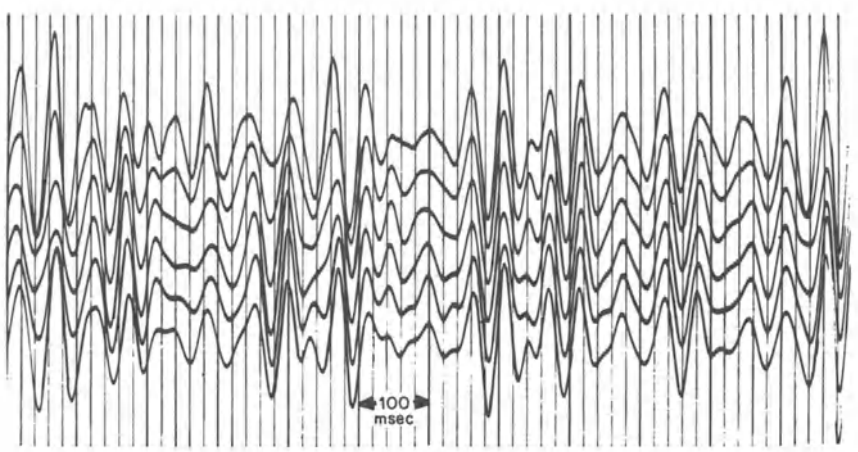

Fig. 7.19 Reflection seismogram.

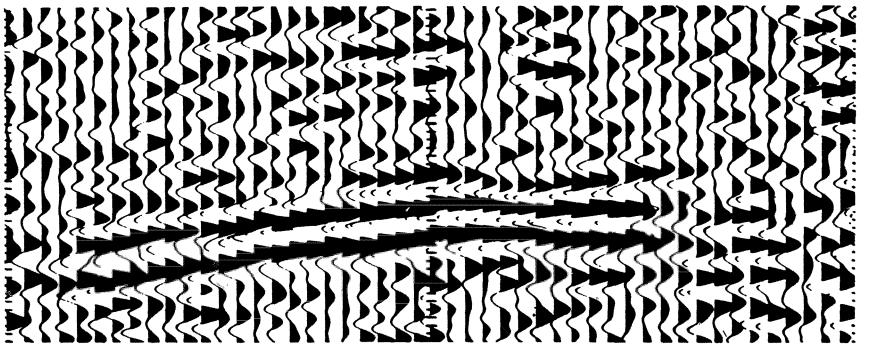

Fig. 7.20 Variable area (VAR) display.

or noise and there would be no means of distinguishing a signal if only one trace were recorded. However, these are unlikely to be exactly in phase at all the geophones, whereas a pulse reflected from a lithologic interface arrives at the various geophones approximately at the same time, as the geophones are close to each other. Therefore, the reflection signals are recognized by the lining-up of the crests and troughs on the adjacent traces across the entire record. The lining-up is almost straight for the later reflections, but for the earlier reflections the pulses may lie on a slightly curved line which is actually the hyperbola represented by Eq. (7.6).

It should be recalled that a ray can be multiply reflected between two or more interfaces before arriving at a geophone, so that although all linings-up on a seismogram indicate distinct reflection events, their number need not correspond to as many actual reflecting horizons.

Fig. 7.20 shows another display of a seismic record. Here one side of the wiggle trace is blacked-in ('variable-area' display) resulting in considerable clarity and ease in picking out the reflections. Another visual display is the 'variable-density' type in which the photographic density along a trace is varied from black to white in proportion to signal variations. There are also hybrid systems.

7.3.2.7 Digital recording

(*a*) *Sampling and anti-aliasing.* The ground motion due to a seismic shot and the consequent geophone/hydrophone output are continuous functions of time. Modern seismic data acquisition systems are built with a view to computer processing so that the ground motion needs to be digitised (sampled at equal intervals of time) before entry to the computer. In order to simplify equipment, conserve magnetic tape and reduce computer time, it needs to be digitised with as few samples as possible without distorting the signal.

Consider a sinusoidal wave as in Fig. 7.21(a). If it is very finely sampled there

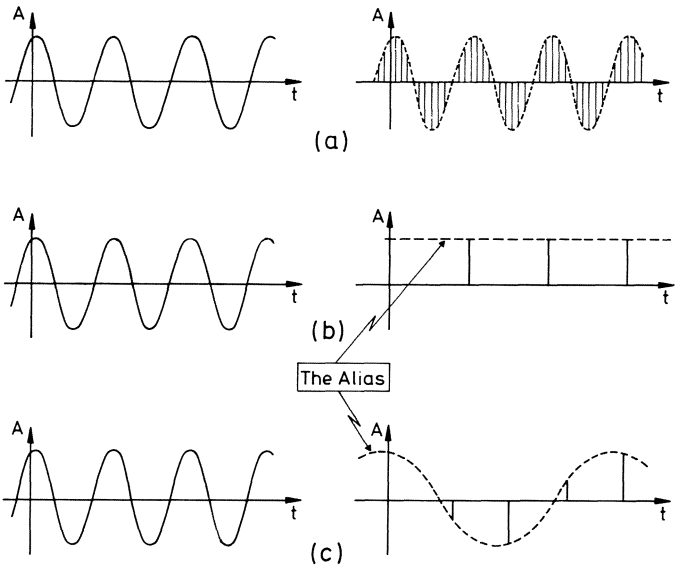

Fig. 7.21 Effect of sampling interval. (a) finely sampled; (b) 1 sample per period; (c) $1\frac{1}{2}$ sample per period.

is no difficulty in reconstructing the original wave as the right-hand part of the figure shows. In fact, with proper interpolation a sine wave may be exactly recovered from samples at equal intervals, *provided* that there are more than two samples per period. If there are less than two samples per period, then reconstruction with the same interpolation procedure will generate a lower frequency sine wave, i.e. the original sine wave will appear under the guise or alias of another sine wave. For example, if we take only one sample per period the simplest interpolation will yield the false result (Fig. 7.21(b)) that the ground moves up and stays up for all time. Again, Fig. 7.21(c) shows how 3 samples per two periods ($1\frac{1}{2}$ sample per period) will lead after interpolation to a ground motion that is of lower frequency than the true one.

According to sampling theory, if samples are taken at a time interval Δt, any frequency $\nu > 1/(2\Delta t)$ will appear as a lower frequency in the reconstruction of the wave. The frequency $1/(2\Delta t)$ is known as the Nyquist frequency. In other words, if the highest frequency in a signal is ν then the sampling interval must not be greater than $1/(2\nu)$ if the signal is to be faithfully reproduced from the samples. In seismic prospecting the maximum frequency in a reflected wave is usually less than 100 Hz. The most common sampling interval is 4 ms giving a Nyquist frequency of $1/(8 \times 10^{-3}) = 125$ Hz. However, much of the seismic noise (e.g. air wave, water wave, wind, instrumental etc.) has frequency components above 125 Hz. Therefore these must be eliminated *before* sampling, otherwise they will be converted to frequencies less than 125 Hz and

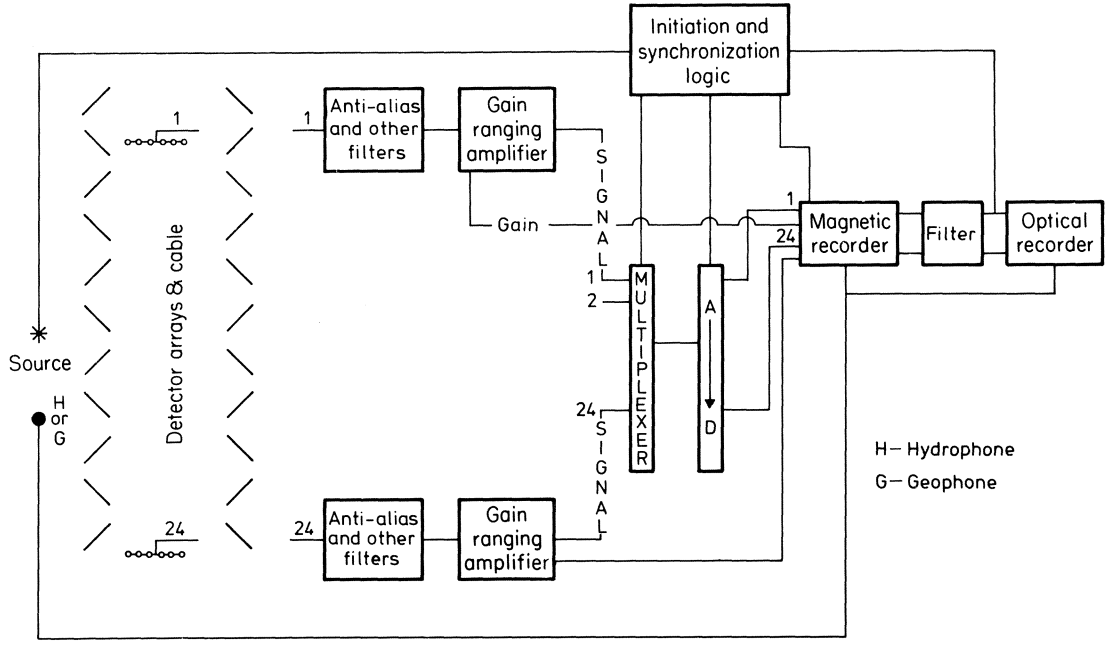

Fig. 7.22 Outline of a reflection seismic data acquisition system.

become inextricably mixed with reflections. The elimination is effected by an *anti-aliasing filter* which is always an analogue electric circuit.

(*b*) *Amplification, multiplexing and A/D conversion.* As with analogue recording the signal from each detector group is fed into an amplifier (one for each group). In digital recording this is a so-called binary gain amplifier in which the gain changes in steps of a factor 2. From the instant of one gain change to the instant of the next, the gain remains constant. If the amplifier output exceeds (or falls below) a defined level, the gain suddenly changes to half (or double) the current value. The gain values at every instant are recorded on one of the channels on a magnetic tape so that it is always possible in later processing to recover the true amplitude of the incoming signal.

In the next stage in digital recording, a *multiplexer*, essentially a high-speed electronic switch, connects each amplifier in turn to an *analogue–digital (A/D) converter* for a short time, during which the signal magnitude is read and converted into a binary-form number that is transcribed onto a magnetic tape. To gauge the speed of the multiplexer operation suppose there are 48 channels. The device connects channel 1 through 48 sequentially in one round and repeats the procedure on the second round and so on. If the sampling rate is, say, 4 ms one complete round must take exactly this much time so that the reading and channel-to-channel switching time is then of the order of $4/48 \approx 0.08\ \text{ms} = 80\ \mu\text{s}$ of which about $25\ \mu\text{s}$ are needed for reading.

If there are N detectors the record on the tape will begin with N binary-form numbers $a_{11}, a_{21}, \ldots, a_{N1}$ representing the first N samples and this series will be followed by the one consisting of the next N samples, each taken 4 ms (or any other predetermined interval) later than the corresponding previous one and so on, ending with the series $a_{1M}, a_{2M}, \ldots, a_{NM}$ of the Mth samples from the N detectors. The binary-number sequence obtained after multiplexing and digitization is thus

$$\{a_{11}, a_{21}, \ldots, a_{N1}, a_{12}, a_{22}, \ldots, a_{N2}, \ldots, a_{1M}, a_{2M}, \ldots, a_{NM}\} \qquad (7.13)$$

The sampling is usually carried out for about 5 seconds, that is, $M \approx 1250$ for a 4 ms sampling interval. In addition to this series, auxiliary channels on the magnetic tape record other data such as the amplifier gain at each instant, elevation of shot and detector etc. Information common to several traces can, of course, be recorded on a separate tape for use in later processing.

Fig. 7.22 shows the outline of a seismic data acquisition system. For further details reference should be made to specialized literature [166, 170, 171].

7.3.3 Data processing

7.3.3.1 General

Nearly all processing of modern reflection seismic data is automatic. A broad overview of the units involved in the processing is shown in Fig. 7.23. The main

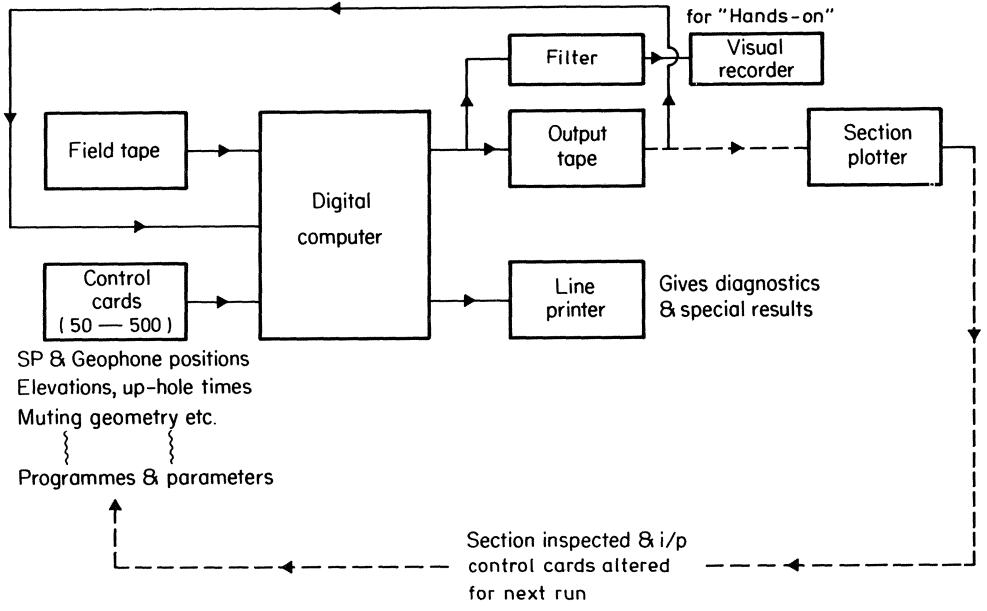

Fig. 7.23 Overview of reflection seismic data processing procedure.

unit is, of course, the digital computer and it will be noticed that it is not only fed by the field tape and the control cards with sundry relevant information but also by information from the output tape. This latter 'feedback' can be used for modifying some of the corrections, to be described presently, applied to the input data. A similar feedback comes from the section plotter but this is shown by dotted lines as it is not an on-line operation as far as the computer is concerned.

It should be realized that data processing is not a remedy for bad field procedures or poor data quality and that, once acquired, data cannot be improved or enhanced short of faking them. The data are numbers and information, measured or acquired, and the object of processing is to sort and rearrange the data, add further data (corrections), reject some data (filtering) and finally display the outcome. Ideally, the outcome would consist of only one component of the total data, to the exclusion of all other components, namely the 'hidden' component that is considered to be of interest. These remarks apply to all geophysical (indeed all scientific) work. In our present context the data of interest are reflection signals.

The principal steps in the processing of reflection seismic data are described briefly below. It should be noted that the dividing line between data acquisition and data processing is not a sharp one and some of the steps described here might very well be executed in practice as data acquisition while some described in Section 7.3.2 might be called processing steps rather than acquisition ones. Much depends, for example, on the equipment and procedures being used. Similarly, the line between processing and interpretation is also not absolutely sharp. From a practical point of view, however, we may roughly classify the activities in the field as data acquisition and those at the base or office as processing and interpretation.

7.3.3.2 Demultiplexing and amplitude recovery

The demultiplexing procedure is essentially a rearrangement of the record in the expression (7.13) so that the M samples belonging to each detector channel (trace) appear as separate sequences, namely

$$\begin{array}{llll} a_{11}, & a_{12}, & \ldots, & a_{1M} \quad \text{Trace 1} \\ a_{21}, & a_{22}, & \ldots, & a_{2M} \quad \text{Trace 2} \\ \vdots & \vdots & \vdots & \vdots \\ a_{N1}, & a_{N2}, & \ldots, & a_{NM} \quad \text{Trace } N \end{array}$$

Amplitude recovery involves compensating a measured amplitude a in the above table for the attenuation suffered by the waves due to geometrical divergence and absorption as well as for the amplification (G) at any instant in question. Several methods exist for the purpose [171], the most straight-

forward one being that each a is multiplied by the factor

$$\frac{Cx\exp(\alpha x)}{G} = \frac{C\bar{V}t\exp(\alpha\bar{V}t)}{G} \tag{7.14}$$

where x is the distance source–reflector–detector, $\bar{V}$ is the average velocity, usually a function of depth and hence of the two-way time t, C is a scaling constant and α is the absorption coefficient. The numerator in (7.14) compensates for spherical divergence and absorption, as will be evident from Section 7.2.6.2.

7.3.3.3 Editing and CDP gather

Editing mainly involves the removal of any obviously unusable data, for example a record or part of it that may have come out too weak for one or other reason. The traces or the relevant parts of the traces are eliminated from further processing by setting all amplitudes concerned to zero.

Following the editing, the traces contributing to each CDP are collected together (cf. Fig. 7.18) and the gather identified by the depth point.

7.3.3.4 Deconvolution (dereverberation, deghosting etc.)

This important operation on the data aims at removing the effect of water-layer multiples (reverberation), ghosts and other types of multiples (Fig. 7.15). As an illustration of the process consider the marine situation in Fig. 7.24 where the reflector of interest is supposed to be so deep compared with the source–hydrophone distance that all the rays may be assumed to be near-vertical, although for convenience of illustration they are shown to be slanting. Thus, C, H and H' are almost identical points and so also are A and A'. We assume for simplicity that the source pressure pulse is a single spike of unit amplitude and that the deep reflector is a perfect one. The seabed reflection coefficient is assumed to be $+R$ for pulses coming from above and reflected back into the water.

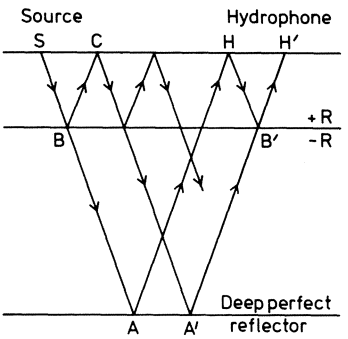

Fig. 7.24 Reverberation of seismic signal.

The direct reflection received at the hydrophone is SAH producing the signal 1.0 on the seismic trace. Besides this, the hydrophone will receive the pulse $SBCA'H'$ reflected first at B on the sea bottom, next at the air–water interface at C and then at A'. The first reflection reduces the pulse amplitude to R. On reflection from the water–air interface ($R = -1.0$) the amplitude becomes $-R$ while there is no further change of amplitude at A' as the deep reflector is perfect. This pulse, which is doubly reflected within the water layer, arrives $2h/V$ seconds later than the primary reflection, which is the additional time for the path SBC, since SB and BC are near-vertical. Another doubly reflected pulse, also arriving at the same time, is $SAHB'H'$. Its amplitude is also $-R$ so that the total signal on the trace at this time will be $-2R$.

Continuing in this way for pulses reflected three and more times between the water surface and the sea bottom we find that the seismic trace will consist of spikes $1.0, -2R, 3R^2, -4R^3, \ldots$, (Fig. 7.24) following each other at the same interval $2h/V$. Strictly speaking all the amplitudes in this should be multiplied by T_1, the transmission coefficient from sea to rock and by T_2, the transmission coefficient from rock to sea at the seabed.

The processing problem is now to remove the water layer multiples (reverberation, ringing or singing as the phenomenon is also called) from the trace to obtain a series $1, 0, 0, \ldots$, that corresponds only to the response of the deep reflector. We treat this desired series as the series c in Eq. (7.11) and the known series $1.0, -2R, 3R^2, \ldots$, as a string of pulses b. Hence the problem reduces to finding a series a such that b convolved with a gives c. Using the deconvolution procedure described in Section 7.3.1.6 it is easily shown that $a = [1, 2R, R^2, 0, 0, \ldots]$ is the *dereverberation operator* to be applied to the seismic trace.

There are, of course, many other multiple reflections. For example, the energy taking the path SAH will be reflected at H and then behave in the same way as the energy along the path SB. The resulting response at the hydrophone will be additional pulses of amplitude $1, 0, -2R, 0, 3R^2, 0, -4R^3, \ldots$, etc. at intervals of $2h/V$. The complexity of the reverberation phenomenon should now be apparent and the reader will realize that the deconvolution operator in practice must be much more sophisticated than the series $[a]$ above.

Suppose that the water depth is 25 m in the above example. Then the interval between the spikes in Fig. 7.24 will be 34.5 ms, which must also be the interval between the terms of the series $[a]$. As there are three terms in this series the interval between the first and the last term is 69 ms. This is called the length of the deconvolution filter or operator $[a]$. In general, the terms of an ideal deconvolution series do not all necessarily become zero after a certain term. In fact, there may be an infinite number of non-zero terms (Problem 7.4), in which case the length of the operator can be chosen by suitably truncating the series.

The deconvolution process described in this section is called *spiking*

deconvolution as it aims at producing a perfect spike output by applying the filter [a] to the observed trace. It is also called *deterministic* for the reason that the model causing the distortion of the source pulse 1.0 into the trace 1.0, $-2R, 3R^2, \ldots$, is known and the filter could be found in a direct manner. In practice, however, the situation is never so simple as Fig. 7.24 implies and the filter coefficients have to be determined by a statistical analysis of the data, but the details of the topic lie outside the scope of this book and the interested reader is referred to other literature [166, 172, 173].

7.3.3.5 Static correction

This correction arises primarily because the seismic source and detector are not in general at the same elevation as is tacitly assumed (cf. Fig. 7.5) and, in land work, also because the near-surface weathered layer varies in thickness and seismic velocity so that small time differences, that would not exist under ideal conditions, are present in the arrivals of reflections reaching the various detectors. The weathered layer is often referred to as the low-velocity layer (LVL) since the seismic velocity in it is relatively low.

Fig. 7.25 shows the situation in principle in a land survey and the time

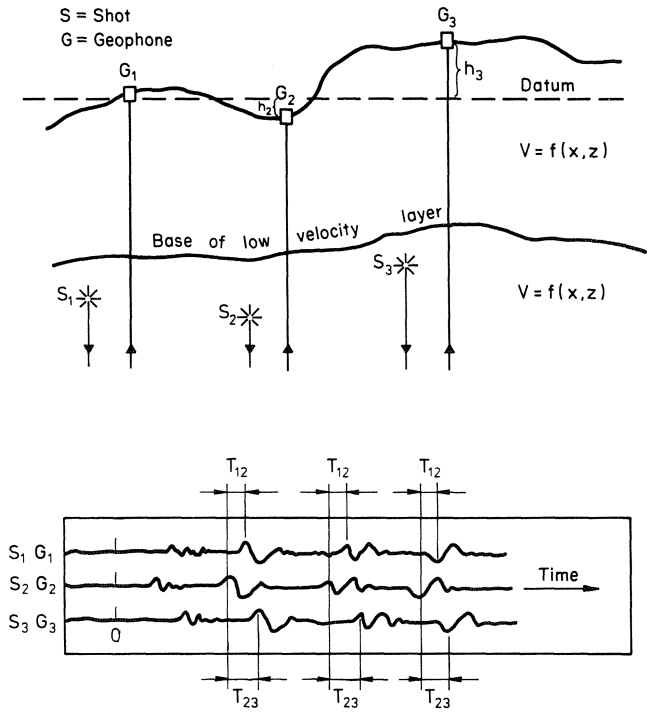

Fig. 7.25 Static corrections to arrival times.

differences T_{12} and T_{23} between the arrivals of the crests of three reflections at G_1, G_2 and G_2, G_3.

If the topography is irregular it is desirable to refer all arrival times to a datum plane, here shown as the horizontal plane through G_1, but it may be any convenient plane with known elevation above mean sea level. It is often put below the base of the LVL but this is not necessary.

Referring to the pair S_2, G_2 we see that if S_2 were on the datum plane the TWT for a reflection reaching G_2 would be greater by an amount $2d_2/V_2$ seconds where d_2 is the depth of S_2 below the datum plane and V_2 is the average seismic velocity between the datum plane and S_2. Again, if h_2 is the depth of G_2 below the datum, there would be a corresponding delay $2h_2/V'_2$ if G_2 were on the datum plane where V'_2 is the average velocity between the datum and G_2 assuming in this case the empty space to be filled by the LVL material in the vicinity of G_2. The two average velocities V_2 and V'_2 may differ since the velocity in the LVL is usually a function of depth. Referred to the datum plane the arrival times of reflections reaching G_2 must therefore be increased by the amount

$$2\left(\frac{d_2}{V_2}+\frac{h_2}{V'_2}\right) \tag{7.15}$$

This is the static correction for the pair S_2, G_2 and it is applied by shifting the entire trace for G_2 by this amount with respect to the time fiducial (marked 0 in Fig. 7.25).

The *relative* shifts T_{12}, T_{23} are seen to be

$$\begin{aligned} T_{12} &= (\text{TWT at } G_1) - (\text{TWT at } G_2) \\ &= 2\left(\frac{d_2}{V_2}-\frac{h_2}{V'_2}\right)-\frac{2d_1}{V_1} \end{aligned} \tag{7.16a}$$

$$T_{23} = 2\left(\frac{d_3}{V_3}-\frac{h_3}{V'_3}\right)-2\left(\frac{d_2}{V_2}+\frac{h_2}{V'_2}\right) \tag{7.16b}$$

The estimation of the average velocities needed for accurate static correction is by no means easy because the LVL is often very inhomogeneous. They can be obtained from a knowledge of shot depth and the 'uphole time' for the pulse reaching a detector placed near the top of the shot hole. There are also automatic statistical procedures involving smoothing of reflections [166, 172].

Marine static corrections are usually no more than adjustments for source and streamer depth and are then calculable much more exactly than in land work since the seismic velocity in water is constant and well known.

7.3.3.6 Dynamic or NMO correction

Although source–receiver separations (or offsets or moveouts as they are also called) are small compared with reflector depths they are not (and cannot be)

zero as required by the concept of vertical incidence (Sections 7.3.1.3). Eq. (7.6) for the two-way travel time for an offset x can be written as

$$t = \left(t_0^2 + \frac{x^2}{V^2} \right)^{1/2} \tag{7.17}$$

where $t_0 (= 2h/V)$ is the vertical or zero-offset TWT. Obviously

$$\Delta t = t - t_0 \tag{7.18a}$$

$$= \left(t_0^2 + \frac{x^2}{V^2} \right)^{1/2} - t_0 \tag{7.18b}$$

is the difference between the TWT at the detector and the zero-offset TWT. This is known as the *normal moveout*. From the definition of Δt (7.18a) it is obvious that subtracting Δt from t gives the vertical TWT at a detector. If $x \ll V t_0$ we get the approximate expression

$$\Delta t \approx \frac{x^2}{2 t_0 V^2} \tag{7.18c}$$

while (7.18b) is exact.

If Δt is calculated for each sample on a trace and the sample value placed at $t - \Delta t$, then instead of a hyperbola in Fig. 7.18 or 7.7 we shall obtain a straight line through the vertex of the hyperbola, provided V is correctly chosen.

The main problem in NMO corrections is thus to estimate V. In practice V is, in effect, chosen so that the reflection hyperbolas are transformed into horizontal straight lines. A method of determining V that is theoretically exact is to plot t^2 against x^2. This gives a straight line whose slope is $1/V^2$ and whose intercept is t_0^2 as Eq. (7.17) shows.

The velocity that gives a satisfactory straight line alignment of the reflections seen on a CDP gather (Fig. 7.18) is called the *stacking velocity*. The velocity is different for different hyperbolas on the same gather.

All NMO corrections involve some interpretation of data (e.g. for sorting out diffraction hyperbolas, multiples, overlapping events etc.) and visual checks are always needed even if automated schemes are used to estimate stacking velocities.

Since Δt is a function of the record time and varies with the TWT at a sample it is also called the *dynamic correction*.

7.3.3.7 Muting

This is in a way a form of editing and involves setting to zero the amplitudes in any undesired part of a trace and leaving the rest as it is. Generally, however, muting is done gradually over the interval concerned by a scaling function that goes smoothly from zero to unity.

The first part of a trace is nearly always muted to avoid stacking non-

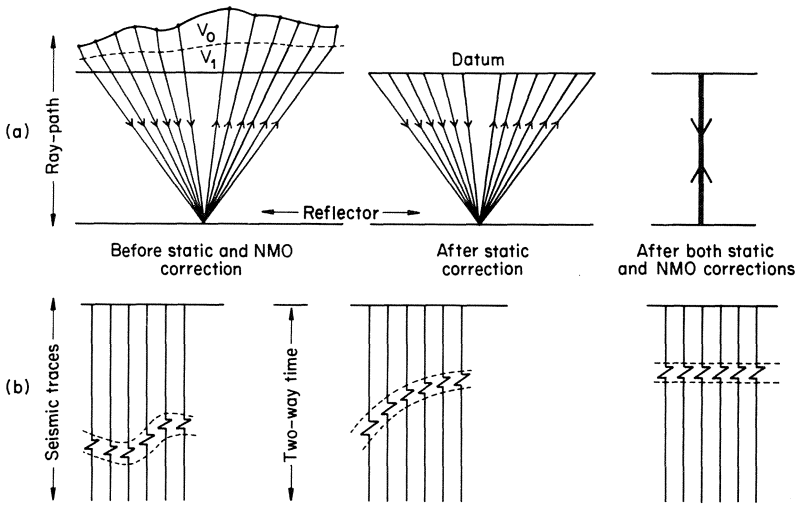

Fig. 7.26 Processing sequence. After [171].

reflection events like direct waves and refracted arrivals. Muting can be undertaken at any convenient stage in the processing sequence.

7.3.3.8 CDP stack

By this time in the processing sequence the recorded TWTs have been reduced to vertical TWTs as the schematic diagram (Fig. 7.26) shows and the CDP gather can now be stacked to obtain the single trace shown in Fig. 7.18. Generally, however, the degree of match between the traces is tested by some suitable statistical measure and a new stacking velocity is assumed and the NMO calculation repeated a few times to obtain a satisfactory match, before stacking is actually undertaken.

Stacking means adding the amplitude values at corresponding times on each of the traces. The sum is divided by the number of traces in the stack and the mean is placed as the amplitude at the time in question.

7.3.3.9 Time-variant deconvolution and filtering

The deconvolution operators to remove reverberations, ghosting etc. (Section 7.3.3.4) that are applied to the seismic record are constant for the entire record. However, reflection signals normally tend to show lower frequencies with record time since high frequencies are damped more rapidly than low ones in propagation. In addition, the peg-leg multiples (cf. Fig. 7.15) in particular, and other multiples also, broaden the seismic record. Therefore some further deconvolution adapted to the frequency content in different parts (times) of the record is generally undertaken with a view to improving the

clarity of reflections by 'compressing' the pulses. This time-variant deconvolution ('TV decon') is sometimes followed by time-variant bandpass filtering designed to filter out noise and improve the signal-to-noise ratio.

Figs 7.27 and 7.28 show an example of a variable area display before and

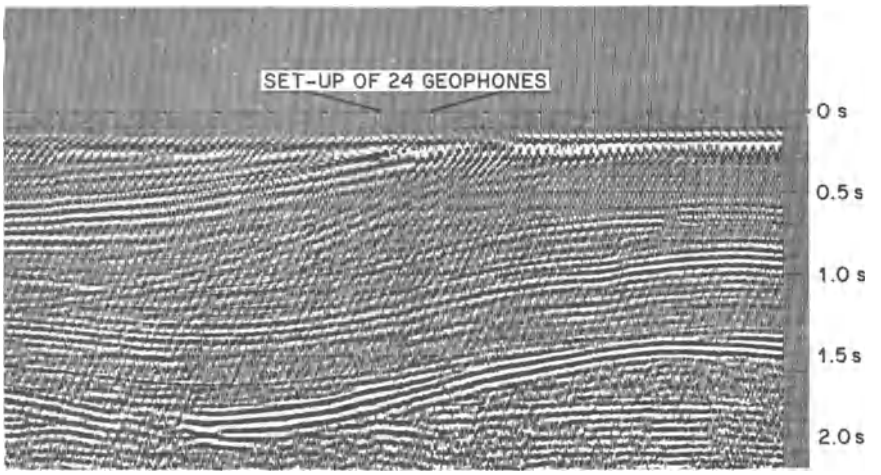

Fig. 7.27 Display of juxtaposed VAR records from consecutive geophone set-ups. Each geophone trace is a CDP stack of signals as explained in the text. (Courtesy of Seismograph Service Ltd. Holwood, England, and Amoco/Gas Council North Sea group.)

Fig. 7.28 Section of Fig. 7.27 after deconvolution. (Courtesy of Seismograph Service Ltd. Holwood, England, and Amoco/Gas Council North Sea Group.)

after deconvolution respectively. It will be seen that a lot of noise in the original display has weakened considerably in the deconvolved display rendering the reflections clearer. It must not be imagined, however, that deconvolution would always improve the clarity of reflections. Cases do occur when the deconvolution operator magnifies unwanted signal.

7.3.3.10 Velocity analysis and CVL

Velocities are required for two main purposes, CDP stacking, as we have already seen, and conversion of time sections into depth sections. If the stacking velocity for each reflector is estimated a plot of it against the record time gives the velocity function for that location. When no wells have been drilled these stacking velocities are the only ones available for time–depth conversion. For this reason, a great deal of effort goes into velocity analysis, which is probably one of the most expensive stages in seismic data processing.

However, lateral velocity changes, local reflector curvature, three-dimensional structure, errors in static correction etc. can render useless the results of internal velocity analysis. Reliable depth maps are, in general, only obtained using results from velocity surveys made in nearby wells.

If t is the two-way time of a reflection, the depth to the reflector is $\bar{V}t/2$ where $\bar{V}$ is the average velocity down to the reflector. This is defined as the total distance travelled divided by the total time. If there are n layers above a reflecting interface and the thickness of the jth layer in the sequence is h_j while the velocity in it is V_j, then

$$\bar{V} = \sum_1^n h_j \Big/ \sum_1^n (h_j/V_j) \tag{7.19}$$

If a well is available a geophone can be lowered in it and shots are fired on the surface in the vicinity of the hole. Knowing the arrival time of the seismic pulse and the shot–geophone distance, $\bar{V}$ is easily calculated.

Another method is the CVL (continous velocity log) first introduced by Vogel [174] and Summers and Broding [175]. The idea is to measure the seismic velocity over very small intervals by lowering a suitable apparatus in a borehole. The acoustic pulse is produced by a powerful electric arc discharge in a small transmitter and the signal is picked up by a receiver only about 1–2 m away in the hole.

A part of a CV log is shown in Fig. 7.29 together with the corresponding geologic section. The total travel time curve shown is obtained by integrating the interval times. The solid triangle at a depth of about 2330 ft indicates the position of the geophone used to calibrate the CVL. The travel time to this geophone was 0.243 s.

Although CVL is subject to various corrections and inaccuracies it is generally assumed that the local velocity variations evinced by it are geologically significant and used in Eq. (7.19).

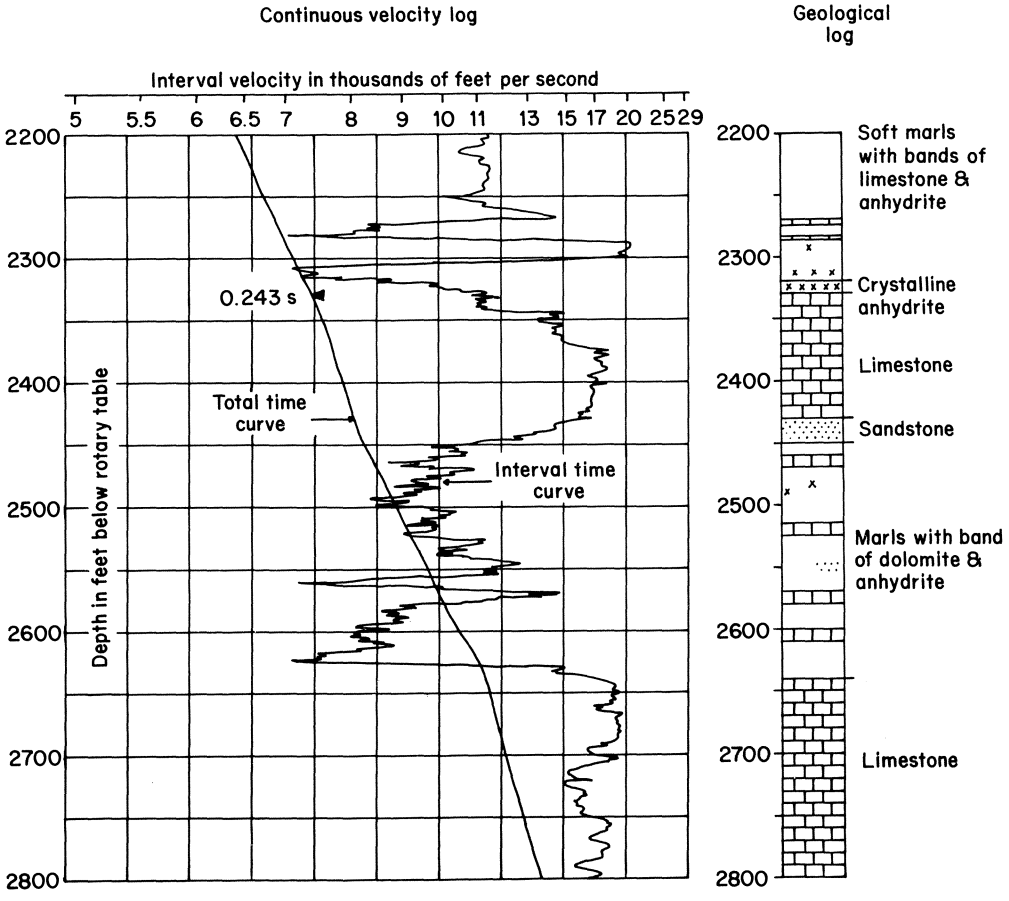

Fig. 7.29 Continuous velocity log.

7.3.3.11 Migration

Behind the stack-trace method of display lies the concept of normal incidence as Fig. 7.26 makes clear. As long as the dips are small and the layering almost horizontal the display portrays the geological structure fairly faithfully but Fig. 7.9 shows that the appearance of a normal-incidence section can be quite different from that of the geological structure when dips are appreciable since the reflector point is not plotted in its true horizontal position. The object of migration is to remedy this situation and move all the apparent reflector and diffractor events to their correct horizontal positions along the seismic profile, usually leaving the vertical axis in time. A migration program is used at the end of a normal data processing sequence.

There are many migration procedures [166, 171, 172] but we shall only deal with the *diffraction-hyperbola method.* It is convenient to start by considering the case of an earth which is homogeneous except for one diffractor point (Fig. 7.30(a)). The resulting normal-incidence section will be a single hyperbolic curve given $t^2 = t_0^2 + 4x^2/V^2$. Each *trace* on the section will contain only one data point of, say, unit amplitude. Evidently the geological structure suggested by the time section is quite different from the true earth depth section. The procedure described below converts the recorded time section to the true depth section.

Consider the recorded trace at shot point A (Fig. 7.31(a)). It consists of a zero at every sample position except at the time where the reflection of unit amplitude is present. Now a 'sampling hyperbola' is placed with its apex at a sample point of trace A. Where its flanks cross successive seismic traces the amplitudes are noted, added together and the sum placed on a new trace (the output trace, Fig. 7.31(b)) at a time equal to the time of the sampling point in question. Since the sampling hyperbola cuts the diffractor-point hyperbola only once the plotted output value will be unity. The sampling hyperbola is then placed with its apex on the second sampling point of trace A and the process repeated. It is easy to see that the output trace at A will consist of samples of unit amplitude at the sampling interval.

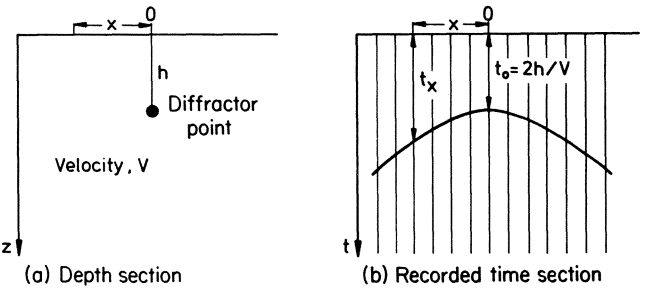

Fig. 7.30 Diffractor point and corresponding normal-incidence section.

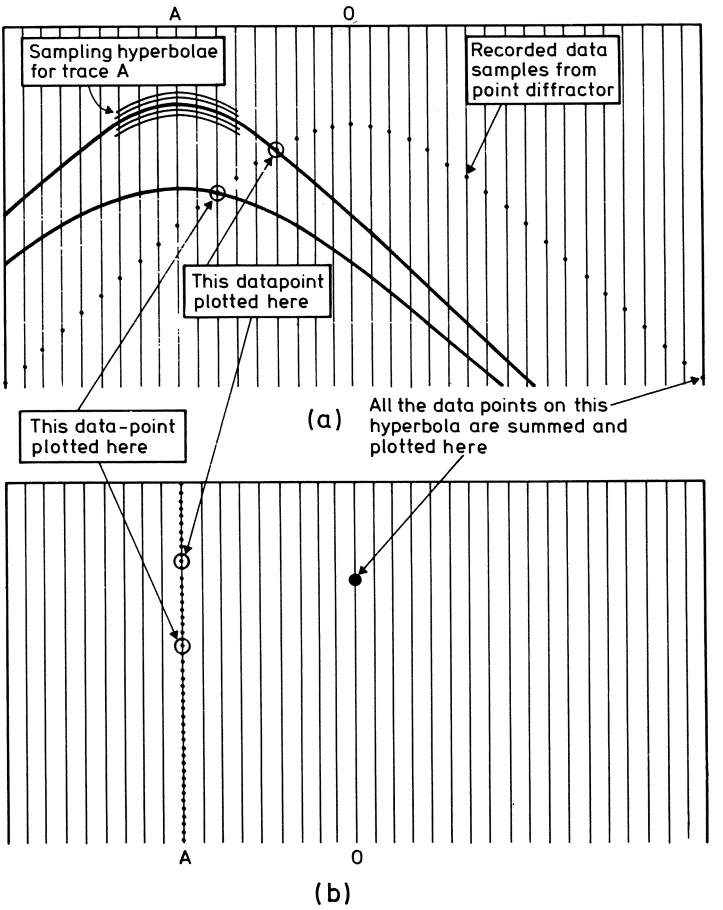

Fig. 7.31 Migration of a single diffraction event by means of diffractor hyperbola.

Note that the equation of the sampling hyperbola is of the form $t = t_0^2 + x^2/V^2$ where t_0 increases by the sampling interval as the apex of the hyperbola is moved while V ('the migration velocity') is constant. Consequently, the sampling hyperbola gets progressively 'flatter' as its apex is positioned progressively later down the trace.

The above procedure is repeated for every trace. Evidently, the result is the same for all output traces except the trace 0. At 0 the sampling hyperbola and the diffraction hyperbola never touch or intersect except when they are coincident. The output trace for 0 will therefore consist of zero at every sample point except for the one corresponding to the diffractor point itself. At this point the value will be m, the total number of traces within the span ('migration

aperture') of the sampling hyperbola. Usually $m \approx 200$, so that the output time section will consist of this one very large amplitude point in the correct position and a very small amount of 'computational noise' (the unit amplitudes).

The same migration procedure as above can be used for a dipping reflector (Fig. 7.32). At early times the sampling hyperbola cuts the reflection signal only once and so the early output samples are of unit amplitude. As the apex moves downwards a stage is reached, as shown in the figure, when the hyperbola is tangential to the reflection. In the example, the output value at

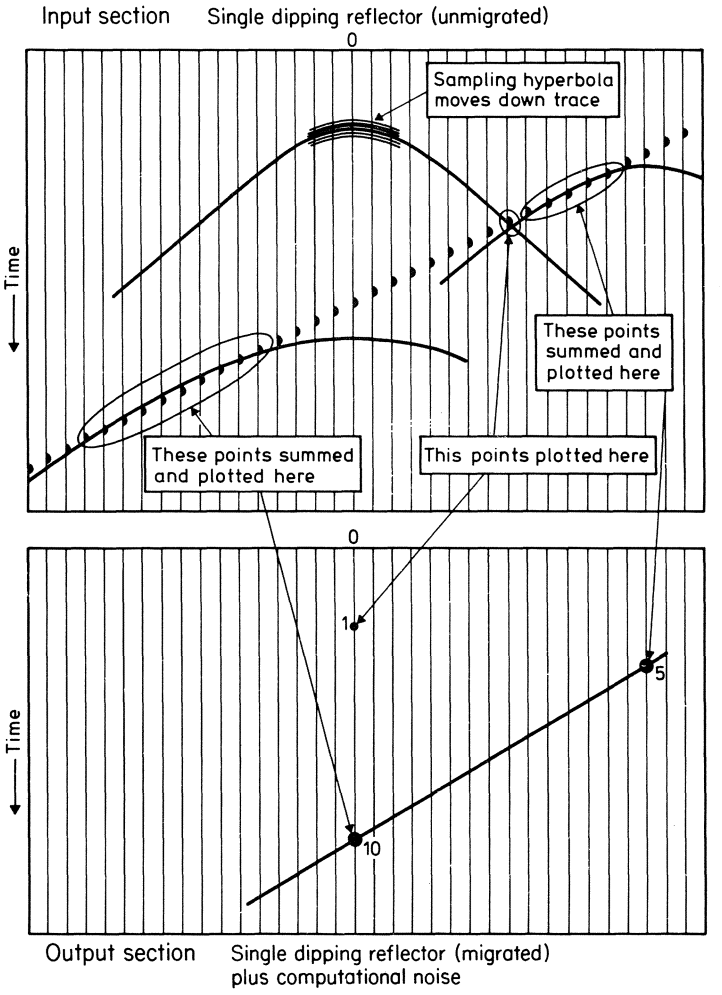

Fig. 7.32 Migration of a dipping reflector.

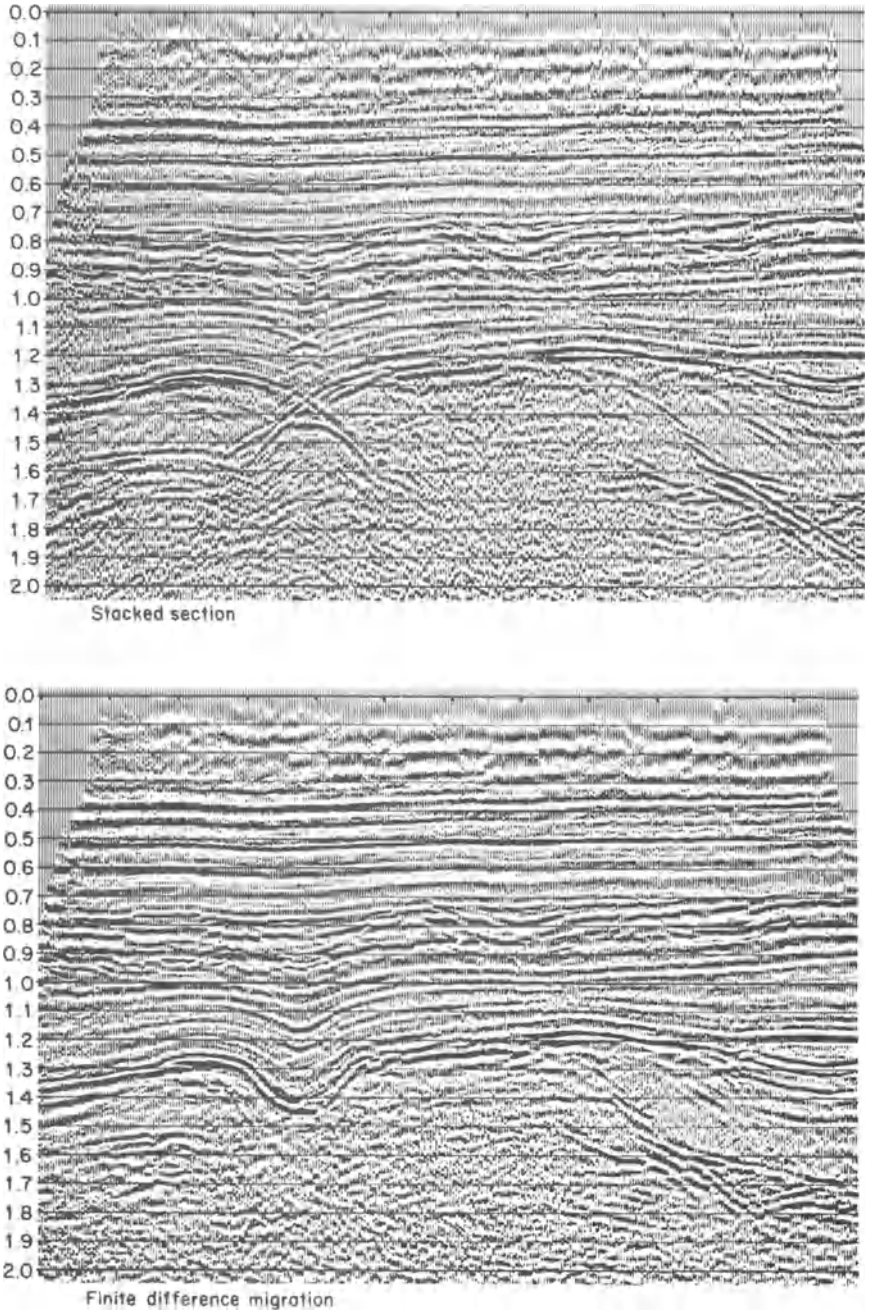

Fig. 7.33 *Upper:* Stacked time section. *Lower:* Migrated time section. (From Prakla-Seismos Information No. 2, 1978.)

this stage would be 10 units and this would be plotted under shot point 0 at the time corresponding to the apex of the hyperbola. Each output trace is built up in exactly the same way with maximum amplitudes occurring at the apices of hyperbolas that are tangent to the reflection on the original section.

It can be shown that if α_U is the dip of the reflector in the unmigrated section and α_M that in the migrated one, $\sin \alpha_M = \tan \alpha_U$.

Any curve may be represented by a series of short, straight-line segments. The diffraction-hyperbola procedure can be applied to each of these and the migrated (true depth) position of a curved reflector can be obtained as the curve formed by the migrated positions of the linear segments.

The process described above implies a reflector dip in the plane of the time section only and other simplifications. For the migration methods suggested for more complicated cases the reader should consult the seismic literature already cited and research papers in geophysical journals.

Fig. 7.33 shows a striking example of the effect of migration applied to a real section. The correct positioning of the dipping reflectors in the lower right-hand corner is evident but above all we should note the syncline at 1.41 s in the migrated section and its counterpart in the unmigrated time section. A comparison of Fig. 7.33 and Fig. 7.9 will be found instructive in this respect. Note also the many diffraction hyperbolas in the stacked unmigrated section and how migration reveals the abrupt discontinuities that are their cause.

7.3.4 Examples of interpretation

7.3.4.1 General remarks

While the acquisition and processing of reflection seismic data may now be said to be very largely a matter of technique their interpretation in terms of geological structures is an art. The principal features of a geological structure can usually be glanced more or less directly from a migrated section but the main task of interpretation is to incorporate these into a geological picture of the area that is consistent with other sections as well as other geophysical and geological data. This might at times require reprocessing a part or whole of the data since, as has already been pointed out above, processing implicitly contains some interpretation of the data and this might need to be modified when the processed data are examined in a larger context.

The geological situations in practice vary enormously from area to area and few general rules can be framed for interpretation, but the examples below should indicate some of the problems involved. Fuller accounts of geologic interpretation of seismic data will be found elsewhere [166, 176, 177].

7.3.4.2 Case of Fig. 7.28

Fig. 7.34 shows the geologic interpretation of the section in Fig. 7.28. It traces the course of bedding planes and shows parts of two salt pillows between

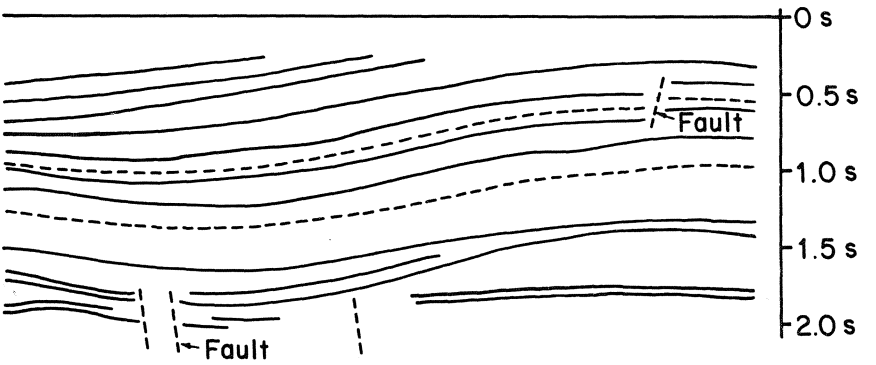

Fig. 7.34 Geologic interpretation (by Dr A.A. Fitch) of the section in Fig. 7.28.

about 1.4 and 1.8 s. The peripheral sink between the pillows is also apparent. Faults as indicated by the seismic sections are also marked.

7.3.4.3 Coal exploration in Eastern Ruhr (Federal German Republic)

This is an example of a so-called 3D survey in which shots and profiles were laid out over an area [178]. The object of the survey was to establish the position of the Carboniferous surface below the 600–700 m thick Cretaceous overburden that lies uncomformably over it and, above all, to find out the extent of the coal-bearing Carboniferous syncline as well as to study its large- and medium-scale tectonics.

Recordings were made with a 120-trace acquisition system with a rather complex pattern of shots and geophones on a grid and 2-fold coverage. The sampling interval was 2 ms. Frequencies above 128 Hz were filtered out.

Time sections (0.3–0.7 s) along two mutually perpendicular profiles are shown in Fig. 7.35 with the interpretation overlaid. One of the main results of the survey was that faults in the Upper Carboniferous with throws considerably less than 25 m could be recognized.

7.3.4.4 Tertiary–Cretaceous boundary (Central America)

This example is from a survey by Western Geophysical Inc., USA [179]. Fig. 7.36(a) shows the migrated time section. Above the most prominent reflector (at 1.4 s on the left side), the rocks are Tertiary clastics with seismic velocities of approximately 2500–3000 m s^{-1}. The strong reflector marks the boundary between these rocks and the underlying Cretaceous carbonate/anhydrite sequence in which the velocities are approximately 6000 m s^{-1}. The upper part of the Tertiary geologic section is strongly folded and faulted. A near-vertical fault is seen at about 7–8 km along the profile.

There is a deep reflector at about 3.1–3.6 s. The proper imaging of this

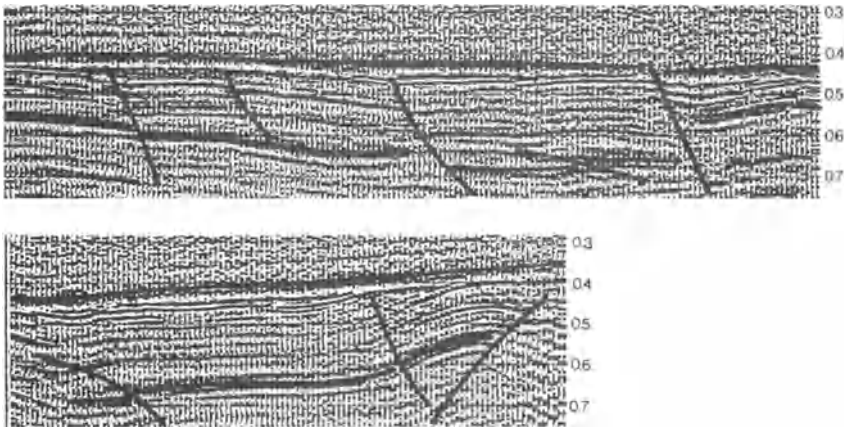

Fig. 7.35 Example of seismic survey for coal exploration. After [178].

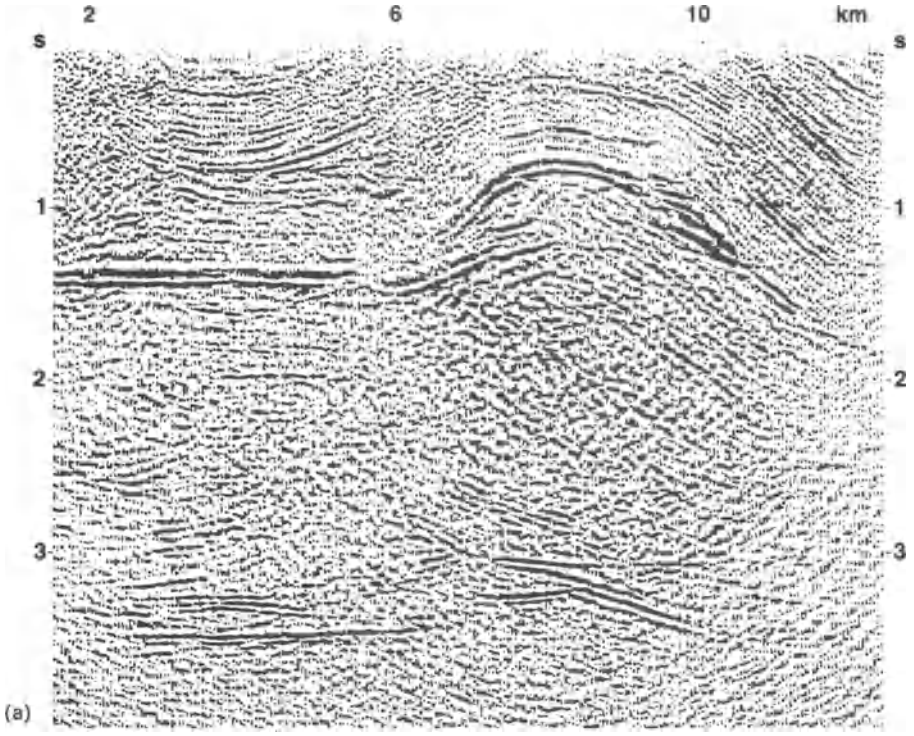

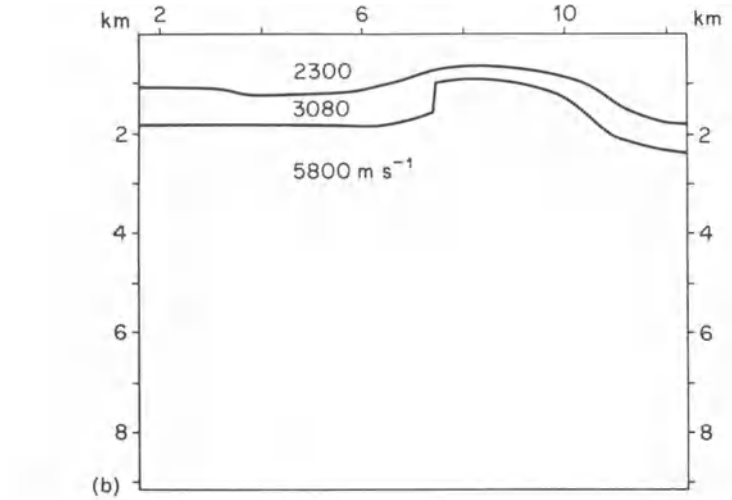

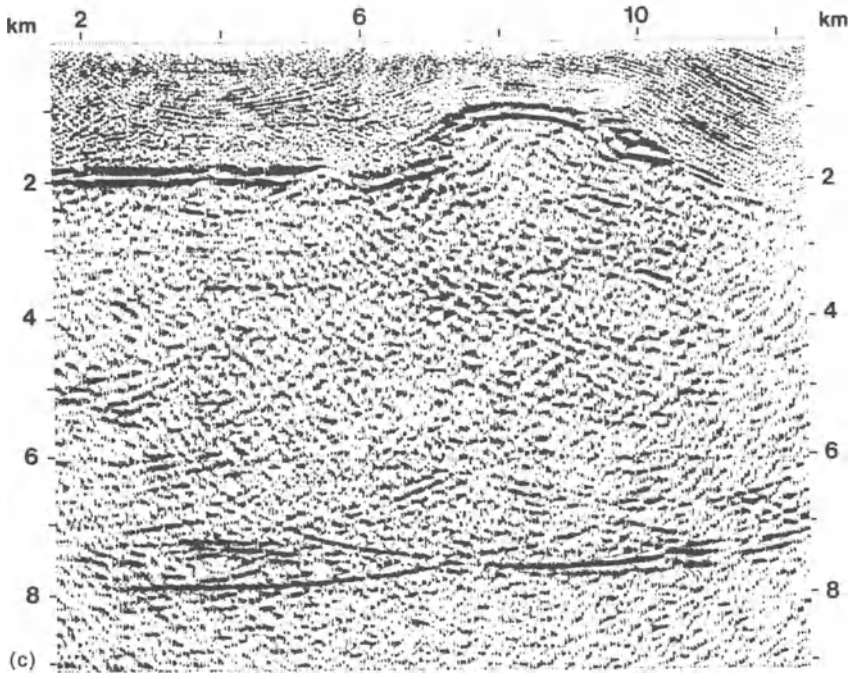

Fig. 7.36(a) Migrated time section in an area in Central America; (b) velocity model used for depth conversion; (c) migrated depth section corresponding to (a). After [179].

reflector, which is believed to be continuous (and not interrupted as it appears to be), on to a depth section requires a wave-theoretical approach. If the reflector were truly discontinuous there would be diffraction hyperbolas at its edges (cf. Fig. 7.8) in the stacked CDP section (not reproduced here) but these were found to be absent. The correct depth conversion cannot be effected simply by multiplying the TWT by $\bar{V}/2$. Essentially this means that a velocity model has to be postulated and proper account has to be taken of Snell's law.

The velocity model used is shown in Fig. 7.36(b). The velocities given are interval velocities (Section 7.3.3.10) determined from well logs. The depth-converted section is shown in Fig. 7.36(c). The deep reflector appears as a continuous and flat interface at approximately 8 km depth.

7.3.5 Vibroseis

This ingenious system of seismic exploration (a trademark of the Continental Oil Company) uses a vibratory instead of an impulse source. The source introduces a definite band of frequencies in the earth by means of a linear frequency sweep of the form shown in Fig. 7.37(a). In radar technology such signals are often called 'chirps' or 'pulse compressions'. Typically, the frequency is swept from 15 to 90 Hz in about 7 seconds. The signal is

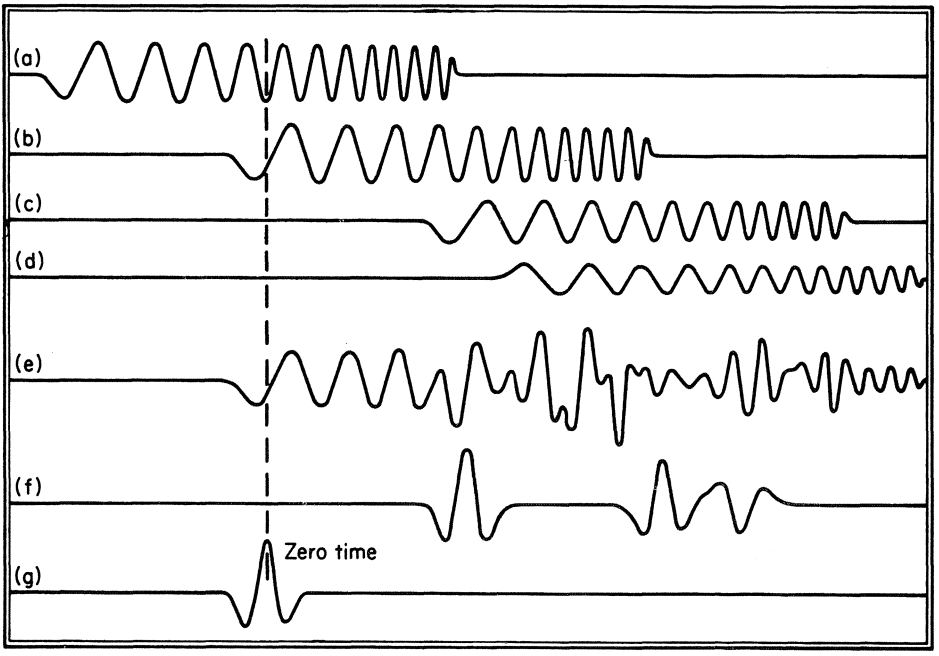

Fig. 7.37 Principle of Vibroseis.

introduced by truck-mounted hydraulic or electromagnetic vibrators capable of exerting a total thrust of several tons on the earth. The input seismic pulse of the impulse sources to which the Vibroseis signal corresponds is given by the autocorrelation function of the signal. This operation is very similar to convolution (p. 264) except that the sliding trace is the same as the stationary trace (nor is it folded on itself). The centre of the pulse thus obtained (Fig. 7.37(g)) corresponds to the time break of the conventional methods.

The returning signal from each reflector in the earth is likewise a frequency-swept signal. Three such signals are shown in Figs 7.37(b), (c) and (d). They add up to the recorded signal (Fig. 7.37(e)). To recover the reflected pulses, the total signal is cross-correlated with the input signal. Computationally this procedure is again the same as autocorrelation, except that the cross-correlated trace is different from the reference trace. For each position of it, the ordinates on the two traces are multiplied and summed. This leads to Fig. 7.37(f) which is nothing but a conventional seismic trace. The rest of the processing (deconvolution, stacking, filtering etc.) is the same as that described in Section 7.3.3.

Theoretically, the Vibroseis system is equivalent to conventional seismic exploration, but differs from it in the method of recovering the seismic information. However, it has several operational and practical advantages.

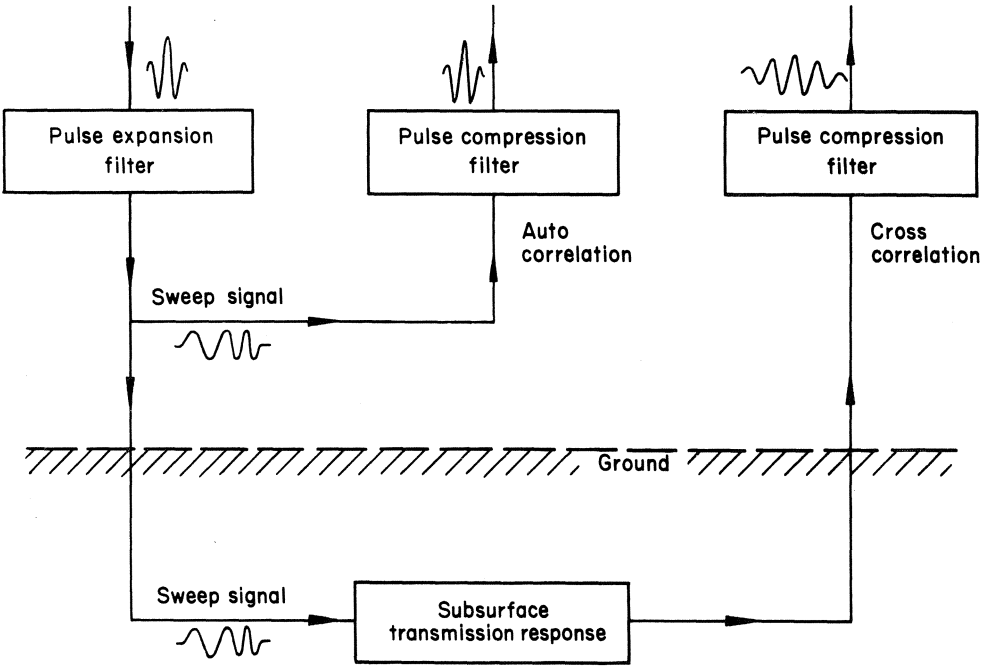

Fig. 7.38 Block diagram of a Vibroseis system.

First, the system is inherently safer and more convenient than one using explosives. Secondly, the sweep rates and frequencies can be optimally selected to suit the geologic conditions in the area so that power is not wasted in generating frequencies which the earth will not transmit. Finally, the energy injected into the earth can be increased almost without limit by coupling together as many vibrators as desired and making them work in phase from a master vibrator.

A block diagram of the system is shown in Fig. 7.38. The reader will find further details about Vibroseis elsewhere [172, 180, 181].

7.4 THE REFRACTION METHOD

7.4.1 Scope

The refraction method in which, besides the direct waves, the waves refracted at various interfaces in the ground and re-emerging at the surface are studied, was much used before 1930 for oil prospecting but has now been replaced by the reflection method, and is used in that work only as an auxiliary procedure for obtaining velocity data, depth of weathering layer etc. The present-day applications of the refraction method are mainly in civil engineering projects for bedrock investigations in connection with dam sites, hydroelectric power

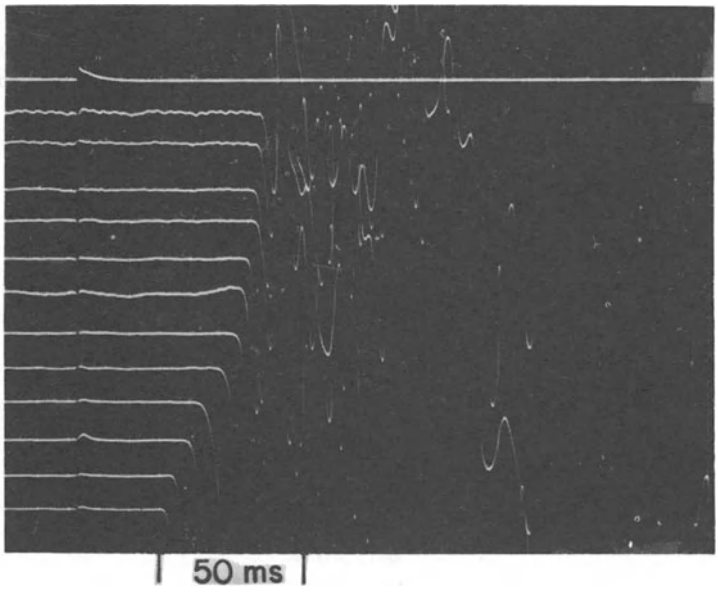

Fig. 7.39 Refraction seismic traces on a photographic record showing shot instant (in uppermost trace) and kicks due to first arrivals.

stations, large-scale building constructions etc. Another important application is in the detection of fracture zones in hard rocks in connection with ground-water prospecting, nuclear waste disposal programmes etc.

In contrast to the reflection method the maximum shot–detector distances in the refraction method are much larger than the depths of the interfaces of interest and, generally, only the first *P* wave arrivals are recorded. Most of the refraction recording at present is in analogue form, the display being on instantly developed photographic or copying paper or on CRO screens. Fig. 7.39 shows a typical recording with the shot instant, twelve geophone traces, the 'kicks' due to first arrivals and the time lines (10 ms apart). Note that the accuracy in time readings aimed at in refraction work is of the order of a millisecond or better. The figure in reflection work is about 0.1 s.

7.4.2 Parallel interfaces

We consider first a situation where a layer in which the waves have a velocity V_1 is underlain by another with velocity V_2. Then by Snell's law (Eq. (7.4)),

$$V_1/V_2 = \sin i_1/\sin i_2 \tag{7.20}$$

where i_1, i_2 are the angles of incidence and refraction for the seismic ray (Fig. 7.40). The ray SA with the *critical angle* of incidence $i_c = \sin^{-1}(V_1/V_2)$ is refracted so that $i_2 = 90°$ and travels along the boundary between the two media. Obviously, this is possible only if $V_2 > V_1$.

Due to this ray the interface is subjected to oscillatory stress and each point

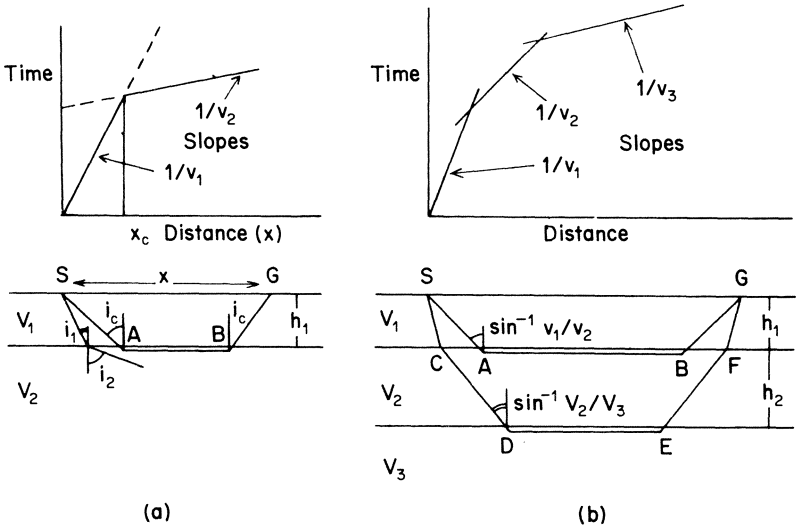

Fig. 7.40 Time–distance graphs in the refraction seismic method.

on it sends out secondary waves and rays such as BG emerge in the top layer at the angle i_c to reach the geophone G.

If G is near to the shot S (which is assumed to be on the surface) the first 'kick' of the galvanometer will be due to the arrival of the direct wave along SG. After some time a second kick will be observed corresponding to the arrival of the refracted wave. However, if SG is sufficiently great the first arrival will correspond to the wave $SABG$ which will have overtaken the direct wave because of a higher velocity along the path AB.

The travel time for the direct wave is $t = x/V_1$ and its plot against x will obviously be a straight line through the origin, that is the coordinate of the shot point, with the slope $1/V_1$ (Fig. 7.40). Remembering that $\sin i_c = V_1/V_2$ it is easily proved that the travel time equation for the ray $SABG$ is

$$t = \frac{x}{V_2} + \frac{2h_1(V_2^2 - V_1^2)^{1/2}}{V_1 V_2} \tag{7.21}$$

which is also a straight line but with a slope $1/V_2$ and an intercept on the t axis given by the second term in (7.21). This term is also called the delay time (t_1) and can also be written as $2h_1 \cos i_c/V_1$.

Equating (7.21) with x/V_1 gives the distance coordinate at which the two straight lines intersect. Beyond this critical distance (x_c) the refracted wave arrives first at the detector. It is easy to show that

$$x_c = 2h_1\sqrt{\left(\frac{V_2 + V_1}{V_2 - V_1}\right)} \tag{7.22a}$$

Thus a time–distance graph of the first arrivals to geophones planted at various distances from the shot will show two intersecting straight lines whose slopes give V_1 and V_2. The point of intersection x_c yields the thickness h_1 of the top layer. Alternatively h_1 may also be determined from the intercept (t_1) on the t axis (7.21).

Clearly, $h_1 = V_1 t_1/(2 \cos i_c) = V_2 t_1/(2 \cot i_c)$.

For three layers with velocities V_1, V_2, V_3 ($V_3 > V_2 > V_1$) there will be two critically refracted rays, $SABG$ along the first interface and $SCDEFG$ along the second one (Fig. 7.40). As before, at short distances the direct ray SG will arrive first. As the distance increases the ray $SABG$ will overtake SG and arrive first while at still greater distances the first kick of the galvanometer will signify the arrival of the ray $SCDEFG$. The time–distance plot then consists of three intersecting straight segments with slopes $1/V_1$, $1/V_2$ and $1/V_3$. The thickness h_1 of the top layer is calculated from (7.22a) and it can be shown that the thickness of the second layer is given by

$$x'(V_3 - V_2) = \frac{2h_1}{V_1}[V_2\sqrt{(V_3^2 - V_1^2)} - V_3\sqrt{(V_2^2 - V_1^2)}] + 2h_2\sqrt{(V_3^2 - V_2^2)} \tag{7.22b}$$

where x' is the second intersection point.

In terms of the intercepts t_1, t_2 of the second and third segments we have the following formulae:

$$h_1 = V_1 t_1 / 2\cos i_1 \tag{7.23a}$$

$$h_2 = \frac{V_2[t_2 - t_1(1 + \cos 2i_3)/(2\cos i_3 \cos i_1)]}{2\cos i_2} \tag{7.23b}$$

where $i_1 = \sin^{-1}(V_1/V_2), i_2 = \sin^{-1}(V_2/V_3)$ and $i_3 = \sin^{-1}(V_1/V_3)$.

These relations can be extended to any number of horizontal layers, one below the other, provided the velocity in each layer is greater than that in the layer immediately above. In general there will then be as many distinct segments on the time–distance curve as there are layers. If, however, a layer is not sufficiently thick or does not have a sufficient velocity contrast with the adjacent layers, the segment corresponding to it may be missing on the time–distance graph of the *first* arrivals. This obviously introduces errors in the depths to the lower interfaces. Such thin layers can however be detected sometimes by recording the later arrivals.

If the velocity increases continuously with the depth, for instance approximately linearly as is often the case, the time–distance graph will be a smooth curve concave towards the x axis.

If a layer has a *lower* velocity than the one on top of it there cannot be any critically refracted ray because i_2 will always be less than i_1 in Fig. 7.40. No energy can be transported along such an interface and no segment corresponding to the lower layer will appear in the time–distance curve. It is worth noting, however, that such layers *could* be detected if account is also taken of shear waves.

7.4.3 Non-parallel interfaces

In Fig. 7.41 is shown a case where the interface between two layers is dipping at an angle with the horizontal. It is readily shown that an 'up-dip' ray such as

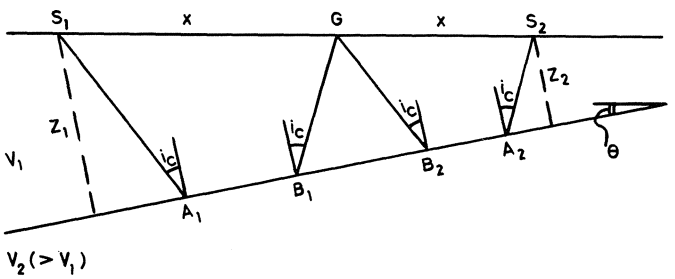

Fig. 7.41 Dipping interface.

$S_1A_1B_1G$ originating at S_1 takes a time

$$t = \frac{2z_1 \cos i_c}{V_1} + \frac{x}{V_1} \sin (i_c - \theta) \tag{7.24}$$

to arrive at the geophone while for a 'down-dip' ray $S_2A_2B_2G$ from a shot at S_2,

$$t = \frac{2z_2 \cos i_c}{V_1} + \frac{x}{V_1} \sin (\theta + i_c) \tag{7.25}$$

These relations, it may be noted in passing, will be interchanged if the surface is sloping and the interface horizontal.

The time–distance curve for the direct ray has the slope $1/V_1$ whether the ray comes from the shot S_1 or shot S_2. However, the segment corresponding to the refracted ray has a slope $\sin (i_c - \theta)/V_1$ when shooting up-dip but $\sin (\theta + i_c)/V_1$ when shooting down-dip. The reciprocals of these slopes are the up-dip and down-dip velocities, V_u and V_d respectively, and it is immediately seen that

$$\theta = \tfrac{1}{2}[\sin^{-1}(V_1/V_d) - \sin^{-1}(V_1/V_u)] \tag{7.26}$$

and

$$i_c = \tfrac{1}{2}[\sin^{-1}(V_1/V_d) + \sin^{-1}(V_1/V_u)] \tag{7.27}$$

(Both V_u and V_d are reckoned positive.)

The dip is directly determined from (7.26) while the depths z_1 and z_2 which complete the information about the configuration in Fig. 7.41 are obtained from the intercepts of the lines represented by (7.24) and (7.25) on the t axis after substituting for i_c from (7.27).

The up-dip velocity $V_u = V_1/\sin (i_c - \theta)$ is positive if $\theta < i_c$ and negative if $\theta > i_c$. If $\theta = i_c$ it becomes infinite so that the corresponding time–distance segment is horizontal. Of course, the infinite velocity is only apparent; no energy is transmitted at this velocity. Noting that the down-dip velocity $V_d = V_1/\sin (i_c + \theta)$ and $\sin i_c = V_1/V_2$ the reader should not find it difficult to prove that

$$V_2 = 2 \cos \theta \frac{V_u V_d}{V_u + V_d} \tag{7.28}$$

Since interface dips are generally small in practice we may put $\cos \theta \approx 1$ and write

$$V_2 \approx \frac{V_u V_d}{(V_u + V_d)/2} \tag{7.29}$$

The value is correct to better than 5% even if the dip is as much as 20°.

The numerator in (7.29) is the product and the denominator the mean of V_u and V_d so that we can frame an easy-to-remember rule 'Product divided by

mean' for the estimate of V_2. If there are more than two layers the rule is valid for the true velocity in each layer provided we can identify the corresponding up-dip and down-dip velocity segments in the time–distance graphs.

The case of an arbitrary number of dipping, but not necessarily parallel, interfaces has been dealt with in an interesting manner by Mota [182] and by Johnson [183]. Nomograms for the rapid determination of interface depths and dips have been published by several authors [184, 185]. It is very rarely, however, that more than three layers can be identified with certainty in shallow refraction seismics.

7.4.4 Computational refinements and examples

7.4.4.1 Need for refinements

The topographic and layering conditions in reality are generally quite different from the idealized ones considered above and the time–distance graphs very rarely consist of regular straight line segments as in Fig. 7.40. An example of a refraction profile that is particularly difficult to interpret is shown in Fig. 7.42 [186]. The profile was shot for a hydroelectric project in northern Sweden.

Each dot or cross represents the travel time to a geophone placed vertically

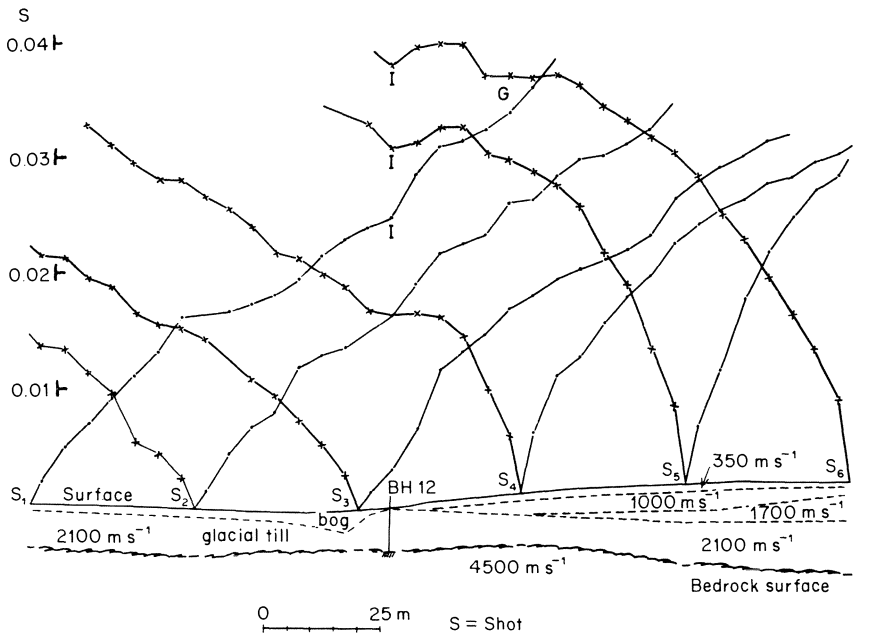

Fig. 7.42 Example of complicated time–distance graphs in a shallow refraction survey. After [186, p. 269].

below it on the ground surface. The depths sounded on this profile are relatively shallow but the results nevertheless illustrate a number of points discussed above.

The steep initial segments near each shot point correspond to the upper layers and at large distances from the shots these are replaced by less steep segments. This is most clearly indicated by the left-hand geophone set-up from shot 4. The break-points between segments or intercept times can only be determined after appropriately correcting for the irregularities (such as I) caused by local inhomogenities. They may, on the other hand, be due to variations in interface dips, for which case it is useful to remember that they are, qualitatively speaking, mirror images of an interface undulation. It should also be noted that very small dip variations can cause very pronounced irregularities of this type in the time–distance curves.

The apparent velocity in the bedrock when the geophones occupy positions around G is less when the shot is fired from S_1 (steeper time–distance segment). Evidently the ground surface and the bedrock are not parallel to each other in this region.

In the right-hand part of the figure the time–distance curves are more or less smooth indicating a fairly continuous downward increase in velocity. The interpretation of the profile is also shown in the figure together with a borehole that checked the depth, but it is clear from the above that some refinements in the treatment of the data are needed before the formulae in the previous section can be used.

The basic problems are: (1) to determine the various velocities and (2) to determine the intercept times. It is preferable to use intercept times rather than break-points for depth calculations.

Many different methods for the correct estimation of the above two basic parameters have been suggested. We shall consider three of them here in brief. These and other ones have been dealt with in great detail by Sjögren in a monograph [187]. An article by Green [188] will also be found to be useful in this connection.

7.4.4.2 The mean-minus-T method

This is a rapid method for estimating the velocity and its variations in a refractor in detail. If T_A and T_B are the arrival times at one and the same geophone from two sufficiently distant shot points A and B (Fig. 7.43) and if $\Delta T = T_B - T_A$ then obviously

$$\frac{\Delta T}{2} = \frac{T_B + T_A}{2} - T_A \tag{7.30}$$

The first term is the mean of the arrival times while the second is the time itself. The time differences ΔT_1, etc., between the refractor velocity curves A and B (for the same refractor) are measured and plotted, with due regard to sign, from

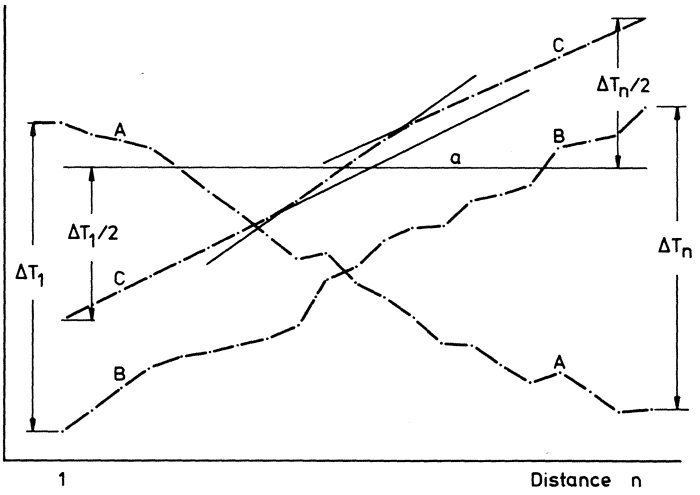

Fig. 7.43 Mean-minus-T method. After [187].

any arbitrary, conveniently placed horizontal time line (a). The points thus obtained are connected by straight line segments. It can be shown that the inverse slope of each segment gives the velocity over that portion of the refractor, the accuracy being the same as that for formula (7.29) above.

The low-velocity segments in the central portion of the mean-minus-T curve in Fig. 7.43 indicate a fracture zone. The edges of the zone are given very nearly by the intersections of the segments. The velocities in the fresh bedrock on either side appear to be slightly different from each other.

The construction of a mean-minus-T curve should normally be the first step in the interpretation, as it provides the refractor velocities needed for other adjustments of the time–distance segments described and subsequent depth calculations.

7.4.4.3 The ABEM correction method

The object of this method is to obtain the correct intercept time T_i corresponding to a velocity segment. An intercept time is made up of two 'delay times', one originating at the shot point and the other below the geophone. If the refractor velocity is the same at the point of critical incidence (A in Fig. 7.40 or A_1 in Fig. 7.41) as at the point of critical emergence (B, B_1 respectively) the two delay parts are equal (assuming V_1 to be the same). (This is why a factor 2 appears in the intercept time in Eqs (7.21), (7.24) or (7.25).) There is no problem in this case in finding T_i from the time–distance graph.

If the refractor velocity is different at points of incidence and emergence, however, the delay times are unequal. A correction method introduced in the

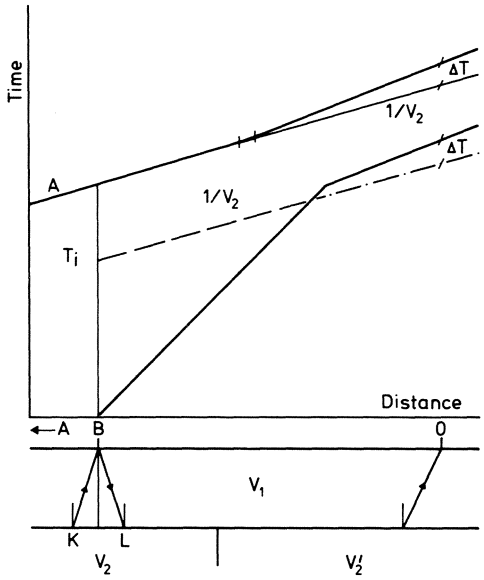

Fig. 7.44 Principle of the ABEM correction method. After [187].

late 1940s by the ABEM Company in Sweden removes the influence of unequal refractor velocities. The procedure is illustrated in Fig. 7.44.

An overlapping time–distance graph A from a sufficiently offset shot will show a segment of slope $1/V_2$ in the region of the shot point B and of slope $1/V_2'$ in the region of the detector O. In general, the slopes will have been determined by the mean-minus-T method using the graph A and the graph from a distant offset shot in the reverse direction, since it is not possible to tell whether the refractor interface in the vicinity of B is dipping or not. An auxiliary line of true slope $1/V_2$ is now drawn from a point on graph A exactly above B, after which the points on the refractor velocity segment of graph B are moved down (or up, as the case may be for individual points) by distances equal to the time difference ΔT between the auxiliary line and the graph A in this part.

The segment thus obtained (dashed line) has the slope $1/V_2$ and its intercept on the time axis through B gives the true intercept time T_i. It is interesting to note (cf. Problem 7.6) that the T_i thus obtained is only affected by the geological conditions within the triangle KBL where KB is the critically emergent ray from shot A and BL the critically incident one from shot B. The refractor configuration outside this triangle does not matter! Hence the procedure is equally applicable whether the interface is horizontal (as shown), dipping, curved or irregular (outside KBL). For the method to give a correct T_i it is only necessary that the interface over the distance KL be *plane* and the refractor velocity over this distance be constant!

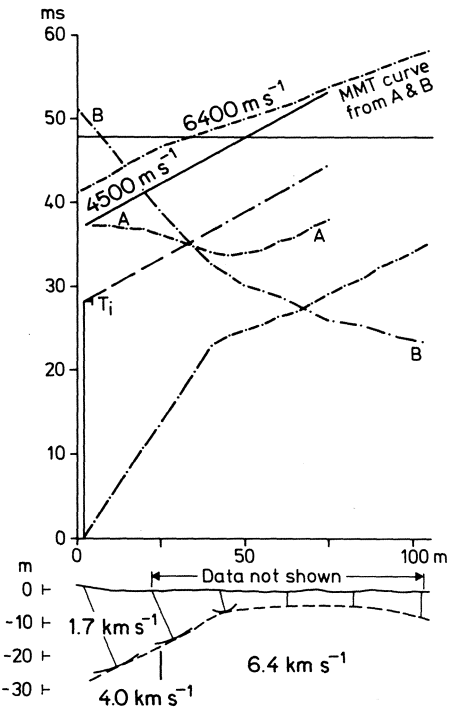

Fig. 7.45 Application of the ABEM correction method. After [187].

Having determined T_i we get the vertical depth of the interface below B (or the perpendicular distance from B in case of dip) from the formula

$$z = \frac{T_i V_1}{2 \cos i_c} \tag{7.31}$$

When there are two or more refractor velocity segments on the time–distance graphs the above correction procedure can be applied to each of them separately provided there are appropriate overlapping graphs from offset shots.

Fig. 7.45 shows the application of the method to some field data.

7.4.4.4 The ABC method

This method uses the concept of reciprocity that the travel time T_{ApC} from a point A to C via a particular path p is the same as the time in the reverse direction via p. Let A and C be two shot points on opposite sides of an observation point B (Fig. 7.46). Then, assuming critically refracted rays, it is

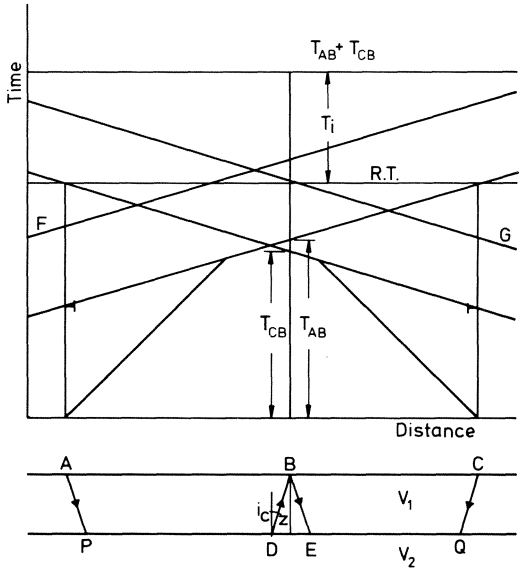

Fig. 7.46 The ABC method. After [187].

quite easy to show that

$$T_{APDB} + T_{CQEB} - T_{APQC} = T_{DB} + T_{EB} - T_{DE} = \frac{2z\cos i_c}{V_1} \tag{7.32}$$

The right-hand side is nothing but the intercept time in Eqs (7.21), (7.24) or (7.25) while the left-hand side is the sum of the times T_{AB} and T_{CB} at B, via the refractor, minus the time T_{AC} (usually called the reciprocal time), also via the refractor. It is absolutely essential that all three times refer to one and the same refractor. Obviously, the estimate of T_i is only affected by the geological conditions within the triangle BDE, a situation analogous to that in the ABEM method.

The ABC method also requires an overlap of recorded arrivals from the relevant refractor. If in Fig. 7.46 the only available time–distance graphs were those of shots from A and C, the procedure would be limited to the area around B where there is an overlap of refracted arrivals from the second layer. However, if records of shots from offset points on either side (F, G) are available the summation of times can be carried out along the entire traverse between A and C by appropriately shifting the offset graphs when necessary.

Fig. 7.47 shows the treatment of the data in the example of Fig. 7.45 by the ABC method. Curve 1 is the summation curve of times from shots at 0 and

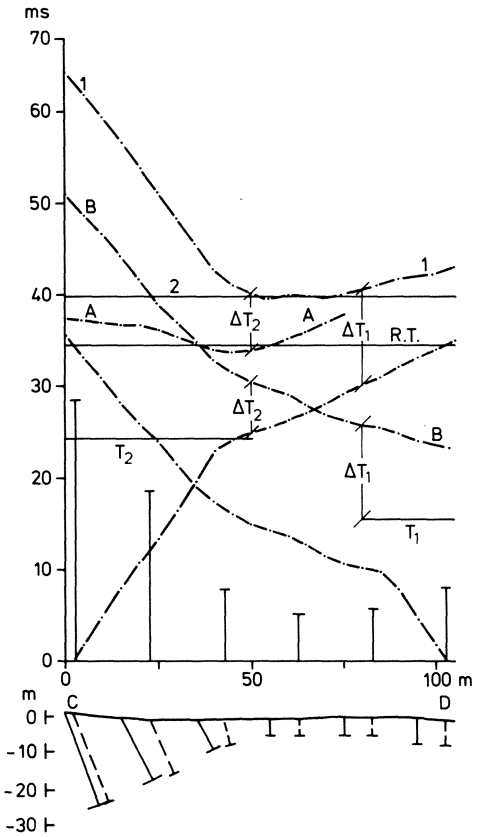

Fig. 7.47 Application of the ABC method. After [187].

100 m. The summation can be carried out directly between 50 and 80 m but outside this range the overlapping curves of shots *A* and *B* must be used as auxiliary curves by shifting them appropriately and joining them to the graphs from 0 and 100 at the last points where direct summation is possible. Instead of shifting the curves it is more convenient to measure the times on them from bases shifted by appropriate distances (T_1 and T_2 as shown in the figure).

The line marked R.T. is the horizontal line drawn through the point on the refractor segment above one of the two shots (0 or 100 m) and represents the reciprocal time. The distance between curve 1 and R.T. directly gives the intercept time at the geophone station. It is useful to note that an ABC curve resembles, qualitatively speaking, a mirror image of the interface for which it is constructed.

Under ideal conditions the ABEM and ABC methods give identical results.

The principal difference between them from the practical point of view is that while the former gives the depths at shot points, the latter gives them at geophone locations.

PROBLEMS

7.1 Construct a normal-incidence section for the model shown in Fig. 7.48 showing the water bottom reflection, the first water bottom multiple and the reflection from R and any diffraction.

(Hint: Rays emerging near A, B, C, D are sufficient to define the section, except for the diffracted wave.)

7.2 The amplitudes of a seismic pulse at 1 ms interval are given by the series [2, 4, −3, −2, −1]. Thirteen sub-surface reflectors have the relative reflection coefficients 3, 2, −1, 4, 1, 1, 2, −3, 0, 3, 2, −2, −4. The pulse takes 0.5 ms to go from one reflector to the next. Calculate the amplitudes on the seismic record neglecting transmission losses and all but primary reflections.

7.3 What is the common depth point for the six traces in Fig. 7.17 for the shot detector pairs 1–21, 2–17,..., etc.

7.4 Consider the primary reflection of a shot signal that is a unit pulse and its ghost from a deep reflector (cf. Fig. 7.15, top left) and determine the series [a] in Section 7.3.3.4 for the following two cases:

(a) The shot is on land and the ground surface has a reflection coefficient $-R$ for waves coming from below while the deep reflector is perfect.

(b) The shot is in water and the deep reflector has a reflection coefficient $+R$ for waves coming from above.

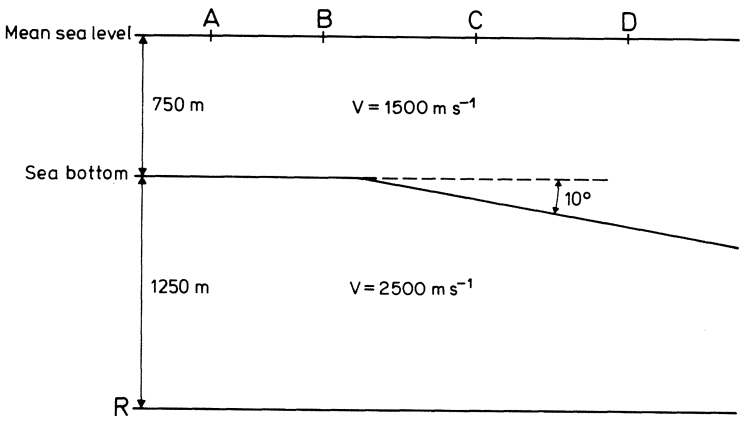

Fig. 7.48

7.5 The velocity of seismic waves V in a semi-infinite medium with horizontal free surface can be expressed as $V = V_0 + kz$ where z is the vertical depth and $k > 0$. Seismic rays from a point source on the surface travel in all directions. Consider the ray that makes, at the surface, an angle α_0 with the surface. What is the maximum depth attained by the ray before it bends upwards?

(Note and hint: The answer can be obtained in three simple algebraic steps by noting that the ray must necessarily be horizontal at its deepest point.)

7.6 Prove the statement that the estimate of T_i in the ABEM method (Fig. 7.45) is only affected by conditions in the triangle KBL by verifying that

$$T_{AB} + T_{BO} - T_{AO} = T_{KB} + T_{BL} + T_{KL}$$

where the times on the left-hand side are all via the refractor.

8

Radioactivity methods

8.1 INTRODUCTION

The geophysical methods employing radioactivity came into prominence with the demand for uranium metal in atomic reactors. However, the methods are not restricted in scope only to the search after the ores of radioactive metals or minerals associated with them (e.g. placer deposits of titanium or zirconium) but can often be used with advantage in geological and structural investigations as well.

8.2 THEORETICAL BACKGROUND

The nucleus of an element X with an atomic number Z has a positive electric charge of Z (atomic) units and is made up of nucleons (protons and neutrons). The number of nucleons is the mass number A of the element and the nucleus is symbolically denoted as ${}^{A}_{Z}\mathrm{X}$. Elements with the same Z but with different A are said to be *isotopes* of each other.

Certain nuclei disintegrate spontaneously emitting α particles (helium nuclei ${}^{4}_{2}\mathrm{He}$) and β particles (electrons and positrons). This is the phenomenon of radioactivity. These emissions alter the nuclear charge, α by $-2, \beta^{+}$ (positron) by -1 and β^{-} (electron) by $+1$. This means that the disintegrating nucleus is transformed into a nucleus of another element. Very often the daughter nucleus is also radioactive in its turn.

The nucleus is generally in an excited energy state after a β emission and returns to its ground state with the emission of a further particle, the γ quantum or ray. In some rare instances an α emission too is followed by a γ ray, e.g. in radium. The γ particle is a purely electromagnetic radiation which does not alter the nuclear charge.

The disintegration of a given quantity of any radioactive element can be expressed by the formula $N = N_0 \exp(-\lambda t)$ where N_0 is the number of nuclei

initially present and N the number remaining after a time t. λ is known as the decay constant and after a time $1/\lambda$ the number of nuclei present is reduced to $1/e \approx 1/3$ of the initial number.

A given quantity of a radioactive element is halved after a time $T = \ln 2/\lambda = 0.693/\lambda$. This time is known as the *half-life* of the element.

About 50 natural and more than 800 artificial radioactive nuclei are known. Natural radioactivity is confined principally to four *radioactive series* which start from the following isotopes of neptunium, uranium and thorium: $^{239}_{93}Np$, $^{238}_{92}U$, $^{235}_{92}U$ and $^{232}_{90}Th$. The transformations of the ^{238}U series are shown in Table 8.1.

The uranium and thorium series end in the stable isotopes of lead $^{206}_{82}Pb$, $^{207}_{82}Pb$, $^{208}_{82}Pb$. The neptunium series ends in the bismuth isotope $^{209}_{83}Bi$.

Besides the members of the four radioactive series, at least 10 other naturally occurring isotopes, all of elements with atomic numbers less than that of lead, are known to be radioactive. Chief among these is the isotope $^{40}_{19}K$ of potassium with a half-life of 4.5×10^8 years. About 42% of ^{40}K is transformed with an emission of β particle into calcium-40 and about 58% with the capture of an electron from the K shell of potassium into argon – 40. The transformation is accompained by high energy γ radiation of a wavelength of about 0.8 pm.

Table 8.1 Radioactive disintegration of the uranium-238 series

Element	Z	Emission	Half-life	Product
Uranium-238	92	α	4.51×10^9 y	^{234}Th
Thorium-234	90	β, γ	24.1 d	^{234}Pa
Protactinium 234	91	β, γ	1.14 min	^{234}U
or		β	6.7 h	^{234}U
Uranium-234	92	α	2.52×10^5 y	^{230}Th
Thorium-230	90	α	80,000 y	^{226}Ra
Radium-226	88	α, γ	1622 y	^{222}Em (Radon)
Emanation-222	86	α	3.825 d	^{218}Po
Polonium-218	84	α, β	3.05 min	^{214}Pb, ^{218}At
Lead-214	82	β, γ	26.8 min	^{214}Bi
Astatine-218	85	α	2 s	^{214}Bi
Bismuth-214	83	β, α, γ	19.7 min	^{214}Po, ^{210}Tl
Polonium-214	84	α	1.6×10^{-4} s	^{210}Pb
Thallium-210	81	β, γ	1.3 min	^{210}Pb
Lead-210	82	β, γ	20 y	^{210}Bi
Bismuth-210	83	β, α	5.0 d	^{210}Po, ^{206}Tl
Polonium-210	84	α	138.4 d	^{206}Pb (stable)
Thallium-206	81	β	4.2 min	^{206}Pb(stable)

The α and β particles lose their energy in passing through matter by collisions, ionization, etc. and are bought to a virtual stop within a certain distance which is called their *range*. In air at 18° C the range of α particles is only a few centimetres, in denser substances, e.g. mica or aluminium, it is still smaller, being of the order 30 μm. Even the β particles whose range is several hundred times greater are completely stopped by a thin sheet of lead or, for example, a few centimetres of sand.

The intensity of γ rays in traversing matter decreases exponentially with distance so that we cannot speak of a definite range in this case. Theoretically, γ rays could be detected across any thickness of matter but a practical limit is set by the sensitivity of the detecting instruments and the background effects due to cosmic radiation. For practical geophysical purposes γ radiation may be taken to be entirely absorbed by 1–2 m of rock.

Evidently, the α and β particles are not of much avail in geophysical field work since they will be undetectable as soon as a radioactive deposit has the thinnest cover of overburden. Thus, the search for radioactive minerals is, to a large extent, a search for places with abnormally high γ radiation. Uranium, for example, is located *indirectly* from the powerful γ radiation emitted by two products of the uranium series: $^{214}_{82}$Pb and $^{214}_{83}$Bi.

According to the quantum theory, electromagnetic radiation consists of discrete 'particles', namely photons. The energy of a photon is given by hc/λ, where h is Planck's constant, $c = 3 \times 10^8$ m s^{-1} is the velocity of light, and λ is the wavelength of the radiation. The energy is commonly expressed in electron volts (eV). One eV is the energy (1.602×10^{-19} J) acquired by an electron in falling through a potential difference of one volt.

Since $h = 6.625 \times 10^{-34}$ J s $= 4.14 \times 10^{-15}$ eV s, the energy of a photon is $1.24 \times 10^{-6}/\lambda$ eV. The wavelengths of γ rays are of the order of 10^{-11}–10^{-12} m (0.1–0.01 Å) and the corresponding energies are of the order of 0.1–1 MeV.

A radioactive series, such as that in Table 8.1, is said to be in equilibrium when as many atoms of any unstable element in it are being formed per second as are disintegrating. Such a series then emits a definite spectrum of γ rays. It is customary to describe the spectrum in terms of energy levels, instead of wavelengths as for the spectrum of ordinary light. The γ spectrum of ^{238}U contains lines at various levels from about 0.1 MeV to about 2.4 MeV. The spectrum of ^{40}K consists of a single line at 1.46 MeV. A spectral line is never perfectly sharp but has a finite, although usually small, energy width.

By measuring the energy emitted at a level it is possible to determine the amount of the particular γ emitting nuclide present in the sample, if at least this nuclide is in radioactive equilibrium with respect to its parent and daughter. If the whole sample is in radioactive equilibrium and if energy lines from other nuclides or other radioactive series are not overlapping the measured line, the content of the parent element of the series (U, Th) can be assessed by comparison with a standard of known content. Conditions are never as ideal in measurements on rock outcrops, but postulating radioactive equilibrium

the measured intensities can still be converted to U or Th content, which then is referred to as equivalent content (eU, eTh).

8.3 RADIOACTIVITY OF ROCKS

Minute traces of radioactive minerals are present in all igneous and sedimentary rocks, in oceans, rivers and springs, in oil, and in peat and humus.

The average amounts of U, Th and ^{40}K in a few materials of the earth's crust are shown in Table 8.2. From this we see that there is a large difference between the radioactivity of basalts and granites. Moreover, the latter have a remarkably high content of ^{40}K. This fact is of great consequence because granites are very common rocks and the γ radiation from their potassium produces a radioactive background which may make it difficult to locate uranium and thorium ores. Sometimes the radioactivity of potassic feldspars in pegmatite dikes may be misinterpreted as being due to a concentration of uranium and thorium.

The high uranium but low thorium content of oil is also striking.

8.4 RADIATION DETECTORS AND FIELD PROCEDURE

8.4.1 Detectors

The α, β and γ radiations are detected by their ionizing action. In geophysical work only the γ rays can normally be detected because the α and β particles are easily stopped by matter.

Table 8.2 Radioactive contents

	U *g/t*	Th *g/t*	^{40}K %
Basalt	0.9	4.2	0.75
Diabase	0.8	2.0	
Granite	3–5	13.0	4.4
Sediments	~ 1.0	5–12	
Limestone	1.3	1.1	
Oil	100		
Ocean water	0.000 15–0.0016	0.0005	
	%	%	
Uraninite	38–80	0–0.3	
Carnotite	50–63†	0–15	
Thorianite	23–26	53–57	
Monazite	0.02–0.7	3.5–16.5	

†Contents of uranium oxide

One common type of detector is the Geiger counter. It consists of a glass tube containing some gas (usually argon with a small amount of alcohol or amyl acetate) with cylindrical cathode round a wire anode. The electrodes are kept at a high potential difference. When a γ ray passes through the gas it produces ions which are accelerated by the field and produce further ions. The momentary current passing through the tube can be amplified and registered on a meter or heard as 'click' in a pair of headphones.

The Geiger counters respond to only 1% or less of the incident γ rays. On the other hand they register practically all *corpuscles* in the cosmic rays.

A more efficient type of detector is the scintillation counter. This utilizes the fact that certain crystals such as thallium-activated sodium iodide, anthracene, para-terphenyl, etc. scintillate when they absorb γ rays. The scintillations can be detected by a photocathode in a photomultiplier tube and recorded suitably after amplification.

The scintillation counters are almost 100% efficient in detecting γ rays. Their sensitivity to cosmic rays is about the same as that of Geiger counters so that their relative response to γ rays is much higher.

Detectors are constructed in two basic modes. The *differential spectrometer* records only radiation falling within predetermined upper and lower energy limits. If the limits are very close together (say a few tens of keV at the most) the spectrometer is said to respond to a channel or a line, while for wider separation of limits (several hundred keV) it is said to respond to a window.

The *integral spectrometer* is set to exclude radiation below a predetermined energy level, the threshold, and records all radiation having photon energies greater than this level. In some instruments the threshold can be varied. There exist also mixed-mode instruments. The choice of the spectrometer will depend to a large extent on the purpose and the requirements of a survey. Window and threshold spectrometers are more rugged, more rapid and require less checking than channel spectrometers. But the latter allow precise determinations of the various nuclides. Under controlled conditions determinations within a few gram per tonne U or Th are possible. Channel spectrometers are, however, expensive.

8.4.2 Field procedure

Radioactive surveys may be made either as 'spot examinations' or, more systematically, on a grid pattern of lines and points with the observer walking along pre-laid lines holding the detector some 40–50 cm above the ground. They can also be carried out from a car by mounting the detector on the roof provided the roads are unsurfaced, for the radioactivity of the materials in 'metalled' roads vitiates the observations.

The intensities are often recorded as counts-per-minute but most instruments are nowadays calibrated in milliröntgens-per-hour. The röntgen is the

quantity of γ (or X-) radiation which produces 2.083×10^9 pairs of ions per cm^3 of air at NTP. It corresponds to an energy absorption of 8.38×10^{-6} joules per kg of air.

The intensities recorded are the integrated effects of the radiation from a finite area on the ground. In foot-surveys most of the intensity comes from within a circle of about 3 m radius while in car-borne surveys about 90% of it comes (because of the greater detector height) from within a radial distance of 15–20 m.

Topographic irregularities, absorption and scattering of radiation in the earth materials, the dispersion of radioactive materials due to weathering, etc. and the 'background radiation' are some of the factors affecting instrument readings. These must be carefully considered in the interpretation.

The background is due mainly to cosmic rays, potassium-40 and the minute quantities of uranium and thorium which are almost always present in rocks. It may vary from one area to another as well as within a single area. A reading cannot be considered significant in general unless it is 3–4 times the background.

An example of a radioactive survey is shown in Fig. 8.1, after Moxham [189]. The area (Pumpkin Buttes area, north-eastern Wyoming, USA) is underlain by sandstone, shale and coal of Paleocene and Eocene age. Deposits of secondary uranium are found in 'rolls' and disseminated in several sandstone layers of the Eocene.

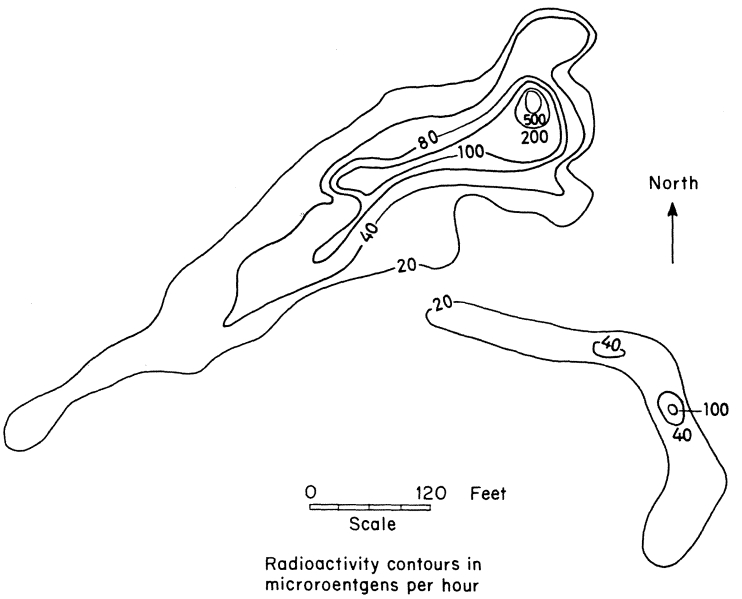

Fig. 8.1 Radioactive survey. After [189].

Contrary to the above example of high radioactivity over ores, Zeschke [190] has reported that 20 deposits of mangniferous ore in south-eastern Europe showed a systematic *decrease* in activity as one approached the outcrops. Above the outcrops the activity was practically nil (i.e. = background). Apparently, the ore deposits have been formed by descending solutions, and the water that flowed through the openings now occupied by ore probably leached most of the radioactive material from the surrounding marble rocks which, it is presumed, had originally a higher radioactivity than at present. This example indicates that the interpretation of radioactivity surveys, like that of all other geophysical surveys, must be done in conjunction with geological information.

8.5 RADON MEASUREMENTS

If radium is present at a place its disintegration product, radon gas (an α emitter with $T = 3.825$ days), may seep towards the surface with currents of water, diffuse through permeable rocks or escape through fissures and cracks.

Radon is present in suspension in nearly all well and river waters and in oil. In some cases the concentration may be very high as in the waters from Valdemorillo, Spain or Manitou, Colorado whose radon activities are 0.22 and $0.03\,\mu c\,l^{-1}$. (One curie is the activity corresponding to 3.7×10^{10} disintegrations per second = activity of 1 g radium.)

Radon measurements have been used as a geophysical method [19]. A small tube is thrust into the ground to a depth of one metre, or thereabouts. A sample of gas is drawn by means of a hand-pump into a container connected to the tube and is analysed for its α activity. A high activity may be due to radon and may in turn indicate faults, fissures, uranium veins, etc.

8.6 RADIOACTIVE DENSITY DETERMINATIONS

The absorption of γ rays has been employed for determining soil density in foundation investigations and hydrological problems. For this purpose an artificial radioactive isotope such as ^{60}Co ($T = 5.26$ years) or ^{137}Cs ($T =$ 33 years) is used. The former emits γ rays during beta disintegration, the latter changes to an excited ^{137}Ba which in turn emits γ rays in returning to the ground state.

A metal probe with the γ source at the end is driven vertically to a depth (z) of about 50–100 cm. The count of a detector placed on the surface at various horizontal distances (x) along a line is noted. The soil will absorb γ rays so that the count will depend upon its density ρ.

If the detector is assumed to be very small it can be shown that

$$N = \frac{N_0}{4\pi r^2}\,\mu \exp(-\mu r) \tag{8.1}$$

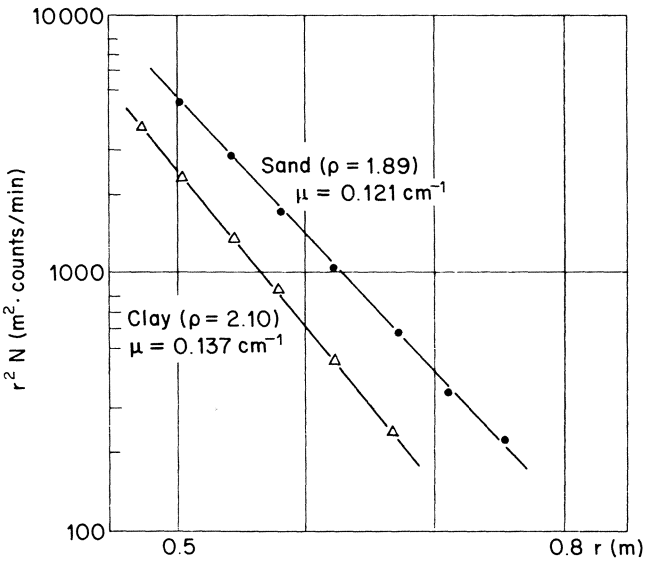

Fig. 8.2 Density determinations by radioactivity. After [192].

where N_0 is the total number of γ quanta emitted, N the number reaching the detector, $r = \sqrt{(x^2 + z^2)}$, the source–receiver distance, and μ is an absorption coefficient.

The plot of $\ln(r^2 N)$ against r will evidently be a straight line with a slope μ. It can be proved however that $\mu = \mu'\rho$ where μ' depends only upon the energy of the radiation. The mean values of $1/\mu'$ are $18.4\,g\,cm^{-2}$ for ^{60}Co and $14.2\,g\,cm^{-2}$ for ^{137}Cs but are affected slightly by test conditions. For the examples shown in Fig. 8.2 (after Homilius and Lorch) using ^{137}Cs, $1/\mu' = 15.33\,g\,cm^{-2}$ (clay) and $15.65\,g\,cm^{-2}$ (sand).

Density values accurate to 1% or better can be obtained with this method whose chief advantage is that the density can be determined *in situ*, without having to take samples.

A rigorous and detailed discussion of the method has been given by Homilius and Lorch in two interesting papers [192, 193].

8.7 AIRBORNE RADIOACTIVITY MEASUREMENTS

As with the other methods, airborne radioactivity work differs from the ground work mainly in respect of the operational procedure. The general principles of measurement and interpretation are the same in either case.

The intensity of the radiation from radioactive sources such as uranium veins decreases rapidly with the height of the observation point above the

earth's surface. The effect is due, in part, to geometrical divergence and, in part, to absorption and scattering in the air. Needless to say, scintillometers of the highest sensitivity are needed in airborne work and flight heights must be kept relatively low (50–70 m). The United States Geological Survey, for example, has used instruments with up to six thallium-activated NaI crystals (some ten centimetres in diameter and five centimetres thick) coupled in parallel. Such a detection system is reported to be sensitive to differences as small as 10 parts per million in the uranium content of rocks.

The detectors are generally shielded (except for the face of the crystal which is directed downward) from cosmic rays by means of a lead shield. The radiation intensities are recorded continuously and the deflections on the recording chart are calibrated by flying the detector over naturally occurring or artificially placed radioactive sources of known strength.

Considerable attention has been paid to devising methods for quantitative estimations of the radioactive content of rocks from the strength and nature of airborne anomalies and great progress has been made in this direction. Moxham [189] states that the content of sources with large dimensions, e.g. marine phosphate deposits, can be determined within a few thousandths of a per cent uranium (or its equivalent). The accuracy decreases with the areal extent of the source.

It should be realized that on account of the shallow depths (generally 1 m or less) sensed by radioactivity, the method is often better described as a technique for mapping soils, except where barren rock is exposed. However, Schwarzer and Adams have reported in an extremely interesting paper [194] that the concentrations of K, U and Th determined from the air in their survey in Payne County, Oklahoma, USA, suggested that the 'signatures' of these elements in the rock are preserved in the overlying *in situ* soils. In such a case it should be possible to map lithologies and lithologic contacts by airborne radioactivity measurements.

9

Well logging in oil fields

9.1 INTRODUCTION

Contrary to what one might expect, little information is obtained on the production potential of an oil well as it is being drilled. The reason is that, for from hydrocarbons 'gushing out', they are actually pushed back by the drilling mud and although cuttings reveal the general lithology in the well and may perhaps show traces of hydrocarbons, they furnish no estimates of oil and gas in place. It is through the data of measurements of various kinds in the wells that such estimates can be made.

If $A\,(\mathrm{m}^2)$ and h (m) are the area and thickness of an oil reservoir then

$$\text{Oil in place} = Ah(1 - S_w)\phi\,\mathrm{m}^3 \tag{9.1}$$

where ϕ is the porosity of the oil-bearing stratum and S_w is the fraction of total pores that contains water so that the fraction $1 - S_w$ contains oil. An exactly similar equation can be written down for gas in place but the gas volume exists at the temperature t (°C) and pressure P (Pa) at the depth in question. Using Boyle's law, however, it is very easy to show that at standard pressure (P_0) and temperature (t_0), usually atmospheric pressure and surface temperature,

$$\text{Gas volume} = \frac{P}{P_0}\frac{273 + t}{273 + t_0}(1 - S_w)\phi\,\mathrm{m}^3 \tag{9.2}$$

where t, t_0 are in degrees Celsius. If P at the depth d(m) is not known it may be taken as $10\,000d$(Pa), this being the hydrostatic pressure assuming the water throughout the geologic column to be freely communicating.

9.2 PERMEABLE ZONES

While porosity is effective in determining the quantity of oil or gas in place it is not in itself sufficient to ensure recovery. A high porosity with little or no

connection between pores (and between fractures and other similar spaces) will not lead to any recovery. For recovery it is also necessary that the formation be permeable, that is, allow the flow of hydrocarbons under a pressure gradient.

Permeability is expressed in the oil industry in *darcy* (or the subunit *millidarcy*), after H. Darcy who first studied the flow of fluids through porous media in the 19th century. Physically, it has the dimensions (length)^2 and, in particular, 1 darcy $= 0.987 \times 10^{-12}$ m^2. The quantitative aspects of rock permeability will not concern us since they belong to the province of reservoir engineering. Suffice it to say that permeabilities are usually such that the recoverable quantity of oil is about 20% of the *in situ* estimate, that for gas may be as much as 70%.

From the point of view of estimating hydrocarbon quantities in place the primary aim of logging is to locate permeable zones and determine ϕ and S_w in Eqs (9.1) and (9.2). The logs easily yield h for the bed in question but not A. If no other information is available, A can be taken as the square of the spacing between two wells in which the bed has been observed.

The most important hydrocarbon-bearing rocks are sandstones, limestones and dolomites, all of which can have high porosities and permeabilities. The porosity of sandstones is largely a primary one due to spaces between sand grains. It is rather uniform and averages about 20%. Limestones and dolomites possess in addition secondary porosity due to fractures and due to cavities formed by the solution of some rock matrix through the action of water. The porosity of limestones and dolomites is much less uniform than that of sandstones.

Besides the above three rock types, shales, a category that also includes clays in the present context, are an important constituent of the sedimentary rocks of oil and gas fields. Shales may have high porosity but their permeability is practically zero since the clay fraction is them effectively binds practically all water and renders it immobile.

Briefly, then, the impermeable sections on a log are shales, the permeable ones non-shales. The latter may be clean, that is, devoid of any shaly beds, or dirty, containing shales to a greater or smaller extent. Accounting for the shaly fraction in non-shales can be a major problem in estimating hydrocarbons in place.

9.3 ARCHIE'S LAW

Using the notation common in the logging industry this law (Section 4.4.1) can be written as

$$R_t = \frac{R_w}{\phi^m S_w^n} \tag{9.3}$$

where R_t is the true resistivity of a geologic formation in place and R_w that of the water in the pores. The resistivity of oil or gas is virtually infinite and does not influence R_t. It will be sufficient for our purpose to put $m = 2$, $n = 2$ (cf. Section 4.4.1). Equation (9.3) can be rewritten then as

$$S_w = (R_w/R_t)^{1/2}\phi \tag{9.4}$$

This is sometimes stated with the right-hand side multiplied by an empirical 'correction factor' depending on rock type. The factors are usually close to unity and their values and the practice of using them varies from one logging company to another.

S_w can be calculated from (9.4) if R_t, R_w and ϕ are known. It is no exaggeration to say that the entire logging industry is based on Eq. (9.4).

It will be evident from the discussion hitherto that there are basically three logs that we must consider, namely (i) permeability-zone logs, (ii) resistivity logs and (iii) porosity logs.

9.4 PERMEABILITY-ZONE LOGS

9.4.1 Self-potential

The SP log is obtained simply by lowering an electrode (usually a lead piece) and registering the electric potential at different points in the hole with respect to a fixed point at the surface. The hole must, of course, be filled with conductive mud. The recording is continuous, the logging rate being about 1500 m per hour. A typical SP log is shown in Fig. 9.1. The SP is constant as long as the electrode is opposite one and the same formation but jumps more or less suddenly to another level on crossing the boundary between two formations. The maximum SP gradient is usually observed almost exactly opposite the boundary. This enables h in Eq. (9.1) or (9.2) to be estimated fairly accurately in most cases.

The SP against permeable zones is strongly negative in general with respect to that opposite shales. The observation can be explained by a system of two principal electrochemical potentials as shown in Fig. 9.2, where E_{sh} is the e.m.f. across the shale–non-shale interface and E_{mw} that across the interface between the water in the permeable zone and the mud filtrate (dotted in the figure) that has invaded the zone. There may also be electrokinetic potentials at the well wall but these can be neglected if the flow of water across the wall is small. Assuming that the current in the circuit $ABCD$ is vanishingly small, the application of Kirchhoff's law to the circuit yields the result

$$E_{mw} + E_{sh} + U_B - U_A = 0 \tag{9.5}$$

if U_A, U_B are the potentials in the borehole mud at points just on either side of the shale–non-shale interface. Equation (9.5) gives the SP jump:

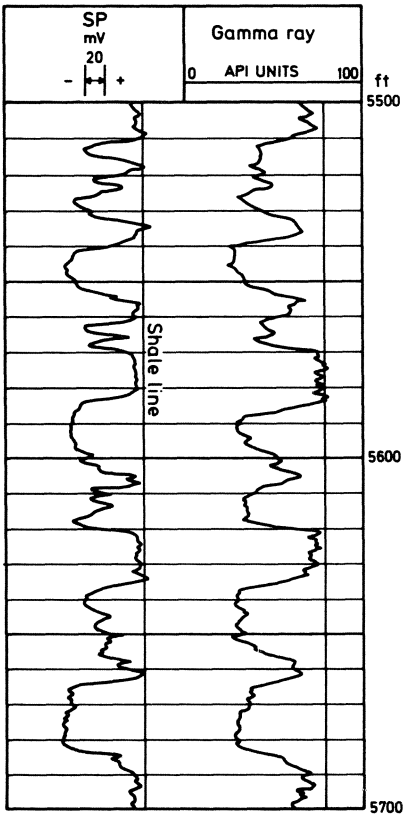

Fig. 9.1 SP and gamma-ray logs.

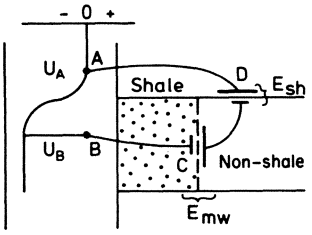

Fig. 9.2 Simplified electrochemical circuit to explain SP jump.

$$SP = U_B - U_A = -(E_{mw} + E_{sh}) \tag{9.6}$$

The geologic formations and the mud contain many different species of ions but it is now *assumed* that the e.m.f. $E_{mw} + E_{sh}$ arises essentially due to an equivalent concentration cell as in Fig. 4.4 with only Na^+ and Cl^- ions participating and with C_2, C_1 representing respectively the ionic concentrations in the mud filtrate and formation water of the permeable zone. Equation (4.2) in Section 4.2.3.2 can then be applied. However, as the resistivities of (dilute) electrolytes are proportional to ionic concentrations, the ratio C_1/C_2 can be replaced by R_{mf}/R_w where R_{mf} is the resistivity of the mud filtrate.

Inserting the experimentally determined values of the ionic velocities in Eq. (4.2) and changing the base of logarithms to 10, Eq. (9.6) can be written as

$$SP = -(65 + 0.24t)\log_{10}(R_{mf}/R_w) \tag{9.7}$$

if t is the temperature (°C) at the observation point.

In practice, therefore a shale line representing U_A is identified on the log and the SP jump measured with respect to it. Since R_{mf} can be measured directly on a sample of the mud filtrate, Eq. (9.7) can be solved for R_w.

It will be realized that a number of assumptions, some of them already stated above, are implicit in this method so that the water resistivities obtained are called equivalent resistivities R_{we}. To obtain the true values R_w it is necessary to use empirical correction charts [195].

9.4.2 Gamma-ray logging

This technique utilizes the natural radioactivity of rocks and is used chiefly for correlating sedimentary strata in petroleum prospecting. The apparatus consists, in principle, of a γ ray detector and its preamplifier suspended in a borehole by means of a waterproof electrical cable. The output of the detector is further amplified on the surface and recorded continuously as the detector is lowered (or raised) in the hole. The logging rate is about $330\,m\,h^{-1}$.

Generally speaking, shales and shaly sandstones show a very high radioactivity (the highest in sedimentary rocks) while salt, coal, anhydrite, limestone, quartz sands, etc. are weakly radioactive. Thus in a γ ray log the peaks in the intensity will correspond, in general, to shales while the lows will indicate the presence of limestones, salt, etc. and other non-shale formations (cf. Fig. 9.1).

Owing to the statistical nature of radioactive decay the γ ray log is not quantitatively exactly reproducible, in contrast to SP which reproduces itself remarkably well in successive runs. The standard γ ray log is not put to any quantitative use in log interpretation but in a semi-quantitative way it is an important indicator of the shaliness of a possible non-shale formation.

9.5 RESISTIVITY AND CONDUCTIVITY LOGS

The object of these logs is to estimate the true formation resistivity R_t of permeable zones for insertion in Eq. (9.4). A major problem in estimating R_t is that the mud filtrate invades the permeable zone up to a longer or shorter distance from the well bore and the apparent resistivity or conductivity obtained with any device will be influenced to a greater or smaller extent by the 'invasion profile' and the mud resistivity. Moreover the resistivity of all strata above and below the zone in question will also affect the measurements.

Analogously to the electric soundings in Chapter 4 an attempt is made in logging to determine R_t by means of 'deep' logs, e.g. by varying electrode separations. However, a deep log is necessarily more influenced, owing to its large electrode separations, by beds adjacent to the one being investigated so that the apparent resistivity obtained usually needs large and uncertain corrections before R_t can be estimated.

9.5.1 Resistivity logs

In one of the earliest resistivity log devices ('Normal array'), one current electrode A and one potential electrode M are lowered in the hole while B and N are kept at the surface. The standard short normal log uses a spacing $AM = 16$ inches, the long or deep one a spacing of 64 inches. The apparent resistivity is calculated in the appropriate manner using Eq. (4.24) in Section 4.4.2. Although a number of theoretical, empirical and semi-empirical corrections to the measured apparent resistivities to obtain R_t have been proposed over the years, the present consensus of logging experts seems to be that neither the short normal nor the long normal array is useful for estimating R_t with any degree of reliability [196, 197], although the short normal, in particular, is of considerable help in geologic correlation.

Another early device is the lateral array in which, besides A, both M and N are in the borehole at a relatively short distance from each other. The arrangement is basically a pole–dipole array (Section 4.4.3.5). While efficient in locating interfaces the array is no better for obtaining R_t than the normal arrays.

The present tendency in resistivity logging is to use the 'Laterolog' device in which a system of guard electrodes besides the main A and B electrodes is intended to prevent the spreading of the current over the ground at large and to confine it instead between two horizontal planes at a distance roughly equal to the length of the electrode spread [198]. The concept works in homogeneous media (in which case it is, on the other hand, not needed) but in inhomogeneous media like a stratified earth a 'focusing' of the current cannot be achieved without a prior knowledge of the resistivity distribution in the ground. Notwithstanding this fundamental objection the Laterolog is now used routinely.

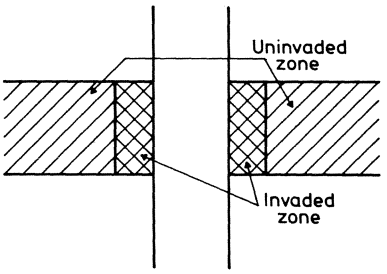

Fig. 9.3 Permeable bed invaded uniformly.

An empirical method of estimating R_t from the Laterolog apparent resistivity R_a, provided the permeable bed is thick and invaded uniformly up to a constant distance (Fig. 9.3), is as follows.

The invaded and uninvaded zones are assumed to contribute to R_a in proportion to their resistivities, R_i and R_t respectively, and in proportion to their 'weights'. If w is the weight of the invaded zone, that of the deep zone is 1-w so that

$$R_a = R_i w + R_t(1 - w) \tag{9.8}$$

The weight w depends on the diameter of the invaded zone, on the ratio R_i/R_t and on the array parameters. The problem of estimating the weights, or the pseudo-weights as they might better be called, for the situation shown in Fig. 9.3 is somewhat similar to finding the effect of the superficial layer on ρ_a in electric sounding on a two-layer earth (Chapter 4).

An estimate of R_t can be obtained from (9.8) if R_i and w are given reasonable values. There are also various other empirical methods for estimating R_t from R_a [199].

9.5.2 Induction logs

The induction log instrument is basically the electromagnetic coaxial coil system (Fig. 6.17) with the axis along the well axis. Frequencies used are in the range 20–30 kHz. In earlier instruments only one transmitting and one receiving coil were used. More recent constructions use an array of auxiliary coils spaced above, below or between the main coils (spacing c. 1 m) to focus the primary field. Much the same objection can be raised to the concept as in the case of the Laterolog instrument.

In homogeneous media the secondary voltage in the receiver coil is approximately proportional to the conductivity. In inhomogeneous media the readings give an apparent conductivity. An empirical formula like Eq. (9.8), with the resistivities replaced by conductivities, is used to estimate the true

conductivity $C_t = 1/R_t$ of the permeable zone. For other empirical methods of determining C_t, reference should be made to specialized literature [197, 199, 200].

In contrast to the other logs discussed so far, the induction log can be run in empty holes or in holes filled with non-conductive mud. Logging speeds for resistivity and conductivity logs are of the order of 1500–2000 m per hour. The resistivity logs are generally preferred in relatively high resistivity formations ($R_t > 200\,\Omega$ m) and the induction logs in low resistivity ($R_t < 200\,\Omega$ m) formations.

An example of resistivity and conductivity logs is shown in Fig. 9.4.

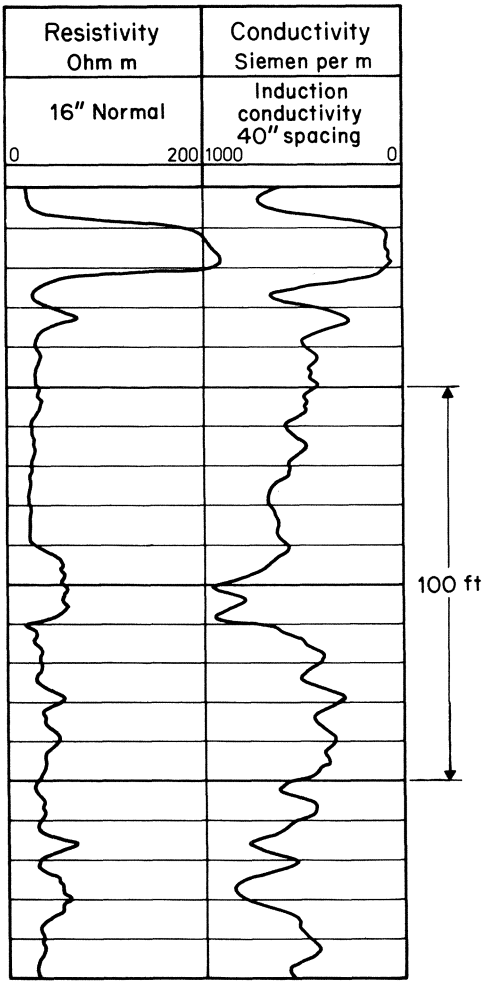

Fig. 9.4 Resistivity and conductivity logs. After [196].

9.6 POROSITY LOGS

Porosity is the last remaining parameter needed to calculate S_w from Eq. (9.4). Three methods, density, neutron and sonic logs are in common use to measure ϕ.

9.6.1 Density log

If ρ_{ma} be the matrix density of a clean formation, ρ_f the density of the fluid filling the pores and ρ_b the bulk density then

$$\rho_b = \phi\rho_f + (1 - \phi)\rho_{ma}$$

from which

$$\phi = (\rho_{ma} - \rho_b)/(\rho_{ma} - \rho_f) \tag{9.9}$$

ρ_b is measured by lowering a γ ray source in the hole and counting the number of high energy γ rays arriving at a fixed distance when the source radiation is scattered by collisions with the electrons in the rock material. This type of scattering is called *Compton scattering*. The method is essentially an adaptation to borehole work of the procedure described in Section 8.6.

In modern density logging there are two detectors, one at a distance of about one metre from the source, the other nearer, and the sonde on which these and the source are mounted is pressed against the borehole wall. Owing to its short distance from the source, the near detector gives greater weight to any mud cake on the wall so that corrections can be estimated for the scattering in the cake. The dual-detector density log is therefore called a compensated density log (CDL).

The depth of investigation of the CDL is about 10 cm from the borehole wall which means that the log senses mud filtrate in the invaded zone, the density of which (ρ_f in Eq. (9.9)) is very nearly 1000 kg m^{-3}. Standard values used for ρ_{ma} are typically 2650 for sandstones and sands, 2680 for limey sands or sandy limes, 2710 for limestones, and 2870 kg m^{-3} for dolomites.

A further development of the CDL is the Litho-density tool (LDT) based on registering very low-energy γ rays within a narrow band in addition to the high-energy rays in the CDL. The absorption of low-energy γ rays is a photoelectric phenomenon and not a loss of energy due to collision with electrons as in the Compton scattering of high-energy rays. The long-spacing detector is calibrated to measure P_e, the photoelectric absorption coefficient per electron present in the medium through which the γ rays have passed. P_e is strongly dependent on the average atomic number of the formation and is therefore a good indicator of the type of rock matrix, making possible a more accurate estimate of ρ_{ma} in Eq. (9.9) than would otherwise be possible in cases of complex lithology.

9.6.2 Neutron log

There are two borehole methods known as neutron–γ and neutron–neutron logging which employ neutrons [201, 202]. A convenient source of neutrons often used is a mixture of radium and powdered beryllium. The beryllium is bombarded by α particles from the radium and fast neutrons are produced according to the reaction

$$^{9}_{4}\mathrm{Be} + {}^{4}_{2}\mathrm{He} \rightarrow {}^{12}_{6}\mathrm{C} + {}^{1}_{0}\mathrm{n} + \text{energy}$$

In collisions with nuclei neutrons are gradually slowed down until they reach thermal velocities. Hydrogen nuclei are particularly efficient in producing such 'thermal' neutrons and then capturing them according to the reaction

$$^{1}_{0}\mathrm{n} + {}^{1}_{1}\mathrm{H} \rightarrow {}^{2}_{1}\mathrm{H} + \gamma$$

with the production of γ radiation.

In rocks, hydrogen nuclei are present in oil, water, natural gas, etc. and the γ radiation to which they give rise can be detected by lowering a neutron source just ahead of a γ ray counter.

In the neutron–neutron method the intensity of the neutrons scattered by the hydrogen nuclei, rather than the intensity of the γ radiation due to their capture, is detected. Neutrons do not produce appreciable ionization so that a special device is needed for their detection. One such device is a Geiger tube filled with boron trifluoride gas. The neutrons react with the boron transforming it into lithium and releasing an α particle which in turn ionizes the gas and reveals the presence of neutrons.

In passing through matter with a high hydrogen content the neutrons are slowed down and captured by the hydrogen nuclei at a very small distance from the source. On the other hand, if the hydrogen content is low they travel a relatively large distance before reaching thermal velocities. Since virtually all hydrogen in rocks is in the pore fluids, the tool can be calibrated to record the porosity directly by measuring its response in reference models of known porosity in which the pores are filled with water. The matrix in the reference model also has some effect on neutron velocities. Most neutron tools have dual calibrations made by using two different reference models having limestone or sandstone respectively as the matrix.

The logging engineer has the option on the well site to record the porosity using one of the two calibrations depending on his judgement of the local geology. If a certain rock formation in the well does not conform to the selected option, only an 'apparent limestone (or sandstone) porosity' will be obtained. This can be converted to the true porosity by means of experimentally obtained charts such as that in Fig. 9.5 which is valid for readings recorded using the option 'limestone matrix'. Thus, e.g., if the recorded porosity value is 14% at some depth where the rock happens to be a dolomite the true porosity will be 11%.

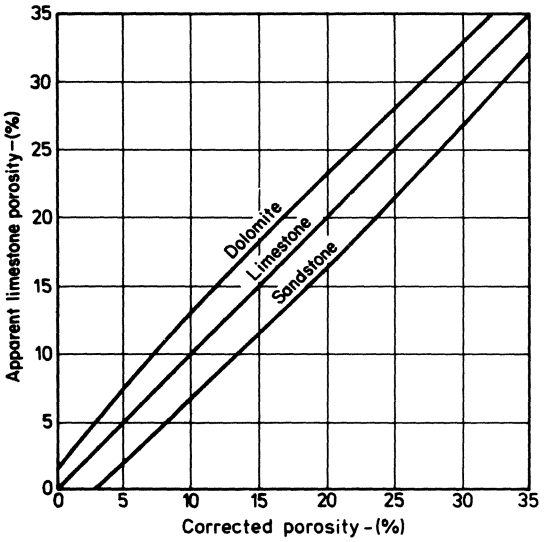

Fig. 9.5 Example of chart for matrix correction. After [196].

The neutron–γ and the single-detector neutron–neutron have now been largely superseded by the compensated neutron log (CNL) in which there are two detectors about 25 and 40 cm respectively from the neutron source and the ratio N_n/N_f of the neutron intensities in the near and far detectors is measured. The ratio increases with porosity for obvious reasons and as with the older instruments the porosity is recorded directly. The depth sensed is about 30 cm.

The neutron log is generally run together with the density log (and the natural γ log) and seldom by itself. Normally, the neutron log indicates a somewhat higher porosity than the density log as the neutron tool also senses the bound water in the clay particles that are nearly always present, and also due to dolomitization which, as it makes the rock denser, leads to a higher neutron absorption than in pure limestones or sandstones. Empirically, the true porosity is found to be very nearly the mean of the two values.

However, if the pore space in a formation is filled with gas the bulk density as well as the hydrogen content will decrease and the neutron log will indicate a lower porosity than the density log. This so-called 'cross-over' in a combined record of neutron and density logs is therefore a clear indicator of gas (Fig. 9.6). False cross-overs can, however, be obtained if the porosity is recorded assuming a limestone matrix where the actual matrix is sandstone while cross-overs may be suppressed if the matrix in this case is dolomite instead.

The logging rate for neutron and density logs is about 550 m per hour, that is, the same as for the natural γ ray. In fact, all three tools are usually mounted in tandem on one and the same sonde, about 8 m long.

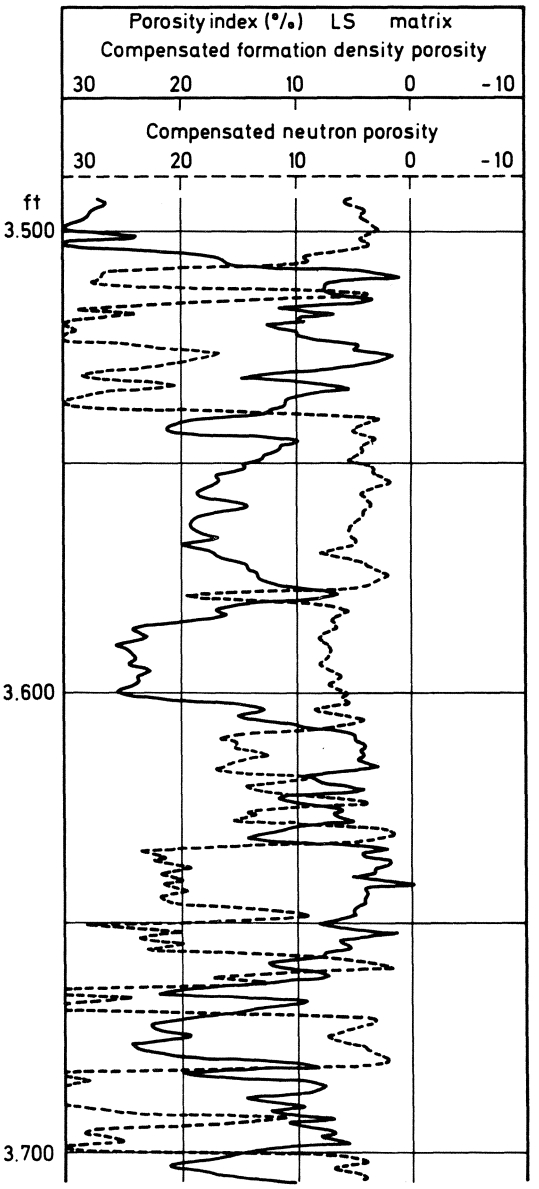

Fig. 9.6 Neutron and density logs with cross-over. After [197].

9.6.3 Sonic or acoustic log

The sonic log is based on the observation that the velocity of sound in a porous rock depends upon the velocity in the matrix as well as that in the fluid occupying the pore space. The effect is extremely complex in reality and no simple theoretical description of it can actually be given even for highly idealized systems [see, e.g. 203 pp. 190 ff]. However, as an empirical aid in estimating the porosity ϕ it is assumed that the travel time through a block of porous rock is the same as if the matrix material were all pressed as a uniform medium at one end and all the fluid filling the pores into a second contiguous medium. This concept leads to the following simple formula (the Wyllie relation) for the travel time t:

$$t = \phi t_f + (1 - \phi) t_{ma} \tag{9.10}$$

where t_f, t_{ma} are the travel times through the fluid part and the matrix part respectively. Equation (9.10) gives

$$\phi = \frac{t - t_{ma}}{t_f - t_{ma}} \tag{9.11}$$

We have already come across velocity logging (Section 7.3.3.10). However, the sonic log does not measure the velocity as such but the time taken by the compressional wave to go through the distance (typically about 0.6–0.7 m) between two receivers, the near one of which is about 1 m from the source. Modern versions use a system of two sound transmitters and four receivers between them to compensate for borehole effects. Logging speeds are about 1500–1600 m per hour.

The observed time is converted to a *specific time* t, $\mu s\, m^{-1}$, needed for the wave to go 1 m. The t_f in Eq. (9.11) is assumed to be that for the mud filtrate (typically 620 $\mu s\, m^{-1}$) whereas t_{ma} depends on the rock type concerned, which must be known if accurate ϕ values are to be obtained. Standard recommended values for t_{ma} are 144, 161 and 177 $\mu s\, m^{-1}$ for dolomite, limestone and sandstone respectively.

9.6.4 Electromagnetic propagation travel-time log

The EPT log, as this is called, measures primarily the specific travel time of very high frequency electomagnetic waves (50 MHz–1 GHz) in the zone invaded by the mud filtrate. The velocity, the specific travel time and the penetration of such waves depend only on the dielectric constant (cf. Eq. (6.33)) and not on the frequency. By an assumption similar to that underlying Eq. (9.11), the porosity can be calculated by the same algebraic formula, using the times for EM propagation instead.

The dielectric constant of a porous medium depends strongly on the water

content. Consequently the EPT-derived porosity ϕ_{EP} indicates essentially that part of the pore space which is water filled whereas the porosity ϕ obtained from a neutron/density log combination provides a measure of all the pore space that is fluid filled. If the pore space contains water as the only fluid then $\phi_{EP} = \phi$. If not, the difference between ϕ_{EP} and ϕ can be attributed to the presence of oil.

The EPT log is a comparatively new addition to the various logging methods and for a fuller account of it the interested reader is referred to Dewan [197].

9.7 AUXILIARY LOGS AND MEASUREMENTS

Besides the above described primary logs that measure a physical property of the formations, a few other types of measurements are also routinely carried out in well logging. These are needed principally for applying various corrections to the data of the primary logs.

An estimate of the temperature is required to correct for the dependence of resistivity (conductivity) on it. Usually it is only measured at a few points in the well (often only at the top and the bottom) and the temperature at intermediate points is estimated by simple linear interpolation.

The well diameter and its variations are recorded by the continuous *caliper log*. This information is needed to estimate the effect of borehole mud on resistivity measurements and the effect of the rugosity of the hole on density and neutron logs.

Another auxiliary log that is included in many routines is the *dipmeter log* which records the dip of a formation. This is required for determining where in a geologic structure a well is located, the kind of faulting encountered, etc. [196]. It is not primarily a log for calculating hydrocarbon in place.

9.8 BASIC LOG INTERPRETATION PROCEDURE

The physical background of well-log interpretation should be evident from the previous pages but it will be convenient in concluding this chapter to recall and summarize the principal steps. These are:

(1) Scan the SP and/or γ ray log (always Track 1) and pick out non-shales, that is, permeable zones (high negative SP, low γ ray count) after determining the shale line.
(2) Estimate R_w from the SP jump using Eq. (9.7) and read bed thickness h from the log.
(3) Scan resistivity (conductivity) curves, usually Track 2, looking for high apparent resistivities (low conductivities). These may be due to the presence of hydrocarbons.

(4) Estimate R_t from Eq. (9.8) or its counterpart if conductivity is scanned.
(5) Read porosities ϕ in the zones of interest (usually Track 3 but sometimes separately executed logs). Locate any 'cross-overs' in density and neutron logs to identify gas occurrence.
(6) Calculate S_w in the zone of interest from Eq. (9.4).
(7) Finally, calculate hydrocarbons-in-place from Eqs (9.1) and (9.2) assuming a reasonable estimate of A.

The above steps show only the fundamental logic involved. A considerable amount of detailed log interpretation is based on empirical and semi-empirical observations requiring special charts, correction tables, etc. For a description of these, reference should be made to specialized logging literature [196, 197, 199, 200].

10

Miscellaneous methods and topics

As the requirements of modern oil and mining exploration, hydrological investigations and civil engineering have grown, a number of special techniques suited to particular problems have been proposed and applied with varying degrees of success. The purpose of this chapter is to mention a few of these techniques and also discuss some topics which are of common interest in all geophysical surveys.

10.1 BOREHOLE MAGNETOMETER

The measurement of electric resistivity, self-potential and elastic wave velocities in boreholes has already been mentioned (pp. 333, 329, 292). It may be added that magnetic intensities too can be measured in a borehole by lowering a fluxgate or a proton magnetometer in it.

The borehole magnetometer has been used chiefly in iron-ore prospecting as an auxiliary instrument. If, for instance, a borehole has failed to encounter an expected ore zone, magnetic measurements can frequently reveal whether the zone is present in the vicinity of the hole and also indicate its distance. Weak and erratic mineralization often makes it difficult or impossible to establish the precise limits of a magnetic impregnation zone by an inspection of the drill cores alone. In such cases, the borehole magnetometer may be of considerable assistance.

The instrument can also be employed sometimes for correlating zones of the same grade in different parts of a magnetite ore deposit.

10.2 *MISE-À-LA-MASSE* METHOD

This technique, sometimes called 'charged-body potential method' in English, involves the placing of one current electrode in a conducting body (e.g. an ore

mass) with the other electrode at a distant point. The electric potentials are measured at points on the ground surface or in boreholes when a current is passed, care being taken, of course, before passing the current to compensate for any SP between the potential electrodes. On homogeneous ground the equipotentials on the surface will evidently be circles with the epicentre of the electrode as the centre. The form of the equipotential surfaces in three dimensions may be visualized by imagining Fig. 4.12 to be rotated around a vertical axis through the buried point electrode. In general, however, the equipotentials will be distorted in practice from their pattern in homogeneous ground due to electrically conducting inhomogeneities.

The *mise-à-la-masse* technique is particularly useful in finding out whether an ore outcrop (or an ore width encountered in a borehole) is a small mass or part of a much larger mass. In the former case the equipotentials on the surface will be more or less circular, while their pattern in the latter case will reflect the strike and geometry of the larger mass. The technique is also useful for testing whether (conducting) ore widths encountered in different holes are interconnected or isolated from each other [204]. Several examples of the application of the technique in ore prospecting have been given by Ketola [205] and it has also been used to study the geometry of electrically well conducting fracture zones in a highly resistive environment [206].

Very few general rules can be formulated to interpret *mise-à-la-masse* measurements. Every case is studied individually and an attempt is made to build a physically plausible model to explain the observed potentials. A theoretical approach has nevertheless been made by Eloranta [207].

10.3 LOGGING IN CRYSTALLINE ROCKS AND COAL FIELDS

Geophysical measurements in boreholes in crystalline rocks have become of great importance in recent years with the need for finding safe repositories for used nuclear fuel [208]. All techniques of well logging described in Chapter 9 can be employed in crystalline rocks but the object is to delineate fracture-free zones of fresh rock. Fractured rock is indicated generally by relatively very low values of apparent resistivity, density and seismic velocity. Of particular use in this connection, because it can indicate even minor fractures, is the single-point resistance log that simply measures the contact resistance between a short brass rod and the borehole wall. Fractures are also indicated by characteristic irregularities in the temperature in a hole provided the hole is water filled.

Logging in coal fields is mainly used for geologic correlation and to estimate the shaliness of a coal formation [209]. Shales and non-shales are distinguished in this case by the same criteria as in oil fields (Chapter 9).

10.4 GEOTHERMAL METHODS

Owing to the radioactivity of the crustal rocks heat is being continuously transported to the surface of the earth from its interior at a mean rate of about $50\,\mathrm{mW\,m^{-2}}$. The lateral variations of this heat flow over the surface of the earth are small. If there are any appreciable local variations they are superimposed on the thermal effects due to vegetation, microclimates, etc. The latter are so large that surface temperature measurements cannot (as a rule) be used for deducing the thermal conductivity of rocks at depth or for determining the position of structures such as buried domes, anticlines, etc. They have, however, been successfully applied in finding fissures and cracks along which convective transfer of heat has taken place from the depth through the agency of water [210].

Also, Pooley and van Steveninck have shown in an excellent paper [211] that temperatures only about 2 m below the ground surface are substantially free from the above effects and measurements in short drill-holes are capable of revealing shallow salt domes and similar structures by anomalies of the order of 1–2° C (50–100 times the measurement accuracy!).

Contrary to the behaviour of the total heat flow, the vertical gradient of the temperature in the earth varies within wide limits ($5–70°\,\mathrm{C\,km^{-1}}$) depending upon the thermal conductivity of rock formations, and temperature logs in deep boreholes can be used with advantage in correlating stratigraphic horizons.

10.5 GEOCHEMICAL PROSPECTING

Indications of oil, ore and other minerals can be sought by chemical analysis of the solid, and gaseous substances of which the earth's crust is composed. Such geochemical prospecting can be carried out in the bedrock, in loose overburden or in the uppermost layer of the earth's crust, namely the surface soils [212, 213].

The analysis of the gases slowly diffusing from very great depths to the surface of the earth has been employed in petroleum prospecting for quite some time. In this case the contents of hydrocarbons like methane, ethane, propane, etc. (which are intimately associated with oil) are determined in samples of gas collected just below the surface of the earth.

In mineral prospecting the object is to determine the metallic contents at different places on the earth. Metal ions can migrate through a number of agencies like weathering, leaching, wind transport, etc. several tens or even hundreds of metres from the parent ore body and create 'haloes' of mineralization around it. The metal concentrations in such haloes are in general very small and refined colorimetic and spectrographic methods are needed for reliable determinations.

The tracing of haloes is reported to have led to the discovery of a large number of mineralized zones in different parts of the world.

The phenomenon of the migration of metals within the earth's crust is an exceedingly complex one. Nevertheless, great progress has been made in its study, particularly in the USSR [212]. The importance of geochemical prospecting will be apparent from the fact that many metals like molybdenum, tungsten, vanadium, etc. which are of vital importance in modern industry, occur in the earth's crust in quantities far too small to alter appreciably the physical properties of the host rock so that their detection by geophysical means is out of the question.

10.6 OPTIMUM POINT AND LINE SPACING

It is clear that the amount of information that can be extracted about subsurface features from geophysical measurements will be greater the denser the network of the observation points. A maximum amount of information will be available when the points are infinitely close to each other. However, this ideal cannot be realized, first due to the finite size of any instrument and secondly due to economic and practical considerations. Therefore a balance must be struck between the extent of information desired and the amount of detail to be mapped.

Geophysical observations are most conveniently made at a number of consecutive points along a set of parallel straight lines. It is advantageous to stake the lines perpendicular to the known or presumed geological strike, which is the direction of the trace made on the earth's surface by inclined strata.

The geological conditions tend to be uniform over relatively large distances along a line in the strike direction but may vary considerably within short distances in the perpendicular direction (Fig. 10.1). If the lines of measurement are normal to the strike their mutual distance may be kept large while the

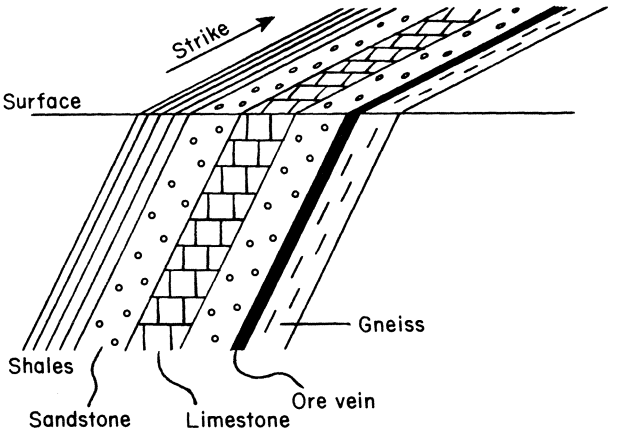

Fig. 10.1

geophysical observations are taken along each of them at relatively close intervals.

The distance between observation points must be adjusted to the anticipated depth of the feature one is seeking. The anomalies of shallow features are narrow while those of deep-lying features extend over greater distances. As a rule geophysical observations cannot be expected to yield information about features whose depth is much smaller than the distance between the observation points.

The optimum distance between the lines is dependent upon the length of the sub-surface feature, or more correctly, upon the estimated length of its measurable surface anomaly. If the distance is too large there may be no line which crosses a short anomaly and the corresponding feature may be undetected. On the other hand, if the line distance is too small there may be quite a number of lines crossing a long anomaly. In general, such lines tend to add to the cost of the survey without providing very much additional information.

Mathematically, the problem of optimum line spacing is that of finding the probability of detecting a geophysical anomaly of given dimensions by surveys with a particular line spacing. This is actually an old problem in 'continuous geometric probabilities' [214] whose solution is well known. For example, if the length of an unknown anomaly is L, the probability that one of a set of lines with spacing $S(\geqslant L)$ crosses the anomaly is $2L/\pi S$. If a number of ore bodies each of which produces an anomaly of length L are randomly distributed in an area the probability of detecting them by a survey with a line spacing $S = L$ is 0.636.

For $S \leqslant L$ the probability that at least one line crosses the anomaly is

$$\frac{2L}{\pi S}[1 - \sqrt{(1 - S^2/L^2)}] + \frac{2}{\pi}\cos^{-1}(S/L)$$

If the length of the ore bodies is, say 100 m the probability of detecting them all with a line spacing of 20 m is 0.974.

Other aspects of optimum line spacing have been considered by Agocs [215].

10.7 POSITION LOCATION IN AIRBORNE SURVEYING

The interpretation of airborne geophysical anomalies and the subsequent ground follow-up require a knowledge of the altitude of the aircraft and its position in the horizontal plane.

The altitude is measured by a barometric or a radio altimeter and is recorded continuously alongside the data representing the results of the geophysical measurements. The position of the aircraft in the horizontal plane is much more difficult to determine. If detailed large-scale maps or good aerial

photographs are available the following method is commonly used for this purpose.

The line to be flown is drawn on the map or the photograph and the pilot takes his bearing on a suitable distant landmark on the line. A navigator sitting beside the pilot watches for details on the flight lines such as rivers, lakes, brooks, railways, houses, etc. At intervals, when flying over a clearly identifiable feature he makes a mark on the map and at the same time presses a signal button which puts another mark on a trace on the recording paper. The succession of marks on the map and the recording paper can be correlated at the end of the flight. The navigator also informs the pilot of any adjustments necessary in the course of the plane.

If maps or air photographs are not available a camera is installed in the plane and exposures are made at regular intervals during flight. The number and the instant of an exposure are, of course, automatically registered on the recording paper. The interval between exposures is usually such that a certain amount of overlap between two adjacent photographs is obtained.

The above position location systems function satisfactorily only so long as there are a sufficient number of distinct topographic features in the area. In flying over dense jungles, deserts, seas, etc. the paucity or absence of such features severely limits the value of photographic methods and some form of radio location must be used. Some of these methods employ radar pulses while others are operated on continuous radio frequency waves. The general principle of the latter methods (Decca, Raydist, Lorac, etc.) is to send out radio waves simultaneously from two transmitter stations at fixed and precisely known locations and measure the phase difference between them at the receiver station (aeroplane). The phase difference is essentially a measure of the difference between the travel times of the two electromagnetic waves and is therefore proportional to the difference of the transmitter distances from the aeroplane.

Another method of radio location uses the Doppler effect. Four radio beams directed towards the ground are sent out making a small angle with the vertical from a transmitter in the aeroplane, two in the forward and aft directions and two sideways. The Doppler frequency shifts of the reflected waves due to the motion of the aeroplane are made to yield the deviations of the plane from the flight line. Thus, starting from a given station and a given initial bearing the actual flight path can be reconstructed from the continuous record of the Doppler shifts.

10.8 COMPOSITE SURVEYS

The choice of the method for a geophysical survey is guided by a number of considerations such as the object of the survey, the geology and topography of the area to be investigated and the type of information sought about the sub-

surface. The last mentioned factor is, of course, of fundamental importance.

It is frequently advantageous to use two or more suitable methods within a given area. Such a composite survey gives additional information about the physical properties of the sub-surface and helps (in combination with the geological knowledge) to reduce the uncertainty inherent in the interpretation of geophysical data.

For example, an electromagnetic anomaly may indicate an electric conductor but sometimes the conductor may be so good that the strong eddy currents in it will screen other less good conductors in the vicinity from the primary field and these will not be detected. In such a case an earth resistivity (or a self-potential) survey will often reveal their presence. A magnetic survey will further eliminate (or confirm) the possibility whether these conductors contain magnetite (pyrrhotite) or are composed purely of non-magnetic conducting minerals. A gravity survey will often help to distinguish between compact, massive ore bodies and zones of poor, disseminated mineralization since the density contrast with the host rock will be large in the first case and small in the second.

Faults, domes, anticlines and other geological structures indicated by a seismic survey can also be 'screened' by gravity observations to obtain information about the density contrasts involved, while magnetic measurements can frequently reveal diabase and gabbro dikes which may not be indicated by the seismic survey owing to their insufficient velocity contrast with the country rock.

Examples of the advantages of composite surveys can be easily multiplied. The results along one of the profiles in a composite electromagnetic, magnetic, self-potential, earth resistivity and induced polarization survey in a lead–zinc–copper sulphide mineralization district in central Sweden are shown in Fig. 10.2, where the scale is in metres. Many of the above-mentioned effects will be recognized in this example. For instance, the electromagnetic indication is due to a thin sulphide vein but the resistivity survey reveals a broad low-resistivity zone of which only a part seems, to judge from the IP profile, to be electronically conducting. The SP profile differentiates two tops corresponding probably to two separate sulphide concentrations within the broad impregnation zone.

Another example in which a combination of two methods supplies extra information is shown in Fig. 10.3. The upper part shows aeromagnetic anomalies. We notice two long and parallel, narrow belts to the west. On the airborne electromagnetic map (lower part) only one of them appears strongly. Evidently, the north-western magnetic anomaly must be caused by a long ultrabasic dike whereas the other anomaly is due to a pyrrhotite-bearing black-shale horizon which, incidently, is a key horizon for ore prospecting in this region. It should also be noticed that a small part of the ultrabasic dike does appear on the electromagnetic map giving weak negative anomalies.

With the coil configuration used (wing-tip mounted coils with dipole axes in

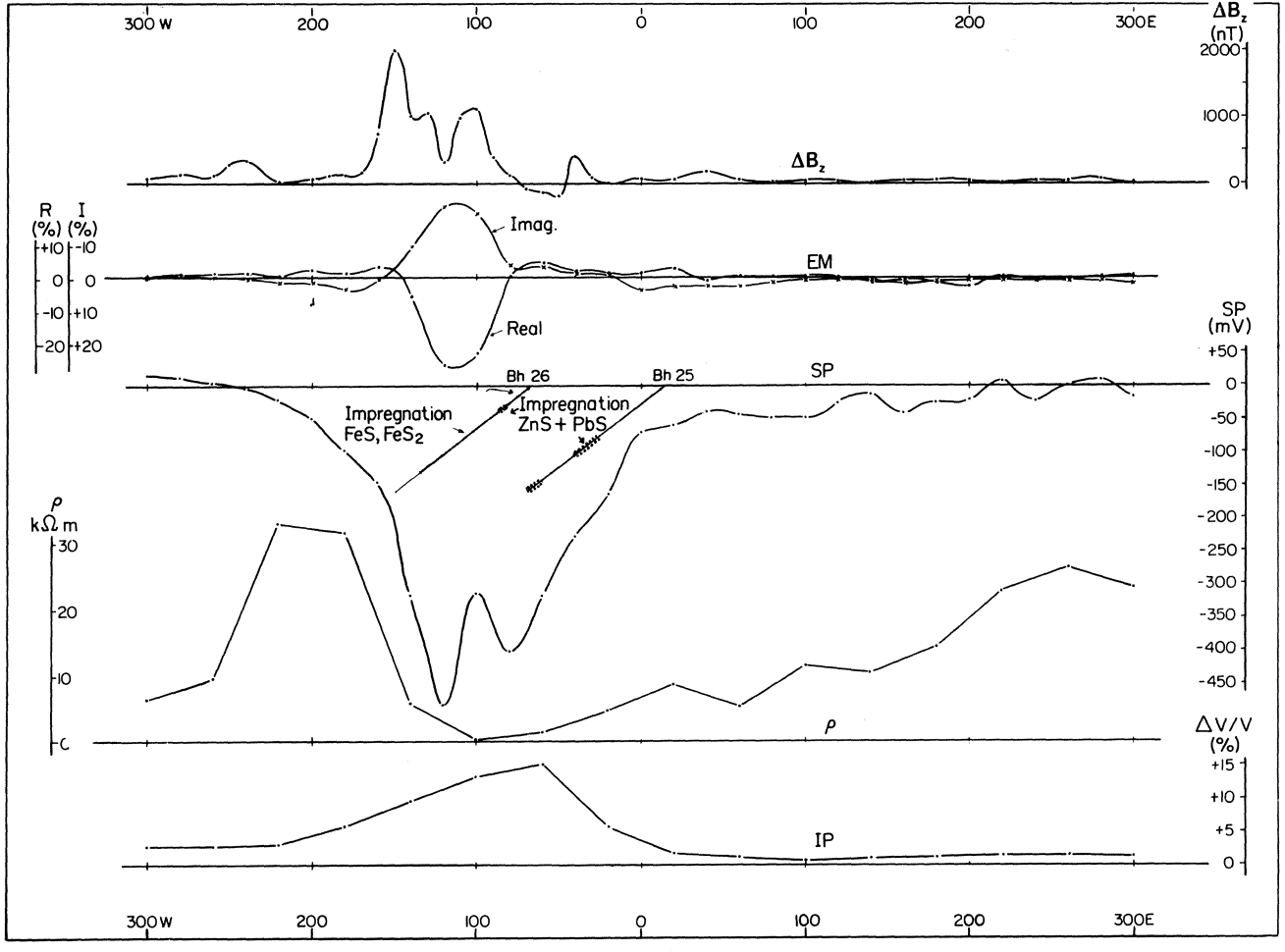

Fig. 10.2 Example of a composite survey.

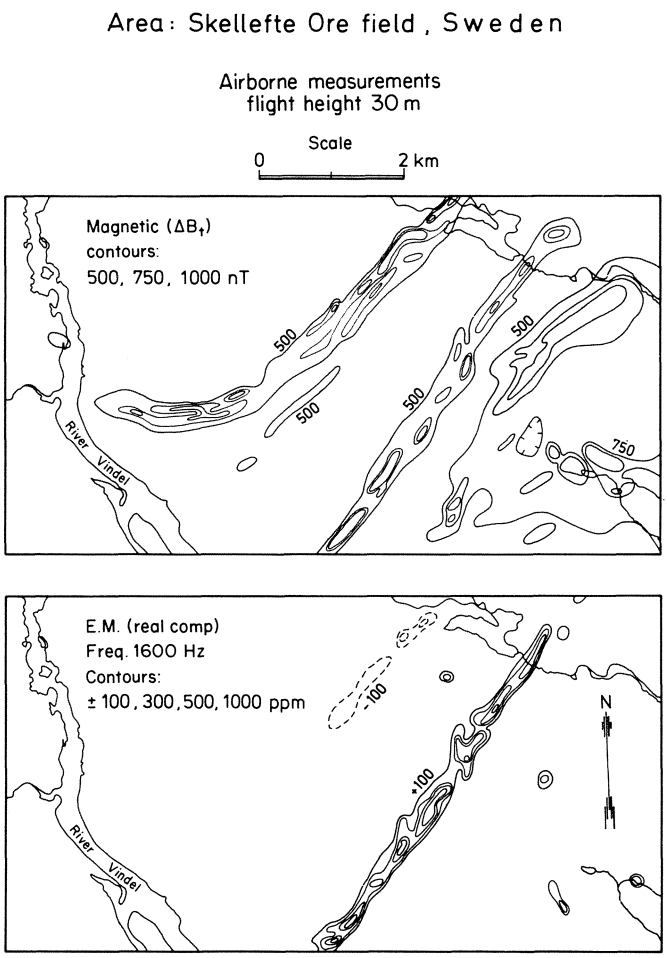

Fig. 10.3 Combination of electromagnetic and magnetic surveys.

the flight direction) tabular conductors give positive anomalies as, for instance, the shale horizon does. The weak negative electromagnetic anomalies of the ultrabasic dike are actually due to the magnetic permeability of the dike (cf. Section 6.13). The eastern magnetic complex, on the other hand, does not give electromagnetic anomalies, either positive or negative. It is clear that not only is this complex a poor electric conductor but also that it has a low magnetic permeability. Presumably this is also basic rock but its content of magnetic material is much smaller than that of the ultrabasic dike.

Several examples of composite surveys and references to case histories will be found elsewhere [102, 127, 216].

Appendices

APPENDIX 1

The magnetic potential

Like the mechanical force (joule per metre = newton) or the electrical force (volt per metre), a static magnetizing force **H** (ampere per metre) is also postulated to be derivable from a corresponding (scalar) potential ϕ (ampere) so that

$$H_x = -\frac{\partial \phi}{\partial x}, \qquad H_y = -\frac{\partial \phi}{\partial y}, \qquad H_z = -\frac{\partial \phi}{\partial z} \tag{A1.1}$$

The H field produces a flux density $\mathbf{B} = \mu\mathbf{H}$.

No sources or sinks of magnetic flux have ever been found to exist. The 'pole' of a magnet is not a source or a sink of flux, for if it were, we would be able to isolate it as such, by cutting the magnet, but no subdivision of a magnet, however fine, succeeds in this respect.

It is easy to show that in a field of flux that contains no sources or sinks of flux, the divergence of the flux density vector is zero. For the magnetic flux we have thus

$$\operatorname{div} \mathbf{B} = \frac{\partial B_x}{\partial x} + \frac{\partial B_y}{\partial y} + \frac{\partial B_z}{\partial z} = 0 \tag{A1.2}$$

From the sets of equations (2.4) and (A1.1) in combination with (A1.2) it follows immediately that

$$\nabla^2 \phi = \operatorname{div} \mathbf{M} \tag{A1.3}$$

We shall now solve Eq. (A1.3) in order to find ϕ when **M** is given.

According to Green's theorem if U, V are two functions with sufficient

differentiability in a region R (volume element dv), then

$$\iiint_R (U\nabla^2 V - V\nabla^2 U)\,dv = \iint_S \left(U\frac{\partial V}{\partial n} - V\frac{\partial U}{\partial n}\right) dS \qquad \text{(A1.4)}$$

where S is the surface bounding R and $\partial/\partial n$ denotes differentiation with respect to the outward normal to dS.

Let R denote the *whole* of space, M_ξ, M_η, M_ζ the components of magnetization at any point of it and ϕ the magnetic potential. Put $U = \phi$, $V = 1/r$ where r is the distance between an arbitrary point $Q(\xi, \eta, \zeta)$ in R and a definite point $P(x, y, z)$ in R. We have

$$r^2 = (x-\xi)^2 + (y-\eta)^2 + (z-\zeta)^2$$

Surround P by a sphere Σ with P as centre and let R_1 denote the region of R external to Σ. The surface σ of Σ is one boundary of R_1, the other boundary being, of course, at infinity. It can be verified by direct differentiation that $\nabla^2 V = 0$ in R_1. Then from (A1.4),

$$\iiint_{R_1} \left(-\frac{\nabla^2\phi}{r}\right) dv = \iint_\sigma \left[\phi\frac{\partial}{\partial n}\left(\frac{1}{r}\right) - \frac{1}{r}\frac{\partial\phi}{\partial n}\right] d\sigma$$

Since the direction of n is opposite to the radius vector ε from P to $d\sigma$, $\partial/\partial n = -\partial/\partial\varepsilon$. Furthermore $r = \varepsilon$ on σ, so that

$$\iiint_{R_1} \left(-\frac{\nabla^2\phi}{r}\right) dv = \iint_\sigma \left(\frac{\phi}{\varepsilon^2} + \frac{1}{\varepsilon}\frac{\partial\phi}{\partial\varepsilon}\right) d\sigma$$

But $d\sigma = \varepsilon^2\, d\Omega$ where $d\Omega$ is the solid angle subtended by $d\sigma$ at P. Hence

$$\iiint_{R_1} \left(-\frac{\nabla^2\phi}{r}\right) dv = \iint_\sigma \left(\phi + \varepsilon\frac{\partial\phi}{\partial\varepsilon}\right) d\Omega$$

which reduces as $\varepsilon \to 0$ (and consequently $R_1 \to R$) to

$$\iiint_R \left(-\frac{\nabla^2\phi}{r}\right) dv = \phi(P)\iint d\Omega = 4\pi\phi(P) \qquad \text{(A1.5)}$$

Since $\nabla^2\phi = \operatorname{div}\mathbf{M}$ (equation A1.3) we get

$$\phi = -\frac{1}{4\pi}\iiint_R \frac{\operatorname{div}\mathbf{M}}{r}\, dv \qquad \text{(A1.6)}$$

where it is *implicit that M is continuous throughout R.*

It is more or less obvious that

$$\frac{\operatorname{div}\mathbf{M}}{r} \equiv \frac{1}{r}\left(\frac{\partial M_\xi}{\partial\xi} + \frac{\partial M_\eta}{\partial\eta} + \frac{\partial M_\zeta}{\partial\zeta}\right)$$

$$\equiv \operatorname{div}\left(\frac{\mathbf{M}}{r}\right) - \sum M_\xi \frac{\partial}{\partial \xi}\left(\frac{1}{r}\right)$$

Hence

$$\phi = -\frac{1}{4\pi}\left[\int_R \operatorname{div}\left(\frac{\mathbf{M}}{r}\right) dv - \int_R \sum M_\xi \frac{\partial}{\partial \xi}\left(\frac{1}{r}\right) dv\right]$$

If M is discontinuous on some surface bounding a volume R_1, encapsulate the surface by two surfaces S_1, S_2 (dashed lines in Fig. A1.1) on either side of it, enclosing an infinitesimal volume $\Delta\tau$. Then

$$\begin{aligned}\phi &= -\frac{1}{4\pi}\left[\int_{R_1} \frac{\operatorname{div}\mathbf{M}}{r} dv + \int_{\Delta\tau} \frac{\operatorname{div}\mathbf{M}}{r} dv + \int_{R_2} \frac{\operatorname{div}\mathbf{M}}{r} dv\right] \\ &= -\frac{1}{4\pi}\left[\int_{R_1} \operatorname{div}\left(\frac{\mathbf{M}}{r}\right) dv + \int_{\Delta\tau} \operatorname{div}\left(\frac{\mathbf{M}}{r}\right) dv + \int_{R_2} \operatorname{div}\left(\frac{\mathbf{M}}{r}\right) dv\right. \\ &\quad \left. - \int_{R_1} \sum M_\xi \frac{\partial}{\partial \xi}\left(\frac{1}{r}\right) dv - \int_{\Delta V} \sum M_\xi \frac{\partial}{\partial \xi}\left(\frac{1}{r}\right) dv - \int_{R_2} \sum M_\xi \frac{\partial}{\partial \xi}\left(\frac{1}{r}\right) dv\right]\end{aligned} \tag{A1.7}$$

However, by the divergence theorem

$$\int_V \operatorname{div}\left(\frac{\mathbf{M}}{r}\right) dv = \int_S \frac{lM_\xi + mM_\eta + nM_\zeta}{r} dS \tag{A1.8}$$

where S is the bounding surface of a volume V and l, m, n are the direction cosines of the outward normal of dS. It is easy to see that S for R_1 is S_1; for $\Delta\tau$ it is S_1 and S_2 and for R_2 it is S_2.

However, dS_1 considered as an element of the bounding surface of R_1 has an outward normal that is exactly opposite to the outward normal when dS_1 is considered as an element bounding $\Delta\tau$. Hence the integrals over S_1 cancel each other. Similarly the integrals over S_2 cancel each other. Hence in view of (A1.8)

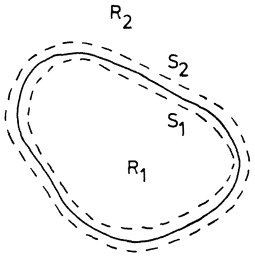

Fig. A1.1

the first three terms of the right-hand side of (A1.7) sum to zero and when $\Delta\tau \to 0$ the equation reduces to

$$\phi = \frac{1}{4\pi}\iiint_R \left[M_\xi \frac{\partial}{\partial \xi}\left(\frac{1}{r}\right) + M_\eta \frac{\partial}{\partial \eta}\left(\frac{1}{r}\right) + M_\zeta \frac{\partial}{\partial \zeta}\left(\frac{1}{r}\right)\right] dv \qquad \text{(A1.9)}$$

It should be noted that the integral is to be taken over *all* space and not merely throughout the bounded volume R_1. Only if the subspace outside R_1 is non-magnetic ($M = 0$ outside R_1) does the integral reduce to one over R_1 alone.

Dipole potential

If $M \neq 0$ within an infinitesimal volume Δv and 0 elsewhere, the derivatives in (A1.9) may be considered to be constant throughout Δv and

$$\begin{aligned}\phi &= \frac{1}{4\pi}\left[\frac{\partial}{\partial \xi}\left(\frac{1}{r}\right)\int_{\Delta v} M_\xi \, dv + \frac{\partial}{\partial \eta}\left(\frac{1}{r}\right)\int_{\Delta v} M_\eta \, dv + \frac{\partial}{\partial \zeta}\left(\frac{1}{r}\right)\int_{\Delta v} M_\xi \, dv\right] \\ &= \frac{1}{4\pi}\left[m_\xi \frac{\partial}{\partial \xi}\left(\frac{1}{r}\right) + m_\eta \frac{\partial}{\partial \eta}\left(\frac{1}{r}\right) + m_\zeta \frac{\partial}{\partial \zeta}\left(\frac{1}{r}\right)\right] \qquad \text{(A1.10)}\end{aligned}$$

The integrals of M_ξ, M_η, M_ζ over the small volume Δv are the magnetic moments (A m^2) in the x, y, z directions. In the limit $\Delta v \to 0$ Eq. (A1.10) gives the potential of point dipole whose moment **m** has the components m_ξ, m_η, m_ζ in the x, y, z directions.

In the case of a point dipole there is no loss of generality in rotating the coordinate axes so that the components of **m** along the new y and z directions vanish, in which case

$$\begin{aligned}\phi_{\text{dipole}} &= \frac{m}{4\pi}\frac{\partial}{\partial \xi}\left(\frac{1}{r}\right) \\ &= -\frac{m}{4\pi}\frac{\partial}{\partial x}\left(\frac{1}{r}\right) = \frac{m}{4\pi}\frac{1}{r^2}\frac{\xi - x}{r} \\ &= \frac{m}{4\pi}\frac{1}{r^2}\cos\theta \qquad \text{(A1.11)}\end{aligned}$$

where θ is the angle between the dipole axis and the line joining the dipole at Q to the point P (Fig. A1.2).

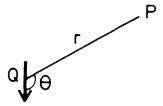

Fig. A1.2 Magnetic dipole.

APPENDIX 2

Magnetized sphere and a magnetic dipole

A2.1 Isotropic, homogeneous sphere subject to a uniform external field strength $H_0(\mathrm{A\,m^{-1}})$

Since the potential due to magnetization is given by Eq. (A1.9) the net magnetizing force at any point $P(x, y, z)$ in, say, the x direction is

$$H_x = H_{0x} + \left(-\frac{\partial \phi}{\partial x}\right) \tag{A2.1}$$

We shall calculate the components H_{ix}, H_{iy}, H_{iz} of the magnetizing force H_i when P is inside the sphere, assuming a susceptibility κ for the sphere and zero for the outside redium so that $\mathbf{M} = \kappa \mathbf{\Pi}_i$. Without loss of generality it may be assumed that x, y, z and ξ, η, ζ are rectangular coordinates with O, the centre of the sphere, as origin.

Then from Eqs (A2.1) and (A1.9):

$$H_{ix} = H_{0x} - \frac{\kappa}{4\pi}\frac{\partial}{\partial x}\iiint_{\text{sphere}}\left[H_{ix}\frac{\partial}{\partial \xi}\left(\frac{1}{r}\right) + H_{iy}\frac{\partial}{\partial \eta}\left(\frac{1}{r}\right) + H_{iz}\frac{\partial}{\partial \zeta}\left(\frac{1}{r}\right)\right] \mathrm{d}v \tag{A2.2}$$

with two similar equations for H_{iy}, H_{iz}.

To solve Eq. (A2.2) for H_{ix} assume as a first guess that H_i is constant within the sphere. Then the three integrals to be evaluated on the right-hand side become

$$\iiint_{\text{sphere}}\frac{\partial}{\partial \xi}\left(\frac{1}{r}\right)\mathrm{d}v, \qquad \iiint_{\text{sphere}}\frac{\partial}{\partial \eta}\left(\frac{1}{r}\right)\mathrm{d}v, \qquad \iiint_{\text{sphere}}\frac{\partial}{\partial \zeta}\left(\frac{1}{r}\right)\mathrm{d}v$$

These can be converted into the surface integrals

$$\iint\frac{l\,\mathrm{d}S}{r}, \qquad \iint\frac{m\,\mathrm{d}S}{r}, \qquad \iint\frac{n\,\mathrm{d}S}{r}$$

where l, m, n are the direction cosines of the surface element $\mathrm{d}S$.

The integrals are elementary and each can be readily evaluated by choosing the lines Ox, Oy or Oz as the respective polar axis of a spherical polar coordinate system.

Since

$$\frac{1}{r} = \frac{1}{[(x-\xi)^2 + (y-\eta)^2 + (z-\zeta)^2]^{1/2}}$$

the integrals turn out to be $4\pi x/3$, $4\pi y/3$, and $4\pi z/3$ (when P is inside the

sphere) so that from (A2.2)

$$H_{ix} = H_{0x} - \tfrac{1}{3}\kappa H_{ix}$$

or

$$H_{ix} = \frac{H_{0x}}{1 + \kappa/3} \tag{A2.3}$$

By symmetry

$$H_{iy} = \frac{H_{0y}}{1 + \kappa/3}, \qquad H_{iz} = \frac{H_{0z}}{1 + \kappa/3}$$

It will be obvious on a moment's reflection that if these values of H_{ix}, H_{iy}, H_{iz} are used as the next guess in Eq. (A2.2) the new values will again be the same. Hence it follows that the internal field in the sphere is uniform, as also its magnetization intensity

$$\mathbf{M} = \frac{\kappa \mathbf{H}_0}{1 + \kappa/3} \tag{A2.3a}$$

The factor $\frac{1}{3}$ in the denominator is *the demagnetization factor.*

A2.2 Magnetic potential of a uniformly magnetized sphere at external points

There is no loss of generality in rotating the coordinate axes in Eq. (A1.9) so that the x axis, say, coincides with the direction of **M**. Then $M_y = M_z = 0$ and $M_x = M$.

Hence

$$\phi = \frac{M}{4\pi} \int\int\int \frac{\partial}{\partial \xi}\left(\frac{1}{r}\right) \mathrm{d}v$$

The quickest way to evaluate the integral here is to note that formally it represents the x component of the external gravitational attraction of a sphere of unit density. Its value is therefore $\frac{4}{3}\pi b^3(\cos\theta)/R^2$ where b is the radius of the sphere, R is the distance of P from O, the centre of the sphere, and θ is the angle between OP and the x axis, that is, M.

Thus

$$\phi = \frac{m}{4\pi} \frac{1}{R^2} \cos\theta$$

where $m = \frac{4}{3}\pi b^3 M$ is the magnetic moment of the sphere, a result that, after comparison with Eq. (A1.11), shows that the potential of a homogeneously magnetized sphere at external points is the same as that of a dipole of identical moment placed at the sphere's centre.

For a sphere in a uniform field, then,

$$m = \frac{4\pi}{3} b^3 \frac{3\kappa H_0}{3+\kappa} \quad (\mathrm{A\,m^2})$$

A2.3 Magnetic field strengths parallel and perpendicular to a dipole

Starting from Eq. (A1.11) we have

$$-\frac{\partial \phi}{\partial r} = \frac{m}{4\pi} \frac{2}{r^3} \cos\theta$$

and

$$-\frac{1}{r}\frac{\partial \phi}{\partial \theta} = \frac{m}{4\pi} \frac{1}{r^3} \sin\theta$$

for the magnetizing forces in the direction of and perpendicular to the radius vector r from the dipole. Each of these can be resolved in the direction parallel and perpendicular to the dipole and it is quite easily shown that the magnetizing forces parallel and perpendicular to the dipole are

$$H_{\parallel} = \frac{m}{4\pi} \frac{1}{r^3} (3\cos^2\theta - 1) \tag{A2.4a}$$

$$H_{\perp} = \frac{m}{4\pi} \frac{3\sin\theta\cos\theta}{r^3} \tag{A2.4b}$$

APPENDIX 3

Magnetic anomaly of a sphere

We shall consider the general case of sphere whose magnetic moment vector **m** is not necessarily in the direction of T_0, the earth's undisturbed magnetizing force, thus implying a remanent magnetization besides that induced by T_0. The surrounding medium is assumed to be non-magnetic.

Let $i(\neq I)$ be the inclination of **m** with the horizontal and ε the angle between the vertical plane through m and the magnetic meridian. Other notations will be (Fig. A3.1):

x = coordinate along the earth's surface measured from an origin O vertically above the sphere's centre.
a = depth of centre below the surface.
$r^2 = a^2 + x^2$ (square of distance from centre) and
γ = angle between the magnetic meridian and the line Ox.

The z axis is directed downwards.

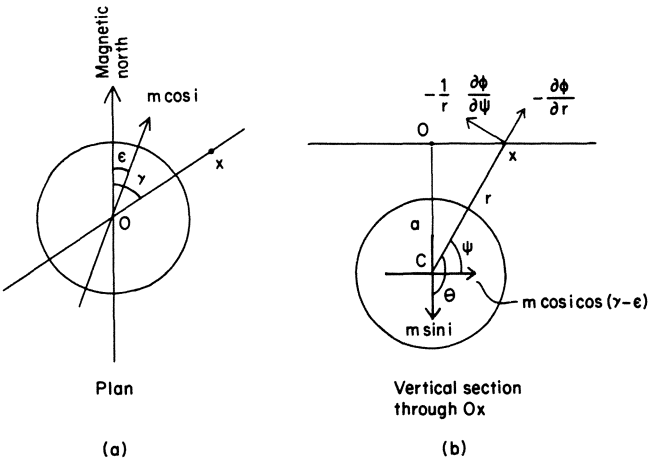

Fig. A3.1 Magnetized sphere.

The moment **m** can be resolved into a vertical component of magnitude $m \sin i$ and two horizontal components of magnitude $m \cos i \cos(\gamma - \varepsilon)$ and $m \cos i \sin(\gamma - \varepsilon)$. With the angles as shown in Fig. A3.1, the potential at x can be written down from equation (A1.11) as

$$\phi = \frac{m \sin i}{4\pi} \frac{\cos\theta}{r^2} + \frac{m \cos i \cos(\gamma - \varepsilon)}{4\pi} \frac{\cos\Psi}{r^2}$$

$$= -\frac{m \sin i}{4\pi} \frac{\sin\Psi}{r^2} + \frac{m \cos i \cos(\gamma - \varepsilon)}{4\pi} \frac{\cos\Psi}{r^2} \qquad \text{(A3.1)}$$

The component $m \cos i \sin(\gamma - \varepsilon)$ does not contribute to ϕ as it makes an angle of $\pi/2$ with Cx. It does, however, contribute to the anomalous flux density at x by the amount

$$\Delta B_y = \mu_0 \frac{m \cos i \sin(\gamma - \varepsilon)}{4\pi r^3} \qquad \text{(A3.2)}$$

directed outwards from the plane of Figure A3.1(b), that is, in the y direction.

From the components of the magnetizing force $-(\partial\phi/\partial r)$ and $-(1/r)(\partial\phi/\partial\Psi)$ along and perpendicular to Cx we get the anomalous flux densities due to the sphere

$$\Delta B_x = -\mu_0 \frac{\partial\phi}{\partial r} \cos\Psi + \mu_0 \frac{1}{r} \frac{\partial\phi}{\partial\Psi} \sin\Psi$$

$$\Delta B_z = \mu_0 \frac{\partial\phi}{\partial r} \sin\Psi + \mu_0 \frac{1}{r} \frac{\partial\phi}{\partial\Psi} \cos\Psi \qquad \text{(A3.3)}$$

Using (A3.1) we easily obtain

$$\Delta B_x = \frac{\mu_0}{4\pi}\frac{m\cos i}{r^3}\left[\left(\frac{3x^2}{r^2}-1\right)\cos(\gamma-\varepsilon)-\frac{3ax}{r^2}\tan i\right] \tag{A3.4}$$

$$\Delta B_z = \frac{\mu_0}{4\pi}\frac{m\sin i}{r^3}\left(\frac{3a^2}{r^2}-\frac{3ax}{r^2}\cot i\cos(\gamma-\varepsilon)-1\right) \tag{A3.5}$$

To calculate ΔB_t in the sense of Eq. (2.21) we must, of course, first calculate $\Delta B_h = (\Delta B_x^2 + \Delta B_y^2)^{1/2}$.

If there is no remanent magnetization **m** lies in the magnetic meridian ($\varepsilon = 0, i = I$) and its magnitude is

$$\tfrac{4}{3}\pi b^3 \frac{3\kappa}{3+\kappa} T_0 \quad (\mathrm{A\,m^2})$$

where b is the radius of the sphere and κ the susceptibility. In this case, for a profile along the magnetic meridian ($\gamma = 0°$) we get from (A3.4), (A3.5) and (2.21):

$$\Delta B_t = \frac{\mu_0}{4\pi}\frac{m}{r^3}\left(\frac{3x^2\cos^2 I - 3ax\sin 2I + 3a^2\sin^2 I}{r^2}-1\right) \tag{A3.6}$$

APPENDIX 4

Measurement of susceptibility and remanence

The intensity of magnetization of rocks can be determined in two basically different ways, either by measuring the field produced by a rock sample or by measuring the effect of the sample on the inductance of an electromagnetic circuit.

A4.1 Magnetometer method

We shall start with the magnetometer method and for simplicity consider a spherical sample (volume v) placed vertically below a vertical-field magnetometer. If H, Z are the earth's horizontal and vertical magnetizing forces, the induced magnetization intensities are $\kappa_e H$ and $\kappa_e Z$ where $\kappa_e = \kappa/(1 + \kappa/3)$ (Eq. (A2.3a), Appendix 2). If the components of the remanent intensity in the sample, M_{rh} and M_{rz}, are directed in the same direction as the induced components, the net horizontal and vertical components of the magnetization intensity will be $\kappa_e H + M_{rh}$ and $\kappa_e Z + M_{rz}$. The components of the magnetic moment are then $(\kappa_e H + M_{rh})v$ and $(\kappa_e Z + M_{rz})v$.

It follows from Eq. (A2.4b), Appendix 2 that directly above the centre of the spherical sample the vertical magnetizing force due to the horizontal moment is zero. The vertical flux density anomaly $\Delta B_z(1)$ read by the magnetometer

will be due to the moment $(\kappa_e Z + M_{rz})v$ only and this is easily seen from Eq. (A3.5) to be

$$\Delta B_z(1) = \frac{\mu_0}{4\pi} \frac{2(\kappa_e Z + M_{rz})v}{a^3} \tag{A4.1}$$

where a = distance between the sample centre and the sensitive element of the magnetometer.

If now the sample is turned upside down, its net magnetic moment in the vertical direction will be $(\kappa_e Z - M_{rz})v$ giving an anomaly

$$\Delta B_z(2) = \frac{\mu_0}{4\pi} \frac{2(\kappa_e Z - M_{rz})v}{a^3} \tag{A4.2}$$

Hence, adding (A4.1) and (A4.2)

$$\kappa_e = \pi \frac{a^3}{v} \frac{\Delta B(1) + \Delta B(2)}{4B_{0z}} \tag{A4.3}$$

where $B_{0z} = \mu_0 Z$ is the normal geomagnetic flux density at the place.

Similarly, by subtraction,

$$M_{rz} = \pi \frac{a^3}{v} \frac{\Delta B(1) - \Delta B(2)}{4\mu_0} \quad (\mathrm{A\,m^{-1}}) \tag{A4.4}$$

The true susceptibility and remanent magnetization intensity are given by $\kappa_e/(1 - N\kappa_e)$ and $M_{rz}/(1 - NM_{rz})$ respectively where N is the demagnetization factor ($\frac{1}{3}$ for a sphere).

In a low magnetic latitude ($B_{0z} \approx 0$) a spherical sample directly below the magnetometer will produce practically no anomaly at it in the vertical direction. In this case the sample should be displaced sideways. It can be easily shown from equation (A2.4), Appendix 2 that at the magnetic equator itself the optimum displacement is such that the line joining the magnetometer element and the centre of the sphere makes an angle $\tan^{-1}\sqrt{2}$ with the horizontal. Equations (A4.2)–(A4.4) must, of course, be replaced then by appropriate equations obtained from (A3.5) since $x \neq 0$.

In any case only samples with relatively high magnetic susceptibility ($\kappa \gtrsim 1$ if $v \approx 0.5$ litre and $a \approx 1$ m) can be measured in this fashion. For weakly magnetic samples it is necessary to use a more sensitive apparatus, for example an astatic magnetometer. Further, a strong magnetizing force such as that due to a current-carrying solenoid is required instead of the earth's magnetizing force. Werner [217] has described in detail an apparatus for measuring weakly magnetic rock samples.

A4.2 Electromagnetic method

The principle of the electromagnetic method of measuring the susceptibilities of rocks is to determine the change in the inductance of a solenoid when a

magnetic body is introduced in the solenoid. The inductance is usually measured on an alternating current bridge. The change in inductance is related basically to the permeability of the rock material. An apparatus in which the change that results in the mutual inductance of two flat coils when the coils are placed on a smooth outcrop of a rock has been described by Mooney [218]. Apparatuses of this type are also commercially available.

An ingenious, but apparently little known, electromagnetic method with which both the relative magnetic permeability (μ_r) and the electric conductivity (σ) of a cylindrical drill core sample can be determined simultaneously has been described by Malmqvist [219]. In this, a long solenoid is fed by an alternating current (frequency $\nu \sim 10$–$30\,\text{kHz}$) and the flux density ϕ_0 at its centre is measured by a small flat coil. The cylindrical sample (radius a) is then inserted in the small coil, which is dimensioned to fit tightly round the sample, and the new flux density ϕ is measured. Actually ϕ differs in phase from ϕ_0 and hence the complex ratio $\phi/\phi_0 = M + iN$ must be measured.

It can be shown that

$$M + iN = \frac{2\mu_r J_1(i^{1/2}ka)}{kaJ_0(i^{1/2}ka)} e^{-i\pi/4} \tag{A4.5}$$

where J_1, J_0 are Bessel functions of order 1 and 0 respectively and $ka = (2\pi\mu_r\mu_0\sigma\nu)^{1/2}\, a$. Writing

$$J_1(i^{1/2}ka) = b_1 e^{i\pi\beta_1/2} \tag{A4.6}$$

$$J_0(i^{1/2}ka) = b_0 e^{i\pi\beta_0/2} \tag{A4.7}$$

we get

$$\beta_0 - \beta_1 = -\left(\frac{1}{2} + \frac{2}{\pi}\tan^{-1}(N/M)\right) \tag{A4.8}$$

Jahnke and Emde [220] have tabulated $\beta_0 - \beta_1$ and b_0/b_1 as functions of ka (denoted by them as r). Knowing the measured value of $\beta_0 - \beta_1$ from the right-hand side of Eq. (A4.6), we can read the corresponding ka and b_0/b_1 from the table (by inverse interpolation, in general). Then it follows from the definition of ka and from Eqs (A4.5)–(A4.7) that

$$\sigma = \frac{(ka)^2}{\mu_r\mu_0 2\pi\nu a^2} \tag{A4.9}$$

$$\mu_r = M\frac{ka}{2}\frac{b_0}{b_1}\frac{1}{\cos[\tan^{-1}(N/M)]} \tag{A4.10}$$

It should be noted that this electromagnetic method cannot give the remanent intensity since this, being constant in time, cannot cause any induced electromagnetic force in the coil.

The development of palaeomagnetic research has led to the construction of some highly sophisticated apparatuses for determining the vector of extremely weak remanent intensities in small rock samples. For a discussion of these reference may be made to Collinson *et al.* [221].

APPENDIX 5

Magnetic potential of a linear dipole and the anomalies of thin and thick sheets

A5.1 Potential of a linear dipole

Let σ be the cross-section of a linear dipole extending, say, in the y direction from $y = y_1$ to $y = y_2$. Then dv in Eq. (A1.9) $= \sigma\, dy$. If the point of observation P is chosen as the origin of coordinates and if M_x, M_y, M_z are independent of y, Eq. (A1.9) can be written immediately as

$$\begin{aligned}\phi &= \frac{1}{4\pi} M_x \sigma \frac{\partial}{\partial x} \int_{y_1}^{y_2} \frac{dy}{(x^2+y^2+z^2)^{1/2}} + \frac{1}{4\pi} M_y \sigma \int_{y_1}^{y_2} \partial\left(\frac{1}{r}\right) \\ &\quad + \frac{1}{4\pi} M_z \sigma \frac{\partial}{\partial z} \int_{y_1}^{y_2} \frac{dy}{(x^2+y^2+z^2)^{1/2}} \\ &= \frac{1}{4\pi} M_x \sigma \frac{\partial}{\partial x} \ln \frac{R_2 + y_2}{R_1 - y_1} + \frac{1}{4\pi} M_y \sigma \left(\frac{1}{R_2} - \frac{1}{R_1}\right) \\ &\quad + \frac{1}{4\pi} M_z \sigma \frac{\partial}{\partial z} \ln \frac{R_2 + y_2}{R_1 - y_1} \end{aligned} \tag{A5.1}$$

where $R_2 = (x^2 + y_2^2 + z^2)^{1/2}$ and $R_1 = (x^2 + y_1^2 + z^2)^{1/2}$. ($R_1, R_2$ are the distances of P from the end points of the dipole).

For an infinitely long dipole ($y_2 = \infty, y_1 = -\infty$) the second term vanishes whereas the limit of the logarithmic terms can be shown to be $-2\ln (x^2 + z^2)^{1/2} + C_\infty$, where C_∞ is an infinite constant, after expressing R_1, R_2 as

$$y_1\left(1 + \frac{x^2+z^2}{y_1^2}\right)^{1/2} \quad \text{and} \quad y_2\left(1 + \frac{x^2+z^2}{y_2^2}\right)^{1/2}$$

Hence, for an infinitely long dipole striking in the y direction

$$\phi = -\frac{1}{4\pi} 2M_x \sigma \frac{\partial}{\partial x} \ln \rho - \frac{1}{4\pi} 2M_z \sigma \frac{\partial}{\partial z} \ln \rho + C_\infty \tag{A5.2}$$

where $\rho = (x^2 + z^2)^{1/2}$ is obviously the shortest distance from P to the dipole. $M_x\sigma, M_z\sigma$ are the magnetic moments μ_x, μ_z in the x and z directions per unit length of the dipole.

A5.2 Magnetic anomaly of a thin sheet

Figs 2.7(a) and 2.7(b) show a uniformly magnetized thin dipping sheet of infinite length and depth extent and of width b in plan and section.

It is clear from Section 2.9.3 that the component of M in the cross-section of the sheet is $M' = M(1 - \cos^2 i \cos^2 \delta)^{1/2}$ inclined at an angle $i' = \tan^{-1}(\tan i / \sin \delta)$.

Choosing x and z axes perpendicular and parallel to the sheet as shown, the potential at $P(x, z)$ can be found by integration of the potential $\mathrm{d}\phi$ due to an element of the sheet having the infinitesimal cross-section $b\,\mathrm{d}\zeta$. If ξ, ζ are the coordinates of such an element then by Eq. (A5.2) above,

$$\mathrm{d}\phi = -\frac{1}{4\pi} M_\xi b\,\mathrm{d}\zeta \frac{\partial}{\partial \xi} \ln \rho^2 - \frac{1}{4\pi} M_\zeta b\,\mathrm{d}\zeta \frac{\partial}{\partial \zeta} \ln \rho^2 + C_\infty$$

where

$$\rho^2 = (\xi - x)^2 + (\zeta - z)^2$$

If the origin is chosen at the top edge of the sheet, we can put $\xi = 0$ *after differentiation*, obtaining

$$\mathrm{d}\phi = \frac{1}{4\pi} M_\xi 2b\,\mathrm{d}\zeta \frac{x}{x^2 + (\zeta - z)^2} - \frac{1}{4\pi} M_\zeta b\,\mathrm{d}\zeta \frac{2(\zeta - z)}{x^2 + (\zeta - z)^2}$$

Integration between $\zeta = 0$ and $\zeta = \infty$ gives

$$\phi = \frac{1}{4\pi} 2M'_\perp b \left(\frac{\pi}{2} + \tan^{-1} \frac{z}{x} \right) + \frac{1}{4\pi} M'_\parallel b \ln(x^2 + z^2) + C_\infty \qquad \text{(A5.3)}$$

where C_∞ is an infinite constant and the notation M_ξ, M_ζ is replaced by $M'_\perp$ and $M'_\parallel$ to denote magnetizations (components of M') perpendicular and parallel to the sheet.

The magnetizing force in any direction whose direction cosines are l, n with respect to the x and y directions is

$$\left(-\frac{\partial \phi}{\partial x} \right) l + \left(-\frac{\partial \phi}{\partial z} \right) n \qquad \text{(A5.4)}$$

In particular, $(l, n) \equiv (\sin \theta, \cos \theta)$ for the horizontal direction and $(-\cos \theta, \sin \theta)$ for the vertical direction. It is then a matter of elementary algebra to show that the flux densities in the two directions are

$$\Delta B_\mathrm{h} = \frac{\mu_0}{4\pi} 2b \frac{xM'_\parallel + aM'_\perp}{a^2 + x^2} \qquad \text{(A5.5)}$$

$$\Delta B_\mathrm{z} = \frac{\mu_0}{4\pi} 2b \frac{aM'_\parallel - xM'_\perp}{a^2 + x^2} \qquad \text{(A5.6)}$$

where x is now used to denote the distance of P from the point O (Fig. 2.7(b)) on the same level as P and is positive in the direction from which θ is measured.

A5.3 Magnetic anomaly of a thick sheet: Derivation of Equation (2.48a)

The infinitely long thick sheet in Fig. A5.1 may be considered to be built up of elementary thin sheets of thickness $d\varepsilon$ as shown. If $d(\Delta B_h), d(\Delta B_z)$ are the horizontal and vertical flux densities of an elementary sheet, the flux density in a direction with direction cosines $(l, 0, n)$ is given by

$$d[\Delta B(l, 0, n)] = l\,d(\Delta B_h) + n\,d(\Delta B_z)$$

If ξ is the horizontal coordinate of the elementary sheet we get from equations (A5.5) and (A5.6)

$$d(\Delta B) = \frac{\mu_0}{4\pi} 2d\varepsilon \left(l \frac{(x-\xi)M'_{\parallel} + aM'_{\perp}}{a^2 + (x-\xi)^2} + n \frac{aM'_{\parallel} - (x-\xi)M'_{\perp}}{a^2 + (x-\xi)^2} \right)$$

However $d\varepsilon = d\xi \sin\theta$ and the above equation may be integrated from $\xi = -b/2$ to $\xi = +b/2$. The integrations are elementary. Noting further (cf. Fig. 2.7) that $M'_{\parallel} = M' \cos(\theta - i')$ and $M'_{\perp} = M' \sin(\theta - i')$ the result stated in Eq. (2.48a) is obtained without difficulty.

A5.4 Proof of scheme in Section 2.9.4.1

It is convenient to start from Eq. (2.48a) and put α_1, α_2 as:

$$\alpha_1 = \pi - \tan^{-1} \frac{a}{x + b/2} \quad \text{and} \quad \alpha_2 = \pi - \tan^{-1} \frac{a}{x - b/2}.$$

Since $\tan^{-1} u + \tan^{-1} v = \tan^{-1}[(u+v)/(1-uv)]$ we have

$$\alpha_1 - \alpha_2 = \tan^{-1} \frac{ab}{x^2 + a^2 - b^2/4} \tag{A5.7}$$

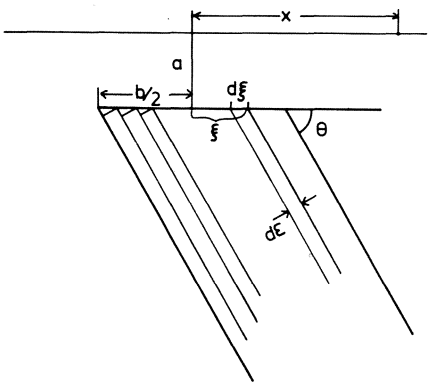

Fig. A5.1 Thick sheet built up of thin sheets.

(a) The condition $\partial \Delta B/\partial x = 0$ for extreme points leads to the quadratic equation

$$kx^2 - 2ax - k\left(\frac{b^2}{4} + a^2\right) = 0$$

If x_1, x_2 are the two roots then, from elementary algebra,

$$x_1 + x_2 = \frac{2a}{k} \qquad \text{(A5.8)} \quad \text{cf. Eq. (2.55)}$$

$$x_1 x_2 = -\left(\frac{b^2}{4} + a^2\right) \qquad \text{(A5.9)} \quad \text{cf. Eq. (2.50)}$$

$$x_1 = (a + \Delta)/k, \qquad x_2 = (a - \Delta)/k \qquad \text{(A5.10)}$$

where

$$\Delta = [a^2 + k^2(b^2/4 + a^2)]^{1/2}$$

It is obvious that $|x_1| > |x_2|$. The proof for $|\Delta B(2)| > |\Delta B(1)|$ is left to the reader (Problem 2.5).

(b) For $x = 0$, Eq. (2.48a) and Eq. (A5.7) above give

$$\Delta B(0) = F \tan^{-1} \frac{ab}{a^2 - b^2/4}$$

$$= F\, 2\tan^{-1} \frac{b}{2a} \qquad \text{(A5.11)}$$

where F denotes the factor outside the square bracket in Eq. (2.48a).

(c) Form now the sum $\Delta B(1) + \Delta B(2)$ where $\Delta B(1) = \Delta B$ at x_1 and $\Delta B(2) = \Delta B$ at x_2. The arctangent term in the sum is

$$F\left(\tan^{-1} \frac{ab}{x_1^2 + a^2 - b^2/4} + \tan^{-1} \frac{ab}{x_2^2 + a^2 - b^2/4}\right) \qquad \text{(A5.12)}$$

After inserting values of x_1, x_2 from (A5.10) and expressing the sum as a single arctangent it can be shown to be

$$F \tan^{-1} \frac{ab}{a^2 - b^2/4} \qquad \text{(A5.13)}$$

that is, $\Delta B(0)$.

The numerator of the argument of the logarithmic term in the sum $\Delta B(1) + \Delta B(2)$ is:

$$\left[\left(x_1 + \frac{b}{2}\right)^2 + a^2\right]\left[\left(x_2 + \frac{b}{2}\right)^2 + a^2\right]$$

$$= \left(x_1^2 + \frac{b^2}{4} + bx_1 + a^2\right)\left(x_2^2 + \frac{b^2}{4} + bx_2 + a^2\right)$$

$$= (x_1^2 - x_1x_2 + bx_1)(x_2^2 - x_1x_2 + bx_2) \qquad \text{using (A5.9)}$$

$$= x_1x_2(x_2 - x_1 - b)(x_1 - x_2 - b) \qquad \text{(A5.14)}$$

The denominator in the argument of the logarithmic term is easily seen to be obtained by replacing x_1 by $-x_1$ and x_2 by $-x_2$. But this replacement obviously does not change (A5.14). Hence the argument of the logarithmic term in $\Delta B(1) + \Delta B(2)$ is unity and the term vanishes. Therefore $\Delta B(1) + \Delta B(2)$ is simply given by (A5.13). This proves the statement that the point $x = 0$ is a point at which the value of ΔB is the algebraic sum of the two extreme values of ΔB. (d) The arctangent term in $\Delta B(1) - \Delta B(2)$ is obtained by replacing the plus sign between the two $\tan^{-1}$ terms in (A5.12) by a minus sign. The result can be expressed as a single arctangent and after using (A5.8) we get

$$F\tan^{-1}\left(\frac{bk(x_2 - x_1)/2}{k^2[(x_2 - x_1)/2]^2 - b^2/4}\right)$$

$$= F\tan^{-1}\left(\frac{2b/k(x_2 - x_1)}{1 - b^2/k^2(x_2 - x_1)^2}\right)$$

$$= F\,2\tan^{-1}\frac{b}{k(x_2 - x_1)}$$

$$= F\,2\tan^{-1}\left(\frac{b}{2a}\frac{x_2 + x_1}{x_2 - x_1}\right)$$

The logarithmic term in $\Delta B(1) - \Delta B(2)$ is

$$-\frac{Fk}{2}\ln\frac{[(x_1 + b/2)^2 + a^2][(x_2 - b/2)^2 + a^2]}{[(x_1 - b/2)^2 + a^2][(x_2 + b/2)^2 + a^2]}$$

Using the same device as number (c) above, this can be shown to be

$$F\frac{2a}{x_2 + x_1}\ln\frac{x_2 - x_1 + b}{x_2 - x_1 - b}$$

Hence

$$\Delta B(1) - \Delta B(2) = 2F\left[\tan^{-1}\left(\frac{b}{2a}\frac{x_2 + x_1}{x_2 - x_1}\right) + \frac{a}{x_2 + x_1}\ln\frac{x_2 - x_1 + b}{x_2 - x_1 - b}\right] \qquad \text{(A5.15)}$$

(e) Equation (A5.9) gives

$$a^2 = -x_1x_2 - \frac{b^2}{4}$$

$$= \tfrac{1}{4}[(x_2 - x_1)^2 - (x_2 + x_1)^2 - b^2] \qquad \text{(A5.16)}$$

Put

$$b' = \frac{b}{x_2 - x_1}, \qquad d' = \frac{x_2 + x_1}{x_2 - x_1}, \qquad a' = \frac{a}{x_2 - x_1}$$

Then Eq. (A5.16) gives

$$a' = \frac{a}{x_2 - x_1} = \tfrac{1}{2}(1 - d'^2 - b'^2)^{1/2}$$

Hence

$$\frac{b}{a} = \frac{b'}{(1 - d'^2 - b'^2)^{1/2}}$$

Since $\Delta B(1) + \Delta B(2) = \Delta B(0)$, Eqs (A5.11) (A5.15) and (A5.8) yield

$$Q = \frac{\Delta B(1) + \Delta B(2)}{\Delta B(1) - \Delta B(2)}$$

$$= \frac{\tan^{-1}[b'/(1 - d'^2 - b'^2)^{1/2}]}{\tan^{-1}[b'd'/(1 - d'^2 - b'^2)^{1/2}] + [(1 - d'^2 - b'^2)^{1/2}/2d'] \ln[(1 + b')/(1 - b)]} \tag{A5.17}$$

Eq. (A5.17) is the transcendental equation, involving only the dimensionless quantities b', d', from which Fig. 2.17 is constructed.

APPENDIX 6

Demagnetization 'factors' for a rectangular parallelepiped

As mentioned in Section 2.10 the concept of a demagnetization factor is only meaningful for a body bounded by a second-degree surface. In an arbitrarily shaped body the internal magnetic field is non-uniform and can only be calculated approximately at best.

If $\kappa/4\pi$ is sufficiently small, H_{ix} in Eq. (A2.2) is evidently almost equal to H_{0x}. Also, if the body is homogeneous and the material isotropic, an external field H_{0x} may be expected to produce negligible internal fields in the y and z directions. Under these assumptions H_{ix} can be calculated for a rectangular parallelepiped (Fig. A6.1) in terms of elementary functions. Putting H_{ix} on the right-hand side of (A2.2) equal to H_{0x}, only the integral

$$\int\int \frac{l \, dS}{r}$$

needs to be evaluated then over the surface of the parallelepiped. The result is

$$H_{ix} = (1 - \kappa N_{xx}) H_{0x} \tag{A6.1}$$

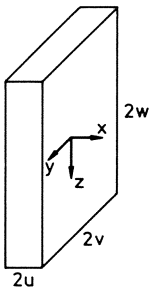

Fig. A6.1 Rectangular parallelepiped.

where, with the origin of the rectangular coordinate system at the centre of the parallelepiped,

$$N_{xx} = \frac{1}{4\pi}[g(x,y,z) + g(-x,y,z) + g(x,-y,z) + g(x,y,-z) + g(-x,-y,z) + g(x,-y,-z) + g(-x,y,-z) + g(-x,-y,-z)] \tag{A6.2a}$$

and

$$g(x,y,z) = \cot^{-1}\left(\frac{[(u-x)^2 + (v-y)^2 + (w-z)^2]^{1/2}(u-x)}{(v-y)(w-z)}\right) \tag{A6.2b}$$

If $\kappa/3 \ll 1$, Eq. (A2.3) may be written as

$$H_{ix} \approx \left(1 - \frac{\kappa}{3}\right) H_{0x}$$

N_{xx} is therefore called, by analogy, the demagnetization factor. It is obviously a function of the position of a point in the body. If the external field is in the y or z directions N_{yy} or N_{zz} can be obtained from Eq. (A6.2a) and Eq. (A6.2b) by cyclic permutations of the symbols x, y, z and u, v, w.

It $u = 0$ (a thin plate) then x is necessarily zero so that

$$g(x,y,z) = \cot^{-1} 0 = \pi/2$$

and

$$N_{xx} = 1 \tag{A6.3}$$

If $v \to \infty$, Eq. (6.2b) gives

$$g(x,y,z) = \cot^{-1}\frac{u-x}{w-z} \tag{A6.4}$$

At the centre of a thick sheet of width $2u$, therefore,

$$N_{xx} = \frac{2}{\pi}\cot^{-1}\frac{u}{w} \tag{A6.5}$$

and, by interchange of symbols,

$$N_{zz} = \frac{2}{\pi}\cot^{-1}\frac{w}{u} \tag{A6.6}$$

N_{yy}, the demagnetization 'factor' in the strike direction is obviously zero since $\cot^{-1}(\infty) = 0$. Similarly if the sheet has infinite depth extent ($w = \infty$), $N_{zz} = 0$ at the centre.

An approximation to the right-hand side of (A6.5) that is sometimes used is

$$\frac{2}{\pi}\cot^{-1}\frac{u}{w} \approx \frac{w}{u+w}$$

The corresponding expression for (A6.6) is, of course, $u/(u+w)$.

For further, and more rigorous, discussion of internal fields in magnetized bodies reference should be made to Joseph *et al.* [222], Joseph [223] and, especially, Eskola [224].

APPENDIX 7

Electric potential

A7.1 Basic equations and conditions

If j_x, j_y, j_z are the current densities at any point then it is easily shown that

$$\frac{dj_x}{dx} + \frac{dj_y}{dy} + \frac{dj_z}{dz} \equiv \text{div}\,\mathbf{j} \tag{A7.1}$$

is the total current emanating out of an infinitesimal unit volume. At a point in a medium where there is no source or sink of current $\text{div}\,\mathbf{j} = 0$, by definition.

From Eq. (4.17) in Chapter 4 it is obvious that, for example, $j_x = -(1/\rho)/(dV/dx)$ with corresponding equations for j_y and j_z. Substituting in Eq. (A7.1) we then get

$$\frac{d}{dx}\left(\frac{1}{\rho}\frac{dV}{dx}\right) + \frac{d}{dy}\left(\frac{1}{\rho}\frac{dV}{dy}\right) + \frac{d}{dz}\left(\frac{1}{\rho}\frac{dV}{dz}\right) = 0 \tag{A7.2}$$

as the equation satisfied by the electric potential V at a point where there is no source or sink of current.

In a homogeneous, isotropic medium ρ is constant and Eq. (A7.2) reduces to Laplace's equation

$$\frac{d^2V}{dx^2} + \frac{d^2V}{dy^2} + \frac{d^2V}{dz^2} = 0 \tag{A7.3}$$

Everywhere on the boundary between two homogeneous media, V satisfies the

following two boundary conditions: (i) V is continuous, (ii) the component of current density normal to the boundary is continuous.

The simple form (A7.3) for Laplace's equation exists only in a rectangular coordinate system. For transformation to other coordinate systems and for the derivation of the boundary conditions, reference may be made to almost any standard book on vector analysis and electricity respectively.

The practical problem in many geophysical situations is to solve (A7.3) under the two boundary conditions and the additional condition that V is finite at any point where there is no source or sink of current.

A7.2 Outcropping vertical contact (Fig. 4.35)

To solve (A7.3) in each of the two media it is assumed that the potential V_1 in the first medium is the sum of a normal potential on a semi-infinite earth $I\rho_1/(2\pi R)$ due to the point current electrode A and a disturbance potential $\beta_1 I\rho_1/(2\pi R')$ due to a fictitious electrode A' that is the image of A in the contact and that emanates a current $\beta_1 I$, R and R' being the distances from A and A'. The potential in medium V_2 is assumed to be $\beta_2 I/2\pi R$ due to an electrode A emanating a current $\beta_2 I$.

We choose A as the origin, the line through it perpendicular to the contact as the x axis (positive towards the right), the vertical direction as the z axis and the line through A perpendicular to the paper as the y axis. Then

$$R = (x^2 + y^2 + z^2)^{1/2}$$
$$R' = [(2a - x)^2 + y^2 + z^2]^{1/2}$$

The contact is defined by $x = a$ so that the boundary conditions are that at $x = a$:

$$V_1 = V_2$$
$$\frac{1}{\rho_1}\frac{dV_1}{dx} = \frac{1}{\rho_2}\frac{dV_2}{dx}$$

Applying these we get

$$\beta_1 = \frac{\rho_2 - \rho_1}{\rho_2 + \rho_1}, \qquad \beta_2 = \frac{2\rho_2}{\rho_2 + \rho_1}$$

In Eq. (4.68) the distance along a line on the surface through A has been denoted by r instead of by x.

APPENDIX 8

Apparent resistivities for dipole–dipole configurations

The electric fields of a current dipole in the radial and azimuthal directions as well as parallel and perpendicular to the dipole are immediately obtained from

the formulae in Appendix A2.3 on replacing ϕ by V, and $m/4\pi$ by $I\rho(AB)/2\pi$, as a comparison of Eqs (4.30) and (A1.11) will show. Thus, for example, for the azimuthal configuration (Fig. 4.15),

$$\frac{\Delta V}{(MN)} \approx E = \frac{I\rho(AB)\sin\theta}{2\pi r^3}$$

from which the apparent resistivity for the configuration is defined as

$$\rho_a = \frac{2\pi r^3}{(AB)(MN)\sin\theta}\frac{\Delta V}{I}$$

The reader should have now no difficulty in verifying the following formulae:

Axial configuration $$\rho_a = \frac{\pi r^3}{(AB)(MN)}\frac{\Delta V}{I}$$

Radial $$\rho_{ar} = \frac{\pi r^3}{(AB)(MN)\cos\theta}\frac{\Delta V}{I}$$

Parallel $$\rho_{ax} = \frac{2\pi r^3}{(AB)(MN)}\frac{1}{3\cos^2\theta - 1}\frac{\Delta V}{I}$$

Perpendicular $$\rho_{ay} = \frac{2\pi r^3}{3(AB)(MN)}\frac{1}{\sin\theta\cos\theta}\frac{\Delta V}{I}$$

Equatorial $$\rho_{eq} = \frac{2\pi r^3}{(AB)(MN)}\frac{\Delta V}{I}$$

All these formulae are valid only provided AB, $MN \ll r$.

APPENDIX 9

Potential of a point current electrode on the surface of a horizontally-layered earth

Let $n-1$ layers rest on an nth 'layer', the infinite substratum (Fig. A9.1). Choosing a cylindrical coordinate system R, θ, z with the electrode C as the origin and z positive downwards, Laplace's equation for the electric potential V in each layer can be written as

$$\frac{\partial^2 V}{\partial R^2} + \frac{1}{R}\frac{\partial V}{\partial R} + \frac{\partial^2 V}{\partial z^2} = 0 \qquad \text{(A9.1)}$$

since, by symmetry, V is independent of θ.

Assuming $V(R,z) = F(R)G(z)$ where F is a function of R only and G of z only, the equation is separated into the two equations

$$\frac{\mathrm{d}^2 G}{\mathrm{d}z^2} - \lambda^2 G = 0 \qquad \text{(A9.2)}$$

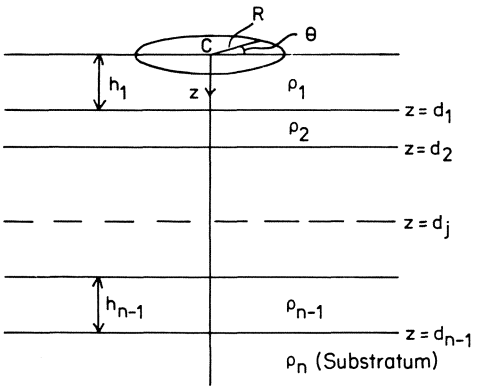

Fig. A9.1 Point electrode on a stratified earth and the cylindrical coordinate system.

$$\frac{d^2F}{dR^2}+\frac{1}{R}\frac{dF}{dR}+\lambda^2F=0 \tag{A9.3}$$

where λ is a constant independent of R and z.

Equation (A9.3) is Bessel's equation of order zero with fundamental solutions $J_0(\lambda R)$, $Y_0(\lambda R)$. $J_0(\lambda R)$ is finite for $R\to\infty$ only if λ is real, and since $Y_0(\lambda R)$ is always ∞ for $R\to\infty$, it must be rejected. The solutions of (A9.2) are $\exp(-\lambda z)$ and $\exp(\lambda z)$.

The most general solution for the potential in any layer j ($j\neq 1$ or n) is then

$$V_j=\int_0^\infty [A_j(\lambda)e^{-\lambda z}+B_j(\lambda)e^{\lambda z}]J_0(\lambda R)\,d\lambda \tag{A9.4}$$

On account of the occurrence of $\exp(\lambda z)$ as well as $\exp(-\lambda z)$, there is no loss of generality in restricting λ to positive real values only.

For $j=n$, the term in $\exp(\lambda z)$ must be excluded since the potential in the substratum must be finite as $z\to\infty$. Thus

$$V_n=\int_0^\infty A_n(\lambda)e^{-\lambda z}J_0(\lambda R)\,d\lambda \tag{A9.5}$$

In the topmost layer ($j=1$), V_1 is the sum of the normal potential (cf. p. 117)

$$V_0=\frac{I\rho}{2\pi}\frac{1}{(R^2+z^2)^{1/2}}$$

and a disturbance potential

$$V_d=\int_0^\infty A_1(\lambda)(e^{-\lambda z}+e^{\lambda z})J_0(\lambda R)\,d\lambda$$

The coefficients of $\exp(-\lambda z)$ and $\exp(\lambda z)$ in V_d are equal since $(1/\rho_1)(\partial V_d/\partial z) = 0$ at $z = 0$ (no current flow across the earth's surface except at C). Using Lipschitz's integral in Bessel function theory for V_0 we have

$$V_1 = \frac{I\rho_1}{2\pi}\int_0^\infty e^{-\lambda z} J_0(\lambda R)\,d\lambda + \int_0^\infty A_1(\lambda)(e^{-\lambda z} + e^{\lambda z})J_0(\lambda R)\,d\lambda \quad \text{(A9.6)}$$

From the continuity of V_j and the current density normal to the layer interfaces we have, for depths $z = d_j$ $(j = 1, 2, \ldots, n-1)$,

$$V_{j-1} = V_j \quad \text{(A9.7a)}$$

$$\frac{1}{\rho_{j-1}}\frac{\partial V_{j-1}}{\partial z} = \frac{1}{\rho_j}\frac{\partial V_j}{\partial_z} \quad \text{(A9.7b)}$$

There are altogether $2n-2$ unknown functions $A(\lambda)$, $B(\lambda)$ to be determined ($2n-4$ in (A9.4) and 1 each in (A9.5) and (A9.6)). They can be determined by solving the system of $2n-2$ linear equations obtained from the conditions (A9.7). The solution is tedious but straightforward. For the details reference may be made to Kofoed's monograph [225]. Identifying $A_1(\lambda)$ as $(I\rho_1/\pi)K(\lambda)$ and R as r along the ground surface, it is easily seen that Eq. (A9.6) is the same as Eq. (4.31).

$K(\lambda)$ is a function of the layer parameters, and recurrence formulae for building it for any number of layers on top of each other, starting from its expression for two layers, can be found by solving the system of Eq. (A9.7). Here the recurrence formulae for the transform $T(\lambda)$ of Eq. (4.37) will be given instead, in terms of the *layer thicknesses* h_j $(j = 1, \ldots, n-1)$, rather than the interface depths d_j.

For a layer (ρ_{n-1}, h_{n-1}) on top of a substratum (ρ_n)

$$T_{n-1}(\lambda) = \rho_{n-1}\frac{1 - k_{n-1}u_{n-1}}{1 + k_{n-1}u_{n-1}} \quad \text{(A9.8)}$$

where

$$u_{n-1} = \exp(-2h_{n-1}\lambda)$$
$$k_{n-1} = (\rho_{n-1} - \rho_n)/(\rho_{n-1} + \rho_n)$$

For the transform T_j for a layer (ρ_j, d_j) on top of the sequence $(\rho_{j+1}, \ldots, \rho_n; h_{j+1}, \ldots, h_n)$ with the transform T_{j+1}, we have

$$T_j(\lambda) = \frac{W_j(\lambda)T_{j+1}(\lambda)}{1 + W_j(\lambda)T_{j+1}(\lambda)/\rho_j^2}; \qquad j = n-2, n-3, \ldots, 2, 1 \quad \text{(A9.9)}$$

where

$$W_j(\lambda) = \rho_j\frac{1 - u_j}{1 + u_j}$$

Starting from $T_{n-1}(\lambda)$ the transform $T_1(\lambda) = T(\lambda)$ of Eq. (4.37) can be obtained by recursive application of the expression for $T_j(\lambda)$.

APPENDIX 10

Homogeneous, anisotropic earth (derivation of Eq. (4.73))

If the resistivities ρ_x, ρ_y, ρ_z are different in the x, y and z directions in a medium but are the same at all points we have an anisotropic, homogeneous, medium. Equation (A7.1) for it is

$$\operatorname{div}\mathbf{j} = \frac{1}{\rho_x}\frac{\partial^2 V}{\partial x^2} + \frac{1}{\rho_y}\frac{\partial^2 V}{\partial y^2} + \frac{1}{\rho_z}\frac{\partial^2 V}{\partial z^2} \tag{A10.1}$$

If an element of volume $dx\,dy\,dz$ of the medium encloses a point source of current I then, by definition

$$(\operatorname{div}\mathbf{j})\,dx\,dy\,dz = I \tag{A10.2}$$

For a homogeneous, isotropic medium ($\rho_x = \rho_y = \rho_z = \rho$), Eqs (A10.1) and (A10.2) give

$$\left(\frac{\partial^2 V}{\partial x^2} + \frac{\partial^2 V}{\partial y^2} + \frac{\partial^2 V}{\partial z^2}\right) dx\,dy\,dz = I\rho \tag{A10.3}$$

On making the substitutions

$$\xi = x\sqrt{\rho_x}, \qquad \eta = y\sqrt{\rho_y}, \qquad \zeta = z\sqrt{\rho_z} \tag{A10.4}$$

Eq. (10.2) becomes

$$\left(\frac{\partial^2 V}{\partial \xi^2} + \frac{\partial^2 V}{\partial \eta^2} + \frac{\partial^2 V}{\partial \zeta^2}\right) d\xi\,d\eta\,d\zeta = I\sqrt{(\rho_x\rho_y\rho_z)} \tag{A10.5}$$

Equation (A10.5) shows that at a point where there is no source or sink of current ($I = 0$), the potential in an anisotropic, homogeneous medium also satisfies Laplace's equation, but in the coordinates ξ, η, ζ. The solution of (A7.3) in x, y, z for a semi-infinite, isotropic earth is given by Eq. (4.72) in Chapter 4. For an anisotropic medium x, y, z must be replaced by ξ, η, ζ and, as comparison of (A10.3) with (A10.5) shows, $I\rho$ by $I\sqrt{(\rho_x\rho_y\rho_z)}$. The potential in an anisotropic medium is then immediately shown to be given by Eq. (4.73).

APPENDIX 11

Single-turn loop and other topics in electromagnetic methods

A11.1 Single-turn loop in homogeneous alternating field (Fig. 6.3)

If the field perpendicular to the loop (area A) is $B = B_0 \exp(-i\omega t)$ the electromotive force induced in accordance with Neumann's law (Section 6.2.1) is $-\mathrm{d}(BA)/\mathrm{d}t = i\omega BA$. As a result of the current I that flows if the loop is closed an additional magnetic flux proportional to I, according to the Biot–Savart

law, is associated with the circuit. This can be expressed as LI, the constant of proportionality L being the self-inductance of the loop. The e.m.f. induced by LI is $-L(\mathrm{d}I/\mathrm{d}t)$. The total e.m.f. in the circuit, namely $\mathrm{i}\omega BA - L(\mathrm{d}I/\mathrm{d}t)$ must be equal, according to Ohm's law, to RI where R is the resistance in the loop. We have, therefore, after trivial rearrangement

$$L\frac{\mathrm{d}I}{\mathrm{d}t} + RI = \mathrm{i}\omega BA \tag{A11.1}$$

To obtain a solution, put $I = I_0 \exp(-\mathrm{i}\omega t)$ where I_0 may be complex, since we cannot assume *a priori* that I and B have the same phase. Then (A11.1) yields

$$I = \frac{\mathrm{i}\omega AB_0 \mathrm{e}^{-\mathrm{i}\omega t}}{R - \mathrm{i}\omega L} \tag{A11.2}$$

Equation (A11.2) can be rewritten using the identity $\mathrm{i} = \exp(\mathrm{i}\pi/2)$ as

$$I = \frac{\omega AB_0(R + \mathrm{i}\omega L)\mathrm{e}^{-\mathrm{i}(\omega t - \pi/2)}}{R^2 + \omega^2 L^2} \tag{A11.3}$$

Putting $R = \alpha \cos\phi, \omega L = \alpha \sin\omega$, i.e. $\alpha = (R^2 + \omega^2 L^2)^{1/2}$ and $\phi = \tan^{-1}(\omega L/R)$, we get

$$I = \frac{\omega AB_0}{(R^2 + \omega^2 L^2)^{1/2}} \mathrm{e}^{-\mathrm{i}(\omega t - \pi/2 - \phi)} \tag{A11.4}$$

The secondary field of the loop-current can be written as KI where K is a geometrical factor depending on the position of the observation in relation to the loop. The amplitude and phase of the secondary field are therefore

$$S = \frac{K\omega AB_0}{(R^2 + \omega^2 L^2)^{1/2}} \qquad \text{and} \qquad -\left(\frac{\pi}{2} + \phi\right)$$

The secondary field lags behind the primary field $B_0 \exp(-\mathrm{i}\omega t)$ by an angle $(\pi/2 + \phi)$. Its real and imaginary components are most easily obtained by reference to Fig. 6.4 as

$$\begin{aligned} Re &= -\frac{K\omega AB_0}{(R^2 + \omega^2 L^2)^{1/2}} \sin\phi \\ &= -\frac{KAB_0\omega^2 L}{R^2 + \omega^2 L^2} \end{aligned} \tag{A11.5}$$

$$\begin{aligned} Im &= -\frac{K\omega AB_0}{(R^2 + \omega^2 L^2)^{1/2}} \cos\phi \\ &= -\frac{KAB_0\omega R}{R^2 + \omega^2 L^2} \end{aligned} \tag{A11.6}$$

(The plot in Fig. 6.5 is for the *magnitudes* of *Re* and *Im* as given by (A11.5) and (A11.6).)

A11.2 Maxwell's equations in source-free region

These equations are given here for reference only. No direct use has been made of them in the text.

A region in which there are no external sources of electric current (e.g. batteries) or of magnetic fields (e.g. magnets) is source-free in the present context. Since a knowledge of advanced vector analysis on the part of the reader has not been considered to be a prerequisite for understanding the present text, Maxwell's equations are given below in long notation:

$$(1) \quad \frac{\partial E_z}{\partial y} - \frac{\partial E_y}{\partial z} = -\frac{\partial B_x}{\partial t}$$

(with two other similar equations obtained by cyclic permutation of the symbols x, y, z.)

$$(2) \quad \frac{\partial H_z}{\partial y} - \frac{\partial H_y}{\partial z} = \sigma E_x + \frac{\partial D_x}{\partial t}$$

(with two other similar equations obtained by cyclic permutation of the symbols x, y, z.)

$$(3) \quad \frac{\partial D_x}{\partial x} + \frac{\partial D_y}{\partial y} + \frac{\partial D_z}{\partial z} = 0$$

$$(4) \quad \frac{\partial B_x}{\partial x} + \frac{\partial B_y}{\partial y} + \frac{\partial B_z}{\partial z} = 0$$

$$(5) \quad \mathbf{D} = \varepsilon \mathbf{E}$$

$$(6) \quad \mathbf{B} = \mu \mathbf{H}$$

Eqs (1) express Neumann's law (Section 6.2.1). Eqs (2), when devoid of the terms in D, can be shown ultimately to depend on the Biot–Savart law (Section 6.4.1) although they are associated with the name of Ampere. Maxwell added the second term representing the so-called displacement current density to account for electromagnetic phenomena in dielectrics. Eq. (3) is valid when there are no free charges (sources of **D** field) while Eq. (4) is a statement of the empirical observation that no sources or sinks of magnetic flux exist. Eqs (5) and (6) are called constitutive relations that relate the D and B fields to their causes, namely the electric (E) and magnetic (H) field strengths.

A11.3 Calculation of a and b in Eq. (6.15)

Let

$$\omega^2 \varepsilon \mu = \alpha \cos \psi \qquad \text{(A11.7)}$$

$$\frac{\omega\mu}{\rho} = \alpha \sin\psi \tag{A11.8}$$

Then

$$k^2 = \alpha e^{i\psi}$$

so that

$$\begin{aligned} k &= \alpha^{1/2} e^{i\psi/2} \\ &= \alpha^{1/2} \cos\left(\frac{\psi}{2}\right) + i\alpha^{1/2} \sin\left(\frac{\psi}{2}\right) \end{aligned}$$

Hence

$$a = \alpha^{1/2} \cos\left(\frac{\psi}{2}\right), \qquad b = \alpha^{1/2} \sin\left(\frac{\psi}{2}\right) \tag{A11.9}$$

From (A11.7) and (A.11.8)

$$\alpha = \frac{\omega\mu}{\rho}(\rho^2\varepsilon^2\mu^2 + 1)^{1/2} \tag{A11.10}$$

Now

$$2\cos^2\left(\frac{\psi}{2}\right) = 1 + \cos\psi \tag{A11.11}$$

$$2\sin^2\left(\frac{\psi}{2}\right) = 1 - \cos\psi \tag{A11.12}$$

Substituting for $\cos\psi$ from (A11.7) in (A11.11) and (A11.12.) gives $\cos(\psi/2)$ and $\sin(\psi/2)$, after which Eqs (A11.9) and (A11.10) yield

$$a = \left(\frac{\omega\mu}{2\rho}\right)^{1/2} [(\rho^2\varepsilon^2\omega^2 + 1)^{1/2} + \rho\varepsilon\omega]^{1/2}$$

$$b = \left(\frac{\omega\mu}{2\rho}\right)^{1/2} [(\rho^2\varepsilon^2\omega^2 + 1)^{1/2} - \rho\varepsilon\omega]^{1/2}$$

A11.4 Tilt of the VLF H field

Let $H\cos\omega t$ be the horizontal primary VLF field along the y axis and let $S\cos(\omega t + \psi)$ be the secondary field making an angle γ with the horizontal. We shall assume the two fields to be in the same vertical plane. The fields Y, Z in the horizontal and vertical directions are then

$$Y = H\cos\omega t + S\cos\gamma\cos(\omega t + \psi)$$

$$Z = S\sin\gamma\cos(\omega t + \psi)$$

Eliminating ωt it can be shown [216] that the tilt of the ellipse of polarization is

given by

$$\tan 2\theta = \frac{2(S/H)\sin\gamma(\cos\psi + (S/H)\cos\gamma)}{1 + 2(S/H)\cos\gamma\cos\psi + (S/H)^2\cos^2\gamma - (S/H)^2\sin^2\gamma} \quad \text{(A11.13)}$$

If $S \ll H$ and $(S/H)\cos\gamma \ll \cos\psi$ we may write (A11.13) as

$$\tan 2\theta \approx 2\theta \approx 2\left(\frac{S}{H}\right)\sin\gamma\cos\psi$$

But $S\sin\gamma = \Delta V$, the vertical component of the secondary field, and $\Delta V\cos\psi$ is its real component (cf. Fig. 6.2).
Hence

$$\theta \approx \frac{\Delta V}{H}\cos\psi$$

which verifies the result quoted on page 213.

APPENDIX 12

Acoustic impedance

To illustrate the essential idea we shall only consider a compressional wave motion in a liquid. Suppose the motion to be in the direction Ox. Each particle of the medium vibrates parallel to Ox about a mean position. Let A and B be two planes, each of area α, with equilibrium positions x and $x + \mathrm{d}x$. If the displacement at A at any instant is u, that at B is $u + (\mathrm{d}u/\mathrm{d}x)\,\mathrm{d}x$ and the linear strain (change in length per unit length) is therefore $\mathrm{d}u/\mathrm{d}x$. This is the total dilatational strain as there is no displacement at right angles to Ox. By Hooke's law the stress at A is $P = K(\mathrm{d}u/\mathrm{d}x)$ where K is the compressional modulus, that at B is $P + (\mathrm{d}P/\mathrm{d}x)\,\mathrm{d}x$. The corresponding forces on the planes are α times the stresses. Since the liquid between A and B is not transported as a whole the forces on A and B must be oppositely directed, but this leaves an unbalanced force

$$K\alpha\frac{\mathrm{d}P}{\mathrm{d}x}\mathrm{d}x = K\alpha\frac{\mathrm{d}^2u}{\mathrm{d}x^2}\mathrm{d}x$$

which causes an acceleration $\mathrm{d}^2u/\mathrm{d}t^2$ of the mass $\rho\alpha\,\mathrm{d}x$ of the liquid between A and B, if ρ is the density. Since force = mass × acceleration we get

$$\frac{\mathrm{d}^2u}{\mathrm{d}t^2} = \frac{K}{\rho}\frac{d^2u}{\mathrm{d}x^2}$$

This is the equation of a wave motion with velocity $V = (K/\rho)^{1/2}$ and its general

solution for propagation in the positive Ox direction is

$$u = \phi(x - Vt)$$

It is easy to verify that this satisfies the wave equation above.

The velocity of the particles at x is

$$\frac{du}{dt} = -V\phi'$$

while, as we have seen

$$\text{stress at } x = K\frac{du}{dx}$$

$$= K\phi'$$

The magnitude of the ratio stress/particle velocity is evidently $K/V = KV/V^2 = \rho V$. This is independent of x or t and is a characteristic of the medium and the elastic wave in question only. It is termed 'acoustic impedance', the units being pascal-second per metre (Pa s m^{-1}) or, which is the same thing, newton second per cubic metre (N s m^{-3}).

APPENDIX 13

Fourier transforms and convolution

A13.1 Fourier transforms

Any arbitrary function $f(t)$ (satisfying certain conditions) can be synthesized from a number of sine and cosine waves of different frequencies each with a characteristic amplitude and phase. If $f(t)$ is periodic with the period T the frequencies are discrete multiples of the fundamental frequency $1/T$. If $f(t)$ is non-periodic the frequencies are infinitesimally close to each other and range from 0 to ∞. For mathematical convenience, however, they are usually taken to range continuously from $-\infty$ to $+\infty$. The function $F(v)$ giving the amplitude of the wave of frequency v is known as the amplitude spectrum. It can be obtained, as will appear below, from $f(t)$ while, conversely, if $F(v)$ is given $f(t)$ can be synthesized by essentially the same process.

We shall start with a periodic function $f(t)$ and express it by means of a Fourier series:

$$f(t) = \sum_{m=0}^{\infty} (a_m e^{i(2\pi m/T)t} + b_m e^{-i(2\pi m/T)t})$$

It is easily shown by multiplying both sides by $\exp(i(2\pi n/T)t)$ and $\exp(-i(2\pi n/T)t)$ and integrating from $-T/2$ to $+T/2$ that

$$a_m = (1/T)\int_{-T/2}^{T/2} f(t')e^{-i(2\pi m/T)t'}\,dt'$$

$$b_m = (1/T)\int_{-T/2}^{T/2} f(t')e^{i(2\pi m/T)t'}\,dt'$$

Hence

$$f(t) = (1/T)\sum_{m=0}^{\infty}\int_{-T/2}^{T/2} f(t')(e^{i(2\pi m/T)(t-t')} + e^{-i(2\pi m/T)(t-t')})\,dt'$$

Since the bracketed expression on the right-hand side is an even function of m it is obvious that we may also write

$$f(t) = (1/2T)\sum_{m=-\infty}^{\infty}\int_{-T/2}^{T/2} f(t')(e^{i(2\pi m/T)(t-t')} + e^{-i(2\pi m/T)(t-t')}\,dt'$$

Moreover, since $\exp(x) - \exp(-x)$ is an odd function of x we obviously have

$$0 = (1/2T)\sum_{m=-\infty}^{\infty}\int_{-T/2}^{T/2} f(t')(e^{i(2\pi m/T)(t-t')} - e^{-i(2\pi m/T)(t-t')}\,dt'$$

Adding these two equations we get

$$f(t) = (1/T)\sum_{m=-\infty}^{\infty} e^{i(2\pi m/T)t}\int_{-T/2}^{T/2} f(t')e^{-i(2\pi m/T)t'}\,dt'$$

If $f(t)$ is non-periodic its period may be said to be infinite. Put $m/T = dv$ and let $T \to \infty$. Then, from the definition of the Riemann integral, the sum may be replaced by an integral. Hence

$$f(t) = \int_{-\infty}^{\infty} dv\left[e^{i2\pi vt}\left(\int_{-\infty}^{\infty} f(t')e^{-i2\pi vt'}\,dt'\right)\right]$$

Let

$$F(v) = \int_{-\infty}^{\infty} f(t)e^{-i2\pi vt}\,dt \qquad \text{(A13.1)}$$

Then it follows that

$$f(t) = \int_{-\infty}^{\infty} F(v)e^{i2\pi vt}\,dv \qquad \text{(A13.2)}$$

$F(v)$ is known as the Fourier transform of $f(t)$ while $f(t)$ is called the inverse Fourier transform of $F(v)$. If the one is given the other can be obtained from (A13.1) or (A13.2) respectively.

A square-wave pulse of duration τ and strength 1 is defined by the equations

$$\begin{aligned} f(t) &= 1 && |t| < \tau/2 \\ &= 1/2 && |t| = \tau/2 \\ &= 0 && |t| > \tau/2 \end{aligned}$$

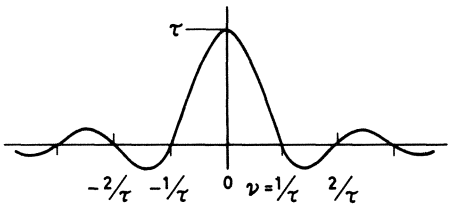

Fig. A13.1 Fourier spectrum of a square-wave pulse.

It is easy to show by means of (A13.1) that the corresponding amplitude spectrum (Fig. A13.1) is given by

$$F(\nu) = \tau \frac{\sin(\pi\nu\tau)}{(\pi\nu\tau)}$$

A13.2 Convolution

Let $f(t)$ represent the response of a linear system to a unit impulse, t seconds after the impulse has been applied. A continuous signal, whose strength at a time λ is $g(\lambda)$, may be considered to consist of an infinite number of successive very closely spaced impulses, each of strength $g(\lambda)\,\mathrm{d}\lambda$. At a time t the system's response to the impulse $g(\lambda)\,\mathrm{d}\lambda$ is evidently $g(\lambda)f(t-\lambda)\,\mathrm{d}\lambda$ since $t-\lambda$ is the time elapsed after the impulse $g(\lambda)\,\mathrm{d}\lambda$. The total response of the system at time t is then

$$r(t) = \int_{-\infty}^{\infty} g(\lambda)f(t-\lambda)\,\mathrm{d}\lambda \tag{A13.3}$$

$$= \int_{-\infty}^{\infty} g(t-\lambda)f(\lambda)\,\mathrm{d}\lambda \tag{A13.4}$$

The integral in (A13.3) or (A13.4) is known as the convolution integral. The limits $-\infty$ and $+\infty$ are chosen merely for the sake of convenience in analysis. Physically if $g(\lambda) \equiv 0$ for $\lambda < t_0$, say and $f(t-\lambda) \equiv 0$ for $t-\lambda < t_1$, that is $\lambda > t - t_1$, the effective limits of integration will be simply t_0 and $t - t_1$.

Taking the Fourier transform of both sides of (A13.4),

$$\begin{aligned} R(\nu) &= \int_{-\infty}^{\infty}\int_{-\infty}^{\infty} g(t-\lambda f(\lambda)\mathrm{e}^{-\mathrm{i}2\pi\nu t}\,\mathrm{d}t\,\mathrm{d}\lambda \\ &= \int_{-\infty}^{\infty}\left(\int_{-\infty}^{\infty} g(t-\lambda)\mathrm{e}^{-\mathrm{i}2\pi\nu(t-\lambda)}\,\mathrm{d}t\right) f(\lambda)\mathrm{e}^{-\mathrm{i}2\pi\nu\lambda}\,\mathrm{d}\lambda \\ &= \int_{-\infty}^{\infty} [G(\nu)]f(\lambda)\mathrm{e}^{-\mathrm{i}2\pi\nu\lambda}\,\mathrm{d}\lambda \\ &= G(\nu)\int_{-\infty}^{\infty} f(\lambda)\mathrm{e}^{-2\mathrm{i}\pi\nu\lambda}\,\mathrm{d}\lambda \\ &= G(\nu)F(\nu) \end{aligned} \tag{A13.5}$$

Equation (A13.5) shows that the Fourier transform of the convolution of two functions is equal to the product of the Fourier transforms of the functions. The same result follows if we start from (A13.3).

A13.2.1 Analytic downward continuation (p. 91)

The formal solution of (3.38) (p. 91) is easily obtained by using the above convolution theorem. Since

$$\frac{1}{r^3} = \frac{1}{[(x-x_0)^2 + (y-y_0)^2 + z^2]^{3/2}}$$

the right-hand side of (3.38) may be regarded as a convolution (in two dimensions) of $1/r^3$ and $(z/2\pi)g(x_0, y_0, z)$. Instead of one frequency as in (A13.1) we then have two spatial frequencies ν, μ (that is, wavenumbers = reciprocals of wavelengths) in the x and y directions. Taking the two-dimensional Fourier transform of both sides in (3.38) we get, by the convolution theorem,

$$G(\nu, \mu) = G_0(\nu, \mu) e^{-\sqrt{(\nu^2+\mu^2)}z} \qquad \text{(A13.6)}$$

since it can be shown that the Fourier transform of $1/r^3$ is

$$\frac{2\pi}{z} e^{-\sqrt{(\nu^2+\mu^2)}z} e^{-i2\pi(\nu x_0 + \mu y_0)}.$$

Therefore

$$G_0(\nu, \mu) = e^{\sqrt{(\nu^2+\mu^2)}z} G(\nu, \mu)$$

Now, $g(x, y, 0)$ being the given function, $G(\nu, \mu)$ can be obtained by the numerical evaluation of two double integrals, namely,

$$\int_{-\infty}^{\infty}\int_{-\infty}^{\infty} g(x, y, 0) \begin{matrix}\cos\\ \sin\end{matrix} (\nu x + \mu y)\, dx\, dy$$

for various values of ν and μ. Then $g(x_0, y_0, z)$ is obtained as the inverse Fourier transform of $G_0(\nu, \mu)$. Towards this end we must numerically evaluate the two double integrals

$$\int_{-\infty}^{\infty}\int_{-\infty}^{\infty} e^{\sqrt{(\nu^2+\mu^2)}z} G(\nu, \mu) \begin{matrix}\cos\\ \sin\end{matrix} (\nu x_0 + \mu y_0)\, d\nu\, d\mu$$

for various values of x_0, y_0.

It should be noticed here that the amplitudes of all frequencies in $g(x, y, 0)$ are magnified in downward continuation on account of the exponential factor. The high frequencies (rapid variations) are magnified more quickly (that is, at smaller depths of continuation).

References

1 Stacey, F.D. and Banerjee, S.K. (1974) *The Physical Principles of Rock Magnetism*, Elsevier, Amsterdam.
2 Green, R. (1960) *Geophys. Prosp.*, **8**, 98–110.
3 Geyger, W.A. (1962) *AIME Trans.*, **81**, 65–73.
4 Gordon, D.I. *et al.* (1968) *IEEE Trans. Mag.*, **Mag.-4**, 397–401.
5 Primdahl, F. (1970) *IEEE Trans. Mag.*, **Mag.-6**, 376–83.
6 Gordon. D.I. *et al.* (1972) *IEEE Trans. Mag.*, **Mag.-8**, 76–82.
7 Waters, G.S. *et al.* (1965) *Geophys. Prosp.*, **4**, 1–9.
8 Guptasarma, D. *et al.* (1966) *Geophys. Prosp.*, **14**, 292–300.
9 Giret, R. *et al.* (1965) *Geophys. Prosp.*, **13**, 225–39.
10 Roy, A. (1970) *Geoexploration*, **8**, 37–40.
11 Lehmann, H. (1971) *Geophys. Prosp.* **19**, 133–55.
12 Werner, S. (1955) *Sveriges Geologiska Undersökning*, Årsbok **43** (1949), No. 6.
13 Gay, S.P. (1967) in *Society of Exploration Geophysicists' Mining Geophysics*, Vol. 2. (ed. D.A. Hansen *et al.*), Society of Exploration Geophysicists, Tulsa.
14 Hjelt, S.E. (1972) *Geoexploration*, **10**, 239–54.
15 Kunaratnam, K. (1981) *Geophys. Prosp.*, **29**, 883–90.
16 Yüngül, S. (1956) *Geophysics*, **21**, 433–54.
17 Zachos, K. (1944) *Beitr. angew. Geophys.*, **11**, 1.
18 Kellogg, O.D. (1953) *Foundations of Potential Theory*, Dover, New York.
19 Jeffreys, H. (1976) *The Earth*, Cambridge University Press, Cambridge.
20 Geodetic reference system 1967, *Publ. Spec. du Bulletin Géodésique*, Bureau Central de L'Association Internationale de Géodesie, Paris.
21 Cook, A.H. (1973) *Physics of the Earth and Planets*, Macmillan, London.
22 Lacoste, L.J.B. (1934) *Physics*, **5**, 178–80.
23 Melton, B.S. (1971) *Geophys. J.*, **22**, 521.

24 Siikarla, T. (1966) *Geoexploration*, **4**, 139–49.
25 Ketelaar, A.C.R. (1976) *Geoexploration*, **14**, 57–65.
26 *Tidal Gravity Corrections for 1978*, European Association of Exploration Geophysicists, The Hague.
27 Nettleton, L.L. (1939) *Geophysics*, **4**, 176–83.
28 Jung, K. (1953) *Zeit. f. Geoph.*, **19**, *Sonderband*, 54–8.
29 Parasnis, D.S. (1952) *Month. Not. Roy. Astr. Soc., Geophys. Suppl.*, **6**, 252.
30 Legge, J.A. (1944) *Geophysics*, **9**, 175–9.
31 Jung, K. (1959) *Gerland Beitr. Geoph.*, **68**, 268–79.
32 Syberg, F.J.R. (1972) *Geophys. Prosp.*, **20**, 47–75.
33 Singh, S.K. (1977) *Geophys. J. Roy. Astr. Soc.*, **50**, 243–6.
34 Coggon, J.H. (1976) *Geoexploration*, **14**, 93–105.
35 Lindblad, A. *et al.* (1938) *Ingenjörs Vet. Akad. Handl. No. 146*, 52.
36 Levine, S. (1941) *Geophysics*, **6**, 180–96.
37 Morgan, N.A. *et al.* (1972) *Geophys. Prosp.*, **20**, 363–74.
38 Jung, K. (1953) *Geophys. Prosp.*, **1**, 29–35.
39 Bott, M.H.P. *et al.* (1958) *Geophys. Prosp.*, **6**, 1–10.
40 Smith, R.A. (1959) *Geophys. Prosp.*, **7**, 55–63.
41 Smith, R.A. (1960) *Geophys. Prosp.*, **8**, 607–13.
42 Skeels, D.C. (1947) *Geophysics*, **12**, 43–56.
43 Roy, A. (1966) *Geoexploration*, **4**, 65–83.
44 Saxov, S. *et al.* (1953) *Geophysics*, **18**, 913–28.
45 Cook A.H. *et al.* (1951) *Quart. J. Geol. Soc. Lond.*, **107**, 287–306.
46 Davis, W.E. *et al.* (1957) *Geophysics*, **22**, 848–69.
47 Dehlinger, P. *et al.* (1972) *Marine Geology*, **12**, 1–41.
48 Gay, S.P. (1967) *Geophys. Prosp.*, **15**, 236–45.
49 Nayak, *et al.* (1981) *Geoexploration*, **18**, 311–320.
50 Schiavone, D. *et al.* (1984) *Geoexploration*, **22**, 47–58.
51 Ogilvy, A.A. *et al.* (1969) *Geophys. Prosp.*, **17**, 36–62.
52 Semenov, A.S. (1980) *Elektrorazvedka metodom Estectvennogo Elektricheskogo Polya*, Nedra, Leningrad.
53 Sato, M. and Mooney, H.M. (1960) *Geophysics*, **25**, 226–49.
54 Kilty, K.T. (1984) *Geophys. Prosp.*, **32**, 51–62.
55 Logn, O. *et al.* (1974) *Geoexploration*, **12**, 11–28.
56 Fitterman, D.V. (1979) *J. Geophys Res.*, **84**, 6031–6040.
57 Ginzburg, A. *et al.* (1977) *Geoexploration*, **15**, 47–56.
58 Shuey, R.T. (1975). *Semi-conducting ore minerals*, Elsevier, Amsterdam.
59 Korvin, G. (1982) *Geoexploration*, **19**, 267–76.
60 Slichter, L.B. (1933) *Physics*, **4**, 307–22.
61 Langer, R.E. (1933) *Amer. Math. Soc. Bull.*, **29**, 814–20.
62 *Standard graphs for resistivity prospecting* (1969), European Association of Exploration Geophysicists, The Hague.
63 Mooney, H.M. and Wetzel, W.W. (1956) *The Potentials about a Point*

Electrode, University of Minnesota Press, Minneapolis.
64 Hummel, J.N. (1929) *Zeit. f. Geoph.*, **5**, 228.
65 Zohdy, A.A.R. (1965) *Geophysics*, **30**, 644–60.
66 Ghosh, D.P. (1971) *Geophys. Prosp.*, **19**, 769–75.
67 Johansen, H.K. (1975) *Geophys. Prosp.*, **23**, 449–58.
68 Guptasarma, D. (1982) *Geophys. Prosp.*, **30**, 501–514.
69 Johansen, H.K. (1977) *Geophys. Prosp.*, **25**, 667–691.
70 Inman, J.R. *et al.* (1973) *Geophysics*, **38**, 1088–1108.
71 Kofoed, O. (1979) *Geosounding Principles*, Elsevier, Amsterdam.
72 Pekeris, C.L. (1940) *Geophysics*, **5**, 31–42.
73 Patella, D. (1975) *Geophys. Prosp.*, **23**, 335–62.
74 Flathe, H. (1955) *Geophys. Prosp.*, **3**, 95–110.
75 Orellana, E. (1966) *Revista de Geofisica*, **25**, 1–40.
76 Maeda, K. (1955) *Geophysics*, **20**, 123–47.
77 De Gery, J.C. *et al.* (1956) *Geophysics*, **31**, 780–93.
78 Lee, T. (1972) *Geophys, Prosp.*, **20**, 847–59.
79 Muskat, M. and Evinger, H.H. (1941) *Geophysics*, **6**, 397–427.
80 Logn, O. (1954) *Geophysics*, **19**, 739–60.
81 Cook, K.L. *et al.* (1954) *Geophysics*, **19**, 761–90.
82 Alfano, L. (1959) *Geophys. Prosp.*, **7**, 311–66.
83 Dieter, K. *et al.* (1969) *Geophysics*, **34**, 615–32.
84 Pridmore, D. *et al* (1981) *Geophysics*, **46**, 1009–24.
85 Maillet, R. (1947) *Geophysics*, **12**, 529–56.
86 Hartshorn, L. (1925) *J. Inst. elect. Engrs.*, **64**, 1152.
87 Bertin, J. and Loeb, J. (1976) *Experimental and Theoretical Aspects of Induced Polarization*, Vols 1 and 2, Gebrüder Borntraeger, Berlin.
88 Sumner, J.S. (1976) *Principle of induced polarization for geophysical exploration*, Elsevier, Amsterdam.
89 Wait, J. (ed.) (1959) *Overvoltage Research and Geophysical Applications*, Pergamon, New York, p. 158.
90 Nilsson, B. (1971) *Geoexploration*, **9**, 35–54.
91 Hohmann, G.W. (1973) *Geophysics*, **38**, 854–63.
92 Rathor, B.S. (1977) *Geoexploration*, **15**, 137–49.
93 Wynn, J.C. *et al.* (1977) *Geophys. Prosp.*, **25**, 29–51.
94 Roy, K.K. *et al.* (1980) *Geoexploration*, **18**, 145–62.
95 Hallof, P. (1967) *IP newsletter cases xxvii and xxviii*, McPhar Geophysics Ltd. Canada.
96 Parasnis, D.S. (1966) *Geoexploration*, **4**, 177–208.
97 Sundberg, K. (1931) *Gerlands Beitr. Geoph., Ergänzungs-Hefte*, **1**, 298–361.
98 Hedström, H. (1937) *Amer. Inst. Min. Met. Eng., Tech. Publ. 827.*
99 Duval, T. *et al.* (1967) *Geoexploration*, **5**, 31–51.
100 Bezvoda, V. *et al.* (1970) *Geophys. Prosp.*, **3**, 343–51.
101 Dizioglu, M.Y. (1967) *Geoxploration*, **5**, 157–64.

102 *Geophysical Surveys in Mining, Hydrological and Engineering Projects* (1958), European Association of Exploration Geophysicists, The Hague.
103 Parasnis, D.S. (1971) *Geophys. Prosp.*, **19**, 163–79.
104 Nair, M.R. *et al.* (1968) *Geoexploration*, **6**, 207–44.
105 Norton, K.A. (1937) *Proc. I.R.E.*, **25**, 1203–36.
106 Paterson, N. *et al.* (1971) *Geoexploration*, **9**, 7–26.
107 Philips, W.J. *et al.* (1975) *Geoexploration*, **13**, 215–26.
108 Eberle, D. (1981) *Geoexploration*, **19**, 103–114.
109 Debye, P. (1909) *Ann. d. Phys.*, **30**, 59.
110 March, H.W. (1953) *Geophysics*, **16**, 671–84.
111 Wait, J.R. (1960) *Geophysics*, **25**, 649–58.
112 Wait, J.R. (1952) *Geophysics*, **17**, 378–86.
113 Wesley, J.P. (1958) *Geophysics*, **23**, 134–43.
114 Graf, A. (1934) *Gerlands Beitr. Geoph.*, **4**, 1.
115 Slichter, L.B. (1951) *Geophysics*, **16**, 431–49.
116 Slichter, L.B. *et al.* (1959) *Geophysics*, **24**, 77–88.
117 Negi, J.G. (1967) *Geophysics*, **32**, 69–87.
118 Lajoie, J.J. *et al.* (1976) *Geophysics*, **41**, 1133–56.
119 Olsson, O. (1978) *Radio Science*, **13**, No. 2.
120 Ward, S.H. (1971) *Geophysics*, **36**, 1–183.
121 Ward, S.H. (1976) *Geophysics*, **41**, 1103–258.
122 Weidelt, P. (1975) *J. Geophys. Res.*, **41**, 85–109.
123 Wait, J. (1982) *Geoelectromagnetism*, Academic Press, London.
124 Harrison, C.H. (1970) *Geophysics*, **35**, 1099–1115.
125 Poddar, M. (1982) *Geophys. Prosp.*, **30**, 86–100.
126 Nabighian, M.N. (1971) *Geophysics*, **36**, 25–37.
127 Morley, L.W. (ed.) (1970) *Mining and Groundwater Geophysics* (1967) Department of Energy, Mines and Resources, Ottawa.
128 Spies, B.R. (1976) *J. Austr. Geol. Geophys.*, **1**, 23–32.
129 Verma, S.K. (1975) *Geophys. Prosp.*, **23**, 292–9.
130 Fokin, A.F. (1971) *Method perekhodnikh protsessov pri poickakh mestorozdeniy sulfidnikh rud*, Nedra, Leningrad.
131 Hjelt, S.E. (1971) *Geoexploration*, **9**, 213–30.
132 Hurley, D.G. (1977) *Geoexploration*, **15**, 77–85.
133 Lee, T. *et al.* (1974) *Geophys. Prosp.*, **22**, 430–44.
134 Singh, R.N. (1972) *Geophysics*, **38**, 864–93.
135 Lee, T. (1975) *Geophys. Prosp.*, **23**, 492–512.
136 Nabighian, M.N. (1979) *Geophysics*, **44**, 1700–5.
137 Nabighian, M.N. (ed.) (1984) *Geophysics*, **49**, 849–1029.
138 Kaufman, A. and Keller, G. (1983) *Frequency and Transient Sounding*, Elsevier, Amsterdam.
139 Ward, S.H. (1961) *Geophys. Prosp.*, **9**, 191–202.
140 Mallick, K. (1972) *Geoexploration*, **11**, 183–6.

141 Kofoed, O. *et al.* (1972) *Geophys. Prosp.*, **20**, 406–20.
142 Tuman, V.S. (1951) *Geophysics*, **16**, 102–14.
143 Niblett, E.R. *et al.* (1960) *Geophysics*, **25**, 998–1008.
144 Yüngül, S. (1977) *Geoexploration*, **15**, 207–38.
145 Cagniard, L. (1953) *Geophysics*, **18**, 605–35.
146 Vozoff, K. (1970) *Mining and Groundwater Geophysics (1967)* (ed. L.W. Morley), Department of Energy, Mines, and Resources, Ottawa.
147 Keller, G. (1971) *Geoexploration*, **9**, 99–148.
148 Porstendorfer, G. (1974) *Principles of Magnetotelluric Prospecting*, Gebrüder Borntraeger, Berlin.
149 Kaufman, A. and Keller, G. (1981) *The Magnetotelluric Sounding Method*, Elsevier, Amsterdam.
150 Hedström, H. *et al.* (1959) *Geophys. Prosp.*, **7**, 448–70.
151 Paterson, N.R. (1961) *Geophysics*, **26**, 601–47.
152 Törnquist, G. (1958) *Geophys. Prosp.*, **6**, 112–26.
153 Hedström, H. *et al.* (1958) *Geophys. Prosp.*, **6**, 322–41.
154 Makowiecki, L.Z. *et al.* (1970) *Inst. Geol. Sci., Geophys. Paper No. 3*, London.
155 Ward, S.H. (1959) *Geophysics*, **24**, 671–89.
156 Gupta Sarma, D. *et al.* (1976) *Geophysics*, **41**, 287–99.
157 Verma, S.K. (1972) *Geophys. Prosp.*, **20**, 752–70.
158 Becker, A. (1967) *Geoexploration*, **5**, 81–8.
159 Ricker, N. (1953) *Geophysics*, **18**, 10–40.
160 Ricker, N.H. (1977) *Transient waves in visco-elastic media*, Elsevier, Amsterdam.
161 Faust, L.Y. (1951) *Geophysics*, **16**, 192–206.
162 Hughes, D.S. *et al.* (1951) *Geophysics*, **16**, 577–93.
163 Baule, H. (1953) *Geophys. Prosp.*, **1**, 111–24.
164 Shumway, G. (1956) *Geophysics*, **21**, 305–19.
165 Datta, S. (1968) *Geoexploration*, **6**, 127–39.
166 Sheriff, R.E. and Geldart, L.P. (1982) *Exploration Seismology* (Vols. 1 and 2), Cambridge University Press, Cambridge.
167 Dennison, A.T. (1953) *Geophys. Prosp.*, **1**, 3–28.
168 Sheriff, R.E. (1973) *Encyclopaedic Dictionary of Exploration Geophysics*, SEG, Tulsa.
169 Mayne, H. (1962) *Geophysics*, **27**, 927–39.
170 Evenden, B.S. and Pieuchot, M. (1984) *Seismic Prospecting Instruments*, Vol. 2, Gebrüder Borntraeger, Berlin.
171 Al-Sadi, H.N. (1980) *Seismic Exploration (Technique and Processing)*, Birkhäuser, Basel.
172 Coffeen, J.A. (1978) *Seismic Exploration Fundamentals*, Penn Well, Tulsa.
173 Kulhanek, O. (1976) *Introduction to Digital Filtering in Geophysics*, Elsevier, Amsterdam.

174 Vogel, C.B. (1952) *Geophysics*, **17**, 586–97.
175 Summers, G.C. *et al.* (1952) *Geophysics*, **17**, 598–614.
176 Jenyon, M.K. and Fitch, A.A. (1985) *Seismic Reflection Interpretation*, Gebrüder Borntraeger, Berlin.
177 McQuillin, R.M. *et al.* (1979) *An introduction to seismic interpretation*, Graham & Trotman, London.
178 Arnetzl, H. (1980) *Prakla-Seismos report*, **2 + 3**, 8–15.
179 *Wave-Theoretical Depth Migration* (1979), Western Geophysical Inc., Houston.
180 Krey, T. (1969) *Geophys. Prosp.*, **17**, 206–18.
181 Edelman, H. (1966) *Geophys. Prosp.*, **14**, 455–69.
182 Mota, L. (1954) *Geophysics*, **19**, 242–54.
183 Johnson, S.H. (1976) *Geophysics*, **41**, 418–24.
184 Meidav, T. (1960) *Geophysics*, **25**, 1035–53.
185 Habberjam, G. (1966) *Geoexploration*, **4**, 219–25.
186 *Geophysical surveys in Mining, Hydrological and Engineering Projects* (1958) European Association of Exploration Geophysicists, The Hague.
187 Sjögren, B. (1984) *Shallow Refraction Seismics*, Chapman and Hall, London.
188 Green, R. (1974) *Geoexploration*, **12**, 259–84.
189 Moxham, R.M. (1960) *Geophysics*, **25**, 408–32.
190 Zeschke, G. (1963) *Econ. Geol.*, **58**, 995–6.
191 Budde, E. (1958) *Geophys. Prosp.*, **6**, 25–34.
192 Homilius, J. *et al.* (1957) *Geophys. Prosp.*, **5**, 449–68.
193 Homilius, J. *et al.* (1958) *Geophys. Prosp.*, **6**, 342–64.
194 Schwarzer, T.F. *et al.* (1973) *Econ. Geol.*, **68**, 1297–312.
195 Gondouin, M. *et al.* (1957) *Trans. Soc. Petr. Eng.*, **210**, 58.
196 *Log Interpretation Fundamentals.* (1975), Dresser Atlas, Houston.
197 Dewan, J.T. (1983) *Essentials of Modern Open-hole Log Interpretation*, Penn Well, Tulsa.
198 Jackson, P.D. (1981) *Geophys. Prosp.*, **29**, 601–26.
199 Pirson, S.J. (1963) *Handbook of Well log Analysis*, Prentice-Hall, Englewood Cliffs.
200 Lynch, E.J. (1962) *Formation Evaluation*, Harper and Row, New York.
201 Fearon, R.E. (1949) *Nucleonics*, **4**, 30.
202 Fearon, R.E. (1949) *Nucleonics*, **4**, 67.
203 Tolstoy, I. (1973) *Wave Propagation*, McGraw Hill, New York.
204 Parasnis, D.S. (1967) *Geophys. Prosp.*, **15**, 407–37.
205 Ketola, M. (1972) *Geoexploration*, **10**, 1–21.
206 Jämtlid, A. (1984) *Geoexploration*, **3/4**, 203–16.
207 Eloranta, E. (1984) *Geoexploration*, **22**, 77–88.
208 Parasnis, D.S. and Soonawala, N.M. (eds) (1984) *Geoexploration*, **3/4** (Special Issue).

209 Kayal, J.R. (1979) *Geoexploration*, **17**, 243–58.
210 Hähnel, R. and Kappelmeyer, O. (1974) *Geothermics with special reference to application*, Gebrüder Borntraeger, Berlin.
211 Pooley, J. Ph. *et al.* (1970) *Geophys. Prosp.*, **18**, 666–700.
212 Ginzburg, I.I. (1960) *Principles of Geochemical Prospecting*, Pergamon Press, New York.
213 Hawkes, H.E. and Webb, J.S. (1962) *Geochemistry in mineral exploration*, Harper, New York.
214 Kendall, M.G. and Moran, P.A.P. (1963) *Geometrical Probability*, Charles Griffin and Co., London.
215 Agocs, W.B. (1955) *Geophysics*, **20**, 871–85.
216 Parasnis, D.S. (1975) *Mining Geophysics*, 2nd ed., Elsevier, Amsterdam.
217 Werner, S. (1945) *Sveriges Geologiska Undersökning* (*Stockholm*), **39** (5), 1–79.
218 Mooney, H. (1952) *Geophysics*, **17**, 531–43.
219 Malmqvist, D. (1957) *Freiberger Forschungshefte*, **C 32**, 20–39.
220 Jahnke, E. and Emde, F. (1945) *Tables of Functions with Formulae and Curves*, Dover, New York.
221 Collinson, D.W. (1983) *Methods in Rock Magnetism and Palaeomagnetism*, Chapman and Hall, London.
222 Joseph, R.I. *et al.* (1965) *J. Appl. Phys.*, **36**, 1579–93.
223 Joseph, R.I. (1976) *Geophysics*, **41**, 1052–4.
224 Eskola, L. and Tervo, T. (1980) *Geoexploration*, **18**, 79–95.
225 Kofoed, O. (1968) *The Application of the Kernel Function in Interpreting Geoelectrical Resistivity Measurements*, Gebrüder Borntraeger, Berlin.

Answers and hints

2.1 61°; 288 m below ground surface.

2.2 (a) Centre may be taken in this case to be at 210E; $a = 32$ m, $b = 148$ m, $k \approx 0$, $\theta \approx 70°$, $M' = 28\ \text{A m}^{-1}$. (The example is actually calculated for $a = 30$ m, $b = 150$ m, $k = 0$, $\theta = 65°$, $M' = 33.7\ \text{A m}^{-1}$.)

(b) 50°.

2.3 149 m.
($I' = I = 90°$, $\theta = 90°$, $T_{0z} = 35.81\ \text{A m}^{-1}$, induced intensity of magnetization $0.4\ \text{m}^{-1}$, $M' = 1.0\ \text{A m}^{-1}$.)

3.1 $2\pi G\rho h\left(1 - \dfrac{4\alpha}{3(1+4\alpha^2)^{1/2}}\right)$ where $\alpha = h/d$.

3.2 $2\pi G\delta\left(\sqrt{(a\lambda)} - (\lambda/2)\ln\dfrac{2\sqrt{(\lambda a)} + \lambda}{\lambda}\right)$

Hint: The anomaly of a thin disc of thickness dz on an axis point is found from Eq. (3.24a) by letting $z_2 \to z_1$ to be $2\pi G\delta[1 - z/(z^2 + a^2)^{1/2}]\,dz$. Integrate this.

3.3 Minimum 27.5 m, maximum 100.6 m.
(Throw of fault h from $\Delta g = 20.5$ m; magnetic equation for fault shows that $\Delta B_z(\text{max})$ is obtained in the present case at $x = 0$.)

3.5 Zero and 2.62 g.u. respectively.

3.8 8.9 km.

4.1 (a) $j_x = 22.8\ \mu\text{A m}^{-2}$, $j_z = 0$.

(b) $j_x = 3.63$, $j_z = \pm 62.75$, $j(\text{total}) = 62.86\ \mu\text{A m}^{-2}$. The value of resistivity is irrelevant if the current is given.

4.2 19.9 m.

4.3 Hint: Observe that if α is written as

$$V_{AM(\alpha)} - V_{BM(\alpha)} - V_{AN(\alpha)} + V_{BN(\alpha)}$$

then β can be written, due to reciprocity, as

$$V_{AN(\alpha)} - V_{BM(\beta)} - V_{AN(\beta)} + V_{BM(\alpha)}$$

and γ as

$$V_{AM(\alpha)} - V_{BM(\beta)} - V_{AN(\beta)} + V_{BN(\alpha)}.$$

4.4 True ρ_3 is about 5500 Ωm. (Principle of equivalence.)

4.5 At the most a three-layer solution will be obtained with the unmodified auxiliary point method. A forward calculation from the model will show systematic differences with the data.

4.6 $T_m = 180\,\Omega$m, $T_1(22.6) = 168.87\,\Omega$m. (The model is not a 'best-fitting' one.)

4.7 68.7 Ωm.

4.8 $$\lambda = \frac{(\rho_1 h_1 + \rho_2 h_2)^{1/2}(\rho_2 h_1 + \rho_1 h_2)^{1/2}}{\rho_m H}$$

where $\rho_m = (\rho_1 \rho_2)^{1/2}$ and $H = h_1 + h_2$.
$\lambda > 1$ follows from the fact that (Numerator)^2 − (Denominator)$^2 > 0$, always.

4.9 (a) Profile on which $\rho_a = 4890\,\Omega$m.
(b) $\lambda = 1.72$, $\rho_l = 2848\,\Omega$m, $\rho_t = 8397\,\Omega$m.
(c) Same as before since ρ_{al} is independent of dip.

4.10 About 75 m. (Use Fig. 4.32.)

4.11 $$\rho_a = \pi \frac{1}{S-T}\frac{\Delta V}{J}$$

where

$$2S = \sinh^{-1}\frac{b-y}{x-l} - \sinh^{-1}\frac{b-y}{2L-(x-l)} +$$

$$\sinh^{-1}\frac{b+y}{x-l} - \sinh^{-1}\frac{b+y}{2L-(x-l)}$$

$2T$ = the same function as $2S$ but with $x-l$ replaced by $x+l$
$2l$ = Distance MN
J = Current per unit electrode length.

4.13 (a) $$\frac{I\rho_1}{2\pi}\left(\frac{1}{l} + \frac{\beta}{2a-l} + \frac{\beta}{2a-5l} - \frac{\beta}{2a-2l} - \frac{\beta}{2a-4l}\right)$$

(b) $\frac{I\rho_1}{2\pi}\left(\frac{1}{l}+\frac{\beta}{2a-l}-\frac{\beta}{2a-2l}+\frac{\beta}{2l}\right)$

(c) $\frac{I}{2\pi}\left(\frac{\rho_1+\rho_2}{2l}-\frac{\beta(\rho_1-\rho_2)}{2l}+\frac{\beta\rho_1}{2a-l}-\frac{\beta\rho_2}{5l-2a}\right)$

where $\beta=(\rho_2-\rho_1)/(\rho_2+\rho_1)$.

5.1 11 Hz.

5.2 E.g. $P_{60}^{120}=0.044$, $P_{900}^{120}=0.014$; $M_{60,100}^{120}=12.15$ s.

6.2 (a) -4.7%.
(b) $-100(\theta^2/2)\%$ (θ in radians).
(c) $-150\ (h/r_0)^2\%$.
(d) No spurious anomaly. Restriction $h \ll r_0$ irrelevant.

6.3 A straight line of definite length through the point (100, 0).

6.5 (a) 5.
(b) 150 Hz.
(c) 10 mm, 3 $\mu\Omega$ m.

6.6 186 m.

6.7 (a) 12 m and 0.063 Ω.
(b) Real -10.0%, Imaginary -13.2%.
(c) $0.57 \times (500/f)$ mm.

7.1 All the three events are bent lines. The sea-bottom reflection is a horizontal line at TWT = 1 s up to the point corresponding to the place of abrupt change in sea-bottom slope and thereafter another straight line inclined at about 6°. The first sea-bottom multiple and the reflection from R are coincident horizontal lines at TWT = 2 s up to the above mentioned point and thereafter straight lines inclined at about 14° and 3° respectively. Diffraction hyperbolas will have vertices at the point where the lines bend.

(Rays must be drawn from C and D, taking account of Snell's law, in such a way that they strike R normally.)

7.2 6, 16, −3, −8, 14, −6, −2, −7, −21, 10, 20, −2, −28, −17, 14, 10, 4.

7.4 (a) $1, R, R^2, R^3, \ldots, R^n, \ldots$
(b) $1, 1, 1, 1, \ldots, 1, \ldots$

7.5 Consider the medium as being built up of a large number of very thin layers in which the velocity is $V_1, V_2, \ldots$ etc. By Snell's law $\cos\alpha_0/V_0 = \cos\alpha_1/V_1 = \cdots = 1/V_s$. The last equality follows because $\alpha = 0°$ at the depth z_s where the ray starts to bend upwards, the velocity there being V_s. But $V_s = V_0 + kz_s$. Hence

$$z_s = V_0(1-\cos\alpha_0)/k\cos\alpha_0.$$

Index